MOLECULAR CONTAINERS BASED ON ARYL-EXTENDED CALIX[4]PYRROLES

Luis Escobar González

UNIVERSITAT ROVIRA I VIRGILI
MOLECULAR CONTAINERS BASED ON ARYL-EXTENDED CALIX[4]PYRROLES
Luis Escobar González

UNIVERSITAT ROVIRA I VIRGILI
MOLECULAR CONTAINERS BASED ON ARYL-EXTENDED CALIX[4]PYRROLES
Luis Escobar González

DOCTORAL THESIS

Luis Escobar González

MOLECULAR RECOGNITION IN ORGANIC SOLVENTS AND WATER USING RECEPTORS BASED ON CALIX[4]PYRROLE SCAFFOLDS

Supervised by Prof. Pablo Ballester Balaguer

UNIVERSITAT
ROVIRA i VIRGILI

Tarragona

2019

UNIVERSITAT ROVIRA I VIRGILI
MOLECULAR CONTAINERS BASED ON ARYL-EXTENDED CALIX[4]PYRROLES
Luis Escobar González

ICIQ
Institut Català d'Investigació Química

Av. Països Catalans, 16
43007 Tarragona, Spain
Tel. (+34) 977 920 200
email: iciq@iciq.es

UNIVERSITAT ROVIRA i VIRGILI
Dept. de Química Analítica i Química Orgànica

Carrer de Marcel·lí Domingo, 1
43007 Tarragona, Spain
Tel. (+34) 977 55 97 69
email: sdn4@urv.cat

I STATE that the present study, entitled "Molecular recognition in organic solvents and water using receptors based on calix[4]pyrrole scaffolds", presented by Luis Escobar González for the award of the degree of Doctor, has been carried out under my supervision at the Institute of Chemical Research of Catalonia (ICIQ).

Tarragona, October 2019

Doctoral Thesis Supervisor

Prof. Pablo Ballester Balaguer

UNIVERSITAT ROVIRA I VIRGILI
MOLECULAR CONTAINERS BASED ON ARYL-EXTENDED CALIX[4]PYRROLES
Luis Escobar González

Acknowledgements

Throughout my PhD Thesis I have received a great deal of support and assistance from many people. First, I would like to thank my supervisor, **Prof. Pablo Ballester**, for giving me the opportunity to join his group at ICIQ and for the continuous support during my research. His patience, motivation and immense knowledge have been essential for my personal and scientific development. I would also like to thank him for the confidence he has placed in me and express my most sincere gratitude for his support in all my decisions.

Besides my supervisor, I would like to acknowledge three postdoctoral researchers, **Alejandro Díaz-Moscoso**, **Frank Arroyave** and **Gemma Aragay**, for helping and teaching me in the laboratory. In addition, I would like to express my gratitude to **Alejandro Díaz-Moscoso**, **Frank Arroyave** and **Rajesh Pudi** for giving me advise and for sharing many moments together in Tarragona.

I would like to thank my former and present lab colleagues, **Jordi Aguilera**, **Nelson Giménez**, **Daniel Hernández-Alonso**, **José Ramón Romero**, **Albano Galán**, **Lluís Martínez**, **Giulia Moncelsi**, **Ricardo Molina**, **Guillem Peñuelas**, **Qingqing Sun, Andrés Felipe**, **Dragoş Dăbuleanu**, **Pedro Ferreira** and **Chiara Mirabella** for their feedback, cooperation, friendship and the fun we have had in the last four years.

I would also like to thank the people that have shared with me a short period of time. Thanks to **Louis Adriaenssens**, **Ryo Sekiya**, **Sasă Korom**, **Martina Piccinno**, **Diana Vargas**, **Kaisa Helttunen**, **Isabell Gruebner**, **Giacomo Berton**, **Ferdinando Malagreca**, **Benedikt Rahe**, **Liam Martin**, **Aina Fitó**, **Angelina Köhler**, **Jia Liang Sun**, **Inmaculada Sempere** and **Cristina Vega**.

I am very grateful to **Sven van Vliet**, **David Villarón** and **Jorn de Jong** for their involvement in the research projects contained in this Thesis. I would also like to thank the opportunity to teach them in the laboratory.

I especially thank **Beatriz Martin** her support, kindness and work throughout the years in our research group. We are all pleased to have you amongst us.

I would also like to thank **Prof. Julius Rebek**, **Yang Yu**, **Prof. Eduardo Peris** and **Carmen Mejuto** for the fruitful collaborations.

Thanks to the ICIQ Research Support Units that have been involved in my research throughout the years. Specifically, I would like to thank **Gabriel González**, **Kerman Gómez** and **Israel Macho** for their help in the NMR experiments. I also thank **Simona Curreli**, **Marta Serrano** and **Noemí Cabello** for their work in the analysis of complex samples and the determination of the mass of our

molecular containers. Thanks to **Eduardo C. Escudero-Adán** for his dedication and grateful discussions about X-ray crystallography.

I would also like to express my sincere thanks to **Prof. Jonathan L. Sessler** for giving me the opportunity to perform a short research stay in his group at Austin. I would like to thank **Gonzalo Anguera**, **Gabriela Vargas**, **Grégory Thiabaud**, **Takehiro Hirao**, **Gretchen Peters**, **Qing He**, **Aaron Lammer**, **Axel Steinbrück**, **Sajal Sen**, **Inhong Hwang**, **Harrison D. Root** and **Ashley Chavana** for the good times. In addition, I would like to express my gratitude to **Gonzalo Anguera** for helping me in Austin since my arrival and for sharing much time together.

Thanks to the **Universitat Rovira i Virgili** and, especially, to **Ricard Boqué**, **Oscar Pamies** and **Francisco Andrade** for giving me the opportunity to teach chemistry to undergraduate students in the laboratory.

Finally, I would like to thank my parents, **Luis Escobar** and **María Victoria González**, and my sister, **Victoria María Escobar**, for supporting me throughout my life and giving me the necessary strength to achieve all the proposed goals.

The work contained in this Thesis has been made possible thanks to the financial support of Ministerio de Educación y Formación Profesional (FPU14/01016), Ministerio de Ciencia, Innovación y Universidades (MCIU), Fondo Europeo de Desarrollo Regional (FEDER), Generalitat de Catalunya and the ICIQ Foundation.

A mis padres y mi hermana,

UNIVERSITAT ROVIRA I VIRGILI
MOLECULAR CONTAINERS BASED ON ARYL-EXTENDED CALIX[4]PYRROLES
Luis Escobar González

Table of Contents

UNIVERSITAT ROVIRA I VIRGILI
MOLECULAR CONTAINERS BASED ON ARYL-EXTENDED CALIX[4]PYRROLES
Luis Escobar González

Chapter 1

Introduction: Molecular Recognition in Water Using Synthetic Receptors

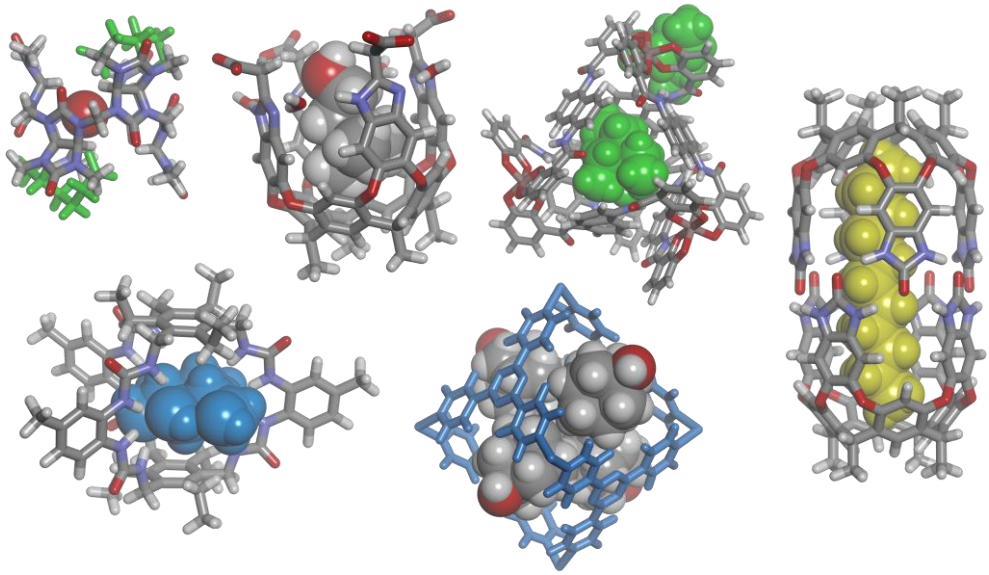

UNIVERSITAT ROVIRA I VIRGILI
MOLECULAR CONTAINERS BASED ON ARYL-EXTENDED CALIX[4]PYRROLES
Luis Escobar González

1.1 Introduction

Molecular recognition in water is a research area that appeared in the 1980's embedded within the field of supramolecular chemistry. The investigated model systems and the results derived from them are key for the understanding and mimicking at proteins' binding affinity, selectivity and catalytic performances that occur in nature.[1,2] In this regard, protein binding pockets are surrounded by aliphatic and/or aromatic groups of amino acid residues that build hydrophobic environments, clefts or cavities, containing polar, ionizable or charged moieties. These hydrophilic groups are commonly buried in the protein's interior, minimizing their solvation with water molecules, for their functional application.[3] In addition, the use of synthetic receptors in molecular recognition overcomes limitations encountered in biological systems, for example, the study of binding processes by spectroscopic techniques and over a wide temperature range.[4]

Binding processes in water are also involved in other appreciated areas of research, such as self-assembly, drug discovery and supramolecular catalysis. Furthermore, applications in nanotechnology and biomedicine are realizing the relevance of non-covalent interactions between discrete molecules.[1] The development of all these research themes entails a deep understanding of the molecular recognition events that occur in aqueous media. Nevertheless, the rules that govern molecular recognition in organic solvents are not practical in water due to its physical and chemical properties.

A water molecule displays a bent geometry of *ca.* 104° and features a dipole moment of 1.85 D (Figure 1a). Water molecules are good hydrogen bond donors (α = 1.17) and acceptors (β = 0.47). In solution, each water molecule adopts mainly a tetrahedral arrangement stablishing between three and four hydrogen bonds with adjacent water molecules (Figure 1b). These water-water interactions create a cohesive hydrogen-bonding network. The dielectric constant of liquid water is ε = 78.5 at 298 K. Water is amphoteric, displaying both Brønsted acid and base properties: weak acid forming hydroxy anions (OH^-) and weak base leading to hydronium cations (H_3O^+).[5,6,7,8,9]

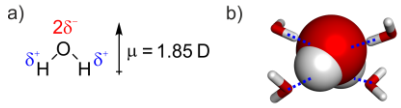

Figure 1. a) Dipole moment and b) tetrahedral hydrogen-bonding arrangement of a water molecule (PM3, water COSMO model). Hydrogen bonds are highlighted with dashed lines (blue).

The physical and chemical properties of water offer both opportunities and challenges for molecular recognition. The main driving forces that operate in water are the hydrophobic effect, dispersion and electrostatic interactions. The hydrophobic effect contributes mainly to the binding affinity, whereas the dispersion and electrostatic interactions play an important role in the selectivity.[10] Additionally, the Hofmeister effect deals with the influence of ions to non-polar

molecules in water.[11] The thermodynamic nature of these forces is discussed in Sections 1.1.1-1.1.3. However, it is worth mentioning here that the enthalpy-entropy compensation effect is observed in most of the complexation processes. This results in a small or no change of binding affinity (K_a).[12]

Another effect is noted in the binding heat capacity, *i.e*. the ability of a system to absorb thermal energy. The sign and magnitude of the heat capacity reflect a dependence of the solvent and the structural and electronic properties of the host and the guest. Heat capacity values are negative in water and larger than in organic solvents. However, the effect of the temperature in binding processes has not been studied with all known synthetic receptors.[13]

The solvation of ions and neutral molecules depends on the properties and forces involved in liquid water. Ions are strongly solvated by water molecules. Cations are solvated through cation-dipole interactions with the electron density of the lone pairs of the oxygen atom of water, whereas anions interact with the partially positively charged hydrogen atoms of water molecules. As a result, the net charge of ions is significantly attenuated by the aqueous medium.[6] Water also interact with polar molecules, which participate in the hydrogen-bonding network. In contrast, non-polar molecules are poorly solvated and tend to associate.[8,9]

Synthetic molecular receptors must meet common requirements to function in water. The receptors must be soluble in water at concentrations that allow spectroscopic and/or calorimetric studies. This limits the number of building blocks used for their syntheses. In general, ionizable or charged groups are incorporated at the periphery of the receptor's scaffold to ensure water solubility and prevent aggregation.[14] The architecture of the receptor must be relatively rigid to prevent the hydrophobic collapse of the binding pocket, which causes lack of binding function. The binding site of the receptor must be complementary to the size, shape and function of the substrate to ensure optimal interactions, high affinity and selectivity. This requires special considerations when polar groups are placed within the binding pocket in order to compensate the high dielectric constant and strong hydrogen-bonding ability of water.[15] The main features of synthetic and natural receptors are summarized in Table 1.[16]

Interestingly, molecules may exhibit unusual chemical and physical properties in confined spaces. The reactivity of bound guests has been exploited using well-defined, hydrophobic synthetic receptors in water. Therefore, synthetic receptors might mimic enzymatic cavities and function as molecular vessels.[17,18]

The prediction of host-guest complexes with quantum or molecular dynamic calculations is still not fully reliable, despite the massive complexation data available in literature and the huge development of computational methods.[5,19]

Table 1. Main features of discrete, synthetic receptors and natural proteins.

	Synthetic receptors	Proteins
Building blocks	Aromatic scaffolds	Amino acids
Synthetic challenges	Water solubility, pre-organization	Geometry (angles/vertices)
Typical length dimensions	1-10 nm	1-100 nm
Cavity environment	Hydrophobic with/without polar functions	

In this chapter, we cover the past decades of recognition of polar and non-polar organic molecules and ions using exclusively synthetic and discrete receptors in water solution. We discuss the role of the hydrophobic effect, the intermolecular forces and the Hofmeister effect involved in reversible binding processes. We review the design development of effective receptors based on cyclic, oligo-cyclic and concave-shaped architectures. This chapter also comprises self-assembled and mechanically-interlocked receptors. Selected examples of hosts that mediate/catalyze chemical transformations are highlighted. Non-cyclic (clips and tweezers), planar (porphyrins) and boronic acid-based receptors are not discussed and the reader is addressed to other literature reviews.[4,15,20,21] Cyclodextrins has been extensively studied in literature and are not included herein. However, they are mentioned for comparison of binding affinity with other receptors discussed in the chapter.

1.1.1 Hydrophobic effect

The hydrophobic effect is involved in natural processes, such as protein folding and membrane self-assembly, and in many chemical phenomena.[22,23] This effect was firstly described as the aggregation of non-polar molecules to minimize the surface area exposed to aqueous solution. The cohesive nature of water is responsible for the hydrophobic effect. Van der Waals interactions between solutes contribute to a lesser extent.[3,14] The hydrophobic effect provides a strong driving force for binding, even though is not specific nor directional.[6] Studies on simple, synthetic models are necessary for the understanding of the hydrophobic effect operating in complex, synthetic or natural systems in water.[5]

The hydrophobic effect is driven by either entropy or enthalpy. An increase of entropy is distinctive of the “classical” hydrophobic effect and is related to the desolvation of non-polar surfaces. On the contrary, the “non-classical” hydrophobic effect results of an increase in the number of hydrogen bonds in the bulk aqueous solution and is enthalpically driven.[4] Independently of the thermodynamic nature of the hydrophobic effect, a binding process in water usually displays a positive entropy and a negative heat capacity (see below), and experiences the enthalpy-entropy compensation effect.[5,24] These thermodynamic earmarks indicate that both non-covalent host-

guest interactions and solvation states of free and bound components need to be considered to predict binding equilibria.[11,25,26]

The transfer of a solute into water requires of the unfavorable creation of an empty cavity and the reorganization of solvent molecules to establish favorable or unfavorable interactions with the solute. It is worth mentioning here that the cavity formation model does not predict changes of heat capacity.[7] The surface/volume of the cavity required to accommodate the solute tends to be minimum, but this effect is modulated by the solute's properties.[3,26,27] In general, a spherical solute of less than 1 nm diameter is solvated by water molecules without breaking their hydrogen bonds, but restricts their mobility in the solvation shell. On the contrary, solvation of a solute featuring a diameter larger than 1 nm provokes the loss of one or more hydrogen bonds per water molecule of the solvation shell.[11] Theoretical calculations suggest that small non-polar molecules prefer to be solvent-separated, whereas large counterparts tend to associate, *i.e.* they aggregate.[5] Furthermore, the effect of a solute on the local structure of water is known as hydrophobic hydration.[22] This effect displays enthalpy-entropy compensation, probably due to solvent-reorganization interactions.[4,28]

The thermodynamic parameters are normally correlated with the surface area of the solute.[3,24] The entropy cost of ordering water molecules around small solutes is *ca.* 25 cal·mol^{-1}·Å^{-2}. This value increases to *ca.* 75 cal·mol^{-1}·Å^{-2} for large solutes owing to the enthalpic cost of breaking hydrogen bonds.[5] Therefore, the energy required to transfer a solute from an organic solvent to water is 20-80 cal·mol^{-1}·Å^{-2}.[3,22,28] As a rule of thumb, the hydrophobic effect accounts for less than 0.3 kcal·mol^{-1} per methylene group of aliphatic substituents.[4]

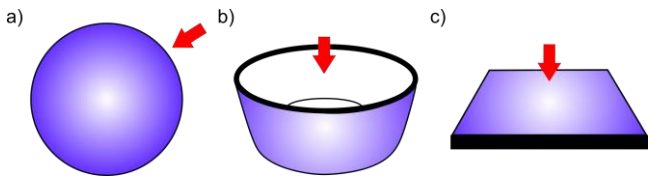

Figure 2. Surfaces of solutes desolvated upon complexation (indicated with arrows): a) Convex; b) concave and c) flat shapes.

The desolvation energy of the surface of a solute depends on its properties. For example, the thermodynamic signature of the desolvation process is related to the shape of the solute. On the one hand, convex surfaces are desolvated by a favorable entropy at room temperature. On the other hand, desolvation of concave surfaces may produce a decrease of enthalpy (favorable).[8] Note that concave surfaces are more hydrophobic than flat counterparts (Figure 2).[7] Desolvation is required for host-guest complexation, among other processes, such as solvent reorganization.[24]

In a hydrophobic cavity, water molecules cannot form four hydrogen bonds between each other and lead to a negative enthalpy when are replaced by non-polar molecules.[29] The desolvation

energy of a cavity increases as water molecules are better stabilized and this may reduce host-guest binding affinity.[30,31] The geometry of the receptor's binding site must minimize the formation of hydrogen bonds between bound water molecules and those with the bulk. *In-silico* calculations predict that cavities featuring a radius lower than 1 nm are expected to be empty ("dry"). Although water molecules can be found in a small cavity if there is a water-host stabilizing interaction. In contrast, large host's cavities are occupied by water molecules ("wet"), even when water-host interactions are unfavorable.[4] The incorporation of functional groups in the receptor's cavity is critical due to the stabilization of included water molecules. The type and arrangement of buried functional groups need to be specially considered in the design of the receptor.[30,32]

The "non-classical" hydrophobic effect is influenced by the shape of the receptor's cavity, the differences in the thermodynamic parameters (enthalpy and entropy) of free and bound water molecules and the surface characteristics of the guest. Whitesides *et al.* suggested that 75% of the free energy of most binding events in water is provided by the hydrophobic effect.[7] This effect is significant when more than 1 nm^2 of the solute's surface area is buried upon complex formation.[8] The binding constants displayed by synthetic host-guest complexes are commonly found in the range between 1 and 10^7 M^{-1}, with some exceptions.[3] The binding affinity of host-guest complexes has been enhanced by increasing the size of the hydrophobic cavity of the receptors.[22] The increase of the receptor's size also leads to the maximization of the number of non-polar contacts between the surface of the cavity and of bound guests. The combination of different non-covalent interactions with the hydrophobic effect is a sensible approach for molecular recognition (see Section 1.1.2).[6,33,34]

The "non-classical" hydrophobic effect was identified by Diederich and co-workers using cyclophane receptors (see Section 1.2.1). They showed that the release of water molecules from the receptor's cavity to the bulk solution upon host-guest complexation produces favorable changes in solvent cohesive interactions and a gain in dispersion forces.[3,22,31] In this respect, the hydrophobic effect is driven by enthalpy and is attributed to the release of bound water molecules to the bulk solution. This explanation is compatible with a wide range of experimental data reported in literature.[7] Diederich *et al.* also observed that all host-guest binding processes in water display negative heat capacity values, ranging from -20 to -130 $cal \cdot mol^{-1} \cdot K^{-1}$.[32]

A negative heat capacity value ($\Delta C_p < 0$) is the hallmark of the hydrophobic effect.[7] The negative sign of heat capacity might be a consequence of the higher heat capacity and lower entropy of water molecules around a non-polar solute than that in bulk solution.[5,28,35,36] The magnitude of the heat capacity depends on the nature of the guest, among other factors. For example, aromatic molecules functionalized with polar and protic groups (*e.g.* OH) lead to large negative ΔC_p values upon complexation, whereas binding of non-protic guests displays relatively low values.[32] Different models for the hydrophobic effect have been proposed. Nevertheless, the understanding of this effect remains elusive.[5]

1.1.2 Electrostatic and dispersion interactions

Together with the hydrophobic effect (Section 1.1.1), non-covalent interactions play key roles in association processes in water. These intermolecular interactions are comprised of either electrostatic or dispersion components, or a combination of both, which are difficult to dissect by experimental or computational methods. Different recognition motifs working in synergy are shared in the receptor's scaffolds to achieve high levels of binding affinity and selectivity. In general, the combined action of the hydrophobic effect with polar binding groups is exploited in molecular recognition in water. It is worth mentioning that dispersion interactions are significant owing to the low polarizability of water molecules.[33,37,38]

Columbic interactions are related with the attraction or repulsion of charged species (Figure 3a). Due to the high dielectric constant of water, ion-pairing is weak. The formation of a salt bridge accounts for *ca.* 1 kcal·mol^{-1}. This interaction is driven by the entropy and accompanied by an increase of enthalpy ($\Delta H > 0$). Yet, association of ions may be enthalpically favorable when hydrogen-bonding interactions take place (see below).[4,6,32]

For example, anion binding in water was firstly dominated by positively charged receptors. The host's counter anions were properly selected in order to minimize their interference in the binding events.[16] Anions are strongly solvated in water and their multiple protonation equilibria can further complicate their recognition. In addition, some charged anion receptors are poorly selective because they only rely on non-directional electrostatic interactions. Recently, neutral anion receptors based on hydrogen-bonding interactions have been designed because they are not affected by the above mentioned drawbacks of charged hosts. Even though, charged receptors are more efficient for the recognition of anions than the neutral counterparts.[29,39]

In the same vein, hydrogen-bonding interactions are weak in water owing to the competition of solvent molecules for hydrogen bond donor/acceptor groups, which are commonly exposed to the bulk solution (Figure 3b). Therefore, the efficient formation of hydrogen-bonded complexes requires the protection of the polar groups from the bulk aqueous solution. For example, incorporation of polar groups in the interior of a hydrophobic cavity minimizes their solvation and, concomitantly, enhances their efficiency. The hydrophobic pocket can be shaped either by molecular design of a pre-defined structure or by association of non-polar molecules holding hydrogen bonds in the interior of the aggregate.[40] In nature, peptide residues are able to establish efficient hydrogen bonds in the hydrophobic interior of proteins.[33,37] The strength of hydrogen-bonding interactions (donor-H···acceptor) increases when decreasing ΔpK_a = pK_a (donor-H) - pK_a (acceptor-H$^+$).[4] Based on the above, the exclusive use of hydrogen bonds to drive an association process in water is not a sensible approach due to the competitive nature of water, even if hydrogen-bonding functions are hidden. Thus, hydrogen bonds are combined with other non-covalent interactions to overcome these limitations.[6,11]

The combination of Columbic and hydrogen-bonding interactions, *a.k.a* charge-assisted hydrogen bonds, may lead to an energetic contribution of *ca*. 1 kcal·mol^{-1} in water, providing selectivity (Figure 3c). This approach has been successfully applied by the Schmuck group using acyclic, acyl guanidinium receptors for the binding of oxoanions (*e.g.* carboxylates, phosphates, etc.).[4,6,41]

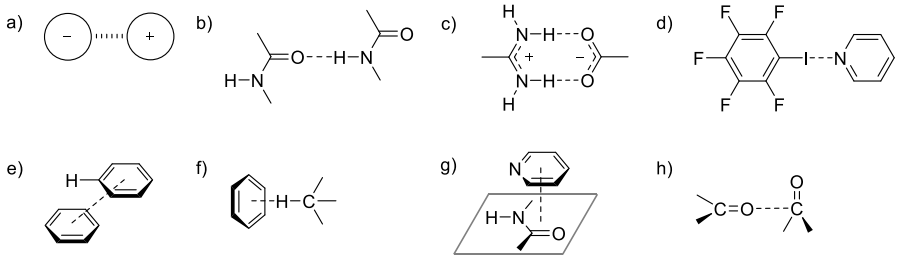

Figure 3. Examples of intermolecular interactions: a) ion-pairing; b) hydrogen bond; c) charge-assisted hydrogen bonds; d) halogen bond; e) offset stacked π-π; f) CH-π; g) amide-π and h) orthogonal C=O···C=O.

In contrast to hydrogen bonds, halogen bonds (XB) are not significantly affected by solvent polarity.[4] However, halogen bonds are relatively weak in polar and non-polar solvents (Figure 3d). The XB donor contains a halogenated atom featuring an electrophilic region (*σ*-hole), whereas the XB acceptor is an electron-donating group in another or the same molecule. The strength of a XB depends on both binding partners. For example, iodinated compounds form stronger halogen bonds than brominated counterparts, and those than chlorinated derivatives. Additionally, electron-withdrawing substituents on the XB donor increases the *σ*-hole potential, reinforcing the halogen-bonding interaction. Likewise, electron-donating groups in the XB acceptor help stabilize the halogen bond. Formation of efficient halogen bonds requires an angle close to linearity (165-180°) and a XB donor-acceptor distance below the sum of their van der Waals radii. Halogen-bonding interactions are driven by enthalpy, along with an entropic cost.[31]

Aromatic interactions are widely encountered in nature.[42,43] Cations are attracted by aromatic rings due to the negative electrostatic potential of the π-face of the aromatic component.[13] The cation-π interaction can enhance the binding free energy by more than 2 kcal·mol^{-1} in synthetic and natural complexes. For example, *ca.* 25% of tryptophan amino acids in nature stablish cation-π interactions with positively charged arginine or lysine residues. The cation-π interaction is formed primarily by an electrostatic component, even though dispersion interactions can be also involved.[4,44]

On the contrary, anion-π interactions are usually repulsive owing to the unfavorable contact of the negatively charged ion and the π-electron cloud of the aromatic ring. Attractive anion-π interactions may be stablished if the aromatic scaffold is decorated with electron-withdrawing groups. For example, the anion-π interaction accounts for *ca.* 2.4 kcal·mol^{-1} in the binding of oxoanions (*e.g.* sulfate and phosphate) by a nitroso-amine-pyrimidine receptor in water (0.1 M

Me_4NCl). The anion-π interaction is entropically favorable, probably due to the desolvation of the non-polar aromatic surface upon anion binding.[45]

Aromatic π-π stacking and CH-π interactions have both electrostatic and dispersion contributions.[38] On the one hand, the binding geometry of two aromatic groups can be edge-to-face, offset stacked or face-face stacked (Figure 3e).[31] On the other hand, CH-π interactions are directional, featuring an angle between 140° and 180° and a distance of 2.3-2.9 Å. The strength of the CH-π interaction increases with the acidity of the CH bond and the increase in the electron density of the aromatic ring (Figure 3f).[4] In general, CH-π interactions contribute less than 2.5 kcal·mol^{-1} to the binding free energy and can be detected by NMR methods when, at least, three CHs are faced to an aromatic ring.[46,47,48] These interactions are particularly interesting in carbohydrate binding, in which the association constants of the complexes between mono-saccharides and proteins are in the order of 10^3-10^4 M^{-1}. In this case, polar and non-polar interactions are key to achieve these levels of affinity with remarkable selectivity.[49]

Likewise, amides are widely spread in nature. They establish π-π and NH-π interactions with aromatic groups. Interestingly, the π-π binding geometry between amides and aromatic heterocycles involves the antiparallel alignment of their dipole moments (Figure 3g).[31] Furthermore, the oxygen atom of the carbonyl group of amides forms hydrogen bonds with hydroxyl groups, among other hydrogen bond donors, in water. Most likely, the NHCO···HO interaction is driven by entropy due to the desolvation of the binding polar groups.[50] Other hetero-atoms, such as sulfur, interact favorably with π-systems through dispersion interactions. The sulfur-π interaction accounts for up to 0.5 kcal·mol^{-1} to the stability of proteins.[16,38]

Finally, orthogonal dipolar interactions, such as C=O···C=O and C-X···C=O, are involved in the stabilization of protein's secondary structure (Figure 3h). The C=O···C=O bond is slightly stronger than the C-X···C=O counterpart, presumably, due to the higher polarizability of the former.[31]

1.1.3 Hofmeister effect

The Hofmeister effect is related with salts and their influence on the solute's properties in aqueous solution. Anions and cations are traditionally grouped into the Hofmeister series according to their effect on salting-in or salting-out proteins, *i.e.* solubilization or aggregation, respectively. However, the implication of ions in water is more general and the effect is more evident in the case of anions. The cation series is poorly defined and depends on the phenomena under investigation. Kosmotropic anions (salting-out effect) feature a small size and high charge density, such as fluoride and sulfate. These anions are strongly solvated, enhancing water structure and the hydrophobic effect. In contrast, chaotropic anions (salting-in effect) are large and charge-delocalized, such as iodide and perchlorate. Chaotropes can undergo partial desolvation and interact with solutes. As a result, they impact negatively on the hydrogen-bonding network of water and disfavor the hydrophobic effect for binding (Figure 4).[4,11,30,40,51]

The influence of chaotropic anions has been termed “chaotropic effect” because it works as a driving force for the association of hydrophobic surfaces. The chaotropic effect is particularly efficient for very large ions that extend the classical Hofmeister scale (Figure 4). The later anions are known as super chaotropic species (*e.g.* borate clusters and polyoxometalates).[51]

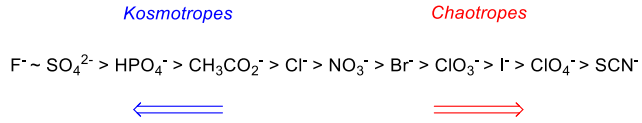

Figure 4. Hofmeister series for anions.

The Hofmeister effect is noticed at high salt concentrations (> 0.1 M). In general, anions impact on the water structure of the first or second solvation shell, but not beyond, because electrostatic interactions are strongly shielded at these salt concentrations.[5,11] In nature, fluoride or sulfate (kosmotropes) decrease the solubility of proteins and favor folding, whereas perchlorate (chaotrope) disrupts the interactions between non-polar surfaces, which causes the breaking of the protein’s quaternary structure and/or induces partial unfolding. Studies using simple, well-defined systems are required for the understanding of the Hofmeister effect in aqueous solution.

In this regard, the Gibb group has put a lot of effort in understanding the Hofmeister effect using a water-soluble deep-cavity cavitand bearing external carboxylic acids (see Section 1.3.2). The cavitand features a hydrophobic binding site suitable for the inclusion of non-polar molecules. The binding of adamantyl carboxylic acid to the receptor involves the deep inclusion of the adamantyl residue (non-polar section) of the guest into the hydrophobic pocket. The addition of kosmotropic anions decreases the binding free energy by $\Delta\Delta G$ = ΔG (with salt) - ΔG (without salt) ~ -0.5 kcal·mol^{-1}, whereas chaotropic anions increase strongly the association energy by $\Delta\Delta G$ ~ +1.4 kcal·mol^{-1}. In the later case, the change in $\Delta\Delta G$ is reasoned in terms of the Hofmeister effect and the competitive binding of chaotropic anions (*e.g.* K_a = 95 M^{-1} for perchlorate). Further studies using the octa-acid cavitand supported that the Hofmeister effect is related with the inclusion of chaotropic anions into the receptor’s cavity and the binding of cations to the peripheral carboxylates.[4]

The binding of super chaotropic anions has been studied by Nau and co-workers using *γ*-cyclodextrin. The association constants of the resulting complexes are in the order of 10^3-10^6 M^{-1}. Interestingly, the binding processes are enthalpically driven and opposed by entropy. These results confirm that certain anions bind efficiently to hydrophobic cavities.[29,51]

1.2 Cyclic and Oligo-Cyclic Covalent Receptors Featuring a Hydrophobic Cavity

In this section, we discuss receptors featuring mono-cyclic or bi-cyclic architectures formed by the covalent bonding of aromatic units. The binding site provided by these cyclic covalent hosts is mainly hydrophobic.

1.2.1 Cyclophanes

Cyclophanes are molecular receptors formed by aromatic scaffolds linked together by alkyl or aryl spacers. The structure of cyclophanes offers a hydrophobic cavity commonly opened at two opposite ends to the bulk solution. Ionizable or charged groups (*e.g.* carboxylic acids, amines, etc.) are appended to the cyclophane's scaffolds to impart solubility in water and minimize their tendency to aggregate. Based on these features, cyclophanes are good candidates for the binding of non-polar molecules or residues in water.[15,52] Nevertheless, cyclophanes incorporating polar binding motifs in the interior of their hydrophobic cavities are still rare.[30]

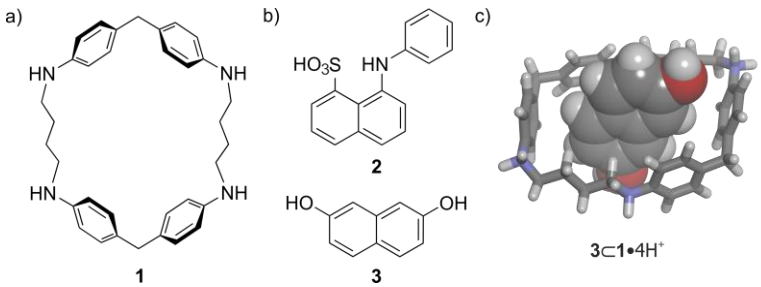

Figure 5. Line-drawing structures: a) cyclophane **1** and b) aromatic guests **2** and **3**; c) energy minimized structure (MM3) of the **3**⊂**1**•4H$^+$ inclusion complex. Host is depicted in stick representation and guest is shown as CPK model.

The first examples of molecular recognition in water using cyclophane receptors were reported by Koga and co-workers in 1980. Cyclophane **1** is based on two rigid, di-phenylmethane units connected by two butane-1,4-di-amine spacers. **1** is soluble in water at pH < 2 owing to the protonation of its secondary amines (Figure 5a). They demonstrated that **1** forms a 1:1 inclusion complex with 1,2,4,5-tetra-methylbenzene in the solid state. The receptor adopts a rhomboid-like conformation (*ca.* 7.9 x 6.5 Å) to accommodate the benzene derivative in the aromatic cavity. They also investigated the binding properties of **1** in acidic aqueous solution. For example, 1-anilinonaphthalene-8-sulfonate **2** (Figure 5b) features emission properties and, therefore, titration experiments were performed by fluorescence spectroscopy. The addition of cyclophane **1** to a solution of **2** enhanced the intensity of the emission band assigned to the guest. The fit of the titration data to a 1:1 binding model using a linear equation (Benesi-Hildebrand plot) returned a binding constant value K_a (**2**⊂**1**•4H$^+$) = 6.3 x 10^3 M^{-1}.[53] However, the binding geometry of the **2**⊂**1**•4H$^+$ complex was not elucidated by NMR spectroscopic techniques.

After these initial studies, Koga *et al.* reported the binding studies of 2,7-di-hydroxynaphthalene **3** (Figure 5b) with cyclophane **1** in DCl/D_2O solution (pD ~ 1) using ^1H NMR spectroscopy. The proton signals of **3** moved upfield with respect to those of the free guest in solution upon the addition of receptor **1**. At the same time, the proton signals of the butyl spacers of **1** experienced upfield shifts, whereas the protons of the methylene bridges of the two *para*-phenyl units did not show appreciable chemical shift changes. These observations supported the inclusion of **3** in the cavity of **1** in water solution. The protons of bound **3** and those of the aliphatic chains of bound **1** suffered the shielding effect exerted by the aromatic rings of both binding partners. The chemical exchange between free and bound components was fast on the ^1H NMR chemical shift timescale. This is related to the existence of two opposite portals in the cyclophane's structure that allows the rapid formation and dissociation of the inclusion complex. The association constant of **3⊂1**•$4H^+$ was estimated to be in the order of 10^3 M^{-1}. Interestingly, a sensible binding geometry was derived from the analysis of the chemical shift changes experienced by the protons of both host and guest. The naphthalene derivative **3** was bound in a pseudo-axial orientation in the aromatic cavity of **1**. In this binding geometry, the two hydroxyl groups of **3** were exposed to the bulk aqueous solution (Figure 5c).[54]

Cyclophane **1** or its octa-*N*-methyl ammonium version were used for the binding studies of a series of charged aromatic guests. The results showed that anionic compounds were bound stronger than structurally related cationic derivatives. This indicated that the formation of 1:1 inclusion complexes derived from cyclophane **1** does not only obey the size and shape complementary principles, but also the complementarity between the charges of the binding partners.[55,56,57]

The length and rigidity of the spacers of **1** were also modified to tune the dimensions and hydrophobicity of the cyclophane's cavity. Remarkably, the incorporation of cyclohexyl units in the spacers boosted the binding constant of 1-anilinonaphthalene-8-sulfonate **2** to $K_a = 5 \times 10^5$ M^{-1}. In the later complex, bound **2** adopts an equatorial orientation in the cavity of the receptor, in which the naphthalene group is buried.[55,58]

Extra water-solubilizing groups were appended to the spacers of the *bis*-(di-phenylmethane) cyclophane **1** with the aim at improving and somehow better controlling the receptor's solubility. Murakami *et al.* incorporated four L-aspartate residues to the four nitrogen atoms of **1**. The attached amino acids allowed to modulate the net charge of the receptor at will. The carboxylic acids of the aspartate residues are ionized at basic pH leading to anionic cyclophanes. On the contrary, protonation of the primary amines of the aspartates at acidic pH gives the cationic counterparts. Using this cyclophane derivative, they observed that electrostatic interactions impact on the thermodynamic stability of the 1:1 complexes by one or two orders of magnitude, depending on the number of charged residues in the binding partners.[59,60]

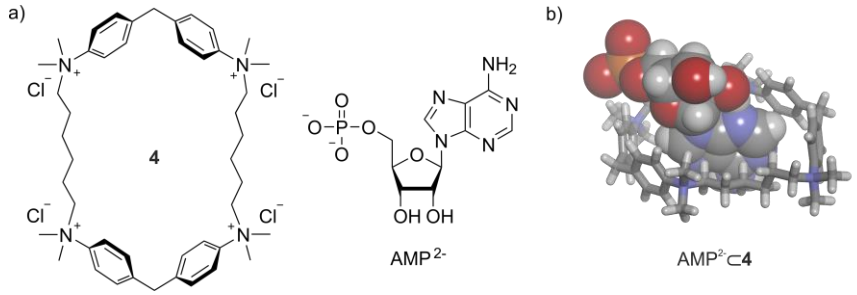

Figure 6. a) Line-drawing structures of **4** and AMP^{2-}; b) energy minimized structure (MM3) of the AMP^{2-}⊂**4** complex. The host is depicted in stick representation and the guest is shown as CPK model.

Based on the above, Schneider and co-workers synthesized a *bis*-(di-phenylmethane) cyclophane receptor, **4**, bearing hexyl chains as spacers and four quaternary ammonium groups (Figure 6a). The cavity size of **4** can accommodate purines and their corresponding nucleosides and nucleotides, stablishing 1:1 complexes. For example, the complex of adenosine mono-phosphate, AMP^{2-}⊂**4**, shows the adenine fragment included in the cavity of **4** and the ribose unit stays near one of the portals of the binding site (Figure 6b). The phosphate group of the guest is exposed to the bulk aqueous solution, even though it can establish electrostatic interactions with the cationic ammonium groups of the receptor. More interestingly, cyclophane **4** displays high-binding selectivity for adenine derivatives.[61]

Cyclophane **4** was also employed as model system to study the effect of salts in the binding of benzoate guests. The increase on the concentration of NaCl resulted in a linear relationship between log K_a and the Debye-Hückel term ($m \times I^{1/2}/[1 + I^{1/2}]$, where I is the ionic strength). The slope of the linear regression (m) was -1.45. This value was significantly lower than the one expected if the host and the guest were treated as normal ions (m = -4.10). Most likely, the inorganic salt, NaCl, impacts on the hydrophobic and Hofmeister effects. In any case, the Debye-Hückel correlation can be used as an indicator of Columbic interactions present in supramolecular host-guest complexes in water.[62]

Velázquez and co-workers introduced four carboxylic acids and four amides in the spacers of a *bis*-(di-phenylmethane) cyclophane, **5** (Figure 7a). **5** is soluble in water at pD ~ 8 due to the conversion of the carboxylic acids into carboxylate groups. The tertiary amines and the amides of **5** also contribute to its water solubility. Cyclophane **5** complexes tyramine **6** and dopamine **7** (as protonated ammonium cations) featuring binding constants between 10 and 10^3 M^{-1} (Figure 7b). The 1:1 inclusion complexes are stabilized by a combination of the hydrophobic effect, π-π and CH-π interactions. Furthermore, the carboxylates of the receptor establish long-range Columbic interactions with the ammonium group of the guests.[17,63] Other *bis*-(di-phenylmethane) cyclophanes bearing triazine spacers have been also reported in the literature.[64]

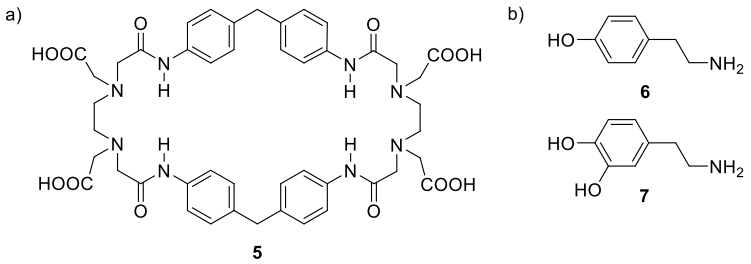

Figure 7. Line-drawing structures: a) cyclophane **5** and b) tyramine **6** and dopamine **7**.

Water-solubilizing groups were also introduced as substituents in the di-phenylmethane walls of the cyclophanes. Cyclophane **8** has four ethyl phosphonate groups and bears *ortho*-substituted pyridines as spacers. This receptor binds the methyl ester of lysine, **9**, through the formation of charge-assisted hydrogen bonds between the ammonium groups of the guest and the phosphonates of the receptor. The protonated ammonium groups of **9** might be also involved in hydrogen-bonding interactions with the pyridines of the receptor **8**. The binding constant of the **9**⊂**8** complex is K_a = 1.2 x 10^3 M^{-1} in water, which is a remarkable value considering that the complex is mainly stabilized by electrostatic interactions (Figure 8).[65]

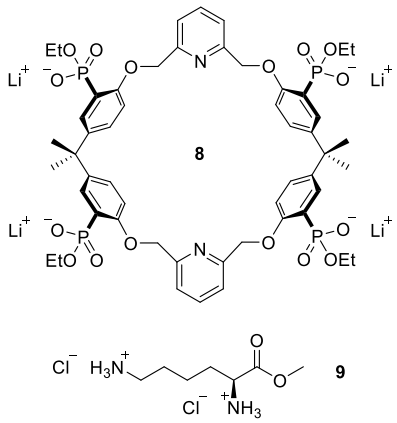

Figure 8. Line-drawing structures of tetra-phosphonate cyclophane **8** and L-lysine di-hydrochloride **9**.

Diederich and co-workers functionalized the methylene bridges of *bis*-(di-phenylmethane) cyclophanes with spiro-piperidinium groups and replaced the amino groups of the spacers by oxygen atoms, **10**-**12** (Figure 9a). These structural modifications allowed to place the quaternary ammonium groups remote from the receptor's cavity, minimizing their effect in the binding events. It is worth mentioning that, in the solid state, the cavity of spiro-piperidinium cyclophanes is occupied by two water molecules.[66] In water solution, the di-piperidinium cyclophane **10** features a critical micellar concentration (cmc) of 1.6 x 10^{-4} M, which limits the implementation of ^{1}H NMR spectroscopy titrations. Nevertheless, the binding constants of the complexes derived from **10**

were determined by solid-liquid or liquid-liquid extraction methods, or by fluorescence spectroscopy titrations. Cyclophane **10** forms 1:1 inclusion complexes with aromatic guests. As in the previous examples reported by Koga, the cyclophane complexes are stabilized by the hydrophobic effect, π-π, CH-π and van der Waals interactions. For example, the complex of 6-[(4-methylphenyl)-amino]-2-naphthalenesulfonate **13** and cyclophane **10** features an association constant value K_a = 4.3 x 10^3 M^{-1} in water (Figure 9b). The binding constant of the **13⊂10** complex is similar to that using *β*-cyclodextrin as receptor.[67]

On the other hand, cyclophane **11** displays a more polarizable and deeper cavity than **10** owing to the presence of *ortho*-methoxy substituents in the phenyl rings (Figure 9a). This also produces an increase of the cmc value to 10^{-2} M^{-1}.[68] Cyclophane **11** binds neutral, aromatic molecules forming thermodynamically stable 1:1 inclusion complexes, K_a = 10^3-10^4 M^{-1}.[66]

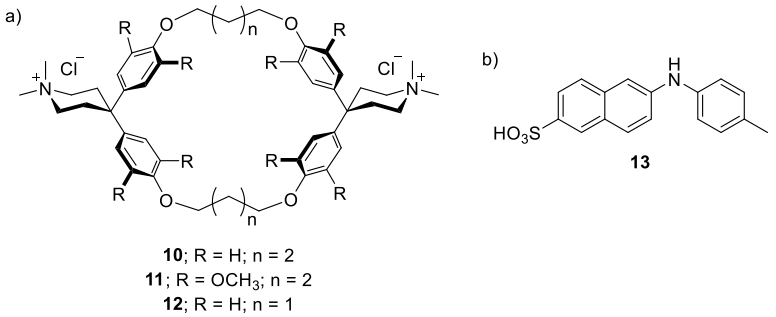

10; R = H; n = 2
11; R = OCH_3; n = 2
12; R = H; n = 1

Figure 9. Line-drawing structures: a) cyclophanes **10**, **11** and **12** and b) guest **13**.

The complexation process of aromatic guests with cyclophanes is mainly driven by the hydrophobic effect, which masks the contribution of π-donor-π-acceptor interactions. In this regard, Diederich *et al.* applied cyclophanes **11** and **12** (Figure 9a) to examine the electronic complementarity between receptor and guest and derive the contribution of donor-acceptor interactions. 1,4-Di-substituted benzene derivatives were chosen as guests because they display an axial binding geometry when bind to the cyclophane receptors, *i.e.* the phenyl group is included in the cavity and the polar groups in *para*-position are exposed to the aqueous solution. The electronic properties of the phenyl group of the guests are tuned by the *para*-substituents and these are expected to impact on the thermodynamic stability of the inclusion complexes. In this regard, cyclophane **12** follows the expected electron donor-acceptor trend. The strength of the interaction between **12** and *para*-substituted benzenes follows the order: acceptor-acceptor > donor-acceptor > donor-donor. However, **11** does not display the later relationship. This result was attributed to the presence of the *ortho*-methoxy groups in the cyclophane's structure (Table 2).[69]

Table 2. Binding constants (K_a, M^{-1}) of *para*-substituted benzenes with cyclophanes **11** and **12** in D_2O at 293 K.

Guest	Electronic nature	K_a (receptor **11**)	K_a (receptor **12**)
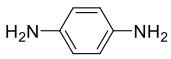	Donor-donor	3.6×10^2	< 10
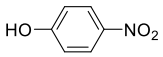	Donor-acceptor	2.3×10^4	6.0×10^2
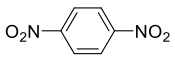	Acceptor-acceptor	7.8×10^3	1.3×10^3

Other cyclophanes bearing O-$(CH_2)_n$-O spacers similar to **10**-**12** (Figure 9a) display a narrow cavity (n = 1), which is suitable for the binding a single methyl group, or a collapsed cavity (n = 2), lacking the binding function.[70]

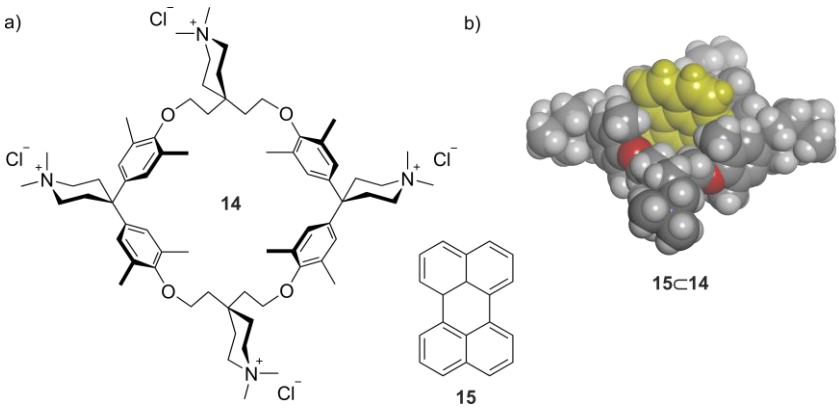

Figure 10. a) Line-drawing structure of cyclophane **14** and perylene **15**; b) energy minimized structure (MM3) of the **15⊂14** inclusion complex. Host and guest (yellow) are shown as CPK models.

The incorporation of two extra spiro-piperidinium groups in the *bis*-(di-phenylmethane) cyclophane scaffold gave **14** (Figure 10a). The tetra-piperidinium **14** is characterized by a cmc value of 7.5×10^{-3} M, which is almost two orders of magnitude larger than that of cyclophane **10**. Furthermore, the *ortho*-methyl substituents of **14** affords a deeper cavity and enhances the hydrophobic effect.[30] **14** is an efficient receptor for neutral poly-aromatic guests, such as pyrene, perylene and fluoranthene, featuring binding constant values in the micromolar range. On top of that, anionic naphthalenes are bound stronger than the neutral counterparts. For comparison, the binding constant value of 1-anilinonaphthalene-8-sulfonate **2** with receptor **14** is almost one order of magnitude larger than that with cyclophane **1** (K_a (**2⊂14**) = 3.2×10^6 M^{-1}). Remarkably, perylene **15** shows a perfect fit for the aromatic cavity of **14**. The **15⊂14** complex is thermodynamically highly stable in water featuring $K_a = 1.6 \times 10^7$ M^{-1} (Figure 10b).[67]

Diederich and co-workers also replaced the spiro-piperidinium groups of the *bis*-(di-phenylmethane) cyclophanes by poly(ether amide) dendrimers bearing terminal carboxylic acids. Remarkably, the resulting dendritic cyclophane, which resembles the core of **10**, displayed slow dynamics between free and bound components on the ^{1}H NMR chemical shift timescale. The densely packed structure of the dendritic cyclophane influences significantly the guest in/out exchange kinetics.[71]

The experimental results obtained by Diederich *et al.* demonstrate the importance of the "non-classical" hydrophobic effect in the binding of aromatic guests by cyclophanes in water. The binding processes are characterized by a strong enthalpy, ΔH = -8 to -12 kcal·mol^{-1}, and an entropic penalty, $T\Delta S$ = -2 to -5 kcal·mol^{-1}. Note that these thermodynamic signatures are in sharp contrast with the ones expected for a process driven by the "classical" hydrophobic effect (ΔH ~ 0 and $T\Delta S$ > 0).[4,68] It was then proposed that the strong negative enthalpic component was derived from the release of enthalpically higher in energy water molecules from the receptor's cavity to the bulk solution, where the enthalpy is lower, and from the establishment of host-guest dispersion interactions.[68]

The van't Hoff analyses of the complexes between **11** and *para*-substituted benzenes by NMR spectroscopy and calorimetric techniques, in a range of 20 K, returned negative heat capacity values. The ΔC_p values were in the order of *ca.* -100 cal·mol^{-1}·K^{-1} for those guests having a strong dipole moment and hydroxyl substituents. These values are in the range of non-polar binding using cyclodextrins.[72]

One of the issues of the di-phenylmethane-based cyclophane receptors is the easy rotation of the aromatic rings leading to multiple conformations. In an effort to reduce their number, Wilcox and co-workers used the Troger's base structure in the construction of cyclophanes. The replacement of one of the di-phenylmethane units by the di-benzodiazocine scaffold gave a relatively more rigid receptor, **16** (Figure 11a). Cyclophane **16** is soluble at concentrations up to 50 mM in 0.1 M KCl/DCl buffer, pD ~ 2. In this acidic solution, three of the four nitrogen atoms of **16** are protonated (one of the diazocine nitrogens remains unprotonated). The interaction of **16**•3H$^+$ with a series of *para*-methyl-substituted benzenes (Figure 11b) was probed by ^{1}H NMR spectroscopy titrations. In all cases, the signal corresponding to the *para*-methyl substituent of the guests experienced the largest upfield shift upon addition of the receptor **16**•3H$^+$. This indicated the deep inclusion of the *para*-methyl group of the guests into the cyclophane's cavity. The fit of the chemical shift changes to a 1:1 binding model, using a non-linear least-square method, returned binding constant values in the range of 40-400 M^{-1}. Neutral electron-rich aromatic guests, such as 4-methylphenol, are weakly bound to **16**•3H$^+$, K_a ~ 50 M^{-1}. However, acceptor-donor guests, such as 4-cianophenol, show an increase in binding affinity, K_a ~ 2 x 10^2 M^{-1}. In the case of anionic aromatic molecules, they are bound to **16**•3H$^+$ featuring K_a values in the order of 10^2-10^3 M^{-1}. For example, the binding

constant of the 4-toluenesulfonate⊂**16**•3H$^+$ complex is 3 x 10^2 M^{-1}. These constant values are in line with those reported by Diederich and co-workers using cyclophanes **10** and **12** (Figure 9a).[73]

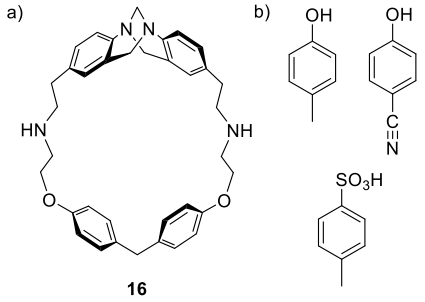

Figure 11. Line-drawing structures: a) cyclophane **16** and b) representative aromatic guests studied by Wilcox and co-workers.

Dougherty and co-workers designed cyclophanes based on the ethenoanthracene scaffold, **17** and **18** (Figure 12a). The ethenoanthracene scaffold is rigid, concave and delivers an electron-rich aromatic surface area to the cyclophane's cavity. The phenyl and cyclohexyl spacers of **17** and **18**, respectively, also aid them to adopt a pre-organized structure. Carboxylate groups are anchored to the ethenoanthracene units in the faces exposed to the bulk solution. In borate buffer at pD = 9, the cyclophanes **17** and **18** are soluble in water and feature cmc values in the range of 0.2-0.8 mM.[74]

These ethenoanthracene cyclophanes adopt two possible conformations for binding: a rhomboid-shaped conformation is preferred for planar guests, such as iminium ions, whereas a toroid-shaped conformation is suitable for the binding of spherical guests, such as tetra-alkylammonium substrates. Neutral electron-deficient aromatic molecules and ethenoanthracene cyclophanes, **17** and **18**, form 1:1 inclusion complexes featuring association constant values K_a = 10^3-10^6 M^{-1}. These guests are preferentially bound to **17** and **18** versus the electron-rich counterparts owing to the donor-acceptor complementarity between the aromatic surfaces of both binding partners. The cyclophanes **17** and **18** also show high-binding affinity for quaternary ammonium guests, such as *N*-methylquinolinium and *N*-methylisoquinolinium. The binding studies indicated that a gain of 3 kcal·mol^{-1} in the complexation free energy is derived from the combination of donor-acceptor and cation-π interactions. The cation-π interaction accounts for 1 kcal·mol^{-1} or more to the thermodynamic stability of these complexes. Long-range Columbic interactions between the external carboxylates of the receptors and the ammonium group of the guests contribute to a lesser extent (< 0.3 kcal·mol^{-1} per carboxylate group).[44,74,75]

Adamantyl tri-methylammonium **19** is a perfect fit for the cavity of the cyclophanes reported by Dougherty and co-workers. The binding free energy of the **19**⊂**17** complex is -6.7 kcal·mol^{-1}. The **19**⊂**17** complex is 1.2 kcal·mol^{-1} thermodynamically more stable than the **19**⊂**18** counterpart in

borate buffer solution (pD = 9). Interestingly, the complexation induced chemical shifts determined from the ^{1}H NMR titration spectra indicated that the tri-methylammonium cation of the guest is deeper in the hydrophobic aromatic cavity of the receptor than the adamantyl group (Figure 12b).[74]

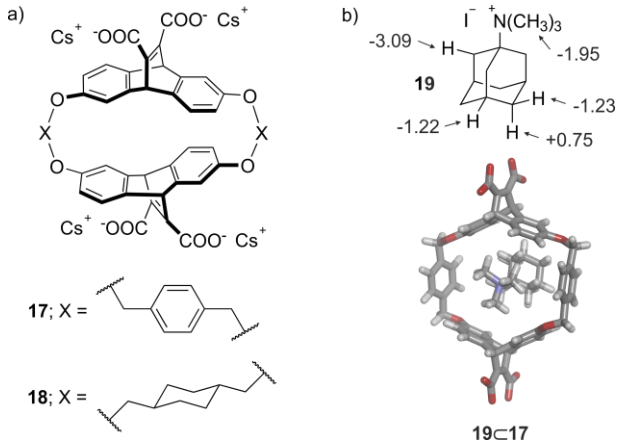

Figure 12. a) Line-drawing structures of cyclophanes **17** and **18**; b) adamantyl tri-methylammonium **19** and energy minimized structure (MM3) of the **19**⊂**17** complex (receptor in the toroid conformation). In b) the chemical shifts (ppm) of proton signals of bound **19** are indicated.

The complexation of cationic organic guests by cyclophanes **17** and **18** in water is driven by enthalpy. The heat capacity values (ΔC_p) for these binding processes are large and negative, and their magnitude coincided with that determined by Diederich and co-workers for the binding of polar *para*-substituted benzene derivatives.[76]

The existence of the cation-π interaction in synthetic and natural host-guest complexes was not obvious at that time. In this regard, the group of Dougherty conducted host-guest binding studies using a series of cyclophane receptors, including **17** and **18**, and a library of cationic guests: alkyliminium, tetra-alkylammonium, sulfonium and guanidinium substrates. The results demonstrated that the cation-π interaction has a remarkable effect in the stability of the host-guest complexes. For example, the complexation of *N*-methylquinolinium is 2.5 kcal·mol^{-1} more favorable than that of the neutral derivative, 4-methylquinoline.[77]

The ethenoanthracene-based cyclophanes were further elaborated by introducing substituents in either the aromatic panels or the spacers.[78,79] For example, Dougherty *et al.* introduced methoxy groups in the ethenoanthracene scaffolds to create a more electron-rich aromatic cavity and increase the cmc value, as discussed above for the spiro-piperidinium cyclophanes (Figure 9a). However, this structural modification was detrimental for guest binding because the cyclophane adopted a conformation in which the methoxy substituents were located in the interior of the cavity, *i.e.* the binding site collapsed.[77,80]

In another example, the phenyl spacers of **17** were decorated with carboxylate groups at their *ortho*-positions providing extra electrostatic interactions and, therefore, enhancing the binding affinity towards cationic organic guests. Conversely, the additional carboxylate groups impact negatively on the recognition of neutral molecules, presumably, owing to the reduction of the hydrophobicity of the binding pocket. Interestingly, the later cyclophane receptor binds efficiently arginine. The complex is stabilized by electrostatic, π-π and cation-π interactions between the guanidinium group of the guest and the ionized aromatic scaffolds of the receptor (K_a = 4.7 x 10^3 M^{-1}). The binding geometry and affinity towards the guanidinium cation of arginine residues allow to selectively recognize di-peptides containing arginine amino acids versus those lacking the guanidinium functionality.[75]

The results obtained in the binding of arginine with cyclophane **17** and other derivatives served for the design of an efficient and selective receptor bearing two ethenoanthracene units and one naphthalene spacer linked together by di-sulfur bonds. This cyclophane selectively binds asymmetric di-methyl arginine versus mono-methyl or symmetric di-methyl arginine residues. The complexes are also stabilized by CH-π interactions stablished between the methyl substituents of the bound guanidinium group and the aromatic panels of the receptor.[81]

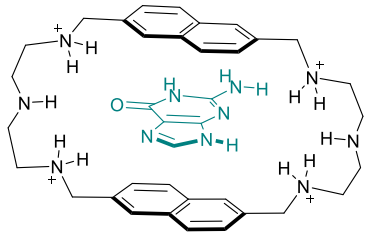

21⊂**20**•4H$^+$

Figure 13. Line-drawing structure of the complex between guanine **21** and cyclophane **20**•4H$^+$ at pH = 6.

Lehn and co-workers used planar, naphthalene panels for the construction of cyclophanes. Receptor **20** features two parallel naphthalene units linked together by two poly-amine linkers (Figure 13). At pH = 6 (pyridine/acetic acid buffer), four of the six amine nitrogen atoms of **20** are protonated. The central nitrogens remain unprotonated because their pK_a values are relatively low. Consequently, the formation of four ammonium groups in **20** is expected to induce a repulsion between the two aromatic sections, “roof” and “floor”, circumventing the hydrophobic collapse of the cavity. ^{1}H NMR and fluorescence titration experiments demonstrated that **20**•4H$^+$ binds aromatic carboxylates and nucleotides. Contrary to the binding selectivity displayed by cyclophane **4** towards adenine (Figure 6), receptor **20**•4H$^+$ selectively binds guanine **21**, K_a (guanine⊂**20**•4H$^+$)/K_a (adenine⊂**20**•4H$^+$) ~ 10 (Figure 13). However, the binding constant ratio drops to *ca.* 4 for the mono-phosphate nucleotides, GMP^{2-} and AMP^{2-}.[52,82]

Water-solubilizing groups were alternatively attached to the naphthalene panels. For example, a tetra-sulfonate 1,5-dinaphtho-32-crown-8 receptor binds bi-pyridinium guests with high-binding affinity (K_a up to 10^7 M^{-1}). The binding processes are enthalpically driven and accompanied by a small entropic gain. The inclusion complexes are highly stabilized by the hydrophobic effect, electrostatic and π-donor-π-acceptor interactions.[17,83]

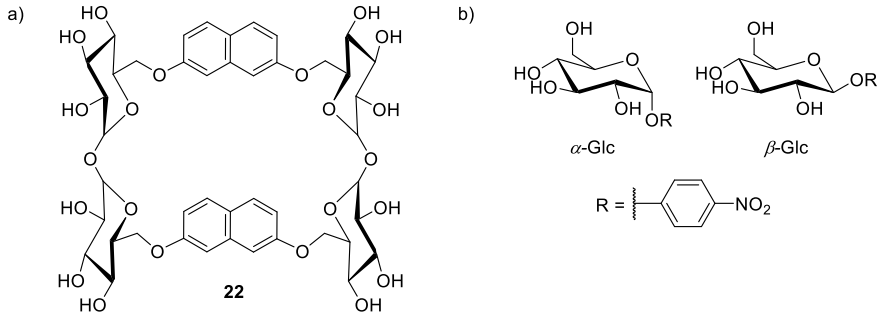

Figure 14. Line-drawing structures: a) cyclophane **22** and b) *α*- and *β*-glucoside derivatives.

Jiménez-Barbero *et al*. modified the spacers of naphthalene-based cyclophanes using saccharide units. Di-saccharide spacers offer additional binding motifs, *i.e.* hydrogen bond donor/acceptor groups, to induce somehow selectivity towards glycoside derivatives (Figure 14). Carbohydrates are highly solvated in water and, therefore, 4-nitrophenyl-substituted glycosides were employed as model substrates. The 4-nitrophenyl group of the modified glycosides is included in the cavity of **22**. The sugar unit of the guests is then involved in hydrogen-bonding interactions with the polar functions of the host. The binding constant values of the complexes using equatorial glycosides are in the order of 10^2 M^{-1}, whereas the constant values of the axial counterparts vary from 80 to 2.4 x 10^2 M^{-1}, depending on the configuration of the anomeric carbon atom. The magnitude of these values is similar to that determined for analogous complexes using *α*-cyclodextrin as receptor. The interaction of glycoside derivatives with cyclophane **22** is driven by enthalpy and opposed by entropy.[84]

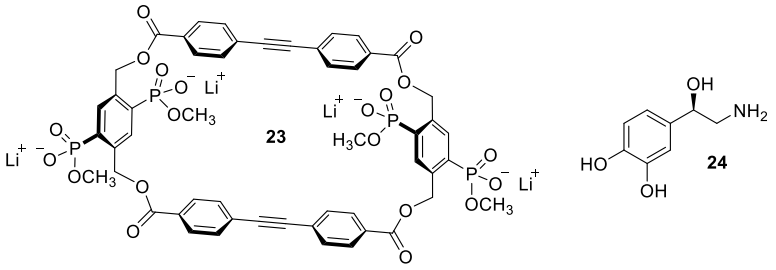

Figure 15. Line-drawing structures of cyclophane **23** and noradrenaline **24**.

Larger aromatic cavities were built using *para*-phenyl-ethynyl-phenyl units as building blocks. Molt *el al.* reported the construction of cyclophane **23** based on the later scaffold at both the "roof" and "floor". The phosphonate groups of the *para*-phenyl spacers impart water solubility to **23**, which features a cmc value of 3 x 10^{-4} M. Most likely, the charge distribution is not ideal to avoid aggregation at millimolar concentrations. Receptor **23** binds noradrenaline **24**, among other catecholamines, forming 1:1 and 2:1 guest/host complexes. The stepwise binding constants are in the order of 10^3 M^{-1} (Figure 15).[85]

On the other hand, structurally simple cyclophanes bearing *para*-benzene derivatives at the "roof" and "floor" have been designed. As discussed above for cyclophane **20**, ammonium groups were incorporated to deliver water solubility. The cationic nature of these simple cyclophanes has been applied in the binding of organic and inorganic anions, such as carboxylate and sulfate, respectively.[86,87,88]

Paraquat units have been also used as building blocks for the synthesis of cyclophanes. They feature an electron-deficient cavity which is ideal for the complexation of electron-rich aromatic molecules. The cationic paraquat scaffolds also impart water solubility. The tetra-cationic cyclo-*bis*-(paraquat-*para*-phenylene) cyclophane **25** was introduced by Stoddart *et al.* in the late 80s (Figure 16a). The receptor **25** features a rectangular cavity of 10.3 x 6.8 Å. In the presence of electron-rich aromatic substrates, such as 1,4-di-methoxybenzene **26** (Figure 16a), 1:1 inclusion complexes are formed in D_2O. The aromatic rings of both host and guest establish charge-transfer interactions. ^1H NMR binding studies showed that the aromatic protons of **26** experienced an upfield shift of $\Delta\delta$ ~ -3 ppm, whereas the protons of the methoxy groups moved only $\Delta\delta$ ~ -0.5 ppm upon complexation. These chemical shift changes indicated that the guest is bound in an axial orientation. The *para*-methoxy substituents are located at the portals of the receptor's cavity (Figure 16b).[89] It is also interesting that the *bis*-paraquat cyclophane **25** binds amino acids containing electron-rich aromatic substituents, such as tryptophan.[52]

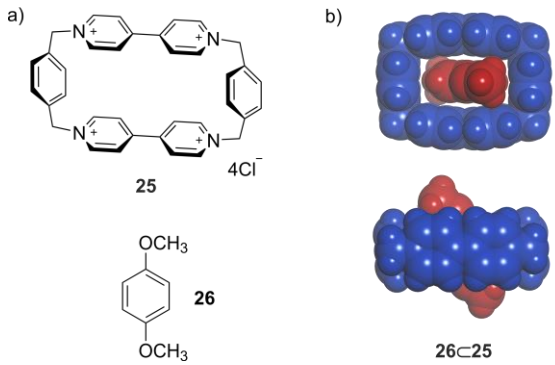

Figure 16. a) Line-drawing structures of cyclophane **25** and 1,4-di-methoxybenzene **26**; b) energy minimized structure (MM3) of the **26⊂25** inclusion complex: side and top views (receptor in blue and guest in red).

The axial binding geometry featured by certain aromatic guests with receptor **25** suggests that 1,4-di-alkoxy-phenyl and 1,5-di-alkoxy-naphthalene derivatives can form pseudo-rotaxanes. Remarkably, the binding constant values of the corresponding 1:1 inclusion complexes are in the range between 10^4 and 10^6 M^{-1}.[90,91]

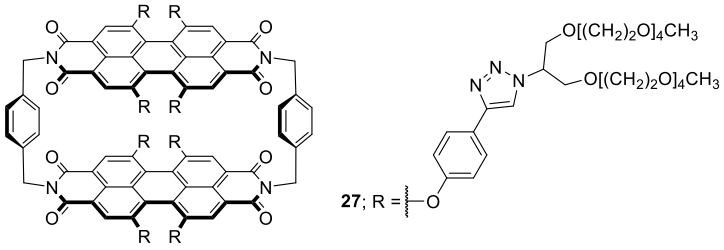

Figure 17. Line-drawing structure of perylene *bis*-imide cyclophane **27**.

Recently, the group of Würthner reported a perylene *bis*-imide cyclophane **27** functionalized at the aromatic panels with oligo(ethylene glycol) chains as water-solubilizing groups (Figure 17). The rigid *para*-xylene spacers avoid the collapse of the aromatic cavity by π-π stacking interactions and the hydrophobic effect. Receptor **27** binds aromatic alkaloids with good finding affinities (K_a = 10^3-10^4 M^{-1}), albeit in a 1:1 acetonitrile:water solution mixture.[92]

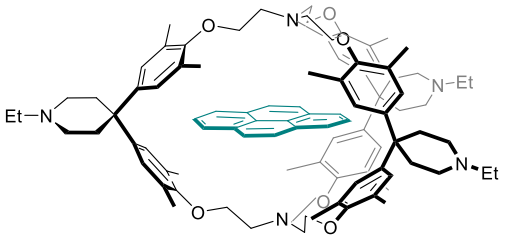

pyrene⊂**28**

Figure 18. Line-drawing structure of the pyrene⊂**28** complex.

Note that the cyclophanes discussed above are mono-cyclic, featuring two-dimensional cavities opened at two opposite ends. The construction of a hydrophobic binding pocket shielded from the bulk aqueous solution requires the design of receptors with pre-organized, three-dimensional structures. This issue was addressed by Diederich and co-workers using bi-cyclic cyclophanes. Cyclophane **28** bears five tertiary amines which deliver solubility in water. The binding pocket of **28** can accommodate poly-cyclic aromatic hydrocarbons. The aromatic guests are sited in the plane defined by the three spiro-carbons of the receptor. Remarkably, the pyrene⊂**28** inclusion complex is thermodynamically highly stable in water, K_a = 6 x 10^6 M^{-1} (Figure 18). The hydrophobic effect, dispersion and dipole-induced-dipole interactions play key roles to achieve high levels of binding affinity in the bi-cyclic cavity of **28**.[68,93]

1.2.2 Pillar[n]arenes

Pillar[n]arenes (n = 5-10) are synthesized by the acid-catalyzed condensation of 1,4-di-alkoxy-substituted benzenes and paraformaldehyde. The *para*-benzene units are connected at their 2- and 5-positions by methylene bridges in a cyclic fashion (Figure 19a). Therefore, the aromatic panels of pillar[n]arenes freely rotate around the methylene bridges. This motion is fast on the ^{1}H NMR chemical shift timescale. The cavity of pillar[n]arenes is electron-rich and hydrophobic, and it is opened at two opposite ends to the bulk solution. They are able to accommodate size and shape complementary electron-deficient guests.[15,17]

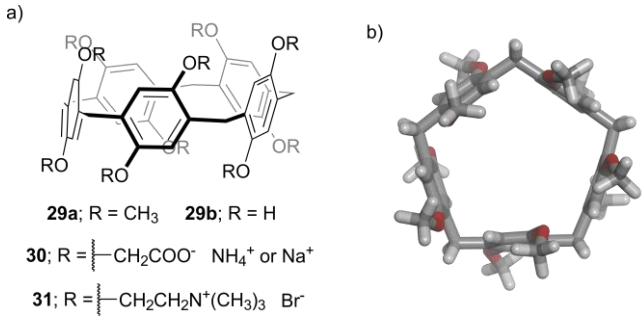

Figure 19. a) Line-drawing structures of pillar[5]arenes **29**-**31** and b) energy minimized structure (MM3) of **29a**. The pillar[5]arene is depicted in stick representation.

Pillar[5]arene was introduced by Ogoshi and co-workers in 2008. The structure of pillar[5]arene resembles a pentagon featuring a cavity diameter of *ca.* 5 Å (Figure 19b). The size of the cavity is similar to that of *α*-cyclodextrin. For example, **29a** and **29b** bear methoxy and hydroxyl substituents, respectively, and are soluble in most common organic solvents.[94] Nevertheless, the functionalization of the phenolic OHs with ionizable or charged groups renders water-soluble pillar[5]arenes.

Water-soluble pillar[5]arenes **30** and **31** are decorated with carboxylate and ammonium residues, respectively (Figure 19a). These pillar[5]arenes and bigger analogs (pillar[n]arenes, n = 6-10) bind charged organic guests in water,[95] stablishing 1:1 inclusion complexes in most cases. The complexes are stabilized by a combination of the hydrophobic effect, π-π, CH-π and charge-transfer interactions. The ionizable or charged groups at the portals of the receptor's cavity establish Columbic interactions with the charged residues of bound guests.[4,30] For example, the deca-carboxylate pillar[5]arene receptor **30** and di-methyl viologen **32** form a 1:1 inclusion complex featuring a binding constant value K_a = 8.2 x 10^4 M^{-1} in water (Figure 20).[96] Interestingly, the di-cationic guest **32** threads the cavity of pillar[5]arene **30**, featuring a pseudo-rotaxane-like topology. The inclusion complexes of pillar[5]arenes and 1,4-*bis*-(pyridinium)butane guests display a similar binding geometry.[97]

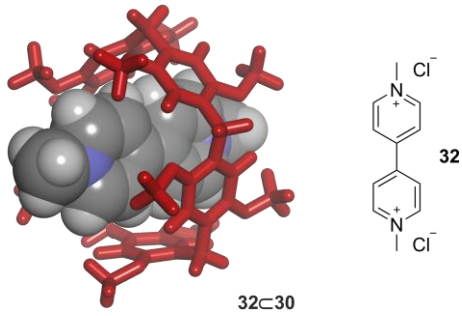

Figure 20. (left) Energy minimized structure (MM3) of the **32⊂30** complex and (right) line-drawing structure of **32**. Pillar[5]arene (red) is depicted in stick representation. Bound guest is shown as CPK model. The alkyl substituents of the receptor are pruned to methyl groups to ease the calculation.

Mukherjee and co-workers investigated the association process of secondary di-alkyl ammonium guests **33a**,**b** with the deca-carboxylate pillar[5]arene **30** (Figure 21a). The analysis of the ^{1}H NMR titration spectra indicated that the receptor, with any of the two guests, experienced fast dynamics on the chemical shift timescale. This is a common feature of receptors opened at two ends. One *N*-alkyl substituent of **33a** or **33b** is bound to the pillar[5]arene's cavity, whereas the other substituent is exposed to the bulk aqueous solution. The ammonium group of the guest is involved in multiple electrostatic interactions with the carboxylate residues at one of the two portals of the cavity. The association constant values are 5.9 x 10^3 M^{-1} and 2.8 x 10^4 M^{-1} for the **33a⊂30** and **33b⊂30** complexes, respectively.[98]

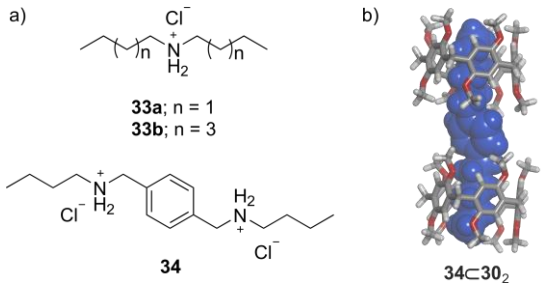

Figure 21. a) Line-drawing structures of **33a**, **33b** and **34**; b) energy minimized structure (MM3) of the putative **34⊂30**$_2$ complex. The pillar[5]arenes are depicted in stick representation and the bound guest (blue) is shown as CPK model. Alkyl substituents are pruned to methyl groups to ease the calculations.

Remarkably, di-ammonium **34** and deca-carboxylate pillar[5]arene **30** form a 1:2 guest/host complex (Figure 21b). The *para*-xylene spacer between the two ammonium cations of **34** is optimal for the formation of the ternary complex in water. Nevertheless, the binding constant values for the first and second binding events, K_a (**34⊂30**) = 6.2 x 10^2 M^{-1} and K_a (**34⊂30** → **34⊂30**$_2$) = 1.7 x 10^2 M^{-1}, indicate that the process is not cooperative ($\alpha = 4 \times K_{1:2}/K_{1:1} \sim 1$).[98]

The deca-carboxylate receptor **30** also binds L-arginine, L-lysine and L-histidine with high-binding affinity (K_a ~ 10^3 M^{-1}). The binding selectivity towards these amino acids is remarkable owing to the additional electrostatic interactions established between the ammonium group at the side chain of the amino acids and the carboxylate residues at the portals of the receptor.[27]

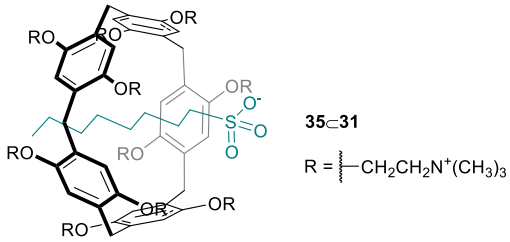

Figure 22. Line-drawing structure of the **35⊂31** inclusion complex.

As discussed above, deca-carboxylate pillar[5]arene **30** is a good receptor for positively charged guests, but it cannot bind negatively charged counterparts. In this respect, deca-ammonium pillar[5]arene **31** (Figure 19a) recognizes negatively ionized or charged guests, such as carboxylic acids and sulfonates. Huang *et al.* reported the binding studies of 1-octylsulfonate **35** with the deca-ammonium receptor **31**. The **35⊂31** complex features an inclusion binding geometry in which the octyl chain of the guest is bound into the receptor's cavity. The sulfonate group of **35** is then involved in electrostatic interactions with the ammonium groups of the receptor (Figure 22). The combination of the host-guest interactions involved in **35⊂31** translates into K_a = 1.3 x 10^4 M^{-1}. The magnitude of this constant value is in line with the affinities displayed by the deca-carboxylate receptor **30** towards cationic guests.[27,99] Other examples using 4-methylbenzene sulfonate as guest have been reported by García-Rio *et. al*.[100,101]

The deca-ammonium pillar[5]arene **31** acts as a wheel in the complexation of long-chain *α,ω*-di-acids in water. The aliphatic chain of the later guests threads the aromatic cavity of **31**, aided by the hydrophobic effect and the establishment of multiple CH-π interactions. The ionized carboxylic acids of the guest and the cationic groups at the portals of the host are attracted by Columbic forces. In general, the binding constants of the di-carboxylate⊂**31** complexes are in the order of 10^4 M^{-1}.[102]

The binding properties of the deca-ammonium receptor **31** were also investigated using a series of neutral guests (alkanes, aliphatic alcohols, xylenes, etc.) in water. The complexation of neutral substrates by the pillar[5]arenes is driven by the hydrophobic effect, π-π, CH-π and van der Waals interactions. The binding constant values of the later complexes are in the order of 10-10^2 M^{-1}. This results from the lack of Columbic interactions. For example, the binding constant of aliphatic alcohols increases with the length of the non-polar substituent: *n*-pentanol > *n*-butanol > *n*-propanol.[103]

Pillar[6]arene possesses an hexagonal cavity of *ca.* 6.7 Å diameter. The size of the cavity is slightly larger than that of *β*-cyclodextrin. Water-soluble pillar[6]arenes **36**-**39** are functionalized with carboxylate, tri-methylammonium, pyridinium or 1-methyl-1H-imidazolium groups (Figure 23). Huang and co-workers reported a dodeca-carboxylate pillar[6]arene **36** featuring a cmc value of *ca.* 10^{-4} M. The binding studies of receptor **36** were conducted from dilute solutions by UV/Vis and fluorescence spectroscopies. Dodeca-carboxylate **36** binds pyridinium cations, in agreement with the previous results discussed for deca-carboxylate pillar[5]arene. For example, the binding constant value of the 1:1 inclusion complex between 1-octylpyridinium **40** and pillar[6]arene **36** is 3.3 x 10^5 M^{-1} in aqueous solution. Note that the association constant value of the later complex, **40**⊂**36**, is one order of magnitude larger than that for the complex of 1-octylsulfonate **35** and deca-ammonium pillar[5]arene **31**. Most likely, the increase in the number of Columbic interactions in the **40**⊂**36** complex and the hydrophobic character of the pyridinium cation of the guest translate into a larger binding affinity. The pillar[6]arene **36** forms thermodynamically highly stable complexes with pyrene derivatives as well (K_a ~ 10^5 M^{-1}).[17,104]

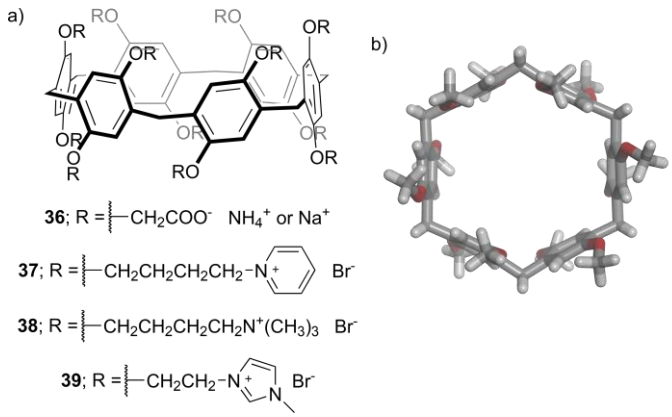

Figure 23. a) Line-drawing structures of pillar[6]arenes **36**-**39** and b) energy minimized structure (MM3) of a pillar[6]arene. The receptor is depicted in stick representation and the water-solubilizing groups are pruned to methyl groups.

The cavity size of pillar[6]arenes can fully accommodate *trans*-azobenzenes. The cationic *trans*-azobenzene **41** (Figure 24a) is included in the aromatic cavity of pillar[6]arene **36**. However, the pillar[6]arene cannot bury the azo bond of the *cis*-isomer **41**. In this case, *cis*-**41** forms an inclusion complex with **36** in which the tri-methylammonium group of the guest is bound into the receptor's cavity (Figure 24b). The establishment of cation-π and CH-π interactions between the ammonium group of the guest and the electron-rich aromatic panels of the receptor are responsible for the binding geometry adopted in the *cis*-**41**⊂**36** complex. The different binding modes in the two complexes, *trans*-**41**⊂**36** and *cis*-**41**⊂**36**, translate into one order of magnitude difference in the constant values, favoring the complexation of *trans*-**41**.[105]

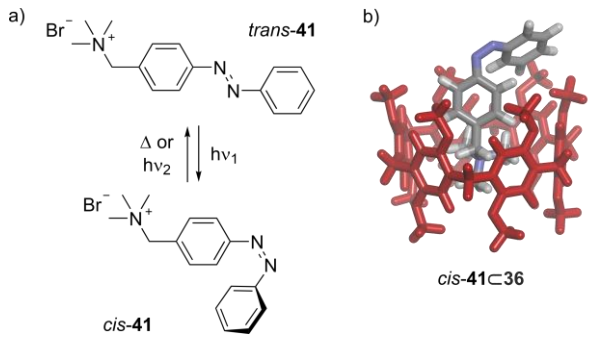

Figure 24. a) *Trans*/*cis* isomerization of azobenzene **41** and b) energy minimized structure (MM3) of the *cis*-**41**⊂**36** complex. The host (red) and the guest are depicted in stick representation. Alkyl substituents of **36** are pruned to methyl groups to ease the calculations.

Chen *et al.* reported a pillar[6]arene **37** decorated with twelve pyridinium cations, which impart water solubility (Figure 23a). They investigated the binding of naphthalene sulfonates, **42** and **43**, with **37** in water. The complexation induced shifts (Δδ) of the aromatic protons of the guests were in the range between -0.3 to -0.5 ppm. This indicated that the naphthalene group of the guests is included in the aromatic cavity of the receptor. The binding constant values of the **42**⊂**37** and **43**⊂**37** inclusion complexes are 3.8 x 10^4 and 2.1 x 10^5 M^{-1}, respectively, by means of fluorescence titration experiments. Remarkably, the binding constant of **43**⊂**37** is almost one order of magnitude larger than that of **42**⊂**37**. This result was explained considering the additional Columbic interactions established between the extra sulfonate group present in **43** and the cationic pyridinium groups of the receptor.[106] The dodeca-tri-methylammonium pillar[6]arene **38** (Figure 23a) binds the naphthalene sulfonate **42** featuring a binding constant value similar to that of the **42**⊂**37** complex.[107]

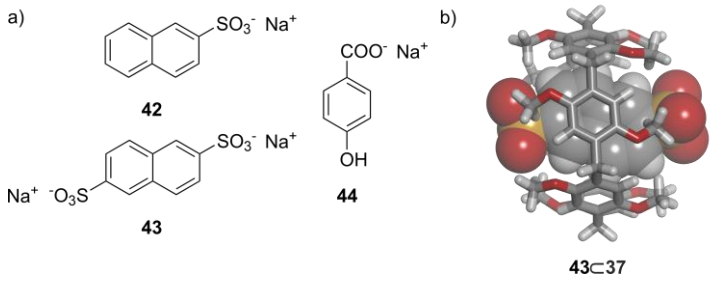

Figure 25. a) Naphthalene sulfonates, **42** and **43**, and 4-hydroxybenzoate **44**; b) energy minimized structure (MM3) of the **43**⊂**37** complex. The host is depicted in stick representation and the guest is shown as CPK model. The alkyl substituents of the receptor are pruned to methyl groups to ease the calculations.

The interaction between 4-hydroxybenzoate **44** (Figure 25a) and dodeca-imidazolium pillar[6]arene **39** (Figure 23a) was studied by fluorescence spectroscopy. Remarkably, the binding

constant value of the **44⊂39** complex was determined to be 3.2 x 10^6 M^{-1}. The authors suggested that, in the **44⊂39** inclusion complex, hydrogen-bonding interactions are established between the carboxylate group of the bound guest and the hydrogen atom of the imidazolium cations, NC*H*N, at one of the two portals of the receptor's cavity. These additional interactions might enhance the binding affinity.[108]

Apart from the applications of pillar[n]arenes in controlling the uptake/release of guests or as artificial channels in lipid membranes,[27] the dodeca-carboxylate pillar[6]arene **36** has been applied in the protection of azastilbene **45** in water (Scheme 1). Azastilbene **45** undergoes hydration upon photo-irradiation at 365 nm in the bulk aqueous solution producing **46** (Scheme 1). Nevertheless, in the presence of receptor **36**, the concentration of free azastilbene **45** is significantly reduced, K_a (**45⊂36**) ~ 10^7 M^{-1}. This produces a dramatically decrease in the rate of the photo-hydration reaction. The pillar[6]arene **36** functions as a supramolecular protecting group for the photo-labile guest **45**, presumably absorbing the high-energy photons from the light source.[109]

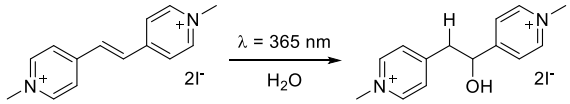

Scheme 1. Photo-hydration reaction of azastilbene **45** to give **46**.

Pillar[7]arene features a cavity diameter of *ca.* 8.7 Å, similar to that shown by *γ*-cyclodextrin. This larger pillar[n]arene derivative is soluble in water when, for example, tri-methylammonium groups are incorporated in the structure. The water-soluble pillar[7]arene **47** binds a pyrene derivative **48** stablishing a 1:1 host/guest inclusion complex (Figure 26). ITC titration experiments indicated that the association constant of the **48⊂47** complex is 1.3 x 10^4 M^{-1}. Interestingly, the binding process is driven by both enthalpy and entropy, ΔH = -2.2 kcal·mol^{-1} and $T\Delta S$ = 3.4 kcal·mol^{-1}. Note that the entropic contribution is larger than the enthalpy. Most likely, this is derived from the desolvation of the large aromatic surface areas of both host and guest upon complexation.[110]

Recently, Ma and co-workers further explored the driving forces involved in the host-guest binding equilibria of carboxylate pillar[n]arenes (n = 5, 6 and 7) and a series of guests. The binding studies were conducted in 20 mM sodium phosphate buffer at pH ~ 7.4. They concluded that di-alkyl ammonium substrates are bound to the negatively charged pillar[n]arenes through the hydrophobic effect, CH-π and Columbic interactions. Similarly, cationic aromatic guests are bound with the help of the later interactions and additional π-π stacking. The binding constant values for these complexes are in the range of 10^3-10^7 M^{-1}, and they support the important role of Columbic interactions to achieve high levels of binding affinity using pillar[n]arene receptors in water.[111]

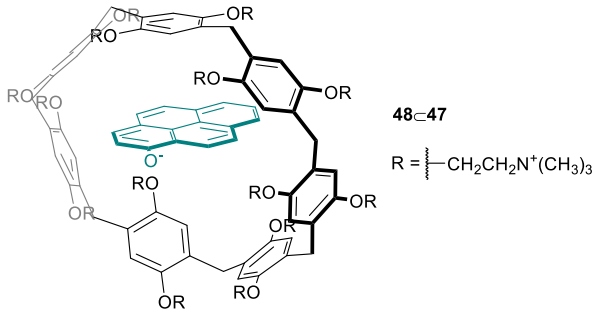

Figure 26. Line-drawing structure of the **48⊂47** complex. The guest **48** is highlighted (green).

1.2.3 Cucurbit[n]urils

The condensation reaction of glycoluril and formaldehyde in acidic media produces cyclic and acyclic cucurbit[n]urils. The cyclic cucurbit[n]urils (n = 5-8, **49**-**52**) feature a pumpkin-like structure, in which the glycoluril units are linked together by 2 x n methylene bridges (Figure 27). In contrast to the pillar[n]arenes (Section 1.2.2), the glycoluril units cannot freely rotate around the methylene junctions, leading to relatively rigid structures.[112] All cyclic cucurbit[n]urils display a cavity depth of *ca.* 9.1 Å, but they have different cavity diameters. The cavity volume of the cyclic cucurbit[n]urils varies from 82 (**49**) to 479 Å^3 (**52**) (Figure 27).[113,114]

Despite the recent applications reported for acyclic cucurbit[n]urils, these receptors are outside the scope of this chapter and the reader is addressed to other literature references.[15,115,116,117,118,119,120]

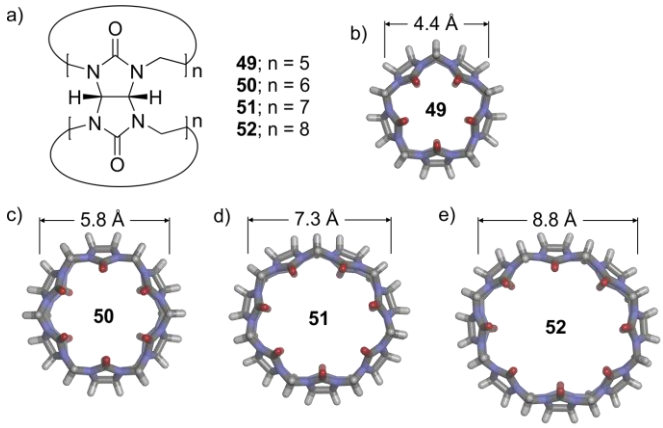

Figure 27. a) Line-drawing structures of cucurbit[n]urils (n = 5-8) **49**-**52**; energy minimized structures (MM3): b) **49**; c) **50**; d) **51** and e) **52**. The structures are depicted in stick representation and the diameter of the cavities is indicated.

The cyclic cucurbit[n]urils feature a hydrophobic cavity opened at two polar ends. The portals of the cavity are defined by the carbonyl moieties of the glycoluril panels. In this respect, the interior

of the cucurbit[n]uril receptors is suitable for the inclusion of non-polar residues. The carbonyl groups of these receptors are keen to be involved in dipole interactions with complementary functional groups of bound guests.[30,112,114] Note that the cavity of cucurbit[n]urils displays a very low polarizability, comparable to the gas phase.[2]

The solubility of the cucurbit[n]urils **49**-**52** in aqueous solution is remarkably different. Cucurbit[6]uril **50** and cucurbit[8]uril **52** are poorly soluble (< 0.1 mM), whereas cucurbit[5]uril **49** and cucurbit[7]uril **51** possess good solubility in water (20-30 mM) (Figure 27).[113] It is worth mentioning that these cucurbit[n]urils are neutral receptors and their polar ureido groups impart water solubility. The protonation or coordination of alkali ions to the carbonyl oxygen atoms increase the solubility of cucurbit[n]urils in water.[27,112]

In general, the inclusion complexes of cucurbit[n]urils **49**-**52** with non-polar or positively charged guests are thermodynamically and kinetically stable. Most likely, the kinetic stability is derived from the shortening of the diameter of the portals in *ca.* 2 Å with respect to the internal cavity.[27,112] The complexes of cucurbit[n]urils with cationic guests are characterized by association constant values that are three orders of magnitude larger than those with structurally related neutral guests. This results from the further stabilization of the charged complexes by cation-dipole interactions.[30] The complexation process of size and shape complementary guests and cucurbit[n]urils is driven by the release of “high-energy” water molecules from the receptor’s cavity to the bulk solution (*i.e.* the “non-classical” hydrophobic effect) and the difference in dispersion interactions between the interior of the cyclic host and the aqueous solution.[30] The “non-classical” hydrophobic effect is maximized in the case of cucurbit[7]uril **51**, in which a modest number of bound water molecules cannot satisfy their hydrogen-bonding characteristics.[30,121] Despite the open cavity featured by cucurbit[n]urils, their inclusion complexes obey the 55% packing coefficient rule reported by Rebek and co-workers.[114]

In general, cucurbit[5]uril **49** binds small molecules, whereas cucurbit[6]uril **50** is able to accommodate aliphatic residues. The larger cavities provided by cucurbit[7]uril **51** and cucurbit[8]uril **52** can accommodate aromatic guests.[114]

In particular, cucurbit[5]uril **49** displays a small cavity volume limiting the number of complementary guests. For example, **49** binds neutral small molecules, such as methanol and acetonitrile, di-atomic gases (*e.g.* N_2, O_2, CO and CO_2) and noble gas atoms (*e.g.* Ar). Owing to the polar character of the cavity portals, **49** also forms complexes with either inorganic or organic cations, such as Pb^{2+} or ammonium salts, respectively. The bound cationic guests seal the hydrophobic cavity of cucurbit[5]uril.[113,114] On the other hand, Nau and co-workers recently demonstrated that the binding process of noble gases to cucurbit[5]uril **49** is driven by differences in cavitation energies, *i.e.* the recovery of the formed void cavities in the receptor’s binding site and in the bulk aqueous solution.[122]

Cucurbit[6]uril **50** features a cavity diameter of 5.8 Å (Figure 27).[112] In the solid state, three water molecules are included in the cavity of **50**. Most likely, the cavity of the receptor is also solvated in water solution, but the bound water molecules are released to the bulk upon guest binding.[113] Aliphatic (di)-ammonium cations bind to **50** stablishing 1:1 inclusion complexes. For example, the *n*-butyl chain of **53**•H^+ fills the cavity volume of **50** and, therefore, it forms the most stable complex of the *n*-alkyl ammonium series, K_a (**53**•H^+⊂**50**) = 1.0 x 10^5 M^{-1} (Figure 28a). For di-ammonium salts, hexane-1,6-di-ammonium **54**•$2H^+$ is a perfect fit for receptor **50** (Figure 28a). **54**•$2H^+$ threads the cavity of the cucurbit[6]uril. This binding geometry places the two ammonium groups of the guest near the two opposite polar portals of the receptor, K_a (**54**•$2H^+$⊂**50**) = 2.8 x 10^6 M^{-1} (Figure 28b). The 1:1 inclusion complexes are stabilized by the combination of the hydrophobic effect, ion-dipole and hydrogen-bonding interactions. The cucurbit[6]uril **50** binds neutral molecules with good binding affinities as well. For example, the complexation of tetrahydrofuran to **50** is characterized by a binding constant value K_a = 1.7 x 10^3 M^{-1}.[112,113,114] It is worth mentioning that the above complexes were formed in a 1:1 formic acid:water solution mixture owing to the low solubility of **50** in pure water. Nevertheless, the binding constant values of the same complexes are similar in 50 mM aqueous NaOAc buffer at pH ~ 4.7 (K_a (**53**•H^+⊂**50**) = 9.1 x 10^5 M^{-1}).[123]

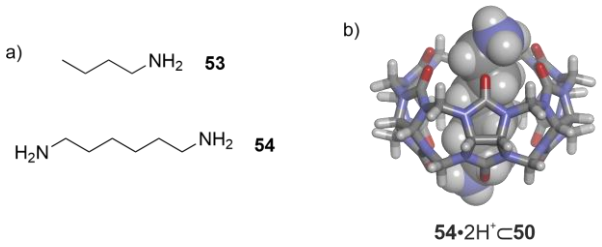

Figure 28. a) Line-drawing structures of **53** and **54**; b) energy minimized structure (MM3) of the **54**•$2H^+$⊂**50** complex. The cucurbit[6]uril is depicted in stick representation and the bound guest is shown as CPK model.

Recently, Nau and co-workers reported the binding studies of di-iodine **55** with cucurbit[6]uril **50**. The corresponding 1:1 inclusion complex, **55**⊂**50**, features a high association constant value, K_a = 1.4 x 10^6 M^{-1}. The complex is stabilized by the hydrophobic effect and, more interestingly, by halogen-bonding interactions between the iodine atoms of **55** and the π-system of the carbonyl groups of **50** (Figure 29).[124]

As discussed above for cucurbit[5]uril **49**, inorganic cations also bind to the polar groups at the cavity portals of **50**. Remarkably, the binding constant value of the later complexes are in the order of 10^2-10^3 M^{-1}. This suggests that cations likely interfere in the formation of inclusion complexes.[113]

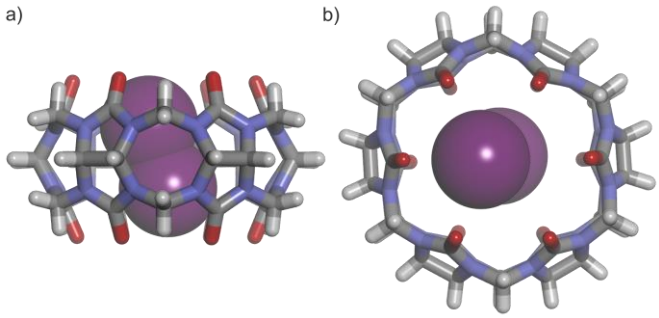

Figure 29. X-ray structure of the **55⊂50** complex: a) side and b) top views. The receptor is depicted in stick representation and the guest is shown as CPK model.

Cucurbit[6]uril **50** has been applied in the construction of (pseudo)-rotaxanes[125] and in chemical transformations. For example, **50** catalyzes the 1,3-dipolar cycloaddition of alkynes and azides, *a.k.a* "click" reaction, in water (Scheme 2). Both alkyne and azide guests, bearing ammonium groups, form inclusion complexes with **50**. The reacting groups of the guests are included in the hydrophobic cavity of the receptor leading to an increase of local concentration. This produces a rate enhancement of the cycloaddition reaction. The dimensions and geometry of the receptor's cavity also impose regioselectivity to the "click" reaction favoring the formation of the 1,4-substituted product.[112,113] However, the catalyst, **50**, suffers product inhibition. This issue is common for many supramolecular containers applied in catalysis.

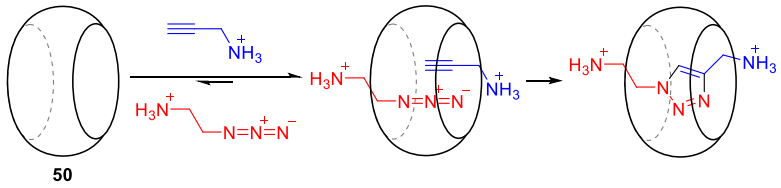

Scheme 2. "Click" reaction catalyzed by cucurbit[6]uril **50**.

One of the main limitations of cucurbit[6]uril **50** is its low solubility in water. However, Kim *et al.* designed a cyclohexyl-substituted cucurbit[6]uril **56** whose solubility is 0.2 M in water (Figure 30a). The cavity of **56** is analogous to that of **50**. In contrast, the binding constant values of the inclusion complexes of **56** in water are two-five orders of magnitude larger than those reported for **50** in 1:1 formic acid:water. For example, the complexes between aliphatic ammonium guests and **56** feature binding constant values K_a = 10^4-10^8 M^{-1}. In the same vein, the binding constants of *α,ω*-aliphatic di-ammonium salts increase up to 10^7-10^{10} M^{-1}. These suggest that both inorganic and ammonium cations compete for binding to the carbonyl groups of receptor **50** in acidic or alkali aqueous solution. Remarkably, the tetra-protonated spermine **57**•$4H^+$ forms a thermodynamically highly stable complex with **56** featuring a binding constant value of 3.4 x 10^{12} M^{-1} (Figure 30b).[123]

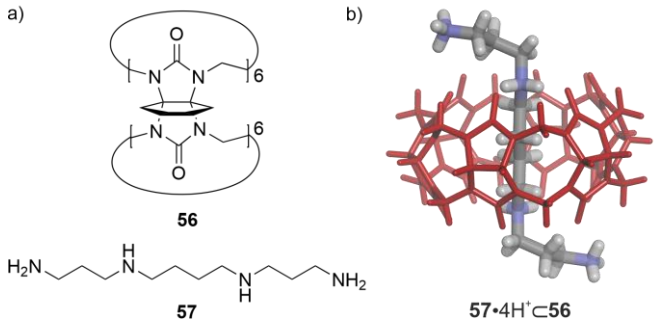

Figure 30. a) Line-drawing structures of cyclohexyl-substituted cucurbit[6]uril **56** and spermine **57**; b) energy minimized structure (MM3) of **57**•4H$^+$⊂**56**. The host (red) and the guest are depicted in stick representation. The cyclohexyl groups of **56** are pruned to hydrogen atoms to ease the calculation.

Cucurbit[7]uril **51**, featuring a cavity volume of 279 Å^3,[113] maximizes the "non-classical" hydrophobic effect for binding (Figure 27). The association constant values of the 1:1 inclusion complexes derived from **51** are in the range of 10^7-10^{17} M^{-1}. As discussed above, complexation is stronger in pure water than in buffer solution due to the competition of metal ions for the oxygen atoms at the portals of the receptor.[2] Cucurbit[7]uril **51** binds neutral and charged guests, such as aromatic, adamantane and ferrocene derivatives.[113]

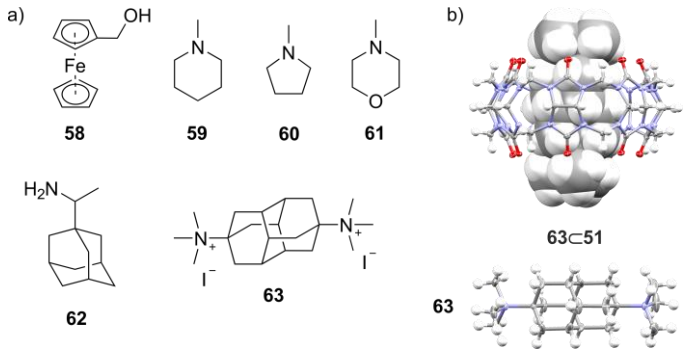

Figure 31. a) Line-drawing structures of ferrocene **58**, tertiary amines **59**-**61**, rimantadine **62** and di-amantane **63**; b) X-ray crystal structures of **63**⊂**51** (top) and **63** (bottom). The structures are shown in ORTEP view with thermal ellipsoids set at 50% probability. Hydrogen atoms are shown as fixed-size spheres of 0.3 Å radius. Bound guest is shown as CPK model.

Neutral ferrocene **58** binds to cucurbit[7]uril **51** with high affinity, K_a = 3.2 x 10^9 M^{-1} (Figure 31a). The ferrocene guest **58** fills the cavity volume of the receptor. Additionally, ferrocene derivatives decorated with ammonium groups boost the binding constant values up to 10^{12}-10^{15} M^{-1}. These results support the significant role of cation-dipole interactions in the formation of supramolecular complexes derived from cucurbit[n]uril receptors.[2,27]

The protonated tertiary amines, *N*-methyl piperidine **59**, *N*-methyl pyrrolidine **60** and *N*-methyl morpholine **61**, form 1:1 inclusion complexes with cucurbit[7]uril **51** in 50 mM sodium acetate buffer at pH ~ 4.7 (Figure 31a). The binding constant values of these complexes are in the order of 10^6-10^7 M^{-1}. Interestingly, the ^{1}H NMR analyses revealed that the ammonium cation of the bound guests is included in the hydrophobic cavity of the receptor **51**.[126]

Cucurbit[7]uril **51** also binds protonated amino-adamantyl derivatives featuring K_a = 10^{12}-10^{14} M^{-1} in water. The adamantyl group is a perfect fit for the cavity of receptor **51**. In these cases, the adamantyl group is buried in the receptor's cavity and the ammonium group is exposed to the bulk solution. The later is involved in cation-dipole interactions with the oxygen atoms at one of the two polar regions of the receptor. For example, the binding constant value of rimantadine **62**•H^+ with **51** is K_a = 4.2 x 10^{12} M^{-1} in aqueous buffer solution at pH ~ 4.7 (Figure 31a).[4,15]

The understanding of the driving forces involved in the binding equilibria of cucurbit[7]uril **51** is required for the design of efficient guests. Di-amantane di-ammonium **63** and receptor **51** form a 1:1 inclusion complex, **63**⊂**51**, characterized by a binding constant value K_a = 7.2 x 10^{18} M^{-1} in pure water and K_a = 1.9 x 10^{15} M^{-1} in 50 mM NaOAc buffer (Figure 31a). The crystal structure of the **63**⊂**51** complex shows that the two ammonium cations of **63** establish a total of fourteen cation-dipole interactions with the carbonyl groups of the receptor (Figure 31b). Furthermore, di-amantane **63** and cucurbit[7]uril **51** are size and shape complementary, maximizing non-polar contacts.[127] The inclusion of the non-polar section of **63** into the hydrophobic cavity of **51** is an enthalpically driven process. On the contrary, the interaction of the ammonium cations with the carbonyl groups of the receptor is favored by entropy.[2,27]

Based on the complexation data obtained by several research groups using cucurbit[7]uril **51**, the introduction of a larger number of cationic charges in the guest's scaffold does not impact on the enthalpic contribution for complex formation (*ca.* -21 kcal·mol^{-1}), but significantly affect the entropic component favoring the binding process (change of *ca.* 4 kcal·mol^{-1}). Certain inclusion complexes of **51** seem to overcome the enthalpy-entropy compensation effect.[2]

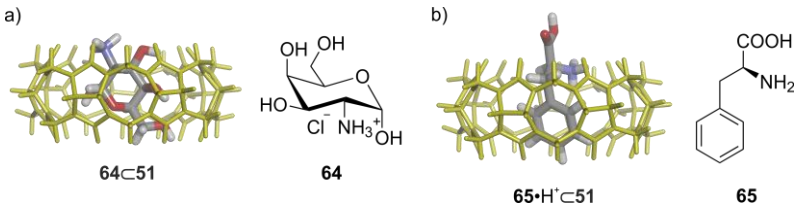

Figure 32. Energy minimized structures (MM3) and line-drawing structures: a) **64**⊂**51** and **64** (*α*-anomer is depicted); b) **65**•H^+⊂**51** and **65**. The cucurbit[7]uril **51** (yellow) and the guests are depicted in stick representation.

Furthermore, receptor **51** binds protonated amino-saccharides, such as D-galactosamine hydrochloride **64**, with good binding affinity (K_a = 10^3-10^4 M^{-1}). It is worth mentioning that the *α*/*β*-

mutarotation of saccharides is slow on the ^{1}H NMR chemical shift timescale and the *α*/*β* ratio is *ca.* 65:35 in water. Nevertheless, 2D NMR experiments demonstrated that the bound amino monosaccharide **64** is the *α*-anomer. Most likely, this isomer is stabilized by multiple cation-dipole interactions when is bound to the cucurbit[7]uril (Figure 32a).[4,128]

Owing to the good binding performance of cucurbit[7]uril towards ammonium guests, **51** is a suitable receptor for the recognition of aromatic amino acids in acidic aqueous solution. In this respect, the aromatic residue of the amino acid is included in the hydrophobic cavity of **51** and the ammonium group interacts electrostatically with one of the receptor's polar portals. The binding constant values of the amino acid complexes are remarkably high. For example, phenylalanine **65** and **51** forms a 1:1 complex, **65**•H^+⊂**51**, featuring K_a = 10^5-10^6 M^{-1} (Figure 32b). More interestingly, the cucurbit[7]uril **51** displays modest binding selectivity for phenylalanine versus other aromatic amino acids.[129] This has been applied by Urbach, Kim and co-workers in the analysis of peptide sequences by mass spectrometry. They showed that receptor **51** enhances the signal in the analysis because, most likely, it facilitates the ionization of the sample.[130]

Cucurbit[7]uril **51** has been applied in supramolecular catalysis. Scherman and co-workers investigated the effect of **51** in the intramolecular Diels-Alder reaction of *N*-allyl-2-furfurylamines, such as **66** (Figure 33a). In the absence of the receptor, **66** reacts to produce the corresponding Diels-Alder product in less than 10% yield after 25 days. However, the yield of the same reaction increases up to 90% in only 6 h when cucurbit[7]uril **51** is present. The cucurbit[7]uril **51** binds the reactant **66**•H^+ in a hairpin-like conformation in which the diene and the dienophile groups are in close proximity (Figure 33b). The stabilization of the bound reactant in this conformation decreases the energy barrier of the intramolecular Diels-Alder reaction.[131]

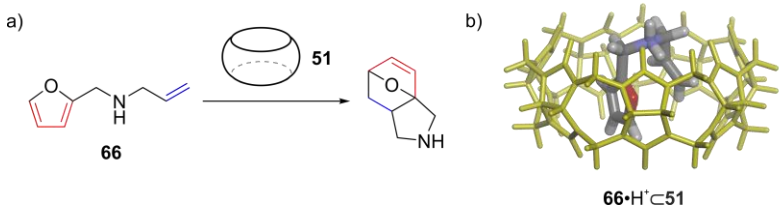

Figure 33. a) Diels-Alder reaction of *N*-allyl-2-furfurylamine **66** and b) energy minimized structure (MM3) of **66**•H^+⊂**51**. The host (yellow) and the guest are depicted in stick representation.

In general, cucurbit[n]urils **49**-**51** cannot form inclusion complexes of stoichiometry larger than 1:1 owing to the limited dimensions of their cavities. Nevertheless, cucurbit[8]uril **52** has a cavity diameter of 8.8 Å (Figure 27) which enables the formation of homo-ternary 2:1 and hetero-ternary 1:1:1 inclusion complexes.[15]

Cucurbit[8]uril **52** and the electron-deficient di-methyl viologen **32** (Figure 20) form a thermodynamically stable 1:1 inclusion complex stabilized by the hydrophobic effect and cation-

dipole interactions. The binding constant value of the **32⊂52** complex is 8.5 x 10^5 M^{-1} by means of ITC titration experiments.[132] Di-methyl viologen **32** fills half of the cavity of **52** and, therefore, the free space is similar to the cavity size of cucurbit[7]uril **51**. However, Columbic repulsions avoid the binding of a second viologen molecule in the cavity of the **32⊂52** complex. Conversely, addition of the electron-rich 2,6-di-hydroxynaphthalene **67** to the **32⊂52** complex leads to the quantitative formation of the hetero-ternary [**67•32**]⊂**52** complex (Figure 34). The co-inclusion of **32** and **67** in the cavity of cucurbit[8]uril **52** is driven by the hydrophobic effect and the establishment of charge-transfer interactions between the two electronically complementary aromatic surfaces of the guests.[4,113,133]

This approach was applied for the recognition of tryptophan residues starting from the pre-formed **32⊂52** inclusion complex. The formation of the corresponding 1:1:1 complex produces the observation of the expected charge-transfer band between the bound viologen **32** and the indole group of tryptophan **68** (Figure 34a). This also produces the quenching of the fluorescence emission of the indole group. The stepwise binding constant for the inclusion of tryptophan **68** into the cavity of **32⊂52** is 4.3 x 10^4 M^{-1} in 10 mM sodium phosphate buffer at pH = 7. This process is enthalpically driven, ΔH = -10.6 kcal·mol^{-1}, and opposed by entropy, $T\Delta S$ = -4.2 kcal·mol^{-1}. The thermodynamic parameters are consistent with the "non-classical" hydrophobic effect operating in the formation of these inclusion complexes.[132,134]

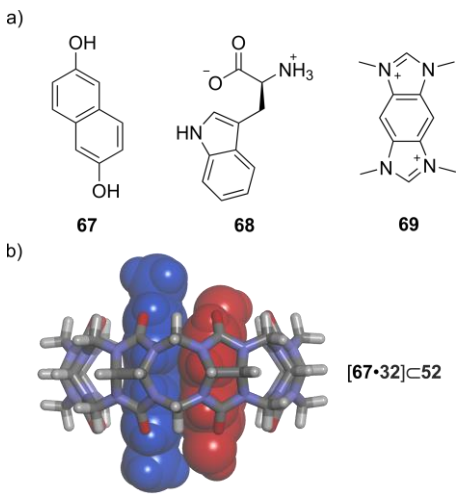

Figure 34. a) Line-drawing structures of molecules **67**-**69** and b) energy minimized structure (MM3) of the [**67•32**]⊂**52** hetero-ternary complex. The host is depicted in stick representation and the guest molecules are shown as CPK models (**32** in blue and **67** in red).

Scherman and co-workers replaced the viologen guest **32** in the **32⊂52** complex by the tetra-methyl benzo-*bis*-imidazolium **69** (Figure 34a). In the same vein, benzo-*bis*-imidazolium **69** and cucurbit[8]uril **52** form a 1:1 inclusion complex (K_a = 5.7 x 10^5 M^{-1}). The stepwise binding constant

for the inclusion of a second guest molecule into the cavity of the pre-assembled **69⊂52** complex lies in the range of 10^3-10^6 M^{-1}. The formation of the hetero-ternary inclusion complex induces the quenching of the fluorescence emission of bound **69**. For example, the association constant of **69⊂52** with **67** to give the [**67•69**]⊂**52** complex is 7.2 x 10^4 M^{-1}.[114,135] Interestingly, the 1:1 inclusion complex between *bis*-imidazolium **70** and cucurbit[8]uril **52** features a cage-like structure (Figure 35). The two terminal imidazolium cations of **70** seal the two opposite portals of the receptor **52**. The binding constant value of **70⊂52** is 1.9 x 10^6 M^{-1}, determined by ITC titration experiments. The **70⊂52** complex can accommodate small guest molecules in the free space of the cavity, leading to 1:1:1 hetero-ternary complexes. The stepwise constant value of this second binding event is in the order of 10^3 M^{-1}. Note that the cage-like **70⊂52** complex imposes size selectivity, precluding the co-inclusion of the larger 2,6-di-hydroxynaphthalene guest **67**.[136]

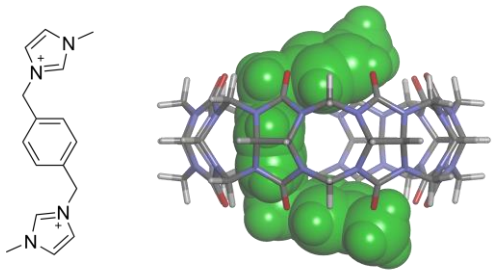

Figure 35. (left) Line-drawing structure of *bis*-imidazolium **70** and (right) energy minimized structure (MM3) of the **70⊂52** complex. The receptor is depicted in stick representation and the guest (green) is shown as CPK model.

Further investigations by Nau and co-workers demonstrated that the binding of an auxiliary guest into the cavity of cucurbit[8]uril **52** produces “high-energy” water molecules in the interior of the 1:1 complex. The bound water molecules are ejected to the bulk solution upon formation of the ternary complex. This process is characterized by a favorable enthalpy ($\Delta H < 0$) and an unfavorable entropy ($T\Delta S < 0$).[27,30,137]

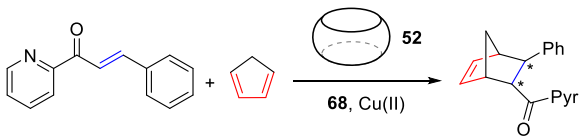

Scheme 3. Diels-Alder reaction of azachalcone and cyclopentadiene. Asterisks denote stereogenic centers.

In addition, cucurbit[8]uril **52** has been applied in catalysis. The outcome of the asymmetric Lewis acid-catalyzed Diels-Alder reaction of azachalcone and cyclopentadiene is significantly affected by the presence of cucurbit[8]uril **52** (Scheme 3). Receptor **52** is not chiral but an included amino acid in its cavity is used as quiral inductor in the later chemical transformation. Using tryptophan **68**, Cu(II) as Lewis acid and cucurbit[8]uril **52**, the yield of the reaction is *ca.* 70% with an enantiomeric

excess (e.e.) of up to 92%. The binding geometry of the inclusion complexes throughout the reaction is difficult to elucidate experimentally.[138]

1.2.4 Bambus[n]urils

Bambus[n]urils are cyclic covalent molecules opened at two opposite ends, whose structure resembles the form of a bamboo plant (Figure 36a). They are synthesized from 2,4-di-substituted-glycoluril and paraformaldehyde in the presence of an acid catalyst. In general, the conjugate base of the acid templates the cyclization step in the reaction. For example, the chloride complex crystallizes from the solution when HCl is used. The X-ray structure of the later complex supports the templating effect of the anion and suggests the application of bambus[n]urils as anion receptors (Figure 36b).[139,140]

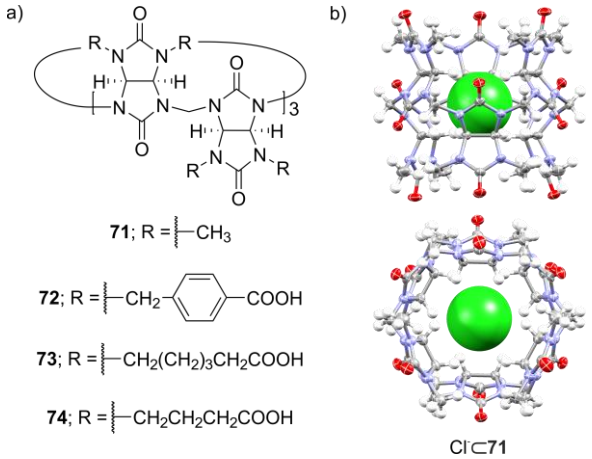

Figure 36. a) Line-drawing structures of bambus[6]urils **71**-**74** and b) X-ray crystal structure of the Cl^-⊂**71** complex. The structure is shown in ORTEP view with thermal ellipsoids set at 50% probability and hydrogen atoms are shown as fixed-size spheres of 0.3 Å radius. Chloride anion is shown as CPK model.

Bambus[n]urils combine the structural features of cucurbit[n]urils and hemi-cucurbit[n]urils (not discussed). The bambus[n]urils offer a hydrophobic cavity but are structurally flexible. The methine hydrogens of the glycoluril panels are oriented to the interior of the hydrophobic cavity. This makes bambus[n]urils as efficient receptors for anions. The bound anion is stabilized by twelve weak C-H···X^- hydrogen bonds. The electrostatic surface map of bambus[n]urils shows a positive region in the interior of the cavity and a negative region at the portals.[139,140] Nevertheless, anion binding using bambus[n]uril receptors is not only electrostatic. The modification of the pH or the ionic strength of the aqueous solutions does not impact on the association constants of these anionic complexes to a significant extent. These results point out that the Hofmeister effect is involved in the complexation process of anions to bambus[6]urils. Therefore, chaotropic anions show binding affinity values larger than kosmotropic counterparts.[141,142]

Bambus[6]uril **71** bears *N*-methyl substituents at the glycoluril panels and is not soluble in water.[140] The cavity of **71** features a diameter of 6.4 Å and a depth of 12.7 Å. Thus, the bambus[6]uril's cavity is *ca.* 4 Å deeper than that of cucurbit[6]uril (Figure 36a).[139] Titration experiments of receptor **71** in 1:1 water:acetonitrile solvent mixture indicated that the binding constants of the complexes with halide anions follow the order: $I^- > Br^- > Cl^- > F^-$. For example, the association constant value for the $I^-\subset$**71** complex is 8.9 x 10^5 M^{-1} in the above mentioned solvent mixture.[139,143]

The functionalization of the available nitrogen atoms of the structure of bambus[6]urils with carboxylic acid groups produces water-soluble receptors, **72**-**74** (Figure 36a). The cavity of bambus[6]urils accommodates a water molecule in the solid state. Hence, it is expected the release of the bound molecule upon anion binding in water solution.[4] The bound anion is then shielded from the bulk aqueous solution. These suggest that solvation/desolvation processes of free and bound species are important in these complexes.[29,141]

Bambus[6]uril **72** bears twelve benzoic acid groups that warrant solubility in water. In general, receptor **72** binds inorganic anions in aqueous solution (20 mM K_2DPO_4 buffer) with high-binding affinity. The anions featuring a modest binding affinity, K_a (F^-,Cl^-,$CN^-\subset$**72**) = 10^2-10^3 M^{-1}, form labile complexes, *i.e.* chemical exchange is fast on the ^{1}H NMR chemical shift timescale. On the contrary, anions that bind strongly to the bambus[6]uril receptor, K_a (Br^-,I^-,$NO_3^-\subset$**72**) = 10^5-10^7 M^{-1}, are kinetically stable. In the halide series, the binding constant for the chloride anion is K_a ($Cl^-\subset$**72**) = 9.1 x 10^2 M^{-1}. This value increases up to 1.0 x 10^7 M^{-1} for the $I^-\subset$**72** complex. Nevertheless, the highest association constant was measured for ClO_4^-, K_a ($ClO_4^-\subset$**72**) = 5.5 x 10^7 M^{-1}.[141] The negatively ionized benzoic acids of **72** do not seem to compete with the inorganic anions for the binding pocket of the bambus[6]uril (see below). Additionally, ITC titration experiments showed that anion binding to **72** is driven by enthalpy and opposed by entropy.[141]

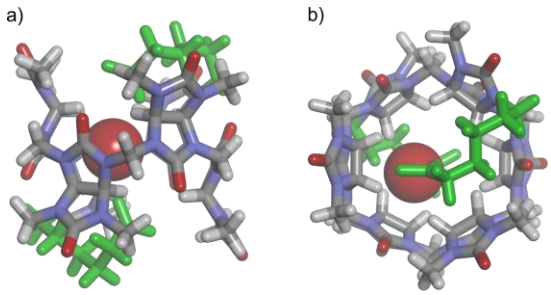

Figure 37. X-ray crystal structure of **73**: a) side and b) top views. Bambus[6]uril is depicted in stick representation and introverted carboxylates are highlighted (green). External carboxylates are pruned to methyl groups for clarity. Bound water molecule is shown as CPK model.

The bambus[6]urils **73** and **74** have pentyl and propyl groups, respectively, functionalized with terminal carboxylic acids. **73** and **74** are soluble in phosphate aqueous buffer at pD ~ 7.5.

Interestingly, the binding constant values for Br^- or I^- decrease in the order: **72** > **73** > **74**. This trend was explained considering the competitive binding of the carboxylate groups of the receptor and the establishment of repulsive Columbic interactions between the carboxylate groups and the bound anion.[142] Remarkably, the crystal structure of **73** shows the inclusion of two of its carboxylate arms in the receptor's cavity. A water molecule bridges these two carboxylate groups (Figure 37). In addition, the authors suggested that the aliphatic carboxylates of **73** and **74** are able to stablish more effective electrostatic repulsions with bound anions than the rigid benzoates present in **72**. In this respect, **74** features the lowest binding constant values because the short, propyl substituents bring the carboxylates close to the portals of the receptor disfavoring anion binding.[142]

1.3 Covalent Receptors Possessing a Concave Hydrophobic Cavity

In this section, we discuss covalent receptors displaying a concave hydrophobic cavity closed at one end and opened at the opposite end. The concave cavity is shallow for calix[n]arenes and resorcin[4]arenes, but becomes deep for cavitands derived from resorcin[4]arene scaffolds.

1.3.1 Calix[n]arenes

Calix[n]arenes **75**-**81** (n = 4-7) are comprised of phenol units linked together by methylene bridges at their *meta*-position (Figure 38a). The calix[n]arene scaffold adopts multiple conformations in solution, cone and alternate, owing to the free rotation of the aromatic panels around the methylene bridges. The rate of interconversion between conformers depends on the size of the substituents attached to the aromatic panels.[13,15] The calix[n]arenes in the cone conformation display a shallow aromatic cavity opened at one end (Figure 38b).[8]

The structure of calix[n]arenes can be modified at either the lower or upper rim, or both. In this respect, water-soluble calix[n]arenes have been prepared using carboxylic acid, phosphonate, sulfonate or ammonium groups.[13,15] The shallow hydrophobic cavity of calix[n]arenes do not isolate the bound water molecules, *i.e.* they are able to stablish hydrogen bonds with those in the bulk solution. Accordingly, it is not expected a high energetic contribution to guest binding from the release of bound water molecules. X-ray crystallography shows that calix[4]arenes bind one water molecule, which is stabilized by OH-π and dispersion interactions. On the contrary, calix[5]arenes accommodate up to three water molecules in the cavity.[30,144]

Tetra-sulfonate calix[4]arenes, such as **75**, bind inorganic cations in water. Mono-charged cations and calix[4]arene **75** form 1:1 complexes featuring an inclusion binding geometry. The binding process is enthalpically driven owing to the establishment of cation-π interactions. However, doubly-charged cations interact with the sulfonate groups at the upper rim of the receptor **75**. As expected for ion-pairing interactions in water, the later is driven by entropy.[15]

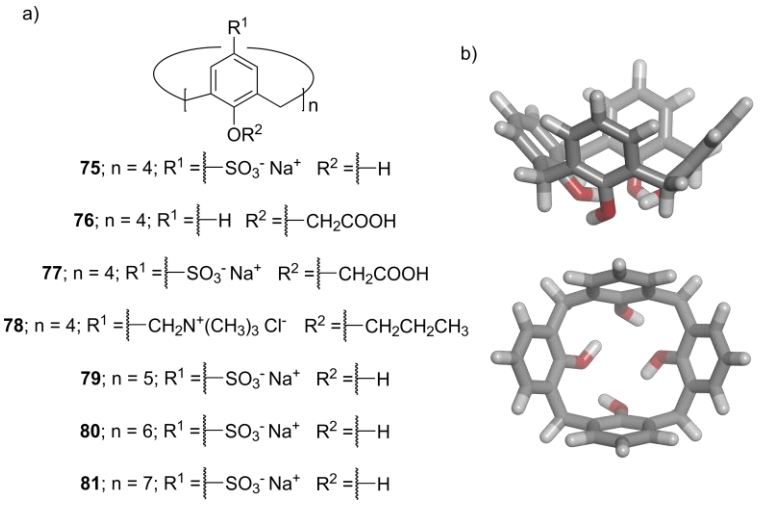

Figure 38. a) Line-drawing structures of calix[n]arenes **75**-**81** and b) energy minimized structure (MM3) of a calix[4]arene in a cone conformation: side and top views. The calix[4]arene is depicted in stick representation.

In general, calix[n]arene receptors bind neutral and charged organic molecules leading to 1:1 inclusion complexes in water. The guest is bound to the shallow hydrophobic cavity of the calix[n]arene. This induces the receptor to adopt a cone conformation. Furthermore, it produces the maximization of host-guest intermolecular interactions and the reduction of the solvent accessible surface area in the complex. The cone (or pinched cone) conformer of calix[4]arenes can be identified by the observation of two separate signals for the methylene bridges in the ^{1}H NMR spectrum.[30,145] At the same time, the proton signals of the bound guest experience upfield shifts owing to the shielding effect exerted by the aromatic cavity of the receptor. For example, a nucleus in the deepest region of the calix[4]arene's cavity displays a complexation induced shift of $\Delta\delta$ ~ -2 ppm.[15] The chemical exchange between free and bound components is fast on the ^{1}H NMR chemical shift timescale in most calix[4]arene complexes.

The inclusion complexes of sulfonate calix[n]arenes and positively charged guests, such as organic ammonium cations, are stabilized by the hydrophobic effect, CH-π, cation-π and Columbic interactions. For example, adamantyl tri-methylammonium **19** and tetra-sulfonate calix[4]arene **75** form a 1:1 complex featuring a binding constant value K_a (**19**⊂**75**) = 2.1 x 10^4 M^{-1}. At first sight, two inclusion binding geometries for **19**⊂**75** are probable because either the adamantyl residue or the tri-methylammonium cation can be buried in the cavity of the receptor. Indeed, the two binding geometries for the **19**⊂**75** complex are present in solution, which interconvert fast on the chemical shift timescale. These two binding modes also explain the ^{1}H NMR spectrum of the complex between calix[4]arene **75** and phenyl tri-methylammonium **82** or benzyl tri-methylammonium **83** (Figure 39).[146]

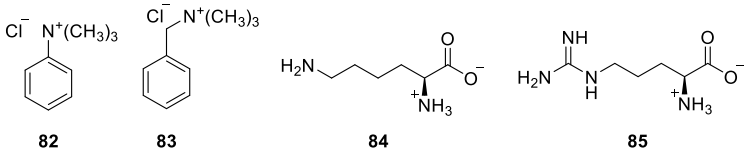

Figure 39. Line-drawing structures of **82**, **83**, lysine **84** and arginine **85**.

The calix[4]arenes **76** and **77** are soluble in phosphate buffer solution at pH = 7.3 owing to the ionization of the carboxylic acid groups at their lower rims (Figure 38a). The lower rim functions lock the receptors in a cone conformation. We anticipate that the later modifications in the structure of calix[4]arenes **76** and **77** affect the binding modes and association constant values of the complexes with organic ammonium cations. For example, the cationic tri-methylammonium group of **82** is selectively included in the cavity of calix[4]arene **76** through cation-π and CH-π interactions. Nevertheless, the phenyl group of the same guest is exclusively bound to the cavity of tetra-sulfonate **77**. The phenyl ring of **82** stablishes π-π and CH-π interactions with the aromatic panels of **77** in the **82⊂77** complex. At the same time, the tri-methylammonium cation is stabilized by the upper rim sulfonate groups of **77** through Columbic interactions. The binding modes and the intermolecular interactions involved in the complexes **82⊂76** and **82⊂77** translate into a difference of one order of magnitude in the association constant values, K_a (**82⊂76**) = 1.6 x 10^2 M^{-1} and K_a (**82⊂77**) = 2.0 x 10^3 M^{-1}.[147]

The 1:1 inclusion complex formed between benzyl tri-methylammonium **83** and calix[4]arene **76** adopts a binding geometry similar to that discussed above for **82⊂76**, but features a drop of one order of magnitude in the binding constant value, K_a (**83⊂76**) ~ 50 M^{-1}. In contrast, the **83⊂77** complex shows two binding geometries that interconvert rapidly on the ^{1}H NMR chemical shift timescale (Figure 40). The binding constant value of **83⊂77** is equal to that of **83⊂76**.[147,148]

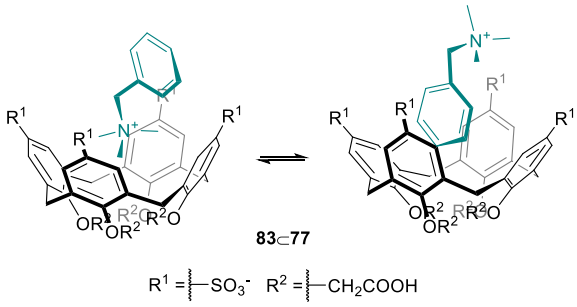

Figure 40. Equilibrium between the two binding geometries featured by the **83⊂77** complex.

Binding of amino acids and short peptides in water has been investigated using tetra-sulfonate **75** and bigger calix[n]arenes (see below). Lysine **84** and arginine **85** form 1:1 inclusion complexes

with the calix[4]arene **75** (Figure 39). The amino acid complexes feature binding constant values in the order of 10^3 M^{-1} in Na_2HPO_4 buffer at pH = 8. Furthermore, di- and tri-peptides containing lysine or arginine residues bind to receptor **75**. Based on the results obtained by 1D and 2D NMR experiments, the terminal protonated amine or the guanidinium group of these amino acids is included in the shallow hydrophobic cavity of the calix[4]arene.[149] Other calix[4]arenes decorated with phosphonic acids at their upper rims have been applied for amino acid sensing.[150]

The calix[4]arenes bearing cationic ammonium groups at their upper rims are efficient receptors for the binding of nucleotides in water. The water-soluble calix[4]arene **78** adopts a cone conformation owing to the appended propyl groups at its lower rim (Figure 38a). The receptor **78** recognizes AMP^{2-}, ADP^{3-} and ATP^{4-} in water. The ammonium cations of **78** are involved in Columbic interactions with the phosphate groups of the bound nucleotide. At the same time, the saccharide residue of the bound nucleotide is partially included in the aromatic cavity of the receptor. The magnitude of the binding constant values for these complexes are in line with the thermodynamic stability for the formation of two salt bridges in water, K_a = 10^3-10^4 M^{-1}.[151]

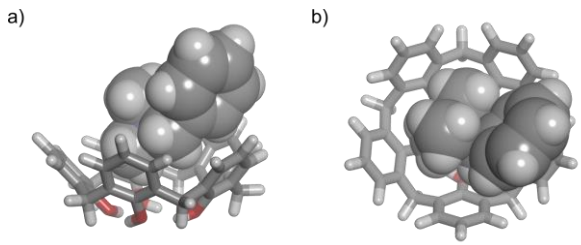

Figure 41. Energy minimized structure (MM3) of **83⊂79**: a) side and b) top views. The calix[5]arene is depicted in stick representation and the bound guest is shown as CPK model.

Penta-sulfonate calix[5]arene **79** possesses six/seven negative charges in aqueous solution owing to the presence of five sulfonate groups at its upper rim and the ionization of one/two phenolic OHs at its lower rim (Figure 38a).[144,152] The molecular recognition properties of calix[5]arene **79** have been investigated using a series of organic ammonium guests and amino acids in water. For example, benzyl tri-methylammonium **83** and **79** form a thermodynamically stable 1:1 inclusion complex featuring an association constant value K_a ~ 10^4 M^{-1}. NMR studies and the energy minimized structure (MM3) of the **83⊂79** complex indicate that the guest is tilted in the electron-rich aromatic cavity of the receptor (Figure 41).[152]

The interaction of amino acids, such as lysine **84** and arginine **85** (Figure 39), with the penta-sulfonate calix[5]arene **79** is weaker than that with calix[4]arenes, even though both complexes feature similar binding modes. In particular, the binding constant values of the amino acid complexes using the calix[5]arene receptor **79** are in the order of 10^2 M^{-1}.[153]

Hexa-sulfonate hexa-hydroxy calix[6]arene **80** (Figure 38a) features eight anionic groups in neutral water: six sulfonates at the upper rim and two ionized phenolic OHs at the lower rim. In the solid state and, most likely, in water solution, the ionized calix[6]arene **80** adopts a double partial cone conformation stabilized by four intramolecular hydrogen bonds (Figure 42).[154] Calix[6]arene **80** forms a 1:1 inclusion complex with the cationic adamantyl guest **19** featuring K_a = 1.0 x 10^3 M^{-1}. The binding constant value of the **19⊂80** complex is one order of magnitude lower than that determined for **19⊂75**. The host-guest intermolecular interactions (non-polar contacts and Columbic forces) are not optimal in the **19⊂80** complex, which produces a decrease in binding affinity (K_a).[146]

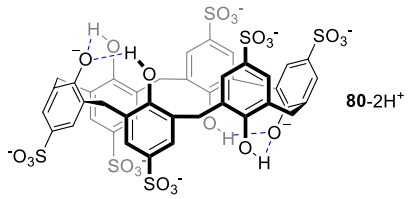

Figure 42. Line-drawing structure of calix[6]arene **80**-$2H^+$. Intramolecular hydrogen-bonding interactions are represented with dashed lines (blue).

The interaction of ferrocene derivatives with the calix[6]arene receptor **80** has been also investigated in aqueous solution. Neutral ferrocene **58** and calix[6]arene **80** form a 1:1 inclusion complex, which is supported by ^{1}H NMR titration experiments. The binding constant of the **58⊂80** complex is K_a = 3.7 x 10^3 M^{-1}, but this magnitude increases up to 10^4 M^{-1} for cationic ferrocene guests.[155]

In the same vein, the hepta-sulfonate calix[7]arene **81** (Figure 38a) supports nine negatively charged groups in aqueous solution at pH ~ 7.3. The structure of calix[7]arene is very flexible. Therefore, **81** adopts multiple conformations in solution. The X-ray crystal structure of **81** and *in-silico* calculations indicate that a double cone pinched conformation is favored. Calix[7]arene **81** also features a large aromatic surface area enabling the binding of aromatic guests. For example, this receptor binds di-methyl viologen **32** in water forming a thermodynamically stable 1:1 complex, K_a ~ 10^4 M^{-1}. However, the binding geometry of the **32⊂81** complex is difficult to elucidate. Most likely, multiple geometries of **32⊂81** are in fast chemical exchange on the NMR chemical shift timescale.[156]

Chiral sulfonate calix[n]arenes and deep-cavity calix[n]arenes have been also reported in the literature.[157,158,159,160]

1.3.2 Resorcin[4]arenes

The cyclic covalent arrangement of four electron-rich, resorcinol units gives the resorcin[4]arene scaffold. The resorcinol panels are connected by methine bridges, in which alkyl substituents (*a.k.a* "feet") are appended. The OH functions of the resorcin[4]arene scaffold form a cyclic seam of hydrogen bonds, aided by water molecules. These inter- and intra-molecular hydrogen-bonding interactions stabilize the resorcin[4]arene in the cone conformer (C_4 symmetry) in analogy to the calix[4]arenes (Figure 43).[161] The resorcin[4]arene in the cone conformation displays a shallow concave hydrophobic cavity.[4]

An included nucleus in the deepest region of the aromatic cavity of resorcin[4]arenes experiences a strong upfield shift of $\Delta\delta$ ~ -2.5 ppm.[162] On the other hand, the chemical exchange between free and bound components in the complexes derived from resorcin[4]arenes is fast on the ^{1}H NMR chemical shift timescale. We will show below that resorcin[4]arenes featuring a deep cavity, *a.k.a* deep cavitands, show remarkably different binding behaviour compared to the shallow receptors.

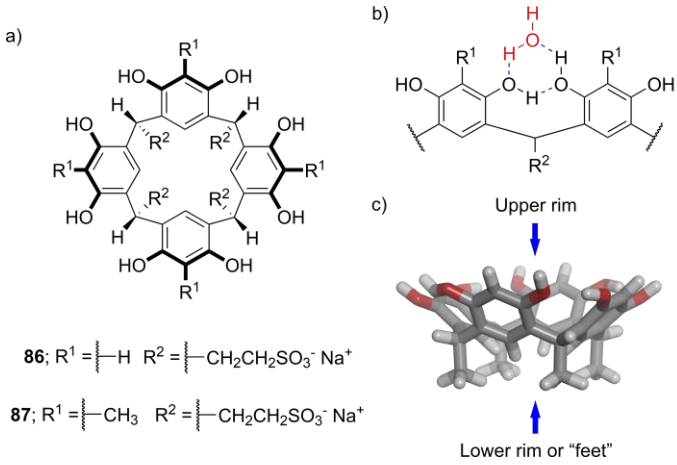

Figure 43. a) Line-drawing structures of resorcin[4]arenes **86** and **87**; b) section of a resorcin[4]arene showing the hydrogen bonds between the resorcinol OHs and a water molecule and c) energy minimized structure (MM3) of a resorcin[4]arene scaffold. The resorcin[4]arene is depicted in stick representation. Upper and lower rims are indicated with arrows (blue).

Ionizable or charged groups, *e.g.* carboxylic acids, sulfonates or phosphates, have been attached at either the upper or lower rim of the resorcin[4]arene scaffold to impart water solubility.[162,163] For example, the resorcin[4]arene bearing sulfonate groups at its lower rim, **86**, is highly soluble in water (Figure 43a). Kobayashi *et al.* demonstrated that the water-soluble resorcin[4]arene **86** forms 1:1 inclusion complexes with cyclic and acyclic alcohols. These complexes show the non-polar section of the cyclic alcohol, **88** or **89**, buried in the cavity of the receptor and the hydroxyl groups of the bound guest are exposed to the bulk aqueous solution (Figure 44). The binding

constant values of the later complexes are lower than 20 M^{-1}. Nevertheless, the *para*-methyl-substituted resorcin[4]arene **87** (Figure 43a) features binding constant values up to 10^2 M^{-1} with the same alcohols. The increase in the binding affinity values results from the deeper hydrophobic cavity featured by **87** versus that shown by **86**.[49,162,164] Van't Hoff analyses of the complexation processes of neutral guests with resorcin[4]arene receptors indicate that the enthalpic contribution is dominant.[163]

It is worth mentioning that ionizable or charged groups at the lower rim of the resorcin[4]arene receptors do not interfere in the binding process of charged guests. On the contrary, the same residues at the upper rim of the receptors affect the thermodynamic and kinetic stability of the inclusion complexes.[162]

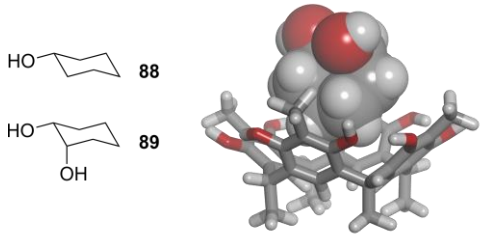

Figure 44. (left) Line-drawing structures of cyclohexanol **88** and *cis*-1,2-cyclohexanediol **89**; (right) energy minimized structure (MM3) of the **89⊂87** complex. The resorcin[4]arene is depicted in stick representation and the guest is shown as CPK model. Water-solubilizing groups were pruned to methyl groups to ease the calculation.

Diederich and co-workers elaborated the aromatic cavity of the resorcin[4]arene scaffold by functionalizing the resorcinol units at the *para*-position with phenyl substituents, **90** (Figure 45a). In addition, ethylene chains were used to connect the resorcinol OHs of the receptor. The incorporation of ethylene bridges produces a more rigid and pre-organized structure, *a.k.a* cavitand.[165] These structural modifications are expected to enhance the hydrophobic effect for the binding of non-polar residues. The cavitand **90** is further decorated with four amidinium groups at the upper rim and four tri(ethylene glycol) mono-methyl ether chains at the feet. The upper and lower rim functions warrant water solubility to **90**. Note that the cationic amidinium groups can assist the binding of guests having charged complementary functions.

In this respect, cavitand **90** was used as receptor for the recognition of organic anions in water. Isophthalates, such as **91** (Figure 45b), form 1:1 and 2:1 guest/host complexes with receptor **90** in pure D_2O (K_a (**91⊂90**) = 8.6 x 10^4 M^{-1} and K_a (**91**$_2$**⊂90**) = 7.7 x 10^3 M^{-1}). On the contrary, 1:1 complexes are established in aqueous borate buffer solution at pH = 9.2 (Figure 45c). The binding constant value of the 1:1 inclusion complex, **91⊂90**, in buffer solution is in line with that determined in pure water. The deep inclusion of isophthalate **91** in the cavity of receptor **90** is driven by the hydrophobic effect and the assistance of electrostatic interactions: ion-pairing and

hydrogen-bonding interactions. These results demonstrate that the formation of high-stoichiometric complexes assembled through electrostatic interactions can be suppressed in certain buffer solutions.[15,27,166,167]

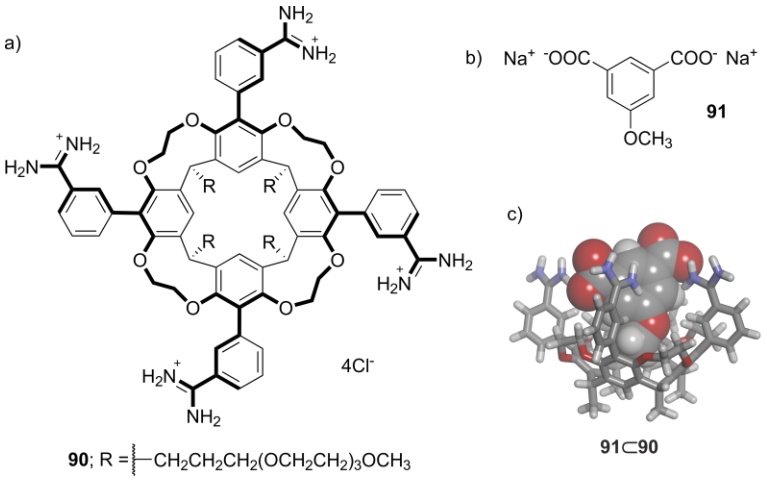

Figure 45. Line-drawing structures: a) tetra-amidinium resorcin[4]arene **90** and b) isophthalate **91**; c) energy minimized structure (MM3) of **91⊂90**. The resorcin[4]rene is depicted in stick representation and the guest is shown as CPK model.

Following a different approach, Rebek and co-workers have connected the resorcinol OHs of the resorcin[4]arene scaffold using aromatic panels. These resorcin[4]arene derivatives are known as deep cavitands. In water solution, the deep cavitands are mainly present as D_{2d} velcrand dimers. However, they are in equilibrium with monomeric C_{2v} "kite" and C_{4v} "vase" conformers, both in low abundance (Figure 46c). The dimerization of resorcin[4]arene cavitands is driven by the hydrophobic effect. Interestingly, the "kite" conformer features a shallow aromatic cavity, whereas the "vase" counterpart displays a deep hydrophobic cavity. Neither the velcrand dimer nor the "kite" conformer are able to stablish highly thermodynamically and kinetically stable host-guest inclusion complexes. Nevertheless, the binding of a size and shape complementary guest induces the resorcin[4]arene dimer to dissociate and, more interestingly, adopt exclusively the "vase" conformation. The bound receptor in the "vase" conformation maximizes non-polar contacts and minimize the solvent accessible surface area in the complex. It is worth mentioning that the "vase" conformer displays a triplet signal for the methine protons at $\delta \sim 5.5$ ppm in the ^{1}H NMR spectrum. The conformational exchange of the free cavitand is slow on the ^{1}H NMR chemical shift timescale and controls the guest in/out exchange kinetics. Thus, it is expected for the resorcin[4]arene deep cavitands to produce kinetically stable inclusion complexes.[27,165,168,169]

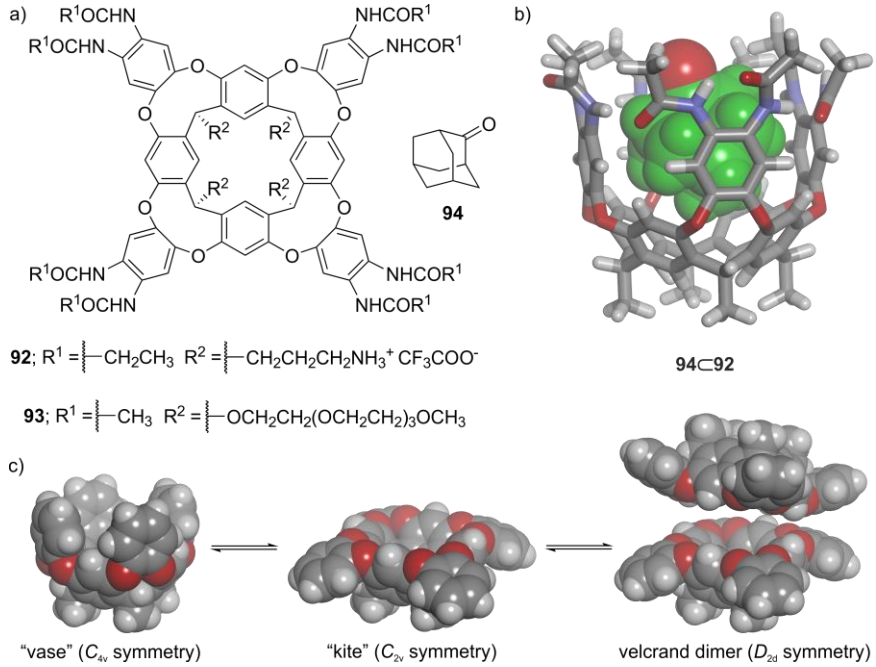

Figure 46. a) Line-drawing structures of resorcin[4]arene cavitands **92**, **93** and adamantanone **94**; b) energy minimized structure (MM3) of **94⊂92** and c) equilibria of resorcin[4]arene cavitands in water. In b) the cavitand is depicted in stick representation and the guest (green) is shown as CPK model. The oxygen atom (red) of bound **94** is highlighted. In c) the cavitands are shown as CPK models and amides at the upper rim are removed for clarity. Water-solubilizing groups were pruned to methyl groups to ease the calculation.

Water-solubilizing groups have been appended at the "feet" of resorcin[4]arene deep cavitands: oligo(ethylene glycol), amine, pyridinium, imidazolium and guanidinium groups.[170,171] The cavitand **92** possesses four ammonium groups at the lower rim and eight amide functions at the upper rim (Figure 46a). Both amides and ammonium groups impart water solubility. Interestingly, the upper rim amides form a hydrogen-bonding belt that stabilizes the "vase" conformation. They might also assist the binding of guests bearing complementary polar functions. The deep cavitand **92** binds size complementary guests featuring constant values in the order of 10^2 M^{-1}. For example, **92** forms a thermodynamically and kinetically stable 1:1 inclusion complex with adamantanone **94** in water, K_a (**94⊂92**) = 1.4 x 10^2 M^{-1}. The adamantyl residue of bound **94** is buried in the deep binding pocket of **92** in the "vase" conformation. On the contrast, the carbonyl group of the bound guest is exposed to the bulk aqueous solution (Figure 46b).[168]

Replacing the cationic ammonium groups at the lower rim by oligo(ethylene glycol) chains produces the neutral deep cavitand **93** (Figure 46a). The later polar groups ensure solubility in water over a wide pH range. The receptor **93** binds adamantyl ammonium and quinuclidium guests featuring K_a values up to 10^2 M^{-1}. The complexation process of the cationic guests with the neutral

deep cavitand is driven by entropy. This thermodynamic signature is derived from the partial desolvation of the charged group of the guest upon binding.[170]

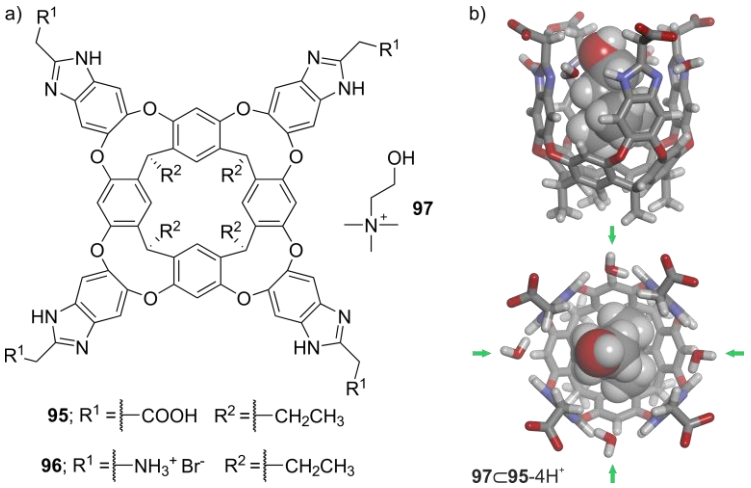

Figure 47. a) Line-drawing structures of cavitands **95**, **96** and choline **97**; b) energy minimized structure (MM3) of **97**⊂**95**-4H$^+$: side and top views. The cavitand is depicted in stick representation and the guest is shown as CPK model. Hydrogen-bonded water molecules at the upper rim are indicated with arrows (green). Substituents at the lower rim were pruned to methyl groups to ease the calculations.

The Rebek group has extended the aromatic panels of the resorcin[4]arene deep cavitands using benzimidazole or benzimidazolone groups, **95** and **96** (Figure 47a). They have also incorporated water-solubilizing groups at the upper rim of the receptors. For example, the tetra-acid resorcin[4]arene cavitand **95** displays a solubility in water of *ca.* 10 mM. The tetra-acid **95** adopts the "vase" conformation in water solution owing to an included, residual THF molecule coming from the last synthetic step of the cavitand. Furthermore, hydrogen-bonded water molecules to the benzimidazoles of **95** further stabilize the "vase" conformation (Figure 47b). The binding of a complementary guest provokes the release of the bound THF molecule from the cavity of **95** to the bulk aqueous solution. Interestingly, the protons of the guest in the binding pocket of benzimidazole or benzimidazolone deep cavitands experience a strong magnetic shielding effect owing to the eight aromatic panels that surround the cavity. For example, a nucleus in the deepest region of the cavity displays an upfield shift of $\Delta\delta$ = -4.4 to -4.9 ppm. The cavitand **95** and the tetra-methylammonium cation form a 1:1 inclusion complex featuring a binding constant value K_a = 3.8 x 10^3 M^{-1}. On the other hand, certain guests bearing both cationic and non-polar residues have binding constant values larger than 10^4 M^{-1}. In this respect, choline **97** or acetylcholine form thermodynamically highly stable 1:1 inclusion complexes with **95** in water (Figure 47). In general, the binding processes using these cavitands are enthalpically driven.[14,169,172]

The deep cavitands **95** and **96** are analogous, but the later bears ammonium cations instead of carboxylic acids at the upper rim (Figure 47a). These two cavitands were applied by Rebek *et al.* to investigate the charge complementarity between host and guest in water. The results showed that the difference in binding affinity (K_a) between the same pair of complexes, guest⊂**95** and guest⊂**96**, is one order of magnitude or more. This supports that charge complementarity is required for the efficient interaction between charged binding partners in water, as discussed previously for cyclophane receptors. On the contrary, neutral guests display similar binding affinities with both cavitands.[173]

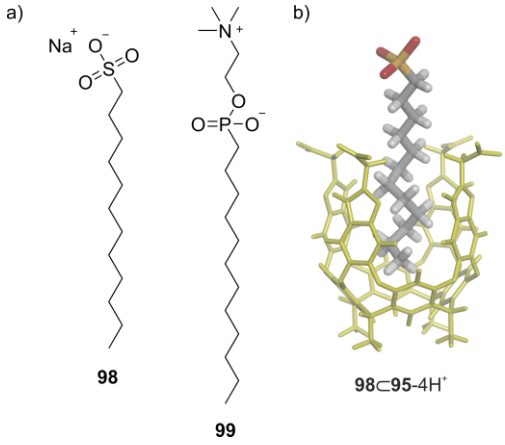

Figure 48. a) Line-drawing structures of surfactants **98** and **99**; b) energy minimized structure (MM3) of **98**⊂**95**-4H$^+$. The resorcin[4]arene (yellow) and the guest are depicted in stick representation. Note that the buried section of **98** in the cavity of **95**-4H$^+$ adopts a helical conformation.

Long-chain guests are bound in unusual conformations in the hydrophobic cavity of benzimidazole and benzimidazolone deep cavitands. Rebek and co-workers observed that surfactants, such as dodecyl sulfate **98** and dodecyl phosphocholine **99** (Figure 48a), adopt a helical conformation in the deep cavity of tetra-acid **95** in water. The terminal methyl group of the bound guest is located in the deepest region of the cavity of the receptor, whereas the polar head is exposed to the bulk aqueous solution. Interestingly, the buried section of the aliphatic chain of **98** and **99** features a coiled conformation to fill the cavity volume and stablish multiple CH-π interactions with the aromatic walls of the receptor **95** (Figure 48b). Note that the helical arrangement of the bound surfactant is *ca.* 3 kcal·mol^{-1} higher in energy than the extended counterpart (0.5-0.6 kcal·mol^{-1} per gauche interaction). Nevertheless, the free energy of binding overcomes the energetic cost of the guest to adopt the coiled structure.[14,167,174]

The coiled arrangement adopted by long-chain guests in the cavity of **95** was also observed for linear hydrocarbons. Interestingly, the ^{1}H NMR spectrum of the 1:1 inclusion complex between *n*-octane **100** and the deep cavitand **95** showed a set of upfield shifted signals displaying a

symmetrical pattern for the bound guest. The comparison of this ^{1}H NMR spectrum with those obtained for the bound surfactants indicated that the chemical shift of each methyl and methylene proton of **100** is the average between two magnetic environments. The signal pattern and chemical shifts of the protons of bound **100** are in agreement with a coiled structure experiencing a fast tumbling motion on the chemical shift timescale (Figure 49). Nevertheless, shorter *n*-alkanes, such as *n*-pentane, feature a staggered conformation in the bound form.[15,175,176,177]

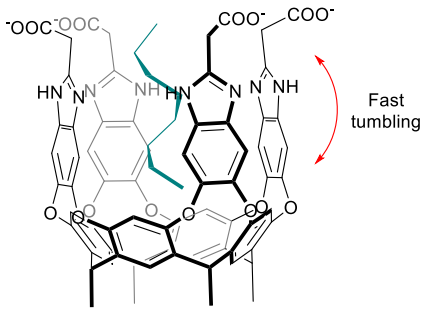

100⊂**95**-4H$^+$

Figure 49. Line-drawing structure of the **100**⊂**95**-4H$^+$ complex. Bound guest (green) adopts a coiled conformation and experiences a fast tumbling motion on the ^{1}H NMR chemical shift timescale.

Resorcin[4]arene cavitands featuring deeper hydrophobic cavities have been designed by Gibb and co-workers (Figure 50). These deep-cavity cavitands are soluble in water when they are decorated with eight external ionizable or charged groups. The water-solubilizing groups are distributed between the upper and lower rims of the cavitand. Remarkably, the deep-cavity cavitands adopt a rigid “vase” conformation in water. In particular, the octa-acid cavitand **101** is soluble in neutral water at micromolar concentrations. However, the solubilization of **101** in water at millimolar concentrations requires a pH > 9 (Figure 50a). Note that the portal of the open-ended cavity of **101** features a large hydrophobic section suggesting that the cavitand might tend to self-associate into high-order species (see Section 1.5.2).[14]

The deep-cavity cavitand **101** has been applied to investigate the role of the Hofmeister effect in the binding of non-polar residues in water. The studies using synthetic model systems are necessary for the understanding of the Hofmeister effect operating in natural complexes. The interaction between the adamantyl carboxylic acid **102** and the cavitand **101** produces a 1:1 inclusion complex in 10 mM phosphate buffer solution at pH ~ 11 (Figure 50a). At this pH, the carboxylic acids of both host and guest are converted into carboxylates. The adamantyl group of **102** is deeply included in the hydrophobic cavity of **101**. Consequently, the carboxylate group of bound **102** is exposed to the bulk aqueous solution and, more interestingly, it prevents the self-association of the cavitand **101**. The binding constant value of the **102**⊂**101** complex is K_a = 4.7 x 10^6 M^{-1} (ΔG = -9.1 kcal·mol^{-1}). In the presence of kosmotropic anions, the free energy of binding

for the **102⊂101** complex is favored by *ca.* 0.5 kcal·mol^{-1} owing to the enhancement of the hydrophobic effect. In contrast, chaotropic anions are detrimental for the binding process. For example, the reduction in the binding free energy of the **102⊂101** complex is notable in the presence of perchlorate, which provokes a loss of *ca.* 1 kcal·mol^{-1}.

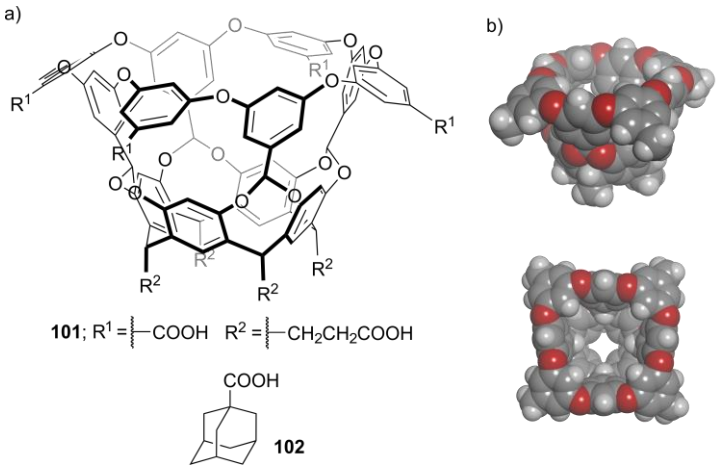

Figure 50. a) Line-drawing structures of octa-acid cavitand **101** and adamantyl carboxylic acid **102**; b) energy minimized structure (MM3) of **101**: side and top views. The deep-cavity cavitand is shown as CPK model. Water-solubilizing groups were pruned to methyl groups to ease the calculation.

The binding of **102** to the hydrophobic cavity of **101** is driven by enthalpy. Conversely, the same complexation process is driven by entropy in the presence of ClO_4^-. The analysis of the ^{1}H NMR titration spectra of ClO_4^- with deep-cavity cavitand **101** revealed that the chaotropic anion binds to the receptor forming a 1:1 host/guest inclusion complex. The binding constant value of the ClO_4^-**⊂101** complex is 95 M^{-1}. Therefore, at high $NaClO_4$ concentrations, the anion effectively competes with the guest **102** for the hydrophobic binding pocket of **101**. These results show how chaotropic anions interfere in non-polar binding processes: they interact with non-polar, aromatic regions of synthetic or natural receptors.[14,178]

The resorcin[4]arene receptors discussed above mainly feature hydrophobic binding pockets and possess water-solubilizing groups at either the upper or lower rim, or both. The ionizable or charged groups at the upper rim impact on the binding affinity value of charged guests. In order to minimize this effect and have access to the polar functionalization of the resorcin[4]arene's cavity, the water-solubilizing groups must be installed exclusively at the lower rim. Based on this, Dalcanale and co-workers have designed tetra-phosphonate resorcin[4]arene cavitands with pyridinium "feet". For example, the tetra-phosphonate cavitand **103** bears four P=O functions inwardly-directed to the cavity of the receptor (Figure 51a). Interestingly, the X-ray crystal structures of related tetra-phosphonate cavitands show that water molecules interact with the polar

functions and the cavity of the receptors is “dry”. This suggest that the cavity of the resorcin[4]arene **103** might be poorly solvated in aqueous solution.

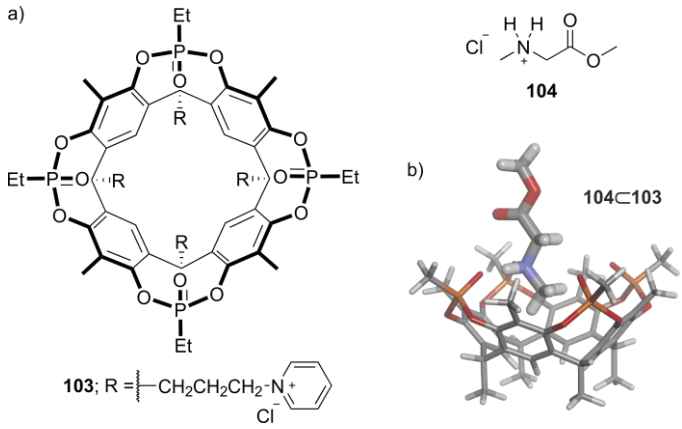

Figure 51. a) Line-drawing structures of tetra-phosphonate cavitand **103** and glycine derivative **104**; b) energy minimized structure (MM3) of the **104⊂103** complex. The cavitand and the guest are depicted in stick representation. Phosphonate substituents and water-solubilizing groups were pruned to methyl groups to ease the calculation.

The tetra-phosphonate cavitand **103** is an efficient receptor for *N*-methylated amino acids in water, K_a = 10^3-10^4 M^{-1}. The binding processes are characterized by a favorable enthalpy and an opposed entropy. For example, the 1:1 inclusion complex of the methyl ester of *N*-methyl glycine **104** and the tetra-phosphonate **103** shows that the *N*-methyl group of the guest is buried in the cavity of the receptor. Therefore, the ammonium cation of **104** is stabilized through cation-dipole and hydrogen-bonding interactions with the four phosphonate oxygen atoms of the receptor (Figure 51b). Remarkably, the amino acids lacking the *N*-methyl group are not recognized by the tetra-phosphonate cavitand **103** in water.[179]

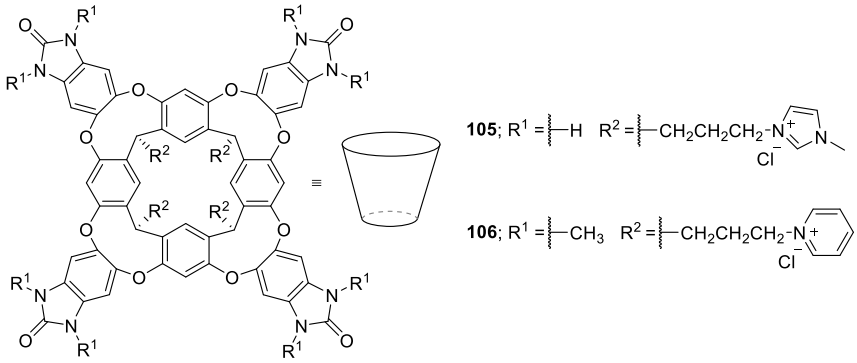

Figure 52. Line-drawing structures of benzimidazolone cavitands **105** and **106**. Cartoon representation of benzimidazolone cavitands is depicted.

Rebek and co-workers have applied benzimidazolone resorcin[4]arene deep cavitands **105** and **106** (Figure 52) to mediate/catalyze chemical transformations in water. For example, cavitand **105** binds long-chain amino acids in a folded conformation, in which the terminal amino and acid groups are brought in close proximity. This favors the cyclization of the bound amino acid to produce the corresponding lactam. Therefore, the cyclization of **107** gives the lactam **108** with a four-fold yield improvement in the presence of the cavitand **105** (Figure 53). Nevertheless, the yield of the lactam product for the same reaction is low in the absence of the cavitand because mainly oligomeric products are formed.

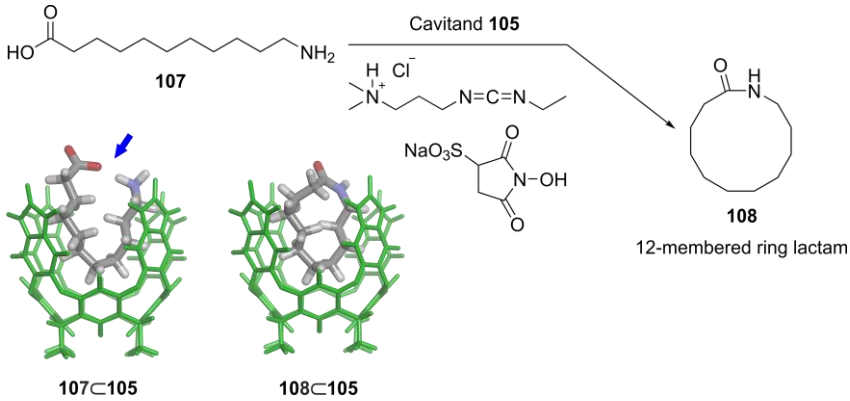

Figure 53. (top) Cyclization of amino acid **107** to give lactam **108**; (bottom) energy minimized structures (MM3) of the inclusion complexes of **107** and **108** with cavitand **105**. The cavitand (green) and the guests are depicted in stick representation. Arrow (blue) highlights the proximity of the two reacting groups in the **107⊂105** complex.

The cyclization reaction of long-chain substrates requires stoichiometric amounts of the cavitand **105**, even though it can be reused after extraction of the product with an organic solvent.[180] Other examples of cyclization reactions using benzimidazolone resorcin[4]arene deep cavitands have been reported by the Rebek group.[181,182]

Another application of the benzimidazolone cavitands is the mono-functionalization of di-symmetric compounds (*i.e.* desymmetrization). Long-chain symmetric molecules bearing two terminal functions react to give the mono-reacted and di-reacted products. When the two reacting groups are independent, the mono-functionalized product can be obtained in 50% yield, together with equal amounts of starting material and di-reacted product. This complicates the purification and isolation of the mono-functionalized product. Using the deep cavitand **106**, the long-chain di-functional substrate is bound in a folded conformation. The cavitand **106** induces a moderate rate acceleration for the reaction of one terminal group of the bound guest but protects the other in the interior of the hydrophobic cavity.

For example, the long-chain di-ester **109** experiences a fast chemical exchange process between two *J*-conformations, known as “yo-yo” motion, when the guest is bound to the cavitand **106**

(Scheme 4). This motion provokes the exposure of one terminal ester group to the bulk aqueous medium, while the other reacting group remains buried in the hydrophobic cavity of the receptor. In this case, the acid hydrolysis occurs at the water/cavitand interface. Thus, the exposed ester group of **109** produces the mono-ester mono-acid product **110** and, more interestingly, the rate of the hydrolysis is enhanced in comparison to the same reaction in the absence of the cavitand. In contrast, the rate of the hydrolysis reaction of the terminal ester group of **110** is reduced because now the bound guest adopts an "static" *J*-conformation. The bound mono-functionalized product **110** shows the terminal ester group buried in the receptor's cavity, where the reaction does not take place, and the carboxylic acid is exposed to the bulk aqueous solution. In other words, the ester group of **110** spends more time buried in the cavity of the receptor, which explains the decrease in the rate of the hydrolysis of **110** to give the di-acid product. Under basic conditions, the mono-ester mono-acid product **110** is produced in more than 90% yield because the **110⊂106** inclusion complex precipitates from the solution.[27,183,184]

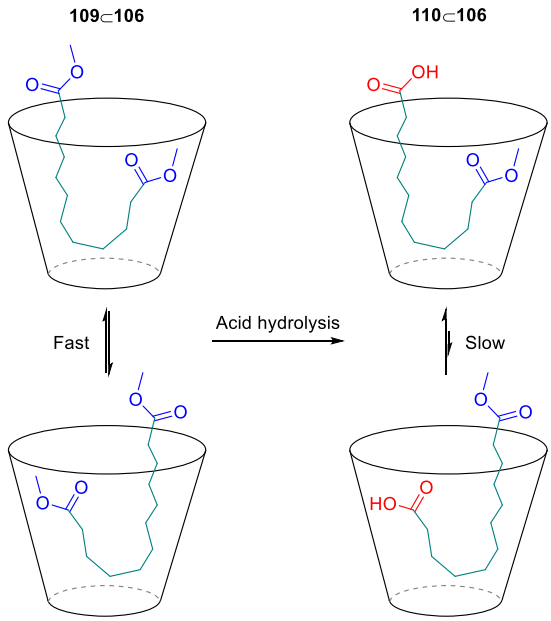

Scheme 4. Cartoon representation of the hydrolysis reaction of di-ester **109** to yield mono-ester mono-acid **110** in the presence of cavitand **106**. Exchange dynamics between *J*-conformations of bound guests are indicated. See Figure 52 for the line-drawing structure of cavitand **106**.

Other applications of water-soluble resorcin[4]arene deep cavitands were discussed by Rebek and co-workers in an excellent review.[185]

1.4 Covalent Receptors Possessing a Hydrophilic Cavity

Polar binding motifs incorporated in the interior of the receptor's cavity offer function selectivity. Furthermore, the hydrophobic cavity of the receptor becomes hydrophilic. In this section, we discuss the binding properties of hydrophilic receptors with polar guests. The inclusion complexes obey the size, shape and function complementary principles.

1.4.1 Temple receptors

Three-dimensional macrocycles formed by two aromatic panels as "roof" and "floor", and relatively rigid polar groups as "pillars" are termed "temple" receptors. The "pillars" avoid the hydrophobic collapse of the "temple" structure and are functionalized with ionizable or charged groups to impart water solubility.[49,186,187]

The hydrophilic cavity of the "temple" receptors can accommodate polar guests, such as carbohydrates. In this respect, lectins are the natural receptors that recognize carbohydrates in aqueous solution. They display a pre-organized aromatic cleft or cavity in which polar groups converge. Therefore, carbohydrate recognition is driven by the hydrophobic effect, hydrogen-bonding and CH-π interactions. The binding constant values of the lectin-carbohydrate complexes are in the range of 10^3-10^4 M^{-1}. Note that carbohydrates are structurally similar and thus, multiple hydrogen bonds and CH-π contacts are required to achieve high levels of binding selectivity.[12,46,49,164,187]

All equatorial saccharides are ideal guests for synthetic "temple" receptors. They feature axial CH groups that interact with the aromatic panels at the "roof" and "floor" of the receptor and equatorial OH functions that can stablish hydrogen-bonding interactions with the "pillars".[49,187] In this regard, the research group of Davis has designed efficient "temple" receptors for the recognition of carbohydrates in water. They have used different aromatic scaffolds (bi-phenyl, ter-phenyl, pyrene, etc.) for the construction of the "roof" and "floor" of the "temple" structures. The "pillars" are usually isophthalamide units, which provide amide groups for hydrogen-bonding interactions. It is worth mentioning here that most of the amide NH protons of the "pillars" are inwardly-oriented to the cavity of the "temple" receptor.[49]

One of the earliest versions of water-soluble "temple" receptors reported by Davis and co-workers was based on bi-phenyl scaffolds. The bi-phenyl structure is twisted owing to steric clashes that arise from the opposite *ortho*-protons of the connected aromatic units. Nevertheless, the bi-phenyl scaffold is a good aromatic platform to stablish CH-π interactions with the axial CHs of bound saccharides. For example, the tri-cyclic receptor **111** bears two bi-phenyl units linked together by four isophthalamide groups ("pillars"). The polar "pillars" offer a total of eight hydrogen bond donors to the binding site, and they also contain small dendritic carboxylate groups to ensure water solubility (Figure 54a). In general, the "temple" receptors form 1:1 inclusion complexes with

mono- and di-saccharides in water. For example, freshly dissolved glucose **112** in water exists as a mixture of *α*- and *β*-anomers in a 72:28 ratio. The apparent binding constant value of the **112⊂111** complex is 4.6 M^{-1}. However, this constant value increases up to 9.2 M^{-1} using equilibrated D-glucose, which features an *α*/*β* ratio equal to 60:40. This result indicates that the "temple" receptor **111** displays binding selectivity for the *β*-anomer of D-glucose **112**. At first sight, the apparent binding constant values can be considered as weighted averages of two putative complexes, *α*-**112⊂111** and *β*-**112⊂111**. Interestingly, 2D NMR spectra revealed the exclusive inclusion of *β*-D-glucose **112** in the cavity of **111**. Thus, the calculated values are minimum estimates for the binding constant of the *β*-**112⊂111** complex. On the contrary, glycosides do not experience mutarotation in water. Methyl *β*-D-glucoside **113** and "temple" receptor **111** form a 1:1 inclusion complex featuring a binding constant value K_a ~ 27 M^{-1}. The receptor **111** also binds di-saccharides in water, such as D-cellobiose **114**. However, the interaction between the "temple" receptor **111** with **114** is weaker (K_a ~ 17 M^{-1}) than with the mono-saccharide **113** (Figure 54b).[188]

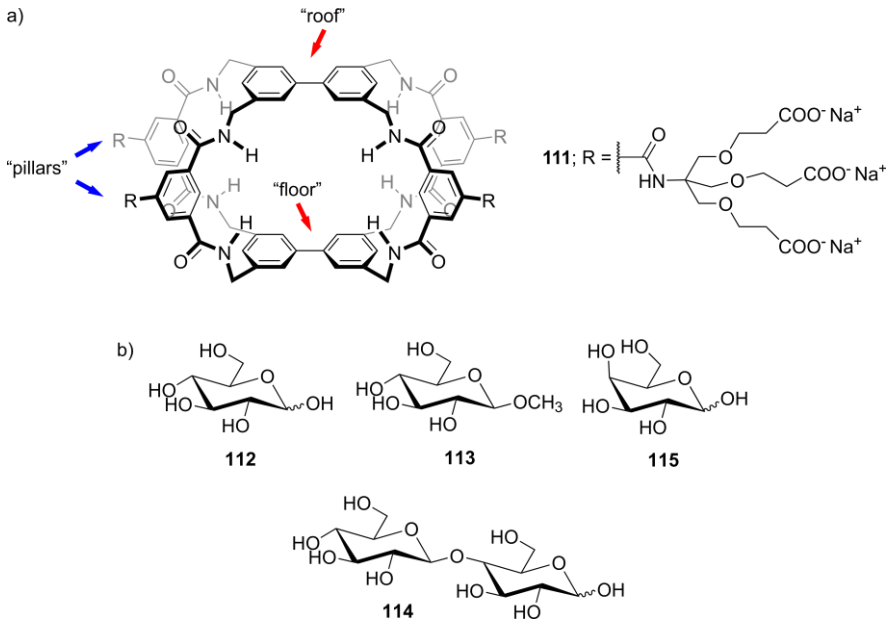

Figure 54. Line-drawing structures: a) tri-cyclic receptor **111** and b) carbohydrates **112**-**115**. Components of the "temple" architecture are indicated with arrows.

The bi-phenyl "temple" receptor **111** displays good binding selectivity for certain mono-saccharides, even though the binding constant values of the corresponding complexes are low. The apparent binding constant value of the **112⊂111** complex is five-fold larger than that of the D-galactose complex, **115⊂111** (Figure 54b). Note that the structural difference between these two mono-saccharides is the orientation of one hydroxyl group. Thus, **112** and **115** are epimers (Figure 54b).[188]

In order to improve the binding affinity of the "temple" receptor **111**, the bi-phenyl units were decorated with alkoxy substituents at the *para*-positions. This was expected to increase the hydrophobic effect of the receptor's cavity and reduce the water solvation of the amide functions. The results showed that the thermodynamic stability of the complexes of all equatorial mono-saccharides was moderately improved.[189] On the other hand, the substituents of the bi-phenyl scaffold also affect the electron density of the π-system and thereby, the strength of the CH-π interactions stablished with bound carbohydrates. The use of bi-phenyl scaffolds functionalized with either OH or F groups produced small changes in the binding constant values. The contribution of the CH-π interactions in the complex is likely masked by other factors, such as changes in the hydrophobicity of the cavity or the conformation of the receptor.[190] Additionally, the "pillar" units of the receptor can be tuned. For example, two isophthalamides of **111** were replaced by two *bis*-aminomethyl pyrrole groups, **116** (structure not shown). The binding constant values of these "temple" receptors, **111** and **116**, are of the same order of magnitude, even though the later displays better selectivity for specific mono-saccharides.[191]

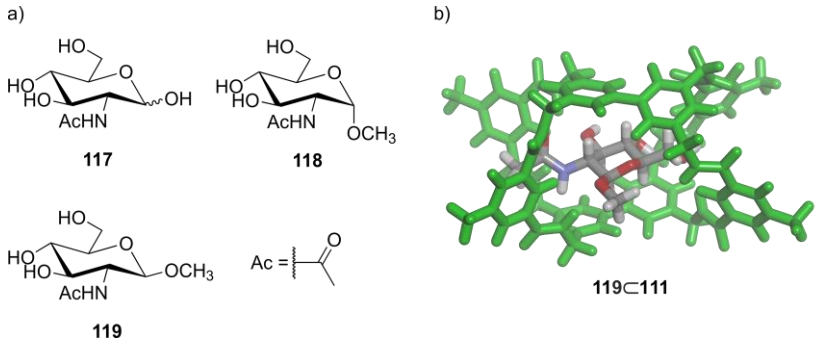

Figure 55. a) Line-drawing structures of *N*-acetyl glucosamines **117**-**119**; b) energy minimized structure (MM3) of the **119⊂111** complex. "Temple" receptor (green) and bound guest are depicted in stick representation. Water-solubilizing groups were pruned to methyl groups to ease the calculation.

N-acetyl-substituted mono-saccharides interact with the tri-cyclic receptor **111** featuring binding constant values larger than the parent compounds. The *β*-anomer of *N*-acetyl glucosamine **117** (*α*/*β* ratio = 64:36 in water) binds exclusively to the receptor **111** featuring an apparent binding constant value K_{app} ~ 1.6 x 10^2 M^{-1} (Figure 55a). The glycoside derivatives of **117**, the *α*-anomer **118** and the *β*-anomer **119**, display different K_a values with the "temple" receptor **111**. The binding constant of the **118⊂111** complex is 27 M^{-1}, whereas the value is 6.3 x 10^2 M^{-1} for **119⊂111**. Note that the binding constant value of the complex for *N*-acetyl glycoside **119** is two orders of magnitude larger than that for glucose **112**. It is worth mentioning here that the binding constant value of the **119⊂111** complex is similar to that of carbohydrate complexes derived from natural wheat germ agglutinin. More interestingly, the synthetic receptor **111** features higher binding selectivity for the *β*-anomer of mono-saccharides than the natural lectin.[192]

The binding mode of the **119⊂111** complex was studied by 2D NMR spectroscopy and molecular modelling (Figure 55b). The energy minimized structure (MM3) of **119⊂111** shows the *N*-acetyl glycoside **119** included in the hydrophilic cavity of the "temple" receptor **111**. The *N*-acetylamino group stays in one of the portals of the cavity. The amide NH of the guest is involved in NH-π interactions with the bi-phenyl units of the receptor.[187] The hydroxymethyl group of bound **119** is placed in the opposite portal of the cavity with respect to the *N*-acetylamino group. The molecular modelling structure of the **119⊂111** complex confirms that the polar substituents of the mono-saccharide must be placed in equatorial positions to avoid steric clashes with the aromatic panels of the receptor and maximize host-guest interactions. These explain the low binding affinities displayed by receptor **111** towards the *α*-anomer of mono-saccharides.[192]

The binding performance of the "temple" receptors was improved replacing the bi-phenyl units in **111** by pyrenes in **120** (Figure 56). The pyrene scaffold is planar and offers a large aromatic surface area. Therefore, the hydrophobic effect and non-polar contacts with bound carbohydrates are enhanced. For example, the *N*-acetyl glycoside **119** (*β*-anomer) and receptor **120** form a thermodynamically and kinetically stable 1:1 inclusion complex in water featuring a binding constant value K_a = 1.8 x 10^4 M^{-1}. On the contrary, the binding constant value drops one order of magnitude for the complex with the *α*-anomer **118**, K_a (**118⊂120**) = 1.6 x 10^3 M^{-1}.[193]

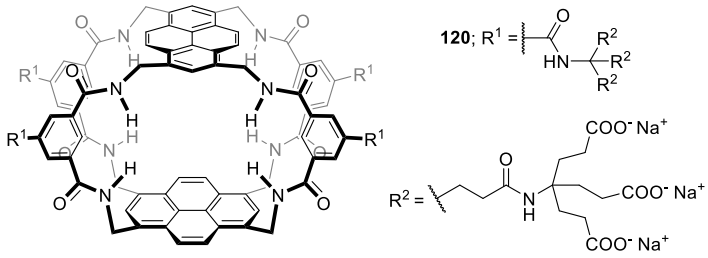

Figure 56. Line-drawing structure of the "temple" receptor **120**.

Davis and co-workers have shown that bigger "temple" receptors can efficiently bind di-saccharides in water.[194,195] For example, the tetra-cyclic receptor **121** bears ter-phenyl units at the "roof" and "floor" of the "temple" structure (Figure 57). Five isophthalamide spacers avoid the hydrophobic collapse of the cavity of **121**. These units are also decorated with a total of fifteen carboxylate groups to ensure the solubility of "temple" **121** in water. In this regard, the "temple" receptor **121** binds the di-saccharide cellobiose **114** (Figure 54b) in water forming a 1:1 inclusion complex with K_{app} = 6.5 x 10^2 M^{-1}. Analyses of 2D NMR spectra of the **114⊂121** complex revealed that the glycosidic bond of **114** adopts a *cis*-conformation in the hydrophilic cavity of the "temple" receptor to satisfy the shape, size and function complementarity principles (Figure 57).

ITC titration experiments indicated that the binding process of the **114⊂121** complex is enthalpically driven (ΔH = -3.2 kcal·mol^{-1}) and accompanied by a small favorable entropy ($T\Delta S$ =

0.6 kcal·mol^{-1}). The enthalpic gain cannot be assigned to the release of "high-energy" water molecules from the receptor's cavity to the bulk solution because the bound solvent molecules are likely stabilized by hydrogen-bonding interactions with the amide functions of the hydrophilic "temple" receptor. Most likely, the hydrogen-bonding and CH-π interactions stablished between the host and the guest upon complexation are responsible for the favorable enthalpic contribution.[49,164,196]

The effect of inorganic anions, such as thiocyanate ($^{-}$SCN), on carbohydrate binding has been investigated using the synthetic "temple" receptors **111** and **121**. In the presence of KSCN, the association constant values of the saccharide complexes decrease more than three-fold. Most likely, the chaotropic anion competes with the carbohydrate guests for the non-polar regions and hydrogen bond donors of the "temple" receptor.[197]

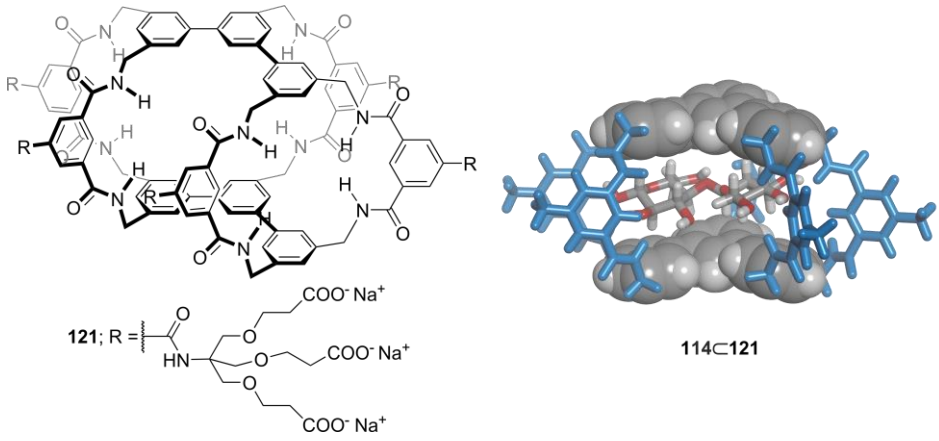

Figure 57. (left) Line-drawing structure of **121** and (right) energy minimized structure (MM3) of **114⊂121**. The "roof" and "floor" of the "temple" receptor are shown as CPK models and the "pillars" (blue) are depicted in stick representation. The bound di-saccharide is depicted in stick representation. Water-solubilizing groups were pruned to methyl groups to ease the calculation.

Sensing of glucose in biological media is a challenging task because it requires the use of water-soluble receptors displaying high-binding affinity and selectivity. In the recent years, the group of Davis has developed "temple" receptors for glucose. The "temple" receptor **122** is based on two anthracene panels and two isophthalamide spacers (Figure 58). The *bis*-anthracenyl receptor **122** binds glucose **112** featuring an apparent binding constant value K_{app} = 56 M^{-1}. Remarkably, the methyl *β*-D-glucoside **113** and the "temple" receptor **122** form a 1:1 inclusion complex featuring an stability constant of 96 M^{-1} (Figure 58). These binding constant values are adequate for sensing glucose in blood. In contrast, the receptor **122** displays low binding affinity towards other mono-saccharides, K_a or K_{app} < 1 M^{-1}.[198]

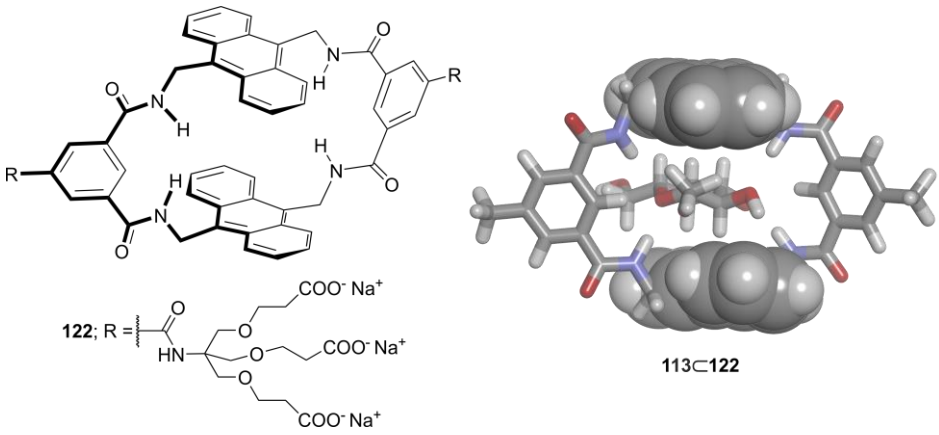

Figure 58. (left) Line-drawing structure of **122** and (right) energy minimized structure (MM3) of the **113⊂122** complex. The "roof" and "floor" of the receptor are shown as CPK models and the "pillars" are depicted in stick representation. The guest is also depicted in stick representation. Water-solubilizing groups were pruned to methyl groups to ease the calculation.

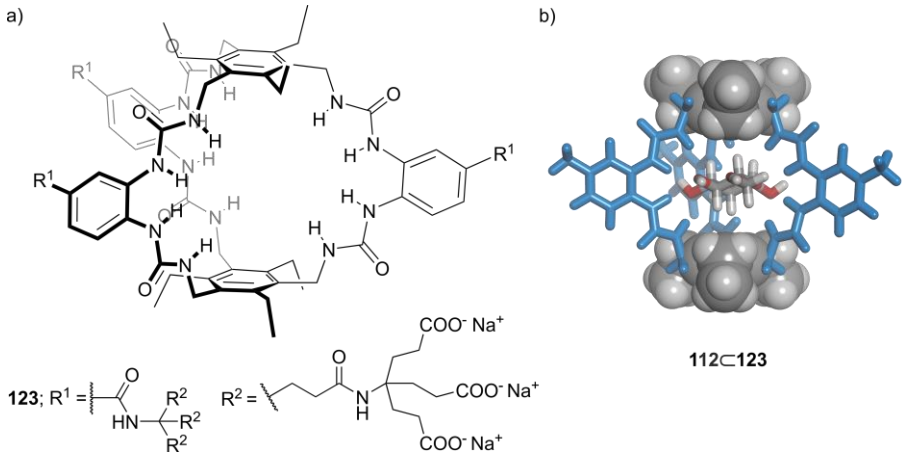

Figure 59. (left) Line-drawing structure of "temple" receptor **123** and (right) energy minimized structure (MM3) of *β*-**112⊂123**. The "roof" and "floor" of the receptor are shown as CPK models and the "pillars" (blue) are depicted in stick representation. The guest is depicted in stick representation. Water-solubilizing groups were pruned to methyl groups to ease the calculation.

More recently, the same research group reported a highly efficient receptor **123** for glucose **112**. The "temple" receptor **123** is based on two tri-ethylmesitylene groups linked together by *ortho*-urea-substituted phenyl units. The six urea groups of **123** offer a total of twelve NH functions that are available to stablish multiple hydrogen-bonding interactions in the interior of the three-dimensional cavity. In this respect, the complex **112⊂123** features a remarkable apparent binding constant value K_{app} = 1.8 x 10^4 M^{-1} in water (Figure 59). Other mono-saccharides have constant values that are one order of magnitude lower than that of the **112⊂123** complex. Additionally, non-

saccharide guests are not included in the cavity of **123**.[199] These results demonstrate that synthetic receptors relying on hydrogen-bonding and CH-π interactions can feature high-binding affinity and selectivity in water.

Other "temple" receptors, which structurally resemble the ones discussed above, have been used to complex poly-saccharides. Note that poly-saccharides, such as cellulose, display low solubility in water. However, the "temple" receptors bind to different regions of the poly-saccharide structure and increase the solubility of the bound form in water. The resulting supramolecular polymer features a poly-rotaxane topology.[195]

1.4.2 Functionalized molecular tubes

Endo-functionalized molecular tubes are based on two *bis*-naphthalene clefts linked together by two amide bonds. The synthesis of these compounds yields a mixture of two isomers: *syn* and *anti*. The *syn*-isomer displays the two *bis*-naphthalene units with the same orientation. On the contrary, the *anti*-isomer features the naphthalene clefts in opposite directions (Figure 60).

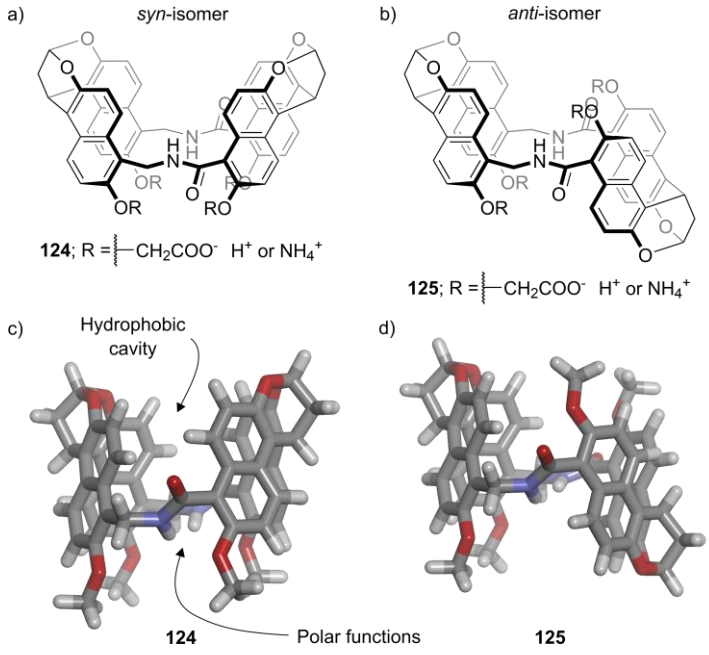

Figure 60. Line-drawing structures of *endo*-functionalized molecular tubes: a) **124** and b) **125**. Energy minimized structures (MM3): c) **124** and d) **125**. The structures are depicted in stick representation. Hydrophobic cavity and polar functions of **124** are indicated. Water-solubilizing groups were pruned to methyl groups to ease the calculations.

The structure of the *syn*-isomer **124** is relatively rigid and enjoys a deep aromatic cavity. However, the *anti*-isomer **125** is structurally flexible and displays a shallow aromatic cavity (Figure 60). The cavity of both isomers is opened at two opposite ends. In addition, the molecular tubes, **124** and

125, bear two amide linkages, whose NHs are inwardly-oriented to the aromatic cavity. The structures of the *endo*-functionalized molecular tubes also contain peripheral carboxylate groups to impart water solubility.[200,201]

In particular, the molecular tube **124** shows a deep hydrophobic cavity with a polar opened end defined by the inwardly-directed amide NHs (Figure 60a,c). Therefore, the NH functions of **124** are partially shielded from the bulk aqueous solution, but the cavity of the tube is likely solvated. The release of bound water molecules from the cavity of the molecular tube **124** to the bulk solution drives the binding of complementary guests.[201]

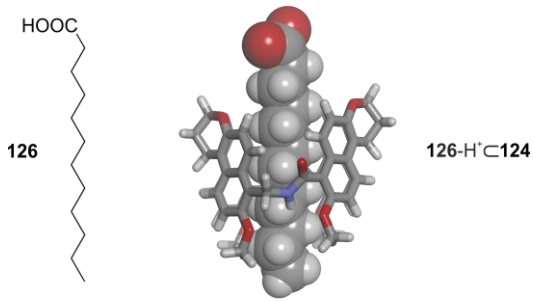

Figure 61. (left) Line-drawing structure of dodecanoic acid **126** and (right) energy minimized structure (MM3) of the **126**-H^+⊂**124** complex. The receptor is depicted in stick representation and the guest is shown as CPK model. Water-solubilizing groups were pruned to methyl groups to ease the calculation.

The water-soluble molecular tubes **124** and **125** were originally reported by Glass and co-workers in 2004. They used the *endo*-functionalized tubes to investigate the binding of long-chain carboxylic acids, *i.e.* fatty acids. The binding experiments were conducted in 20 mM Na_2CO_3 aqueous solution at pH = 8.4. The results showed that the receptors **124** and **125** bind the hydrocarbon chain of fatty acids through the hydrophobic effect. The ionized carboxylic acid of the bound guest is exposed to the bulk aqueous solution (Figure 61). In general, both receptors feature similar constant values with the same fatty acid and the magnitude of these values increases with the chain length of the guest. The largest binding constant value was determined for dodecanoic acid **126**, K_a (**126**⊂**124** or **126**⊂**125**) ~ 2 x 10^4 M^{-1}.[200] Note that the hydrophilic cavity of the receptor **124** is suitable for the inclusion of the carboxylate group of **126**. The bound carboxylate would be involved in charge-dipole and hydrogen-bonding interactions with the amide NHs. However, this binding geometry was not detected by NMR spectroscopic techniques. This is derived from the high-energetic cost of the desolvation of the carboxylate group prior to binding.

Later, Jiang and co-workers applied the *endo*-functionalized molecular tubes **124** and **125** for the recognition of neutral polar guests in water. The hydrophilic cavity of these receptors is appropriate for the binding of small molecules having a non-polar section and one or two hydrogen-bonding acceptor groups. In this regard, the hydrophobic effect and hydrogen-bonding interactions work in

synergy to drive the inclusion of neutral polar molecules to the interior of the *endo*-functionalized receptors. For example, the *syn*-receptor **124** binds di-methylformamide **127** featuring a binding constant value K_a (**127⊂124**) = 3.1 x 10^2 M^{-1}. The complex between tetrahydrofuran and **124** is characterized by a similar constant value. Note that these guests, di-methylformamide and tetrahydrofuran, feature one hydrogen-bonding acceptor group. On the contrary, the *anti*-receptor **125** is not efficient for the binding of these polar guests. The binding affinity of the complexes of **125** is lower than 10^2 M^{-1}.[201]

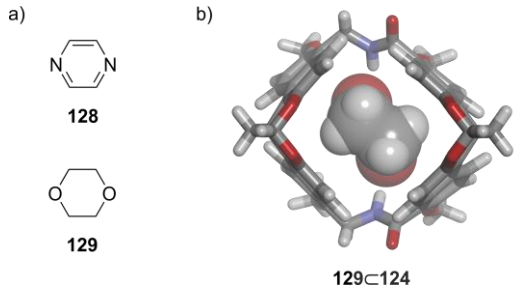

Figure 62. a) Line-drawing structures of guests **128** and **129**; b) energy minimized structure (MM3) of **129⊂124** (top view). The host is depicted in stick representation and the guest is shown as CPK model. Water-solubilizing groups were pruned to methyl groups to ease the calculation.

Pyrazine **128** and 1,4-dioxane **129** possess two polar atoms that are function complementary to the hydrophilic cavity of the molecular tubes (Figure 62a). In addition, they are size and shape complementary to the receptor's cavity. Remarkably, the binding constant value of the 1:1 inclusion complex between **124** or **125** and pyrazine **128** is K_a ~ 2 x 10^3 M^{-1}. More surprisingly, 1,4-dioxane **129** and the *syn*-receptor **124** stablish a thermodynamically highly stable complex featuring K_a = 1.4 x 10^4 M^{-1}. However, the binding constant value drops one order of magnitude for the analogous complex using the *anti*-receptor, K_a (**129⊂125**) = 3.2 x 10^3 M^{-1}. The polar functions of the guests **128** and **129** stablish two simultaneous hydrogen-bonding interactions with the amide NHs of the *syn*-receptor **124** (Figure 62b). ^{1}H NMR titration experiments in 9:1 H_2O/D_2O solution supported the formation of strong hydrogen bonds in the inclusion complexes. The non-polar section of either **128** or **129** is buried in the binding pocket of **124**, defined by the *bis*-naphthalene clefts. It is worth mentioning that the *syn*-receptor **124** displays high-binding selectivity for 1,4-dioxane **129** versus other polar guests (see below).[201,202]

ITC titration experiments revealed that the complexation process of 1,4-dioxane **129** with the *syn*-receptor **124** is enthalpically driven, ΔH = -4.1 kcal·mol^{-1}. The small entropic contribution favors binding, $T\Delta S$ = 1.3 kcal·mol^{-1}. Therefore, the "non-classical" hydrophobic effect and polar interactions are involved in the formation of the **129⊂124** complex in water.[201]

Recently, Jiang and co-workers investigated the driving forces and molecular properties involved in the binding of polar guests by the *endo*-functionalized molecular tubes. Principal component analysis revealed that the hydrophobicity, volume, surface area and polarizability of the guest affect positively on the binding affinity (K_a) of the complex. On the other hand, the dipole moment of the guest has a detrimental effect in the K_a value. It is worth mentioning that these molecular properties are not only the main factors to consider for efficient binding. *In-silico* calculations indicated that the binding process of polar guests with *endo*-functionalized molecular tubes is driven by the hydrophobic effect. In addition, the formation of intermolecular hydrogen bonds is key to achieve high-binding selectivity for polar versus non-polar guests. Based on these findings, the guest must be size, shape and function complementary to the hydrophilic cavity of the *endo*-functionalized receptors. Furthermore, the ideal guest should form two hydrogen bonds with the amide NHs and fill completely the cavity of the receptor. The later would provoke the release of the bound water molecules. In this regard, Jiang and co-workers designed the guest **130**, which shows a perfect fit for the cavity of the *syn*-receptor **124** (Figure 63). The **130⊂124** complex features a binding constant value K_a = 2.2 x 10^6 M^{-1}, which is one of the largest reported to date for the complexation of a small polar molecule by a synthetic host in water. The binding process is characterized by a favorable enthalpy, ΔH = -10.8 kcal·mol^{-1}, and an unfavorable entropy, $T\Delta S$ = -2.4 kcal·mol^{-1}.[202]

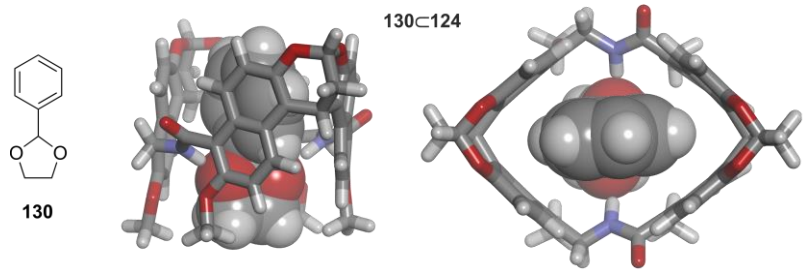

Figure 63. (left) Line-drawing structure of **130** and (right) energy minimized structure (MM3) of the **130⊂124** complex: side and top views. The host is depicted in stick representation and the guest is shown as CPK model.

The *endo*-functionalized molecular tubes **124** and **125** have been applied to the sensing of epoxides. For example, chiral epoxides transfer the chirality to the molecular tube upon host-guest complexation. In this respect, the receptors **124** and **125** serve to quantify the enantiomeric excess of the products derived from asymmetric reactions.[203]

The *endo*-functionalized molecular tubes **124** and **125** has been also used for the assembly of poly(pseudo-rotaxanes). These supramolecular polymers are converted into hydrogels upon metal complexation.[204]

1.4.3 Calix[4]pyrroles

Calix[4]pyrroles are comprised of four pyrrole units linked together by sp^3-carbon atoms, known as *meso*-carbons. The structure of calix[4]pyrroles is relatively flexible and, for this reason, they can adopt multiple conformations in solution. These conformations are characterized by the relative orientation of the pyrrole units of the calix[4]pyrrole core. In non-polar solvents, such as dichloromethane and chloroform, the calix[4]pyrroles adopt an alternate conformation: 1,2- or 1,3-alternate. On the contrary, the calix[4]pyrroles display a cone or partial-cone conformation in polar solvents, such as acetone, acetonitrile and methanol. In the cone conformation, the calix[4]pyrroles are able to stablish four convergent hydrogen-bonding interactions between the four pyrrole NHs and the polar atom of the bound molecule.

The incorporation of aromatic substituents at the *meso*-carbons of calix[4]pyrroles gives aryl-extended derivatives. The relative orientation of the *meso*-aromatic substituents dictates the configuration of the aryl-extended calix[4]pyrroles. Thus, four configurational isomers can exist: *ααββ*, *αβαβ*, *αααβ* and *αααα*. This assignment is in agreement with the literature of porphyrins. For example, the tetra-*α* or *αααα*-isomer of an aryl-extended calix[4]pyrrole in the cone conformation features a deep aromatic cavity closed at one end by a polar binding site and opened at the opposite end (Figure 64).[4,205]

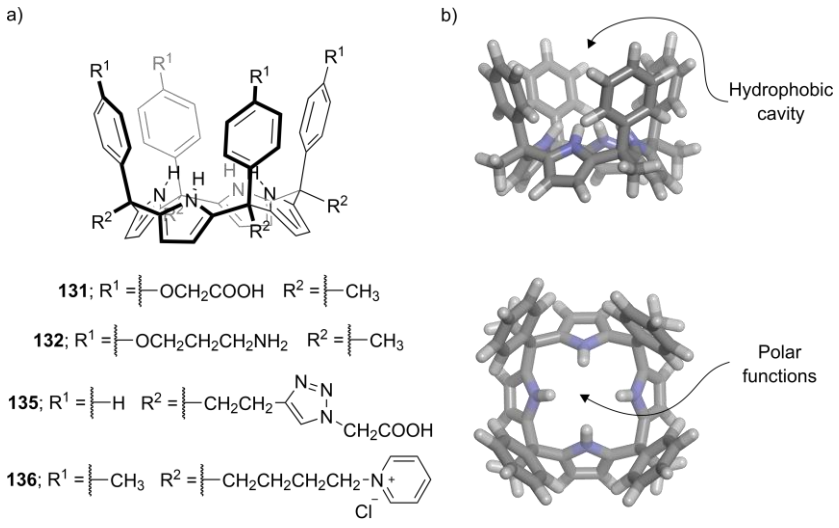

Figure 64. a) Line-drawing structures of aryl-extended calix[4]pyrroles **131**, **132**, **135** and **136**; b) energy minimized structure (MM3) of the tetra-*α* isomer of an aryl-extended calix[4]pyrrole in the cone conformation: side and top views. The receptor is depicted in stick representation. Substituents at the upper and lower rims are removed for clarity.

In water solution, the conformation of the tetra-*α* isomer of aryl-extended calix[4]pyrroles remains elusive. The aryl-extended calix[4]pyrrole may adopt alternate and cone conformations which rapidly interconvert on the ^{1}H NMR chemical shift timescale. In any case, the polar aromatic cavity

of the calix[4]pyrrole is likely solvated by a few number of "high-energy" water molecules. In general, 1:1 inclusion complexes are established between the tetra-*α* isomer of aryl-extended calix[4]pyrroles and neutral polar guests. The inclusion of the guest in the hydrophilic cavity of the calix[4]pyrrole provokes the locking of the receptor in the cone conformation. Furthermore, the binding of the polar guest isolates the hydrogen bond functions of both binding partners in the hydrophobic cavity of the receptor from the bulk aqueous solution. This is a unique characteristic of the inclusion complexes derived from aryl-extended calix[4]pyrrole receptors. In this respect, it is expected a substantial contribution of hydrogen-bonding interactions to the binding free energy.[205] The hydrophobic effect is also involved to achieve high levels of binding affinity.

Tetra-*α* aryl-extended calix[4]pyrroles equipped with ionizable or charged groups at either the upper or lower rim have been reported in the literature. In 2009, we introduced two water-soluble aryl-extended calix[4]pyrroles. The aryl-extended calix[4]pyrroles were functionalized with carboxylic acids, **131**, and amino groups, **132**, at the upper rim (Figure 64a). Both calix[4]pyrroles are soluble at millimolar concentrations in water solution at pH ~ 7. Interestingly, the calix[4]pyrroles **131** and **132** bind pyridyl *N*-oxides, **133** and **134**, forming thermodynamically and kinetically stable 1:1 inclusion complexes (Figure 65a). The binding constant value of pyridine *N*-oxide **133** with any of the two hosts is *ca.* 2 x 10^3 M^{-1}. This value increases up to *ca.* 2 x 10^4 M^{-1} for the *para*-phenyl derivative **134**. The determination of similar binding constant values for the same pair of complexes using neutral guests supports that the nature of the water-solubilizing groups does not impact on their thermodynamic stability.[206] The oxygen atom of the bound pyridyl *N*-oxide stablishes hydrogen-bonding interactions with the four pyrrole NHs of the calix[4]pyrrole core of the receptor. The four aromatic walls of the receptor are engaged in π-π and CH-π interactions with the aromatic groups of the bound guest.

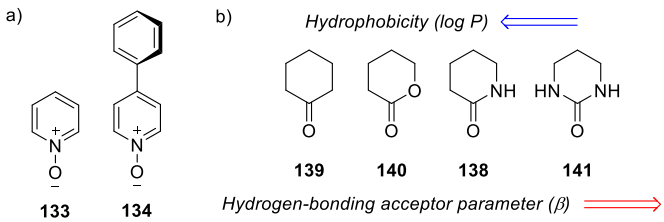

Figure 65. Line-drawing structures of neutral polar guests: a) pyridyl *N*-oxides **133** and **134** and b) six-membered ring guests **138**-**141**. Trends of hydrophobicity (log *P*) and hydrogen-bonding acceptor parameter (*β*) are indicated in the six-membered ring series.

However, the upper rim substituents of the aryl-extended calix[4]pyrroles **131** and **132** might affect the stability of the inclusion complexes by partially blocking the open portal of the receptor's cavity. In this regard, the water-solubilizing groups were moved to the lower rim of the aryl-extended calix[4]pyrrole structure in **135** (Figure 64a). The carboxylic acids of **135** are located at the opposite site of the calix[4]pyrrole's binding pocket. This prevents the interference of the water-

solubilizing groups in the binding process. Nevertheless, the binding constant value of the **133⊂135** complex is similar to that of **133⊂131**. This result indicates that the water-solubilizing groups, at either the upper or lower rim of the aryl-extended calix[4]pyrrole receptor, have a minimum effect in the thermodynamic stability of the inclusion complexes.[207]

ITC titration experiments revealed that the binding process of pyridyl *N*-oxides with aryl-extended calix[4]pyrrole receptors is strongly driven by the enthalpy in water.[207] This thermodynamic signature is characteristic of the "non-classical" hydrophobic effect operating in these host-guest complexes. Polar interactions, such as hydrogen-bonding, are also involved. However, the contribution of the intermolecular forces to the binding free energy is difficult to dissect.

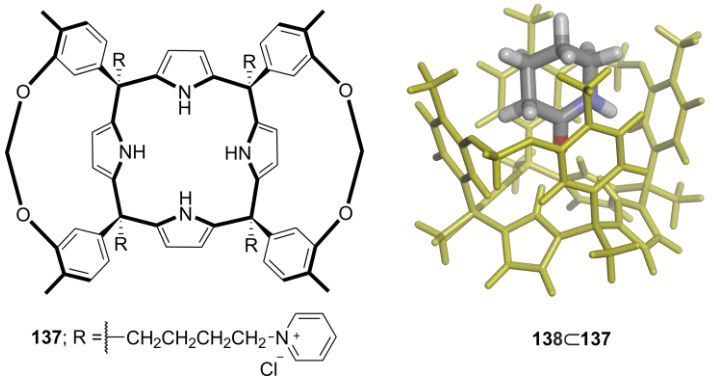

Figure 66. (left) Line-drawing structure of aryl-extended calix[4]pyrrole cavitand **137** and (right) energy minimized structure (MM3) of the **138⊂137** complex. The host (yellow) and the guest are depicted in stick representation. Water-solubilizing groups were pruned to methyl groups to ease the calculation.

The aryl-extended calix[4]pyrrole receptors discussed above are functionalized at either the upper or lower rim. In 2017, the Ballester group reported a synthetic methodology for the synthesis of upper and lower rim functionalized tetra-*α* isomers of aryl-extended calix[4]pyrroles. The method involves the use of methyltributylammonium chloride and 4 M HCl in dioxane. The ammonium chloride salt acts as a template in the formation of the tetra-*α* isomer.[208] For example, the aryl-extended calix[4]pyrrole **136** (Figure 64a) and the calix[4]pyrrole cavitand **137** (Figure 66) were synthesized following this synthetic methodology.[209]

The receptors **136** and **137** display good binding affinities, K_a > 10^4 M^{-1}, towards size complementary lactams, for example, the six-membered ring **138**, in water (Figure 65b). The energy minimized structure (MM3) of the **138⊂137** complex shows the oxygen atom of the amide hydrogen-bonded to the four pyrrole NHs of the calix[4]pyrrole core in the cone conformation. The non-polar section of the lactam is buried in the deep cavity of the receptor, where it establishes multiple CH-π contacts with the *meso*-aromatic walls. The NH of the bound lactam is also engaged in NH-π interactions (Figure 66).[209]

The relevance of hydrogen-bonding interactions in the binding affinity (K_a) of the aryl-extended calix[4]pyrrole complexes in water was demonstrated using a series of cyclic polar guests: cyclic ketone **139**, lactone **140**, lactam **138** and cyclic urea **141** (Figure 65b). These guests feature different polarity (carbonyl oxygen atom) and hydrophobicity. The later decreases from the cyclic ketone **139** (more hydrophobic) to the cyclic urea **141** (less hydrophobic) using calculated log *P* values (partition coefficient between octanol and water). As discussed previously, the binding constant value is expected to increase with the hydrophobicity of the guest, *i.e.* K_a (**139**⊂receptor) should be larger than K_a (**141**⊂receptor). Nevertheless, the calix[4]pyrrole receptors **136** and **137**, having a shielded hydrophilic cavity, display the opposite binding behavior: the less hydrophobic guest, **141**, is bound stronger than the more hydrophobic counterpart, **139**. The polarity of the guest seems to favor binding. Indeed, the binding free energy shows a linear relationship with the hydrogen-bonding acceptor parameter (β) of the carbonyl oxygen atom of the guest series. For example, the 1:1 inclusion complex of the cyclic ketone **139** (less polar, $\beta \sim 6$) features a binding constant value $K_a \sim 10^3\ M^{-1}$. This value increases two orders of magnitude for the cyclic urea **141** (more polar, $\beta \sim 9$). These results indicate that hydrogen-bonding interactions in water not only play a role in the binding selectivity of the calix[4]pyrrole receptors towards polar guests, but also contribute to the binding free energy (ΔG) to a significant extent. The deep cavity of the aryl-extended calix[4]pyrrole receptors places the polar functions in a non-polar environment, where they are able to work efficiently. Furthermore, the binding of these cyclic polar guests **138**-**141** is driven by a strong enthalpic contribution. This indicates that the "non-classical" hydrophobic effect is operative in these host-guest complexes.[209]

Other applications of aryl-extended calix[4]pyrroles were reported in the literature. For example, Sessler and co-workers showed that the tetra-acid **131** self-assembles into high-order aggregates in the presence of a di-topic *bis*-*N*-oxide in aqueous solution. The morphology of the corresponding supramolecular assembly can be controlled by changing the pH of the solution.[210]

1.5 Self-Assembled Receptors

Self-assembly is a supramolecular approach based on the non-covalent interaction of molecular units, *i.e.* building blocks, to produce large, well-defined architectures under thermodynamic control. The information for the assembly is encoded in the binding motifs of the building blocks. In this regard, self-assembled containers have been prepared using metal-ligand coordination bonds or non-covalent forces: hydrophobic effect, Columbic or hydrogen-bonding interactions.[1,14,15,16,18,31]

In this section, we divide self-assembled molecular containers in two categories: cages and capsules. We define cages as self-assembled receptors that feature large portals allowing the reversible passage of guests. They are assembled from flat, rigid multi-topic ligands and metal ions (*i.e.* metal coordination cages). On the other hand, capsules feature an enclosed cavity in which the in/out exchange of the guest requires the partial or total dissociation of the capsular

assembly. In general, capsules are assembled from concave building blocks, such as calix[4]arenes and resorcin[4]arenes (Section 1.3).

1.5.1 Metal coordination cages

The formation of coordination bonds between metal ions and multi-topic ligands leads to metal coordination cages. Metal-ligand coordination bonds are strong in both non-polar and polar solvents, unless a competitive coordinating solvent is used. In general, the metallo-cages are soluble in water owing to the use of multiple metal ions for their assembly. In addition, polar, ionizable or charged groups can be incorporated in the structure of the ligands to improve the water solubility and circumvent the aggregation of the self-assembled metallo-cage.[16]

Most of the metal coordination cages feature a hydrophobic cavity, which can accommodate size and shape complementarity guests. The overall charge of the metallo-assembly imposes charge binding selectivity and affect the stability and reactivity of bound guests.[16]

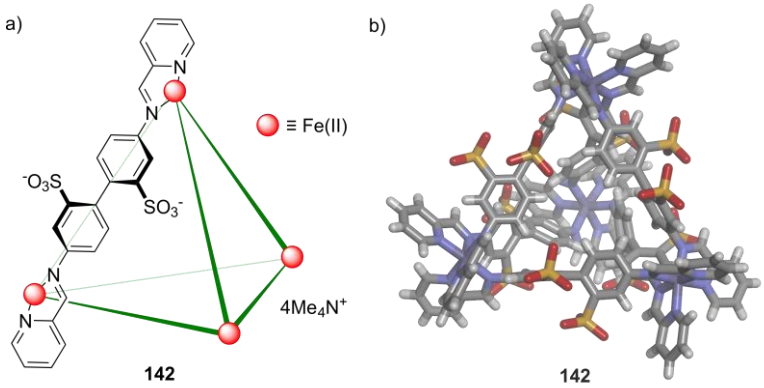

Figure 67. a) Cartoon representation and b) energy minimized structure (MM3) of the tetrahedral Fe(II)-cage **142**. The cage is depicted in stick representation.

Nitschke and co-workers reported the self-assembly of a tetrahedral M_4L_6 cage **142** using Fe(II) metal ions and bi-phenyl imine ligands bearing sulfonate groups (Figure 67). Similar metallo-cages were obtained by replacing the Fe(II) metal centers by Co(II) or Ni(II). The cage **142** is soluble in water owing to the four Fe(II) ions at the vertices and the outwardly-oriented sulfonate groups at the edges of the tetrahedron (overall charge = -4). Interestingly, the configuration of a vertex of **142** is mechanically coupled to the others owing to the ligand rigidity. This leads to a racemic mixture of two homo-quiral assemblies, ΔΔΔΔ and ΛΛΛΛ, both displaying *T* symmetry. The cage **142** features a cavity volume of *ca.* 140 Å^3.[211,212,213]

The Fe(II)-cage **142** binds preferentially neutral non-polar molecules versus polar or cationic guests. The inclusion of a suitable guest in the tetrahedral cavity of **142** is driven by the

hydrophobic effect. For example, cyclohexane and **142** form a 1:1 cage complex in water featuring a binding constant value K_a = 7.1 x 10^4 M^{-1}. In contrast, the cage complex of 1,4-dioxane **129** shows a drop of more than two orders of magnitude in the binding affinity value with respect to the complex of cyclohexane, K_a (**129⊂142**) = 1.5 x 10^2 M^{-1}. Aromatic guests are also included in the hydrophobic cavity of the cage **142**. For example, benzene forms a thermodynamically stable cage complex with **142** in water, K_a = 3.0 x 10^3 M^{-1}.[211,214]

Furthermore, binding studies using the tetrahedral cage **142** and a series of guests indicated that the binding affinity values of the cage complexes are related to the hydrophobicity of the guest: the more hydrophobic guest, the larger the binding constant value. On the other hand, the magnitude of the rate constant for the formation of the cage complex depends on the size and shape of the guest. For example, a bulky guest passes slowly through any of the cage portals. A slippage mechanism, *i.e.* deformation of a cage's face, operates for the entrance/exchange of the guest in the cage complex.[16]

The tetrahedral Fe(II)-cage **142** offers a hydrophobic environment to protect reactive species in water. For example, white phosphorus (P_4) **143** is air sensitive. Nevertheless, white phosphorus **143** can be stored in the cavity of the Fe(II)-cage **142** in water and in the presence of oxygen (Figure 68). The stabilization of **143** is rationalized by the constrictive binding of the guest in the cage's cavity, rather than the unfavorable passage of molecular oxygen through the portals of the cage. Any oxidized product of **143** does not fit in the cavity of the tetrahedron **142**.[18,215,216]

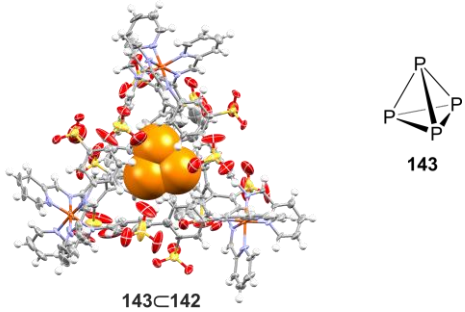

Figure 68. (left) X-ray structure of the **143⊂142** cage complex and (right) structure of white phosphorus **143**. The structure is shown in ORTEP view with thermal ellipsoids set at 50% probability. Hydrogen atoms are shown as fixed-size spheres of 0.3 Å. Bound molecule is shown as CPK model.

The Raymond group also reported a tetrahedral M_4L_6 cage **144**, but using different metal ions and ligands for the assembly: tri-valent or tetra-valent metal ions (Ga(III), Al(III), Fe(III), Si(IV) or Ti(IV)) and a *bis*-catechol-substituted naphthalene ligand (Figure 69). The structures of these M_4L_6 cages are analogous. In this respect, we discuss the properties and applications of the Ga(III)-cage **144**, and we refer to other tetrahedral cages, having different metal centers, for comparison. Note that the *bis*-catechol naphthalene ligand is relatively rigid owing to the formation of an intramolecular

NH···O hydrogen bond. In analogy to the Fe(II)-cage **142**, the Ga(III)-cage **144** is synthesized as a racemic mixture of two *T*-symmetric homo-chiral assemblies, ΔΔΔΔ and ΛΛΛΛ.

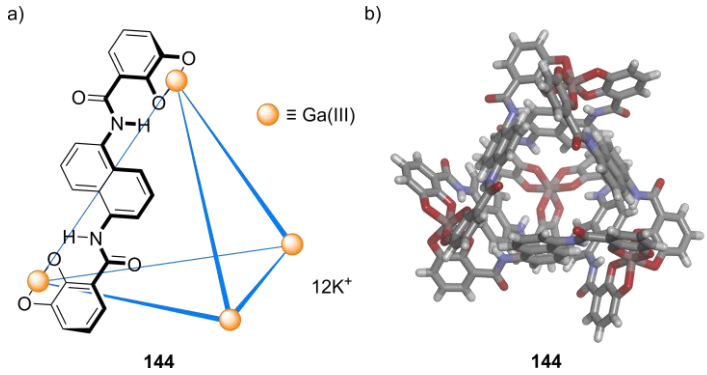

Figure 69. a) Cartoon representation and b) energy minimized structure (MM3) of the tetrahedral Ga(III)-cage **144**. The cage is depicted in stick representation.

The Ga(III)-cage **144** has twelve negative charges imparting water solubility. The binding pocket of **144**, which is surrounded by six naphthalene panels, is hydrophobic. Therefore, neutral or cationic guests bind efficiently to the cavity of **144** through the hydrophobic effect, Columbic, cation-π and CH-π interactions. Furthermore, the cavity size of **144** can suffer subtle expansions/contractions to accommodate the guest. Thus, it can display a maximum volume of *ca.* 450 $Å^3$.

The formation of the cage complex between a neutral or cationic guest and the Ga(III)-cage **144** is driven by the entropy, $T\Delta S$ = 12-24 kcal·mol^{-1}. This thermodynamic signature is derived from the desolvation of the cage's cavity upon complexation and corresponds to the "classical" hydrophobic effect. Cationic guests can also bind to the exterior of the cage through cation-π and Columbic interactions. The later binding process is typically driven by the enthalpy.[1,16,217,218,219]

In general, cyclic and acyclic organic ammonium cations (*e.g.* tetra-alkylammonium, protonated *N*-alkyl aziridines, azetidines, pyrrolidines and piperidines) are bound to the cavity of the Ga(III)-cage **144**. The corresponding cage complexes feature good binding affinities.[17] For example, the binding constant value of the 1:1 complex between tetra-ethylammonium **145** and the cage **144** is K_a (**145**⊂**144**) = 3.5 x 10^4 M^{-1}. The included guest **145** is involved in a slow chemical exchange process on the ^{1}H NMR chemical shift timescale with the free counterpart. The guest in/out exchange process in the cage complex involves a slippage mechanism. On the other hand, the constant value for the binding of the cation **145** to the exterior of the tetrahedral cage **144** is K_a (**145**⊂**144** → **145**[**145**⊂**144**]) ~ 60 M^{-1}. The later binding process shows fast dynamics on the same timescale for the free and bound **145** (Figure 70).[218,220,221]

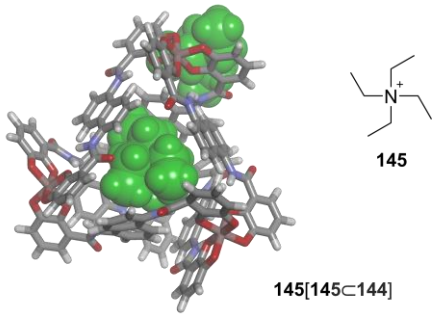

Figure 70. (left) Energy minimized structure (MM3) of **145**[**145**⊂**144**] and (right) tetra-ethylammonium cation **145**. The cage is depicted in stick representation and the guests (green) are shown as CPK models.

In the same vein, protonated secondary and tertiary amines are stabilized in the cavity of the tetrahedral Ga(III)-cage **144** through Columbic and cation-π interactions. Remarkably, the bound protonated amine experiences an increase of 2-5 pK_a units in basicity. Bound protonated phosphines also enjoy an increase in basicity. Additionally, proton-bound homo-dimers of cyclic amines are stabilized in the hydrophobic cavity of the Ga(III)-cage **144**.[215,217,222]

The stabilization of cationic species in water using the Ga(III)-cage **144** has been applied to the isolation of iminium cations, such as **146**. The iminium cation **146** is generated in situ from 2-pentanone and pyrrolidine, and it is then stabilized in the cavity of the cage **144** (Scheme 5). Note that the iminium cation **146** can be rapidly hydrolyzed in water in the absence of the cage.[223]

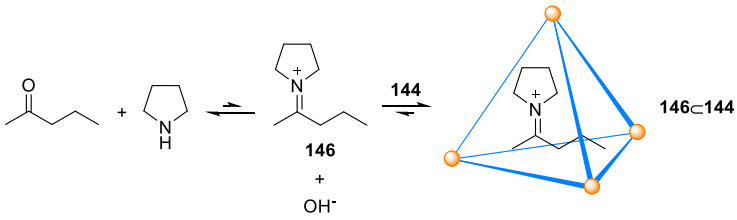

Scheme 5. Protection of the iminium cation **146** in the interior of the Ga(III)-cage **144**.

The results discussed above show that the Ga(III)-cage **144** is able to stabilize cationic species through a combination of Columbic and cation-π interactions. The cage **144** is also hydrophobic, allowing the stabilization of neutral non-polar species. These properties have been exploited by Raymond and co-workers to stabilize transition states or destabilize ground states. Both should produce a rate acceleration for a particular process.[1]

For example, the Ga(III)-cage **144** increases the rate of the C(O)-N bond rotation of bound symmetric tertiary amides in water. The planar ground state of the amide is destabilized in the interior of the cage **144**, where it adopts a twisted conformation. This provokes a decrease of up to

3.6 kcal·mol^{-1} in the energy barrier for amide bond rotation. The C(O)-N bond rotation of *N*,*N*-di-propyl nicotinamide **147** is 450-fold faster in the bound than in the free state (Scheme 6).[224] The inversion-rotation process of bound protonated amines is also accelerated by the Ga(III)-cage **144**.[215,217]

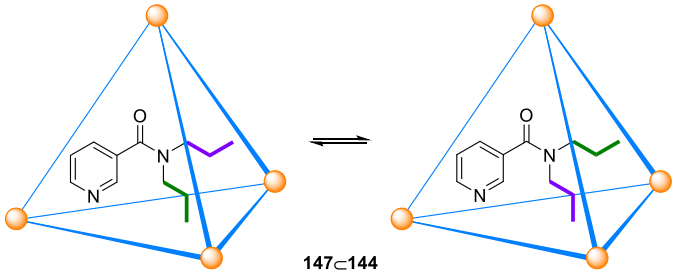

Scheme 6. Amide bond rotation of **147** in the **147⊂144** cage complex.

The binding and stabilization of reactive species and transition states suggested the application of the Ga(III)-cage **144** to mediate or catalyze chemical reactions in water occurring through cationic transition states. The inclusion of the guest in the cavity of the metallo-cage is driven by the hydrophobic effect and Columbic forces. The transition state is then stabilized by electrostatic interactions. Additionally, the application of the Ga(III)-cage **144** as catalyst requires to circumvent the issue of product inhibition, for example, obtaining a product that is a poor guest for the cage's cavity.[7,217] The aza-Cope rearrangement of allylenammonium or propargylenammonium cations involves charged intermediates and transition states, maintaining the net charge throughout the reaction. The Ga(III)-cage **144** accelerates the aza-Cope rearrangement of these bound species, such as **148**, by almost three orders of magnitude with respect to the background reaction under the same experimental conditions. The tetrahedral cage **144** binds the allylenammonium cation **148** in a chair-like conformation suitable to undergo the aza-Cope rearrangement. Interestingly, the product is an iminium cation which is further hydrolyzed to the corresponding aldehyde in the bulk aqueous solution. The neutral aldehyde cannot compete with the cationic guest (starting material) for the cavity of the anionic cage **144**, enabling catalytic turnover (Scheme 7).[225,226]

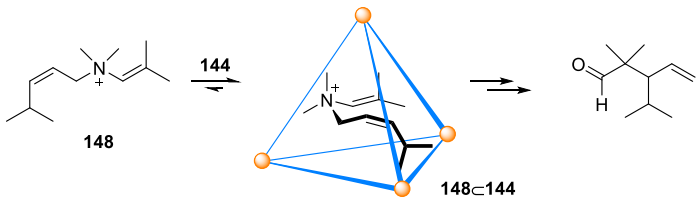

Scheme 7. Aza-Cope rearrangement of allylenammonium cation **148** catalyzed by the Ga(III)-cage **144**.

On the other hand, the Nazarov cyclization of neutral penta-methyl cyclopentadienol involves a positively charged transition state. In this case, the net charge changes throughout the reaction. The Ga(III)-cage **144** catalyzes the Nazarov cyclization through the stabilization of the positively charged transition state leading to a remarkable rate acceleration, $k_{cage}/k_{bulk} \sim 10^6$.[17,18]

The effect of the overall charge of the metallo-cage in the catalytic performance was investigated by the Raymond group using two isostructural tetrahedral cages: the Ga(III)-cage **144** and the Si(IV)-cage. The Si(IV)-cage has eight negative charges, whereas the Ga(III)-cage **144** contains four additional charges of the same sign. As expected, the two cages provide similar rate constant values for the aza-Cope rearrangement because the net charge is constant throughout the reaction. Nevertheless, the Ga(III)-cage **144** induces a rate acceleration of almost three orders of magnitude larger than the Si(IV)-cage for the Nazarov cyclization reaction. In this case, the Ga(III)-cage stabilizes better the cationic transition state, which is generated throughout the reaction, than the Si(IV)-cage.[227]

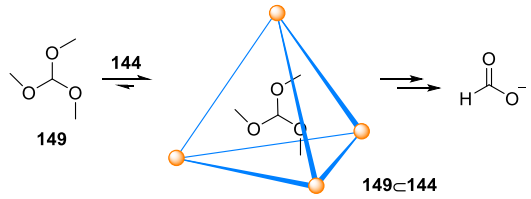

Scheme 8. Hydrolysis of orthoformate **149** catalyzed by the Ga(III)-cage **144** in basic aqueous solution.

Furthermore, the Ga(III)-cage **144** catalyzes the hydrolysis of orthoformate esters, such as **149**, and acetals in basic aqueous solution. Orthoformates and acetals are stable in neutral or basic aqueous solution but are readily hydrolyzed in acidic media. The Ga(III)-cage **144** binds the orthoformate ester or acetal and catalyzes the hydrolysis reaction in water at pH > 10. The hydrolysis of orthoformates gives the formate anion as product, which cannot compete for binding to the anionic metallo-cage (Scheme 8). On the other hand, the hydrolysis of acetals produces the corresponding aldehyde, which is further converted to the aldehyde hydrate in the bulk solution. Both products are less hydrophobic guests than the reactant, which enable catalytic turnover.[217,228,229]

Octahedral M_6L_4 cages have been designed by Fujita and co-workers. They are based on Pd(II) or Pt(II) metal ions and neutral *tris*-pyridyl ligands (Figure 71). The Pd(II)-cage **150** and the analogous Pt(II)-cage are positively charged (overall charge = +12). The metal ions at the vertices of the octahedron impart water solubility. These octahedral cages feature larger portals than those discussed above. The cavity volume of the octahedral Pd(II)-cage **150** is *ca.* 650 Å^3.[15,230]

In the solid state, the Pd(II)-cage **150** shows ten water molecules included in the hydrophobic cavity. The bound water molecules feature an ice-like structure, which is stabilized by water-water

hydrogen-bonding interactions and OH-π interactions with the aromatic panels of the octahedral cage. In this respect, the formation of the cage complexes derived from the Pd(II)/Pt(II)-cage is driven by the entropy owing to the "melting" of the bound water molecules in the cage.[4,15,215]

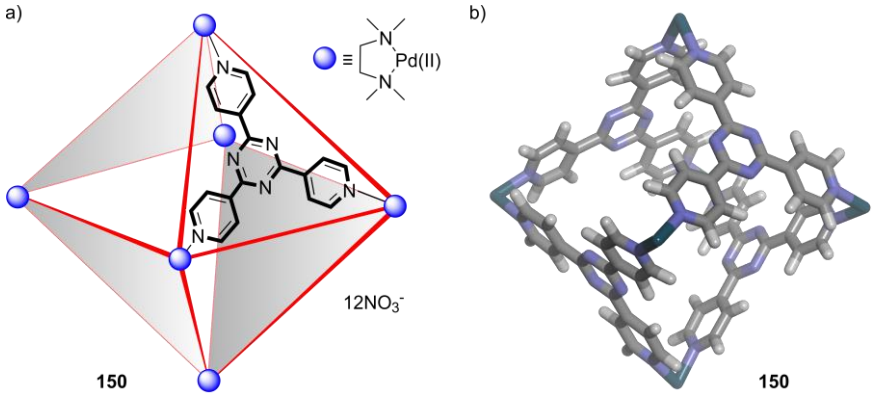

Figure 71. a) Cartoon representation and b) energy minimized structure (MM3) of the Pd(II)-cage **150**. The cage is depicted in stick representation.

The binding properties of the Pd(II)-cage **150** and the Pt(II)-cage are analogous. Neutral guests are bound to the hydrophobic cavity of the Pd(II)-cage **150** through the hydrophobic effect. For example, four molecules of 1-adamantanol **151** are included in the cavity of **150** forming the **151**$_4$⊂**150** cage complex (Figure 72). Interestingly, the inclusion of four molecules of 1-adamantanol is characterized by a strong positive cooperativity. The proton signals of bound **151**, in the **151**$_4$⊂**150** cage complex, appeared upfield-shifted in the ^{1}H NMR spectrum and indicated that the adamantyl group is buried in the cage's cavity. Consequently, the hydroxyl group of the guest is exposed to the bulk aqueous solution.[231]

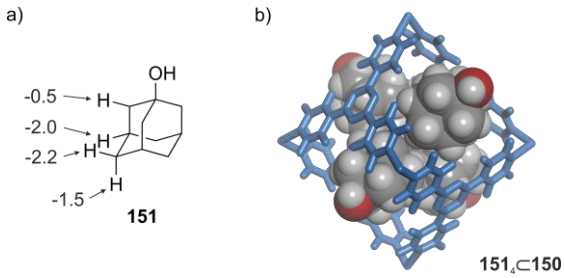

Figure 72. a) Line-drawing structure of 1-adamantanol **151** and b) energy minimized structure (MM3) of the **151**$_4$⊂**150** complex. The cage (blue) is depicted in stick representation and the bound guests are shown as CPK models. In a) complexation induced chemical shifts ($\Delta\delta = \delta_{bound} - \delta_{free}$) are indicated.

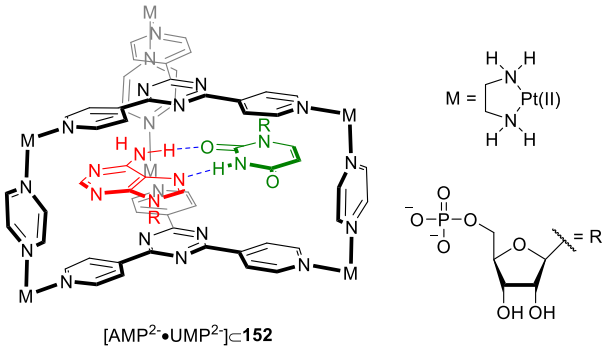

[AMP^{2-}•UMP^{2-}]⊂**152**

Figure 73. Line-drawing structure of the hetero-ternary [AMP^{2-}•UMP^{2-}]⊂**152** cage complex. AMP^{2-} and UMP^{2-} are highlighted in red and green colors, respectively.

The Pt(II)-cage **152** features a trigonal prism structure, $M_6L_2L_3$'. It was used to provide a non-polar environment for the efficient formation of hydrogen-bonded base pairs in water. In separate water solutions, either AMP^{2-} or UMP^{2-} forms a homo-ternary 2:1 cage complex with **152**. Nevertheless, the mixture of the three components in equimolar amounts, AMP^{2-}, UMP^{2-} and **152**, leads to the exclusive formation of the hetero-ternary [AMP^{2-}•UMP^{2-}]⊂**152** cage complex (Figure 73). The cage complexes are stabilized through the hydrophobic effect, π-π and Columbic interactions. Remarkably, [AMP^{2-}•UMP^{2-}]⊂**152** is further stabilized by the formation of two buried hydrogen bonds between the bound bases of the nucleotides. Therefore, the hydrophobic cage allows the formation of stable anti-Hoogsteen-type hydrogen bonds in water.[232]

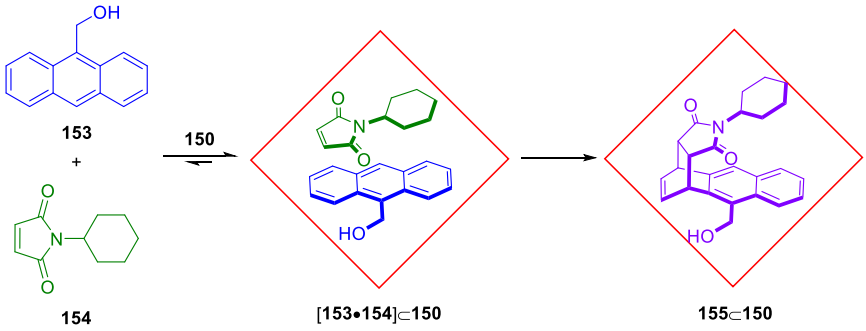

Scheme 9. Diels-Alder reaction between **153** and **154** mediated by the Pd(II)-cage **150**. The octahedral cage is depicted as a diamond (red).

The octahedral Pd(II)-cage **150** has been applied to mediate chemical transformations in water solution. For example, the Pd(II)-cage **150** promotes the Diels-Alder reaction of anthracenes and phthalimides in water. In the presence of **150**, the Diels-Alder reaction between 9-hydroxymethylanthracene **153** and *N*-cyclohexylphthalimide **154** yields the *syn*-isomer **155** in almost quantitative yield. This unusual regioselectivity is only achieved using the octahedral

metallo-cage. The two reactants, **153** and **154**, are included in the cavity of **150** leading to the exclusive formation of the hetero-ternary [**153•154**]⊂**150** cage complex. The double bond of bound **154** is placed in close proximity to the 1,4-position of **153**. Therefore, the reaction gives the 1,4-Diels-Alder product **155** (Scheme 9). The reaction requires the use of stoichiometric amounts of the Pd(II)-cage **150**.[18,233] Nevertheless, the same metallo-cage has been applied as catalyst in the Knoevenagel condensation of aromatic aldehydes in neutral water. The cationic Pd(II)-cage **150** stabilizes the negatively charged intermediate generated throughout the reaction.[234]

Hunter, Ward and co-workers designed a cubic M_8L_{12} cage **156** based on Co(II) metal ions and pyridyl-pyrazolyl ligands (Figure 74). The cationic metal centers and the hydroxymethyl substituents of the ligands impart water solubility. The Co(II)-cage **156** is positively charged (overall charge = +16) and features a cavity volume of *ca.* 400 Å^3.[235,236]

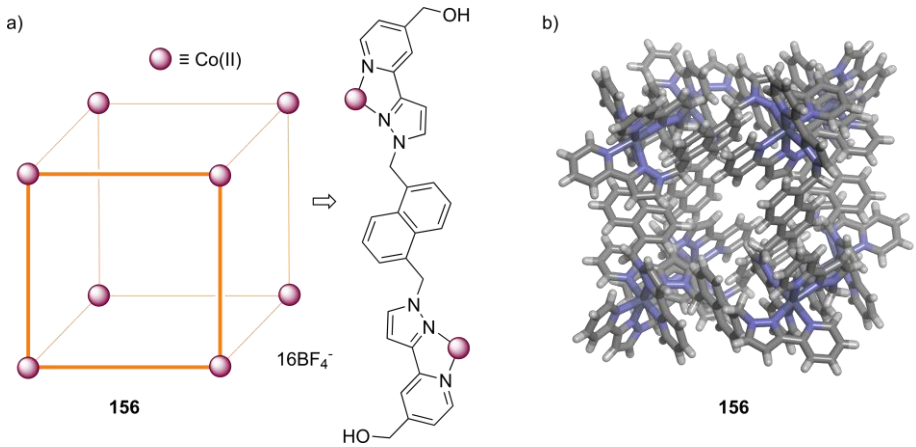

Figure 74. a) Cartoon representation and b) energy minimized structure (MM3) of the cubic Co(II)-cage **156**. The cage is depicted in stick representation. Hydroxymethyl groups are removed for clarity.

In the solid state, the Co(II)-cage **156** shows ten water molecules included in the hydrophobic cavity. The bound water molecules in **156** stablish a fewer number of hydrogen bonds than those in the bulk solution, which leads to enthalpically driven binding processes. This is in contrast with the crystal structure of the octahedral Pd(II)-cage **150**, in which the bound water molecules feature an ice-like structure and, therefore, the binding processes are driven by the entropy.[16,235,236]

The Co(II)-cage **156** binds preferentially neutral guests versus anionic species. Interestingly, the results obtained from the binding studies using a series of cyclic ketones, from cyclopentanone to cycloundecanone **157**, show a linear relationship between the free energy of binding and the surface area of the guest. This relationship quantifies in *ca.* 70 cal·mol^{-1}·Å^{-2} the hydrophobic effect operating in these cage complexes. The energy gain for the inclusion of a methylene group in the hydrophobic cavity of the metallo-cage **156** is 1.2±0.2 kcal·mol^{-1}.[16]

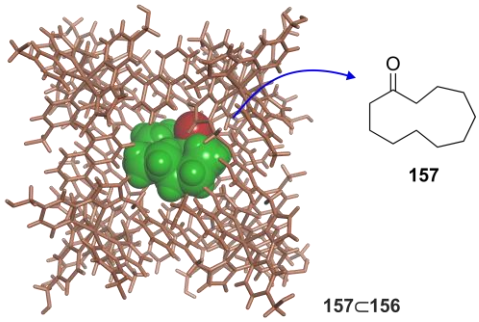

Figure 75. (left) X-ray crystal structure of the **157⊂156** complex and (right) line-drawing structure of the guest **157**. The cage (orange) is depicted in stick representation and the guest (green) is shown as CPK model. The oxygen atom (red) of bound guest is highlighted.

Interestingly, cycloundecanone **157** forms a thermodynamically highly stable complex with the Co(II)-cage **156** in water (Figure 75). The **157⊂156** cage complex features a binding constant value K_a = 1.2 x 10^6 M^{-1}. Nevertheless, more polar guests, such as lactams, are difficult to bind to the Co(II)-cage **156**. For example, the binding constant value for the six-membered ring lactam **138** is 3 M^{-1} and for the pyridine *N*-oxide **133** is 1 M^{-1}. These results are in agreement with the hydrophobic nature of the cavity of the Co(II)-cage and support the idea that hydrogen-bonding interactions play an important role in the binding of polar molecules using aryl-extended calix[4]pyrrole receptors in water (Section 1.4.3).[236,237,238,239]

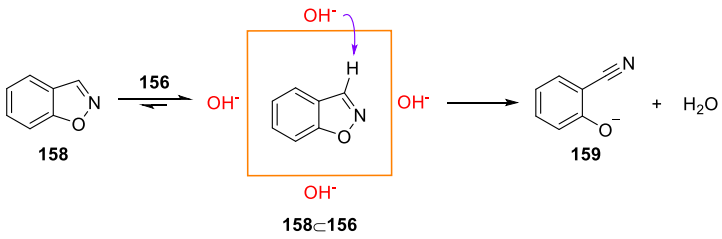

Scheme 10. Kemp elimination reaction of benzisoxazole **158** catalyzed by the Co(II)-cage **156**. The Co(II)-cage is represented as a square (orange).

The Co(II)-cage **156** was applied as catalyst in the Kemp elimination reaction of benzisoxazole **158** to give 2-cyanophenolate **159** in basic water. Benzisoxazole **158** is included in the cavity of the metallo-cage **156** through the hydrophobic effect, stablishing a thermodynamically stable 1:1 cage complex (K_a (**158⊂156**) = 4.0 x 10^3 M^{-1}). At the same time, hydroxy anions are bound to the exterior of the cationic Co(II)-cage via Columbic interactions. This produces an increase in the local concentration of hydroxy anions at the periphery of the cage complex **158⊂156**. The bound benzisoxazole **158** is then converted into the 2-cyanophenolate anion **159**. Note that the anion **159** cannot compete with the reactant **158** for the hydrophobic cavity of the metallo-cage, enabling

catalytic turnover. The reaction rate is remarkably enhanced in the presence of the Co(II)-cage **156** in water at pD = 8.5, k_{cage}/k_{bulk} = 2 x 10^5 (Scheme 10).[235,240]

Some metallo-cages discussed above bear weak inwardly-directed polar functions for the recognition of polar or charged guests. However, Nitschke and co-workers assembled a tetrahedral M_4L_4 Fe(II)-cage **160** from azaphosphatrane ligands using anions as templates (Figure 76). The Fe(II)-cage **160** has the four azaphosphatrane P^+-H groups pointing to the interior of the cavity (*T* symmetry), or one P^+-H group pointing outwards and the other three are inwardly-directed (C_3 symmetry). In both, the binding pocket is hydrophilic, and the cage is negatively charged (overall charge = +12).

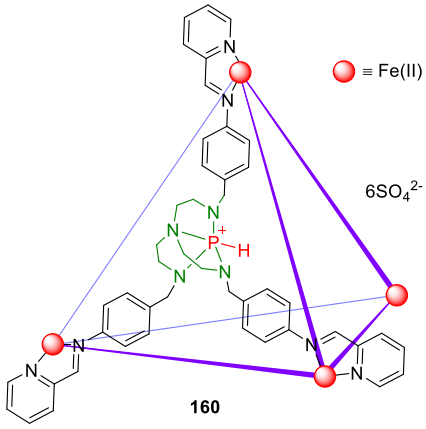

Figure 76. Cartoon representation of the tetrahedral M_4L_4 cage **160**.

The anion used as template controls the symmetry of the Fe(II)-cage **160**. For example, anions having a volume smaller than 53 Å^3 produce mainly the C_3-symmetric cage. On the contrary, anions featuring a larger volume (> 53 Å^3) template the formation of the *T*-symmetric cage. One isomer of the cage **160** can be converted into the other by the addition of the corresponding anion. Remarkably, the tetrahedral Fe(II)-cage **160** is able to bind anions in water. The combination of three/four converging hydrogen-bonding interactions with Columbic forces overcomes the high energetic cost for the desolvation of the anion. The receptor **160** represents one of the few examples of metal coordination cages featuring endohedral polar functions for the efficient recognition of anions in water.[241,242]

Other examples of metal coordination cages and applications in catalysis have been reported in the literature.[18,213,243]

1.5.2 Non-covalent capsules

Non-covalent self-assembled capsules feature an enclosed cavity, which isolates bound guests from the bulk solution. For their construction, concave scaffolds, such as calix[4]arenes and resorcin[4]arenes, have been used. These scaffolds provide the curvature necessary for the capsular assembly. The inner volume of the capsule might accommodate solvent molecules or complementary guests. In general, encapsulation complexes are thermodynamically and kinetically stable.[244,245]

In Section 1.3.2, we discussed the formation of 1:1 inclusion complexes derived from the octa-acid deep-cavity cavitand **101**. Furthermore, the octa-acid **101** self-assembles into a dimeric capsule, **101**$_2$, in the presence of suitable guests (Figure 77). The dimerization of **101** is driven by the hydrophobic effect owing to the desolvation of the aromatic surface area at the cavity portal. The external carboxylic acids of **101**$_2$ are converted into carboxylates in basic water.[215,246]

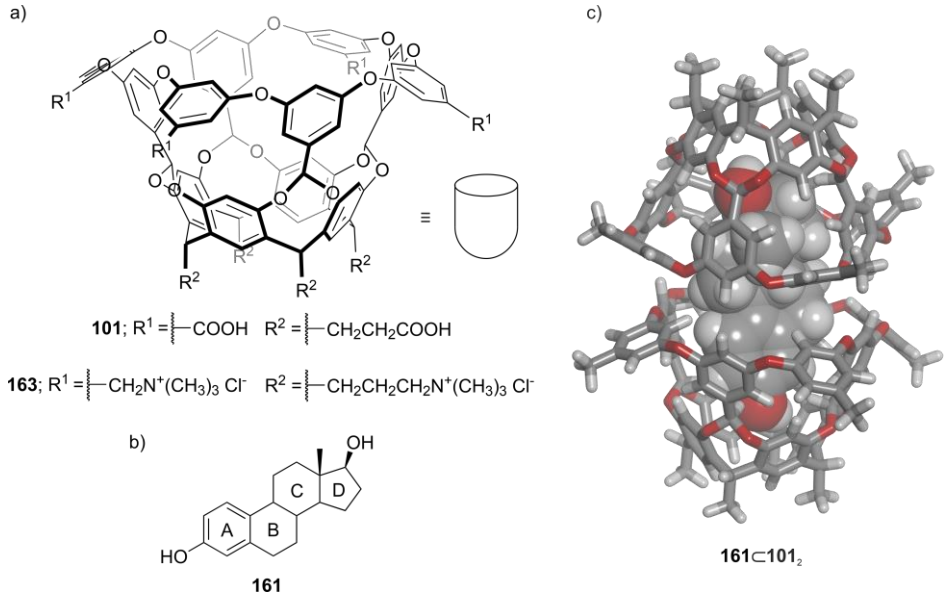

Figure 77. a) Line-drawing structures of **101** and **163** (cartoon representation of the deep-cavity cavitand is depicted); b) structure of estradiol **161** and c) energy minimized structure (MM3) of the **161**⊂**101**$_2$ encapsulation complex. The resorcin[4]arenes are depicted in stick representation and the guest is shown as CPK model. Water-solubilizing groups were pruned to methyl groups to ease the calculation.

The cavity volume of the dimeric capsule **101**$_2$ is large enough to accommodate steroids, such as estradiol **161** (Figure 77b). The A ring of bound **161** is included in one half and the D ring is in the opposite half of the capsule **101**$_2$ (Figure 77c). The quantitative formation of the ternary 1:2 guest/host complex, **161**⊂**101**$_2$, indicates that the binding constant value is larger than 10^8 M^{-2}.[246]

The deep-cavity cavitand **101** also forms self-assembled dimeric capsules with *n*-alkanes, from nonane to heptadecane. Alkanes shorter than *n*-decane fit comfortably in a staggered conformation in the cavity of **101**$_2$. On the contrary, longer *n*-alkanes adopt a high-energy, compacted conformation in the cavity of the dimeric capsule.[14,247]

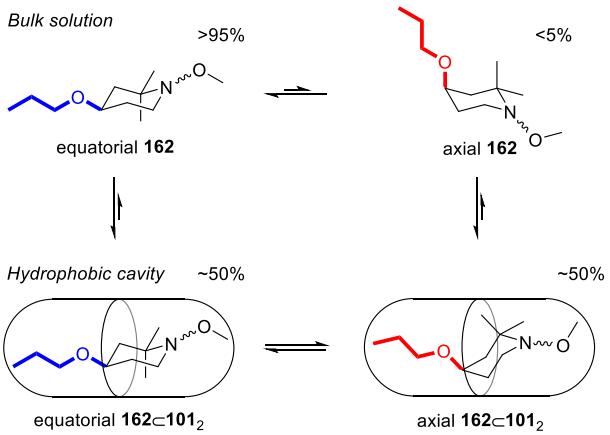

Scheme 11. Equilibria experienced by the piperidine derivative **162** in the presence of capsule **101**$_2$ in water. See Figure 77 for the line-drawing structure of **101**.

The stabilization of high-energy conformers in the cavity of **101**$_2$ was also investigated using piperidine derivatives. For example, free piperidine **162** adopts preferentially an equatorial conformation (propyloxy substituent) in solution. Nevertheless, the addition of **162** to a millimolar solution of deep-cavity cavitand **101** induces the formation of two kinetically stable encapsulation complexes in equimolar amounts. One encapsulation complex features the equatorial conformer of **162**, equatorial **162⊂101**$_2$. Remarkably, the other shows the encapsulated **162** in the axial conformation, axial **162⊂101**$_2$, which is the less energetically stable for the free guest in solution (Scheme 11).[248]

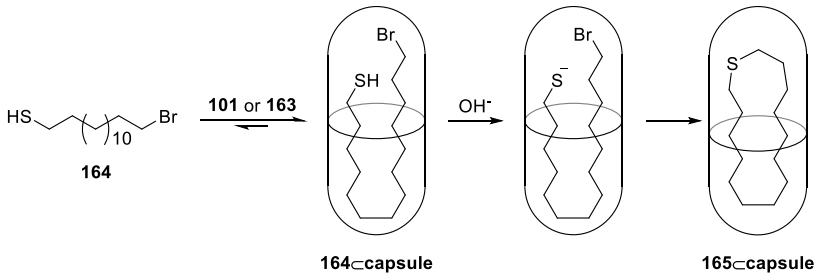

Scheme 12. Cyclization reaction of **164** in the interior of the dimeric capsule, **101**$_2$ or **163**$_2$.

Gibb and co-workers reported a deep-cavity cavitand bearing external quaternary ammonium groups, **163** (Figure 77). Octa-ammonium **163** and octa-acid **101** are analogous. Nevertheless, the dimeric capsules, $\mathbf{101}_2$ and $\mathbf{163}_2$, feature opposite overall charge and electrostatic potential. In analogy to the Columbic stabilization of charged species by metal coordination cages (Section 1.5.1), the electrostatic potential of the non-covalent dimeric capsules should impact on the reactivity of bound guests. Recently, the same group showed the effect of the two dimeric capsules in the cyclization reaction of long-chain *α,ω*-alkanes bearing terminal thiol and halide groups. The cyclization requires the deprotonation of the terminal thiol group at one end of the molecule with a base to produce the corresponding thiolate. The thiolate then reacts with the halide at the other end to give the cyclic product. For example, *α,ω*-thiol **164** is encapsulated in either $\mathbf{101}_2$ or $\mathbf{163}_2$. The pK_a value of the bound thiol is two units larger in the anionic capsule $\mathbf{101}_2$ than in the cationic counterpart $\mathbf{163}_2$. This is translated into an energetic stabilization of the thiolate anion upon deprotonation in $\mathbf{163}_2$ or, in other words, the acidity of the bound thiol is enhanced in the cationic capsule. Therefore, **164** undergoes cyclization in 8 h in the interior of the anionic capsule $\mathbf{101}_2$ in basic water to give the cyclic product **165**. In striking contrast, the same reaction takes place in 2 min using the cationic capsule $\mathbf{163}_2$ (Scheme 12).[249] The dimeric capsule $\mathbf{101}_2$ has been also applied to mediate photo-chemical reactions in water.[247,250,251,252]

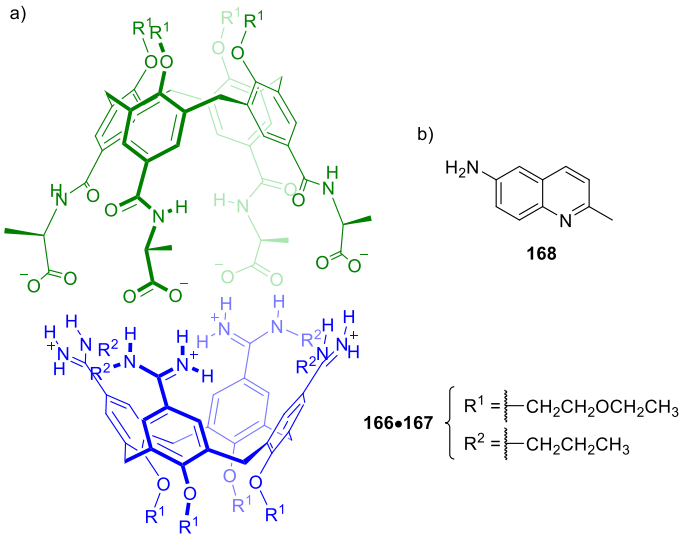

Figure 78. Line-drawing structures: a) dimeric capsule **166•167** (**166** in green and **167** in blue) and b) guest **168**.

Reinhoudt and co-workers reported the self-assembly of dimeric capsules based on calix[4]arene scaffolds through ion-pairing interactions in water. Two self-complementary calix[4]arenes were used for the capsular assembly. One calix[4]arene **166** was decorated with carboxylic acids at the upper rim. The carboxylic acids are ionized in water at basic pH. The other calix[4]arene **167** was functionalized with amidinium groups at the upper rim. The mixture containing the two

calix[4]arenes, **166** and **167**, in water at pH = 9 affords the hetero-dimeric capsule **166•167** (Figure 78a). Interestingly, the propyl substituents of the amidinium groups of **167** are inwardly-oriented to fill the cavity volume of the dimeric capsule. Furthermore, the addition of a size and shape complementary guest, such as 6-amino-2-methyl quinoline **168**, to the solution of **166•167** provokes the release of the bound propyl groups to the periphery of the capsule and the concomitant encapsulation of the guest (Figure 78b).[15,167,253,254]

Despite the lability of hydrogen bonds in water solution, Rebek and co-workers demonstrated that the water-soluble benzimidazolone resorcin[4]arene deep-cavitand **169** self-assembles quantitatively into a cylindrical homo-dimeric capsule in the presence of non-polar guests: large aromatic molecules or long *n*-alkanes, such as undecane **170**. The formation of the dimeric capsule, **169**$_2$, is driven by the hydrophobic effect owing to the encapsulation of the non-polar guest, and the formation of a seam of bifurcated hydrogen-bonding interactions at the equator of the assembly (Figure 79).[14,255]

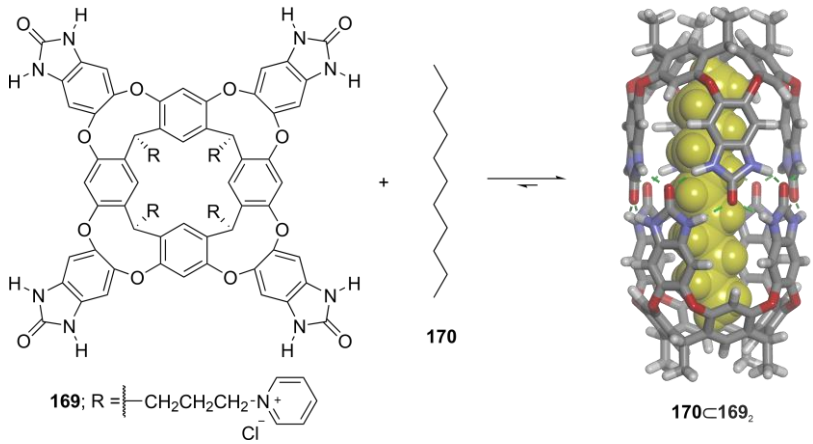

Figure 79. (left) Line-drawing structures of **169** and **170**; (right) energy minimized structure (MM3) of the **170⊂169**$_2$ encapsulation complex. The cavitand is depicted in stick representation and the bound guest (yellow) is shown as CPK model. Hydrogen bonds are highlighted (green lines).

1.6 Mechanically-Interlocked Receptors

Mechanically-interlocked architectures have been constructed with the aid of the molecular recognition properties of the individual components. The three-dimensional cavity provided by the mechanically-interlocked structure can accommodate size, shape and function complementarity guests. In this section, we discuss selected examples of water-soluble rotaxanes and catenanes.

1.6.1 Rotaxanes

[2]Rotaxanes are molecules formed by a macrocycle and a linear component linked together by the mechanical bond. The linear component bears terminal bulky stoppers to avoid the dethreading of the [2]rotaxane structure. The incorporation of ionizable or charged groups at either the macrocycle or the linear component renders water-soluble [2]rotaxanes.[256]

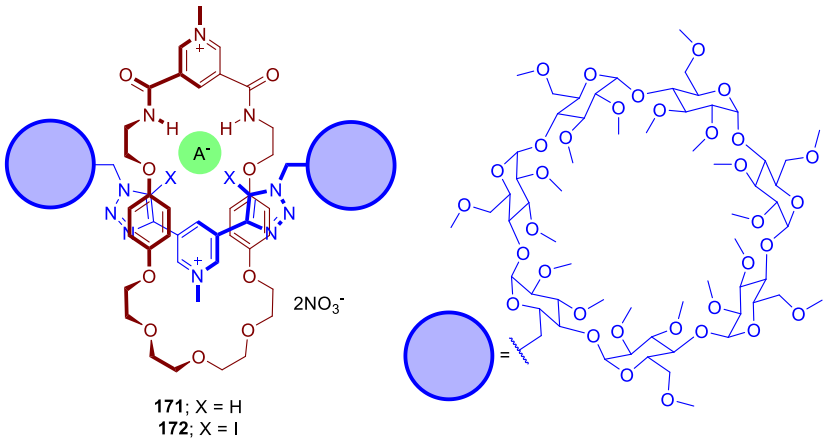

Figure 80. Line-drawing structures of [2]rotaxanes **171** and **172**. Anion binding site (green) is highlighted.

Beer and co-workers have designed [2]rotaxanes, **171** and **172**, for the recognition of anions in water. In this respect, the macrocycle is a pyridinium 3,5-di-carboxamide having a poly(ethylene glycol) chain. The linear component is a 3,5-di-triazole pyridinium derivative functionalized with two *β*-cyclodextrins as stoppers. The [2]rotaxanes **171** and **172** are soluble in water owing to the presence of the pyridinium cations and the *β*-cyclodextrins. On the one hand, **171** bears two amide NHs and two triazole C-H functions converging into the cavity. On the other hand, **172** features two triazole C-I substituents, instead of CHs, together with the amide NHs in the binding pocket (Figure 80). The different substituents on the triazole groups of the linear component serve to explore the role of hydrogen- and halogen-bonding interactions for anion binding in water.

For example, the hydrogen-bonding receptor **171** and the iodide anion form a 1:1 inclusion complex featuring a binding constant value K_a ($I^-\subset$**171**) = 20 M^{-1} in water. Remarkably, the binding affinity value of I^- increases up to 2.2 x 10^3 M^{-1} using the halogen-bonding receptor **172**. This result

supports that halogen bonds are less affected by solvent polarity than hydrogen bonds. The inclusion of the anion in the three-dimensional cavity of the [2]rotaxanes in water is driven by electrostatic interactions. The Hofmeister effect might be also involved in the binding of the anion.[29,257,258]

1.6.2 Catenanes

[2]Catenanes are molecules formed by the mechanical connection of two macrocycles. In general, water-soluble [2]catenanes are synthesized from aromatic components. The aromatic units are brought together through the hydrophobic effect and the establishment of π-donor-π-acceptor interactions prior to the catenation reaction.[256]

Stoddard and co-workers synthesized a water-soluble [2]catenane **173** from the *bis*-pyridinium cyclophane **25** and the 1,5-di-alkoxynaphthalene **174**. The later is functionalized with terminal alkynyl groups. The equimolar mixture of **25** and **174** in water produces the corresponding [2]pseudo-rotaxane that is then converted into the [2]catenane **173** by a Glaser-Hay coupling reaction (Scheme 13). The formation of the [2]pseudo-rotaxane is driven by the hydrophobic effect and the π-donor-π-acceptor interactions between the aromatic surfaces of **25** and **174**.[1,259] Therefore, the naphthalene group of one macrocycle is included in the electron-deficient cavity provided by the cyclophane **25** in the [2]catenane **173**.

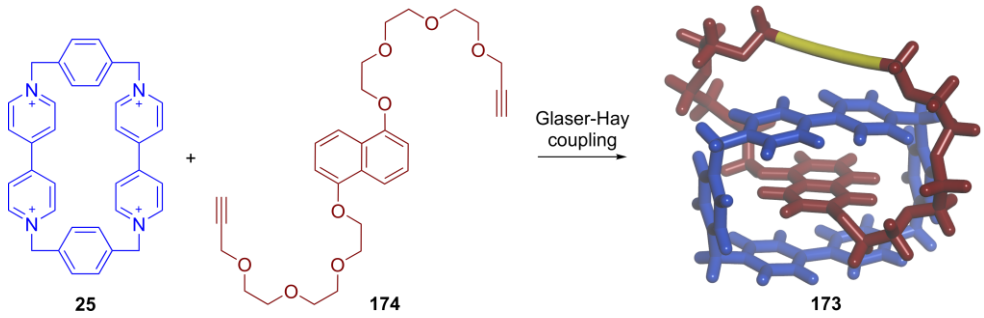

Scheme 13. Synthesis of [2]catenane **173** from **25** and **174**. The energy minimized structure (MM3) of **173** is depicted in stick representation. Triple bonds (yellow) are highlighted in the model.

Dynamic covalent chemistry has been applied in the preparation of catenanes. For example, Sessler and co-workers used hydrazone linkages (C=N-N) in the synthesis of a water-soluble [2]catenane.[260] In another example, Sanders and co-workers reported the synthesis of a [2]catenane **175** using di-sulfur bonds (Scheme 14a). Both naphthalenediimide **176** and 1,6-di-alkoxynaphthalene **177** were functionalized with thiol and carboxylic acid groups. The carboxylic acids were incorporated to warrant water solubility. The reaction between the thiol groups of both aromatic components, **176** and **177**, yields a complex mixture of products containing di-sulfur bonds. Interestingly, the [2]catenane **175** is present in the mixture and, therefore, can be isolated

and characterized. The [2]catenane **175** is composed of two macrocycles. Each macrocycle is formed by one unit of **176** and one unit of **177** linked together by di-sulfur bonds. The naphthalene units are situated at the exterior and the naphthalenediimide units are found in the interior of the [2]catenane **175**. The two naphthalenediimides create a hydrophobic and electron-deficient three-dimensional cavity. The cavity of the [2]catenane **175** is suitable for the inclusion of electron-rich aromatic guests. For example, the guest **178** is intercalated in the aromatic cavity of **175**, where it stablishes π-donor-π-acceptor interactions with the naphthalenediimide units (Scheme 14b). The binding constant value of the **178⊂175** complex is K_a = 7.7 x 10^3 M^{-1} in water.[261]

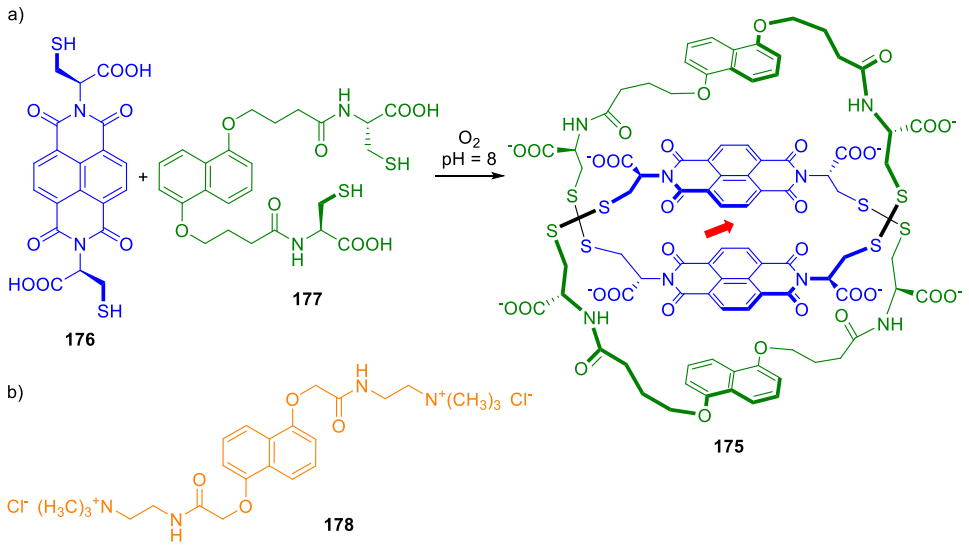

Scheme 14. a) Synthesis of [2]catenane **175** from **176** and **177**; b) line-drawing structure of guest **178**. The binding site of **175** is indicated (red arrow).

1.7 Conclusions

In the Introduction of this Thesis, we revised the design development and molecular recognition properties of water-soluble synthetic receptors featuring solvent-exposed and enclosed cavities. Since the early examples of cyclophanes, many synthetic receptors of different size, shape and function have been reported in the literature. Cyclic and oligo-cyclic covalent receptors feature hydrophobic cavities and establish thermodynamically stable complexes. Nevertheless, these complexes are labile owing to the presence of multiple cavity portals in the receptors' structures. The development of receptors possessing concave cavities, which are closed at one end and opened at the opposite end, allows the formation of thermodynamically and kinetically stable complexes. The nature of the cavity of concave receptors impacts on the binding properties. Concave hydrophobic receptors are abundant in the literature, whereas the hydrophilic counterparts are still scarce. We believe that hydrophilic receptors are good candidates for the

efficient and selective recognition of polar guests in water. Therefore, they require further development in the next few years.

We also discussed the binding properties of self-assembled molecular containers in water: metal coordination cages and non-covalent capsules. Both assemblies feature hydrophobic cavities that surround the bound guest. However, self-assembled receptors bearing endohedral polar functions have been poorly developed. The incorporation of polar binding motifs in the interior of cages and capsules should enhance the selectivity for the encapsulation of polar guests. Additionally, we included selected examples of the application of synthetic molecular containers in water. The water-soluble receptors can mediate/catalyze chemical transformations and achieve unusual reaction selectivities.

1.8 Aims of the Thesis

The aim of the research work included in this Thesis is the design and synthesis of deep-cavity covalent receptors, self-assembled metal coordination cages and non-covalent capsules, featuring polar interiors and operating in organic solvents and water. For their construction, we selected the aryl-extended calix[4]pyrrole scaffold, which delivers a concave hydrophilic cavity. We aim at studying the molecular recognition properties of the synthesized calix[4]pyrrole receptors and characterizing thermodynamically and kinetically their host-guest complexes. The understanding of the formation and dissociation of the host-guest complexes, as well as the intermolecular forces involved, should provide valuable knowledge for the design of new molecular receptors with improved functions.

Specifically, we pursued the following objectives:

O.1) **Design and synthesis of calix[4]pyrrole receptors featuring deep hydrophilic cavities: super aryl-extended calix[4]pyrroles.**

The tetra-*α* isomer of aryl-extended calix[4]pyrroles in the cone conformation feature a deep aromatic cavity closed at one end by a polar binding site and opened at the opposite end to the bulk solution. Despite the deep aromatic cavity provided by the aryl-extended calix[4]pyrroles, the polar functions are likely solvated in water solution. In addition, water molecules compete with polar guests for the hydrophilic binding pocket of the aryl-extended receptors. We envisaged that the extension of the aromatic cavity of the aryl-extended calix[4]pyrroles with ethynyl-phenyl substituents should afford derivatives featuring deeper hydrophilic cavities, that we termed super aryl-extended calix[4]pyrroles. The super aryl-extended receptors should enhance the hydrophobic effect for the binding of non-polar residues and shield better the polar closed end from water solvation, improving the efficiency and selectivity in the recognition of function complementary guests. We aim at mimicking the binding performance of natural receptors, such as proteins, in water using these synthetic hydrophilic containers.

O.2) **Self-assembly of metallo-cages and non-covalent capsules based on super aryl-extended calix[4]pyrrole scaffolds.**

We aim at designing molecular containers with a pre-organized and enclosed cavity based on super aryl-extended calix[4]pyrrole scaffolds. In this regard, we envisaged that these containers could be prepared following two approaches: a) coordination of a metal ion at the upper rim of the super aryl-extended calix[4]pyrrole affording a mono-metallic cage, and 2) self-assembly of the super aryl-extended calix[4]pyrrole into non-covalent dimeric capsules. We investigated these two approaches in the Thesis. In particular, we thought that mono-metallic Pd(II)/Pt(II)-cages could be assembled from super aryl-extended calix[4]pyrrole ligands functionalized with four pyridyl substituents at the upper rim. The coordination of the metal ion to the tetra-pyridyl calix[4]pyrrole

ligand should seal the open cavity of the container. In the second approach, we proposed the synthesis of a super aryl-extended calix[4]pyrrole decorated with four terminal urea groups at the upper rim. In this respect, the upper rim urea groups have encoded the information for the assembly of the super aryl-extended derivative into a hydrogen-bonded dimeric capsule. This second approach was previously applied by Rebek and Böhmer using tetra-urea calix[4]arenes, and by our research group using tetra-urea aryl-extended calix[4]pyrroles.

O.3) **Thermodynamic and kinetic characterization of host-guest complexes from aryl-extended and super aryl-extended calix[4]pyrroles in organic solvents and water.**

The driving forces involved in the formation of host-guest complexes in organic solvents and water are remarkably different. We wanted to evaluate the binding performance of the synthesized super aryl-extended calix[4]pyrroles in different solvents using a series of neutral polar guests, such as pyridyl *N*-oxides, and compare their properties with those of the parent aryl-extended calix[4]pyrroles. The thermodynamic characterization of the host-guest complexes consisted of the determination of the association constant values and the thermodynamic parameters (enthalpy and entropy) involved in the binding processes. The accurate binding constant values could be determined by ^{1}H NMR spectroscopy, ITC and/or UV-Vis spectroscopy titrations. On the other hand, the kinetic characterization of the supramolecular complexes could be done by NMR spectroscopic techniques. To this end, we though to apply dynamic NMR techniques at equilibrium and/or kinetic ^{1}H NMR studies (slow processes). The analyses of the kinetic data afford the rate constants for the formation and dissociation of the investigated complexes. The characterization of the host-guest complexes derived from aryl-extended and super aryl-extended calix[4]pyrroles with neutral polar guests should provide valuable information about the effect of the solvent and the depth of the receptor's cavity in the strength and kinetics of the binding processes.

O.4) **High-binding affinity and selectivity in the complexation of neutral polar molecules in water.**

We sought to apply aryl-extended and super aryl-extended calix[4]pyrrole receptors in the molecular recognition of polar guests in water. Both receptors should bind size, shape and function complementary guest molecules. In this respect, we proposed to investigate the complexation of a series of pyridyl *N*-oxides in water. We also though that the size and shape of the deep hydrophilic cavity of aryl-extended calix[4]pyrrole receptors should impose conformational selectivity. To this end, we used aryl-extended calix[4]pyrrole receptors for the selective recognition of the *cis*-rotamer of acyclic mono-amides. The *trans*-rotamer should not bind to the receptor's cavity owing to shape complementary issues. Furthermore, we though that the combination of the hydrophobic effect, hydrogen-bonding, NH-π and CH-π interactions between the aryl-extended calix[4]pyrrole receptor and the *cis*-isomer of the bound amide should afford thermodynamically stable inclusion complexes in water.

O.5) **Investigation of the guest exchange mechanisms operating in the inclusion and cage complexes of super aryl-extended calix[4]pyrrole receptors and self-assembled metallo-cages, respectively.**

The kinetic characterization of the host-guest complexes should provide information related with the mechanisms involved in the inclusion/exchange of the guests in the molecular containers. We sought to investigate and propose the guest in/out mechanisms operating in the inclusion complexes of the super aryl-extended calix[4]pyrrole receptors and in the complexes of the mono-metallic Pd(II)/Pt(II)-cages. The magnitude of the rate constant values for the formation and the dissociation of the complexes, as well as the energy barriers associated to these processes, should be related with the intermolecular interactions involved in the complex and conformational changes of the receptors, among others, to allow the reversible passage of the guests. Therefore, the kinetic characterization of the host-guest inclusion and cage complexes should serve to propose viable pathways for the in/out exchange of the guests.

1.9 Outline of the Thesis

This doctoral Thesis is divided in seven Chapters: the present introduction (Chapter 1), six chapters containing the results and their discussion (Chapters 2-7) and a final section including the general conclusions of this work.

In **Chapter 2**, we describe the enlargement of the aromatic cavity defined by the four *meso*-phenyl walls of aryl-extended calix[4]pyrroles (AE-C[4]Ps) with *para*-ethynyl-phenyl substituents affording unprecedented calix[4]pyrroles that we termed “super aryl-extended” (SAE-C[4]Ps). We compared the binding properties of an aryl-extended calix[4]pyrrole with its super aryl-extended counterpart in chloroform solution by ^{1}H NMR spectroscopy and ITC titration experiments. The binding studies using a series of pyridyl and aliphatic *N*-oxides demonstrated the formation of thermodynamically and kinetically stable 1:1 inclusion complexes with both calix[4]pyrrole receptors. Nevertheless, the elaboration of the aromatic cavity in the SAE-C[4]P receptor provided a larger thermodynamic stability to the complexes than the AE-counterpart. We also explored the water solubility of SAE-C[4]Ps functionalized at the upper rim with ionizable or charged groups. We concluded that the incorporation of four ionizable or charged residues is not enough to gain access to water solubility.

Chapter 3 deals with the preparation of SAE-C[4]Ps bearing eight ionizable (carboxylates) or charged (pyridinium or imidazolium) groups at the periphery of their scaffolds: four groups located at the upper rim and the other four at the lower rim. We show that the synthesized calix[4]pyrroles are soluble in neutral or basic water at millimolar concentration. We used the water-soluble SAE-C[4]Ps as model systems for the quantification of the hydrophobic effect in the binding of non-polar residues. The investigated non-polar residues are the *para*-substituents of a series of pyridyl *N*-oxide derivatives. We observed that the energy scale associated with the hydrophobic effect operating in these simple model systems is in line with the values derived from protein mutagenesis and the transfer of non-polar molecules from organic solvents to water.

In **Chapter 4**, we report the synthesis of tetra-*α* tetra-pyridyl aryl-extended and super aryl-extended calix[4]pyrrole ligands. We describe the coordination studies of the tetra-pyridyl ligands with Pd(II) and Pt(II) salts. The tetra-pyridyl super aryl-extended ligand self-assembles into a mono-metallic Pd(II)/Pt(II)-cage, whereas the aryl-extended counterpart produces ill-defined aggregates. We monitored the inclusion and exchange processes of planar pyridyl *N*-oxides and quinuclidine *N*-oxide, a sterically more demanding guest, with the mono-metallic Pd(II)/Pt(II)-cages by NMR spectroscopy. Finally, we disclosed the inclusion/exchange mechanisms operating in the reversible encapsulation of the neutral polar guests with the mono-metallic cages.

We applied a water-soluble tetra-cationic pyridinium aryl-extended calix[4]pyrrole receptor for the selective conformational binding of the *cis*-rotamer of amides in **Chapter 5**. We describe the results of the binding studies of the tetra-pyridinium calix[4]pyrrole receptor with a series of acyclic mono-amides in water. The tetra-pyridinium receptor displayed conformational selectivity and high-

binding affinity towards the *cis*-rotamers of *N*-phenyl amides. We also report the complexation of a long-chain di-formamide with a super aryl-extended calix[4]pyrrole in water. The reported findings demonstrate that the water-soluble calix[4]pyrroles function as minimal chaperones, increasing the concentration of amide *cis*-rotamers in solution through selective binding.

Chapter 6 deals with the synthesis of a calix[4]pyrrole decorated with four light-responsive azobenzene groups at the upper rim. We report the results of light-induced isomerization studies of the all-*trans* receptor, monitored by ^{1}H NMR and UV/Vis spectroscopies. We selected 4-phenyl pyridine *N*-oxide and a bi-phenyl carboxylate as guests. We describe the binding properties of the all-*trans* receptor, as well as the *cis*-enriched isomeric mixture produced by light-irradiation at 365 nm. In the photostationary state, the all-*cis* isomer is present in an extent larger than 80%. We show that the binding constant value is one order of magnitude larger for the complexes of the all-*trans* receptor than those of the *cis*-enriched mixture of isomers.

Finally, we report in **Chapter 7** our initial studies on the self-assembly of non-covalent dimeric capsules from a tetra-urea super aryl-extended calix[4]pyrrole derivative. We describe the synthesis of a super aryl-extended calix[4]pyrrole equipped with four urea groups at the upper rim and *meso*-alkyl substituents at the lower rim. We performed solution studies of the self-assembly of the tetra-urea SAE-C[4]P using mono- and di-topic pyridyl *N*-oxides as templating guests. The tetra-urea SAE-C[4]P, with any of the two templating guests, self-assembles into a homo-dimeric capsule. Interestingly, the equimolar mixture of the tetra-urea SAE-C[4]P, a tetra-urea calix[4]arene and the mono-topic pyridyl *N*-oxide affords exclusively a hetero-dimeric capsular assembly.

1.10 References and Notes

[1] K. Ariga, H. Ito, J. P. Hill, H. Tsukube, *Chem. Soc. Rev.* **2012**, *41*, 5800-5835.

[2] D. Shetty, J. K. Khedkar, K. M. Park, K. Kim, *Chem. Soc. Rev.* **2015**, *44*, 8747-8761.

[3] K. N. Houk, A. G. Leach, S. P. Kim, X. Y. Zhang, *Angew. Chem., Int. Ed.* **2003**, *42*, 4872-4897.

[4] F. Biedermann, H.-J. Schneider, *Chem. Rev. (Washington, DC, U. S.)* **2016**, *116*, 5216-5300.

[5] K. A. Dill, T. M. Truskett, V. Vlachy, B. Hribar-Lee, *Annu. Rev. Biophys. Biomol. Struct.* **2005**, *34*, 173-199.

[6] T. H. Rehm, C. Schmuck, *Chem. Soc. Rev.* **2010**, *39*, 3597-3611.

[7] P. W. Snyder, M. R. Lockett, D. T. Moustakas, G. M. Whitesides, *Eur. Phys. J. Spec. Top.* **2014**, *223*, 853-891.

[8] M. B. Hillyer, B. C. Gibb, in *Annu. Rev. Phys. Chem., Vol. 67* (Eds.: M. A. Johnson, T. J. Martinez), Annual Reviews, Palo Alto, **2016**, pp. 307-329.

[9] E. Brini, C. J. Fennell, M. Fernandez-Serra, B. Hribar-Lee, M. Luksic, K. A. Dill, *Chem. Rev. (Washington, DC, U. S.)* **2017**, *117*, 12385-12414.

[10] H. J. Schneider, A. K. Yatsimirsky, *Chem. Soc. Rev.* **2008**, *37*, 263-277.

[11] B. C. Gibb, *Isr. J. Chem.* **2011**, *51*, 798-806.

[12] R. U. Lemieux, *Acc. Chem. Res.* **1996**, *29*, 373-380.

[13] R. M. Izatt, K. Pawlak, J. S. Bradshaw, R. L. Bruening, *Chem. Rev. (Washington, DC, U. S.)* **1995**, *95*, 2529-2586.

[14] J. H. Jordan, B. C. Gibb, *Chem. Soc. Rev.* **2015**, *44*, 547-585.

[15] G. V. Oshovsky, D. N. Reinhoudt, W. Verboom, *Angew. Chem., Int. Ed.* **2007**, *46*, 2366-2393.

[16] L. L. K. Taylor, I. A. Riddell, M. M. J. Smulders, *Angew. Chem., Int. Ed.* **2019**, *58*, 1280-1307.

[17] E. A. Kataev, C. Muller, *Tetrahedron* **2014**, *70*, 137-167.

[18] C. J. Brown, F. D. Toste, R. G. Bergman, K. N. Raymond, *Chem. Rev. (Washington, DC, U. S.)* **2015**, *115*, 3012-3035.

[19] H. J. Schneider, *J. Phys. Chem. B* **2018**, *122*, 2825-2826.

[20] T. D. James, K. Sandanayake, S. Shinkai, *Angew. Chem., Int. Ed.* **1996**, *35*, 1910-1922.

[21] S. Striegler, *Curr. Org. Chem.* **2003**, *7*, 81-102.

[22] W. Blokzijl, J. Engberts, *Angew. Chem., Int. Ed.* **1993**, *32*, 1545-1579.

[23] H. J. Bakker, *Nature* **2012**, *491*, 533-535.

[24] D. H. Leung, R. G. Bergman, K. N. Raymond, *J. Am. Chem. Soc.* **2008**, *130*, 2798-2805.

[25] A. Biela, N. N. Nasief, M. Betz, A. Heine, D. Hangauer, G. Klebe, *Angew. Chem., Int. Ed.* **2013**, *52*, 1822-1828.

[26] P. S. Cremer, A. H. Flood, B. C. Gibb, D. L. Mobley, *Nature Chem.* **2017**, *10*, 8-16.

[27] J. Murray, K. Kim, T. Ogoshi, W. Yao, B. C. Gibb, *Chem. Soc. Rev.* **2017**, *46*, 2479-2496.

[28] D. Ben-Amotz, *Annu. Rev. Phys. Chem.* **2016**, *67*, 617-638.

[29] M. J. Langton, C. J. Serpell, P. D. Beer, *Angew. Chem., Int. Ed.* **2016**, *55*, 1974-1987.

[30] F. Biedermann, W. M. Nau, H. J. Schneider, *Angew. Chem., Int. Ed.* **2014**, *53*, 11158-11171.

[31] E. Persch, O. Dumele, F. Diederich, *Angew. Chem., Int. Ed.* **2015**, *54*, 3290-3327.

[32] F. Diederich, D. B. Smithrud, E. M. Sanford, T. B. Wyman, S. B. Ferguson, D. R. Carcanague, I. Chao, K. N. Houk, *Acta Chem. Scand.* **1992**, *46*, 205-215.

[33] D. A. Uhlenheuer, K. Petkau, L. Brunsveld, *Chem. Soc. Rev.* **2010**, *39*, 2817-2826.

[34] F. J. Rizzuto, L. K. S. von Krbek, J. R. Nitschke, *Nat. Rev. Chem.* **2019**, *3*, 204-222.

[35] N. R. Syme, C. Dennis, S. E. V. Phillips, S. W. Homans, *ChemBioChem* **2007**, *8*, 1509-1511.

[36] J. Mecinovic, P. W. Snyder, K. A. Mirica, S. Bai, E. T. Mack, R. L. Kwant, D. T. Moustakas, A. Heroux, G. M. Whitesides, *J. Am. Chem. Soc.* **2011**, *133*, 14017-14026.

[37] H. J. Schneider, *Angew. Chem., Int. Ed.* **1991**, *30*, 1417-1436.

[38] H. J. Schneider, *Acc. Chem. Res.* **2015**, *48*, 1815-1822.

[39] S. Kubik, *Chem. Soc. Rev.* **2010**, *39*, 3648-3663.

[40] J. M. Zayed, N. Nouvel, U. Rauwald, O. A. Scherman, *Chem. Soc. Rev.* **2010**, *39*, 2806-2816.

[41] P. Blondeau, M. Segura, R. Perez-Fernandez, J. de Mendoza, *Chem. Soc. Rev.* **2007**, *36*, 198-210.

[42] E. A. Meyer, R. K. Castellano, F. Diederich, *Angew. Chem., Int. Ed.* **2003**, *42*, 1210-1250.

[43] L. M. Salonen, M. Ellermann, F. Diederich, *Angew. Chem., Int. Ed.* **2011**, *50*, 4808-4842.

[44] D. A. Dougherty, *Acc. Chem. Res.* **2013**, *46*, 885-893.

[45] P. Arranz-Mascaros, C. Bazzicalupi, A. Bianchi, C. Giorgi, M. L. Godino-Salido, M. D. Gutierrez-Valero, R. Lopez-Garzon, M. Savastano, *J. Am. Chem. Soc.* **2013**, *135*, 102-105.

[46] E. Jimenez-Moreno, G. Jimenez-Oses, A. M. Gomez, A. G. Santana, F. Corzana, A. Bastida, J. Jimenez-Barbero, J. L. Asensio, *Chem. Sci.* **2015**, *6*, 6076-6085.

[47] M. Nishio, *Phys. Chem. Chem. Phys.* **2011**, *13*, 13873-13900.

[48] J. L. Asensio, A. Arda, F. J. Canada, J. Jimenez-Barbero, *Acc. Chem. Res.* **2013**, *46*, 946-954.

[49] D. B. Walker, G. Joshi, A. P. Davis, *Cell. Mol. Life Sci.* **2009**, *66*, 3177-3191.

[50] J. P. L. Cox, I. A. Nicholls, D. H. Williams, *J. Chem. Soc., Chem. Commun.* **1991**, 1295-1297.

[51] K. I. Assaf, W. M. Nau, *Angew. Chem., Int. Ed.* **2018**, *57*, 13968-13981.

[52] D. Ramaiah, P. P. Neelakandan, A. K. Nair, R. R. Avirah, *Chem. Soc. Rev.* **2010**, *39*, 4158-4168.

[53] K. Odashima, A. Itai, Y. Iitaka, K. Koga, *J. Am. Chem. Soc.* **1980**, *102*, 2504-2505.

[54] K. Odashima, A. Itai, Y. Iitaka, Y. Arata, K. Koga, *Tetrahedron Lett.* **1980**, *21*, 4347-4350.

[55] K. Odashima, T. Soga, K. Koga, *Tetrahedron Lett.* **1981**, *22*, 5311-5314.

[56] C. F. Lai, K. Odashima, K. Koga, *Tetrahedron Lett.* **1985**, *26*, 5179-5182.

[57] C. F. Lai, K. Odashima, K. Koga, *Chem. Pharm. Bull.* **1989**, *37*, 2351-2354.

[58] T. Soga, K. Odashima, K. Koga, *Tetrahedron Lett.* **1980**, *21*, 4351-4354.

[59] Y. Murakami, J. Kikuchi, T. Ohno, O. Hayashida, M. Kojima, *J. Am. Chem. Soc.* **1990**, *112*, 7672-7681.

[60] J. Kikuchi, K. Egami, K. Suehiro, Y. Murakami, *Chem. Lett.* **1992**, 1685-1688.

[61] H. J. Schneider, T. Blatter, B. Palm, U. Pfingstag, V. Rudiger, I. Theis, *J. Am. Chem. Soc.* **1992**, *114*, 7704-7708.

[62] H. J. Schneider, I. Theis, *J. Org. Chem.* **1992**, *57*, 3066-3070.

[63] M. B. Inoue, E. F. Velazquez, M. Inoue, Q. Fernando, *J. Chem. Soc., Perkin Trans. 2* **1997**, 2113-2118.

[64] S. Kusano, S. Konishi, R. Ishikawa, N. Sato, S. Kawata, F. Nagatsugi, O. Hayashida, *Eur. J. Org. Chem.* **2017**, 1618-1623.

[65] T. Grawe, T. Schrader, P. Finocchiaro, G. Consiglio, S. Failla, *Org. Lett.* **2001**, *3*, 1597-1600.

[66] F. Diederich, *J. Chem. Educ.* **1990**, *67*, 813-820.

[67] F. Diederich, K. Dick, *J. Am. Chem. Soc.* **1984**, *106*, 8024-8036.

[68] S. B. Ferguson, E. M. Seward, E. M. Sanford, M. Hester, M. Uyeki, F. Diederich, *Pure Appl. Chem.* **1989**, *61*, 1523-1528.

[69] S. B. Ferguson, E. M. Sanford, E. M. Seward, F. Diederich, *J. Am. Chem. Soc.* **1991**, *113*, 5410-5419.

[70] J. Huuskonen, J. E. H. Buston, N. D. Scotchmer, H. L. Anderson, *New J. Chem.* **1999**, *23*, 1245-1252.

[71] S. Mattei, P. Wallimann, B. Kenda, W. Amrein, F. Diederich, *Helv. Chim. Acta* **1997**, *80*, 2391-2417.

[72] D. B. Smithrud, T. B. Wyman, F. Diederich, *J. Am. Chem. Soc.* **1991**, *113*, 5420-5426.

[73] M. D. Cowart, I. Sucholeiki, R. R. Bukownik, C. S. Wilcox, *J. Am. Chem. Soc.* **1988**, *110*, 6204-6210.

[74] M. A. Petti, T. J. Shepodd, R. E. Barrans, D. A. Dougherty, *J. Am. Chem. Soc.* **1988**, *110*, 6825-6840.

[75] S. M. Ngola, P. C. Kearney, S. Mecozzi, K. Russell, D. A. Dougherty, *J. Am. Chem. Soc.* **1999**, *121*, 1192-1201.

[76] D. A. Stauffer, R. E. Barrans, D. A. Dougherty, *J. Org. Chem.* **1990**, *55*, 2762-2767.

[77] P. C. Kearney, L. S. Mizoue, R. A. Kumpf, J. E. Forman, A. McCurdy, D. A. Dougherty, *J. Am. Chem. Soc.* **1993**, *115*, 9907-9919.

[78] T. H. Webb, H. S. Suh, C. S. Wilcox, *J. Am. Chem. Soc.* **1991**, *113*, 8554-8555.

[79] F. Zeng, C. F. Chen, *Org. Biomol. Chem.* **2015**, *13*, 1988-1991.

[80] J. E. Forman, R. E. Barrans, D. A. Dougherty, *J. Am. Chem. Soc.* **1995**, *117*, 9213-9228.

[81] L. I. James, J. E. Beaver, N. W. Rice, M. L. Waters, *J. Am. Chem. Soc.* **2013**, *135*, 6450-6455.

[82] M. Dhaenens, J. M. Lehn, J. P. Vigneron, *J. Chem. Soc., Perkin Trans. 2* **1993**, 1379-1381.

[83] L. Chen, H. Y. Zhang, Y. Liu, *J. Org. Chem.* **2012**, *77*, 9766-9773.

[84] J. Jimenez-Barbero, E. Junquera, M. Martinpastor, S. Sharma, C. Vicent, S. Penades, *J. Am. Chem. Soc.* **1995**, *117*, 11198-11204.

[85] O. Molt, D. Rubeling, G. Schafer, T. Schrader, *Chem.--Eur. J.* **2004**, *10*, 4225-4232.

[86] S. Carvalho, R. Delgado, M. G. B. Drew, V. Calisto, V. Felix, *Tetrahedron* **2008**, *64*, 5392-5403.

[87] J. S. Mendy, M. L. Pilate, T. Horne, V. W. Day, M. A. Hossain, *Chem. Commun. (Cambridge, U. K.)* **2010**, *46*, 6084-6086.

[88] R. R. Mittapalli, S. S. R. Namashivaya, A. S. Oshchepkov, T. A. Shumilova, T. Ruffer, H. Lang, E. A. Kataev, *Chem. Commun. (Cambridge, U. K.)* **2017**, *53*, 11345-11348.

[89] B. Odell, M. V. Reddington, A. M. Z. Slawin, N. Spencer, J. F. Stoddart, D. J. Williams, *Angew. Chem., Int. Ed.* **1988**, *27*, 1547-1550.

[90] M. Bria, G. Cooke, A. Cooper, J. F. Garety, S. G. Hewage, M. Nutley, G. Rabani, P. Woisel, *Tetrahedron Lett.* **2007**, *48*, 301-304.

[91] S. T. J. Ryan, J. Del Barrio, I. Ghosh, F. Biedermann, A. I. Lazar, Y. Lan, R. J. Coulston, W. M. Nau, O. A. Scherman, *J. Am. Chem. Soc.* **2014**, *136*, 9053-9060.

[92] M. Sapotta, A. Hofmann, D. Bialas, F. Würthner, *Angew. Chem., Int. Ed.* **2019**, *58*, 3516-3520.

[93] D. B. Smithrud, F. Diederich, *J. Am. Chem. Soc.* **1990**, *112*, 339-343.

[94] T. Ogoshi, S. Kanai, S. Fujinami, T.-a. Yamagishi, Y. Nakamoto, *J. Am. Chem. Soc.* **2008**, *130*, 5022-5023.

[95] Z. T. Li, J. Yang, G. C. Yu, J. M. He, Z. Abliz, F. H. Huang, *Chem. Commun. (Cambridge, U. K.)* **2014**, *50*, 2841-2843.

[96] T. Ogoshi, M. Hashizume, T.-a. Yamagishi, Y. Nakamoto, *Chem. Commun. (Cambridge, U. K.)* **2010**, *46*, 3708-3710.

[97] C. J. Li, X. Y. Shu, J. Li, S. H. Chen, K. Han, M. Xu, B. J. Hu, Y. H. Yu, X. S. Jia, *J. Org. Chem.* **2011**, *76*, 8458-8465.

[98] S. Dasgupta, A. Chowdhury, P. S. Mukherjee, *RSC Adv.* **2015**, *5*, 85791-85798.

[99] Y. Ma, X. Ji, F. Xiang, X. Chi, C. Han, J. He, Z. Abliz, W. Chen, F. Huang, *Chem. Commun. (Cambridge, U. K.)* **2011**, *47*, 12340-12342.

[100] B. Gomez, V. Francisco, F. Fernandez-Nieto, L. Garcia-Rio, M. Martin-Pastor, M. R. Paleo, F. J. Sardina, *Chem.--Eur. J.* **2014**, *20*, 12123-12132.

[101] B. Gomez-Gonzalez, V. Francisco, R. Montecinos, L. Garcia-Rio, *Org. Biomol. Chem.* **2017**, *15*, 911-919.

[102] X.-B. Hu, L. Chen, W. Si, Y. Yu, J.-L. Hou, *Chem. Commun. (Cambridge, U. K.)* **2011**, *47*, 4694-4696.

[103] Y. J. Ma, M. Xue, Z. B. Zhang, X. D. Chi, F. H. Huang, *Tetrahedron* **2013**, *69*, 4532-4535.

[104] G. C. Yu, M. Xue, Z. B. Zhang, J. Y. Li, C. Y. Han, F. H. Huang, *J. Am. Chem. Soc.* **2012**, *134*, 13248-13251.

[105] D. Y. Xia, G. C. Yu, J. Y. Li, F. H. Huang, *Chem. Commun. (Cambridge, U. K.)* **2014**, *50*, 3606-3608.

[106] W. Chen, Y. Y. Zhang, J. Li, X. B. Lou, Y. H. Yu, X. S. Jia, C. J. Li, *Chem. Commun. (Cambridge, U. K.)* **2013**, *49*, 7956-7958.

[107] Y. J. Ma, J. Yang, J. Y. Li, X. D. Chi, M. Xue, *RSC Adv.* **2013**, *3*, 23953-23956.

[108] Y. Yao, J. Y. Li, J. Dai, X. D. Chi, M. Xue, *RSC Adv.* **2014**, *4*, 9039-9043.

[109] D. Y. Xia, P. Wang, B. B. Shi, *Org. Biomol. Chem.* **2017**, *15*, 7618-7622.

[110] Z. H. Zhang, L. Shao, Z. T. Li, G. C. Yu, J. Yang, *Tetrahedron Lett.* **2017**, *58*, 2736-2739.

[111] Y. Liu, F. Zhou, F. Yang, D. Ma, *Org. Biomol. Chem.* **2019**, *17*, 5106-5111.

[112] P. Cintas, *J. Inclusion Phenom.* **1994**, *17*, 205-220.

[113] J. Lagona, P. Mukhopadhyay, S. Chakrabarti, L. Isaacs, *Angew. Chem., Int. Ed.* **2005**, *44*, 4844-4870.

[114] S. J. Barrow, S. Kasera, M. J. Rowland, J. del Barrio, O. A. Scherman, *Chem. Rev. (Washington, DC, U. S.)* **2015**, *115*, 12320-12406.

[115] C. A. Burnett, D. Witt, J. C. Fettinger, L. Isaacs, *J. Org. Chem.* **2003**, *68*, 6184-6191.

[116] D. Ma, P. Y. Zavalij, L. Isaacs, *J. Org. Chem.* **2010**, *75*, 4786-4795.

[117] D. Lucas, L. Isaacs, *Org. Lett.* **2011**, *13*, 4112-4115.

[118] C. Shen, D. Ma, B. Meany, L. Isaacs, Y. H. Wang, *J. Am. Chem. Soc.* **2012**, *134*, 7254-7257.

[119] X. Y. Lu, L. Isaacs, *Org. Lett.* **2015**, *17*, 4038-4041.

[120] X. Y. Lu, L. Isaacs, *Angew. Chem., Int. Ed.* **2016**, *55*, 8076-8080.

[121] F. Biedermann, V. D. Uzunova, O. A. Scherman, W. M. Nau, A. De Simone, *J. Am. Chem. Soc.* **2012**, *134*, 15318-15323.

[122] S. He, F. Biedermann, N. Vankova, L. Zhechkov, T. Heine, R. E. Hoffman, A. De Simone, T. T. Duignan, W. M. Nau, *Nature Chem.* **2018**, *10*, 1252-1257.

[123] Y. Kim, H. Kim, Y. H. Ko, N. Selvapalam, M. V. Rekharsky, Y. Inoue, K. Kim, *Chem.--Eur. J.* **2009**, *15*, 6143-6151.

[124] H. S. El-Sheshtawy, B. S. Bassil, K. I. Assaf, U. Kortz, W. M. Nau, *J. Am. Chem. Soc.* **2012**, *134*, 19935-19941.

[125] D. Tuncel, M. Katterle, *Chem.--Eur. J.* **2008**, *14*, 4110-4116.

[126] M. A. Gamal-Eldin, D. H. Macartney, *Org. Biomol. Chem.* **2013**, *11*, 1234-1241.

[127] L. Cao, M. Šekutor, P. Y. Zavalij, K. Mlinarić-Majerski, R. Glaser, L. Isaacs, *Angew. Chem., Int. Ed.* **2014**, *53*, 988-993.

[128] Y. Jang, R. Natarajan, Y. H. Ko, K. Kim, *Angew. Chem., Int. Ed.* **2014**, *53*, 1003-1007.

[129] J. W. Lee, H. H. L. Lee, Y. H. Ko, K. Kim, H. I. Kim, *J. Phys. Chem. B* **2015**, *119*, 4628-4636.

[130] J. W. Lee, M. H. Shin, W. Mobley, A. R. Urbach, H. I. Kim, *J. Am. Chem. Soc.* **2015**, *137*, 15322-15329.

[131] A. Palma, M. Artelsmair, G. L. Wu, X. Y. Lu, S. J. Barrow, N. Uddin, E. Rosta, E. Masson, O. A. Scherman, *Angew. Chem., Int. Ed.* **2017**, *56*, 15688-15692.

[132] M. E. Bush, N. D. Bouley, A. R. Urbach, *J. Am. Chem. Soc.* **2005**, *127*, 14511-14517.

[133] H. J. Kim, J. Heo, W. S. Jeon, E. Lee, J. Kim, S. Sakamoto, K. Yamaguchi, K. Kim, *Angew. Chem., Int. Ed.* **2001**, *40*, 1526-1529.

[134] L. M. Heitmann, A. B. Taylor, P. J. Hart, A. R. Urbach, *J. Am. Chem. Soc.* **2006**, *128*, 12574-12581.

[135] F. Biedermann, U. Rauwald, M. Cziferszky, K. A. Williams, L. D. Gann, B. Y. Guo, A. R. Urbach, C. W. Bielawski, O. A. Scherman, *Chem.--Eur. J.* **2010**, *16*, 13716-13722.

[136] D. Z. Jiao, F. Biedermann, O. A. Scherman, *Org. Lett.* **2011**, *13*, 3044-3047.

[137] F. Biedermann, M. Vendruscolo, O. A. Scherman, A. De Simone, W. M. Nau, *J. Am. Chem. Soc.* **2013**, *135*, 14879-14888.

[138] L. F. Zheng, S. Sonzini, M. Ambarwati, E. Rosta, O. A. Scherman, A. Herrmann, *Angew. Chem., Int. Ed.* **2015**, *54*, 13007-13011.

[139] J. Svec, M. Necas, V. Sindelar, *Angew. Chem., Int. Ed.* **2010**, *49*, 2378-2381.

[140] M. Stancl, J. Svec, V. Sindelar, *Isr. J. Chem.* **2011**, *51*, 592-599.

[141] M. A. Yawer, V. Havel, V. Sindelar, *Angew. Chem., Int. Ed.* **2015**, *54*, 276-279.

[142] V. Havel, M. Babiak, V. Sindelar, *Chem.--Eur. J.* **2017**, *23*, 8963-8968.

[143] J. Svec, M. Dusek, K. Fejfarova, P. Stacko, P. Klan, A. E. Kaifer, W. Li, E. Hudeckova, V. Sindelar, *Chem.--Eur. J.* **2011**, *17*, 5605-5612.

[144] J. W. Steed, C. P. Johnson, C. L. Barnes, R. K. Juneja, J. L. Atwood, S. Reilly, R. L. Hollis, P. H. Smith, D. L. Clark, *J. Am. Chem. Soc.* **1995**, *117*, 11426-11433.

[145] S. Shinkai, K. Araki, M. Kubota, T. Arimura, T. Matsuda, *J. Org. Chem.* **1991**, *56*, 295-300.

[146] T. Arimura, M. Kubota, K. Araki, S. Shinkai, T. Matsuda, *Tetrahedron Lett.* **1989**, *30*, 2563-2566.

[147] G. Arena, A. Casnati, A. Contino, G. G. Lombardo, D. Sciotto, R. Ungaro, *Chem.--Eur. J.* **1999**, *5*, 738-744.

[148] G. Arena, A. Casnati, A. Contino, F. G. Gulino, D. Sciotto, R. Ungaro, *J. Chem. Soc., Perkin Trans. 2* **2000**, 419-423.

[149] N. Douteau-Guevel, F. Perret, A. W. Coleman, J. P. Morel, N. Morel-Desrosiers, *J. Chem. Soc., Perkin Trans. 2* **2002**, 524-532.

[150] J. Dziemidowicz, D. Witt, J. Rachon, *J. Inclusion Phenom. Macrocyclic Chem.* **2008**, *61*, 381-391.

[151] Y. H. Shi, H. J. Schneider, *J. Chem. Soc., Perkin Trans. 2* **1999**, 1797-1803.

[152] G. Arena, S. Gentile, F. G. Gulino, D. Sciotto, C. Sgarlata, *Tetrahedron Lett.* **2004**, *45*, 7091-7094.

[153] C. Bonaccorso, S. Gentile, F. G. Gulino, D. Sciotto, *Lett. Org. Chem.* **2009**, *6*, 598-603.

[154] J. L. Atwood, D. L. Clark, R. K. Juneja, G. W. Orr, K. D. Robinson, R. L. Vincent, *J. Am. Chem. Soc.* **1992**, *114*, 7558-7559.

[155] L. Zhang, A. Macias, T. B. Lu, J. I. Gordon, G. W. Gokel, A. E. Kaifer, *J. Chem. Soc., Chem. Commun.* **1993**, 1017-1019.

[156] C. Gaeta, T. Caruso, M. Mincolelli, F. Troisi, E. Vasca, P. Neri, *Tetrahedron* **2008**, *64*, 5370-5378.

[157] T. Arimura, H. Kawabata, T. Matsuda, T. Muramatsu, H. Satoh, K. Fujio, O. Manabe, S. Shinkai, *J. Org. Chem.* **1991**, *56*, 301-306.

[158] F. Sansone, S. Barboso, A. Casnati, D. Sciotto, R. Ungaro, *Tetrahedron Lett.* **1999**, *40*, 4741-4744.

[159] S. B. Nimse, J. Kim, V. T. Ta, H. S. Kim, K. S. Song, C. Y. Jung, V. T. Nguyen, T. Kim, *Tetrahedron Lett.* **2009**, *50*, 7346-7350.

[160] S. B. Nimse, J. Kim, K. S. Song, J. T. Lee, V. T. Nguyen, V. T. Ta, T. Kim, *Tetrahedron Lett.* **2011**, *52*, 3751-3755.

[161] Y. Tanaka, Y. Aoyama, *Bull. Chem. Soc. Jpn.* **1990**, *63*, 3343-3344.

[162] K. Kobayashi, Y. Asakawa, Y. Kato, Y. Aoyama, *J. Am. Chem. Soc.* **1992**, *114*, 10307-10313.

[163] X. Gui, J. C. Sherman, *Chem. Commun. (Cambridge, U. K.)* **2001**, 2680-2681.

[164] A. P. Davis, *Org. Biomol. Chem.* **2009**, *7*, 3629-3638.

[165] C. Gropp, B. L. Quigley, F. Diederich, *J. Am. Chem. Soc.* **2018**, *140*, 2705-2717.

[166] L. Sebo, F. Diederich, V. Gramlich, *Helv. Chim. Acta* **2000**, *83*, 93-113.

[167] S. M. Biros, J. Rebek, *Chem. Soc. Rev.* **2007**, *36*, 93-104.

[168] T. Haino, D. M. Rudkevich, A. Shivanyuk, K. Rissanen, J. Rebek, *Chem.--Eur. J.* **2000**, *6*, 3797-3805.

[169] R. J. Hooley, H. J. Van Anda, J. Rebek, *J. Am. Chem. Soc.* **2007**, *129*, 13464-13473.

[170] A. Lledo, J. Rebek, *Chem. Commun. (Cambridge, U. K.)* **2010**, *46*, 8630-8632.

[171] S. Javor, J. Rebek, *J. Am. Chem. Soc.* **2011**, *133*, 17473-17478.

[172] S. M. Biros, E. C. Ullrich, F. Hof, L. Trembleau, J. Rebek, *J. Am. Chem. Soc.* **2004**, *126*, 2870-2876.

[173] C. H. Haas, S. M. Biros, J. Rebek, *Chem. Commun. (Cambridge, U. K.)* **2005**, 6044-6045.

[174] L. Trembleau, J. Rebek, *Science* **2003**, *301*, 1219-1220.

[175] M. P. Schramm, J. Rebek, *Chem.--Eur. J.* **2006**, *12*, 5924-5933.

[176] R. J. Hooley, S. M. Biros, J. Rebek, *Chem. Commun. (Cambridge, U. K.)* **2006**, 509-510.

[177] M. P. Schramm, R. J. Hooley, J. Rebek, *J. Am. Chem. Soc.* **2007**, *129*, 9773-9779.

[178] C. L. D. Gibb, B. C. Gibb, *J. Am. Chem. Soc.* **2011**, *133*, 7344-7347.

[179] R. Pinalli, G. Brancatelli, A. Pedrini, D. Menozzi, D. Hernandez, P. Ballester, S. Geremia, E. Dalcanale, *J. Am. Chem. Soc.* **2016**, *138*, 8569-8580.

[180] S. Mosca, Y. Yu, J. V. Gavette, K. D. Zhang, J. Rebek, *J. Am. Chem. Soc.* **2015**, *137*, 14582-14585.

[181] Q. X. Shi, D. Masseroni, J. Rebek, *J. Am. Chem. Soc.* **2016**, *138*, 10846-10848.

[182] N.-W. Wu, I. D. Petsalakis, G. Theodorakopoulos, Y. Yu, J. Rebek Jr., *Angew. Chem., Int. Ed.* **2018**, *57*, 15091-15095.

[183] D. Masseroni, S. Mosca, M. P. Mower, D. G. Blackmond, J. Rebek, *Angew. Chem., Int. Ed.* **2016**, *55*, 8290-8293.

[184] Q. Shi, M. P. Mower, D. G. Blackmond, J. Rebek, *Proc. Natl. Acad. Sci. U. S. A.* **2016**, *113*, 9199-9203.

[185] Y. Yu, J. Rebek, *Acc. Chem. Res.* **2018**, *51*, 3031-3040.

[186] M. Inouye, K. Fujimoto, M. Furusyo, H. Nakazumi, *J. Am. Chem. Soc.* **1999**, *121*, 1452-1458.

[187] S. Kubik, *Angew. Chem., Int. Ed.* **2009**, *48*, 1722-1725.

[188] E. Klein, M. P. Crump, A. P. Davis, *Angew. Chem., Int. Ed.* **2005**, *44*, 298-302.

[189] N. P. Barwell, M. P. Crump, A. P. Davis, *Angew. Chem., Int. Ed.* **2009**, *48*, 7673-7676.

[190] N. P. Barwell, A. P. Davis, *J. Org. Chem.* **2011**, *76*, 6548-6557.

[191] G. Joshi, A. P. Davis, *Org. Biomol. Chem.* **2012**, *10*, 5760-5763.

[192] Y. Ferrand, E. Klein, N. P. Barwell, M. P. Crump, J. Jimenez-Barbero, C. Vicent, G. J. Boons, S. Ingale, A. P. Davis, *Angew. Chem., Int. Ed.* **2009**, *48*, 1775-1779.

[193] P. Rios, T. S. Carter, T. J. Mooibroek, M. P. Crump, M. Lisbjerg, M. Pittelkow, N. T. Supekar, G. J. Boons, A. P. Davis, *Angew. Chem., Int. Ed.* **2016**, *55*, 3387-3392.

[194] B. Sookcharoenpinyo, E. Klein, Y. Ferrand, D. B. Walker, P. R. Brotherhood, C. F. Ke, M. P. Crump, A. P. Davis, *Angew. Chem., Int. Ed.* **2012**, *51*, 4586-4590.

[195] T. J. Mooibroek, J. M. Casas-Solvas, R. L. Harniman, C. Renney, T. S. Carter, M. P. Crump, A. P. Davis, *Nature Chem.* **2016**, *8*, 69-74.

[196] Y. Ferrand, M. P. Crump, A. P. Davis, *Science* **2007**, *318*, 619-622.

[197] E. Klein, Y. Ferrand, N. P. Barwell, A. P. Davis, *Angew. Chem., Int. Ed.* **2008**, *47*, 2693-2696.

[198] C. F. Ke, H. Destecroix, M. P. Crump, A. P. Davis, *Nature Chem.* **2012**, *4*, 718-723.

[199] R. A. Tromans, T. S. Carter, L. Chabanne, M. P. Crump, H. Li, J. V. Matlock, M. G. Orchard, A. P. Davis, *Nature Chem.* **2019**, *11*, 52-56.

[200] B. J. Shorthill, C. T. Avetta, T. E. Glass, *J. Am. Chem. Soc.* **2004**, *126*, 12732-12733.

[201] G. B. Huang, S. H. Wang, H. Ke, L. P. Yang, W. Jiang, *J. Am. Chem. Soc.* **2016**, *138*, 14550-14553.

[202] H. Yao, H. Ke, X. Zhang, S.-J. Pan, M.-S. Li, L.-P. Yang, G. Schreckenbach, W. Jiang, *J. Am. Chem. Soc.* **2018**, *140*, 13466-13477.

[203] L. L. Wang, Z. Chen, W. E. Liu, H. Ke, S. H. Wang, W. Jiang, *J. Am. Chem. Soc.* **2017**, *139*, 8436-8439.

[204] H. Ke, L.-P. Yang, M. Xie, Z. Chen, H. Yao, W. Jiang, *Nature Chem.* **2019**, *11*, 470-477.

[205] D. S. Kim, J. L. Sessler, *Chem. Soc. Rev.* **2015**, *44*, 532-546.

[206] B. Verdejo, G. Gil-Ramirez, P. Ballester, *J. Am. Chem. Soc.* **2009**, *131*, 3178-3179.

[207] D. Hernandez-Alonso, S. Zankowski, L. Adriaenssens, P. Ballester, *Org. Biomol. Chem.* **2015**, *13*, 1022-1029.

[208] A. Díaz-Moscoso, D. Hernández-Alonso, L. Escobar, F. A. Arroyave, P. Ballester, *Org. Lett.* **2017**, *19*, 226-229.

[209] G. Peñuelas-Haro, P. Ballester, *Chem. Sci.* **2019**, *10*, 2413-2423.

[210] X. D. Chi, H. C. Zhang, G. I. Vargas-Zuniga, G. M. Peters, J. L. Sessler, *J. Am. Chem. Soc.* **2016**, *138*, 5829-5832.

[211] P. Mal, D. Schultz, K. Beyeh, K. Rissanen, J. R. Nitschke, *Angew. Chem., Int. Ed.* **2008**, *47*, 8297-8301.

[212] T. K. Ronson, C. Giri, N. K. Beyeh, A. Minkkinen, F. Topic, J. J. Holstein, K. Rissanen, J. R. Nitschke, *Chem.--Eur. J.* **2013**, *19*, 3374-3382.

[213] J. L. Bolliger, A. M. Belenguer, J. R. Nitschke, *Angew. Chem., Int. Ed.* **2013**, *52*, 7958-7962.

[214] M. M. J. Smulders, S. Zarra, J. R. Nitschke, *J. Am. Chem. Soc.* **2013**, *135*, 7039-7046.

[215] Z. Laughrey, B. C. Gibb, *Chem. Soc. Rev.* **2011**, *40*, 363-386.

[216] P. Mal, B. Breiner, K. Rissanen, J. R. Nitschke, *Science* **2009**, *324*, 1697-1699.

[217] M. D. Pluth, R. G. Bergman, K. N. Raymond, *Acc. Chem. Res.* **2009**, *42*, 1650-1659.

[218] D. L. Caulder, C. Brückner, R. E. Powers, S. König, T. N. Parac, J. A. Leary, K. N. Raymond, *J. Am. Chem. Soc.* **2001**, *123*, 8923-8938.

[219] C. J. Hastings, M. D. Pluth, S. M. Biros, R. G. Bergman, K. N. Raymond, *Tetrahedron* **2008**, *64*, 8362-8367.

[220] A. V. Davis, K. N. Raymond, *J. Am. Chem. Soc.* **2005**, *127*, 7912-7919.

[221] C. Sgarlata, J. S. Mugridge, M. D. Pluth, B. E. F. Tiedemann, V. Zito, G. Arena, K. N. Raymond, *J. Am. Chem. Soc.* **2010**, *132*, 1005-1009.

[222] M. D. Pluth, R. G. Bergman, K. N. Raymond, *J. Am. Chem. Soc.* **2007**, *129*, 11459-11467.

[223] V. M. Dong, D. Fiedler, B. Carl, R. G. Bergman, K. N. Raymond, *J. Am. Chem. Soc.* **2006**, *128*, 14464-14465.

[224] M. D. Pluth, R. G. Bergman, K. N. Raymond, *J. Org. Chem.* **2008**, *73*, 7132-7136.

[225] D. Fiedler, R. G. Bergman, K. N. Raymond, *Angew. Chem., Int. Ed.* **2004**, *43*, 6748-6751.

[226] C. J. Hastings, D. Fiedler, R. G. Bergman, K. N. Raymond, *J. Am. Chem. Soc.* **2008**, *130*, 10977-10983.

[227] C. M. Hong, M. Morimoto, E. A. Kapustin, N. Alzakhem, R. G. Bergman, K. N. Raymond, F. D. Toste, *J. Am. Chem. Soc.* **2018**, *140*, 6591-6595.

[228] M. D. Pluth, R. G. Bergman, K. N. Raymond, *Science* **2007**, *316*, 85-88.

[229] M. D. Pluth, R. G. Bergman, K. N. Raymond, *Angew. Chem., Int. Ed.* **2007**, *46*, 8587-8589.

[230] M. Fujita, M. Tominaga, A. Hori, B. Therrien, *Acc. Chem. Res.* **2005**, *38*, 369-378.

[231] T. Kusukawa, M. Fujita, *Angew. Chem., Int. Ed.* **1998**, *37*, 3142-3144.

[232] T. Sawada, M. Yoshizawa, S. Sato, M. Fujita, *Nature Chem.* **2009**, *1*, 53-56.

[233] M. Yoshizawa, M. Tamura, M. Fujita, *Science* **2006**, *312*, 251-254.

[234] T. Murase, Y. Nishijima, M. Fujita, *J. Am. Chem. Soc.* **2012**, *134*, 162-164.

[235] W. Cullen, M. C. Misuraca, C. A. Hunter, N. H. Williams, M. D. Ward, *Nature Chem.* **2016**, *8*, 231-236.

[236] A. J. Metherell, W. Cullen, N. H. Williams, M. D. Ward, *Chem.--Eur. J.* **2018**, *24*, 1554-1560.

[237] S. Turega, W. Cullen, M. Whitehead, C. A. Hunter, M. D. Ward, *J. Am. Chem. Soc.* **2014**, *136*, 8475-8483.

[238] M. Whitehead, S. Turega, A. Stephenson, C. A. Hunter, M. D. Ward, *Chem. Sci.* **2013**, *4*, 2744-2751.

[239] C. G. P. Taylor, W. Cullen, O. M. Collier, M. D. Ward, *Chem.--Eur. J.* **2017**, *23*, 206-213.

[240] W. Cullen, A. J. Metherell, A. B. Wragg, C. G. P. Taylor, N. H. Williams, M. D. Ward, *J. Am. Chem. Soc.* **2018**, *140*, 2821-2828.

[241] D. Zhang, T. K. Ronson, J. Mosquera, A. Martinez, L. Guy, J. R. Nitschke, *J. Am. Chem. Soc.* **2017**, *139*, 6574-6577.

[242] D. Zhang, T. K. Ronson, J. Mosquera, A. Martinez, J. R. Nitschke, *Angew. Chem., Int. Ed.* **2018**, *57*, 3717-3721.

[243] E. G. Percastegui, J. Mosquera, J. R. Nitschke, *Angew. Chem., Int. Ed.* **2017**, *56*, 9136-9140.

[244] F. Hof, S. L. Craig, C. Nuckolls, J. Rebek, *Angew. Chem., Int. Ed.* **2002**, *41*, 1488-1508.

[245] J. Rebek, *Acc. Chem. Res.* **2009**, *42*, 1660-1668.

[246] C. L. D. Gibb, B. C. Gibb, *J. Am. Chem. Soc.* **2004**, *126*, 11408-11409.

[247] S. Liu, B. C. Gibb, *Chem. Commun. (Cambridge, U. K.)* **2008**, 3709-3716.

[248] M. Porel, N. Jayaraj, S. Raghothama, V. Ramamurthy, *Org. Lett.* **2010**, *12*, 4544-4547.

[249] K. Wang, X. Cai, W. Yao, D. Tang, R. Kataria, H. S. Ashbaugh, L. D. Byers, B. C. Gibb, *J. Am. Chem. Soc.* **2019**, *141*, 6740-6747.

[250] R. Kulasekharan, V. Ramamurthy, *Org. Lett.* **2011**, *13*, 5092-5095.

[251] R. Choudhury, A. Barman, R. Prabhakar, V. Ramamurthy, *J. Phys. Chem. B* **2013**, *117*, 398-407.

[252] V. Ramamurthy, *Acc. Chem. Res.* **2015**, *48*, 2904-2917.

[253] F. Corbellini, L. Di Costanzo, M. Crego-Calama, S. Geremia, D. N. Reinhoudt, *J. Am. Chem. Soc.* **2003**, *125*, 9946-9947.

[254] F. Corbellini, R. M. A. Knegtel, P. D. J. Grootenhuis, M. Crego-Calama, D. N. Reinhoudt, *Chem.--Eur. J.* **2005**, *11*, 298-307.

[255] K. D. Zhang, D. Ajami, J. Rebek, *J. Am. Chem. Soc.* **2013**, *135*, 18064-18066.

[256] J. E. Beves, B. A. Blight, C. J. Campbell, D. A. Leigh, R. T. McBurney, *Angew. Chem., Int. Ed.* **2011**, *50*, 9260-9327.

[257] M. J. Langton, S. W. Robinson, I. Marques, V. Felix, P. D. Beer, *Nature Chem.* **2014**, *6*, 1039-1043.

[258] M. J. Langton, I. Marques, S. W. Robinson, V. Felix, P. D. Beer, *Chem.--Eur. J.* **2016**, *22*, 185-192.

[259] L. Fang, S. Basu, C. H. Sue, A. C. Fahrenbach, J. F. Stoddart, *J. Am. Chem. Soc.* **2011**, *133*, 396-399.

[260] H. Li, H. C. Zhang, A. D. Lammer, M. Wang, X. P. Li, V. M. Lynch, J. L. Sessler, *Nature Chem.* **2015**, *7*, 1003-1008.

[261] H. Y. Au-Yeung, G. D. Pantos, J. K. M. Sanders, *Proc. Natl. Acad. Sci. U. S. A.* **2009**, *106*, 10466-10470.

Chapter 2

Super Aryl-Extended Calix[4]pyrroles: Synthesis, Binding Studies and Attempts to Gain Water Solubility

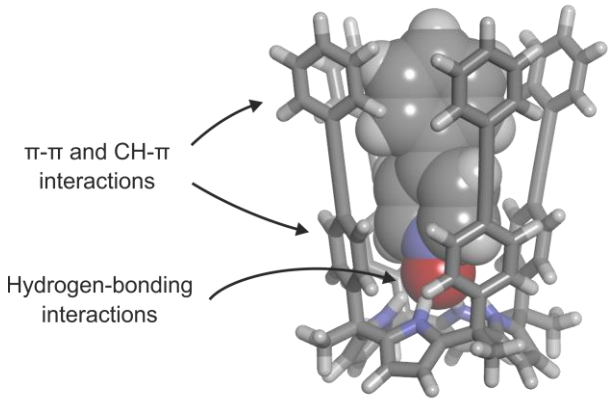

Part of this chapter has been published in:

L. Escobar, G. Aragay, P. Ballester, *Chem.--Eur. J.* **2016**, *22*, 13682-13689.

UNIVERSITAT ROVIRA I VIRGILI
MOLECULAR CONTAINERS BASED ON ARYL-EXTENDED CALIX[4]PYRROLES
Luis Escobar González

2.1 Introduction

Molecular recognition of polar substrates in water using synthetic receptors represents a challenging and exacting endeavor, aiming to mimic natural protein performance.[1,2,3] Encountered difficulties include: 1) the synthesis of receptors that are water-soluble and do not aggregate at the concentrations required for conducting NMR binding studies; 2) the incorporation to the receptor's scaffolds of converging polar groups able to establish hydrogen-bonding interactions with those of the targeted substrates and 3) burying the receptor's polar groups in the interior of hydrophobic cavities of sensible dimensions with the aim to reduce water solvation and induce guest inclusion. Following these guidelines, it is also expected that liberation of solvation water molecules will provide additional enthalpic and/or entropic gains to the thermodynamic stability of the formed complex.[4] In water, the driving force for the binding of polar substrates consists of a combination of hydrophobic, dispersion and polar interactions, which are not obvious to dissect owing to strong interdependences. On the one hand, hydrophobic and dispersion interactions are responsible for the achievement of high levels of affinity. On the other hand, polar interactions provide binding selectivity. In this sense, synthetic receptors deprived of polar groups in the hydrophobic cavities only obey the selectivity principle of size and shape complementarity.

Davis and co-workers achieved remarkable levels of affinity and selectivity in the binding of carbohydrates in water using "temple" receptors (Figure 1).[2,5] These synthetic receptors were rationally designed following the guidelines discussed above. The obtained results proved that it is indeed possible to synthesize receptors that resemble the biological counterparts (*i.e.* lectins). However, the number of examples of synthetic receptors where hydrogen-bonding sites converge in a sizeable three-dimensional hydrophobic cavity to achieve the selective binding in water of polar molecules is scarce.[6] The extensive use of aromatic panels in the construction of hydrophobic cavities makes the adequate positioning of polar groups that can be displayed towards the included polar guest more difficult.

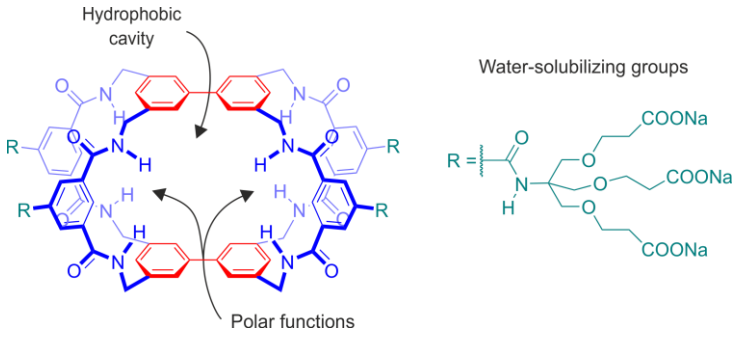

Figure 1. "Temple" receptor reported by Davis and co-workers. Hydrophobic cavity, polar functions and water-solubilizing groups are highlighted.

We and others have demonstrated that the water-soluble tetra-*α* isomers of aryl-extended calix[4]pyrroles (AE-C[4]Ps) are privileged receptors for the recognition of *N*-oxides in this solvent.[7,8,9] Aryl-extended calix[4]pyrroles were introduced originally by Sessler and Floriani.[10,11] In the solid state, the tetra-*α* isomers formed deep inclusion complexes with electron-rich neutral molecules (*e.g.* ethanol, acetic acid and acetone) in which the calix[4]pyrrole core adopted the cone conformation. In this conformation, the aryl-extended calix[4]pyrroles displayed an aromatic cavity open at one end and closed at opposite end by four converging pyrrole units. The included polar guests established four simultaneous hydrogen-bonding interactions between one of its electron-rich oxygen atoms and the four pyrrole NHs.[12] The burying of the polar NHs in a deep aromatic cavity isolates them from solvation with bulk water. The reduced solvation of the polar groups is crucial in maintaining their hydrogen-bonding properties for polar substrates in water.

The elaboration of the aromatic cavity in synthetic receptors is typically associated with modifications of their binding selectivity and affinity. In this chapter, we report the enlargement of the aromatic cavity defined by *meso*-phenyl substituents in the tetra-*α* isomers of aryl-extended calix[4]pyrroles affording unprecedented calix[4]pyrroles that we termed “super aryl-extended” (SAE) (Figure 2). The newly prepared receptors were obtained by Sonogashira reaction of the parent tetra-*α* 4-iodophenyl tetra-methyl calix[4]pyrrole with 4-ethynyl-substituted phenyl derivatives. We compare the binding properties of an aryl-extended calix[4]pyrrole with its SAE counterpart in $CHCl_3$ solution. To explore the water solubility of the SAE-C[4]Ps, we appended ionizable or charged groups at their upper rim. We also show that the incorporation of four ionizable or charged groups is not enough to gain access to water solubility.

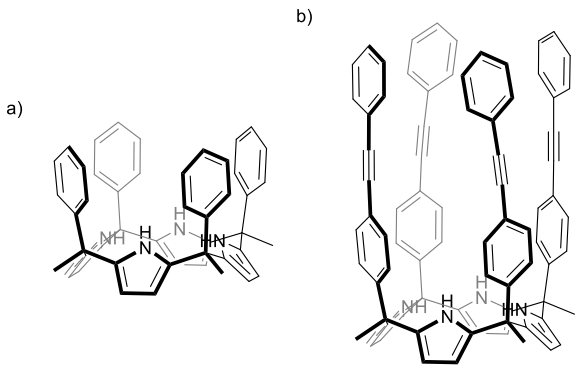

Figure 2. Molecular structures of tetra-*α* isomers: a) aryl-extended and b) super aryl-extended calix[4]pyrroles in cone conformation.

2.2 Results and Discussion

2.2.1 Synthesis

We envisaged the synthesis of water-soluble super aryl-extended calix[4]pyrroles using two different strategies (Scheme 1). Both strategies started from the tetra-*α* isomer of 4-iodophenyl calix[4]pyrrole. The strategy A is planned as a linear synthesis that consists in the construction of the carbon skeleton of the SAE-C[4]P by two consecutive C-C cross-coupling reactions. First, the tetra-iodo calix[4]pyrrole is transformed into a tetra-alkyne derivative. Next, the tetra-alkyne reacts with a *para*-substituted aryl iodide having installed the corresponding water-solubilizing group or a suitable functionalized precursor. The strategy B is a convergent synthesis. In this case, a *para*-substituted aryl alkyne is prepared and is cross-coupled with the tetra-iodo aryl-extended calix[4]pyrrole. Both, the aryl iodide and the aryl alkyne are elaborated with appropriate substituents that can be converted into ionizable (*e.g.* carboxylic acids) or positively charged residues (*e.g*. pyridinium cations).

It is worth mentioning that, in strategy A, the two cross-coupling reactions involve the use of a tetra-aryl-extended calix[4]pyrrole scaffold. In other words, the C-C coupling reaction must take place four times to produce the desired compounds. On the other hand, in strategy B, the calix[4]pyrrole scaffold is only involved in one cross-coupling step with the *para*-substituted aryl alkyne. Besides the advantages described above for strategy B, initial attempts to prepare a tetra-hydroxy super aryl-extended calix[4]pyrrole (R = OH) through the strategy A produced intractable reaction mixtures and the product was only detected in trace amounts. In this regard, we applied the strategy B in the synthesis of SAE-C[4]P derivatives.

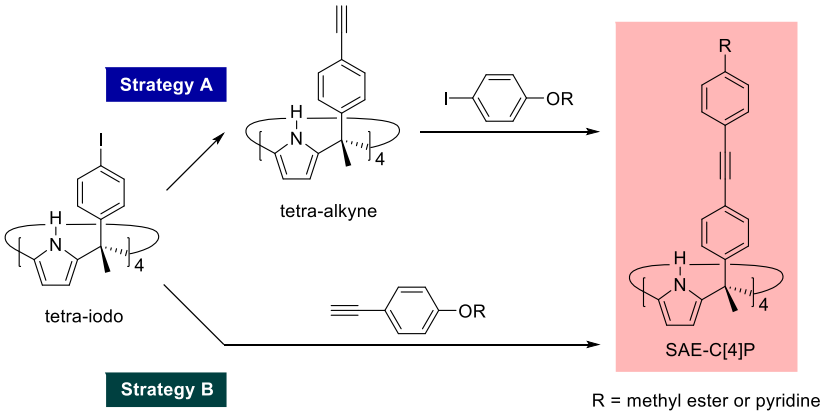

Scheme 1. Synthetic strategies for the preparation of super aryl-extended calix[4]pyrroles involving Sonogashira cross-coupling reactions.

Chapter 2

Tetra-*α* 4-iodophenyl calix[4]pyrrole **1** was prepared by acid-catalyzed condensation of freshly distilled pyrrole with commercially available 4-iodophenyl methyl ketone using a literature procedure.[13] Methyl 4-(ethynylphenoxy)acetate **2a** and *N*-(4-ethynylphenyl)-4-pyridinecarboxamide **2b** were prepared in 54% and 50% yield, respectively, using conditions reported for similar substrates.[14,15] The synthetic procedures are described in detail in the Experimental Section.

The super aryl-extended calix[4]pyrroles **3a** and **3b** were synthesized by coupling the tetra-iodo calix[4]pyrrole **1** with the corresponding 4-ethynyl-substituted derivatives, **2a** and **2b**, under palladium/copper-catalyzed Sonogashira conditions.[16] Column chromatography purification of the crude reaction mixtures allowed the isolation of the pure super aryl-extended calix[4]pyrroles, **3a** and **3b**, as solids in 81 and 50% yield, respectively (Scheme 2). Both SAE-C[4]Ps were characterized by a complete set of high-resolution spectra (NMR and HRMS).

It is worth mentioning that we did not use 4-ethynylphenol in the synthesis of the super aryl-extended calix[4]pyrrole derivatives because this compound was not stable and quickly decomposed after purification by column chromatography.[17]

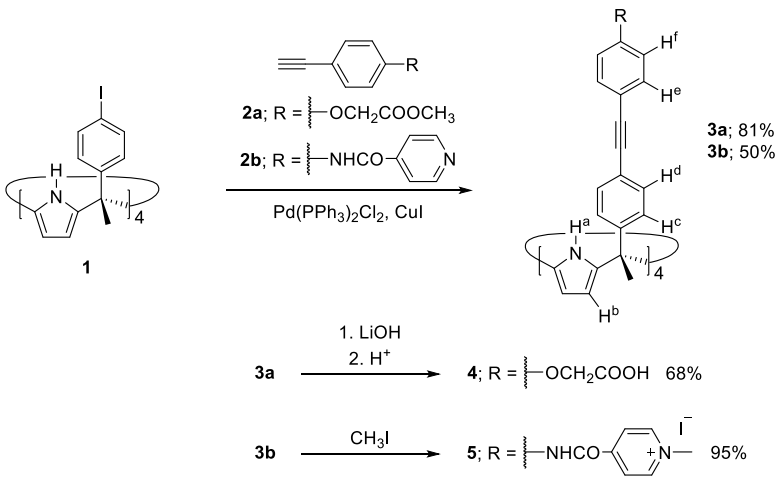

Scheme 2. Synthesis of super aryl-extended calix[4]pyrroles **3a**-**b**, **4** and **5**.

In the particular case of tetra-ester **3a**, single crystals suitable for X-ray diffraction were formed from slow diffusion of acetonitrile vapors into a methylene chloride solution of **3a**. In the solid state, **3a** adopted the cone conformation with one molecule of acetonitrile deeply included in its cavity (Figure 3a). The nitrogen atom of the bound acetonitrile was involved in four hydrogen bonds with the pyrrole NHs. The average N···N distance was 3.24 Å. Remarkably, the aromatic cavity of **3a** collapsed in its upper section owing to the edge-to-face stacking geometry (CH-π interactions) adopted by adjacent terminal phenyl rings of the ethynyl substituents (Figure 3b).

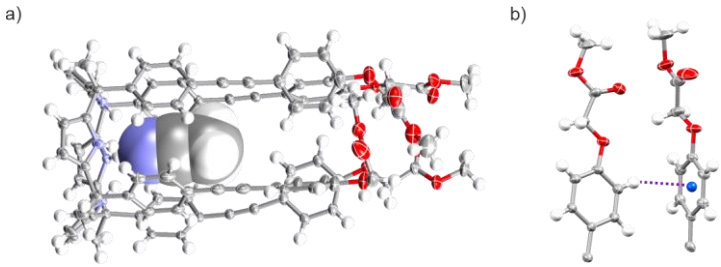

Figure 3. a) X-ray structure of the tetra-ester SAE-C[4]P **3a** and b) selected view of the edge-to-face CH-π interactions established between adjacent terminal phenyl rings. The structures are shown in ORTEP view with thermal ellipsoids set at 50% probability. Hydrogens are shown as fixed-size spheres of 0.3 Å radius. Bound acetonitrile is shown as CPK model. CH-π interaction is highlighted in b) with a dashed line.

The tetra-methyl ester **3a** was hydrolyzed with LiOH, followed by acidification to provide the tetra-acid **4** in 68% yield. In turn, the tetra-pyridyl receptor **3b** was reacted with excess of CH_3I to afford the *N*-methyl tetra-pyridinium derivative **5** (Scheme 2).

Single crystals of the tetra-acid **4** suitable for X-ray diffraction analysis were obtained by slow diffusion of acetonitrile into an acetone solution of the compound. The solid state was very similar to that observed for the parent tetra-ester **3a**. The packing of the crystal revealed that tetra-acid **4** formed dimeric aggregates with a capsular-like topology (Figure 4). The dimeric capsules were stabilized by eight intermolecular hydrogen bonds formed between the carboxylic groups installed at the upper rim of the monomers.

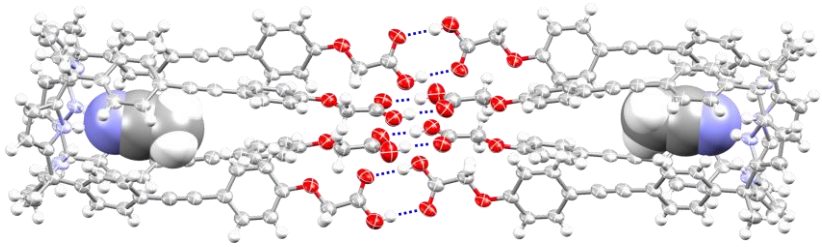

Figure 4. X-ray structure of the dimeric aggregate of tetra-acid **4**. The structure is shown in ORTEP view with thermal ellipsoids set at 50% probability. Hydrogens are shown as fixed-size spheres of 0.3 Å radius. Bound acetonitrile molecules are shown as CPK models. Hydrogen bonds between carboxylic acids are highlighted with dashed lines.

DOSY NMR spectroscopy is an adequate technique to investigate the self-assembly of tetra-acid **4** into dimeric aggregates in solution.[18] The tetra-acid **4** was not soluble in $CDCl_3$ nor CD_3CN. Thus, we performed a DOSY NMR experiment of **4** using [D_8]THF as solvent. The diffusion constant obtained for **4** was 5.6±0.2 x 10^{-10} $m^2 \cdot s^{-1}$ (Figure 5). This constant value was similar to that determined for the tetra-ester precursor **3a** (Figure 6). This result ruled out the existence of dimeric aggregates of tetra-acid **4** in THF solution. Most likely, the tetra-acid **4** does not adopt a cone

conformation in THF and the solvation of the carboxylic acid groups at the upper rim of **4** with THF molecules prevents their association at the studied concentrations.

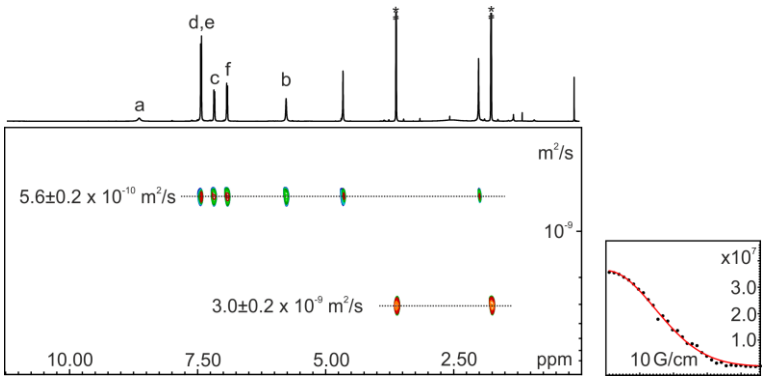

Figure 5. (left) ^{1}H pseudo 2D plot DOSY (500 MHz with cryoprobe, [D$_8$]THF, 298 K, D20 = 0.15 s; P30 = 1 ms) of tetra-acid **4** (3.5 mM). (right) Fit of the decay of signal b to a mono-exponential function. Errors are indicated as standard deviations. See Scheme 2 for proton assignment. *Residual solvent peaks.

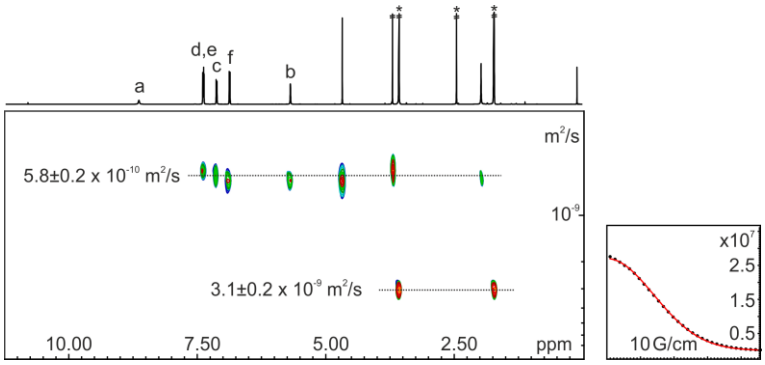

Figure 6. (left) ^{1}H pseudo 2D plot DOSY (500 MHz with cryoprobe, [D$_8$]THF, 298 K, D20 = 0.15 s, P30 = 1 ms) of tetra-ester **3a** (3.5 mM). (right) Fit of the decay of signal b to a mono-exponential function. Errors are indicated as standard deviations. See Scheme 2 for proton assignments. *Residual solvent peaks.

2.2.2 Binding studies of the tetra-ester SAE-C[4]P **3a** with *N*-oxides

We probed the interaction of the tetra-ester **3a** with pyridyl *N*-oxides **6a**-**c** and alkyl *N*-oxides **7a**-**b** (Figure 7) by ^{1}H NMR spectroscopy. *N*-oxides have relevant biological activity. They are known to act as a novel class of antiviral drugs by inhibiting the replication processes and to control the osmotic pressure of fish tissues, among others.[19,20,21] Previous investigations by our research group have established that *N*-oxides bind aryl-extended calix[4]pyrroles through the formation of four convergent hydrogen bonds between the oxygen atom of the *N*-oxide and the pyrrole NHs.[7,8]

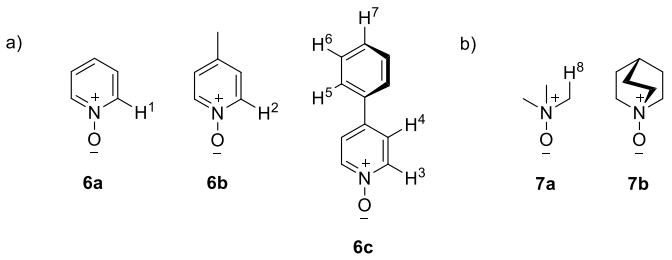

Figure 7. Line-drawing structures: a) pyridyl *N*-oxides **6a**-**c** and b) alkyl *N*-oxides **7a**-**b**.

Pyridyl *N*-oxides **6a**-**c**

The ^{1}H NMR spectrum of a millimolar $CDCl_3$ solution of **3a** displayed sharp and well-defined proton signals that are in agreement with a C_{4v} symmetry. The pyrrole NHs (H^a) resonated at δ = 7.6 ppm and the β-pyrrole hydrogen atoms (H^b) appeared at δ = 5.7 ppm (Figure 8a). All together, these observations did not evidence the preferred conformation adopted by the calix[4]pyrrole **3a** in solution. The receptor may be locked in the cone conformation or experiencing an interconversion process between conformers (cone and alternate) at a rate that is fast on the chemical shift timescale. Molecular dynamic simulations have shown that the octa-methyl calix[4]pyrrole **8** (Figure 12) adopted mainly the 1,3-alternate conformation in solvents with reduced hydrogen-bonding acceptor properties (*e.g.* chloroform).[22] They also revealed that in non-polar solvents the conformational space of calix[4]pyrroles was complex and the conformational transitions were fast. Based on the above, we considered that **3a** dissolved in $CDCl_3$ was fluttering mainly between alternate conformations.

We observed that the addition of 0.5 equiv. of pyridine *N*-oxide **6a** to the $CDCl_3$ solution of **3a** induced the appearance of a new set of proton signals (Figure 8b). We assigned this new set of signals to the protons of bound **3a**. Significantly, the β-pyrrole protons and the pyrrole NHs in the bound receptor moved downfield, $\Delta\delta$ = +0.35 and +2.25 ppm, respectively. On the contrary, the aromatic protons of the added *N*-oxide appeared upfield shifted with respect to the free counterpart. In particular, the complexation induced shift experienced by the protons *alpha* to the nitrogen atom (H^1) was larger than -3.5 ppm. When 1 equiv. of **6a** was added, only the proton signals assigned to bound **3a** were detected (Figure 8c). The addition of more than 1 equiv. of **6a** did not produce additional changes in the signals of the receptor but caused the appearance of the proton signals of the free *N*-oxide (Figure 8d).

Taken together, these results indicated that: 1) **3a** binds **6a** forming a 1:1 complex (**6a**⊂**3a**); 2) the chemical exchange between the components of the complex and the free counterparts is slow on the chemical shift timescale; 3) the binding constant is larger than 10^4 M^{-1} and 4) the **6a**⊂**3a** complex features an inclusion binding geometry. That is, **6a** is included in the aromatic cavity displayed by **3a** in the cone conformation where it experiences a strong magnetic shielding

exerted by the *meso*-aryl substituents. The receptor **3a** is locked in the cone conformation upon binding **6a** owing to the establishment of four hydrogen bonds between the oxygen atom of the *N*-oxide and the pyrrole NHs.

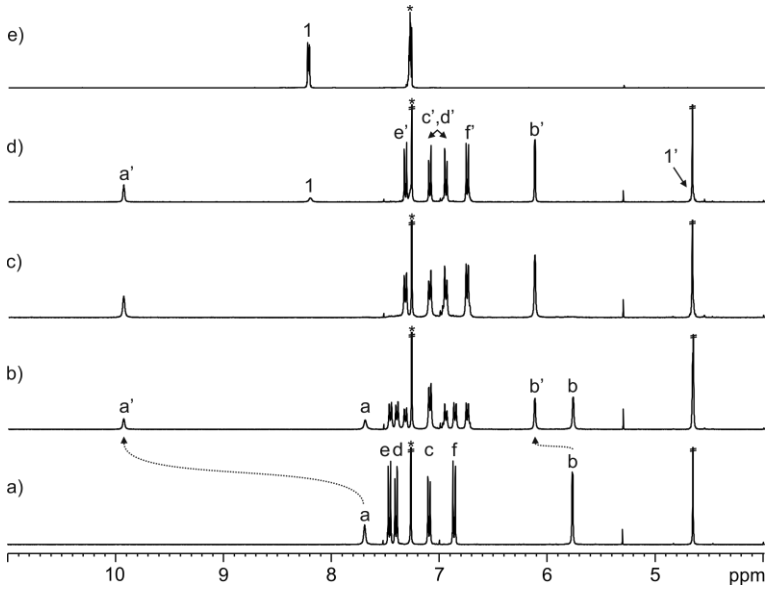

Figure 8. Selected region of the ^{1}H NMR (400 MHz, $CDCl_3$, 298 K) spectra of the titration of **3a** with **6a**: a) 0; b) 0.5; c) 1 and d) 2 equiv.; e) **6a**. Primed letters correspond to proton signals of bound components. See Scheme 2 and Figure 7a for proton assignments. *Residual solvent peak.

We observed completely analogous behaviour in the binding dynamics and chemical shift changes during the titration of **3a** with pyridyl *N*-oxides **6b** and **6c** (see Experimental Section). Remarkably, in the **6c⊂3a** inclusion complex the signals of the *ortho*- and *meta*-protons in the *para*-phenyl substituent of **6c** also experienced significant upfield changes ($\Delta\delta$ = -0.37 and -1.20 ppm, respectively).

We performed simple molecular modelling studies (PM6) to derive the putative structures for the inclusion complexes **6b⊂3a** and **6c⊂3a** (Figure 9). The energy minimized structures of both complexes showed the guest deeply included in the aromatic cavity of the receptor. The oxygen atom of the *N*-oxides formed four hydrogen bonds with NH groups of the pyrrole core that adopted the cone conformation. In addition, the pyridyl ring of the guests establishes π-π and CH-π interactions with the *meso*-phenyl substituents that define the lower section of the aromatic cavity of the receptor. Nonetheless, additional π-π and CH-π interactions exist between the *para*-phenyl ring of guest **6c** and the terminal phenyl groups that define the upper section of the aromatic cavity of bound **3a**. Clearly, the inclusion of the guests disrupts the edge-to-face stacking interactions observed for the CH_3CN⊂**3a** complex in the solid state. The additional π-π and CH-π interactions

displayed in the energy minimized structure of **6c⊂3a** suggested a potential increase in its thermodynamic stability with respect to the **6b⊂3a** analogue.

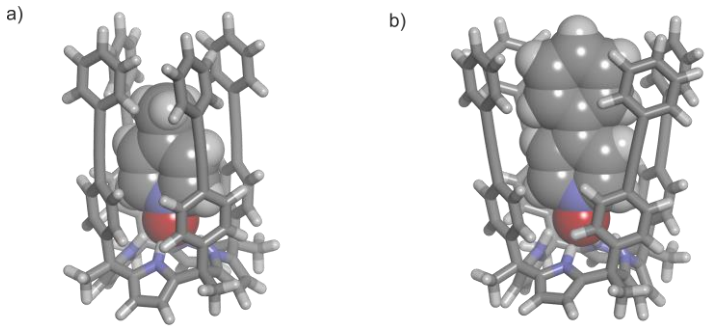

Figure 9. Energy minimized structures (PM6) of the inclusion complexes: a) **6b⊂3a** and b) **6c⊂3a**. Receptors are depicted in stick representation and bound guests are shown as CPK models. Substituents at the *para*-position of the terminal phenyl groups of the SAE-C[4]Ps are omitted for clarity.

We computed the chemical shifts (δ)[23,24,25,26,27] and the nucleus-independent chemical shifts (NICS),[28,29] which are related to complexation induced shifts ($\Delta\delta$), for the hydrogen atoms of the *N*-oxide in the **6c⊂3a** complex (Table 1). The sensible agreement that exists between experimental and calculated values strongly supports the inclusion geometry assigned to the **6c⊂3a** complex in solution.

Table 1. Experimental (δ_{exp}, ppm) and calculated (δ_{calc}, ppm) chemical shifts for the proton signals of bound **6c**. The complexation induced shifts ($\Delta\delta_{exp}$, ppm) and calculated NICS (ppm) are also included. See Figure 7a for proton assignment.

Signal	δ_{exp}	δ_{calc}	$\Delta\delta_{exp}$	NICS
3	4.57	3.69	-3.67	-4.69
4	7.25	7.00	-0.33	-0.48
5	7.13	6.42	-0.37	-0.46
6	6.26	5.17	-1.20	-1.76
7	6.86	4.76[a]	-0.64	-1.62[a]

[a] The calculated chemical shift and NICS of H^7 are very different to the experimental values because this hydrogen, which is in the *para*-position of the phenyl substituent of **6c**, is exposed to the solvent and the calculation was performed in the gas phase.

Alkyl *N*-oxides **7a**-**b**

Next, we investigated the complexation of alkyl *N*-oxides **7a**-**b** with the tetra-ester SAE-C[4]P **3a** in $CDCl_3$ solution by ^{1}H NMR spectroscopy. The addition of 0.5 equiv. of trimethylamine *N*-oxide **7a** to a millimolar solution of **3a** produced two sets of proton signals for the super aryl-extended **3a**, which we assigned to the free and bound receptor (Figure 10b). This observation indicated that free and bound **3a** experienced slow dynamics on the ^{1}H NMR chemical shift timescale. Remarkably, the pyrrole NHs moved $\Delta\delta$ = +2.6 ppm owing to the formation of hydrogen bonds with the oxygen atom of **7a**. The proton signal of the methyl groups (H^8) of **7a** appeared at 1 ppm ($\Delta\delta$ = -2.25 ppm) and that confirmed the deep inclusion of **7a** in the aromatic cavity of the receptor. The addition of 1 equiv. of **7a** provoked the exclusive observation of the proton signals assigned to the bound components (Figure 10c). Finally, the addition of more than 1 equiv. of *N*-oxide **7a** did not induce changes on the proton signals of the bound species. The proton signal of the guest added in excess coincided with that of the free compound in chloroform solution (Figure 10d).

Taken all together, **7a** and **3a** formed a thermodynamically and kinetically stable 1:1 inclusion complex, for which we estimated a binding constant K_a (**7a**⊂**3a**) > 10^4 M^{-1}. The result obtained in the ^{1}H NMR titration experiment of quinuclidine *N*-oxide **7b** with the tetra-ester **3a** produced an analogous result to that described above (see Experimental Section).

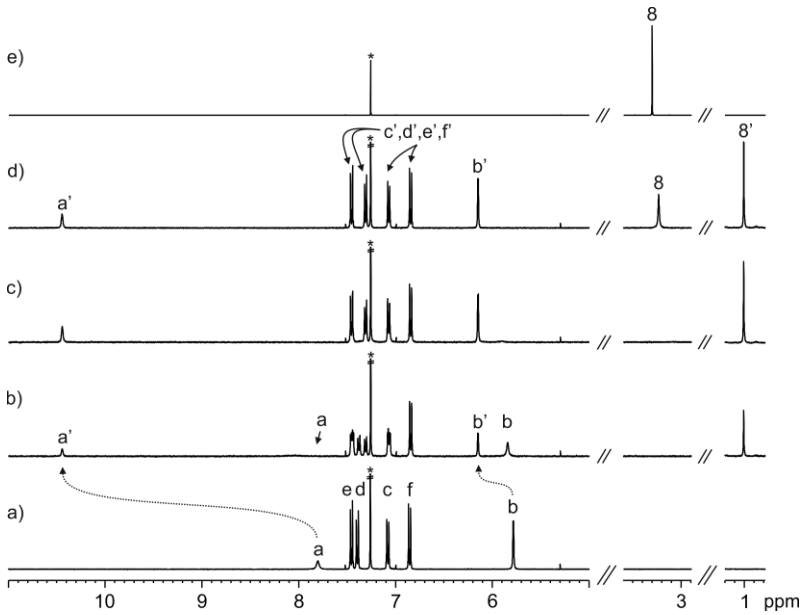

Figure 10. Selected regions of the ^{1}H NMR (400 MHz, $CDCl_3$, 298 K) spectra of the titration of **3a** with **7a**: a) 0; b) 0.5; c) 1 and d) 2 equiv.; e) **7a**. Primed letters correspond to proton signals of bound components. See Scheme 2 and Figure 7b for proton assignments. *Residual solvent peak.

Unfortunately, the tetra-pyridyl receptor **3b** featured reduced solubility in most non-polar and polar organic solvents, except $(CD_3)_2SO$. This characteristic precluded the implementation of titration experiments with this latter receptor.

2.2.3 Thermodynamic characterization of the inclusion complexes

Pair-wise competitive experiment

To quantify the effect of the additional interactions in **6c⊂3a**, we determined the ratio between the stability constant values for the **6b⊂3a** and **6c⊂3a** complexes performing a pair-wise competitive experiment (Figure 11). The analysis of an equimolar $CDCl_3$ solution of **3a** and **6b** using ^{1}H NMR spectroscopy evidenced the quantitative formation of the **6b⊂3a** complex. The addition of 0.7 equiv. of **6c** to the above solution induced not only the observation of the proton signals of free *N*-oxide **6c** (H^3), but also those corresponding to the **6c⊂3a** complex ($H^{3'}$) and free *N*-oxide **6b** (H^2). This observation demonstrated that *N*-oxide **6c** was able to partially replace the bound *N*-oxide **6b** in the **6b⊂3a** complex.

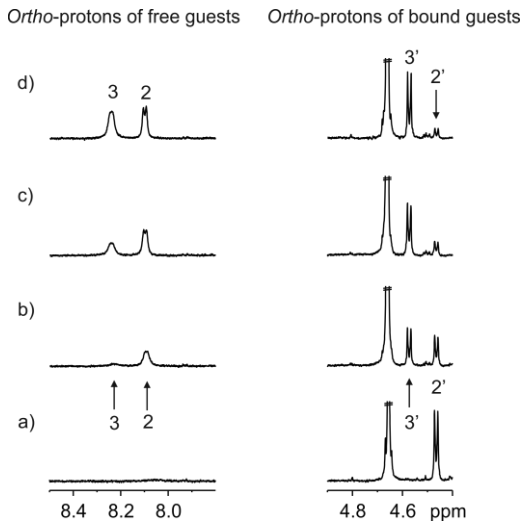

Figure 11. Selected regions of the ^{1}H NMR (500 MHz, $CDCl_3$, 298 K) spectra of the pair-wise competitive binding experiment of *N*-oxides **6b** and **6c** and receptor **3a**: a) 1 equiv. of **6b**; addition of incremental amounts of **6c**: b) 0.7; c) 1.3 and d) 1.9 equiv. Primed letters correspond to proton signals of bound *N*-oxides. See Figure 7a for proton assignments.

The incremental addition of *N*-oxide **6c** (1.3 and 1.9 equiv.) showed that the intensity of the proton signals assigned to the **6c⊂3a** complex ($H^{3'}$) grew at the expense of those of the **6b⊂3a** ($H^{2'}$) counterpart. Using the integral values of selected proton signals from all the species involved in the equilibrium, we determined an averaged ratio of stability constants of K_a (**6c⊂3a**)/K_a (**6b⊂3a**) ~

4 using Equation 1. This value translated into *ca.* 0.8 kcal·mol^{-1} of free energy advantage in favour of the **6c⊂3a** complex.

1) K_{a2}/K_{a1} = ([HG_2] x [G_1])/([HG_1] x [G_2]); where the guests are G_1 and G_2, and the corresponding 1:1 complexes are HG_1 and HG_2.

As mentioned above, the measured increase in thermodynamic stability for the **6c⊂3a** complex can be assigned to additional π-π and CH-π interactions established between the *para*-phenyl substituent of **6c** and the terminal phenyl groups that defined the upper section of the receptor's cavity. Nevertheless, the assessed free energy difference is significantly lower than we expected. We and others have determined an average gain in free energy of *ca.* 1 kcal·mol^{-1} for each CH-π interaction.[30] Likewise, π-π interactions in organic solvents can contribute to about 1 kcal·mol^{-1} in the complex stability.[31] Most likely, solvation effects do not allow a direct translation of enthalpy gain into free energy.

Isothermal titration calorimetry (ITC) experiments

The stability constants of the inclusion complexes, **6a**-**c⊂3a** and **7a**-**b⊂3a**, were too high to be measured accurately using ^{1}H NMR titrations. In this regard, we performed ITC titration experiments in chloroform solution to characterize the binding processes of *N*-oxides **6a**-**c** and **7a**-**b** with the tetra-ester SAE-C[4]P **3a**. We also studied the binding of the *N*-oxides to the octa-methyl calix[4]pyrrole **8** and the aryl-extended calix[4]pyrrole **9** (Figure 12). Receptor **8** is an ideal model to determine the contribution of the hydrogen-bonding interactions between the *N*-oxides and the calix[4]pyrrole core in $CDCl_3$ solution. In turn, the aryl-extended derivative **9** seemed to be a good model to quantify the energy gain provided by the terminal phenyl substituents incorporated at the upper rim of tetra-ester **3a** when *N*-oxide **6c** is bound.

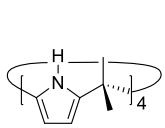

8

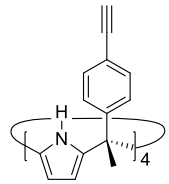

9

Figure 12. Structures of octa-methyl calix[4]pyrrole **8** and tetra-*α* 4-ethynylphenyl calix[4]pyrrole **9** employed as reference models in the binding studies.

In all cases, the obtained experimental binding isotherms were fit to a theoretical 1:1 binding model (Figure 13). The fit data allowed the direct calculation of the stability constant values (K_a) and the enthalpy (Δ*H*) of binding. The free energy (Δ*G*) and the entropy of binding (Δ*S*) were mathematically derived from the thermodynamic constants measured experimentally. In the case

of titrations displaying an abrupt saturation of the measured heat, the binding constant values returned from the fit of the data to a theoretical 1:1 binding model are just estimates (Table 2).

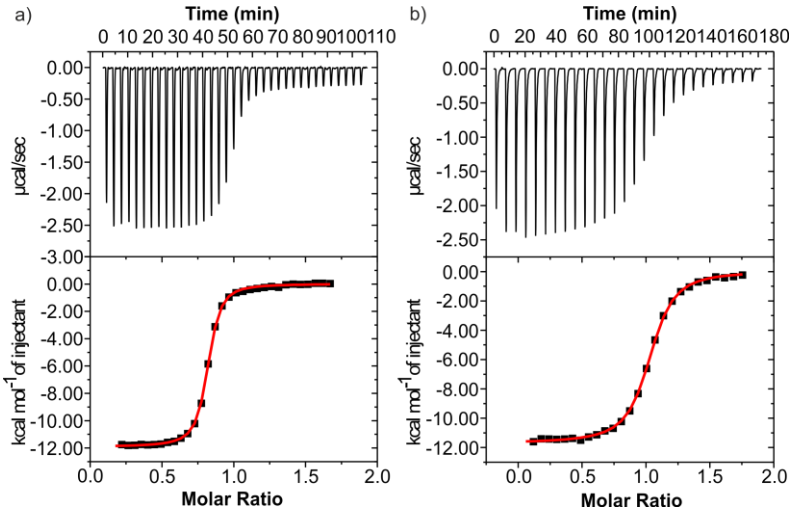

Figure 13. Top panels show raw data (heat *vs.* time) for the titration of guest into the host: a) **6a⊂3a** and b) **7a⊂3a** ($CHCl_3$). Titrations were performed at 298 K. Bottom panels represent integrated data fitted to the theoretical binding isotherm (red line) for a 1:1 binding model.

As expected, all the stability constants determined for the aryl and super aryl-extended calix[4]pyrroles, **9** and **3a**, were larger than 10^4 M^{-1} and the binding processes were driven mainly by enthalpy (see Experimental Section). In addition, enthalpy-entropy compensation effects seemed to be involved in the binding processes.[32]

Considering the inclusion complex of pyridine *N*-oxide **6a** or **6b** and tetra-ester **3a**, as reference to quantify the effect produced by the introduction of the *para*-phenyl group in the *N*-oxide guest **6c**, we assigned, in agreement with the pair-wise competitive experiment, a value of *ca.* 1 kcal·mol^{-1} to the additional π-π and CH-π interactions present in the **6c⊂3a** complex. Alternatively, the energy gain provided by these interactions was estimated using the **6c⊂9** complex as reference, resulting in an equivalent value of *ca.* 1 kcal·mol^{-1} less stable than the **6c⊂3a** counterpart. The obtained results confirmed that the elaboration of the aromatic cavity present in the SAE-C[4]P **3a** enhanced its binding properties towards *N*-oxide **6c** in comparison to the aryl-extended counterpart **9**. On the other hand, the binding processes of *N*-oxide **6a** and **6b** did not show noticeable changes in free energy when comparing the complexes formed with SAE-C[4]P **3a** and the aryl-extended counterpart **9**, supporting the lack of additional CH-π and π-π interactions for the *para*-methyl substituted guest with the upper section of the super aryl-extended **3a**.

Table 2. Binding constants (K_a, M^{-1}) and free energies (ΔG) at 298 K of the 1:1 inclusion complexes of tetra-ester **3a**, octa-methyl **8** and tetra-alkyne **9** in chloroform. Error values are reported as standard deviations.

Guest	Tetra-ester **3a**		Octa-methyl **8**		Tetra-alkyne **9**	
	K_a	ΔG	K_a	ΔG	K_a	ΔG
6a	$4.9\pm0.1 \times 10^6$	-9.1±0.1	<10[a]	-	$3.6\pm0.2 \times 10^6$	-8.9±0.1
6b	$1.2\pm0.5 \times 10^7$	-9.6±0.2	-	-	$1.3\pm0.1 \times 10^7$	-9.7±0.1
6c	$3.6\pm0.2 \times 10^7$	-10.3±0.1	-	-	$1.0\pm0.1 \times 10^7$	-9.5±0.1
7a	$1.1\pm0.1 \times 10^6$	-8.2±0.1	-	-	-	-
7b	$>10^{7}$[,b]	-	80 ± 10[c]	-2.6±0.1	$>10^{7}$[,b]	-

[a] Estimated from ^{1}H NMR titration experiments; [b] estimated from ITC experiments and [c] determined by ^{1}H NMR titration experiments.

The binding constants measured for the complexes of the octa-methyl calix[4]pyrrole **8** with pyridine and quinuclidine *N*-oxides **6a** and **7b**, respectively, are lower than 10^2 M^{-1} in chloroform solution. These values are significantly lower than those obtained with the aryl-extended calix[4]pyrrole **9** and the SAE derivative **3a**. From these results in chloroform solution, three general conclusions can be drawn: 1) the four convergent hydrogen bonds formed between an *N*-oxide and a calix[4]pyrrole contribute in a reduced extent to the thermodynamic stability of the corresponding 1:1 complex; 2) the three-dimensional aromatic cavity displayed by the tetra-*α* isomer of aryl-extended calix[4]pyrroles is necessary for the efficient binding of pyridyl and alkyl *N*-oxides; and 3) multiple π-π and CH-π interactions, probably in combination with solvophobic effects, are mainly responsible for the high thermodynamic stability of the inclusion complexes shown above.

2.2.4 Kinetic characterization of the inclusion complexes with pyridyl *N*-oxides

We performed 2D ^{1}H-^{1}H EXSY NMR experiments using $CDCl_3$ solutions of the super aryl-extended calix[4]pyrrole **3a** and the pyridyl *N*-oxides, **6b** and **6c**, in a 1:0.5 ratio (Figure 14). In both cases, we observed cross-peaks due to chemical exchange between the separate *β*-pyrrole proton signals in the free (H^b) and bound ($H^{b'}$) receptor **3a**. Using the integral values of the exchange cross-peaks and the diagonal peaks, we determined the rate constants (k_1' and k_{-1}') for the two-sites magnetization exchange process with the help of the EXSYCalc software.[33] The magnetization exchange rate constants and the rate constants of the binding equilibrium of **3a** with the *N*-oxides, assuming a one-step process, are related as indicated by Equations 2 and 3.

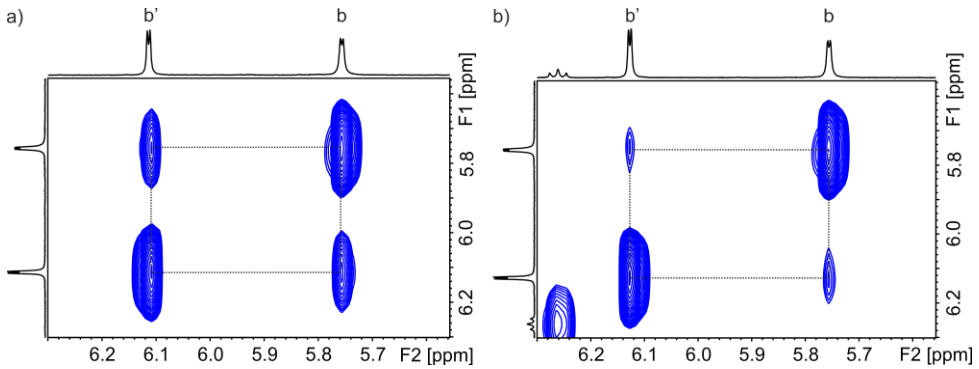

Figure 14. 2D ^{1}H-^{1}H EXSY NMR (500 MHz, $CDCl_3$, 298 K, t_{mix} = 0.3 s) spectra: a) **6b** and **3a** (0.5:1 ratio) and b) **6c** and **3a** (0.5:1 ratio). Primed letters correspond to proton signals of bound **3a**. See Scheme 2 for proton assignments.

$$M(\mathbf{3a}) \underset{k_{-1}'}{\overset{k_1'}{\rightleftharpoons}} M(\mathbf{3a}')$$

$$\mathbf{3a} + N\text{-oxide} \underset{k_{-1}}{\overset{k_1}{\rightleftharpoons}} N\text{-oxide}\subset\mathbf{3a}$$

2) $k_1 = k_1' / [N\text{-oxide}]$

3) $k_{-1} = k_{-1}'$

In turn, the equilibrium constant K_a for the binding process is equal to the forward rate constant (k_1) divided by the inverse rate constant (k_{-1}). Hence, we determined the energy barrier for the dissociation of the complexes as $\Delta G^{\ddagger}$ (**6b⊂3a**) = 17.6±0.1 kcal·mol^{-1} and $\Delta G^{\ddagger}$ (**6c⊂3a**) = 18.4±0.1 kcal·mol^{-1} (Table 3). The greater kinetic stability determined for the **6c⊂3a** complex with respect to the **6b⊂3a** counterpart is in line with the superior thermodynamic stability of the former. This result suggested that the structure of the transition state (TS) must be similar in both cases. We hypothesized that, in the TS, the receptor adopts a conformation that resembles the 1,3-alternate conformer and the *N*-oxide is mainly bound with just two hydrogen bonds. Therefore, the TS structure is more similar to the starting materials than the inclusion complex.

Such TS qualifies as an early TS and, according to Hammond's postulate, it is characteristic of rapid and exothermic reactions. Indeed, the ITC experiments showed that the binding equilibria are highly exothermic. Using the stability constant values determined in the ITC experiments and the assessed rate constants for complex's dissociation (k_{-1}), we calculated the rate constant for the formation of the inclusion complexes (k_1) (Table 3). The determined values were large and close to those expected for a diffusion controlled process ($k_1 \sim 10^7$ M^{-1}·s^{-1}). All together, these results suggested that, to a large extent, the SAE-C[4]P **3a** adopts a 1,3-alternate conformation when dissolved in chloroform solution. A change in the receptor's conformation is not required for the TS formation of the inclusion complex. This finding is in contrast with previous results in our group for

anion binding with aryl-extended calix[4]pyrroles in acetonitrile solution. There, we postulated that the receptor mainly adopted the cone conformation in acetonitrile.[34]

Table 3. Magnetization exchange rate constants ($k = k_1' + k_{-1}'$, s^{-1}) and chemical exchange rate constants (k_1, $M^{-1}\cdot s^{-1}$ and k_{-1}, s^{-1}) of the complexes **6b⊂3a** and **6c⊂3a** determined from 2D ^{1}H-^{1}H EXSY NMR experiments. Energy barriers for the dissociation of the complexes ($\Delta G^{\ddagger}$, kcal·mol^{-1}) were calculated using the Eyring-Polanyi equation. Errors are indicated as standard deviations.

Complex	$k = k_1' + k_{-1}'$	k_1	k_{-1}	$\Delta G^{\ddagger}$
6b⊂3a	1.6±0.1	1.0±0.4 x 10^7	0.8±0.1	17.6±0.1
6c⊂3a	0.4±0.1	7.2±0.5 x 10^6	0.2±0.1	18.4±0.1

Alternatively, the rate constants for the magnetization exchange between spins of free and bound **3a**, in the **6b⊂3a** and **6c⊂3a** complexes, were measured by selective inversion recovery (SIR) NMR experiments[35] (Figure 15). First, the relaxation times (T_1) of the proton signals of free and bound **3a** were determined by non-selective inversion recovery (NSIR) NMR experiments (Table 4). Next, the signal of the *β*-pyrrole protons of free **3a** was selectively inverted and ^{1}H NMR spectra was acquired at different delays (t). The fit of the data to a two-sites model using the CIFIT program[36] returned the rate constants (k) for the magnetization exchange (Table 4). The obtained values were in agreement with those determined above using 2D EXSY NMR experiments.

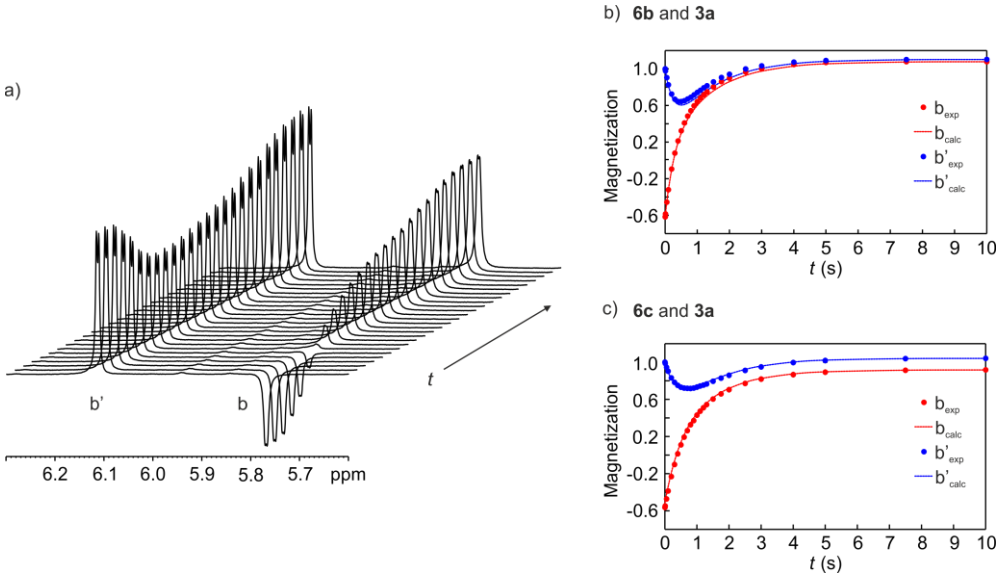

Figure 15. Magnetization *vs.* time (s) for the SIR NMR experiments (signal b) of **6b** and **6c** with **3a**: a) ^{1}H NMR spectra of **6b** and **3a** (0.5:1 ratio); fit of the signals b (free) and b' (bound) to a two-sites magnetization exchange model: c) **6b** and **3a** (0.5:1 ratio) and c) **6c** and **3a** (0.5:1 ratio). See Scheme 2 for proton assignments.

Table 4. Relaxation times (T_1, s) of *β*-pyrrole protons (b) of free and bound **3a**. Magnetization exchange rate constants (k, s^{-1}) of the complexes **6b⊂3a** and **6c⊂3a** determined from SIR NMR experiments. Errors are indicated as standard deviations.

Specie	T_1	Complex	k
3a	1.7±0.1	**6b⊂3a**	1.5±0.1
6b⊂3a	1.1±0.1	**6c⊂3a**	0.5±0.1
6c⊂3a	1.1±0.1		

2.2.5 Attempts to gain water solubility with SAE-C[4]Ps

We investigated the solubility of tetra-acid SAE-C[4]P **4** in basic water (pD > 10). Unfortunately, all our attempts to dissolve **4** in basic water at 1 mM concentration resulted in the formation of suspensions. The addition of 10% (vol.) of acetone to the formed suspensions produced clear solutions. The analysis of the obtained solutions using ^{1}H NMR spectroscopy did not show any signal. The lack of proton signals in the ^{1}H NMR spectrum of the solution suggested the formation of high-order aggregates (*e.g.* micelles) owing to the large hydrophobic section of **4**. Most likely, the concentration used in the ^{1}H NMR experiments was above the critical micellar concentration. In consequence, we could not perform further studies concerning the complexation ability of these aggregates. Dynamic light scattering (DLS) measurements confirmed this hypothesis and revealed the presence of aggregates with a mean hydrodynamic diameter of 127±3 nm in solution (Figure 16).

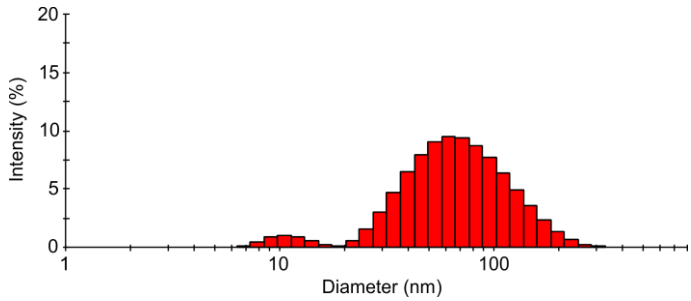

Figure 16. Intensity (%) *vs.* diameter (nm) of a 1 mM solution of **4** in 9:1 water:acetone.

Likewise, the four positive charges located at the upper rim of **5** did not promote its solubility in neutral water at the concentrations required for NMR characterization. The synthesis of super aryl-extended calix[4]pyrroles that are water-soluble as discrete molecules will require the introduction of more than four charged groups in their scaffolds.

2.3 Conclusions

In summary, we described the synthesis of two neutral super aryl-extended calix[4]pyrroles, **3a** and **3b**, and their ionizable or charged derivatives, **4** and **5**. The compounds were characterized by a complete set of high-resolution spectra. The tetra-ester **3a** and the tetra-acid **4** were also characterized by X-ray diffraction analysis of single crystals. In the solid state, these two receptors adopted the cone conformation and deeply included one hydrogen-bonded molecule of acetonitrile in the aromatic cavity. They also displayed intramolecular edge-to-face CH-π interactions between the four terminal phenyl residues that defined the upper section of the aromatic cavity. We performed ^{1}H NMR and ITC titration experiments to characterize the complexation of tetra-ester **3a** with pyridyl *N*-oxides **6a**-**c** and alkyl *N*-oxides **7a**-**b**. The obtained results revealed the formation of thermodynamically and kinetically highly stable 1:1 complexes. The association constant values of the complexes formed in chloroform solution were larger than 10^{6} M^{-1}. The results of the binding experiments indicated that the CH-π and π-π interactions established between the *para*-phenyl ring in *N*-oxide **6c** and the four terminal phenyls that defined the upper section of the aromatic cavity of calix[4]pyrrole **3a** can be estimated to be of the order of 1 kcal·mol^{-1}. Thus, the elaboration of the aromatic cavity present in **3a** endowed this compound with superior binding properties towards *N*-oxide **6c** in comparison to the simple aryl-extended counterpart **9**. We also determined the kinetic stability of the inclusion complexes of **3a** with the pyridyl *N*-oxides and their dissociation energy barriers. Finally, we calculated that the formation of the complexes was close to diffusion control. This finding suggested that **3a** adopts a 1,3-alternate conformation when dissolved in $CDCl_3$ solution. We propose that the TS structure for the dissociation of both complexes is similar and involves **3a** in 1,3-alternate conformation with the *N*-oxide interacting with the receptor just by establishing two hydrogen bonds. The SAE-C[4]P derivatives **4** and **5** having ionizable carboxylic groups and positively charged pyridinium groups, respectively, at their upper rims, turned out to be insoluble in water at the concentration required for ^{1}H NMR spectroscopy.

2.4 Experimental Section

2.4.1 General information and instruments

Reagents were obtained from commercial suppliers and used without further purification unless otherwise stated. All solvents were commercially obtained and used without further purification except pyrrole which was distilled. Dry solvents were taken from a solvent system MB SPS 800. THF, Et_3N, DIPEA and *i*Pr_2NH were distilled and dried. THF, DIPEA and *i*Pr_2NH were degassed by three freeze-pump-thaw cycles before used in the cross-coupling reactions. Routine ^{1}H NMR and ^{13}C{^{1}H} NMR spectra were recorded on a Bruker Avance 300 (300 MHz for ^{1}H NMR and 75 MHz for ^{13}C NMR), Bruker Avance 400 (400 MHz for ^{1}H NMR and 100 MHz for ^{13}C NMR), Bruker Avance 500 (500 MHz for ^{1}H NMR and 125 MHz for ^{13}C NMR) or Bruker Avance 500 with cryoprobe (500 MHz for ^{1}H NMR and 125 MHz for ^{13}C NMR). Deuterated solvents are indicated in

the characterization and chemical shifts are given in ppm. Residual solvent peaks were used as reference.[37] All NMR *J* values are given in Hz. COSY, NOESY, ROESY, HMQC and HMBC experiments were recorded to help with the assignment of ^{1}H and ^{13}C signals. High-resolution mass spectra (HRMS) were obtained on a Bruker HPLC-TOF (MicroTOF Focus) and Bruker HPLC-QqTOF (MaXis Impact). Both with ESI as ionization mode. IR spectra were recorded on a Bruker Optics FTIR Alpha spectrometer equipped with a DTGS detector, KBr beamsplitter at 4 cm^{-1} resolution using a one bounce ATR accessory with diamond windows. Melting points were measured on a MP70 Melting Point System Mettler Toledo. Crystal structure determinations were carried out using Bruker Apex II Duo and Rigaku MicroMax-007HF diffractometers. Both using MoK*α* radiation. Crystal structure solution was achieved using direct methods as implemented in SHELX-2014. Least-squares refinement on F2 using all measured intensities was carried out using the program SHELX-2014. In the case of tetra-acid **4**, residual electron density originating from disordered solvent molecules was treated with the SQUEEZE routine in the PLATON program.[38] ITC titrations were carried out on a MicroCal VP-ITC MicroCalorimeter. Column chromatography was performed with silica gel technical grade, pore size 60 Å, 230-400 mesh particle size, 40-63 μm particle size. Thin layer chromatography (TLC) silica gel 60 F254.

2.4.2 Synthesis and characterization data

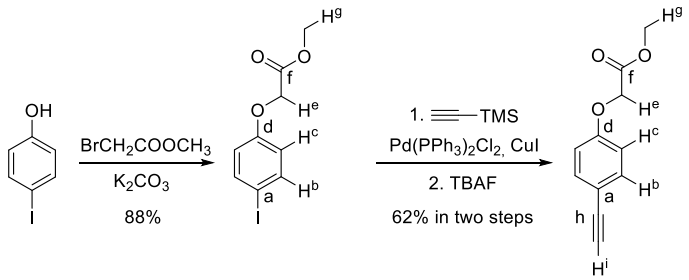

Scheme 3. Synthesis of methyl 4-(ethynylphenoxy)acetate **2a**.

Methyl 4-(iodophenoxy)acetate: 4-Iodophenol (0.70 g, 3.18 mmol, 1 equiv.), K_2CO_3 (0.66 g, 4.77 mmol, 1.5 equiv.) and dry DMF (100 mL) were added to a round-bottom flask. The mixture was stirred for 2 h and, after that, methyl bromoacetate (0.36 mL, 3.82 mmol, 1.2 equiv.) was added. The reaction was stirred for 24 h. 1 N HCl was added until pH = 5 and the product was extracted with CH_2Cl_2 (4x50 mL) and H_2O (50 mL). The organic layer was washed with water (3x100 mL), dried (Na_2SO_4), filtered and concentrated under vacuum to afford the product as a white solid (0.82 g, 2.81 mmol, 88% yield). Rf = 0.3 (1:1 CH_2Cl_2:Hexane). ^{1}H NMR (300 MHz, $CDCl_3$, 298 K): *δ* (ppm) = 7.59-7.56 (m, 2H); 6.70-6.67 (m, 2H); 4.61 (s, 2H); 3.80 (s, 3H). $^{13}C\{^{1}H\}$ NMR (100 MHz, $CDCl_3$, 298 K): *δ* (ppm) = 169.1; 157.8; 138.5; 117.2; 84.3; 65.4; 52.5. FTIR *ν* (cm^{-1}) = 2949; 1757; 1485; 1437; 1212; 1174; 1061; 835; 811; 715; 597; 511. M.p. = 71-73°C.

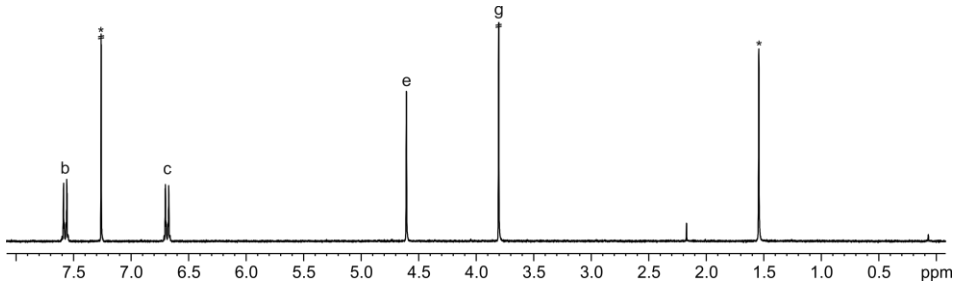

Figure 17. ^{1}H NMR (300 MHz, $CDCl_3$, 298 K) spectrum of methyl 4-(iodophenoxy)acetate. See Scheme 3 for proton assignment. *Residual solvent peak.

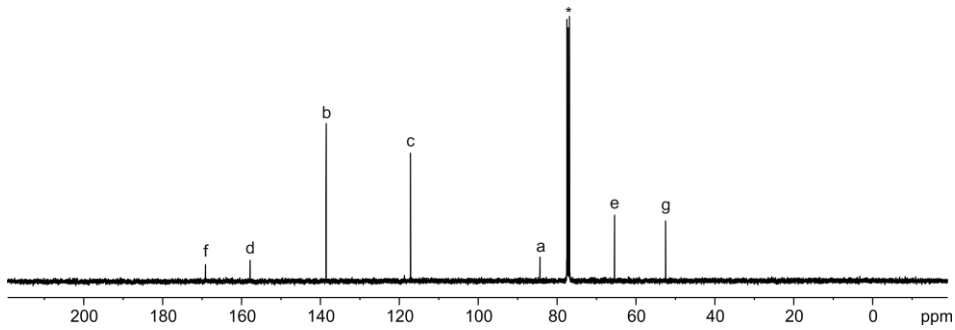

Figure 18. $^{13}C\{^{1}H\}$ NMR (100 MHz, $CDCl_3$, 298 K) spectrum of methyl 4-(iodophenoxy)acetate. See Scheme 3 for carbon assignment. *Residual solvent peak.

Methyl 4-(ethynylphenoxy)acetate 2a: Step 1. Methyl 4-(iodophenoxy)acetate (200 mg, 0.69 mmol, 1 equiv.), $Pd(PPh_3)_2Cl_2$ (35 mg, 0.05 mmol, 0.07 equiv.), CuI (35 mg, 0.18 mmol, 0.27 equiv.) were kept under Argon atmosphere for 5 min. Dry THF (10 mL) and dry DIPEA (0.36 mL, 2.05 mmol, 3 equiv.) were added to the reaction flask. Ethynyltrimethylsilane (0.29 mL, 2.05 mmol, 3 equiv.) was added. The color of the mixture changed from orange to black. The reaction was stirred at 45ºC for 3 h. Then, the solvent was removed under vacuum and the solid was dissolved in CH_2Cl_2 (10 mL). The crude was washed with 1 N HCl (10 mL) and brine (10 mL). The organic layer was dried (Na_2SO_4), filtered and concentrated. The product was purified by column chromatography on silica gel (12 g, 1:1 CH_2Cl_2:Hexane, product Rf = 0.3 85:15 Hexane:EtOAc). Evaporation of the solvent afforded the product as an orange oil (163.70 mg, 91% yield). Step 2. Deprotection was performed by dissolving the protected compound in dry THF (10 mL) and slow addition of TBAF (1.3 mL from 1 M solution in THF, 1.18 mmol, 1.1 equiv.). The reaction was stirred under Argon atmosphere for 15 min. The color changed from yellow to brown. The reaction was quenched by adding saturated NH_4Cl (10 mL). EtOAc (10 mL) and water (10 mL) were added to the crude. The organic layer was separated and extracted again from the aqueous layer with EtOAc (10 mL). The organic layers were washed with brine (10 mL), dried (Na_2SO_4), filtered and concentrated under vacuum to yield a brown oil. The product was purified by column

chromatography on silica gel (8 g, 1:1 CH_2Cl_2:Hexane). Evaporation of the solvent afforded the product as a white solid (149.8 mg, 0.79 mmol, 68% yield). Rf = 0.3 (85:15 Hexane:EtOAc). ^{1}H NMR (400 MHz, $CDCl_3$, 298 K): δ (ppm) = 7.44-7.42 (m, 2H); 6.86-6.84 (m, 2H); 4.64 (s, 2H); 3.81 (s, 3H); 3.00 (s, 1H). $^{13}C\{^1H\}$ NMR (100 MHz, $CDCl_3$, 298 K): δ (ppm) = 169.1; 158.2; 133.8; 115.6; 114.7; 83.4; 76.4; 65.3; 52.5. FTIR ν (cm^{-1}) = 3236; 2960; 2912; 1750; 1605; 1505; 1435; 1238 1214; 1172; 1078; 844. M.p. = 80-81ºC. The characterization data are in agreement with those previously reported in the literature.[15]

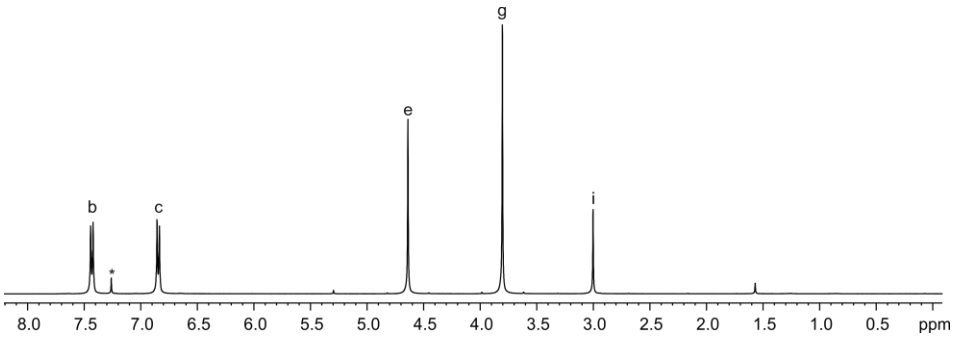

Figure 19. ^{1}H NMR (400 MHz, $CDCl_3$, 298 K) spectrum of **2a**. See Scheme 3 for proton assignment. *Residual solvent peak.

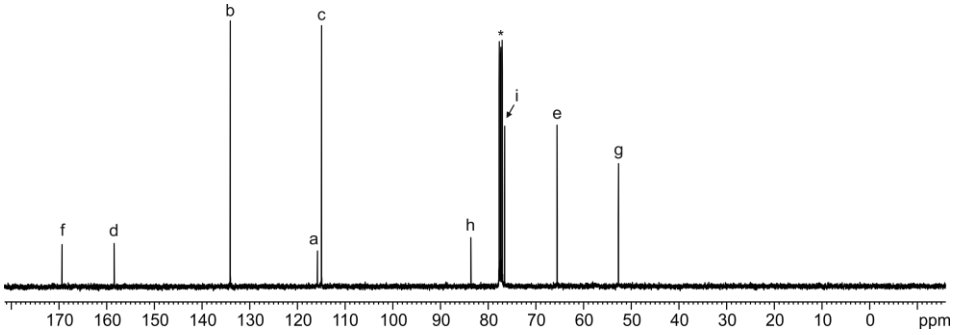

Figure 20. $^{13}C\{^1H\}$ NMR (100 MHz, $CDCl_3$, 298 K) spectrum of **2a**. See Scheme 3 for carbon assignment. *Residual solvent peak.

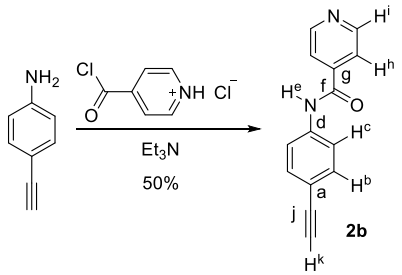

Scheme 4. Synthesis of *N*-(4-ethynylphenyl)-4-pyridinecarboxamine **2b**.

***N*-(4-ethynylphenyl)-4-pyridinecarboxamide 2b:** 4-Ethynylaniline (500 mg, 4.27 mmol, 1 equiv.) was dissolved in dry CH_2Cl_2 (20 mL) and dry Et_3N (0.71 mL, 5.12 mmol, 3 equiv.). The mixture was stirred at r.t. and isonicotinoyl chloride hydrochloride (362 mg, 2.56 mmol, 1.5 equiv.) was added slowly. The mixture was stirred for 5 h. After that, the organic layer was washed with 0.1 N NaOH (10 mL), dried (Na_2SO_4), filtered and concentrated. The solid was washed with CH_2Cl_2 (5 mL) affording the product as a white solid (183.3 mg, 0.82 mmol, 50% yield). ^{1}H NMR (400 MHz, $CDCl_3$, 298 K): δ (ppm) = 8.82-8.81 (m, 2H); 7.87 (br s, 1H); 7.70-7.69 (m, 2H); 7.64-7.62 (m, 2H); 7.54-7.51 (m, 2H); 3.09 (s, 1H). ^{13}C{^{1}H} NMR (125 MHz, $CDCl_3$, 298 K): δ (ppm) = 163.7; 151.1; 141.9; 137.7; 133.3; 120.9; 120.0; 119.0; 83.2; 77.5. HRMS (ESI-TOF) m/z: $[M-H]^-$ Calcd for $C_{14}H_9N_2O$ 221.0720; Found 221.0724. FTIR ν (cm^{-1}) = 3326; 3185; 1660; 1586; 1508; 1488; 1405; 1316; 1291; 834; 654; 536. M.p. = 211-213°C.

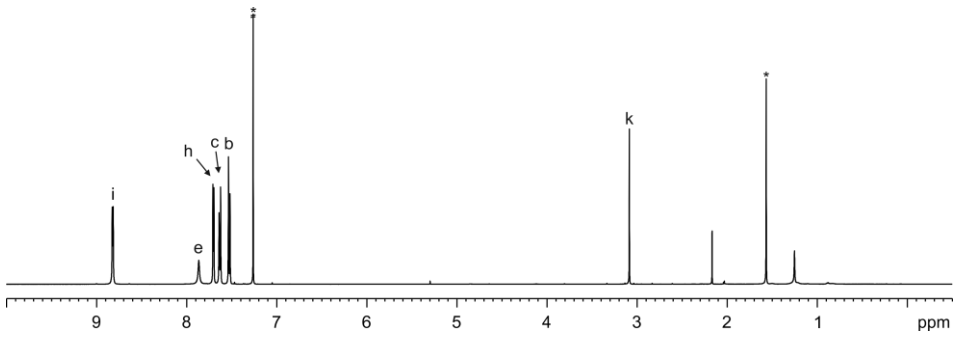

Figure 21. ^{1}H NMR (400 MHz, $CDCl_3$, 298 K) spectrum of **2b**. See Scheme 4 for proton assignment. *Residual solvent peaks.

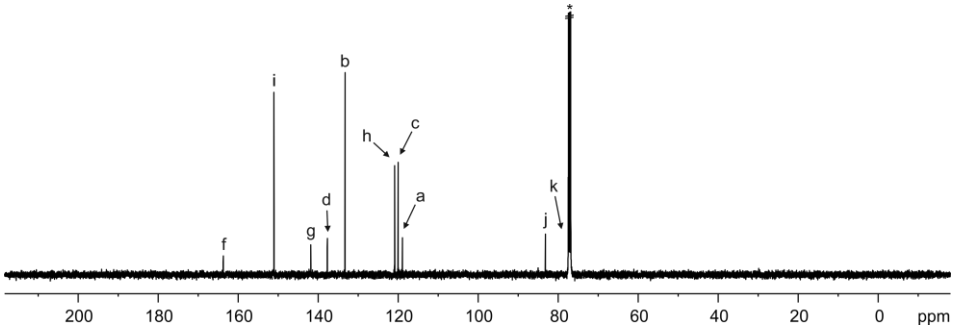

Figure 22. $^{13}C\{^{1}H\}$ NMR (125 MHz, $CDCl_3$, 298 K) spectrum of **2b**. See Scheme 4 for carbon assignment. *Residual solvent peak.

Tetra-ester super aryl-extended calix[4]pyrrole 3a: Tetra-iodo **1** (50 mg, 0.04 mmol, 1 equiv.), $Pd(PPh_3)_2Cl_2$ (14.86 mg, 0.02 mmol, 0.13 equiv.), CuI (6.45 mg, 0.03 mmol, 0.2 equiv.) and methyl 4-(ethynylphenoxy)acetate **2a** (48.30 mg, 0.25 mmol, 1.5 equiv.) were kept under Argon atmosphere in a round-bottom flask. Dry THF (5 mL) and dry *i*Pr_2NH (5 mL) were added. The reaction was stirred at 45°C for 5 h. The color of the mixture changed from yellow to black. After that, the reaction was stopped and concentrated. The crude was redissolved in CH_2Cl_2 (10 mL) and washed with 0.2 N HCl (10 mL) and brine (10 mL). The organic layer was dried (Na_2SO_4), filtered and concentrated to dryness. The product was purified by column chromatography on silica gel (4 g, 99:1 CH_2Cl_2:EtOAc) to afford **3a** as a white solid (40 mg, 0.03 mmol, 81% yield). Rf = 0.3 (99:1 CH_2Cl_2:EtOAc). ^{1}H NMR (300 MHz, $CDCl_3$, 298 K): δ (ppm) = 7.69 (br s, 4H); 7.46-7.44 (m, 8H); 7.41-7.39 (m, 8H); 7.10-7.08 (m, 8H); 6.86-6.84 (m, 8H); 5.76 (s, 8H); 4.61 (s, 8H); 3.81 (s, 12H); 1.98 (s, 12H). $^{13}C\{^{1}H\}$ NMR (100 MHz, $CDCl_3$, 298 K): δ (ppm) = 169.3; 157.8; 148.1; 136.3; 133.3; 131.0; 127.6; 121.8; 116.8; 114.8; 106.7; 89.1; 88.4; 65.4; 52.5; 44.8; 27.9. HRMS (ESI-TOF) m/z: $[M+Na]^+$ Calcd for $C_{92}H_{76}N_4NaO_{12}$ 1451.5352; Found 1451.5330. FTIR ν (cm^{-1}) = 3395; 1758; 1739; 1601; 1511; 1434; 1204; 1173; 1074; 828; 771; 533. M.p. > 265ºC (decompose).

Chapter 2

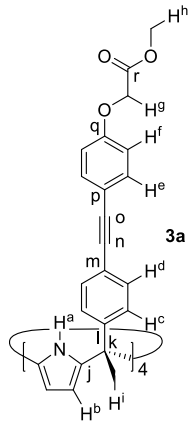

Figure 23. Line-drawing structure of **3a**.

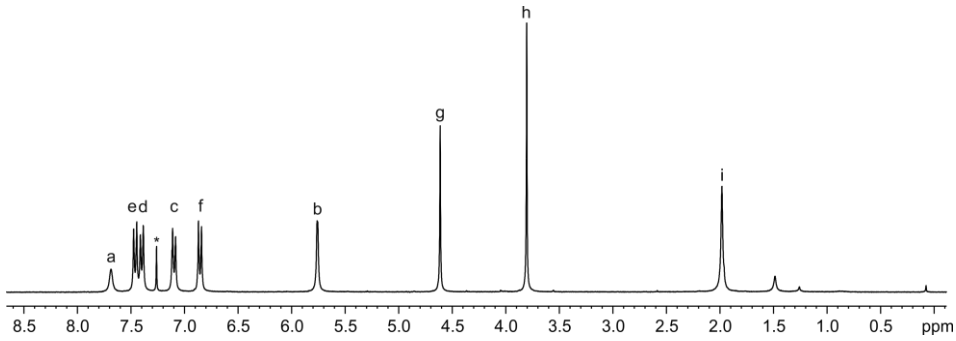

Figure 24. ^{1}H NMR (300 MHz, $CDCl_3$, 298 K) spectrum of **3a**. See Figure 23 for proton assignment. *Residual solvent peak.

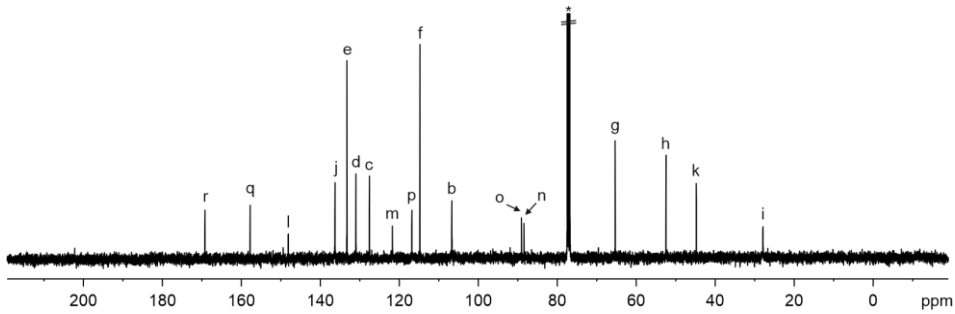

Figure 25. $^{13}C\{^{1}H\}$ NMR (100 MHz, $CDCl_3$, 298 K) spectrum of **3a**. See Figure 23 for carbon assignment. *Residual solvent peak.

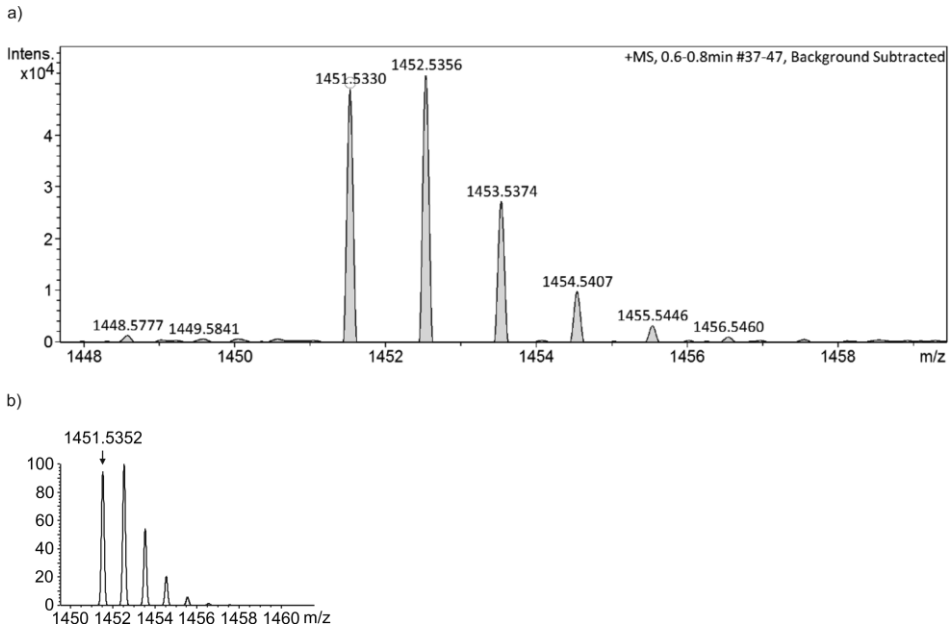

Figure 26. a) Experimental and b) theoretical isotopic distributions of $[M+Na]^+$. The exact mass for the monoisotopic peak in a) and b) is indicated.

Tetra-pyridine super aryl-extended calix[4]pyrrole 3b: Tetra-iodo **1** (50 mg, 0.04 mmol, 1 equiv.), $Pd(PPh_3)_2Cl_2$ (14.86 mg, 0.02 mmol, 0.12 equiv.), CuI (6.45 mg, 0.03 mmol, 0.2 equiv.) and *N*-(4-ethynylphenyl)-4-pyridinecarboxamide **2b** (56.50 mg, 0.25 mmol, 1.5 equiv.) were kept under Argon atmosphere for 5 min. Dry THF (5 mL) and dry iPr$_2$NH (5 mL) were added. The color of the mixture changed from yellow to black. The reaction was stirred at 45°C for 3 h. After that, a white precipitate appeared in the solution. The mixture was filtered and the solid was resuspended in an aqueous solution of saturated $NaHCO_3$ (5 mL). Then, the solid was filtered and washed with aqueous saturated $NaHCO_3$ (2 mL). The product was purified by column chromatography on silica gel (4 g, THF) to afford tetra-pyridine **3b** as a white solid (32.85 mg, 0.04 mmol, 50% yield). Rf = 0.5 (99:1 THF:CH_3OH). ^{1}H NMR (500 MHz, $(CD_3)_2SO$, 298 K): δ (ppm) = 10.59 (s, 4H); 9.54 (br s, 4H); 8.73-8.72 (m, 8H); 7.79-7.77 (m, 16H); 7.59-7.57 (m, 8H); 7.52-7.50 (m, 8H); 7.01-6.99 (m, 8H); 5.99 (s, 8H); 1.85 (s, 12H). $^{13}C\{^1H\}$ NMR (125 MHz with cryoprobe, $(CD_3)_2SO$, 298 K): δ (ppm) = 164.1; 150.5; 141.7; 139.0; 136.9; 132.0; 131.3; 127.3; 121.5; 120.6; 120.3; 117.5; 105.3; 89.4; 88.7; 67.0; 44.3; 30.7. HRMS (ESI-TOF) m/z: $[M+H]^+$ Calcd for $C_{104}H_{77}N_{12}O_4$ 1557.6185; Found 1557.6117. FTIR v (cm^{-1}) = 3335; 3306; 1676; 1655; 1587; 1517; 1406; 1323; 1017; 833; 751; 525. M.p. > 245ºC (decompose).

Chapter 2

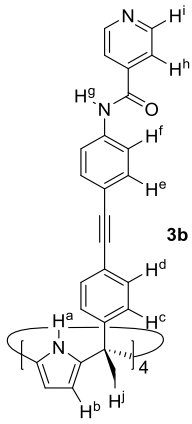

Figure 27. Line-drawing structure of **3b**.

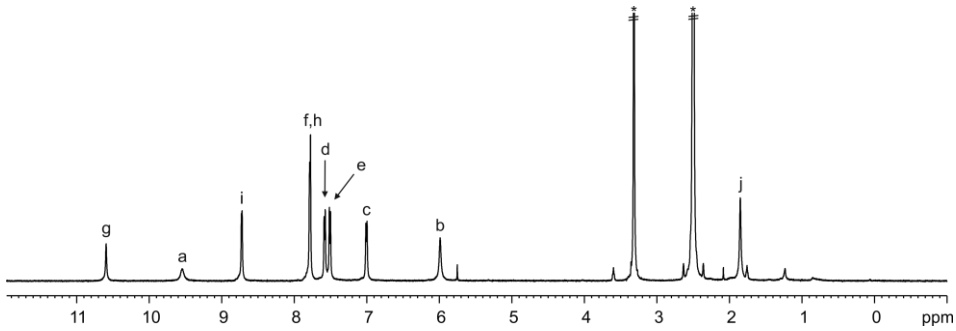

Figure 28. ^{1}H NMR (500 MHz with cryoprobe, $(CD_3)_2SO$, 298 K) spectrum of **3b**. See Figure 27 for proton assignment. *Residual solvent peaks.

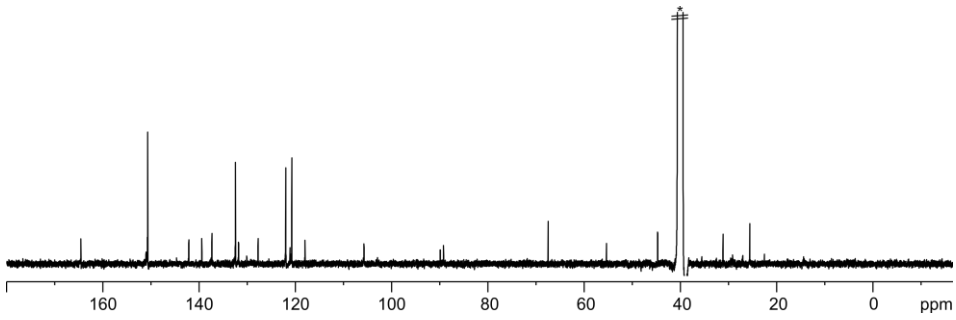

Figure 29. $^{13}C\{^{1}H\}$ NMR (500 MHz with cryoprobe, $(CD_3)_2SO$, 298 K) spectrum of **3b**. *Residual solvent peak.

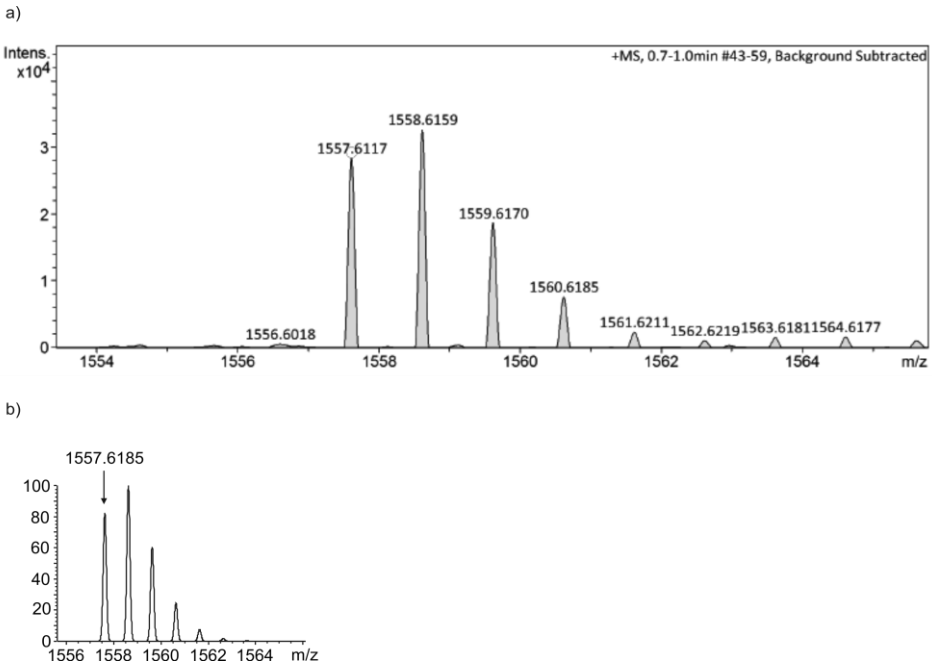

Figure 30. a) Experimental and b) theoretical isotopic distributions of $[M+H]^+$. The exact mass for the monoisotopic peak in a) and b) is indicated.

Tetra-acid super aryl-extended calix[4]pyrrole 4: Tetra-ester **3a** (49.30 mg, 0.03 mmol, 1 equiv.) was dissolved in 1:1 THF:H_2O (10 mL) and LiOH (6.61 mg, 0.28 mmol, 2 equiv.) was added. The reaction was stirred at r.t. for 5 h. After that, the THF was removed under vacuum. Water (10 mL) was added to the mixture and it was washed with CH_2Cl_2 (10 mL). Then, the aqueous layer was acidified with 1 N HCl until pH = 3 and a white precipitate appeared which was extracted with EtOAc (3x10 mL). The organic layer was washed with brine (20 mL), dried (Na_2SO_4), filtered and concentrated to afford **4** as a white solid (32.10 mg, 0.02 mmol, 68% yield). ^{1}H NMR (500 MHz with cryoprobe, $(CD_3)_2CO$, 298 K): δ (ppm) = 8.91 (br s, 4H); 7.47-7.45 (m, 8H); 7.41-7.39 (m, 8H); 7.05-7.03 (m, 8H); 6.93-6.91 (m, 8H); 5.97 (d, J = 2.5 Hz, 8H); 4.77 (s, 8H); 3.30 (br s, 4H); 1.94 (s, 12H). ^{13}C{^{1}H} NMR (125 MHz with cryoprobe, $(CD_3)_2CO$, 298 K): δ (ppm) = 170.2; 159.3; 150.9; 138.1; 133.8; 131.9; 128.5; 122.5; 116.7; 115.8; 106.6; 89.9; 88.5; 65.4; 45.5; 29.8. HRMS (ESI-TOF) m/z: $[M-H]^-$ Calcd for $C_{88}H_{67}N_4O_{12}$ 1371.4761; Found 1371.4769. FTIR v (cm^{-1}) = 3412; 2922; 2853; 1724; 1514; 1429; 1282; 1240; 1176; 832; 771; 524. M.p. > 150ºC (decompose).

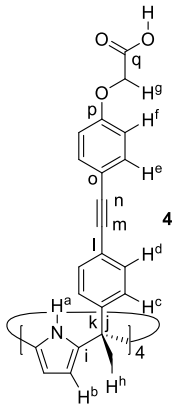

Figure 31. Line-drawing structure of **4**.

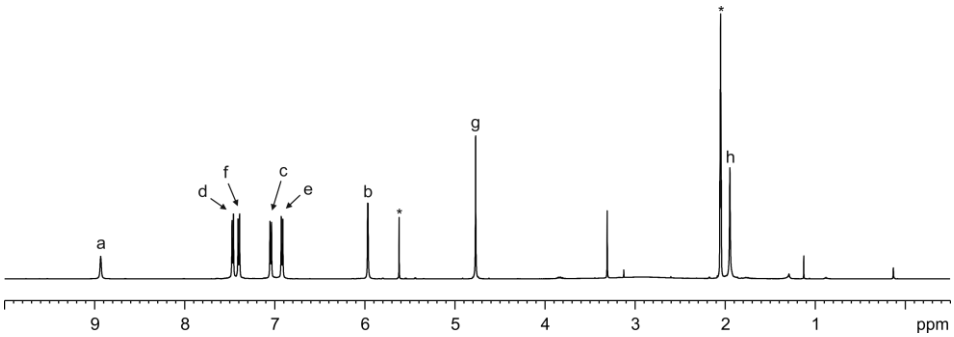

Figure 32. ^{1}H NMR (500 MHz with cryoprobe, $(CD_3)_2CO$, 298 K) spectrum of **4**. See Figure 31 for proton assignment. *Residual solvent peaks.

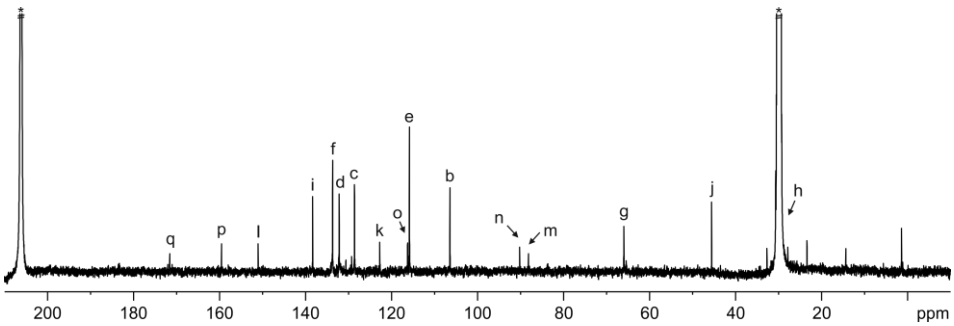

Figure 33. $^{13}C\{^{1}H\}$ NMR (500 MHz with cryoprobe, $(CD_3)_2CO$, 298 K) spectrum of **4**. See Figure 31 for carbon assignment. *Residual solvent peaks.

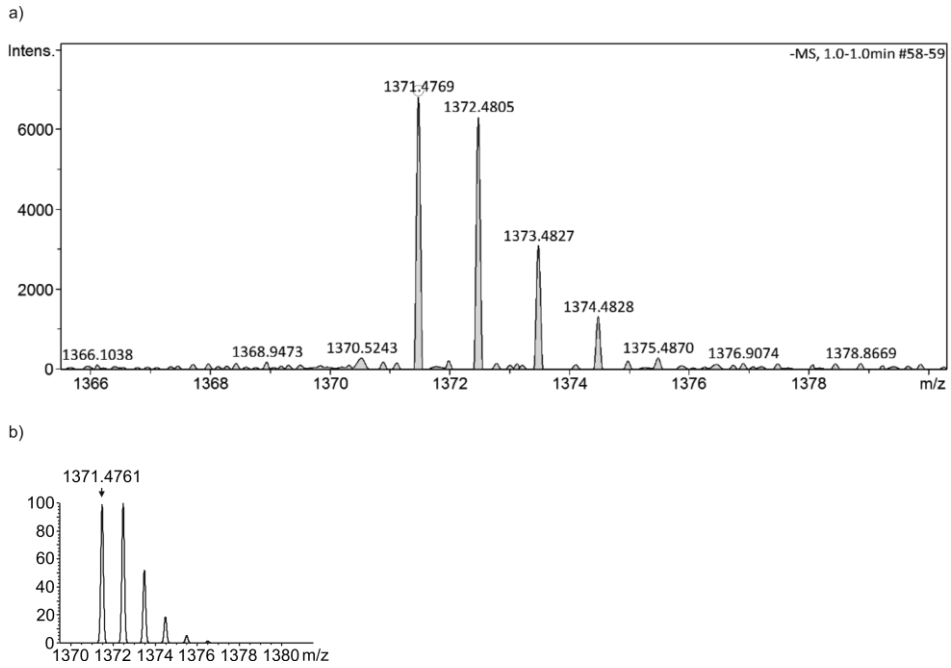

Figure 34. a) Experimental and b) theoretical isotopic distributions of $[M\text{-}H]^-$. The exact mass for the monoisotopic peak in a) and b) is indicated.

Tetra-methyl pyridinium super aryl-extended calix[4]pyrrole 5: Tetra-pyridine **3b** (10 mg, 0.01 mmol, 1 equiv.) was dissolved in dry DMF (1 mL) and stirred for 5 min. After that, methyl iodide was added (0.04 mL, 0.64 mmol, 25 equiv.). The mixture was stirred at 45°C under Argon atmosphere for 24 h. The reaction was stopped and the solvent was removed under vacuum. THF (20 mL) was added and the mixture was heated at 45°C for 2.5 h. The product was collected by filtration (13 mg, 0.01 mmol, 95% yield). ^{1}H NMR (500 MHz, $(CD_3)_2SO$, 298 K): δ (ppm) = 10.83 (br s, 4H); 9.78 (br s, 4H); 9.19-9.17 (m, 8H); 8.50-8.48 (m, 8H); 7.83-7.81 (m, 8H); 7.61-7.57 (m, 16H); 7.08-7.06 (m, 8H); 5.87 (br s, 8H); 4.42 (s, 12H); 1.90 (s, 12H).

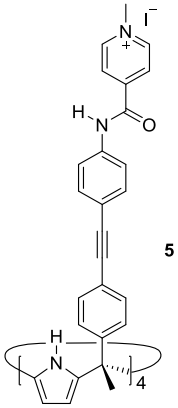

Figure 35. Line-drawing structure of **5**.

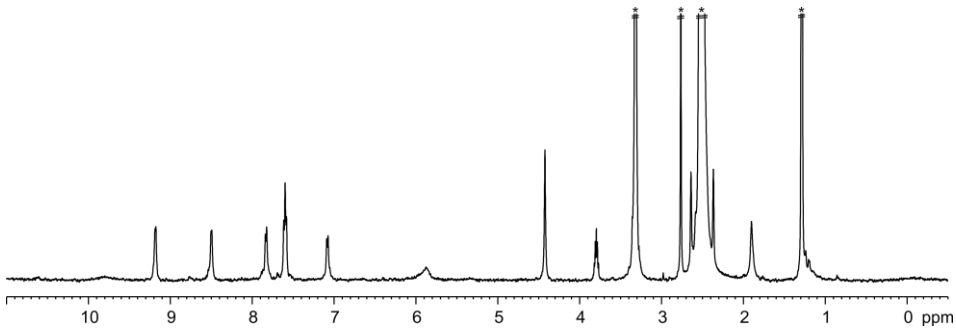

Figure 36. ^{1}H NMR (500 MHz, $(CD_3)_2SO$, 298 K) spectrum of **5**. *Residual solvent peaks.

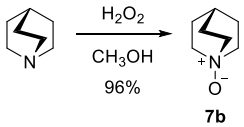

7b

Scheme 5. Synthesis of quinuclidine *N*-oxide **7b**.

Quinuclidine (100 mg, 0.90 mmol, 1 equiv.) was dissolved in CH_3OH (1.80 mL) and added to a sealed tube. The solution was stirred and H_2O_2 (0.17 mL from a 33% aqueous solution, 1.80 mmol, 2 equiv.) was added dropwise to the previous solution. The solution was heated at 90°C for 3 h. After that, the reaction was stopped and the crude was concentrated obtaining an oily residue. The crude was purified by filtration through basic alumina (1 g, 9:1 CH_2Cl_2:isopropanol) affording the product as a white solid (110 mg, 0.86 mmol, 96% yield). The ^{1}H NMR ($CDCl_3$, 298 K) spectrum was in agreement with that reported in literature.[39]

2.4.3 ^{1}H NMR binding studies

A solution of tetra-ester **3a** (1-3 mM) was prepared in $CDCl_3$. Subsequently, 0.5 mL of the solution were transferred to a NMR tube. A solution of pyridyl *N*-oxide **6a**-**c** or alkyl *N*-oxide **7a**-**b** was prepared in $CDCl_3$ using the receptor's solution at higher concentration ([G] = 10-30 mM and [**3a**] = 1-3 mM). Immediately, the 0.5 mL of the receptor's solution was titrated by manually injecting incremental amounts of the *N*-oxide's solution using a micro syringe. A ^{1}H NMR spectrum of the mixture was acquired after each injection and vigorous hand shaking of the NMR tube for few seconds.

Pyridyl *N*-oxides

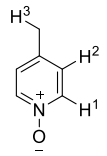

Figure 37. Line-drawing structure of **6b**.

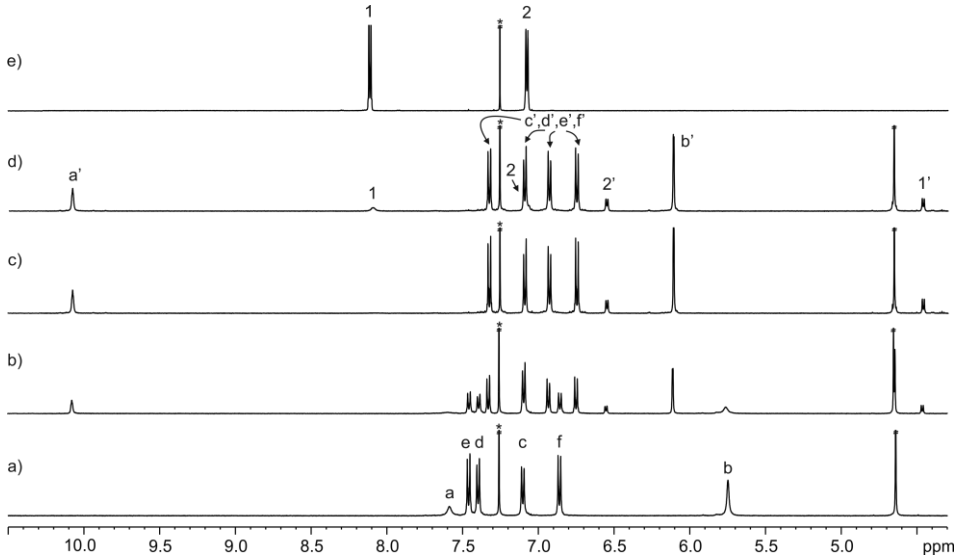

Figure 38. ^{1}H NMR (500 MHz, $CDCl_3$, 298 K) spectra of the titration of **3a** with **6b**: a) 0; b) 0.5; c) 1 and d) 1.5 equiv.; e) **6b**. Primed letters correspond to proton signals of bound components. See Figure 23 and Figure 37 for proton assignments. *Residual solvent peak.

Table 5. Chemical shifts (δ, ppm) of the protons of free and bound **6b** (**6b⊂3a**) and complexation induced shifts ($\Delta\delta$, ppm).

Signal	δ_{free}	δ_{bound}	$\Delta\delta$
1	8.12	4.46	-3.66
2	7.08	6.55	-0.53
3	2.35	1.25	-1.10

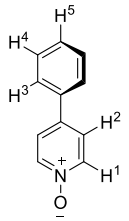

Figure 39. Line-drawing structure of **6c**.

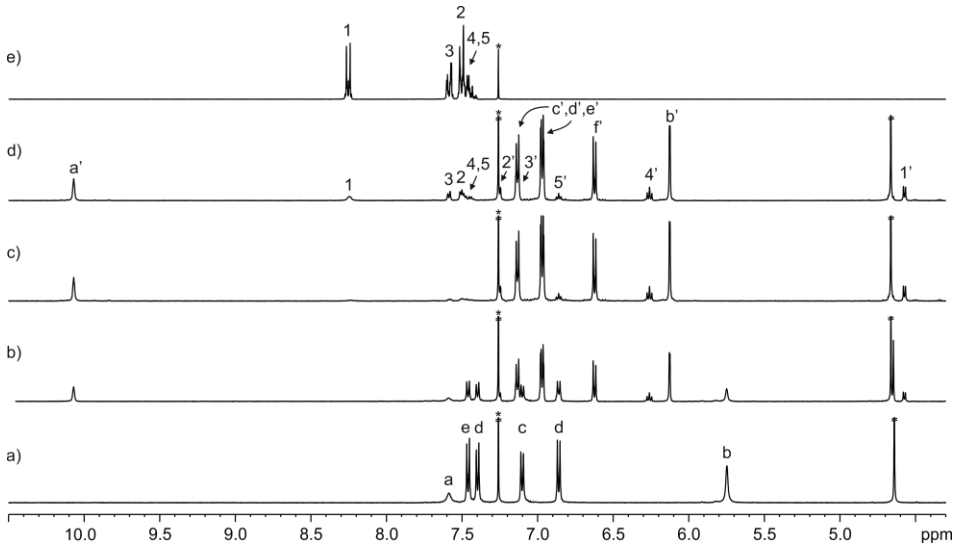

Figure 40. ^{1}H NMR (500 MHz, $CDCl_3$, 298 K) spectra of the titration of **3a** with **6c**: a) 0; b) 0.6; c) 1.2 and d) 1.7 equiv.; e) **6c**. Primed letters correspond to proton signals of bound components. See Figure 23 and Figure 39 for proton assignments. *Residual solvent peak.

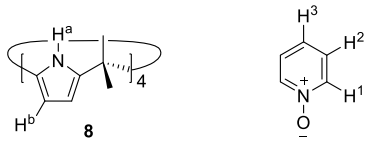

Figure 41. Line-drawing structures of octa-methyl calix[4]pyrrole **8** and **6a**.

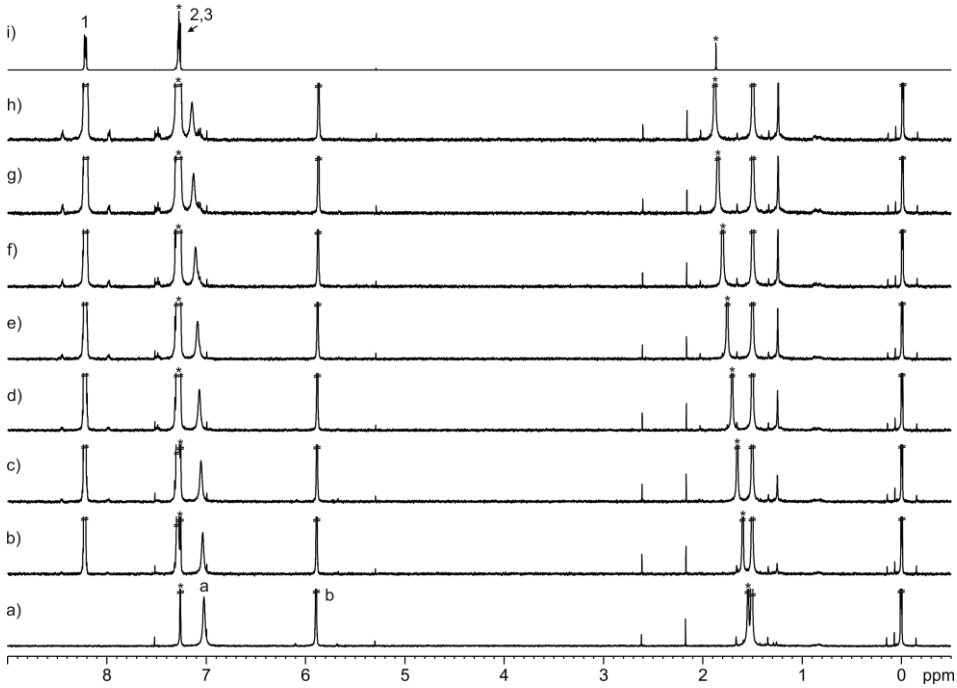

Figure 42. ^{1}H NMR (400 MHz, $CDCl_3$, 298 K) spectra of the titration of octa-methyl **8** with **6a**: a) 0; b) 5; c) 10; d) 15; e) 20; f) 25; g) 30 and h) 35 equiv.; i) **6a**. See Figure 41 for proton assignments. *Residual solvent peaks.

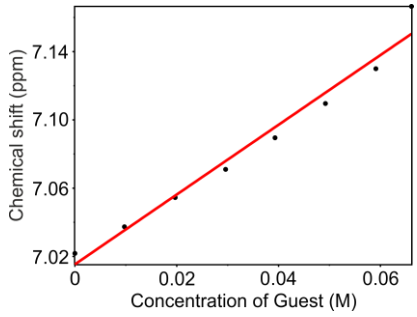

Figure 43. Fit of the chemical shift of signal a to a theoretical 1:1 binding model. The binding constant for the **6a⊂8** complex is estimated to be lower than 10 M^{-1}.

Chapter 2

Alkyl *N*-oxides

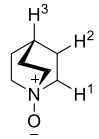

Figure 44. Line-drawing structure of **7b**.

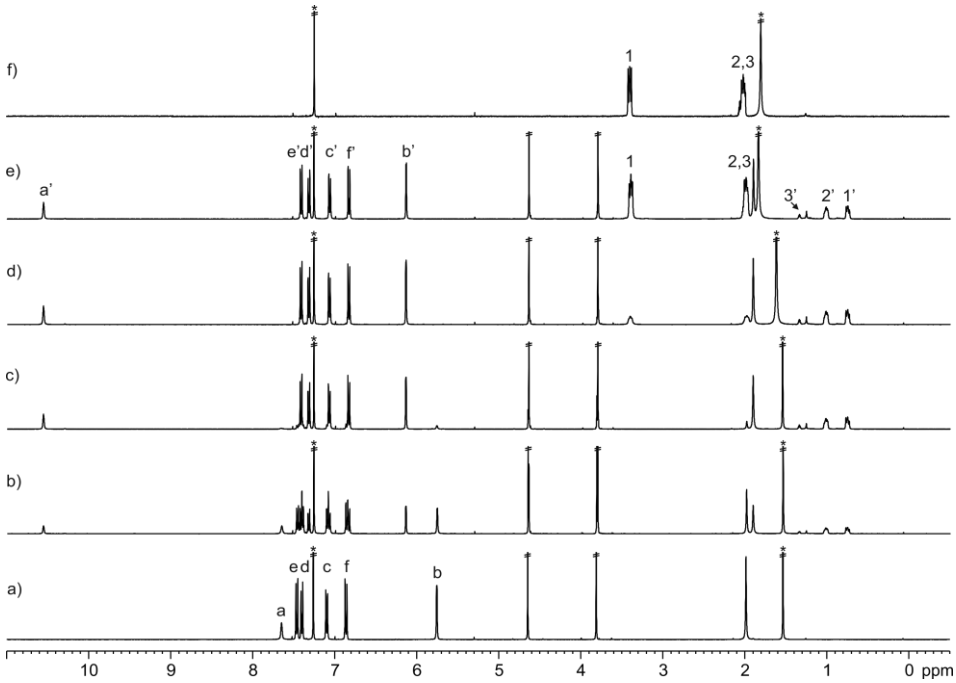

Figure 45. ^{1}H NMR (400 MHz, $CDCl_3$, 298 K) spectra of the titration of **3a** with **7b**: a) 0; b) 0.5; c) 1; d) 2 and e) 5 equiv.; f) **7b**. See Figure 23 and Figure 44 for proton assignments. *Residual solvent peaks.

Table 6. Chemical shifts (δ, ppm) of the protons of free and bound **7b** (**7b**⊂**3a**) and complexation induced shifts ($\Delta\delta$, ppm).

Signal	δ_{free}	δ_{bound}	$\Delta\delta$
1	3.40	0.75	-2.65
2	1.99	1.01	-0.98
3	1.99	1.34	-0.65

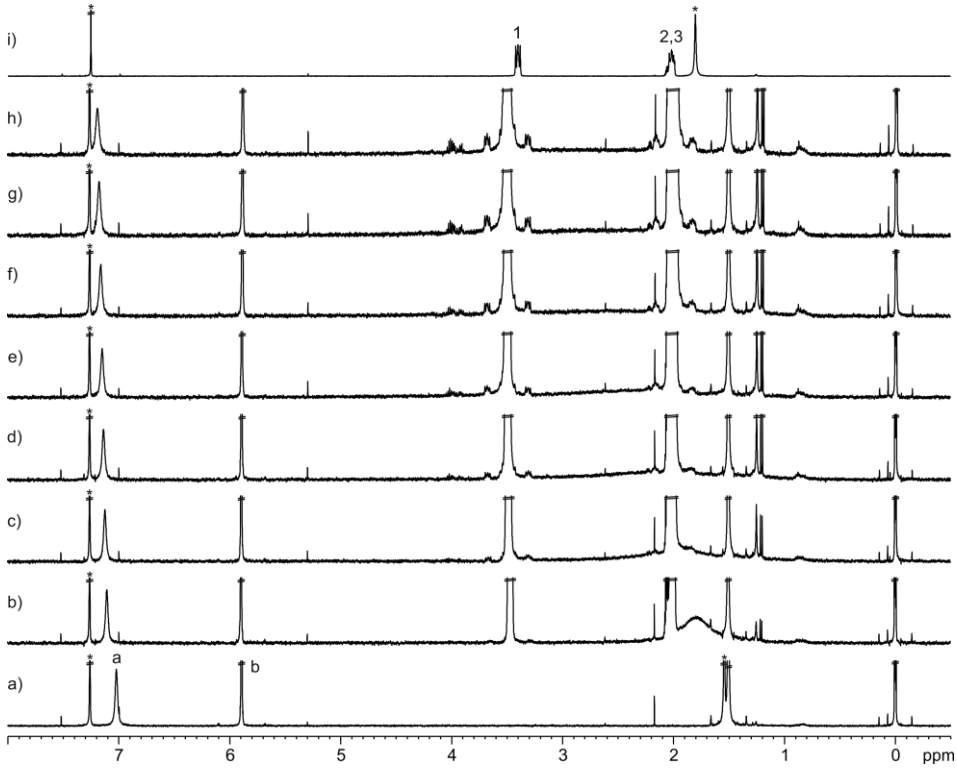

Figure 46. ^{1}H NMR (400 MHz, $CDCl_3$, 298 K) spectra of the titration of **8** with **7b**: a) 0; b) 4; c) 8; d) 12; e) 16; f) 20; g) 24 and h) 28 equiv.; i) **7b**. See Figure 41 and Figure 44 proton assignments. *Residual solvent peaks.

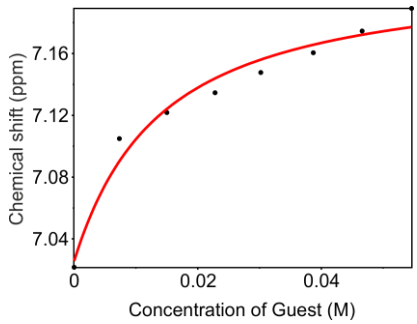

Figure 47. Fit of the chemical shift of signal a to a theoretical 1:1 binding model. The binding constant for the **7b⊂8** complex is 80±10 M^{-1}.

2.4.4 ITC titration experiments

Titrations of calix[4]pyrrole receptors (**3a** and **9**) with guest molecules (**6a**-**c** and **7a**-**b**) were carried out in chloroform solution by the addition of small aliquots (8-10 µL) of a solution of the guest into a solution of the host in the same solvent. The concentration of guest solutions was approximately

seven-ten times more concentrated than receptor solutions ([H] = 0.05-0.10 mM). The association constants and the thermodynamic parameters were obtained from the fit of the titration data to a simple 1:1 binding model using the Microcal ITC Data Analysis module.

Pyridyl *N*-oxides

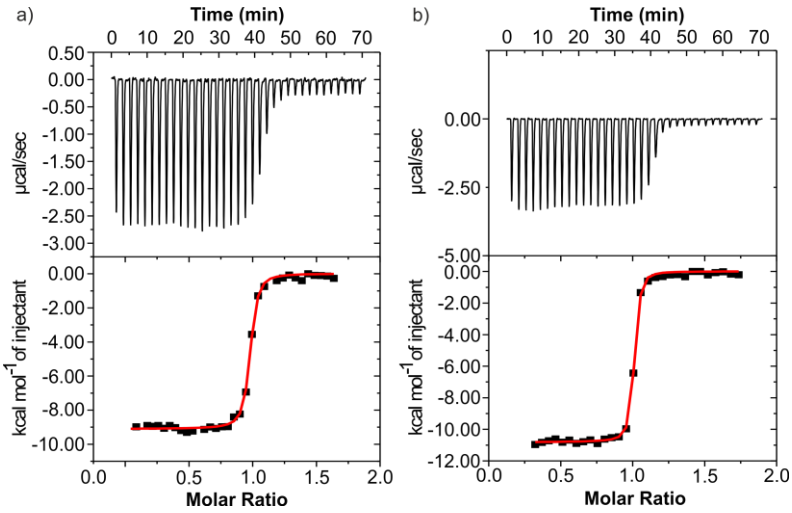

Figure 48. Top panels show raw data (heat *vs.* time) for the titration of guest into the host: a) **6b⊂3a** and b) **6c⊂3a** ($CHCl_3$). Titrations were performed at 298 K. Bottom panels represent integrated data fitted to the theoretical binding isotherm (red line) for a 1:1 binding model.

Table 7. Binding constants (K_a, M^{-1}) and thermodynamic parameters (ΔG, ΔH and $T\Delta S$, $kcal \cdot mol^{-1}$) obtained from the ITC titration experiments of **3a** with **6a**-**c** in $CHCl_3$ at 298 K. Error values are reported as standard deviations.

Guest	K_a	ΔG	ΔH	$T\Delta S$
6a	$4.9\pm0.1 \times 10^6$	-9.1±0.1	-11.6±0.2	-2.5±0.1
6b	$1.2\pm0.5 \times 10^7$	-9.6±0.2	-9.3±0.2	0.3±0.3
6c	$3.6\pm0.2 \times 10^7$	-10.3±0.1	-11.3±0.5	-1.0±0.5

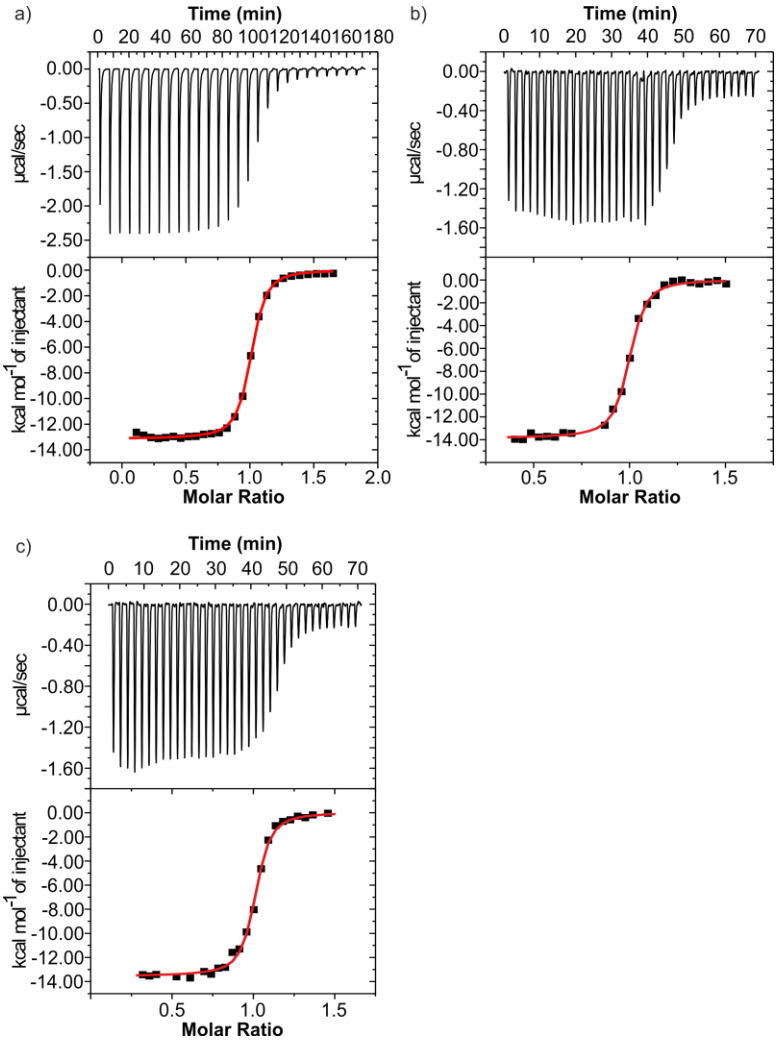

Figure 49. Top panels show raw data (heat *vs.* time) for the titration of guest into the host: a) **6a⊂9**; b) **6b⊂9** and c) **6c⊂9** ($CHCl_3$). Titrations were performed at 298 K. Bottom panels represent integrated data fitted to the theoretical binding isotherm (red line) for a 1:1 binding model.

Table 8. Binding constants (K_a, M^{-1}) and thermodynamic parameters (ΔG, ΔH and $T\Delta S$, kcal·mol^{-1}) obtained from the ITC titration experiments of **9** with **6a**-**c** in $CHCl_3$ at 298 K. Error values are reported as standard deviations.

Guest	K_a	ΔG	ΔH	$T\Delta S$
6a	3.6±0.2 x 10^6	-8.9±0.1	-13.2±0.1	-4.3±0.1
6b	1.3±0.1 x 10^7	-9.7±0.1	-13.7±0.4	-4.0±0.4
6c	1.0±0.1 x 10^7	-9.5±0.1	-14.2±0.2	-4.7±0.2

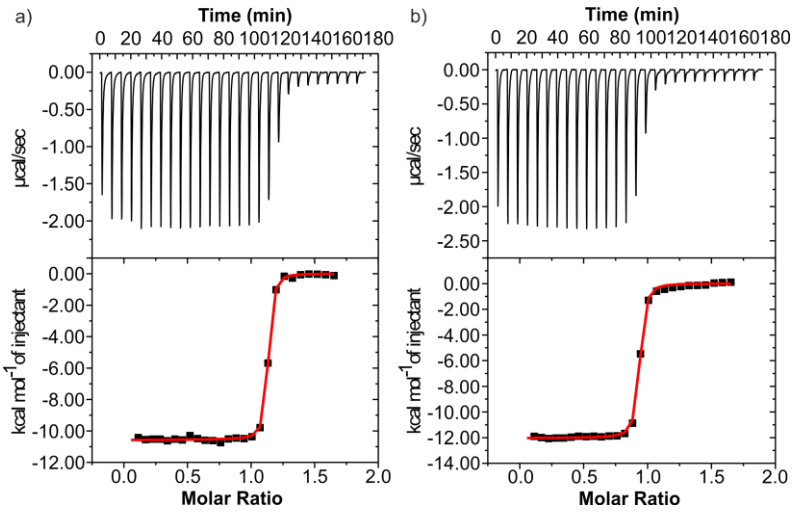

Figure 50. Top panels show raw data (heat *vs.* time) for the titration of guest into the host: a) **7b⊂3a** and b) **7b⊂9** ($CHCl_3$). Titrations were performed at 298 K. Bottom panels represent integrated data fitted to the theoretical binding isotherm (red line) for a 1:1 binding model.

Table 9. Binding constants (K_a, M^{-1}) and thermodynamic parameters (ΔG, ΔH and $T\Delta S$, kcal·mol^{-1}) obtained from the ITC titration experiments of **3a** and **9** with **7a**-**b** in $CHCl_3$ at 298 K. Error values are reported as standard deviations.

Guest	Host	K_a	ΔG	ΔH	$T\Delta S$
7a	**3a**	1.1±0.1 x 10^6	-8.2±0.1	-11.2±0.5	-3.0±0.5
7b	**3a**	> 10^7		-10.8±0.3	
7b	**9**	> 10^7		-11.9±0.2	

2.4.5 Determination of longitudinal relaxation times (T_1)

The longitudinal relaxation times (T_1) of the *β*-pyrrole protons of **3a** in the free and bound states (**6b⊂3a** and **6c⊂3a**) were determined by non-selective inversion recovery ^{1}H NMR experiments. The data were fit to Equation 4 using Dynamics Center from Bruker.

4) $f(t) = I_0 \times (1-e^{-t/T1})$

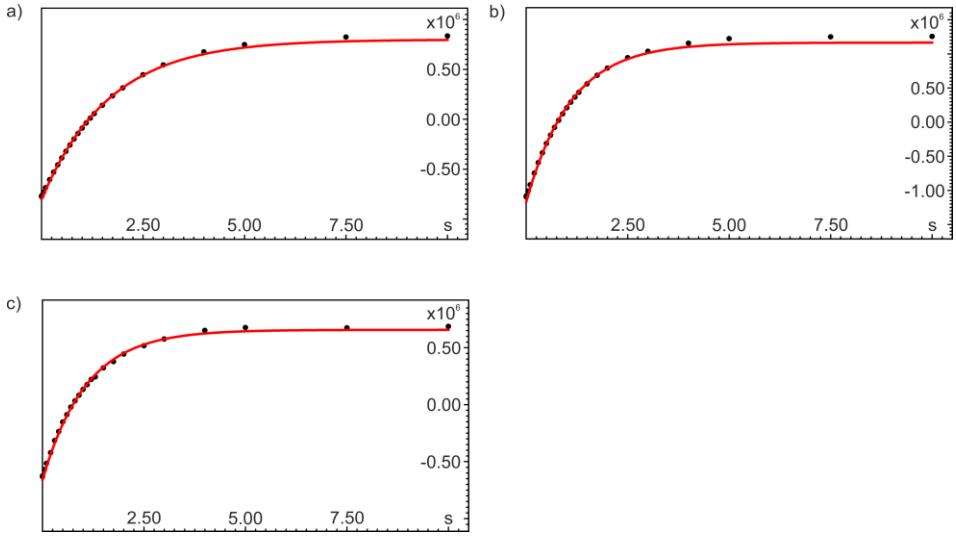

Figure 51. Fit of the signal b to Equation 4 from the non-selective inversion recovery NMR experiments: a) **3a**; b) **6b⊂3a** and c) **6c⊂3a**.

2.4.6 Molecular modelling studies

The energy minimized structures showed in the chapter were obtained from SCIGRESS Version FJ 2.6. The structures were optimized using MM3 or PM6 force field. For the chemical shift calculations and NICS, the structure of **6c⊂3a** was optimized using DFT+Dispersion method and BP86-D3/def2-SVP level of theory using Turbomole Version 4.1.[23,24,25,26,27,28]

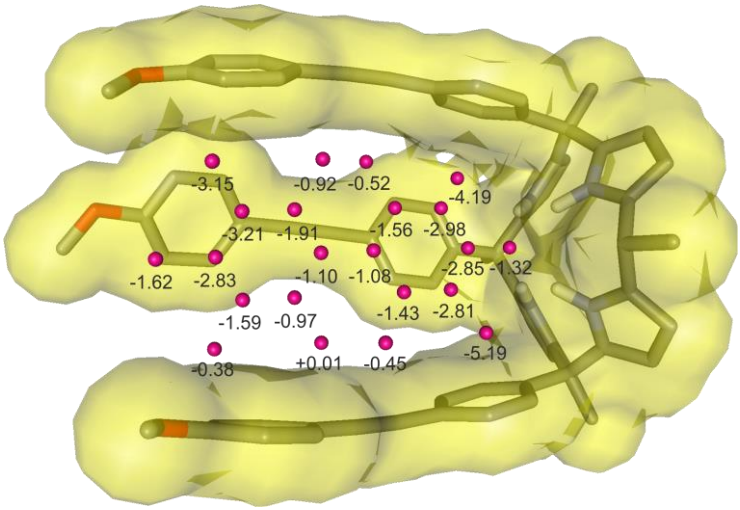

Figure 52. NICS values in the position of the atoms of bound **6c**. One *meso*-aromatic wall of the receptor has been omitted for clarity.

2.4.7 X-ray structures

CCDC 1486376 (tetra-ester **3a**) and 1486387 (tetra-acid **4**) contain the supplementary crystallographic data for this chapter. These data can be obtained free of charge from The Cambridge Crystallographic Data Centre.

2.4.8 Dynamic light scattering (DLS) measurements

DLS measurements were carried out on the solutions of tetra-acid **4** in glass cuvettes using a Malvern Zetasizer Nano-ZS instrument at a 173º scattering angle using a 633 nm laser at 25°C. Ultra-pure MilliQ water (conductivity = 0.055 $\mu S \cdot cm^{-1}$) and acetone (HPLC grade) were used. The solutions were filtered through a 0.2 μm filter and sonicated 10 min before measuring. Each sample was measured three times with five runs and thirty seconds each run. The solvent refractive index (1.336) and viscosity (1.066 cP) for 9:1 water:acetone mixture were determined using the Solvent Builder function of the Zetasizer software Version 6.12.

2.5 References and Notes

[1] G. V. Oshovsky, D. N. Reinhoudt, W. Verboom, *Angew. Chem., Int. Ed.* **2007**, *46*, 2366-2393.

[2] A. P. Davis, *Org. Biomol. Chem.* **2009**, *7*, 3629-3638.

[3] E. A. Kataev, C. Mueller, *Tetrahedron* **2014**, *70*, 137-167.

[4] F. Biedermann, W. M. Nau, H. J. Schneider, *Angew. Chem., Int. Ed.* **2014**, *53*, 11158-11171.

[5] H. Destecroix, C. M. Renney, T. J. Mooibroek, T. S. Carter, P. F. N. Stewart, M. P. Crump, A. P. Davis, *Angew. Chem., Int. Ed.* **2015**, *54*, 2057-2061.

[6] M. Torneiro, W. C. Still, *J. Am. Chem. Soc.* **1995**, *117*, 5887-5888.

[7] B. Verdejo, G. Gil-Ramírez, P. Ballester, *J. Am. Chem. Soc.* **2009**, *131*, 3178-3179.

[8] D. Hernández-Alonso, S. Zankowski, L. Adriaenssens, P. Ballester, *Org. Biomol. Chem.* **2015**, *13*, 1022-1029.

[9] X. Chi, H. Zhang, G. I. Vargas-Zúñiga, G. M. Peters, J. L. Sessler, *J. Am. Chem. Soc.* **2016**, *138*, 5829-5832.

[10] P. Anzenbacher, K. Jursikova, V. M. Lynch, P. A. Gale, J. L. Sessler, *J. Am. Chem. Soc.* **1999**, *121*, 11020-11021.

[11] L. Bonomo, E. Solari, G. Toraman, R. Scopelliti, M. Latronico, C. Floriani, *Chem. Commun. (Cambridge, U. K.)* **1999**, 2413-2414.

[12] L. Adriaenssens, P. Ballester, *Chem. Soc. Rev.* **2013**, *42*, 3261-3277.

[13] A. Galan, G. Aragay, P. Ballester, *Chem. Sci.* **2016**, *7*, 5976-5982.

[14] A. Spurg, S. R. Waldvogel, *Eur. J. Org. Chem.* **2008**, 337-342.

[15] Y. T. He, S. J. Liu, A. Menon, S. Stanford, E. Oppong, A. M. Gunawan, L. Wu, D. J. Wu, A. M. Barrios, N. Bottini, A. C. B. Cato, Z. Y. Zhang, *J. Med. Chem.* **2013**, *56*, 4990-5008.

[16] R. Chinchilla, C. Najera, *Chem. Soc. Rev.* **2011**, *40*, 5084-5121.

[17] G. Q. Lai, S. L. Liu, J. F. Xu, Y. J. Shen, *J. Chem. Res.* **2006**, 203-204.

[18] L. Avram, Y. Cohen, *Chem. Soc. Rev.* **2015**, *44*, 586-602.

[19] J. Balzarini, M. Stevens, G. Andrei, R. Snoeck, R. Strunk, J. B. Pierce, J. A. Lacadie, E. De Clercq, C. Pannecouque, *Helv. Chim. Acta* **2002**, *85*, 2961-2974.

[20] M. A. Bain, G. Fornasini, A. M. Evans, *Curr. Drug Metab.* **2005**, *6*, 227-240.

[21] M. Stevens, C. Pannecouque, E. De Clercq, J. Balzarini, *Biochem. Pharmacol.* **2006**, *71*, 1122-1135.

[22] J. R. Blas, J. M. Lopez-Bes, M. Marquez, J. L. Sessler, F. J. Luque, M. Orozco, *Chem.--Eur. J.* **2007**, *13*, 1108-1116.

[23] J. P. Perdew, *Phys. Rev. B* **1986**, *33*, 8822-8824.

[24] A. D. Becke, *Phys. Rev. A* **1988**, *38*, 3098-3100.

[25] R. Ahlrichs, M. Bar, M. Haser, H. Horn, C. Kolmel, *Chem. Phys. Lett.* **1989**, *162*, 165-169.

[26] M. Kollwitz, J. Gauss, *Chem. Phys. Lett.* **1996**, *260*, 639-646.

[27] S. Grimme, J. Antony, S. Ehrlich, H. Krieg, *J. Chem. Phys.* **2010**, *132*.

[28] P. V. Schleyer, C. Maerker, A. Dransfeld, H. J. Jiao, N. J. R. V. Hommes, *J. Am. Chem. Soc.* **1996**, *118*, 6317-6318.

[29] D. Ajami, T. Iwasawa, J. Rebek, *Proc. Natl. Acad. Sci. U.S.A.* **2006**, *103*, 8934-8936.

[30] G. Aragay, D. Hernandez, B. Verdejo, E. C. Escudero-Adan, M. Martinez, P. Ballester, *Molecules* **2015**, *20*, 16672-16686.

[31] J. Rebek, B. Askew, P. Ballester, C. Buhr, S. Jones, D. Nemeth, K. Williams, *J. Am. Chem. Soc.* **1987**, *109*, 5033-5035.

[32] J. D. Dunitz, *Chem. Biol.* **1995**, *2*, 709-712.

[33] J. C. Cobas, M. Martín-Pastor, EXSYCalc Version 1.0.

[34] G. Gil-Ramirez, E. C. Escudero-Adan, J. Benet-Buchholz, P. Ballester, *Angew. Chem., Int. Ed.* **2008**, *47*, 4114-4118.

[35] T. J. Williams, A. D. Kershaw, V. Li, X. P. Wu, *J. Chem. Educ.* **2011**, *88*, 665-669.

[36] A. D. Bain, CIFIT Version 2.0.

[37] G. R. Fulmer, A. J. M. Miller, N. H. Sherden, H. E. Gottlieb, A. Nudelman, B. M. Stoltz, J. E. Bercaw, K. I. Goldberg, *Organometallics* **2010**, *29*, 2176-2179.

[38] P. Vandersluis, A. L. Spek, *Acta Crystallogr. Sect. A* **1990**, *46*, 194-201.

[39] G. L. Kenyon, D. H. Eargle, C. W. Koch, *J. Org. Chem.* **1976**, *41*, 2417-2421.

Chapter 3

Quantification of the Hydrophobic Effect Using Water-Soluble Super Aryl-Extended Calix[4]pyrroles

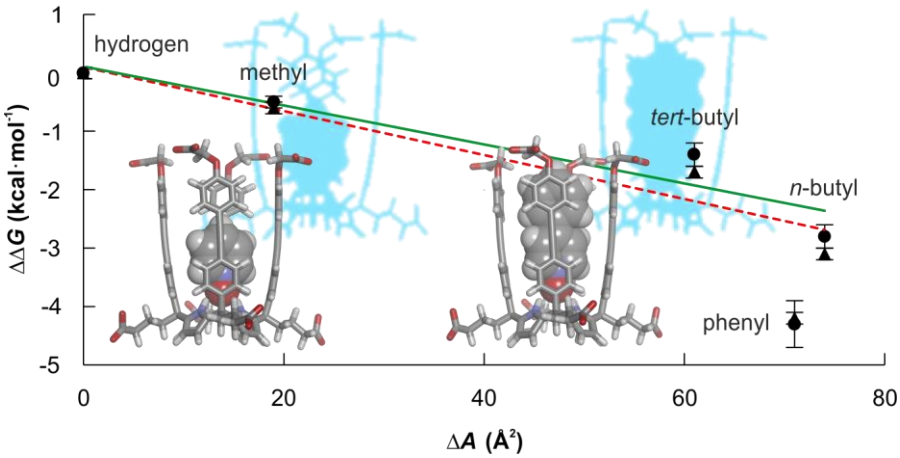

Part of this chapter has been published in:

L. Escobar, P. Ballester, *Org. Chem. Front.* **2019**, *6*, 1738-1748.

Volume 6 | Number 11 | 7 June 2019

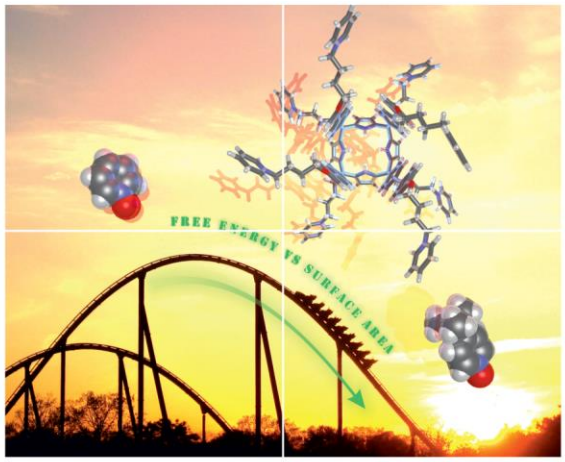

ORGANIC CHEMISTRY FRONTIERS

CCS 中国化学会 CHINESE CHEMICAL SOCIETY
SIOC 1950
ROYAL SOCIETY OF CHEMISTRY | Celebrating IYPT 2019
rsc.li/frontiers-organic

3.1 Introduction

Molecular recognition in water using synthetic receptors aims at mimicking protein binding performance, since binding events in nature take place in this solvent. In this regard, protein binding pockets possess structured hydrophobic environments, clefts or cavities, in which polar groups converge (*e.g.* amides, protonated amines, carboxylates, etc.) being somewhat hidden from solvation by bulk water molecules.[1,2,3]

The binding of neutral polar molecules in water is mainly driven by the combination of the hydrophobic effect with dispersion and polar interactions.[4,5,6,7] Most likely, the hydrophobic effect is the most important driving force.[8,9,10,11,12,13,14] Hydrophobic binding has been extensively used to account for the thermodynamic signatures observed in the binding of polar and non-polar molecules by synthetic and biological hosts in water.[15,16,17,18,19,20,21]

The binding of polar molecules using water-soluble synthetic hosts is challenging because the receptors must feature not only the size and shape complementarity to the targeted guests but also a bespoke functional group complementarity.[7,22,23] On the one hand, the solubility of the synthetic receptors in water solution demands the incorporation of polar, ionizable or charged groups in their scaffold's periphery. On the other hand, water-soluble synthetic receptors make an extensive use of aromatic panels in shaping their hydrophobic cavities and clefts. This latter synthetic strategy complicates the installation of converging polar binding sites (*e.g.* hydrogen bond donors) in the interior of hydrophobic environments. However, the placement of converging polar binding sites in hydrophobic cavities reduces exposure to water solvation and represents a sensible approach in the development of effective hosts for the hydrophobic binding of polar substrates assisted by hydrogen-bonding interactions.

In this vein, Davis and co-workers described the complexation, with good binding affinities, of mono-, di- and poly-saccharides in water using "temple" receptors.[24,25,26,27] The research group of Jabin explored the binding of cyclic ureas and lactams with a calix[6]cryptamide receptor in aqueous solution (1:2 water:methanol), determining binding constants in the order of 10^2 M^{-1} by NMR spectroscopic techniques.[28] More recently, Jiang and co-workers synthesized *endo*-functionalized molecular tubes and studied their interaction with polar neutral substrates of small molecular weight, obtaining binding constants up to 10^6 M^{-1}.[29,30,31] Other examples of synthetic water-soluble receptors displaying polar and non-polar cavities have been described.[19,32,33,34]

The cone conformation of the tetra-*α* isomer of aryl-extended calix[4]pyrroles (AE-C[4]Ps) displays a deep aromatic cavity closed at one end by a polar binding site with an opposite open portal. The buried polar site consists in four converging pyrrole NHs. Thus, the calix[4]pyrrole's binding site resembles a minimalist protein binding pocket. We reported the synthesis of water-soluble aryl-extended calix[4]pyrroles and studied their binding properties with neutral polar molecules: pyridyl *N*-oxides and amides.[35,36,37,38] The obtained results demonstrated the formation of kinetically and

thermodynamically highly stable 1:1 inclusion complexes (K_a > 10^3 M^{-1}). The formed inclusion complexes are stabilized by a combination of the hydrophobic effect, hydrogen-bonding, π-π and CH-π interactions.

In Chapter 2, we described the synthesis of super aryl-extended calix[4]pyrroles (SAE-C[4]Ps) soluble in chloroform solution and reported their complexation properties with pyridyl *N*-oxide derivatives. The SAE-C[4]Ps feature an extension of the *meso*-aromatic substituents compared to the parent aryl-extended, AE-C[4]Ps. The elaboration of the aromatic cavity was expected to deliver an increase of the hydrophobic effect for the binding of substrates in aqueous solution. In addition, the polar binding site of the SAE-C[4]Ps in cone conformation is buried more deeply in its aromatic cavity than in the AE-C[4]P counterparts. We surmised that this structural modification may protect even better the polar site from water solvation. Unfortunately, all our attempts to produce SAE-C[4]Ps soluble in water, at typical NMR concentrations, by installing four ionizable or charged groups at their upper rims were unsuccessful.[39]

Herein, we report the syntheses of three SAE-C[4]Ps bearing eight ionizable (carboxylates) or charged (pyridinium or 1-methyl-1H-imidazolium) groups at the periphery of their scaffolds: four groups located at the upper rim and the other four at the lower rim. We demonstrate that the synthesized calix[4]pyrroles are soluble in neutral or basic water at millimolar concentration. The deep aromatic cavity displayed by the SAE-C[4]Ps in cone conformation is suitable for the inclusion of sizeable polar molecules. We report the results obtained in the binding of a series of pyridyl *N*-oxide derivatives with the SAE-C[4]P receptors. We probed the binding of the *N*-oxides using ^{1}H NMR spectroscopy titrations and isothermal titration calorimetry (ITC) experiments. We used two of the prepared SAE-C[4]P receptors as model systems for the quantification of the hydrophobic effect in the binding of non-polar residues. The investigated non-polar residues are constituted by the *para*-substituents of the pyridyl *N*-oxide derivatives. The energy scale associated with the hydrophobic effect determined using the model systems is in line with the values derived from protein mutagenesis and the transfer of non-polar molecules from organic solvents to water.

3.2 Results and Discussion

3.2.1 Synthesis

We synthesized the AE-C[4]Ps **1a** and **1b** by acid-mediated cyclocondensation of the aryl-alkyl ketones, **2a** and **2b**, respectively, with pyrrole (see Experimental Section). The tetra-(4-iodophenyl) calix[4]pyrrole **1a** functionalized with four terminal methyl ester groups at its lower rim was prepared with aqueous concentrated 37% HCl to promote the cyclocondensation with pyrrole. For the AE-C[4]P analogue **1b** bearing four *meso*-(4-chlorobutyl) groups at its lower rim, we used 4 M HCl (added as dioxane solution) and methyltributylammonium chloride as template in the

cyclocondensation step. Our research group recently described this later synthetic methodology.[40] Both AE-C[4]Ps, **1a** and **1b**, were isolated in 10% yield after column chromatography purification.

Next, the quadruple Sonogashira cross-coupling reactions of the tetra-iodo tetra-*α* isomers, **1a** and **1b**, with methyl (4-ethynylphenoxy)acetate **3a**[39,41,42] and (1-chlorobutyloxy-4-ethynyl)benzene **3b**, respectively, afforded the corresponding octa-ester and octa-chloro SAE-C[4]Ps, **4a** and **4b**, in 70% and 60% isolated yields. Finally, the octa-ester **4a** was hydrolysed with LiOH in a THF:H_2O mixture followed by acidification of the solution,[35] obtaining the octa-acid derivative **5** as a white solid in 96% yield. The octa-pyridinium **6** and octa-(1-methyl-1H-imidazolium) **7** derivatives were obtained as chloride salts in 90% and 84% yields, respectively, by heating the parent octa-chloro compound **4b** overnight at 110°C in separate solution of pyridine[43] and 1-methyl-1H-imidazole[33] (Scheme 1). All the synthesized compounds were fully characterized by a set of high-resolution spectra (NMR and HRMS).

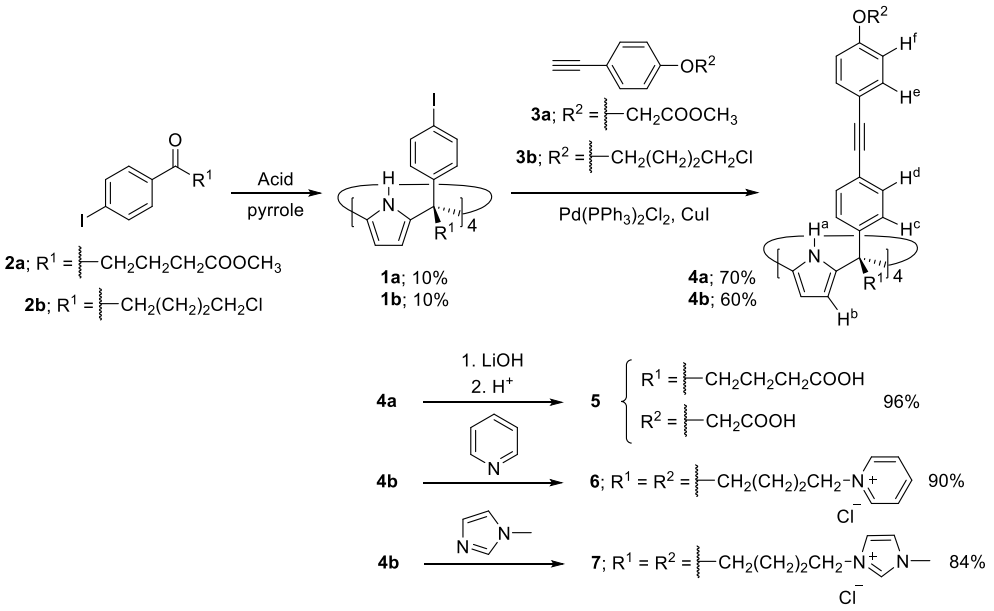

Scheme 1. Synthesis of super aryl-extended calix[4]pyrroles **4**-**7**.

In the case of the tetra-iodo calix[4]pyrroles **1a** and **1b**, single crystals suitable for X-ray diffraction were obtained by slow diffusion of methanol into methylene chloride solutions of **1a** and **1b** (Figure 1). The preliminary solution of the crystal structures supported that the isolated AE-C[4]Ps **1a** and **1b** were the tetra-*α* isomers. In the solid state, **1a** and **1b** adopt a partial cone conformation by stablishing three hydrogen bonds between three pyrrole NHs and the oxygen atom of a methanol molecule, which is included in the aromatic cavity defined by the four *meso*-(4-iodophenyl) substituents. The forth pyrrole NH forms a hydrogen bond with the carbonyl's oxygen atom of a

meso-alkyl ester of an adjacent calix[4]pyrrole **1a**. In contrast, the remaining pyrrole NH of **1b** is hydrogen-bonded to an extra methanol molecule that occupies the shallow aromatic cavity defined by the pyrrole units.

Unluckily, we did not obtain single crystals suitable for X-ray diffraction analysis of the super aryl-extended calix[4]pyrroles **4**-**7**.

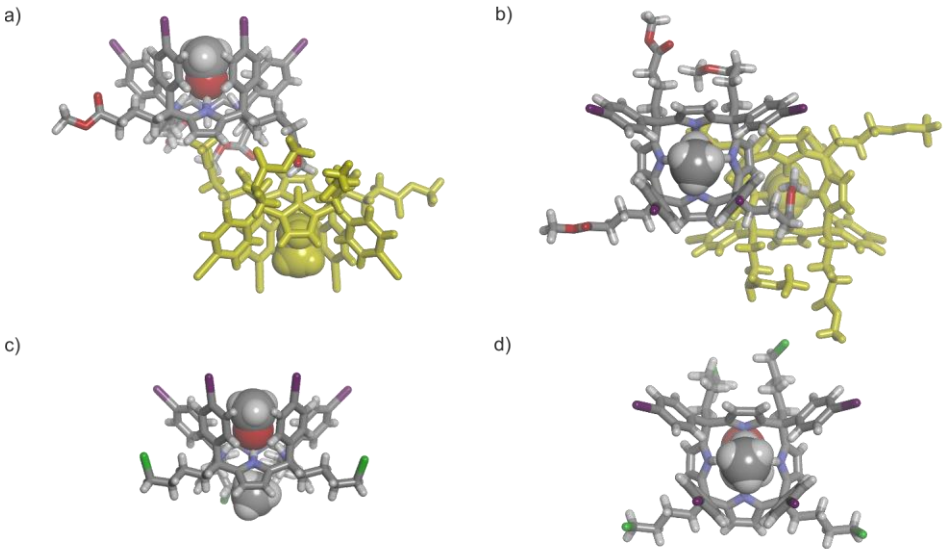

Figure 1. Preliminary solution of the X-ray crystal structures of **1a** and **1b**: a) side and b) top views of $[CH_3OH]_2\subset[\mathbf{1a}]_2$; c) side and d) top views of $[CH_3OH]_2\subset\mathbf{1b}$. Calix[4]pyrroles are depicted in stick representation and methanol molecules are shown as CPK models. In a) and b), one molecule of CH_3OH and a calix[4]pyrrole are highlighted in yellow.

The synthesized SAE-C[4]Ps **5**, **6** and **7** are functionalized either with eight carboxylic groups, which are ionizable in water at basic pH, or eight positively charged ammonium groups. All the polar groups were placed at the periphery of the receptor's aromatic scaffolds. Four of them are the end groups of the *meso*-alkyl substituents at their lower rims. The other four are placed at their upper rims, as terminal groups of the *para*-substituent of the *meso*-phenyl-ethynyl-phenyl walls. We envisaged that loading the SAE-C[4]P derivatives, **5**-**7**, with eight positive or negative charges would warrant their water solubility at millimolar concentrations.

Remarkably, the synthesized SAE-C[4]Ps structurally resemble the Gibb's octa-acid and octa-ammonium resorcin[4]arene deep-cavity cavitands.[19,44] However, the SAE-C[4]P derivatives in cone conformation display four convergent hydrogen bond donor groups in the interior of their aromatic cavities.

3.2.2 Solution studies of the super aryl-extended calix[4]pyrroles

The ^{1}H NMR spectrum of a 1 mM solution of the octa-acid **5** in D_2O at pD ~ 10 (adjusted using NaOD) displayed sharp and well-defined proton signals in agreement with a C_{4v} symmetry (Figure 2a). At this pD, most likely, the octa-acid **5** is converted into the octa-carboxylate derivative. The aromatic protons of octa-carboxylate **5** ($H^{c\text{-}f}$) appeared as four separate signals between 7.6 and 6.8 ppm, and its *β*-pyrrole protons (H^b) resonated as a sharp singlet at 6.1 ppm. The signal of the pyrrole NHs (H^a) of **5** was not detected owing to the fast H/D exchange. Conversely, the ^{1}H NMR spectrum (water-suppression pulse program) of **5** in 9:1 H_2O:D_2O solution mixture revealed the signal of the NHs (H^a) centered at 8.9 ppm (see Experimental Section).

We performed a DOSY experiment to determine the diffusion coefficient of the octa-carboxylate **5**. The experiment assigned a diffusion constant of 1.9±0.1 x 10^{-10} $m^2 \cdot s^{-1}$ to the calix[4]pyrrole (Figure 2b). The determined diffusion constant translated into a putative diffusing sphere having a hydrodynamic radius of 10.6 Å. The volume of the sphere is consistent with the size of the energy minimized structure of a discrete molecule of the octa-carboxylate **5**.

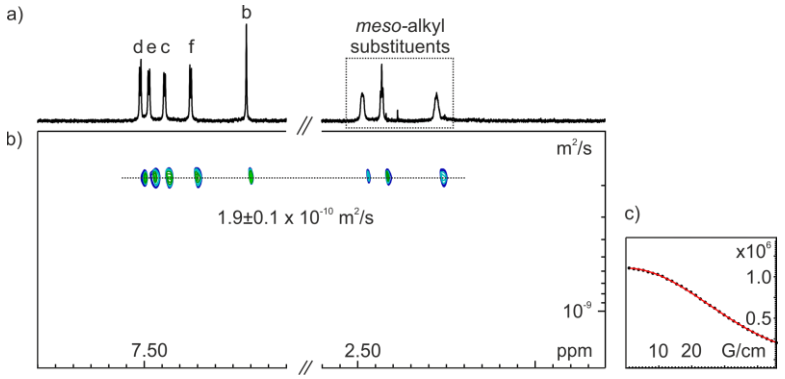

Figure 2. a) ^{1}H NMR (500 MHz with cryoprobe, D_2O, pD ~ 10, 298 K) spectrum of octa-acid **5**; b) pseudo 2D plot of ^{1}H DOSY (500 MHz with cryoprobe, D_2O, pD ~ 10, 298 K, D20 = 0.15 s, P30 = 1 ms) of **5** and c) decay of proton b fitted to a mono-exponential function. See Scheme 1 for proton assignment.

Taken together, these results indicated that the octa-carboxylate **5** is soluble in basic water at millimolar concentrations and does not show signs of aggregation. Additionally, the parent octa-acid **5** is soluble in acetone and dimethyl sulfoxide, showing well-resolved proton signals that are in agreement with C_{4v} symmetry.

The SAE-C[4]Ps derivatives **6** and **7** bear eight positively charged ammonium groups conveying water solubility independently of the pH. This feature renders **6** and **7** more compatible for solubilization in biological media than the octa-acid **5**. The ^{1}H NMR spectra of D_2O solutions of **6** and **7** showed broad proton signals at 298 K (Figure 3a). Thus, we performed variable-temperature (VT) ^{1}H NMR experiments using the above D_2O solutions (Figure 3 and Experimental

Section). At T > 318 K, the ^{1}H NMR spectra showed sharp and well-defined proton signals that were in agreement with C_{4v} symmetry. We also used ^{1}H NMR spectroscopy to monitor dilution experiments (1-0.05 mM) with **6** and **7** in D_2O (see Experimental Section). The broad proton signals of the SAE-C[4]Ps were unchanged by dilution. Most likely, at 298 K, the observed broadening of the proton signals is caused by the equilibrium (chemical exchange process) between conformers (cone and alternate) of the octa-cationic SAE-C[4]Ps, **6** and **7**, taking place at an intermediate rate on the ^{1}H NMR chemical shift timescale.

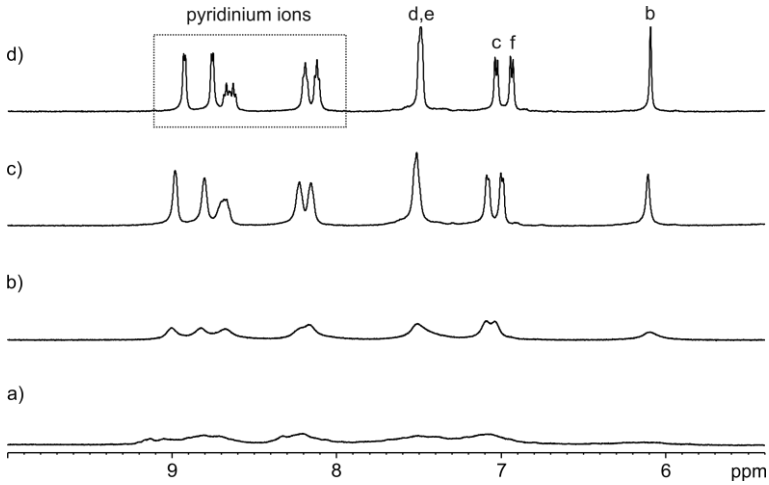

Figure 3. Selected region of the VT ^{1}H NMR (500 MHz, D_2O) spectra of **6**: a) 298; b) 318; c) 338 and d) 358 K. See Scheme 1 for proton assignment.

This hypothesis is substantiated by the observation of sharp and well-defined proton signals in the ^{1}H NMR spectra for the 1:1 inclusion complexes of the octa-cationic SAE-C[4]Ps with pyridyl *N*-oxide derivatives (see below). The inclusion of the guests locks the SAE-C[4]P in the cone conformation. Nevertheless, the reduced aggregation of the 1:1 inclusion complex compared to the parent hosts cannot be ruled out.

We hypothesize that the different dynamics observed for the conformational exchange equilibria experienced by the octa-anionic **5** and octa-cationic **6** and **7** could be related to differences in the energetics of the solvation/desolvation processes experienced by the conformers owing to the substantially different nature of the installed water-solubilizing groups.

The chloride salts of the octa-ammonium SAE-C[4]Ps, **6** and **7**, are also soluble in methanol and dimethyl sulfoxide. Remarkably, the ^{1}H NMR spectra of **6** and **7** in $(CD_3)_2SO$ solution displayed two sets of sharp proton signals in a 70:30 ratio based on integral values. The number of proton signals in each set was in agreement with C_{4v} symmetry for the host (Figure 4a). The pyrrole NHs (H^a) of the minor component of the mixture appeared at δ = 11.1 ppm. On the other hand, the

singlet for the pyrrole NHs of the major component was upfield shifted (δ = 9.2 ppm). We assigned the signals of the minor component to the protons of the receptors in the Cl^-⊂SAE-C[4]P complexes. This assignment was corroborated by the addition of an excess of TBACl to the above $(CD_3)_2SO$ solutions of the SAE-C[4]Ps (Figure 4b). The incremental addition of the TBACl salt produced the increase of the signals assigned to the protons of the Cl^-⊂SAE-C[4]P complex at the expenses of those of the major component in the mixture, putatively the free SAE-C[4]P.

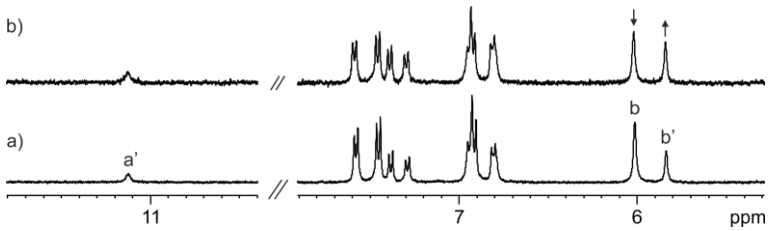

Figure 4. Selected regions of the ^{1}H NMR (400 MHz, $(CD_3)_2SO$, 298 K) spectra of **6** with TBACl: a) 0 and b) 20 equiv. Primed letters correspond to proton signals of the Cl^-⊂SAE-C[4]P complex. Arrows indicate the change of the intensity of the proton signals. See Scheme 1 for proton assignment.

When the octa-cationic SAE-C[4]Ps, **6** and **7**, were dissolved in CD_3OD, the ^{1}H NMR spectra of the solutions revealed the presence of a single set of proton signals (Figure 5 and Experimental Section). Thus, the SAE-C[4]Ps, **6** and **7**, are not efficient receptors for chloride in the presence of the competitive polar and protic solvent.

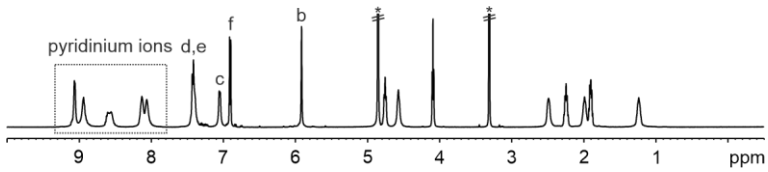

Figure 5. ^{1}H NMR (500 MHz with cryoprobe, CD_3OD, 298 K) spectrum of **6**. See Scheme 1 for proton assignment. *Residual solvent peaks.

3.2.3 ^{1}H NMR binding studies

First, we probed the interaction of the SAE-C[4]Ps **5** and **6** with a series of pyridyl *N*-oxides, **8a**-**f**, and aliphatic *N*-oxides, **9a**-**b** (Figure 6) using ^{1}H NMR spectroscopy titrations. The binding properties of receptor **5** were investigated in D_2O solutions at basic pD, whereas those of the octa-cationic counterpart **6** were evaluated in neutral un-buffered D_2O solutions. The pyridyl *N*-oxide guests, **8a**-**d**, are substituted with phenyl, *n*-butyl, *tert*-butyl and methyl groups, respectively, at the pyridyl's *para*-position. We were interested in assessing the hydrophobic effect exerted by the non-polar substituents in the binding of the guest series. To this end, we used pyridine *N*-oxide **8e** as reference. Additionally, we evaluated the binding of the isoquinoline *N*-oxide derivative **8f** to the SAE-C[4]P receptors. The phenyl substituent in **8f** is co-planar with respect to the pyridyl residue

displaying a tilted geometry of *ca.* 30° with respect to **8a**. We wanted to find out how these structural differences will translate in binding affinity values. The binding of the aliphatic *N*-oxides **9a**-**b** to the SAE-C[4]Ps in water was also investigated.

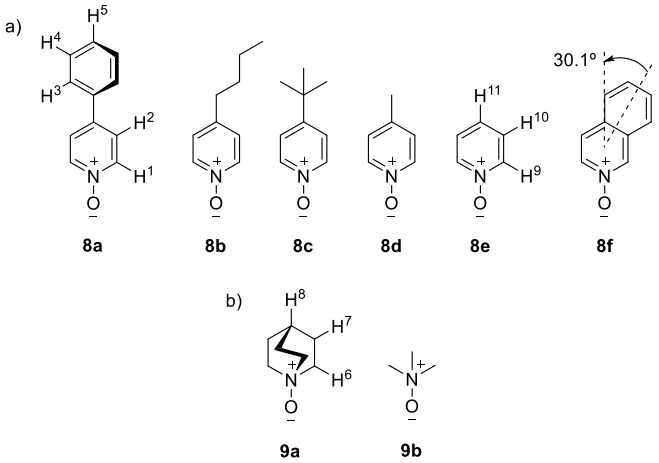

Figure 6. Line-drawing structures of a) pyridyl *N*-oxides **8a**-**f** and b) aliphatic *N*-oxides **9a**-**b**. The depicted angle in **8f** was determined from its energy minimize structure (PM3, water COSMO model implemented in SCIGRESS Version FJ 2.6).

Pyridyl *N*-oxides **8a**-**f**

The addition of 0.6 equiv. of *N*-oxide **8a** to a millimolar solution of **5** in water at pD ~ 10 (adjusted using NaOD) produced the appearance of a new set of proton signals for the receptor. We assigned this new set of proton signals to bound **5** (Figure 7b). The observation of two separate sets of signals for free and bound **5** was indicative of a slow chemical exchange on the ^{1}H NMR chemical shift timescale. At this point, the proton signals of the phenyl pyridine *N*-oxide **8a** appeared upfield shifted with respect to those of free **8a** in water solution. Notably, the doublet of the aromatic protons *alpha* to the nitrogen atom of **8a** resonated at δ = 4.5 ppm, displaying the largest complexation induced shift, $\Delta\delta$ = -3.8 ppm. All protons of bound **8a** experienced the anisotropic effect exerted by the *meso*-aromatic substituents of **5** and moved upfield (Table 1). This observation confirmed the complete inclusion of **8a** in the aromatic cavity of **5**. The binding of **8a** by **5** is driven by the formation of hydrogen-bonding interactions between the calix[4]pyrrole core of the receptor and the oxygen atom of the guest, the hydrophobic effect and additional aromatic interactions (π-π and CH-π). The addition of 1 equiv. of **8a** produced the quantitative formation of the **8a**⊂**5** complex (Figure 7c). The addition of more than 1 equiv. of *N*-oxide **8a** did not produce changes on the proton signals of the bound components. The proton signals of the guest added in excess coincided with those of the free guest in water solution (Figure 7d). In short, 4-phenyl pyridine *N*-oxide **8a** and negatively ionized octa-acid **5** formed a thermodynamically and

kinetically highly stable 1:1 complex featuring a deep inclusion binding geometry. A binding constant lager than 10^4 M^{-1} can be estimated for the **8a⊂5** complex.

The results of the ^{1}H NMR spectroscopy titrations of octa-acid **5** in D_2O at pD ~ 10 with other pyridyl *N*-oxide derivatives **8b**-**f** produced analogous results to those described above (see Experimental Section).

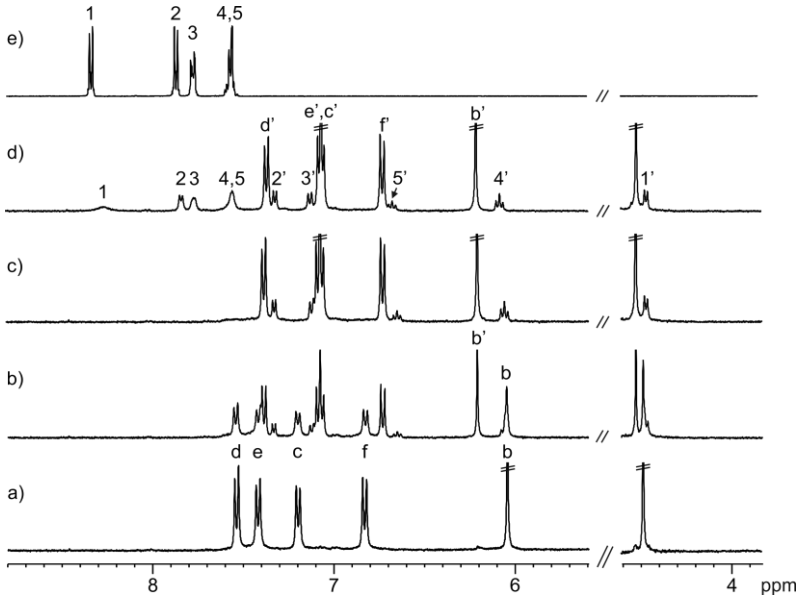

Figure 7. Selected regions of the ^{1}H NMR (400 MHz, D_2O, pD ~ 10, 298 K) spectra of the titration of **5** with **8a**: a) 0; b) 0.6; c) 1 and d) 2.3 equiv.; e) **8a**. Primed letters and numbers correspond to proton signals of bound components. See Scheme 1 and Figure 6a for proton assignments.

Next, we studied the binding of 4-phenyl pyridine *N*-oxide **8a** with the octa-pyridinium SAE-C[4]P **6** in neutral un-buffered D_2O solution. As mentioned above, the ^{1}H NMR spectrum of a 1 mM solution of the octa-pyridinium **6** in D_2O showed broad proton signals (Figure 8a). However, the addition of 0.5 equiv. of pyridyl *N*-oxide **8a** to the D_2O solution of **6** produced the emergence of a set of sharp and well-defined proton signals (Figure 8b). We assigned the new set of signals to the protons of the bound receptor. The aromatic protons of **8a** appeared upfield shifted and the calculated $\Delta\delta$ values were similar to those determined for the **8a⊂5** complex (Table 1), supporting its deep inclusion in the aromatic cavity of **6**. The addition of 1 equiv. of **8a** produced the exclusive observation of the proton signals assigned to the **8a⊂6** complex (Figure 8c). In brief, the octa-pyridinium SAE-C[4]P **6** formed a kinetically and thermodynamically highly stable 1:1 inclusion complex with **8a**, **8a⊂6**, for which a stability constant larger than 10^4 M^{-1} can be estimated. The sharpening of the proton signals of **6** in the **8a⊂6** complex is assigned to the conformational locking of the bound receptor in the cone conformation.

Chapter 3

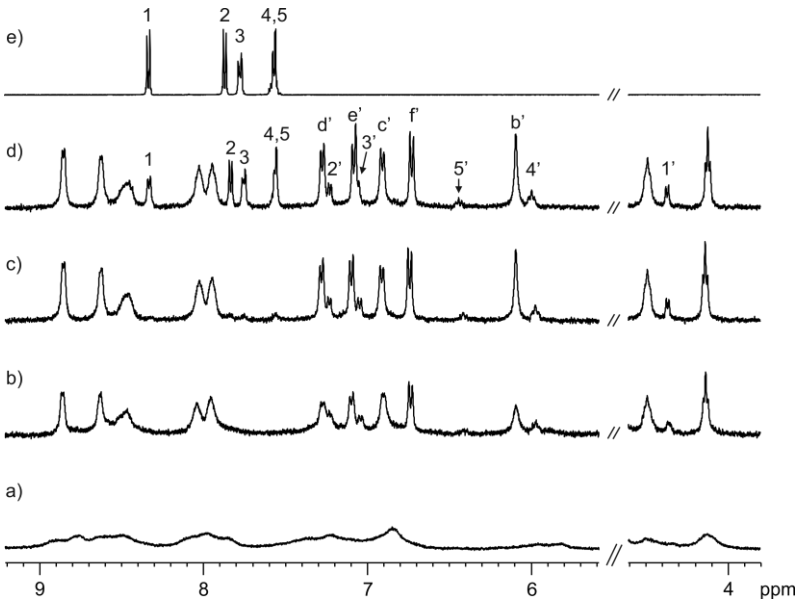

Figure 8. Selected regions of the ^{1}H NMR (400 MHz, D_2O, 298 K) spectra of the titration of **6** with **8a**: a) 0; b) 0.5; c) 1 and d) 2 equiv.; e) **8a**. Primed letters and numbers correspond to proton signals of bound components. See Scheme 1 and Figure 6a for proton assignments.

Table 1. Chemical shifts of the proton signals of free **8a** (δ_{free}, ppm) and bound **8a** (δ_{bound}, ppm) in the **8a⊂5** and **8a⊂6** complexes, and complexation induced shifts ($\Delta\delta$, ppm). See Figure 6a for proton assignment.

Signal	δ_{free}	Octa-acid **5**		Octa-pyridinium **6**	
		δ_{bound}	$\Delta\delta$	δ_{bound}	$\Delta\delta$
1	8.27	4.42	-3.85	4.37	-3.90
2	7.83	7.27	-0.56	7.23	-0.60
3	7.75	7.08	-0.67	7.06	-0.69
4	7.53	6.05	-1.48	6.00	-1.53
5	7.53	6.64	-0.89	6.45	-1.08

We performed simple molecular modelling studies aiming at providing structural information on the formed 1:1 inclusion complexes. The energy minimized structures (BP86-D3-def2-SVP DFT level of theory, water COSMO model implemented in Turbomole Version 7.0)[45,46,47] of the 1:1 inclusion complexes of **8a** and **8e** with a pruned SAE-C[4]P lacking the water-solubilizing substituents installed at the upper and lower rims are shown in Figure 9.

The receptor adopts the cone conformation by establishing four hydrogen bonds between the pyrrole NHs and the oxygen atom of the *N*-oxide unit. The SAE-C[4]P and the bound *N*-oxide are also engaged in π-π and CH-π interactions.[48,49] The pyridyl *N*-oxides are deeply included in the polar and aromatic cavity of the super aryl-extended calix[4]pyrrole. It is worth mentioning that the upper section of the aromatic cavity in the **8e**⊂SAE-C[4]P complex collapses owing to edge-to-face CH-π interactions. We observed the collapse of this cavity in the X-ray structures of organic soluble SAE-C[4]Ps.[39,50]

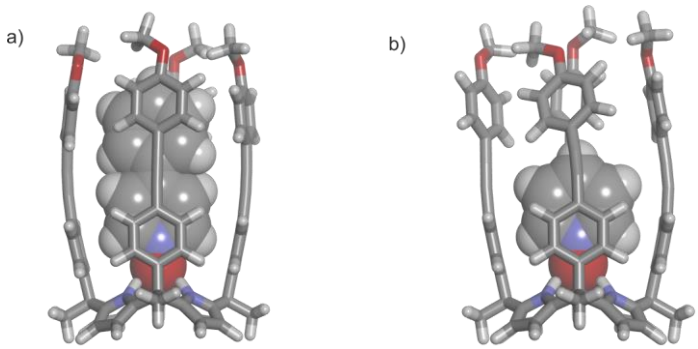

Figure 9. Energy minimized structures (BP86-D3-def2-SVP DFT level of theory, water COSMO model implemented in Turbomole Version 7.0) of the 1:1 inclusion complexes of SAE-C[4]Ps with a) **8a** and b) **8e**. The calix[4]pyrroles are depicted in stick representation and the *N*-oxides are shown as CPK models. The alkyl substituents at the upper and lower rims of the SAE-C[4]Ps are pruned to methyl groups to ease the calculations.

We also computed the structure of the octa-anionic **8a⊂5** complex at the DFT level of theory using water COSMO model. The optimized structure of octa-anionic **8a⊂5** displays the receptor in a cone conformation similar to the one shown in the Figure 9a for the neutral host (see Experimental Section).

Aliphatic *N*-oxides **9a-b**

We investigated the binding of quinuclidine *N*-oxide **9a** and tri-methylamine *N*-oxide **9b** to the octa-acid **5** in D_2O at pD ~ 10. The addition of incremental amounts of the *N*-oxide **9a** to a millimolar solution of **5** produced a new set of proton signals assigned to the bound host (Figure 10). The observation of separate set of signals for the free and bound receptor is indicative of a slow chemical exchange on the ^{1}H NMR chemical shift timescale. At the same time, the signals of the *N*-oxide **9a** appeared upfield shifted with respect to those of the free guest in solution. For example, the *α*-protons respect to the *N*-oxide of **9a** (H^6) appeared at 0.6 ppm ($\Delta\delta$ = -2.7 ppm), due to its inclusion in the aromatic cavity of the SAE-C[4]P in a cone conformation. The integration of the proton signals of bound receptor **5** and *N*-oxide **9a** confirmed the formation of a 1:1 complex. Likewise, a binding constant value K_a = 1.3±0.1 x 10^2 M^{-1} for the **9a⊂5** complex was calculated using the integral values of the protons signals of the free and bound components.

Next, we titrated the octa-acid **5** with tri-methylamine *N*-oxide **9b** under the same experimental conditions. In this case, the ^{1}H NMR spectra showed negligible chemical shift changes in the proton signals of **5** upon addition of incremental amounts of **9b** (see Experimental Section). This result indicated that the interaction between **9b** and **5** is very weak in aqueous solution and a binding constant K_a (**9b**⊂**5**) < 10 M^{-1} can be estimated.

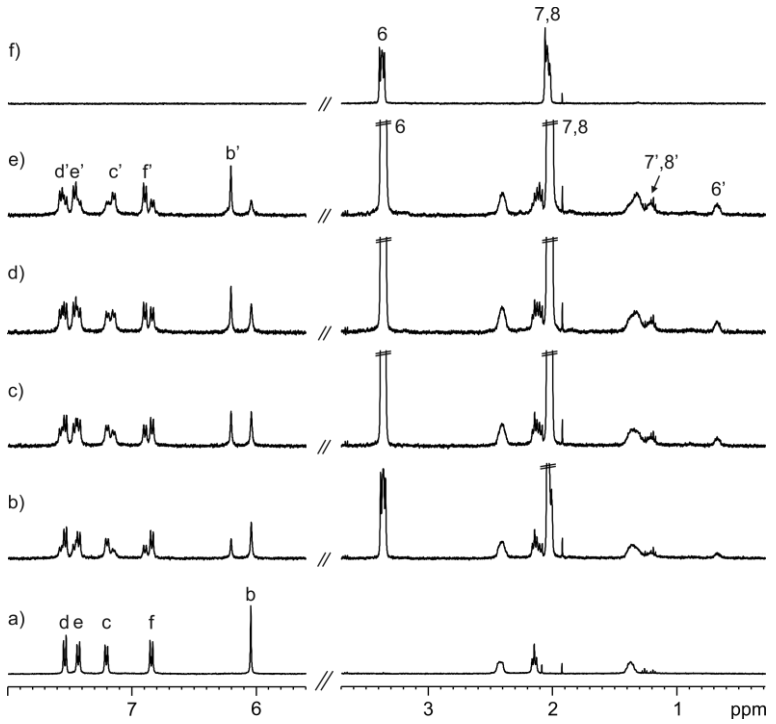

Figure 10. Selected regions of the ^{1}H NMR (400 MHz, D_2O, pD ~ 10, 298 K) spectra of the titration of **5** with **9a**: a) 0; b) 5; c) 7.5; d) 10 and e) 15 equiv.; e) **9a**. Primed letters and numbers correspond to proton signals of bound components. See Scheme 1 and Figure 6b for proton assignments.

The water-soluble SAE-C[4]Ps **5** and **6** show high binding affinity (K_a > 10^4 M^{-1}) towards pyridyl *N*-oxides **8a**-**f**. Interestingly, the receptors also feature high selectivity for pyridyl *N*-oxides versus the aliphatic counterparts **9a**-**b**. Most likely, the higher polarizability of the aromatic molecules[51] and the establishment of π-π and CH-π interactions are responsible for the superior binding affinity and selectivity displayed by the SAE-C[4]Ps in water towards them.

3.2.4 Isothermal titration calorimetry experiments

In order to determine accurate values for the binding constants of the SAE-C[4]P complexes, we performed isothermal titration calorimetry (ITC) experiments. Ideally, ITC experiments provide binding constant value (K_a), enthalpy of binding (Δ*H*) and complex stoichiometry in a single experiment. Nevertheless, as it happens with other titration techniques the accurate determination

of a binding constant value by ITC requires performing the experiment at the adequate concentration of host and guest. The accurate determination of large binding constant values demand performing the titration experiment at very dilute conditions, which may challenge the sensibility and accuracy of the instrument in measuring the heat released or absorbed due to the complex formation.

The measured binding isotherms for the different ITC experiments were fitted to the theoretical 1:1 binding model ("one set of sites") implemented in the calorimeter software. The fit of the ITC titration data returned the stability constant value (K_a) of the complex and the enthalpy of binding (ΔH). The free energy (ΔG) and the entropy (ΔS) values were derived from the thermodynamic constants measured experimentally.

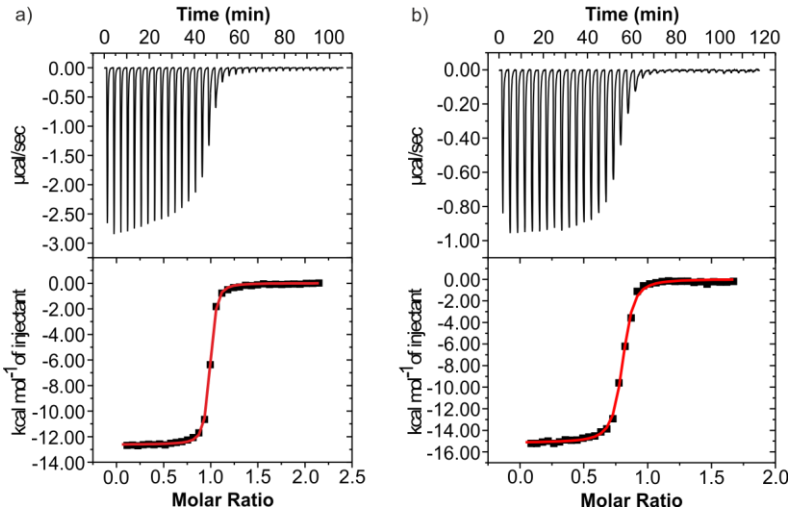

Figure 11. Top panels show raw data (heat *vs.* time) for the titration of guest into the host: a) **8a⊂5** (H_2O at pH ~ 10) and b) **8a⊂6** (H_2O). Titrations were performed at 298 K. Bottom panels represent integrated data fitted to the theoretical binding isotherm (red line) for a 1:1 binding model.

It is important to realize that some binding constant values returned from the fit of the titration data to the theoretical 1:1 model are just estimates. This is the case for the titrations displaying an abrupt saturation of the measured heat (Figure 11). That is, a small number of experimental points define the saturation phase of the binding isotherm. These titrations correspond to complexes featuring larger binding constants. The accurate determination of their binding constant value requires performing a titration under more dilute conditions. However, these dilute conditions are incompatible with the sensibility and accuracy of the ITC instrument. For this reason, the accurate values for the binding constant of the thermodynamically more stable inclusion complexes were derived from pair-wise competitive titration experiments that were analyzed using ^{1}H NMR spectroscopy. These experiments only provide useful information on the binding constant ratio if the thermodynamic stability of the two competing complexes differ in less than two orders of

magnitude. Thus, starting from the complex having the larger binding constant value that we could measure accurately using ITC experiments and performing a series of designed pair-wise competitive experiments between complexes of incremental binding affinities, we determined the binding constant values of those complexes for which the ITC experiments provided only estimates ($K_a > 10^7$ M^{-1}).

The determination of accurate binding constant values was a necessary step in order to derive the magnitudes of the hydrophobic effect provided by the non-polar *para*-substituent to the binding. The results of the ITC experiments and the pair-wise competitive experiments are summarized in Table 2.

Table 2. Binding constants (K_a, M^{-1}), free energies (ΔG) at 298 K of the 1:1 inclusion complexes of the octa-acid **5** and octa-pyridinium **6** in basic and neutral water, respectively, and calculated surface areas (A, $Å^2$) of the guests (Swiss-PDB Viewer Version 4.1.0). Error values are reported as standard deviations.

Guest	Area	Octa-acid **5**		Octa-pyridinium **6**	
		K_a	ΔG	K_a	ΔG
8a	180	$>10^{7,a}$		$>10^{7,a}$	
		$1.2\pm0.5 \times 10^{9,b}$	-12.4 ± 0.4^b	$2.6\pm0.6 \times 10^{9,b}$	-12.8 ± 0.1^b
8b	183	$>10^{7,a}$		$>10^{7,a}$	
		$1.0\pm0.4 \times 10^{8,b}$	-10.9 ± 0.2^b	$3.7\pm0.6 \times 10^{8,b}$	-11.7 ± 0.1^b
8c	170	$9.1\pm3.0 \times 10^{6,b}$	-9.5 ± 0.2^b	$3.7\pm0.6 \times 10^{7,b}$	-10.3 ± 0.1^b
8d	128	$2.0\pm0.1 \times 10^{6,c}$	-8.6 ± 0.1^c	$6.1\pm0.1 \times 10^{6,c}$	-9.2 ± 0.1^c
8e	109	$8.6\pm0.5 \times 10^{5,c}$	-8.1 ± 0.1^c	$1.9\pm0.1 \times 10^{6,c}$	-8.6 ± 0.1^c
8f	151	$2.2\pm0.2 \times 10^{6,c}$	-10.0 ± 0.1^c	$7.1\pm0.2 \times 10^{6,c}$	-9.3 ± 0.1^c

[a] Estimated from ITC experiments; [b] determined by pair-wise ^{1}H NMR competitive experiments and [c] determined by ITC experiments.

Several conclusions can be drawn from the tabulated and determined data. All binding constant values for the SAE-C[4]P complexes determined/estimated using ITC experiments are larger than 10^4 M^{-1}. This finding is in agreement with the results obtained from the ^{1}H NMR titration experiments. All binding processes are mainly driven by enthalpy, along with favourable or unfavourable entropic contributions (see Experimental Section). Enthalpy and entropy compensation effects seem to be operative.[52] The binding constants are similar for the analogous pair of complexes: the same pyridyl *N*-oxide bound with the octa-acid **5** and the octa-pyridinium **6**. Therefore, the nature of the water-solubilizing groups placed at the receptor's scaffolds periphery

and the pH of the water solutions do not affect significantly the affinity of the complex. This result is consistent with previous studies reported by Rebek and co-workers in the binding of resorcin[4]arene deep cavitands with neutral guests.[53]

Remarkably, the increase in surface area of the non-polar residue at the *para*-position of the pyridyl *N*-oxides translates into a gain in binding affinity. This energy gain must be related to the hydrophobic effect caused by the reduction in the solvent accessible surface area of the substituent upon complex formation and the concomitant increase in non-polar surface contact between the binding partners (see below).[1]

It is worth mentioning that the SAE-C[4]P receptors feature nanomolar affinities for the complexation of 4-phenyl pyridine *N*-oxide **8a** in water. To the best of our knowledge, the magnitude of the binding constant is unprecedented for complexes of small polar molecules with synthetic receptors in aqueous media.

The binding constant values for the isoquinoline *N*-oxide **8f** are two orders of magnitude lower than those of the *para*-phenyl derivative **8a**. Most likely, steric clashes between the fused aryl rings in **8f** and the *meso*-aromatic walls of the receptor do not allow the establishment of an ideal geometry for the hydrogen-bonding interactions between the guest's oxygen atom and the four pyrrole NHs. Likewise, the reduced shape complementarity between host and guest negatively impacts on the π-π and CH-π interactions of the complex. The high binding affinities measured for the complexes of the pyridyl *N*-oxides and the SAE-C[4]Ps are several orders of magnitude larger than the ones reported by Hunter, Ward and co-workers using a metallo-cage receptor.[32,54]

3.2.5 Relationship between the free energies of binding and the surface area of the non-polar *para*-substituent

We wanted to quantify the hydrophobic effect exerted by the non-polar *para*-substituents in the binding of the guests. To this end, we subtracted the value of the free energy of the pyridine *N*-oxide complex, **8e**⊂SAE-C[4]P, from the free energy values determined for the *N*-oxide derivatives having a *para*-substituent. In doing so, we assume that the overall free energy of binding can be dissected as the sum of the free energies of binding of the pyridine *N*-oxide residue and the *para*-substituent (Equation 1). We also consider that the free energy of binding provided by the pyridine *N*-oxide residue is constant throughout the guest series. Similarly, the surface area of the *para*-substituent of the pyridyl *N*-oxide guests was calculated by subtracting the surface area of the guest **8e** from the surface area of the guests **8a**-**d** (Equation 2).

1) $\Delta\Delta G = \Delta G$ [(**8a**-**d**)⊂SAE-C[4]P] – ΔG [**8e**⊂SAE-C[4]P]

2) $\Delta A = A$ [**8a**-**d**] – A [**8e**]

The plots of the calculated ΔΔ*G* values *vs.* the surface areas of the *para*-alkyl substituents (Δ*A*) (Table 2) showed good linear relationships (r ~ 0.95), thus providing some insight into the origin of the variation (Figure 12). The most likely explanation is consistent with the existence and the variation of the hydrophobic effect, involving the non-polar *para*-substituent and the surface of the four aromatic rings defining the upper cavity of the SAE-C[4]Ps.

The slopes of the lines provide magnitudes on the order of 33-38 cal·mol^{-1}·Å^{-2} for the hydrophobic effect operating in the thermodynamic stabilization of the SAE-C[4]P's complexes. Notably, the energy values assigned to the hydrophobic effect using these simple host-guest systems, are in line with those reported in literature from studies of site-directed mutagenesis of protein residues (30-60 cal·mol^{-1}·Å^{-2}) and the transfer of solutes from non-polar solvents to water (20-50 cal·mol^{-1}·Å^{-2}).[1,55,56]

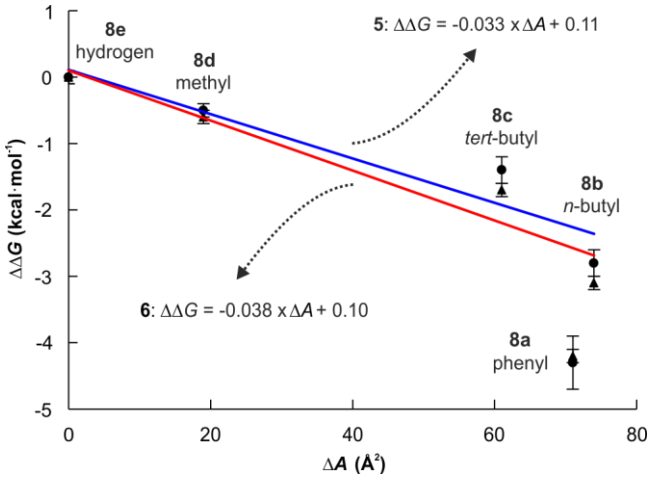

Figure 12. Difference in free energy (ΔΔ*G*) *vs.* surface area (Δ*A*) of the non-polar *para*-substituent for the complexes of the pyridyl *N*-oxide derivatives with water-soluble SAE-C[4]Ps. The data of the complexes of **5** and **6** are shown as circles and triangles, respectively. The linear fits of the data are represented as solid lines for complexes of **5** (blue) and **6** (red), respectively. Error bars are standard deviations.

The *para*-phenyl residue **8a** turns out to be an outlier of the linear trend deduced for the alkyl substituents. The **8a**⊂SAE-C[4]P complexes are stabilized by an additional 2 kcal·mol^{-1} with respect to our estimate based on the reduction of solvent surface accessibility of the phenyl group. We propose the formation of a cluster of aromatic interactions (π-π and CH-π) in the upper section of the SAE-C[4]P complexes as the putative origin of the extra stabilization. Aromatic-aromatic interactions are known to provide thermodynamic stabilization to protein folding but to a lesser extent than our estimate. Nevertheless, the binding geometry observed in the cluster of aromatic-aromatic interactions present in the **8a**⊂SAE-C[4]P complexes might be a rare motif in nature.[48,49,57]

3.2.6 Further binding studies by NMR spectroscopy and ITC

Binding studies in aqueous buffer solution

We examined the binding of pyridine *N*-oxide **8e** to octa-acid **5** in 0.1 M borate/sodium hydroxide buffer (pH or pD ~ 10) and 0.1 M NaCl with the aim to explore the effect of salts in the binding constant of the **8e⊂5** complex. The ^{1}H NMR spectrum of a millimolar solution of **5** in aqueous buffer solution showed broad proton signals (Figure 13a). Most likely, the signal broadening is produced by a modification in the exchange kinetics of the equilibria between conformers in the buffered solution. As might be expected, the addition of incremental amounts of **8e** to the aqueous buffer solution of **5** produced sharp and well-defined proton signals for the bound host. The binding of the guest locks the host in the cone conformation. The signals of the bound guest **8e** appeared upfield shifted with respect to those of free *N*-oxide in solution (Figure 13). The complexation induced shifts ($\Delta\delta$) for bound **8e** are similar to the ones calculated from the same titration experiment in un-buffered water at pD ~ 10. These results indicated that, in buffer aqueous solution, **8e** and **5** formed a 1:1 inclusion complex for which a binding constant larger than 10^4 M^{-1} can be estimated.

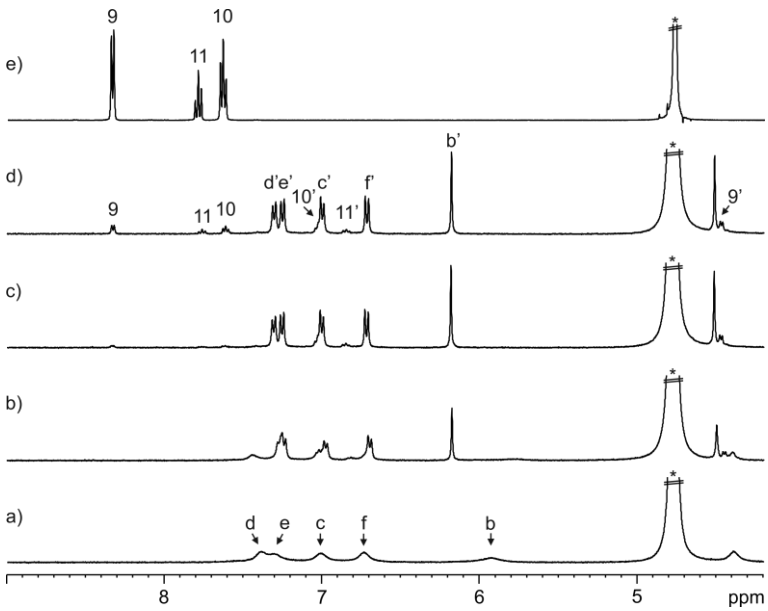

Figure 13. Selected region of the ^{1}H NMR (400 MHz, D_2O, 0.1 M borate/sodium hydroxide buffer, pD ~ 10, 0.1 M NaCl, 298 K) spectra of the titration of **5** with **8e**: a) 0; b) 0.6; c) 1.1 and d) 1.8 equiv.; e) **8e**. Primed letters and numbers correspond to proton signals of bound components. See Scheme 1 and Figure 6a for proton assignments. *Residual solvent peak.

The accurate binding constant value of the **8e⊂5** complex in borate/sodium hydroxide buffer solution was determined by ITC titrations. The integrated heat derived from the titration of **5** with

8e was fitted to the theoretical 1:1 binding model ("one set of sites") (Figure 14). The fit returned a binding constant value K_a (**8e⊂5**) = 8.9±0.1 x 10^5 M^{-1}. This constant is equivalent, within the experimental error, to the **8e⊂5** complex formed in un-buffered water solution at basic pH.

These results indicated that the presence of salts in aqueous solution (0.1 M borate/sodium hydroxide buffer and 0.1 M NaCl) does not affect noticeably the association constant of the octa-acid SAE-C[4]P **5** with the pyridyl *N*-oxide derivative **8e**.

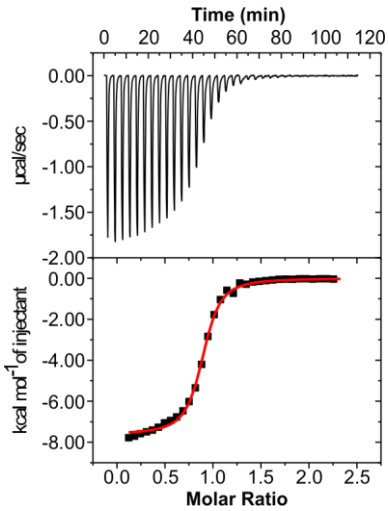

Figure 14. Top panel shows raw data (heat *vs.* time) for the titration of guest into the host: **8e⊂5** (H_2O, 0.1 M borate/sodium hydroxide buffer, pH ~ 10, 0.1 M NaCl). Titration was performed at 298 K. Bottom panel represents integrated data fitted to the theoretical binding isotherm (red line) for a 1:1 binding model.

In striking contrast with the result obtained above, preliminary ITC titration experiments using the octa-pyridinium **6** and the pyridyl *N*-oxides produced binding isotherms which are characteristic of more complicated equilibria (*e.g.* formation of 1:2 or 2:1 host:guest complexes). Further investigations are necessary to improve our understanding of the binding behaviour of octa-pyridinium **6** in aqueous buffer solution.

Variable-temperature ITC experiments in neutral un-buffered water

The sign and magnitude of the heat capacity (ΔC_p) associated to a binding process depend significantly on the intermolecular forces involved in the formation of the complex and the solvation/desolvation processes of the free and bound components. In general, ΔC_p is negative for hydrophobic binding processes in water. For example, the heat capacity value for the binding of polar benzene derivatives (*e.g.* 4-nitrophenol) or organic cations (*e.g.* adamantyl tri-methylammonium) to cyclophane receptors is *ca.* -100 $cal \cdot mol^{-1} \cdot K^{-1}$.[58,59]

In this regard, we performed variable-temperature (VT) ITC titration experiments, from 298 to 328 K, using the pyridine *N*-oxide **8e** and the octa-pyridinium **6** in neutral un-buffered water solutions. The plot of the enthalpy, ΔH, versus the temperature showed a linear relationship. The slope of the fitted line returned the sign and magnitude of ΔC_p (Figure 15). For the **8e⊂6** complex, we determined a value of ΔC_p equal to -170±30 cal·mol^{-1}·K^{-1}. The negative sign of ΔC_p indicates that the binding process of the pyridyl *N*-oxide derivative **8e** to the water-soluble SAE-C[4]P **6** is mainly driven by the hydrophobic effect. Additionally, the magnitude of ΔC_p for the formation of the SAE-C[4]P's complex is in line with those determined for other synthetic host-guest systems in water.[58,59]

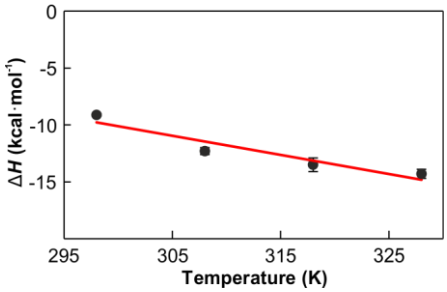

Figure 15. Enthalpy (ΔH, kcal·mol^{-1}) *vs.* temperature (K) derived from the VT ITC titration experiments of **8e⊂6**. The experimental data are fitted to a linear regression equation (red line). Error bars are standard deviations.

It is worth mentioning that the binding constant of the **8e⊂6** complex was not dramatically affected by the change in temperature in the range of temperatures under investigation (K_a (328 K)/K_a (298 K) ~ 0.2).

3.2.7 Initial synthetic steps towards super aryl-extended calix[4]pyrrole cavitands

Aryl-extended calix[4]pyrrole cavitands have been previously reported by our research group. The cavitands adopt a more pre-organized conformation for binding than the parent aryl-extended calix[4]pyrroles, enhancing the association constants.[38,60] We envisaged that super aryl-extended calix[4]pyrroles **10a** and **10b** (Scheme 2) can be used as precursors for the synthesis of deep-cavity cavitands based on the SAE-C[4]P architecture. The tetra-hydroxy derivative **10a** would react with two equivalents of a di-functional linker (*e.g.* ethylene or propylene di-(*para*-toluenesulfonate) leading to a cavitand with two bridged units at its upper rim. In the same vein, the octa-hydroxy **10b** would give a tetra-bridged cavitand from its reaction with four equivalents of the later linker. As a result, the SAE-C[4]P cavitands would be less conformationally flexible than the parent SAE-C[4]Ps.

The cavitand's precursors **10a** and **10b** were prepared in two synthetic steps (Scheme 2). First, a quadruple palladium/copper-catalyzed cross-coupling reaction between the tetra-iodo **1a** and the alkynyl derivatives **11a**[61] and **11b**,[62] respectively, having protecting *tert*-butyl di-methyl silyl ether

groups (OTBDMS), produced the SAE-C[4]Ps **12a** and **12b** in 77% and 70% yields, respectively. After that, deprotection of the hydroxy groups of **12a** and **12b** using TBAF gave **10a** and **10b**, respectively. The SAE-C[4]Ps **10a** and **10b** were isolated after column chromatography purification in 82% and 60% yields, respectively.

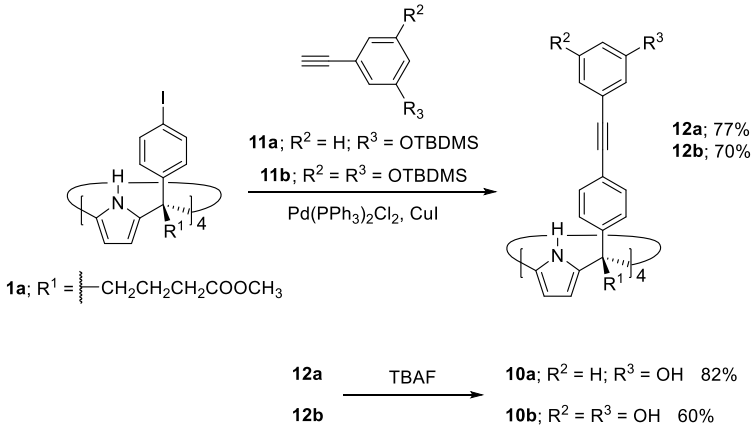

Scheme 2. Synthesis of cavitand's precursors **10a**-**b**. OTBDMS = *tert*-butyl di-methyl silyl ether.

3.3 Conclusions

In summary, we report the syntheses of three unprecedented super aryl-extended calix[4]pyrroles bearing either eight ionizable or charged groups at the periphery of their scaffolds, **5**-**7**. The super aryl-extended derivatives are soluble in neutral or basic water solutions at mM concentration. We show that the free receptors display dissimilar rates in their conformation exchange equilibria owing to the different nature of the installed water-solubilizing groups.

The SAE-C[4]Ps bind pyridyl *N*-oxides **8a**-**f** with association constants larger than 10^5 M^{-1}. The increase in the surface area of the non-polar substituent at the *para*-position of the pyridyl *N*-oxide translates into a gain in the thermodynamic stability of the 1:1 inclusion complexes. The analysis of the free energies of binding and the surface area of the non-polar *para*-substituent of the guests allowed the quantification of the hydrophobic effect operating in these SAE-C[4]P complexes. The results obtained with these simple host-guest complexes are in line with those reported previously in literature using other methodologies, such as protein mutagenesis and phase-transfer experiments.

Remarkably, the SAE-C[4]P receptors display nanomolar affinities for the complexation of 4-phenyl pyridine *N*-oxide **8a** due to a combination of the binding characteristics of the pyridine *N*-oxide group and the formation of a cluster of aromatic interactions between the *para*-phenyl ring of **8a** and the *meso*-aromatic substituents at the upper section of the cavity of the receptors.

3.4 Experimental Section

3.4.1 General information and instruments

All reagents were obtained from commercial suppliers and used without further purification unless otherwise stated. All solvents were commercially obtained and used without further purification excess pyrrole that was distilled and freshly used. Dry solvents were taken from a solvent system MB SPS 800 or obtained after drying with appropriate desiccants. Routine ^{1}H NMR and $^{13}C\{^{1}H\}$ NMR spectra were recorded on a Bruker Avance 300 (300 MHz for ^{1}H NMR and 75 MHz for ^{13}C NMR), Bruker Avance 400 (400 MHz for ^{1}H NMR and 100 MHz for ^{13}C NMR), Bruker Avance 500 (500 MHz for ^{1}H NMR and 125 MHz for ^{13}C NMR) or Bruker Avance 500 with cryoprobe (500 MHz for ^{1}H NMR and 125 MHz for ^{13}C NMR). Deuterated solvents used are indicated in the characterization and chemical shifts are given in ppm. Residual solvent peaks were used as reference.[63] All NMR *J* values are given in Hz. COSY, NOESY, ROESY, HMQC and HMBC were recorded to help with the assignment of ^{1}H and ^{13}C signals. High-resolution mass spectra (HRMS) were obtained on a Bruker HPLC-TOF (MicroTOF Focus) and Bruker HPLC-QqTOF (MaXis Impact). Both with ESI as ionization mode. IR spectra were recorded on a Bruker Optics FTIR Alpha spectrometer equipped with a DTGS detector, KBr beam splitter at 4 cm^{-1} resolution using a one bounce ATR accessory with diamond windows. Melting points were measured on a MP70 Melting Point System Mettler Toledo instrument. ITC titrations were carried out on a Microcal VP-ITC MicroCalorimeter. Column chromatography purifications were performed with silica gel technical grade, pore size 60 Å, 230-400 mesh particle size, 40-63 µm particle size and Thin layer chromatography (TLC) analyses on silica gel 60 F254.

3.4.2 Synthesis and characterization data

Tetra-(4-iodophenyl) calix[4]pyrrole 1a: A solution of methyl 5-(4'-iodophenyl)-5-oxopentanoate **2a** (1 g, 3.01 mmol, 1 equiv.) in CH_2Cl_2 (10 mL) was stirred under Argon atmosphere and protected from the light by covering the flask with foil. Then, 37% HCl (0.51 mL, 6.02 mmol, 2 equiv.) was added dropwise over 5 min. Finally, distilled pyrrole (0.25 mL, 3.61 mmol, 1.2 equiv.) was added dropwise over 5 min. The mixture was stirred at r.t. under Argon atmosphere for 72 h. After that, the crude was concentrated, redissolved in CH_2Cl_2 (10 mL) and washed with aqueous saturated $NaHCO_3$ (2x10 mL) and water (10 mL). The organic layer was dried (Na_2SO_4), filtered and concentrated to dryness. The crude was purified by column chromatography on silica gel (50 g, 80:19:1 CH_2Cl_2:Hexane:MTBE) affording *αααα*-**1a** as a white solid. Compound *αααα*-**1a** was recrystallized from 3:2 CH_3OH:CH_2Cl_2 (108 mg, 0.07 mmol, 10% yield). Rf = 0.2 (80:19:1 CH_2Cl_2:Hexane:MTBE). ^{1}H NMR (400 MHz, $CDCl_3$, 298 K): *δ* (ppm) = 8.01 (br s, 4H); 7.53-7.51 (m, 8H); 6.95-6.93 (m, 8H); 5.81 (s, 8H); 3.62 (s, 12H); 2.29 (m, 16H); 1.59 (m, 8H). ^{13}C{^{1}H} NMR (125 MHz, $CDCl_3$, 298 K): *δ* (ppm) = 174.4; 145.4; 136.5; 135.2; 130.9; 106.7; 92.4; 51.7; 49.1; 38.4; 33.4; 20.3. HRMS (ESI-TOF) m/z: $[M-H]^-$ Calcd for $C_{64}H_{63}I_4N_4O_8$ 1523.0830; Found 1523.0835. FTIR *v* (cm^{-1}) = 3393; 2920; 1731; 1572; 1482; 1434; 1259; 1169; 1004; 770; 723; 507. M.p > 130°C (decompose).

Other calix[4]pyrrole isomers of **1a** were isolated from the crude. Compounds *αααβ*-**1a** and *ααββ*-**1a** were isolated in 5% and 3% yields, respectively. Characterization for *αααβ*-**1a**: Rf = 0.3 (80:19:1 CH_2Cl_2:Hexane:MTBE). ^{1}H NMR (400 MHz, $CDCl_3$, 298 K): *δ* (ppm) = 7.82 (br s, 2H); 7.63-7.61 (m, 2H); 7.55-7.52 (m, 6H); 7.21-7.19 (m, 2H); 6.93-6.88 (m, 6H); 5.92 (dd, *J* = 2.4 Hz; *J* = 2.4 Hz, 2H); 5.87 (dd, *J* = 2.4 Hz; *J* = 2.4 Hz, 2H); 5.83 (dd, *J* = 2.4 Hz; *J* = 2.4 Hz, 2H); 5.81 (dd, *J* = 2.4 Hz; *J* = 2.4 Hz, 2H); 3.64 (s, 3H); 3.62 (s, 9H); 2.34-2.14 (m, 16H); 1.57-1.33 (m, 8H). ^{13}C{^{1}H} NMR (125 MHz, $CDCl_3$, 298 K): *δ* (ppm) = 173.9; 173.8; 144.8; 137.4; 136.8; 136.8; 135.3; 135.0; 134.8; 134.5; 130.7; 130.6; 130.4; 107.0; 106.8; 106.6; 106.3; 92.5; 51.7; 49.0; 48.8; 34.0; 33.6; 20.5. HRMS (ESI-TOF) m/z: $[M+Na]^+$ Calcd for $C_{64}H_{64}I_4N_4O_8Na$ 1547.0795; Found 1547.0774. FTIR *v* (cm^{-1}) = 3396; 2947; 1734; 1483; 1413; 1565; 1170; 1145; 1005; 770; 726; 511. M.p > 125°C (decompose). Characterization for *ααββ*-**1a**: Rf = 0.6 (80:19:1 CH_2Cl_2:Hexane:MTBE). ^{1}H NMR (400 MHz, $CDCl_3$, 298 K): *δ* (ppm) = 7.56 (br s, 2H); 7.53-7.51 (m, 8H); 7.30 (br s, 2H); 6.93-6.91 (m, 8H); 5.89 (d, *J* = 2.4 Hz, 4H); 5.86 (d, *J* = 2.4 Hz, 4H); 3.64 (s, 12H); 2.34-2.08 (m, 16H); 1.50-1.46 (m, 8H). ^{13}C{^{1}H} NMR (125 MHz, $CDCl_3$, 298 K): *δ* (ppm) = 174.0; 144.3; 137.1; 135.3; 134.4; 130.3; 106.8; 106.5; 51.7; 48.9; 33.8; 20.5. HRMS (ESI-TOF) m/z: $[M+Na]^+$ Calcd for $C_{64}H_{64}I_4N_4O_8Na$ 1547.0795; Found 1547.0778. FTIR *v* (cm^{-1}) = 2963; 1734; 1570; 1483; 1413; 1260; 1146; 1002; 769; 729; 662; 512. M.p > 120°C (decompose).

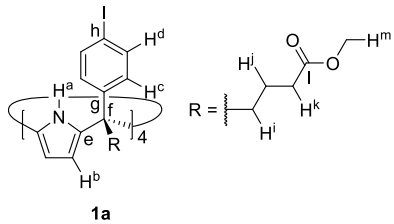

1a

Figure 16. Line-drawing structure of tetra-*α* **1a**.

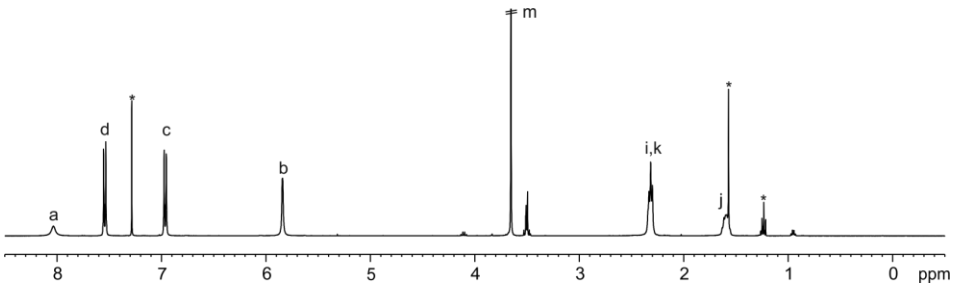

Figure 17. ^{1}H NMR (400 MHz, $CDCl_3$, 298 K) spectrum of tetra-*α* **1a**. See Figure 16 for proton assignment. *Residual solvent peaks.

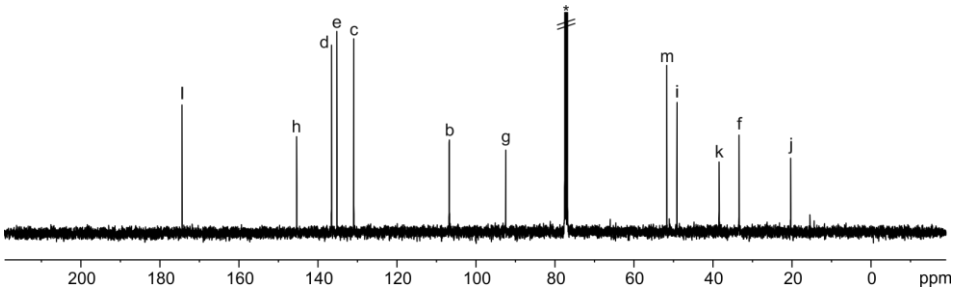

Figure 18. $^{13}C\{^{1}H\}$ NMR (125 MHz, $CDCl_3$, 298 K) spectrum of tetra-*α* **1a**. See Figure 16 for carbon assignment. *Residual solvent peak.

Reaction conditions for the synthesis of tetra-(4-iodophenyl) calix[4]pyrrole **1a**:

Table 3. Conditions for the synthesis of **1a**:

Entry	Acid (equiv.)	Additive[a] (equiv.)	Solvent (0.3-0.5 M)	Time (h)	Result (% yield)[c]
1	4 M HCl in dioxane (2)	-	CH_2Cl_2	72	**2a** and oligomers
2	4 M HCl in dioxane (2)	3	CH_2Cl_2	72	**2a** and oligomers
3	CH_3SO_3H (2/2)[b]	-	CH_3OH/CH_2Cl_2	24/48	*ααββ*- (10) and *αααβ*-**1a** (10)
4	37% HCl (2)	-	CH_2Cl_2	72	*ααββ*- (3), *αααβ*- (5) and *αααα*-**1a** (10)
5	37% HCl (2)	3	CH_2Cl_2	72	**2a** and oligomers

[a] Tricaprylmethylammonium chloride (mixture C_8-C_{10}; C_8 is dominant) or methyltributylammonium chloride. [b] Reaction performed in two steps: Reaction using 1) CH_3SO_3H in CH_3OH for 24 h and 2) CH_3SO_3H in CH_2Cl_2 for 48 h. [c] Reaction crudes were analyzed by ^1H NMR spectroscopy and yields are given for isolated compounds.

Reaction crude from the synthesis of **1a** using 37% HCl (entry 5, Table 3) was analyzed by HPLC (method: Spherisorb silica gel column (80 Å, 5 µm, 4.6 mm x 250 mm); 97.5:2.5 CH_2Cl_2:MTBE; flux = 1 mL/min; injections of 10 µL; detection at 250, 240 and 235 nm).

Table 4. Results obtained from Figure 19:

Peak	Retention time (min)	Relative area	Compound
1	3.78	1	*ααββ*-**1a**
2	4.29	2	*αααβ*-**1a**
3	5.10	5.5	**2a**
4	5.77	4	*αααα*-**1a**

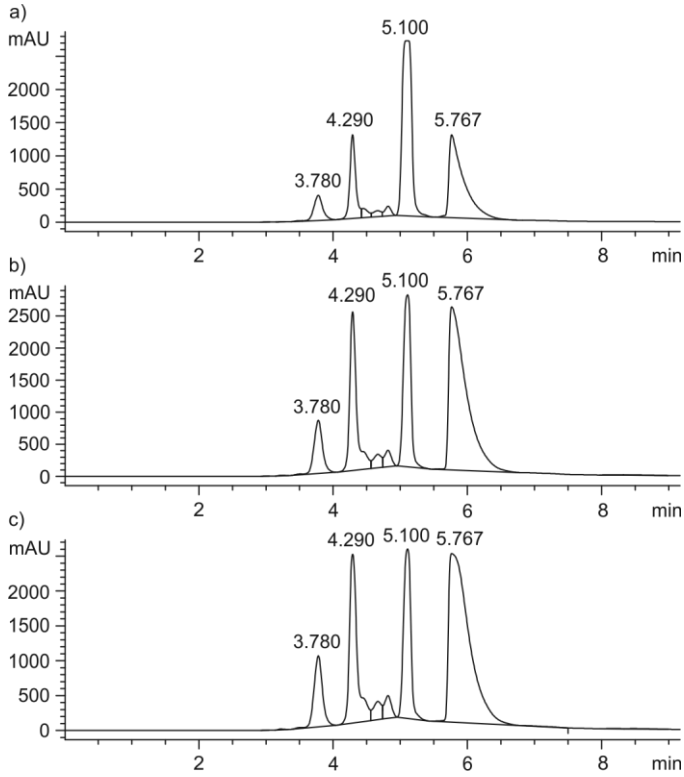

Figure 19. Chromatograms of the reaction crude (10 mg/mL solution) using different detection wavelengths: a) 250; b) 240 and c) 235 nm.

Tetra-(4-iodophenyl) calix[4]pyrrole 1b: Compound *αααα*-**1b** was synthesized following a methodology previously described by our research group.[40] 4-Iodophenyl 4'-chlorobutyl ketone **2b** (1 g, 3.10 mmol, 1 equiv.) and methyltributylammonium chloride (2.19 g, 9.30 mmol, 3 equiv.) were dissolved in dry CH_2Cl_2 (6.2 mL). The mixture was stirred at r.t. under Argon atmosphere and pyrrole (0.22 mL, 3.10 mmol, 1 equiv.) was added dropwise. HCl (2.33 mL from a 4 M solution in dioxane, 9.30 mmol, 3 equiv.) was added dropwise. The flask was covered with foil and stirred for 72 h. After that, the crude was diluted with CH_2Cl_2 (50 mL) and washed with aqueous saturated $NaHCO_3$ (2x50 mL) and water (50 mL). The organic layer was dried (Na_2SO_4), filtered and concentrated. The crude was suspended in 4:6 CH_2Cl_2:Hexane, filtered and purified by column chromatography on silica gel (80 g, 4:6 CH_2Cl_2:Hexane). The product was further purified by recrystallization from 1:1 CH_2Cl_2:CH_3OH affording *αααα*-**1b** as a white solid (119 mg, 0.08 mmol, 10% yield). Rf = 0.3 (4:6 CH_2Cl_2:Hexane). ^{1}H NMR (400 MHz, $CDCl_3$, 298 K): δ (ppm) = 7.54-7.52 (m, 8H); 7.27 (br s, 4H); 6.85-6.83 (m, 8H); 5.84 (s, 8H); 3.49 (t, J = 6.0 Hz, 8H); 2.24 (m, 8H); 1.73 (m, 8H); 1.34 (m, 8H). ^{13}C{^{1}H} NMR (100 MHz, $CDCl_3$, 298 K): δ (ppm) = 144.3; 137.0; 135.2; 130.4; 106.8; 92.6; 48.8; 44.8; 39.5; 32.9; 22.8. HRMS (ESI-TOF) m/z: $[M+H]^+$ Calcd for

$C_{60}H_{61}Cl_4I_4N_4$ 1484.9824; Found 1484.9780. FTIR *v* (cm^{-1}) = 2948; 2867; 1567; 1483; 1416; 1390; 1306; 1187; 1046; 1004; 768. M.p. > 110ºC (decompose).

Other calix[4]pyrrole isomers of **1b** were isolated from the crude. A mixture of *ααα*β-**1b** and *αα*ββ-**1b** was isolated in a total 30% yield.

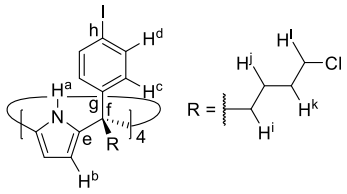

1b

Figure 20. Line-drawing structure of tetra-*α* **1b**.

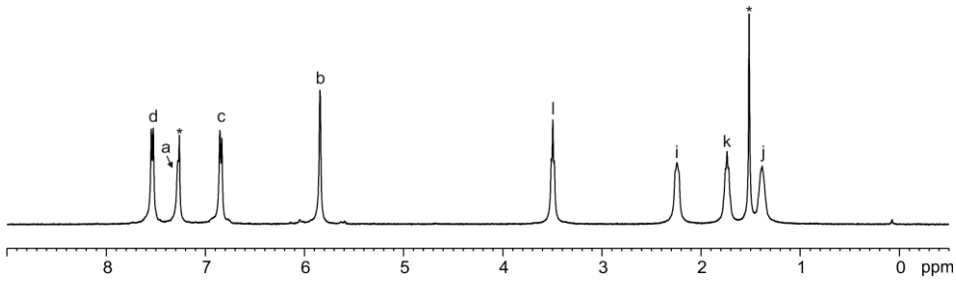

Figure 21. ^{1}H NMR (400 MHz, $CDCl_3$, 298 K) spectrum of tetra-*α* **1b**. See Figure 20 for proton assignment. *Residual solvent peaks.

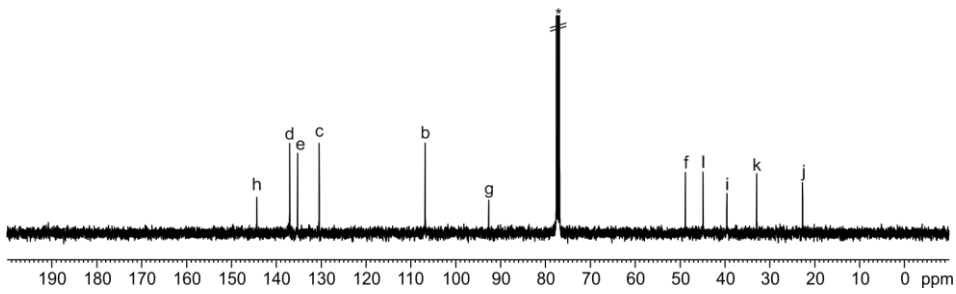

Figure 22. $^{13}C\{^1H\}$ NMR (125 MHz, $CDCl_3$, 298 K) spectrum of tetra-*α* **1b**. See Figure 20 for carbon assignment. *Residual solvent peak.

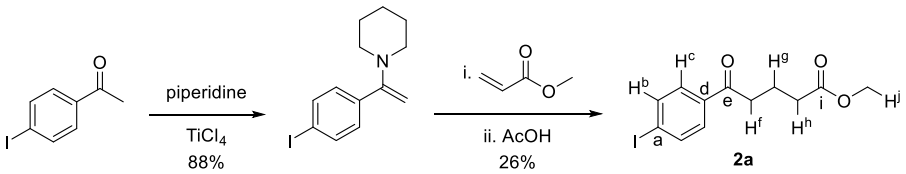

Scheme 3. Synthesis of 5-(4'-iodophenyl)-5-oxopentanoate **2a**.

5-(4'-Iodophenyl)-5-oxopentanoate 2a: Compound **2a** was synthesized following a procedure reported by our group.[40] 4-Iodoacetophenone (20 g, 81 mmol, 1 equiv.) was dissolved in piperidine (40 mL, 406 mmol, 5 equiv.) and hexane (500 mL) was added. The mixture was stirred at 0°C for 10 min. Then, $TiCl_4$ (5.4 mL, 48 mmol, 0.6 equiv.) was added slowly during 5 min. The reaction was stirred for 30 min more at 0°C and 24 h at r.t. Then, the solids were filtered off and washed with hexane (200 mL). The combined organic phases were concentrated under vacuum. The resulting enamine was obtained as brown oil (22.50 g, 71.80 mmol, 88% yield) and used in the next synthetic step. Step i. The enamine (18 g, 57.47 mmol, 1 equiv.) was dissolved in dried EtOH (180 mL). The solution was stirred under Argon atmosphere at r.t. and methyl acrylate (10.35 mL, 115 mmol, 2 equiv.) was added. Step ii. After six days, methanol (50 mL), water (50 mL) and acetic acid (27 mL) were added and the reaction was heated at 45°C for 1 h. The organic solvent was evaporated and EtOAc (100 mL) was added. The organic phase was washed with 1 N HCl (2x100 mL) and water (100 mL), dried (Na_2SO_4), filtered and concentrated to dryness. The product was purified by column chromatography on silica gel (8:2 CH_2Cl_2:Hexane → 8:1.9:0.1 CH_2Cl_2:Hexane:Et_2O) to afford **2a** as a white solid (5.50 g, 16.56 mmol, 26% yield). Rf = 0.3 (8:1.9:0.1 CH_2Cl_2:Hexane:Et_2O). ^{1}H NMR (400 MHz, $CDCl_3$, 298 K): δ (ppm) = 7.83-7.80 (m, 2H); 7.67-7.64 (m, 2H); 3.67 (s, 3H); 3.00 (t, J = 7.1 Hz, 2H); 2.43 (t, J = 7.1 Hz, 2H); 2.05 (m, 2H). ^{13}C{^{1}H} NMR (75 MHz, $CDCl_3$, 298 K): δ (ppm) = 198.8; 173.8; 138.1; 136.2; 129.6; 101.2; 51.8; 37.5; 33.1; 19.3. HRMS (ESI-TOF) m/z: $[M+Na]^+$ Calcd for $C_{12}H_{13}INaO_3$ 354.9802; Found 354.9818. FTIR v (cm^{-1}) = 2944; 2883; 1731; 1675; 1579; 1437; 1358; 1313; 1217; 1169; 1004; 874; 807; 714. M.p. = 70-71°C.

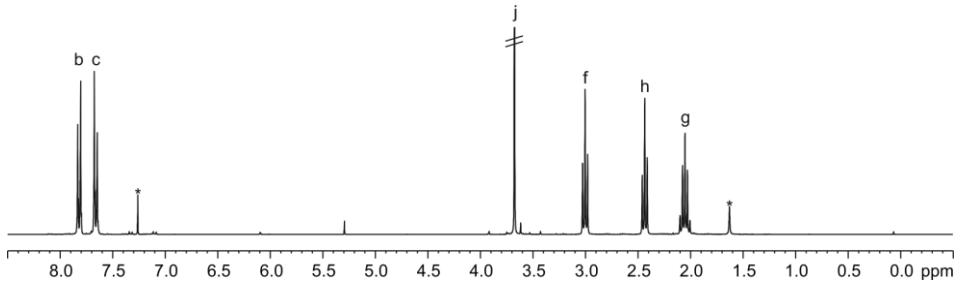

Figure 23. ^{1}H NMR (400 MHz, $CDCl_3$, 298 K) spectrum of **2a**. See Scheme 3 for proton assignment. *Residual solvent peaks.

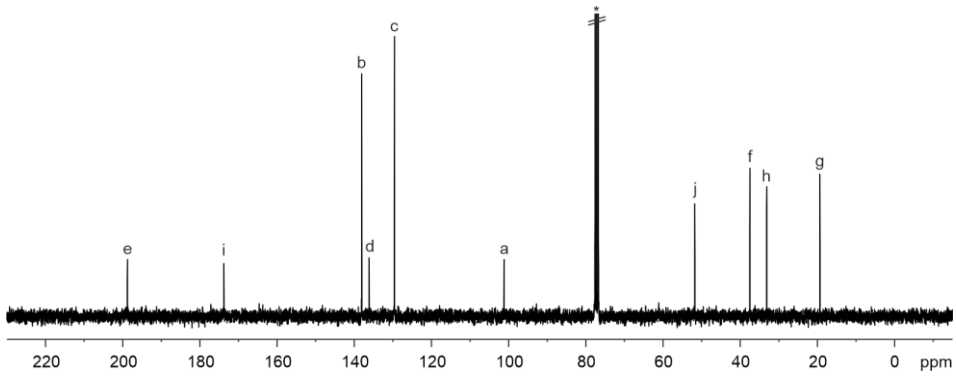

Figure 24. $^{13}C\{^{1}H\}$ NMR (75 MHz, $CDCl_3$, 298 K) spectrum of **2a**. See Scheme 3 for carbon assignment. *Residual solvent peak.

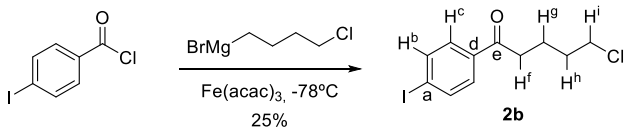

Scheme 4. Synthesis of 4-iodophenyl 4'-chlorobutyl ketone **2b**.

4-Iodophenyl 4'-chlorobutyl ketone 2b: Compound **2b** was synthesized following a similar procedure described in literature.[64,65] Part 1. Magnesium turnings (0.46 g, 18.76 mmol, 1 equiv.) were added to an oven-dried round-bottom flask and purged with Argon. Dry THF (2 mL) was added and the mixture was sonicated for 10 min. Then, the flask was connected to an addition funnel and it was slowly stirred under Argon atmosphere. 1-Chloro-4-bromo butane (2.16 mL, 18.76 mmol, 1 equiv.) was added to the addition funnel and diluted with dry THF (12 mL). The 1-chloro-4-bromo butane solution was added dropwise to the magnesium for 1 h. The temperature was controlled with an ice bath. After the addition, dry THF (4 mL) was added to the addition funnel and added dropwise to the reaction. The reaction was stirred at r.t. for 30 min and the magnesium was totally consumed. Part 2. 4-Iodobenzoyl chloride (5 g, 18.76 mmol, 1 equiv.), $Fe(acac)_3$ (0.33 g, 0.94 mmol, 0.05 equiv.) and dry THF (13 mL) were added to an oven-dried round-bottom flask. The mixture was stirred under Argon atmosphere and cooled at -78ºC. The freshly prepared Grignard reagent was added dropwise for 5 min. The reaction flask was covered with foil. THF (4 mL) was added to the flask of the Grignard reagent and added to the reaction. The reaction was stirred at -78ºC for 1 h and at r.t. for 23 h. After that, the reaction was stopped and water (30 mL) was added. The crude was extracted with CH_2Cl_2 (3x30 mL) and the organic layer was washed with 1 N HCl (30 mL) and water (2x30 mL). The organic layer was dried, filtered (Na_2SO_4) and concentrated. A mixture of 4:6 CH_2Cl_2:Hexane was added to the crude and filtered. The crude was purified by column chromatography on silica gel (400 g, 4:6 CH_2Cl_2:Hexane) affording the product as a white solid (1.51 g, 4.69 mmol, 25% yield). Rf = 0.2 (4:6

CH_2Cl_2:Hexane). ^{1}H NMR (400 MHz, $CDCl_3$, 298 K): δ (ppm) = 7.84-7.82 (m, 2H); 7.67-7.65 (m, 2H); 3.58 (t, J = 6.2 Hz, 2H); 2.97 (t, J = 6.8 Hz, 2H); 1.88 (m, 4H). $^{13}C\{^1H\}$ NMR (100 MHz, $CDCl_3$, 298 K): δ (ppm) = 199.0; 138.1; 136.2; 129.6; 101.1; 44.8; 37.6; 32.1; 21.5. HRMS (ESI-TOF) m/z: $[M+Na]^+$ Calcd for $C_{11}H_{12}ClOINa$ 344.9514; Found 344.9514. FTIR ν (cm^{-1}) = 2943; 2898; 1689; 1581; 1560; 1467; 1390; 1293; 1178; 1058; 1005; 974. M.p. = 74-75°C.

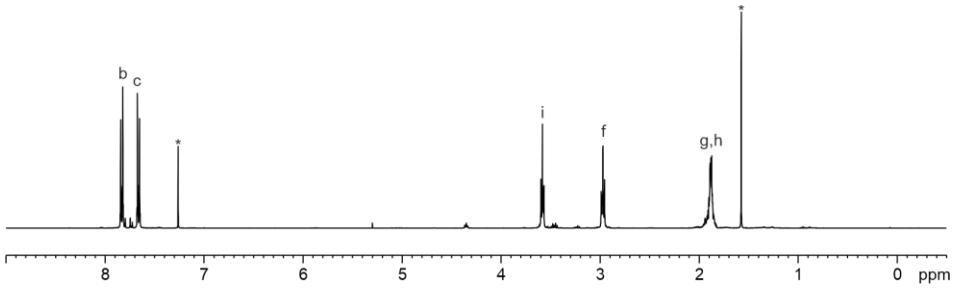

Figure 25. ^{1}H NMR (400 MHz, $CDCl_3$, 298 K) spectrum of **2b**. See Scheme 4 for proton assignment. *Residual solvent peaks.

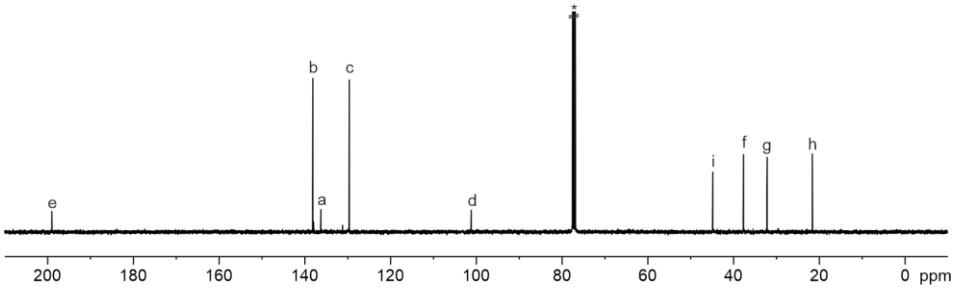

Figure 26. $^{13}C\{^1H\}$ NMR (125 MHz, $CDCl_3$, 298 K) spectrum of **2b**. See Scheme 4 for carbon assignment. *Residual solvent peak.

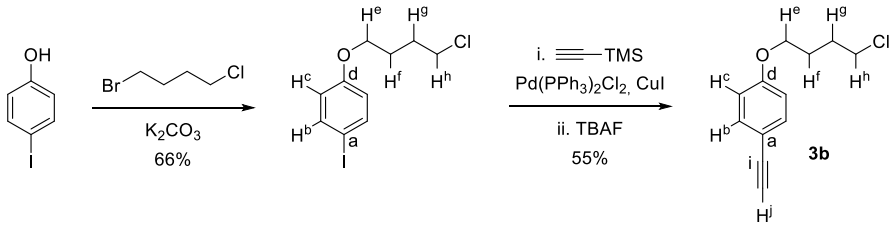

Scheme 5. Synthesis of (1-chlorobutyloxy-4-ethynyl)benzene **3b**.

1-(4'-Chlorobutyloxy)-4-iodobenzene: 4-Iodophenol (0.50 g, 2.27 mmol, 1 equiv.) was dissolved in dry DMF (50 mL) and stirred at r.t. under Argon atmosphere. K_2CO_3 (0.47 g, 3.41 mmol, 1.5 equiv.) was added and the reaction was stirred for 2 h. 1-Bromo-4-chlorobutane (0.31 mL, 2.73 mmol, 1.2 equiv.) was added and the reaction was stirred for 22 h. After that, the reaction was

stopped and 1 N HCl was added until pH = 5. The compound was extracted by adding CH_2Cl_2 and water (4x15 mL of CH_2Cl_2 and 4x15 mL of water). The organic layer was washed with water (3x50 mL), dried (Na_2SO_4), filtered and concentrated. The crude was purified by silica gel column chromatography (20 g, 3:7 CH_2Cl_2:Hexane) affording the product as a colorless oil (0.47 g, 1.51 mmol, 66% yield). Rf = 0.5 (3:7 CH_2Cl_2:Hexane). ^{1}H NMR (300 MHz, $CDCl_3$, 298 K): δ (ppm) = 7.56-7.53 (m, 2H); 6.68-6.65 (m, 2H); 3.96 (t, J = 5.6 Hz, 2H); 3.61 (t, J = 6.1 Hz, 2H); 1.98-1.93 (m, 4H). ^{13}C{^{1}H} NMR (75 MHz, $CDCl_3$, 298 K): δ (ppm) = 158.9; 138.4; 117.0; 82.9; 67.2; 44.8; 29.4; 26.7. HRMS (ESI-TOF) m/z: $[M]^{\cdot+}$ Calcd for $C_{10}H_{12}ClOI$ 309.9616; Found 309.9621. FTIR ν (cm^{-1}) = 2955; 2873; 1585; 1572; 1485; 1469; 1441; 1280; 1239; 1174; 1100; 1049.

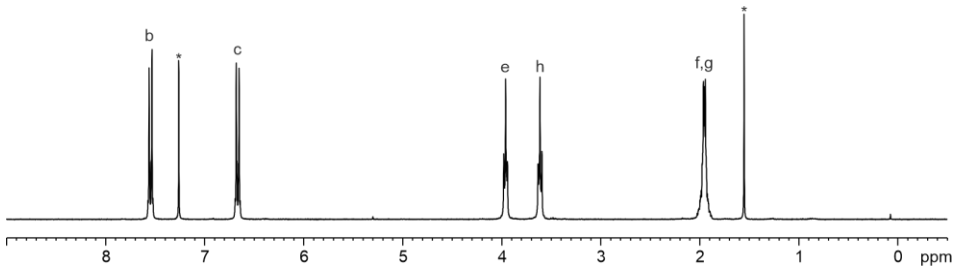

Figure 27. ^{1}H NMR (300 MHz, $CDCl_3$, 298 K) spectrum of 1-(4'-chlorobutyloxy)-4-iodobenzene. See Scheme 5 for proton assignment. *Residual solvent peaks.

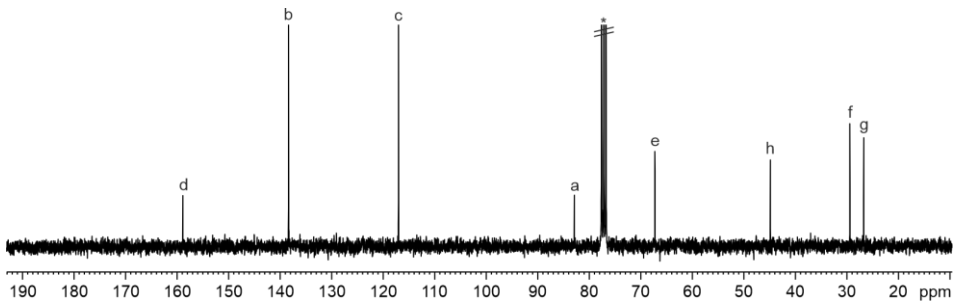

Figure 28. ^{13}C{^{1}H} NMR (75 MHz, $CDCl_3$, 298 K) spectrum of 1-(4'-chlorobutyloxy)-4-iodobenzene. See Scheme 5 for carbon assignment. *Residual solvent peak.

(1-Chlorobutyloxy-4-ethynyl)benzene 3b: Step i. 1-(4'-Chlorobutyloxy)-4-iodobenzene (1 g, 3.22 mmol, 1 equiv.), $Pd(PPh_3)_2Cl_2$ (170 mg, 0.24 mmol, 0.07 equiv.) and CuI (170 mg, 0.90 mmol, 0.28 equiv.) were kept under Argon atmosphere. Dry and degassed THF (32 mL) and DIPEA (1.68 mL, 9.66 mmol, 3 equiv.) were added. Ethynyltrimethylsilane (1.37 mL, 9.66 mmol, 3 equiv.) was added. The reaction was stirred at 45°C for 3 h. After that, the reaction was stopped and the crude was concentrated. The crude was redissolved in CH_2Cl_2 (50 mL) and washed with 1 N HCl (50 mL), brine (50 mL) and water (50 mL). The organic layer was dried (Na_2SO_4), filtered and concentrated. The crude was suspended in 2:8 CH_2Cl_2:Hexane, filtered and purified by column chromatography on silica gel (20 g, 2:8 CH_2Cl_2:Hexane). The protected alkyne was isolated as an

orange oil (697 mg, 2.48 mmol, 77% yield). Step ii. The protected alkyne (697 mg, 2.48 mmol, 1 equiv.) was dissolved in THF (20 mL). TBAF (2.73 mL, 2.73 mmol, 1.1 equiv.) was added dropwise. The reaction was stirred at r.t. under Argon atmosphere for 15 min. After that, the reaction was quenched with NH_4Cl (20 mL). EtOAc (20 mL) and water (20 mL) were added. THF was removed under vacuum. The crude was extracted with EtOAc (3x20 mL) and the organic layer was washed with brine (20 mL), dried (Na_2SO_4), filtered and concentrated. The crude was suspended in 2:8 CH_2Cl_2:Hexane, filtered and purified by silica gel column chromatography (8 g, 2:8 CH_2Cl_2:Hexane). The product was isolated as a pale yellow solid (284 mg, 1.36 mmol, 55% yield). Rf = 0.3 (2:8 CH_2Cl_2:Hexane). ^{1}H NMR (400 MHz, $CDCl_3$, 298 K): δ (ppm) = 7.43-7.41 (m, 2H); 6.84-6.82 (m, 2H); 4.00 (t, J = 5.8 Hz, 2H); 3.62 (t, J = 6.1 Hz, 2H); 2.99 (s, 1H); 1.99-1.94 (m, 4H). $^{13}C\{^1H\}$ NMR (100 MHz, $CDCl_3$, 298 K): δ (ppm) = 159.4; 133.8; 114.6; 114.4; 83.8; 75.9; 67.2; 44.8; 29.4; 26.7. HRMS (ESI-TOF) m/z: $[M+H]^+$ Calcd for $C_{12}H_{14}ClO$ 209.0728; Found 209.0723. FTIR v (cm^{-1}) = 2960; 2939; 2906; 2869; 2100; 1604; 1505; 1398; 1293; 1247; 1174; 1034. M.p. = 53-55°C.

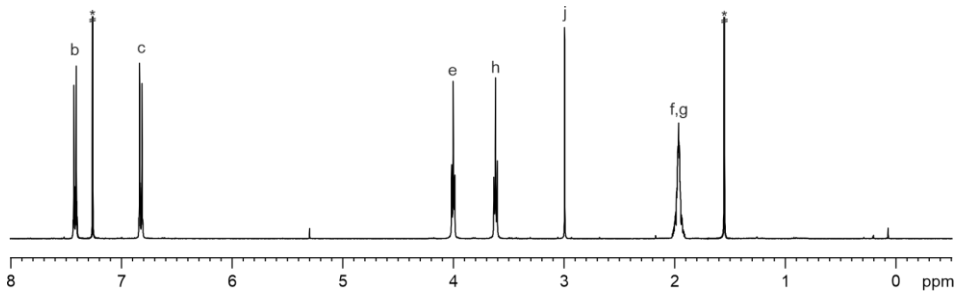

Figure 29. ^{1}H NMR (400 MHz, $CDCl_3$, 298 K) spectrum of **3b**. See Scheme 5 for proton assignment. *Residual solvent peaks.

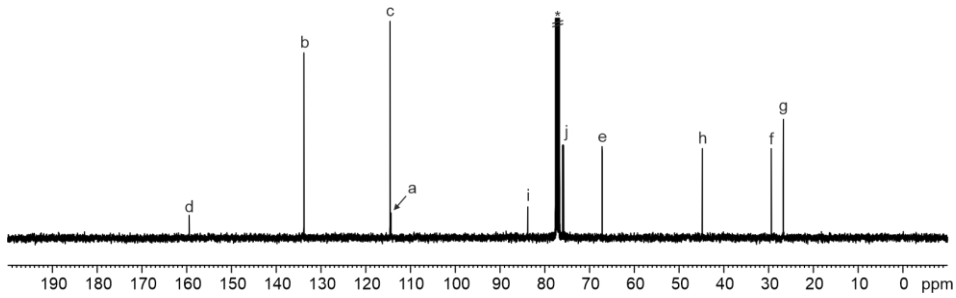

Figure 30. $^{13}C\{^1H\}$ NMR (100 MHz, $CDCl_3$, 298 K) spectrum of **3b**. See Scheme 5 for carbon assignment. *Residual solvent peak.

Chapter 3

Octa-ester super aryl-extended calix[4]pyrrole 4a: Tetra-*α* **1a** (50 mg, 0.03 mmol, 1 equiv.), $Pd(PPh_3)_2Cl_2$ (2.88 mg, 0.004 mmol, 0.03 equiv.), CuI (1.25 mg, 0.007 mmol, 0.05 equiv.) and methyl (4-ethynylphenoxy)acetate **3a** (37.40 mg, 0.20 mmol, 1.5 equiv.) were dissolved in dry THF (5 mL). The mixture was stirred under Argon atmosphere and dry diisopropylamine (5 mL) was added. The reaction was stirred at 45°C for 5 h. After that, the reaction was stopped and the crude was concentrated. The crude was redissolved in CH_2Cl_2 (10 mL) and washed with 0.5 N HCl (10 mL), brine (10 mL) and water (10 mL). The organic layer was dried (Na_2SO_4), filtered and concentrated. The crude was purified by column chromatography on silica gel (6 g silica gel, 98:2 → 95:5 CH_2Cl_2:MTBE) affording **4a** as a white solid. The product was recrystallized from 3:1 CH_3OH:Et_2O (38.40 mg, 0.02 mmol, 70% yield). Rf = 0.25 (98:2 CH_2Cl_2:MTBE). ^{1}H NMR (400 MHz, $CDCl_3$, 298 K): *δ* (ppm) = 8.01 (br s, 4H); 7.47-7.45 (m, 8H); 7.37-7.35 (m, 8H); 7.20-7.18 (m, 8H); 6.87-6.85 (m, 8H); 5.86 (s, 8H); 4.65 (s, 8H); 3.81 (s, 12H); 3.64 (s, 12H); 2.36-2.32 (m, 8H); 2.31 (dd, *J* = 6.6 Hz, *J* = 6.6 Hz, 8H); 1.63-1.59 (m, 8H). ^{13}C{^{1}H} NMR (100 MHz, $CDCl_3$, 298 K): *δ* (ppm) = 174.4; 169.2; 157.8; 145.6; 135.4; 133.3; 130.7; 128.8; 121.7; 117.0; 114.8; 106.7; 89.0; 88.6; 65.4; 52.5; 51.7; 49.3; 38.6; 33.6; 20.5. HRMS (ESI-TOF) m/z: $[M+Na]^+$ Calcd for $C_{108}H_{100}N_4O_{20}Na$ 1795.6823; Found 1795.6824. FTIR *ν* (cm^{-1}) = 3368; 2951; 1733; 1513; 1435; 1284; 1203; 1174; 1076; 830; 773; 538. M.p > 185°C (decompose).

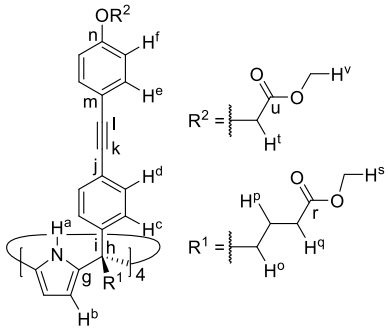

4a

Figure 31. Line-drawing structure of octa-ester **4a**.

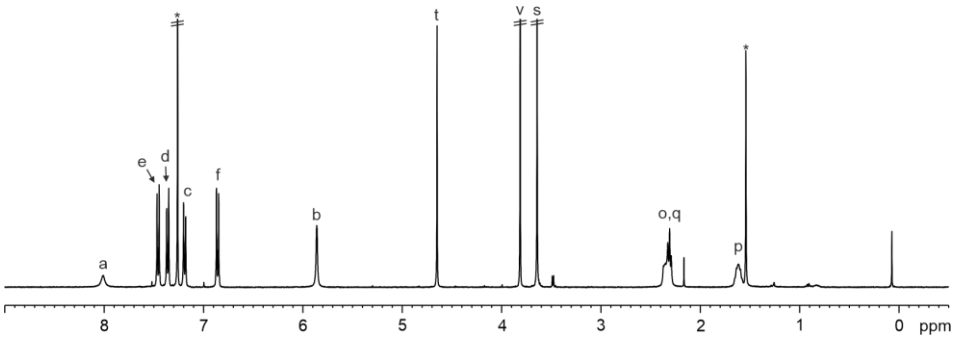

Figure 32. ^{1}H NMR (400 MHz, $CDCl_3$, 298 K) spectrum of **4a**. See Figure 31 for proton assignment. *Residual solvent peaks.

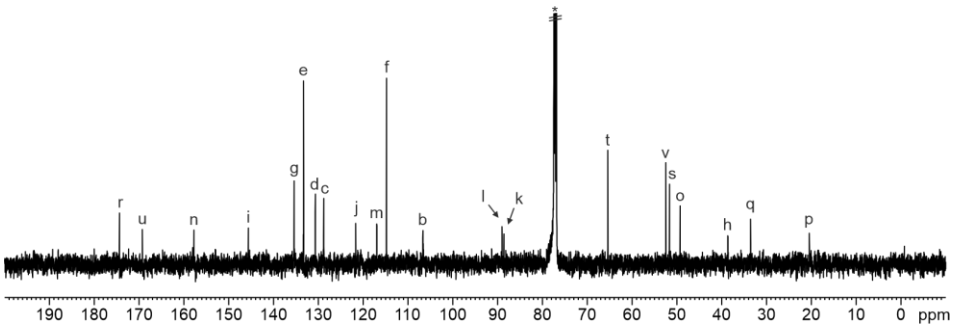

Figure 33. $^{13}C\{^{1}H\}$ NMR (100 MHz, $CDCl_3$, 298 K) spectrum of **4a**. See Figure 31 for carbon assignment. *Residual solvent peak.

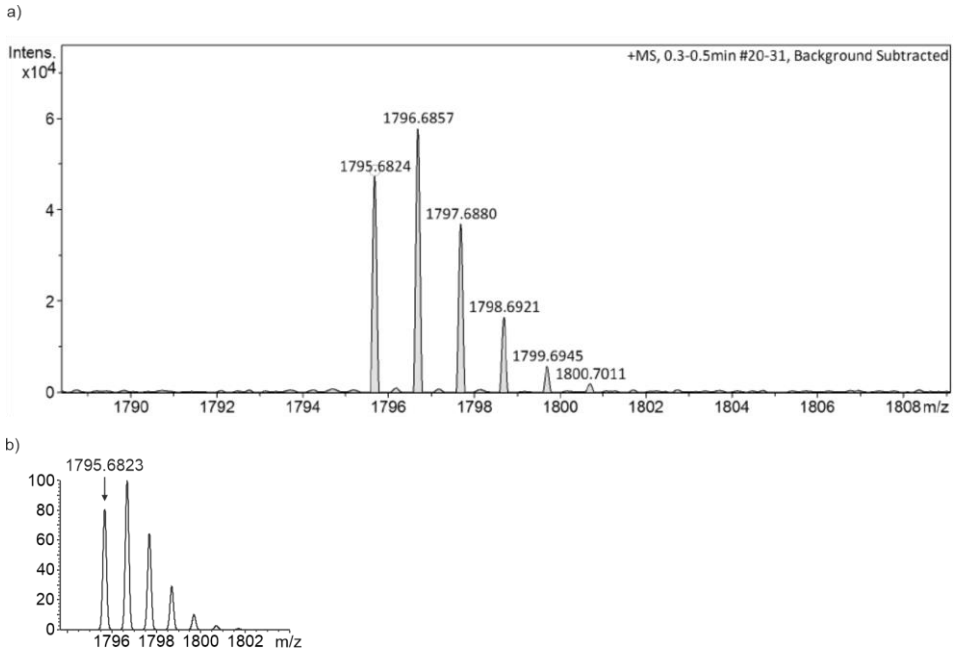

Figure 34. a) Experimental and b) theoretical isotopic distributions of $[M+Na]^+$. The exact mass for the monoisotopic peak in a) and b) is indicated.

Octa-chloro super aryl-extended calix[4]pyrrole 4b: Tetra-*α* **1b** (52 mg, 0.035 mmol, 1 equiv.), (1-chlorobutyloxy-4-ethynyl)benzene **3b** (43.40 mg, 0.208 mmol, 1.5 equiv.), $Pd(PPh_3)_2Cl_2$ (3.07 mg, 0.004 mmol, 0.03 equiv.) and CuI (1.33 mg, 0.007 mmol, 0.05 equiv.) were kept under Argon atmosphere. Dry and degassed THF (5 mL) and diisopropylamine (5 mL) were added. The reaction was stirred at 45°C for 3.5 h. After that, the reaction was stopped and the crude was concentrated. The crude was redissolved in CH_2Cl_2 (10 mL) and washed with 0.5 N HCl (10 mL), brine (10 mL) and water (10 mL). The organic layer was dried (Na_2SO_4), filtered and concentrated. The crude was purified by column chromatography on silica gel (6 g, 1:1 → 8:2 CH_2Cl_2:Hexane, the crude was adsorbed on silica gel) affording the product as white solid. The product was sonicated in CH_3CN (3 mL) and washed with extra CH_3CN (2 mL) (37.98 mg, 0.021 mmol, 60% yield). Rf = 0.6 (8:2 CH_2Cl_2:Hexane). ^1H NMR (400 MHz, $CDCl_3$, 298 K): *δ* (ppm) = 7.44-7.42 (m, 8H); 7.40 (br s, 4H); 7.39-7.37 (m, 8H); 7.10-7.08 (m, 8H); 6.82-6.80 (m, 8H); 5.88 (d, *J* = 2.2 Hz, 8H); 4.00 (t, *J* = 5.5 Hz, 8H); 3.63 (t, *J* = 6.0 Hz, 8H); 3.50 (t, *J* = 6.6 Hz, 8H); 2.32-2.28 (m, 8H); 2.00-1.94 (m, 16H); 1.79-1.72 (m, 8H); 1.45-1.37 (m, 8H). $^{13}C\{^1H\}$ NMR (100 MHz, $CDCl_3$, 298 K): *δ* (ppm) = 159.0; 144.5; 135.5; 133.3; 131.0; 128.3; 122.1; 115.6; 114.6; 106.6; 89.7; 88.0; 67.2; 48.9; 44.9; 44.8; 39.6; 33.1; 29.4; 26.8; 22.7. MS (MALDI-TOF) m/z: $[M-C_4H_8Cl]^+$ Calcd for $C_{104}H_{100}Cl_7N_4O_4$ 1713.6; Found 1713.4. FTIR *ν* (cm^{-1}) = 2952; 2871; 1607; 1569; 1515; 1473; 1286; 1253; 1174; 1050; 1030; 833. M.p. > 205°C (decompose).

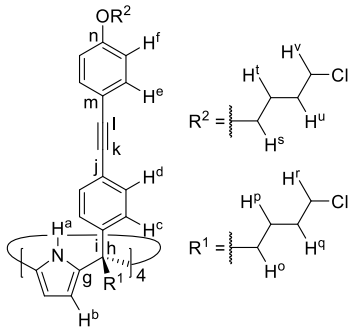

4b

Figure 35. Line-drawing structure of octa-chloro **4b**.

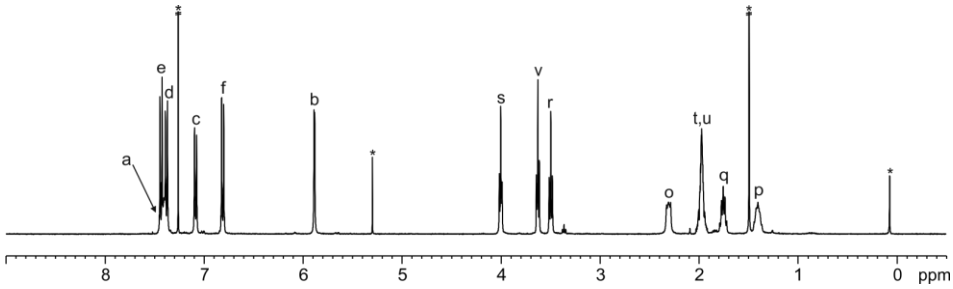

Figure 36. ^{1}H NMR (400 MHz, $CDCl_3$, 298 K) spectrum of **4b**. See Figure 35 for proton assignment. *Residual solvent peaks.

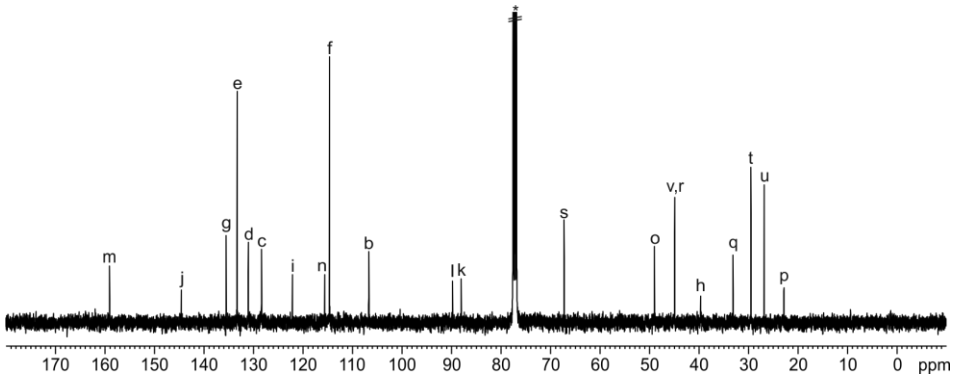

Figure 37. $^{13}C\{^{1}H\}$ NMR (100 MHz, $CDCl_3$, 298 K) spectrum of **4b**. See Figure 35 for carbon assignment. *Residual solvent peak.

Octa-acid super aryl-extended calix[4]pyrrole 5: Octa-ester calix[4]pyrrole **4a** (38 mg, 0.02 mmol, 1 equiv.) was dissolved in THF (10 mL). LiOH (8.21 mg, 0.34 mmol, 2 equiv.) was dissolved in water (3 mL) and added to the previous solution. The reaction was stirred at 40°C for 24 h. After that, the reaction was stopped and the organic solvent was evaporated under reduced pressure.

Additional water (7 mL) was added to the crude and the aqueous layer was washed with CH_2Cl_2 (10 mL). Then, the aqueous layer was acidified with 1 N HCl until pH = 3 and the white precipitate was extracted with EtOAc (3x10 mL). The organic layer was dried (Na_2SO_4), filtered and concentrated affording the product as a white solid (34 mg, 0.02 mmol, 96% yield). ^{1}H NMR (400 MHz, $(CD_3)_2CO$, 298 K): δ (ppm) = 8.44 (br s, 4H); 7.51-7.49 (m, 8H); 7.39-7.36 (m, 8H); 7.08-7.06 (m, 8H); 6.90-6.88 (m, 8H); 6.10 (d, J = 2.4 Hz, 8H); 4.78 (s, 8H); 2.48-2.44 (m, 8H); 2.28 (dd, J = 7.2 Hz, J = 7.2 Hz, 8H); 1.45-1.41 (m, 8H). ^{13}C{^{1}H} NMR (100 MHz, $(CD_3)_2CO$, 298 K): δ (ppm) = 174.6; 170.4; 159.3; 147.2; 137.6; 133.8; 131.9; 130.0; 122.8; 116.6; 115.8; 106.5; 90.3; 88.4; 65.5; 49.3; 40.6; 34.2; 21.5. HRMS (ESI-TOF) m/z: $[M-3H]^{3-}$ Calcd for $C_{100}H_{81}N_4O_{20}$ 552.5154; Found 552.5176. FTIR v (cm^{-1}) = 3409; 2925; 1703; 1601; 1514; 1407; 1174; 1108; 1068; 827; 768; 527. M.p > 170°C (decompose).

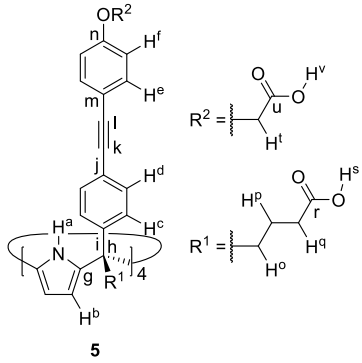

5

Figure 38. Line-drawing structure of octa-acid **5**.

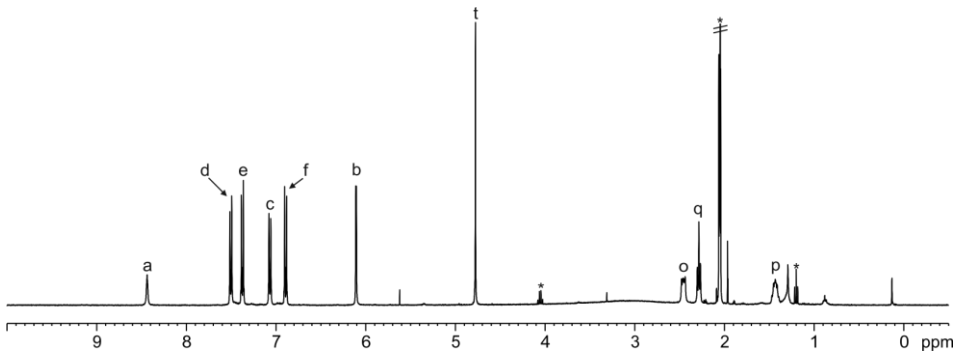

Figure 39. ^{1}H NMR (400 MHz, $(CD_3)_2CO$, 298 K) spectrum of **5**. See Figure 38 for proton assignment. *Residual solvent peaks.

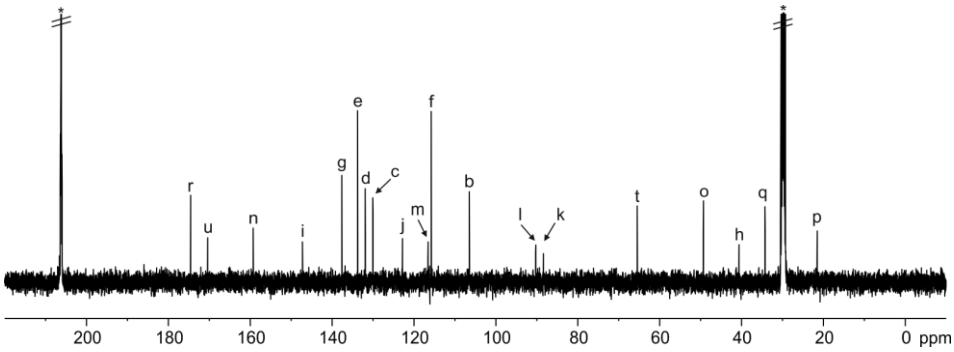

Figure 40. ^{1}H NMR (100 MHz, $(CD_3)_2CO$, 298 K) spectrum of **5**. See Figure 38 for carbon assignment. *Residual solvent peaks.

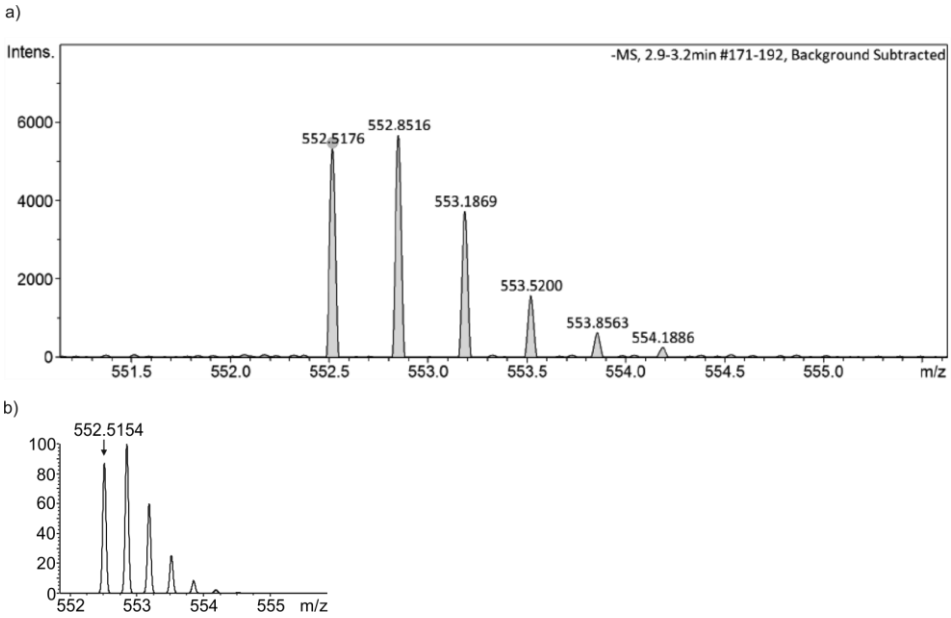

Figure 41. a) Experimental and b) theoretical isotopic distributions of $[M-3H]^{3-}$. The exact mass for the monoisotopic peak in a) and b) is indicated.

Octa-pyridinium octa-chloride super aryl-extended calix[4]pyrrole 6: Octa-chloro super aryl-extended calix[4]pyrrole **4b** (30 mg, 0.02 mmol, 1 equiv.) was added to a dry-oven schlenk flask and kept under Argon atmosphere. Fresh distilled and dry pyridine (3 mL) was added and the reaction was stirred at 110°C overnight. After that, the reaction was stopped and allowed to reach r.t. The crude was concentrated and CH_2Cl_2 (5 mL) was added and sonicated. The crude was filtered and washed with CH_2Cl_2 (3 mL) and hexane (3 mL) affording the product as a pale yellow solid (37 mg, 0.015 mmol, 90% yield). ^{1}H NMR (500 MHz with cryoprobe, CD_3OD, 298 K): δ (ppm) = 9.10-9.04 (m, 8H); 8.97-8.92 (m, 8H), 8.60-8.56 (m, 16H); 8.15-8.10 (m, 8H); 8.08-8.04 (m, 8H);

7.43-7.41 (m, 16H); 7.06-7.04 (m, 8H); 6.91-6.89 (m, 8H); 5.91 (s, 8H); 4.77-4.74 (m, 8H); 4.58-4.56 (m, 8H); 4.09 (t, *J* = 6.0 Hz, 8H); 2.50-2.48 (m, 8H); 2.27-2.22 (m, 8H); 2.00-1.97 (m, 8H); 1.91-1.88 (m, 8H); 1.26-1.22 (m, 8H). $^{13}C\{^{1}H\}$ NMR (125 MHz with cryoprobe, CD_3OD, 298 K): *δ* (ppm) = 160.4; 147.0; 146.8; 146.0; 145.9; 137.9; 134.1; 131.8; 129.9; 129.6; 129.5; 123.3; 116.7; 115.8; 106.8; 90.6; 88.6; 68.3; 62.8; 49.9; 40.2; 32.8; 29.5; 27.0; 23.2. HRMS (ESI-TOF) m/z: $[M-8Cl]^{8+}$ Calcd for $C_{148}H_{148}N_{12}O_4$ 269.6463; Found 269.6456. FTIR *v* (cm^{-1}) = 3209; 2936; 2865; 1632; 1601; 1513; 1485; 1283; 1246; 1174; 837; 774. M.p. > 235°C (decompose).

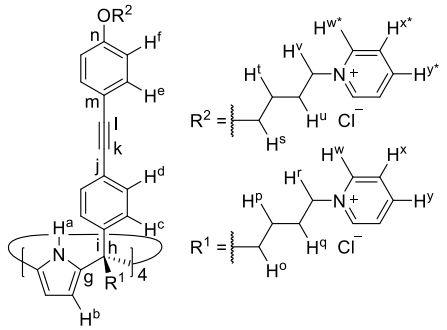

6

Figure 42. Line-drawing structure of octa-pyridinium **6**.

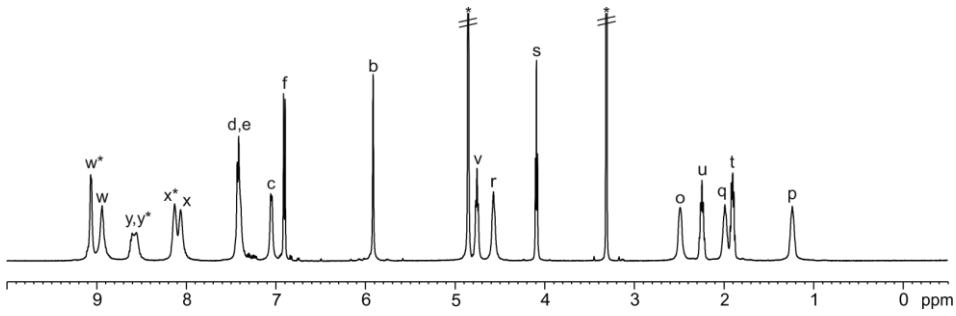

Figure 43. ^{1}H NMR (500 MHz with cryoprobe, CD_3OD, 298 K) spectrum of **6**. See Figure 42 for proton assignment. *Residual solvent peaks.

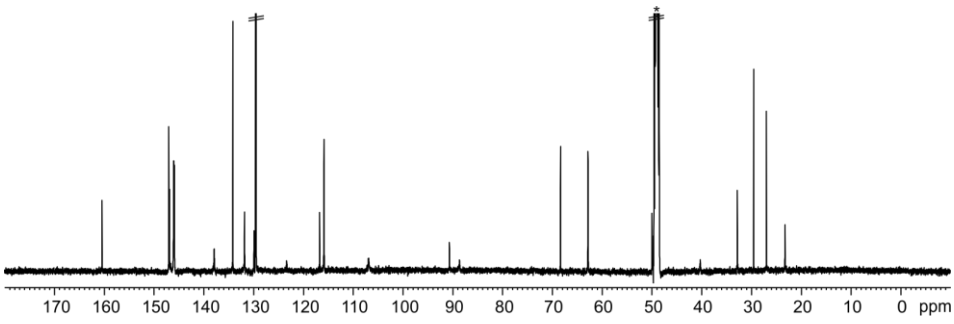

Figure 44. ^{1}H NMR (125 MHz with cryoprobe, CD_3OD, 298 K) spectrum of **6**. *Residual solvent peak.

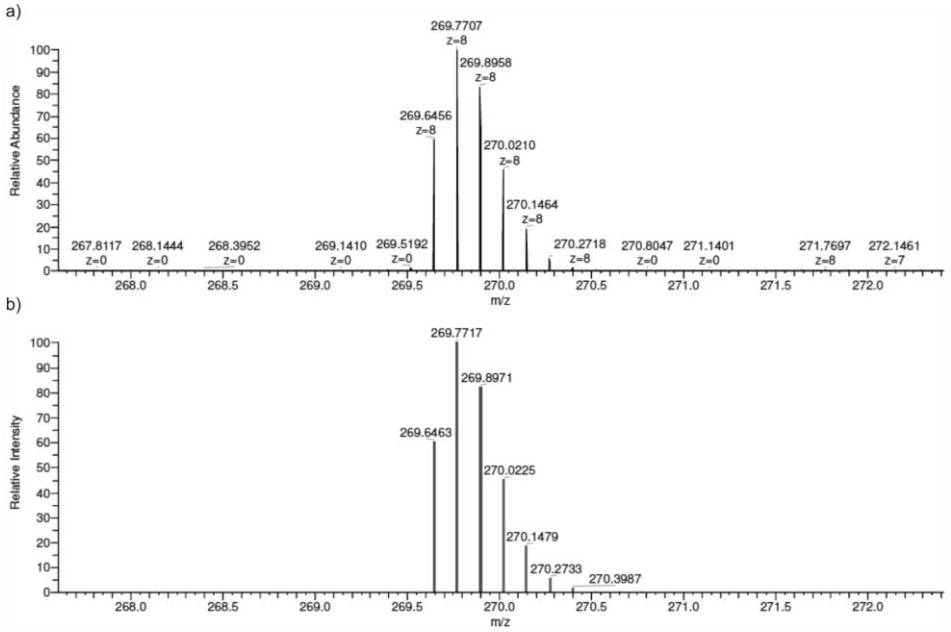

Figure 45. a) Experimental and b) theoretical isotopic distributions of $[M\text{-}8Cl]^{8+}$. The exact mass for the monoisotopic peak in a) and b) is indicated.

Octa-(1-methyl-1H-imidazolium) octa-chloride super aryl-extended calix[4]pyrrole 7: Octa-chloro super aryl-extended calix[4]pyrrole **4b** (35 mg, 0.02 mmol, 1 equiv.) was added to a dry-oven schlenk flask and kept under Argon atmosphere. 1-Methyl-1H-imidazole (3 mL) was added and the reaction was stirred at r.t. for 1 h. After that, the reaction was stirred at 110°C overnight. Next, the reaction was stopped and allowed to reach r.t. The crude was concentrated to dryness and acetone (3 mL) was added and sonicated. The crude was filtered and the solid was washed with acetone (2x3 mL) and CH_2Cl_2 (2x3 mL) affording the product as a pale brown solid (40 mg, 0.016 mmol, 84% yield). ^{1}H NMR (500 MHz with cryoprobe, CD_3OD, 298 K): δ (ppm) = 9.00-8.90 (m, 8H); 7.69-7.67 (m, 4H); 7.57-7.42 (m, 24H); 7.10-7.00 (m, 8H); 6.90-6.89 (m, 8H); 5.91 (s, 8H);

4.33 (t, *J* = 7.2 Hz; 8H); 4.13-4.08 (m, 16H); 3.94-3.89 (m, 24H); 2.47 (s, 8H); 2.11 (t, *J* = 7.4 Hz, 8H); 1.87-1.84 (m, 16H); 1.19 (s, 8H). $^{13}C\{^{1}H\}$ NMR (125 MHz with cryoprobe, CD_3OD, 298 K): *δ* (ppm) = 160.5; 146.6; 137.9; 134.2; 131.8; 129.9; 125.0; 124.9; 123.6; 116.6; 115.8; 106.9; 90.6; 88.6; 68.3; 64.3; 54.8; 50.6; 40.3; 36.5; 31.4; 28.1; 27.1; 23.3. HRMS (ESI-TOF) m/z: $[M-8Cl]^{8+}$ Calcd for $C_{140}H_{156}N_{20}O_4$ 272.6572; Found 272.6564. FTIR *v* (cm^{-1}) = 3366; 3224; 3075; 2947; 1601; 1566; 1513; 1244; 1166; 1017; 833; 620. M.p. > 138°C (decompose).

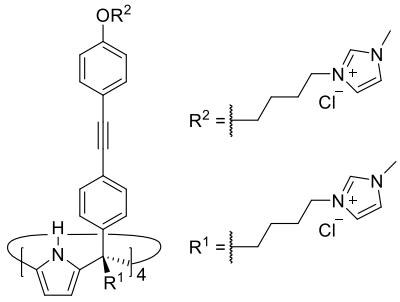

7

Figure 46. Line-drawing structure of octa-(1-methyl-1H-imidazolium) **7**.

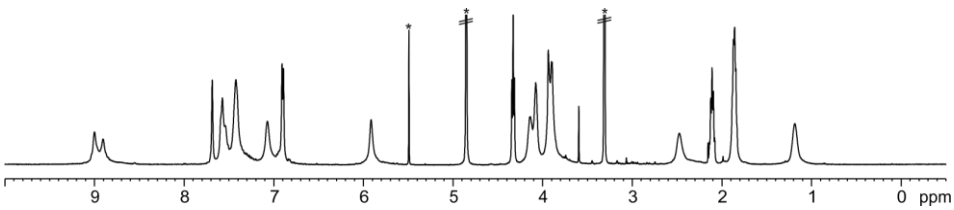

Figure 47. ^{1}H NMR (500 MHz with cryoprobe, CD_3OD, 298 K) spectrum of **7**. *Residual solvent peaks.

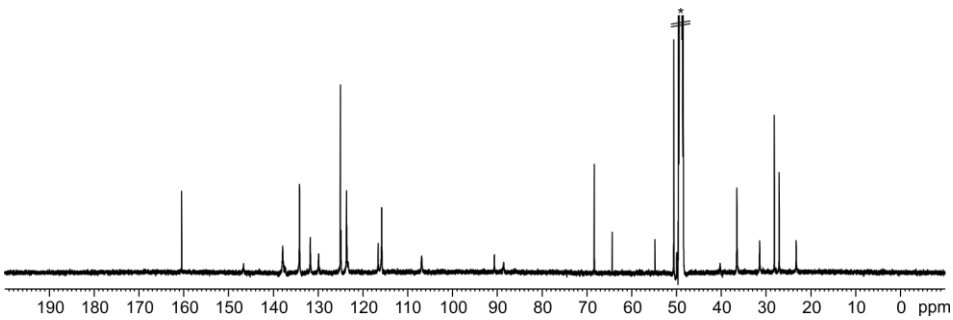

Figure 48. $^{13}C\{^{1}H\}$ NMR (125 MHz with cryoprobe, CD_3OD, 298 K) spectrum of **7**. *Residual solvent peak.

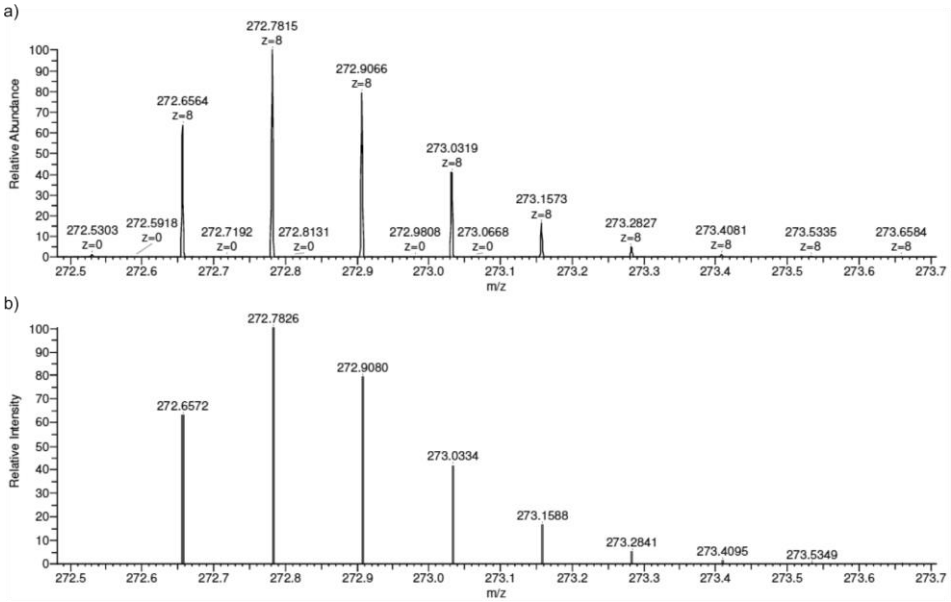

Figure 49. a) Experimental and b) theoretical isotopic distributions of $[M\text{-}8Cl]^{8+}$. The exact mass for the monoisotopic peak in a) and b) is indicated.

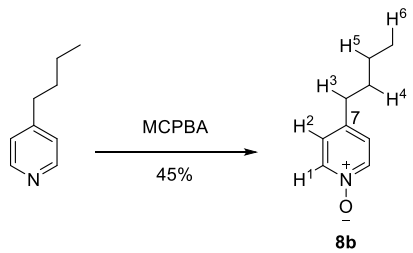

Scheme 6. Synthesis of 4-butyl pyridine *N*-oxide **8b**.

4-Butyl pyridine *N*-oxide 8b: 4-Butyl pyridine (0.22 g, 1.59 mmol, 1 equiv.) was dissolved in CH_2Cl_2 (21 mL). The solution was stirred at 0°C and MCPBA (1.10 g, 4.77 mmol, 3 equiv.) was added portionwise. The reaction was stirred at 0°C for 1 h and at r.t. for 2 h. The reaction was stopped and the crude was concentrated. The crude was purified by neutral alumina column chromatography (40 g, 95:5 CH_2Cl_2:isopropanol) affording the product as a pale brown oil (109 mg, 0.72 mmol, 45% yield). ^{1}H NMR (400 MHz, $CDCl_3$, 298 K): δ (ppm) = 8.11-8.09 (m, 2H); 7.07-7.05 (m, 2H), 2.58 (t, J = 7.6 Hz, 2H); 1.57 (tt, J = 7.6 Hz, J = 7.6 Hz, 2H); 1.33 (tq, J = 7.6 Hz, J = 7.6 Hz, 2H); 0.91 (t, J = 7.6 Hz, 3H). ^{13}C{^{1}H} NMR (100 MHz, $CDCl_3$, 298 K): δ (ppm) = 142.6; 138.8; 126.1; 34.2; 32.4; 22.2; 13.9. The synthesis and the analysis of **8b** by mass spectrometry were previously reported in the literature.[66]

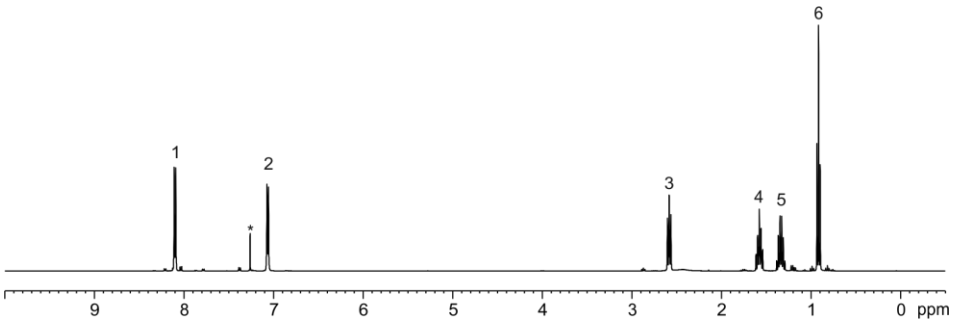

Figure 50. ^{1}H NMR (400 MHz, $CDCl_3$, 298 K) spectrum of **8b**. See Scheme 6 for proton assignment. *Residual solvent peak.

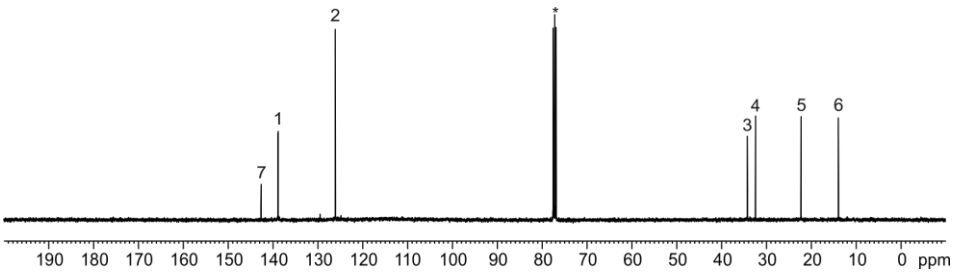

Figure 51. $^{13}C\{^{1}H\}$ NMR (100 MHz, $CDCl_3$, 298 K) spectrum of **8b**. See Scheme 6 for carbon assignment. *Residual solvent peak.

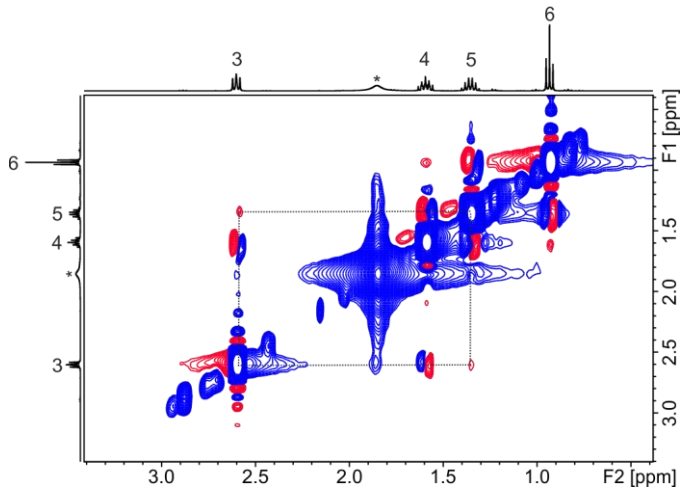

Figure 52. Selected region of the 2D ^{1}H-^{1}H NOESY NMR (400 MHz, $CDCl_3$, 298 K, t_{mix} = 0.3 s) spectrum of **8b**. NOE cross-peaks were observed between H^3 and H^5. See Scheme 6 for proton assignment. *Residual solvent peak.

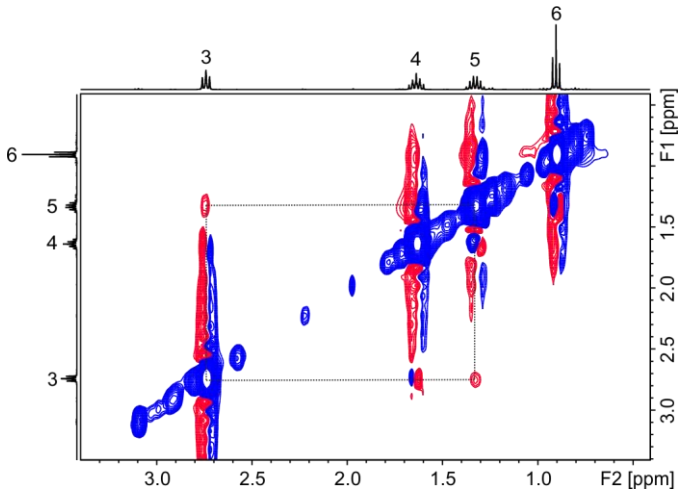

Figure 53. Selected region of the 2D ^{1}H-^{1}H NOESY NMR (400 MHz, D_2O, 298 K, t_{mix} = 0.3 s) spectrum of **8b**. NOE cross-peaks were observed between H^3 and H^5. See Scheme 6 for proton assignment.

4-*tert*-Butyl pyridine *N*-oxide 8c: The compound was prepared following a similar procedure previously described in literature.[67]

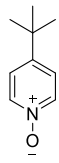

8c

Figure 54. Line-drawing structure of 4-*tert*-butyl pyridine *N*-oxide **8c**.

Quinuclidine *N*-oxide 9a: The experimental procedure for the synthesis of **9a** is described in Chapter 2.

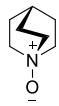

9a

Figure 55. Line-drawing structure of quinuclidine *N*-oxide **9a**.

Tetra-hydroxy super aryl-extended calix[4]pyrrole 10a: Part 1. Tetra-iodo calix[4]pyrrole **1a** (50 mg, 0.03 mmol, 1 equiv.), $Pd(PPh_3)_2Cl_2$ (2.88 mg, 0.004 mmol, 0.03 equiv.), CuI (1.25 mg, 0.007 mmol, 0.05 equiv.) and 1-[(*tert*-butyldimethylsilyl)oxy]-3-ethynyl-benzene **11a**[61] (45.70 mg, 0.20 mmol, 1.5 equiv.) were dissolved in dry THF (5 mL). The mixture was stirred under Argon atmosphere and dry diisopropylamine (5 mL) was added. The reaction was stirred at 45°C under

Argon atmosphere for 24 h. After that, the reaction was stopped and the solvent was removed. The crude was redissolved in CH_2Cl_2 (10 mL) and washed with 0.5 N HCl (10 mL), brine (10 mL) and water (10 mL). The organic layer was dried (Na_2SO_4), filtered and concentrated. The product was purified by column chromatography on silica gel (6 g, 8:1.9:0.1 CH_2Cl_2:Hexane:MTBE, product Rf = 0.3) to afford **12a** as a white solid. The compound was further purified by recrystallization in CH_3OH (49 mg, 0.03 mmol, 77% yield). Part 2. The protected compound **12a** (49 mg, 0.03 mmol, 1 equiv.) was dissolved in dry THF (5 mL). The solution was stirred at 0°C under Argon atmosphere. TBAF (0.11 mL, 0.11 mmol, 1.1 equiv.) was added dropwise. After 30 min, the reaction was quenched with saturated NH_4Cl (10 mL). EtOAc (10 mL) and water (10 mL) were added. The product was extracted in the organic layer and further extracted with additional EtOAc (10 mL). The organic layer was washed with brine (10 mL), dried (Na_2SO_4), filtered and concentrated. The product was purified by column chromatography on silica gel (6 g, 8:2 CH_2Cl_2:THF) to afford **10a** as a white solid. The compound was further purified by recrystallization in CH_2Cl_2 (30.90 mg, 0.02 mmol, 82% yield). Rf = 0.6 (8:2 CH_2Cl_2:THF). ^{1}H NMR (400 MHz, $(CD_3)_2CO$, 298 K): δ (ppm) = 8.59 (br s, 4H); 8.56 (s, 4H); 7.54-7.52 (m, 8H); 7.14 (dd, *J* = 8.4 Hz, *J* = 8.4 Hz, 4H); 7.10-7.08 (m, 8H); 6.98 (dd, *J* = 2.0 Hz, *J* = 2.0 Hz, 4H); 6.94 (dd, *J* = 8.4 Hz, *J* = 2.0 Hz, 4H); 6.85 (ddd, *J* = 8.4 Hz, *J* = 2.0 Hz, *J* = 2.0 Hz, 4H); 6.06 (d, *J* = 2.4 Hz, 8H); 3.60 (s, 12H); 2.44 (m, 8H); 2.29 (tt, *J* = 7.2 Hz, *J* = 7.2 Hz, 8H); 1.42 (m, 8H). ^{13}C{^{1}H} NMR (100 MHz, $(CD_3)_2CO$, 298 K): δ (ppm) = 174.0; 158.3; 147.4; 137.4; 132.0; 130.6; 129.9; 124.8; 123.8; 122.5; 118.8; 116.9; 106.6; 90.4; 89.1; 51.5; 49.3; 40.6; 34.4; 21.5. HRMS (ESI-TOF) m/z: $[M+Na]^+$ Calcd for $C_{96}H_{82}N_4NaO_{12}$ 1507.5978; Found 1507.5955. FTIR *v* (cm^{-1}) = 3393; 2947; 1705; 1589; 1576; 1507; 1437; 1201; 945; 834; 773; 684.

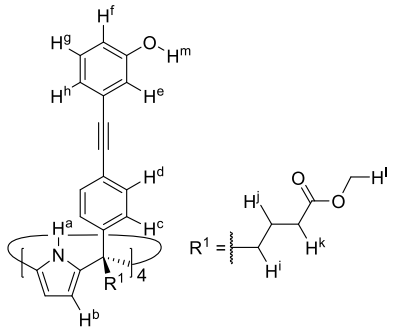

10a

Figure 56. Line-drawing structure of tetra-hydroxy **10a**.

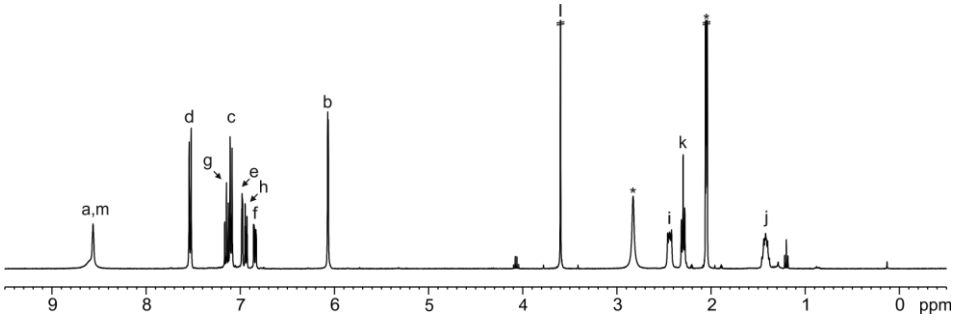

Figure 57. ^{1}H NMR (400 MHz, $(CD_3)_2CO$, 298 K) spectrum of **10a**. See Figure 56 for proton assignment. *Residual solvent peaks.

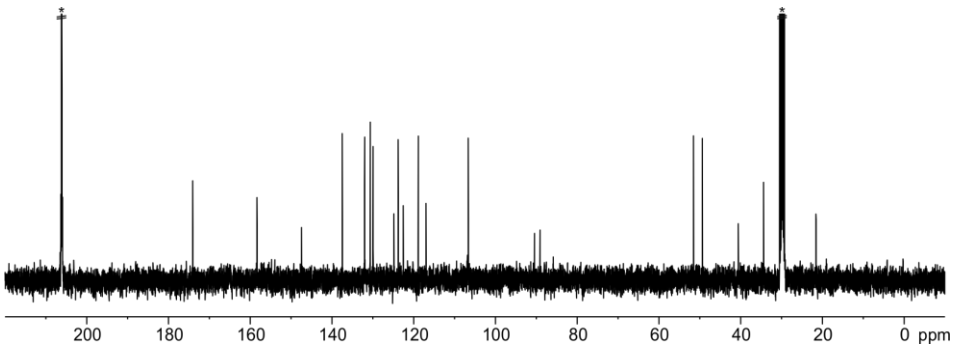

Figure 58. $^{13}C\{^{1}H\}$ NMR (100 MHz, $(CD_3)_2CO$, 298 K) spectrum of **10a**. *Residual solvent peaks.

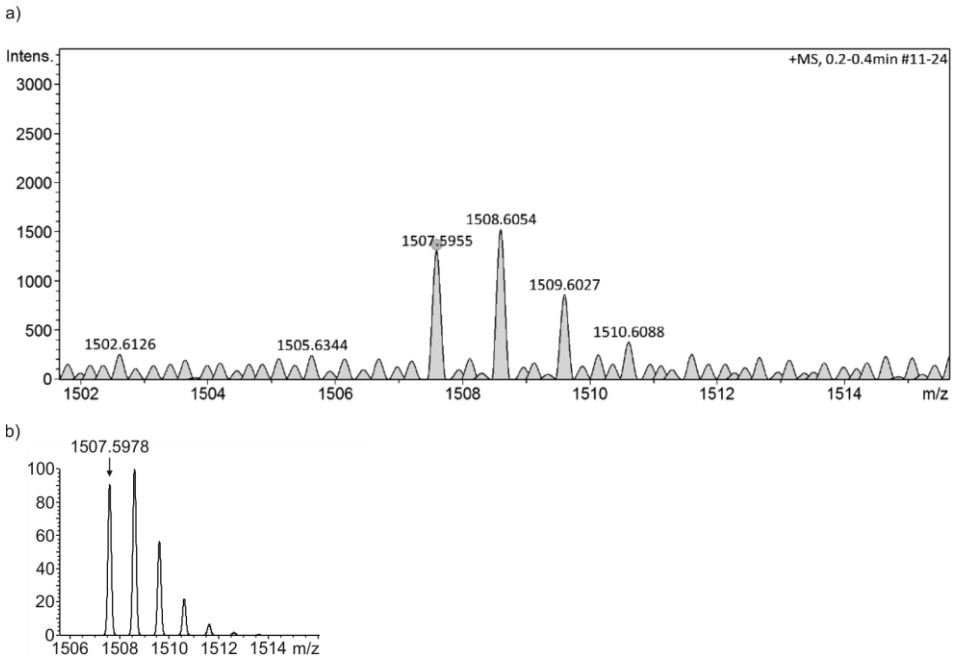

Figure 59. a) Experimental and b) theoretical isotopic distributions of $[M+Na]^+$. The exact mass for the monoisotopic peak in a) and b) is indicated.

Octa-hydroxy super aryl-extended calix[4]pyrrole 10b: Part 1. Tetra-iodo calix[4]pyrrole **1a** (50 mg, 0.03 mmol, 1 equiv.), $Pd(PPh_3)_2Cl_2$ (2.88 mg, 0.004 mmol, 0.03 equiv.), CuI (1.25 mg, 0.007 mmol, 0.05 equiv.) and 1,3-*bis*-[(*tert*-butyldimethylsilyl)oxy]-5-ethynyl-benzene **11b**[62] (71.30 mg, 0.20 mmol, 1.5 equiv.) were dissolved in dry THF (5 mL). The mixture was stirred under Argon atmosphere and dry diisopropylamine (5 mL) was added. The reaction was stirred at 45°C under Argon atmosphere for 5 h. After that, the reaction was stopped and the solvent was removed. The crude was redissolved in CH_2Cl_2 (10 mL) and washed with 0.5 N HCl (10 mL), brine (10 mL) and water (10 mL). The organic layer was dried (Na_2SO_4), filtered and concentrated. The product was purified by column chromatography on silica gel (6 g, 8:1.9:0.1 CH_2Cl_2:Hexane:MTBE, product Rf = 0.3) to afford **12b** as a white solid. The compound was further purified by recrystallization in CH_3OH (56 mg, 0.02 mmol, 70% yield). Part 2. The protected compound **12b** (56 mg, 0.02 mmol, 1 equiv.) was dissolved in dry THF (8 mL). The solution was stirred at 0°C under Argon atmosphere. TBAF (0.19 mL, 0.19 mmol, 1.1 equiv.) was added dropwise. After 30 min, the reaction was stirred at r.t. for 30 min. The reaction was quenched with saturated NH_4Cl (10 mL). EtOAc (10 mL) and water (10 mL) were added. The product was extracted in the organic layer and further extracted with additional EtOAc (10 mL). The organic layer was washed with brine (10 mL), dried (Na_2SO_4), filtered and concentrated. The product was purified by column chromatography on silica gel (6 g, 9:1 THF:CH_2Cl_2) to afford **10b** as a white solid. The compound was further purified by recrystallization in CH_2Cl_2 (28.28 mg, 0.03 mmol, 60% yield). Rf = 0.7 (9:1 THF:CH_2Cl_2). ^1H

NMR (400 MHz, $(CD_3)_2CO$, 298 K): δ (ppm) = 8.70 (s, 4H); 8.51 (br s, 4H); 7.52-7.50 (m, 8H); 7.12-7.10 (m, 8H); 6.50 (d, J = 2 Hz, 8H); 6.37 (t, J = 2 Hz, 4H); 6.01 (d, J = 2.4 Hz, 8H); 3.60 (s, 12H); 2.44 (m, 8H); 2.29 (dd, J = 7.2 Hz, J = 7.2 Hz, 8H); 1.41 (m, 8H). $^{13}C\{^1H\}$ NMR (100 MHz, $(CD_3)_2CO$, 298 K): δ (ppm) = 174.1; 159.4; 147.4; 137.3; 131.9; 129.8; 125.1; 122.5; 110.9; 106.7; 104.7; 90.6; 88.7; 51.5; 49.4; 40.6; 34.4; 21.6. HRMS (ESI-TOF) m/z: $[M-2H]^{2-}$ Calcd for $C_{96}H_{82}N_4O_{16}$ 773.2868; Found 773.2878. FTIR v (cm^{-1}) = 3390; 2959; 1704; 1588; 1509; 1435; 1363; 1259; 1147; 999; 837; 796.

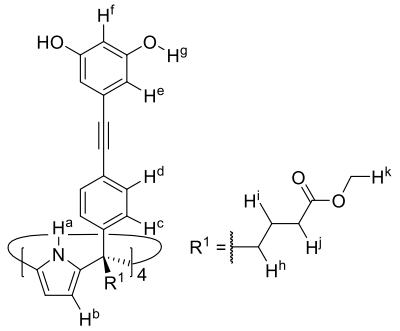

10b

Figure 60. Line-drawing structure of octa-hydroxy **10b**.

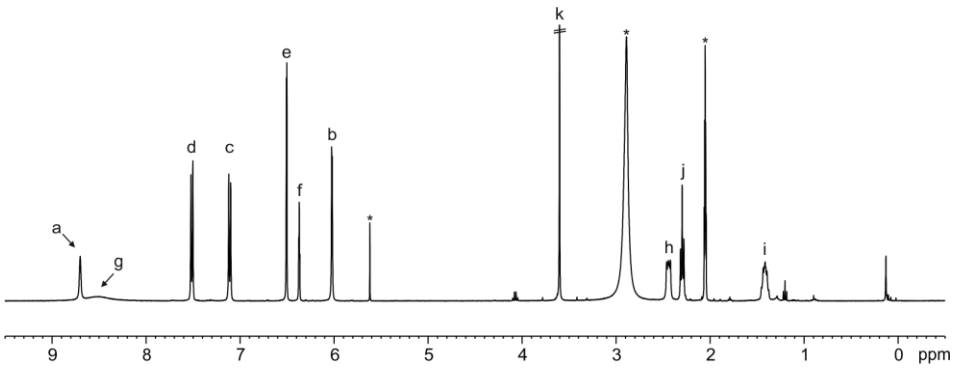

Figure 61. ^1H NMR (400 MHz, $(CD_3)_2CO$, 298 K) spectrum of **10b**. See Figure 60 for proton assignment. *Residual solvent peaks.

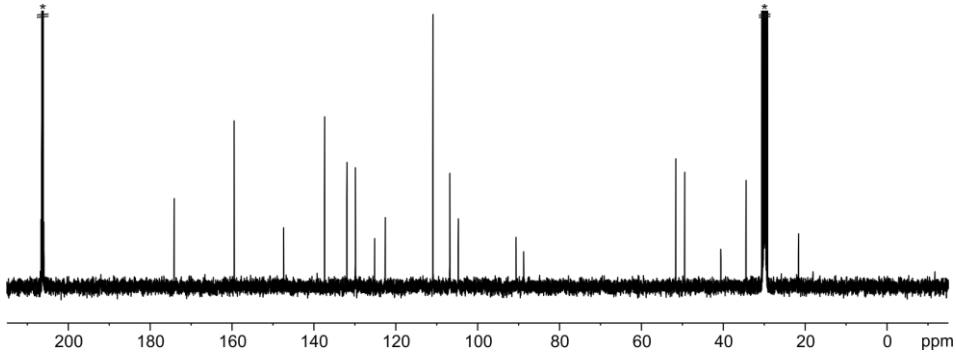

Figure 62. $^{13}C\{^{1}H\}$ NMR (100 MHz, $(CD_3)_2CO$, 298 K) spectrum of **10b**. *Residual solvent peaks.

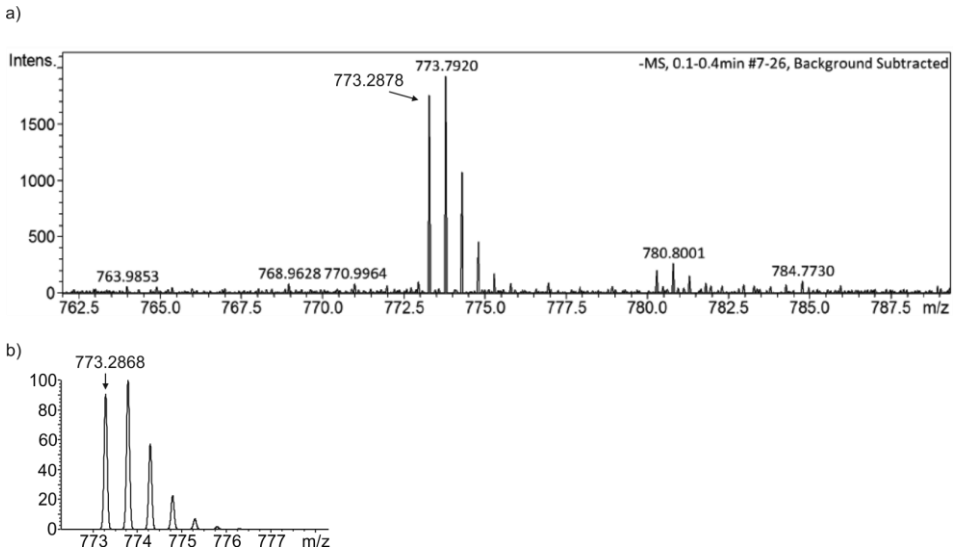

Figure 63. a) Experimental and b) theoretical isotopic distributions of $[M\text{-}2H]^{2-}$. The exact mass for the monoisotopic peak in a) and b) is indicated.

3.4.3 Water-suppression NMR experiment of octa-acid **5**

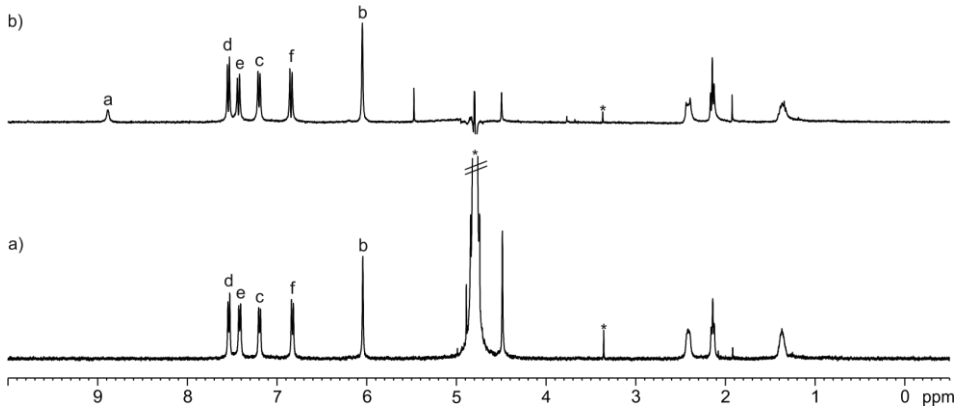

Figure 64. ^{1}H NMR (400 MHz, 298 K) of **5** (1 mM): a) D_2O and b) 9:1 H_2O:D_2O (water-suppression pulse program). See Figure 38 for proton assignment. *Residual solvent peaks.

3.4.4 Dilution and variable-temperature (VT) ^{1}H NMR experiments of **6** and **7**

^{1}H NMR spectra of octa-pyridinium **6** in $(CD_3)_2SO$

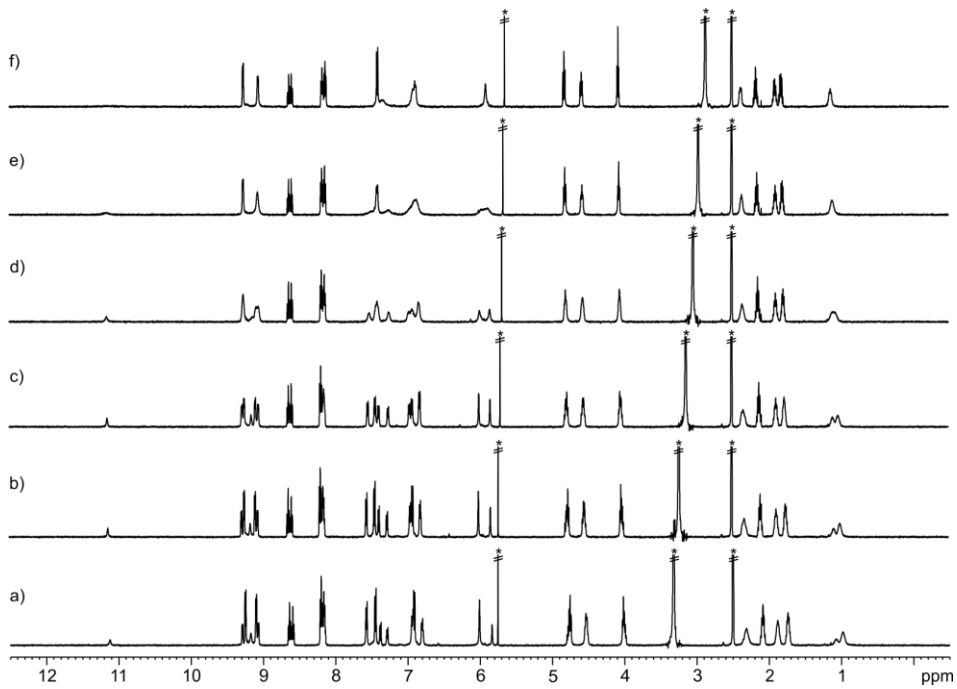

Figure 65. VT ^{1}H NMR (500 MHz, $(CD_3)_2SO$) spectra of **6**: a) 298; b) 318; c) 338; d) 358; e) 373 and f) 393 K. *Residual solvent peaks.

Chapter 3

^{1}H NMR spectra of octa-(1-methyl-1H-imidazolium) **7** in $(CD_3)_2SO$

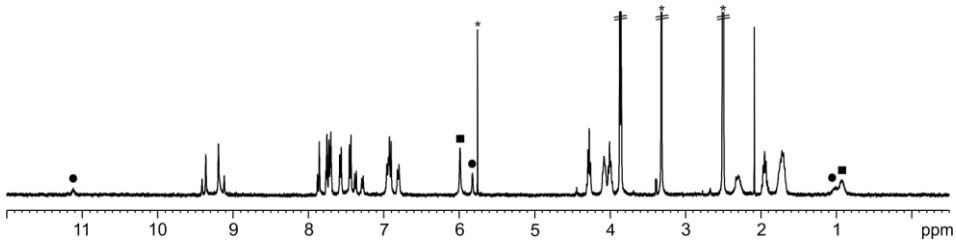

Figure 66. ^{1}H NMR (400 MHz, $(CD_3)_2SO$, 298 K) spectrum of **7**. The ^{1}H NMR spectrum showed two set of signals in a 70:30 ratio, which are assigned to the protons of free SAE-C[4]P (squares) and Cl^-⊂SAE-C[4]P (circles), respectively. *Residual solvent peaks.

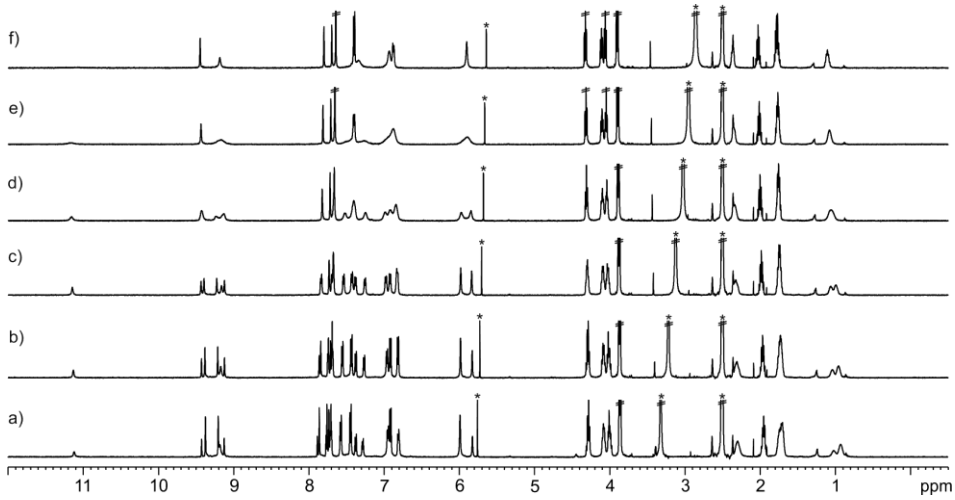

Figure 67. VT ^{1}H NMR (500 MHz, $(CD_3)_2SO$) spectra of **7**: a) 298; b) 318; c) 338; d) 358; e) 373 and f) 393 K. *Residual solvent peaks.

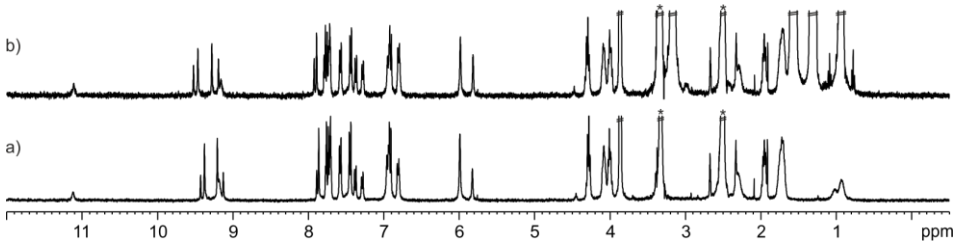

Figure 68. ^{1}H NMR (400 MHz, $(CD_3)_2SO$, 298 K) spectra of **7** and TBACl: a) **7** and b) TBACl + **7** (20:1 ratio). The spectrum b) showed two set of signals in a 60:40 ratio, which are assigned to the protons of free SAE-C[4]P and Cl^-⊂SAE-C[4]P, respectively. *Residual solvent peaks.

Dilution experiments in water

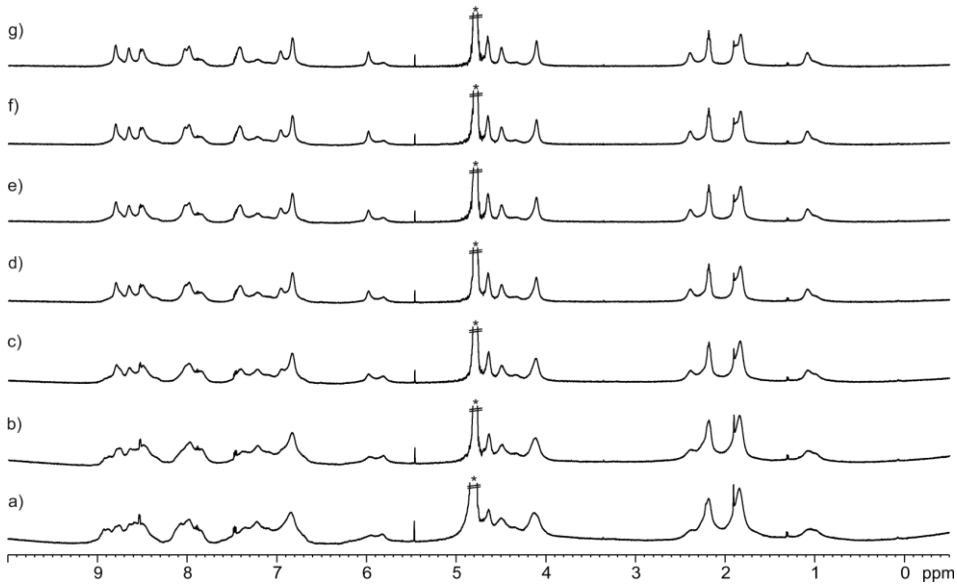

Figure 69. ^{1}H NMR (500 MHz with cryoprobe, D_2O, 298 K) spectra of **6**: a) 1; b) 0.8; c) 0.6; d) 0.4; e) 0.2; f) 0.1 and g) 0.05 mM. *Residual solvent peak.

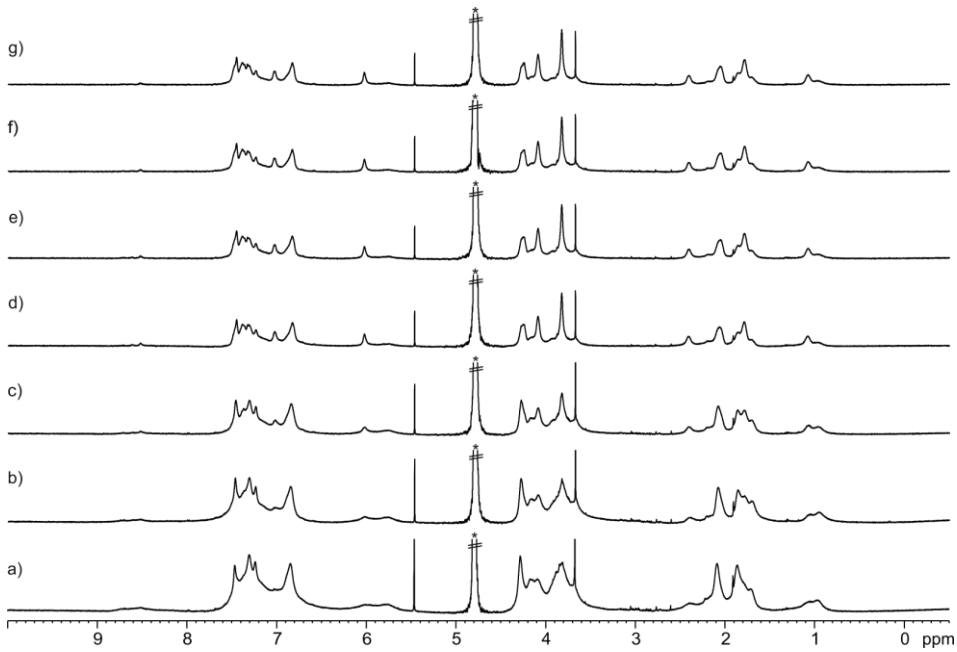

Figure 70. ^{1}H NMR (500 MHz with cryoprobe, D_2O, 298 K) spectra of **7**: a) 1; b) 0.8; c) 0.6; d) 0.4; e) 0.2; f) 0.1 and g) 0.05 mM. *Residual solvent peak.

VT ^{1}H NMR experiment of octa-(1-methyl-1H-imidazolium) **7** in water

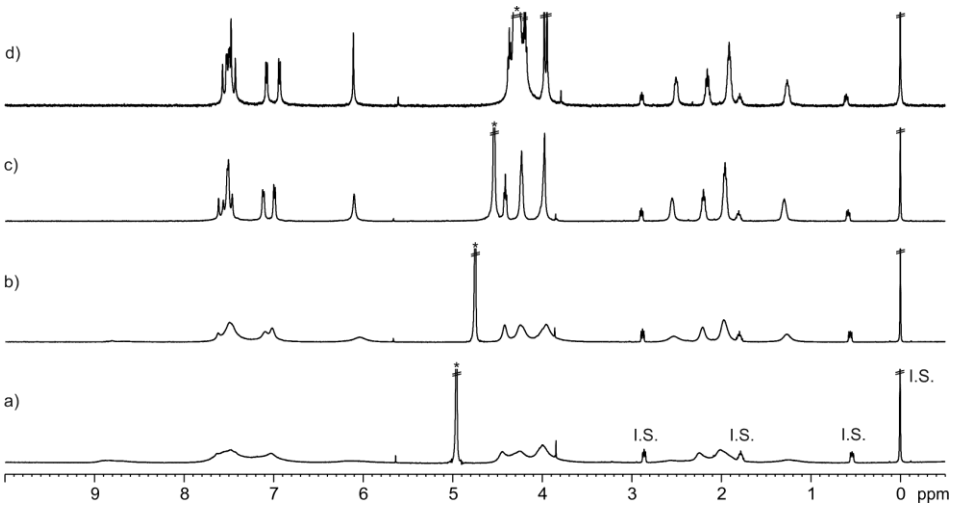

Figure 71. VT ^{1}H NMR (500 MHz, D_2O) spectra of **7**: a) 298; b) 318; c) 338 and d) 358 K. Sodium 3-(trimethylsilyl)propane-1-sulfonate (I.S.). *Residual solvent peak.

3.4.5 ^{1}H NMR spectroscopic titration experiments of **5** with *N*-oxides

A solution of host **5** (1 mM) was prepared in D_2O at pD ~ 10 using NaOD. Subsequently, 0.5 mL of the solution were transferred to a NMR tube. The remaining D_2O solution of the host was used to prepare the titrant's solution, which contained the pyridyl *N*-oxide **8a**-**f** or aliphatic *N*-oxide **9a**-**b** at 20-50 fold higher concentration ([G] = 20-50 mM and [H] = 1 mM). In this manner, the concentration of the host was maintained constant throughout the titration. Immediately, the 0.5 mL of the host solution was titrated by manually injecting incremental amounts of the titrant's solution using a micro syringe. A ^{1}H NMR spectrum of the mixture was acquired after each injection and vigorous hand shaking of the NMR tube for few seconds.

Pyridyl *N*-oxides

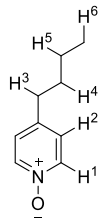

Figure 72. Line-drawing structure of **8b**.

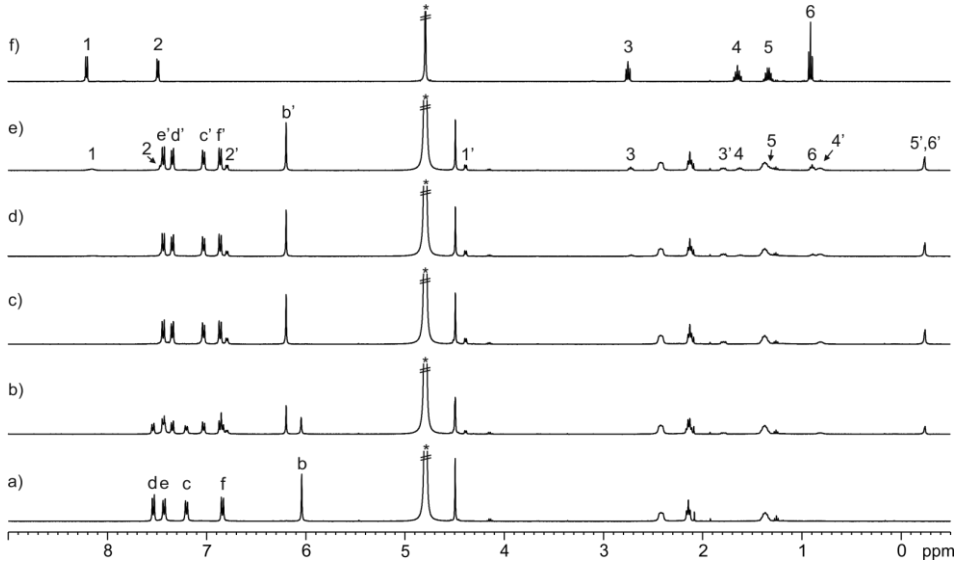

Figure 73. ^{1}H NMR (400 MHz, D_2O, pD ~ 10, 298 K) spectra of the titration of **5** with **8b**: a) 0; b) 0.55; c) 1; d) 1.4 and e) 2 equiv.; f) **8b**. Primed letters and numbers correspond to proton signals of bound components. See Figure 38 and Figure 72 for proton assignments. *Residual solvent peak.

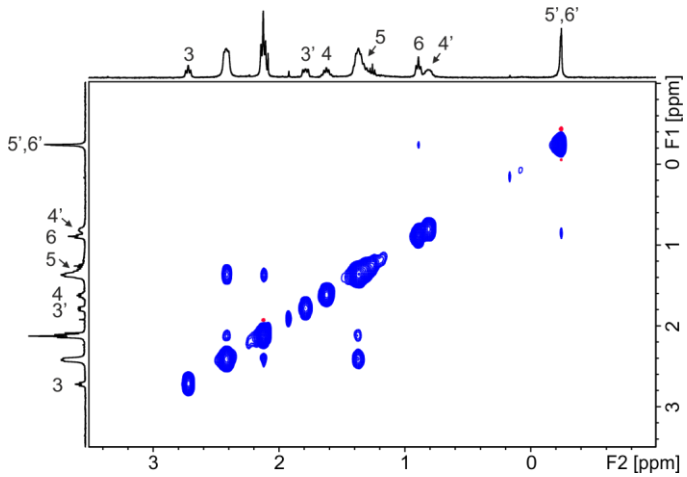

Figure 74. Selected region of the 2D ^{1}H-^{1}H NOESY NMR (400 MHz, D_2O, pD ~ 10, 298 K, t_{mix} = 0.6 s) spectrum of **8b** and **5** (2:1 ratio). Primed numbers correspond to proton signals of bound component. See Figure 72 for proton assignment.

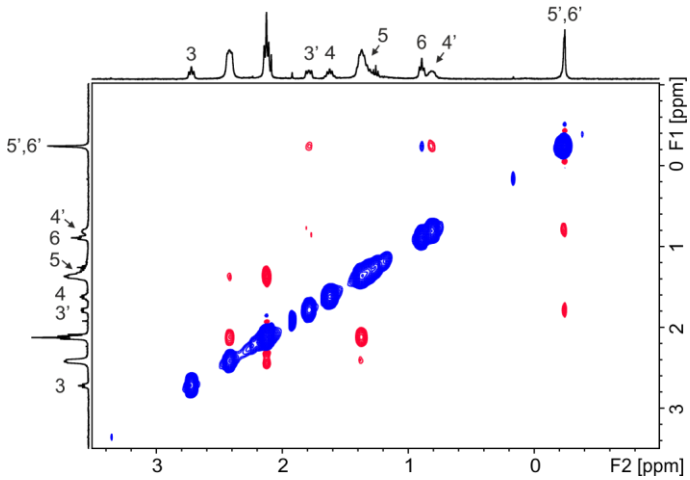

Figure 75. Selected region of the 2D ^{1}H-^{1}H ROESY NMR (400 MHz, D_2O, pD ~ 10, 298 K, spin-lock = 0.4 s) spectrum of **8b** and **5** (2:1 ratio). Primed numbers correspond to proton signals of bound component. See Figure 72 for proton assignments.

Table 5. Chemical shifts (δ, ppm) of the protons of free and bound **8b** (**8b⊂5**) and complexation induced shifts ($\Delta\delta$, ppm).

Signal	δ_{free}	δ_{bound}	$\Delta\delta$
1	8.21	4.38	-3.83
2	7.49	6.79	-0.70
3	2.75	1.79	-0.96
4	1.65	0.81	-0.84
5	1.33	-0.24	-1.57
6	0.91	-0.24	-1.15

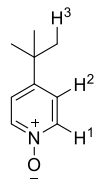

Figure 76. Line-drawing structure of **8c**.

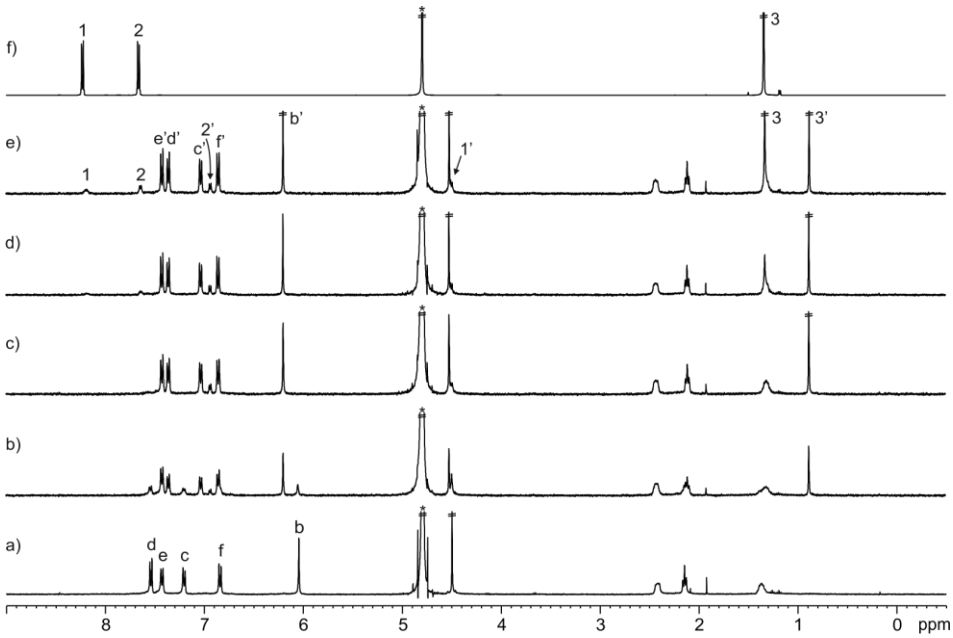

Figure 77. ^{1}H NMR (400 MHz, D_2O, pD ~ 10, 298 K) spectra of the titration of **5** with **8c**: a) 0; b) 0.7; c) 1; d) 1.6 and e) 2.2 equiv.; f) **8c**. Primed letters and numbers correspond to proton signals of bound components. See Figure 38 and Figure 76 for proton assignments. *Residual solvent peak.

Table 6. Chemical shifts (δ, ppm) of the protons of free and bound **8c** (**8c⊂5**) and complexation induced shifts ($\Delta\delta$, ppm).

Signal	δ_{free}	δ_{bound}	$\Delta\delta$
1	8.23	4.50	-3.73
2	7.66	6.94	-0.72
3	1.34	0.88	-0.46

Chapter 3

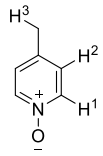

Figure 78. Line-drawing structure of **8d**.

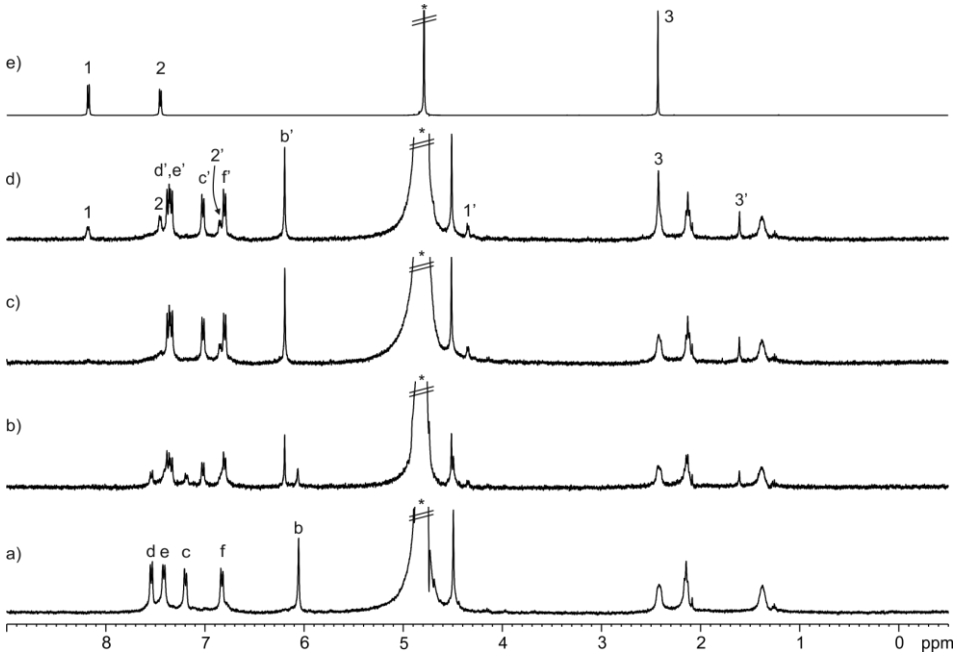

Figure 79. ^{1}H NMR (400 MHz, D_2O, pD ~ 10, 298 K) spectra of the titration of **5** with **8d**: a) 0; b) 0.6; c) 1 and d) 2.2 equiv.; e) **8d**. Primed letters and numbers correspond to proton signals of bound components. See Figure 38 and Figure 78 for proton assignments. *Residual solvent peak.

Table 7. Chemical shifts (δ, ppm) of the protons of free and bound **8d** (**8d⊂5**) and complexation induced shifts ($\Delta\delta$, ppm).

Signal	δ_{free}	δ_{bound}	$\Delta\delta$
1	8.18	4.35	-3.83
2	7.45	6.85	-0.60
3	2.43	1.61	-0.82

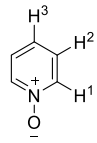

Figure 80. Line-drawing structure of **8e**.

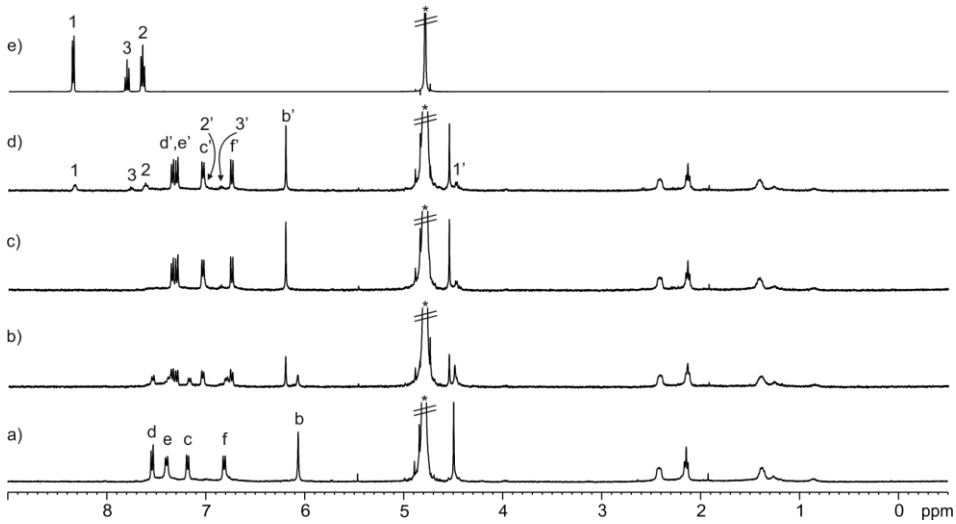

Figure 81. ^{1}H NMR (400 MHz, D_2O, pD ~ 10, 298 K) spectra of the titration of **5** with **8e**: a) 0; b) 0.6; c) 1 and d) 2.2 equiv.; e) **8e**. Primed letters and numbers correspond to proton signals of bound components. See Figure 38 and Figure 80 for proton assignments. *Residual solvent peak.

Table 8. Chemical shifts (δ, ppm) of the protons of free and bound **8e** (**8e**⊂**5**) and complexation induced shifts ($\Delta\delta$, ppm).

Signal	δ_{free}	δ_{bound}	$\Delta\delta$
1	8.33	4.47	-3.86
2	7.62	7.02	-0.60
3	7.76	6.85	-0.91

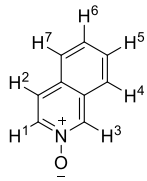

Figure 82. Line-drawing structure of **8f**.

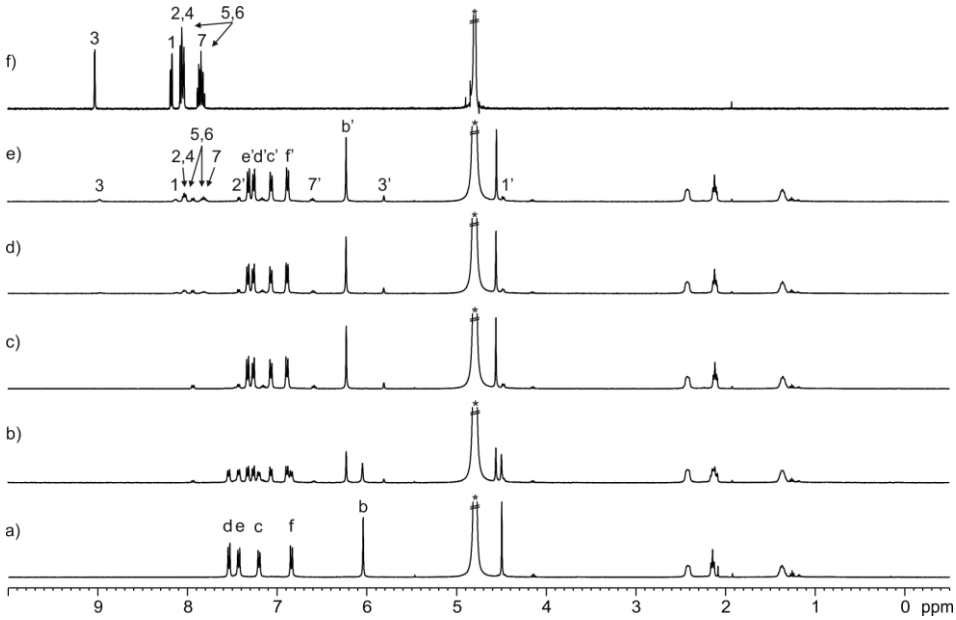

Figure 83. ^{1}H NMR (400 MHz, D_2O, pD ~ 10, 298 K) spectra of the titration of **5** with **8f**: a) 0; b) 0.55; c) 1; d) 1.4 and e) 1.9 equiv.; f) **8f**. Primed letters and numbers correspond to proton signals of bound components. See Figure 38 and Figure 82 for proton assignments. *Residual solvent peak.

Table 9. Chemical shifts (δ, ppm) of the protons of free and bound **8f** (**8f**⊂**5**) and complexation induced shifts ($\Delta\delta$, ppm).

Signal	δ_{free}	δ_{bound}	$\Delta\delta$
1	8.13	4.47	-3.66
2	8.03	7.42	-0.61
3	8.98	5.80	-3.18
7	7.82	6.60	-1.22

Aliphatic *N*-oxides

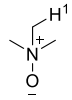

Figure 84. Line-drawing structure of **9b**.

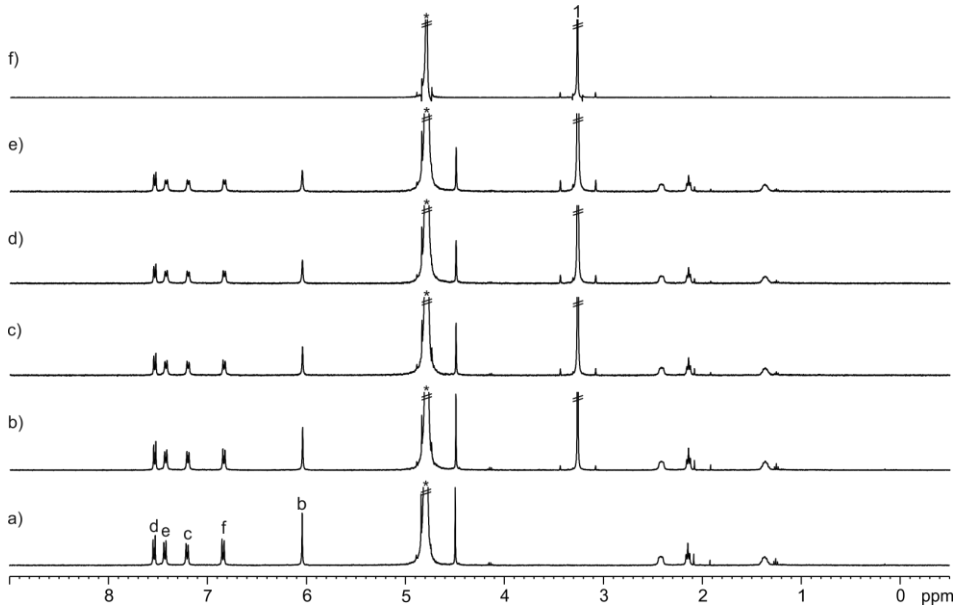

Figure 85. ^{1}H NMR (400 MHz, D_2O, pD ~ 10, 298 K) spectra of the titration of **5** with **9b**: a) 0; b) 10; c) 20; d) 30 and e) 40 equiv.; f) **9b**. See Figure 38 and Figure 84 for proton assignments. *Residual solvent peak.

3.4.6 Pair-wise ^{1}H NMR competitive experiments of **5** with pyridyl *N*-oxides

A series of pair-wise NMR competitive titration experiments were performed using receptor **5** (1 mM) and the pyridyl *N*-oxides **8a**-**f** in basic (pD ~ 10) D_2O solutions. The binding constant ratio between the two competing complexes was determined by integration of selected proton signals in the acquired ^{1}H NMR spectra (K_{a2}/K_{a1} = ([HG_2] x [G_1])/([HG_1] x [G_2]). The binding constant values of the thermodynamically more stable complexes (K_a > 10^7 M^{-1}) were determined using the calculated ratio of the binding constants and the binding constant value of one of the complexes, which was measured either accurately by ITC experiments or from a previous pair-wise competitive experiment.

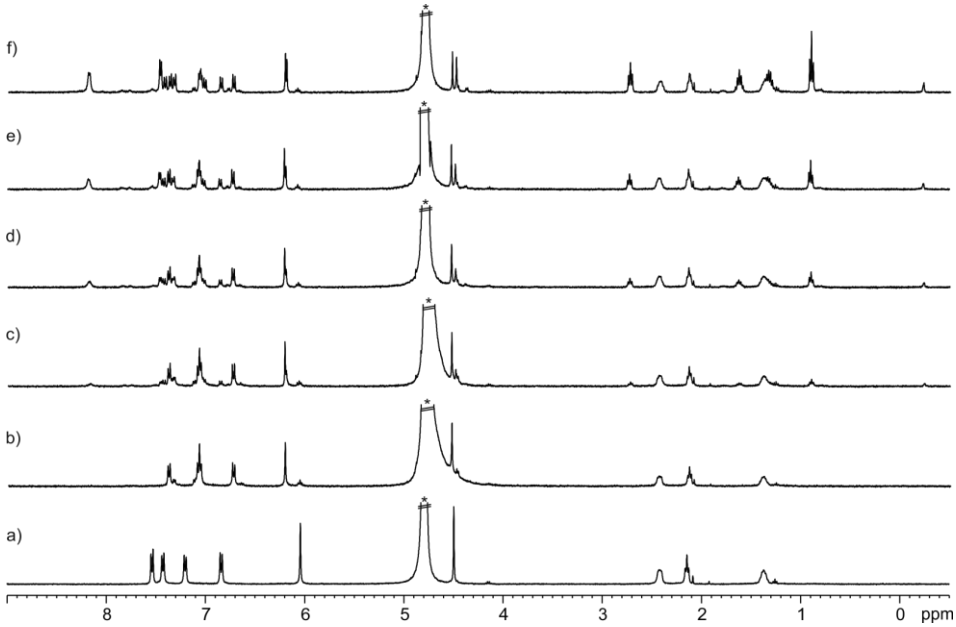

Figure 86. ^{1}H NMR (400 MHz, D_2O, pD ~ 10, 298 K) spectra of the pair-wise competitive experiment of **5**, **8a** and **8b**: a) **5**; b) **8a** + **5** (1:1 ratio); c) **8b** + **8a** + **5** (1:1:1 ratio); d) **8b** + **8a** + **5** (2:1:1 ratio); e) **8b** + **8a** + **5** (3:1:1 ratio) and f) **8b** + **8a** + **5** (5:1:1 ratio). *Residual solvent peak.

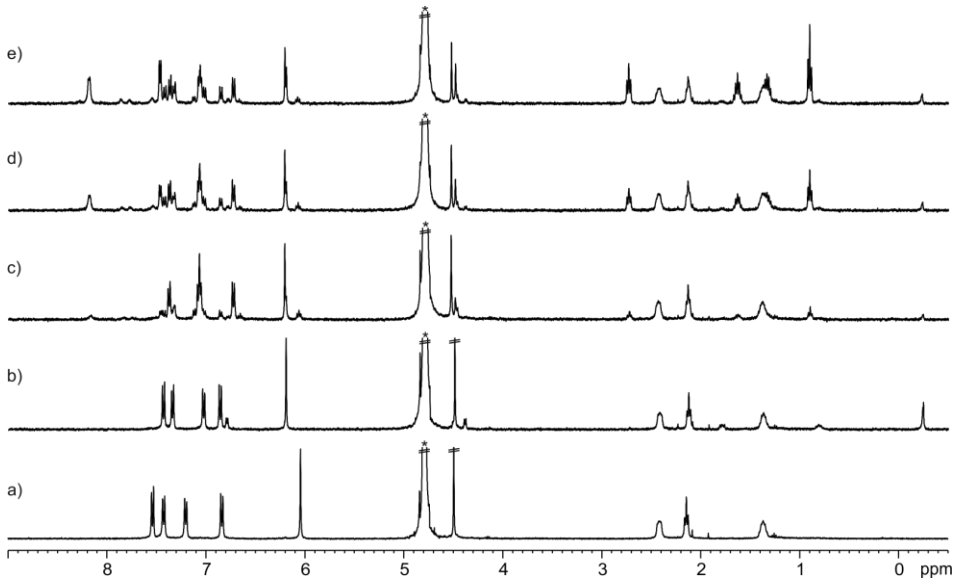

Figure 87. ^{1}H NMR (400 MHz, D_2O, pD ~ 10, 298 K) spectra of the pair-wise competitive experiment of **5**, **8a** and **8b**: a) **5**; b) **8b** + **5** (1:1 ratio); c) **8a** + **8b** + **5** (1.1:1:1 ratio); d) **8a** + **8b** + **5** (1.1:2.8:1 ratio) and e) **8a** + **8b** + **5** (1.1:4.7:1 ratio). *Residual solvent peak.

Integration of selected proton signals in the spectra of the pair-wise competitive experiments indicated that K_a (**8a**⊂**5**) = 12±1 x K_a (**8b**⊂**5**).

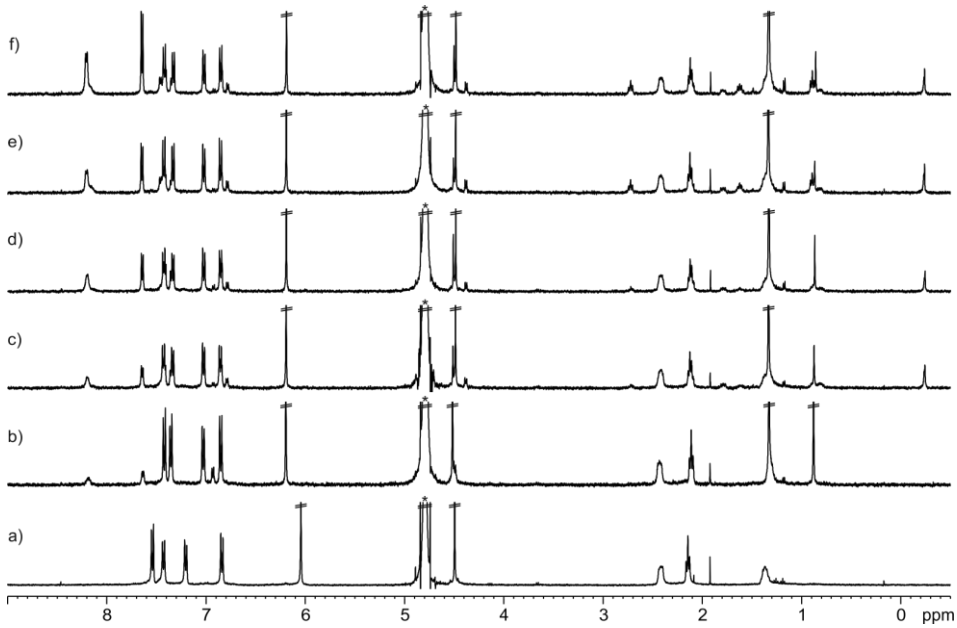

Figure 88. ^{1}H NMR (400 MHz, D_2O, pD ~ 10, 298 K) spectra of the pair-wise competitive experiment of **5**, **8b** and **8c**: a) **5**; b) **8c** + **5** (2.2:1 ratio); c) **8b** + **8c** + **5** (1.1:2.2:1 ratio); d) **8b** + **8c** + **5** (1.1:3.2:1 ratio); e) **8b** + **8c** + **5** (2.1:3.2:1 ratio) and f) **8b** + **8c** + **5** (2.1:5.3:1 ratio). *Residual solvent peak.

Integration of selected proton signals in the spectra of the pair-wise competitive experiments indicated that K_a (**8b**⊂**5**) = 11.0±0.5 x K_a (**8c**⊂**5**).

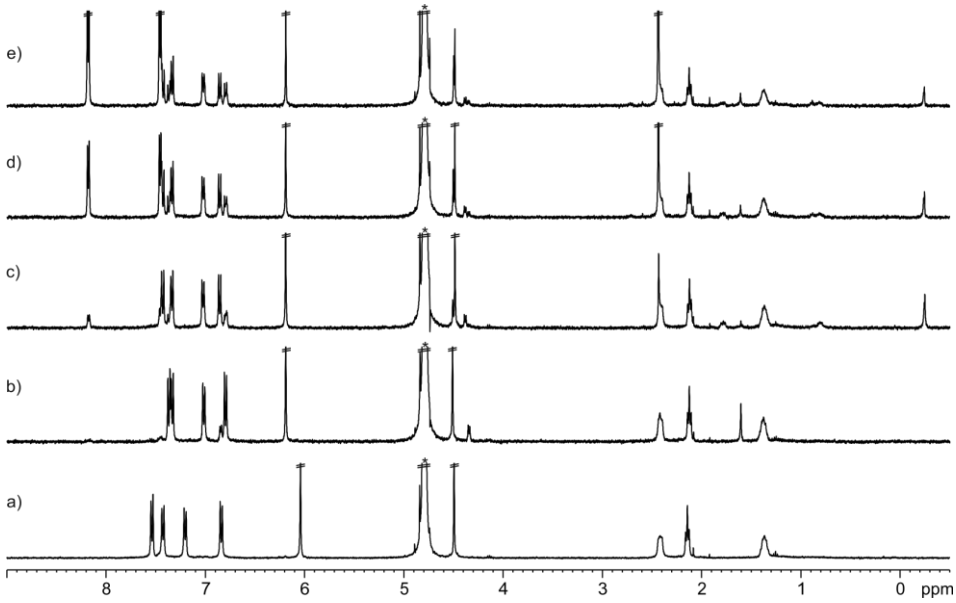

Figure 89. ^{1}H NMR (400 MHz, D_2O, pD ~ 10, 298 K) spectra of the pair-wise competitive experiment of **5**, **8b** and **8d**: a) **5**; b) **8d** + **5** (1.1:1 ratio); c) **8b** + **8d** + **5** (1:1.1:1 ratio); d) **8b** + **8d** + **5** (1:5.1:1 ratio) and e) **8b** + **8d** + **5** (1:11.4:1 ratio). *Residual solvent peak.

Integration of selected proton signals in the spectra of the pair-wise competitive experiments indicated that K_a (**8b**⊂**5**) = 50±20 x K_a (**8d**⊂**5**).

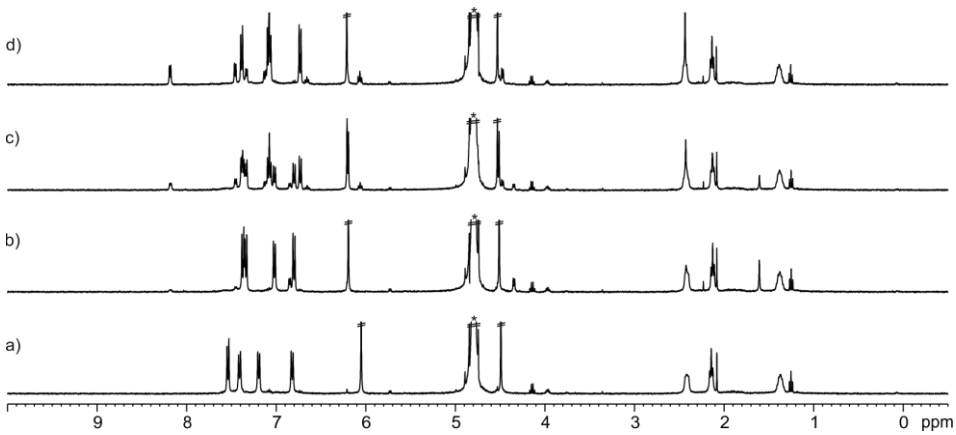

Figure 90. ^{1}H NMR (400 MHz, D_2O, pD ~ 10, 298 K) spectra of the pair-wise competitive experiment of **5**, **8a** and **8d**: a) **5**; b) **8d** + **5** (1.5:1 ratio); c) **8a** + **8d** + **5** (0.5:1.5:1 ratio) and d) **8a** + **8d** + **5** (1:1.5:1 ratio). *Residual solvent peak.

The spectra of the pair-wise competitive experiments indicated that K_a (**8a**⊂**5**) >> K_a (**8d**⊂**5**).

3.4.7 ^{1}H NMR spectroscopic titration experiments of **6** with pyridyl *N*-oxides

A solution of host **6** (1 mM) was prepared in D_2O. Subsequently, 0.5 mL of the solution were transferred to a NMR tube. The remaining D_2O solution of the host was used to prepare the titrant's solution, which contained the pyridyl *N*-oxide **8a**-**f** at 20-30 fold higher concentration ([G] = 20-30 mM and [H] = 1 mM). In this manner, the concentration of the host was maintained constant throughout the titration. Immediately, the 0.5 mL of the host solution was titrated by manually injecting incremental amounts of the titrant's solution using a micro syringe. A ^{1}H NMR spectrum of the mixture was acquired after each injection and vigorous hand shaking of the NMR tube for few seconds.

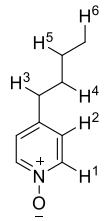

Figure 91. Line-drawing structure of **8b**.

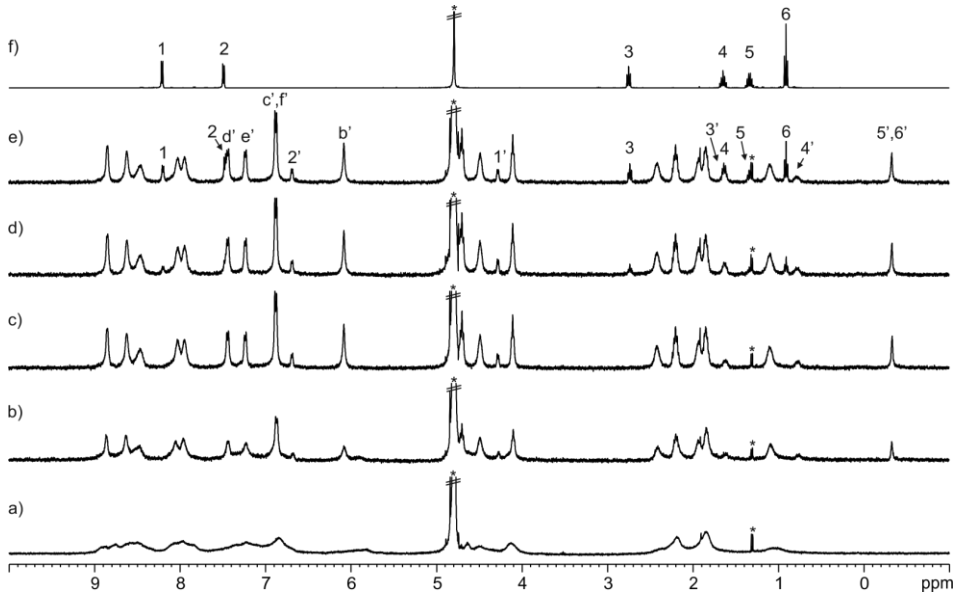

Figure 92. ^{1}H NMR (400 MHz, D_2O, 298 K) spectra of the titration of **6** with **8b**: a) 0; b) 0.5; c) 1; d) 1.5 and e) 2 equiv.; f) **8b**. Primed letters and numbers correspond to proton signals of bound components. See Figure 42 and Figure 91 for proton assignments. *Residual solvent peak.

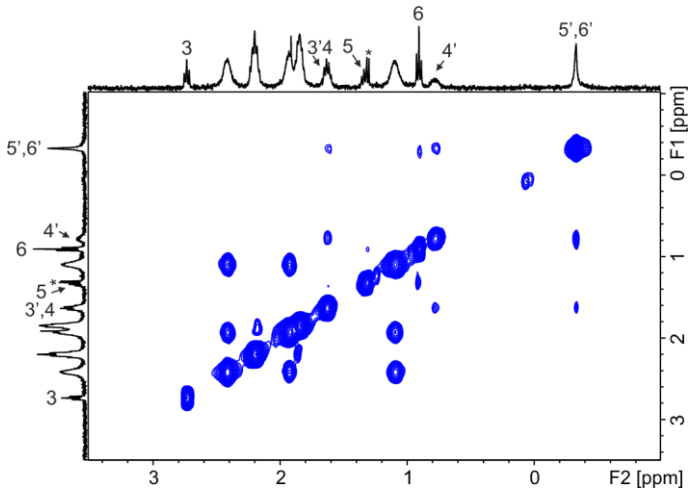

Figure 93. Selected region of the 2D ^{1}H-^{1}H NOESY NMR (400 MHz, D_2O, 298 K, t_{mix} = 0.6 s) spectrum of **8b** and **6** (2:1 ratio). Primed numbers correspond to proton signals of bound component. See Figure 91 for proton assignment. *Residual solvent peak.

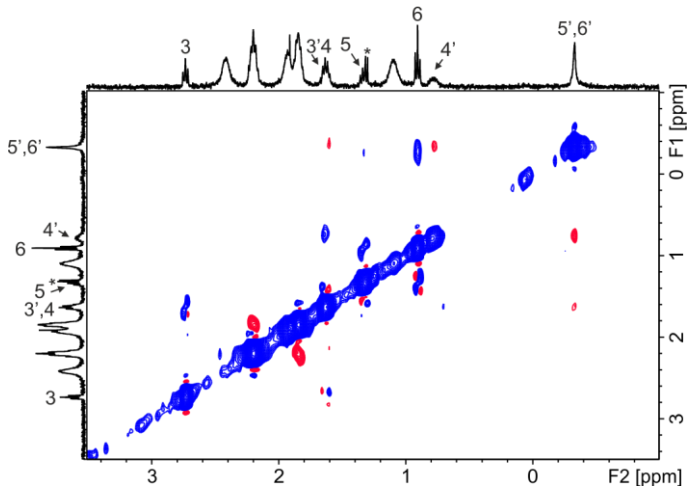

Figure 94. Selected region of the 2D ^{1}H-^{1}H ROESY NMR (400 MHz, D_2O, 298 K, spin lock = 0.4 s) spectrum of **8b** and **6** (2:1 ratio). Primed numbers correspond to proton signals of bound component. See Figure 91 for proton assignment. *Residual solvent peak.

Table 10. Chemical shifts (δ, ppm) of the protons of free and bound **8b** (**8b⊂6**) and complexation induced shifts ($\Delta\delta$, ppm).

Signal	δ_{free}	δ_{bound}	$\Delta\delta$
1	8.21	4.28	-3.93
2	7.49	6.69	-0.80
3	2.75	1.64	-1.11
4	1.65	0.78	-0.87
5	1.33	-0.33	-1.66
6	0.91	-0.33	-1.24

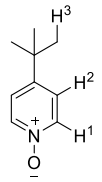

Figure 95. Line-drawing structure of **8c**.

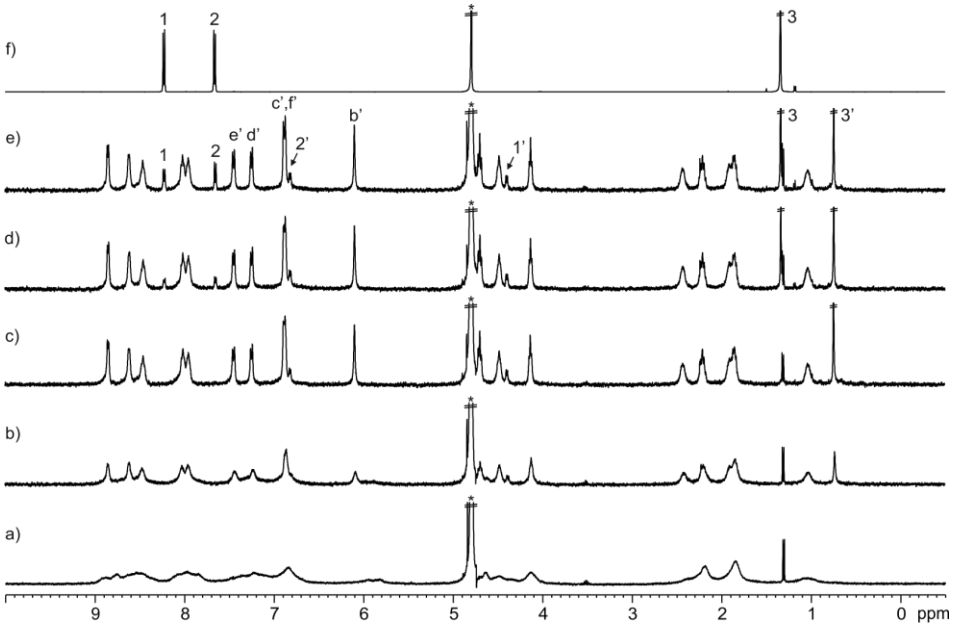

Figure 96. ^{1}H NMR (400 MHz, D_2O, 298 K) spectra of the titration of **6** with **8c**: a) 0; b) 0.7; c) 1; d) 1.6 and e) 2.2 equiv.; f) **8c**. Primed letters and numbers correspond to proton signals of bound components. See Figure 42 and Figure 95 for proton assignments. *Residual solvent peak.

Table 11. Chemical shifts (δ, ppm) of the protons of free and bound **8c** (**8c⊂6**) and complexation induced shifts ($\Delta\delta$, ppm).

Signal	δ_{free}	δ_{bound}	$\Delta\delta$
1	8.23	4.39	-3.84
2	7.66	6.82	-0.84
3	1.34	0.74	-0.60

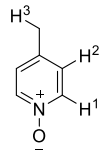

Figure 97. Line-drawing structure of **8d**.

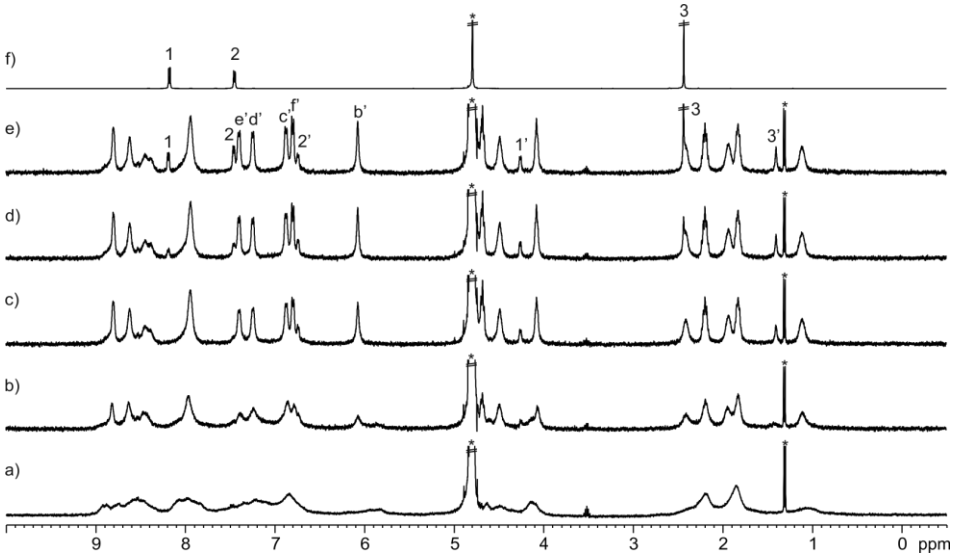

Figure 98. ^{1}H NMR (400 MHz, D_2O, 298 K) spectra of the titration of **6** with **8d**: a) 0; b) 0.5; c) 1; d) 1.5 and e) 2 equiv.; f) **8d**. Primed letters and numbers correspond to proton signals of bound components. See Figure 42 and Figure 97 for proton assignments. *Residual solvent peak.

Table 12. Chemical shifts (δ, ppm) of the protons of free and bound **8d** (**8d⊂6**) and complexation induced shifts ($\Delta\delta$, ppm).

Signal	δ_{free}	δ_{bound}	$\Delta\delta$
1	8.18	4.26	-3.92
2	7.45	6.74	-0.71
3	2.43	1.40	-1.03

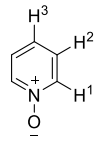

Figure 99. Line-drawing structure of **8e**.

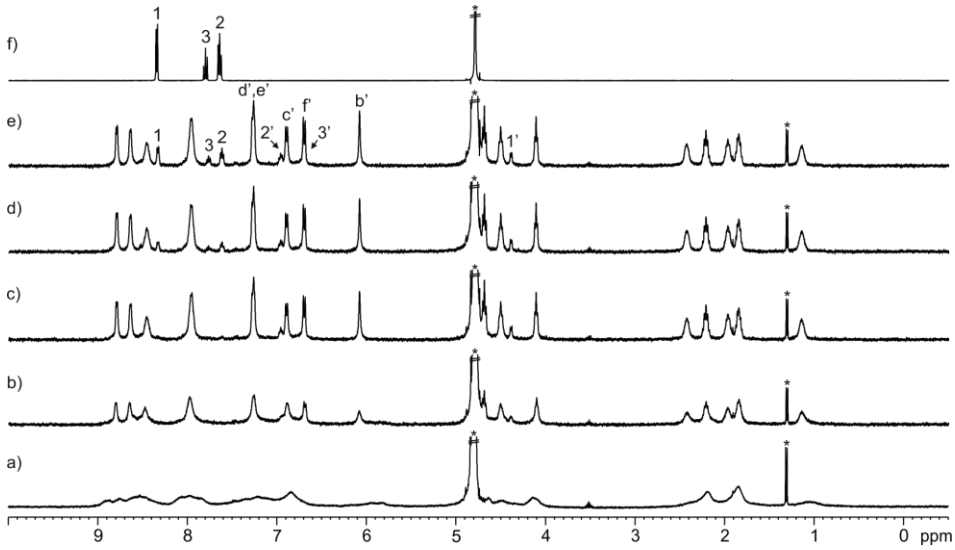

Figure 100. ^{1}H NMR (400 MHz, D_2O, 298 K) spectra of the titration of **6** with **8e**: a) 0; b) 0.5; c) 1; d) 1.5 and e) 2 equiv.; f) **8e**. Primed letters and numbers correspond to proton signals of bound components. See Figure 42 and Figure 99 for proton assignments. *Residual solvent peaks.

Table 13. Chemical shifts (δ, ppm) of the protons of free and bound **8e** (**8e⊂6**) and complexation induced shifts ($\Delta\delta$, ppm).

Signal	δ_{free}	δ_{bound}	$\Delta\delta$
1	8.35	4.39	-3.96
2	7.65	6.96	-0.69
3	7.80	6.70	-1.10

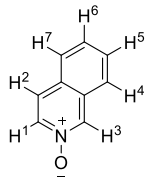

Figure 101. Line-drawing structure of **8f**.

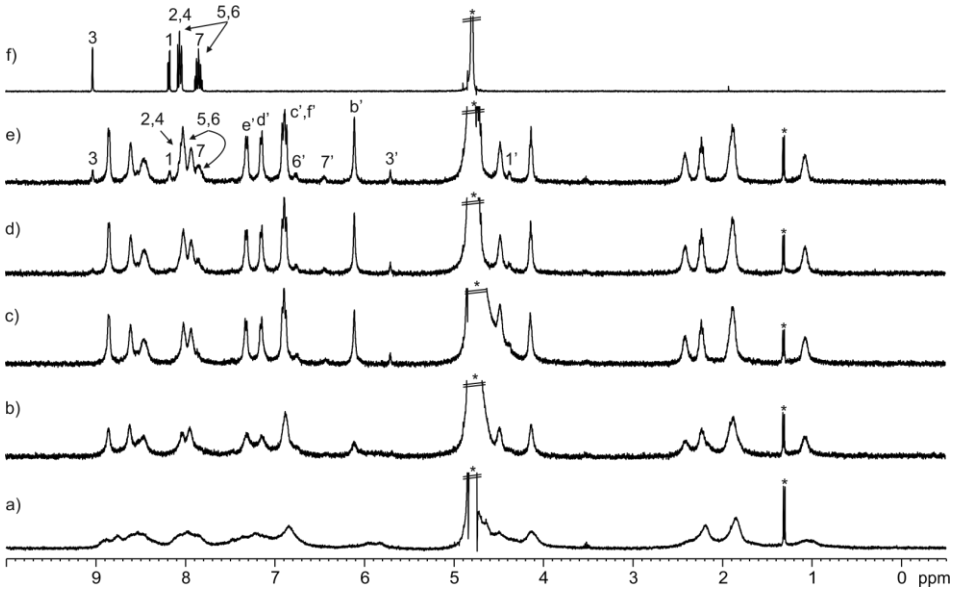

Figure 102. ^{1}H NMR (400 MHz, D_2O, 298 K) spectra of the titration of **6** with **8f**: a) 0; b) 0.5; c) 1; d) 1.5 and e) 2 equiv.; f) **8f**. Primed letters and numbers correspond to proton signals of bound components. See Figure 42 and Figure 101 for proton assignments. *Residual solvent peaks.

Table 14. Chemical shifts (δ, ppm) of the protons of free and bound **8f** (**8f**⊂**6**) and complexation induced shifts ($\Delta\delta$, ppm).

Signal	δ_{free}	δ_{bound}	$\Delta\delta$
1	8.16	4.37	-3.79
3	9.03	5.70	-3.33
6	7.84	6.76	-1.08
7	7.84	6.44	-1.40

3.4.8 Pair-wise ^{1}H NMR competitive experiments of **6** with pyridyl *N*-oxides

A series of pair-wise NMR competitive titration experiments were performed using receptor **6** (1 mM) and the pyridyl *N*-oxides **8a**-**f** in un-buffered D_2O solutions. The binding constant ratio between the two competing complexes was determined by integration of selected proton signals in the acquired ^{1}H NMR spectra (K_{a2}/K_{a1} = ([HG_2] x [G_1])/([HG_1] x [G_2]). The binding constant values of the thermodynamically more stable complexes (K_a > 10^7 M^{-1}) were determined using the calculated ratio of the binding constants and the binding constant value of one of the complexes, which was measured either accurately by ITC experiments or from a previous pair-wise competitive experiment.

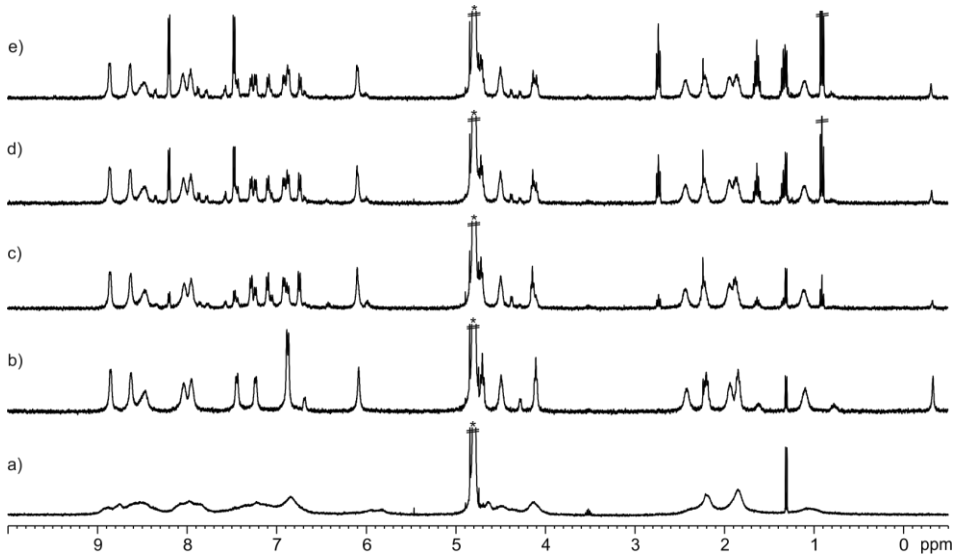

Figure 103. ^{1}H NMR (400 MHz, D_2O, 298 K) spectra of the pair-wise competitive experiment of **6**, **8a** and **8b**: a) **6**; b) **8b** + **6** (1:1 ratio); c) **8a** + **8b** + **6** (1.1:1:1 ratio); d) **8a** + **8b** + **6** (1.1:2.9:1 ratio) and e) **8a** + **8b** + **6** (1.1:4.4:1 ratio). *Residual solvent peak.

Integration of selected proton signals in the spectra of the pair-wise competitive experiments indicated that K_a (**8a**⊂**6**) = 7±1 x K_a (**8b**⊂**6**).

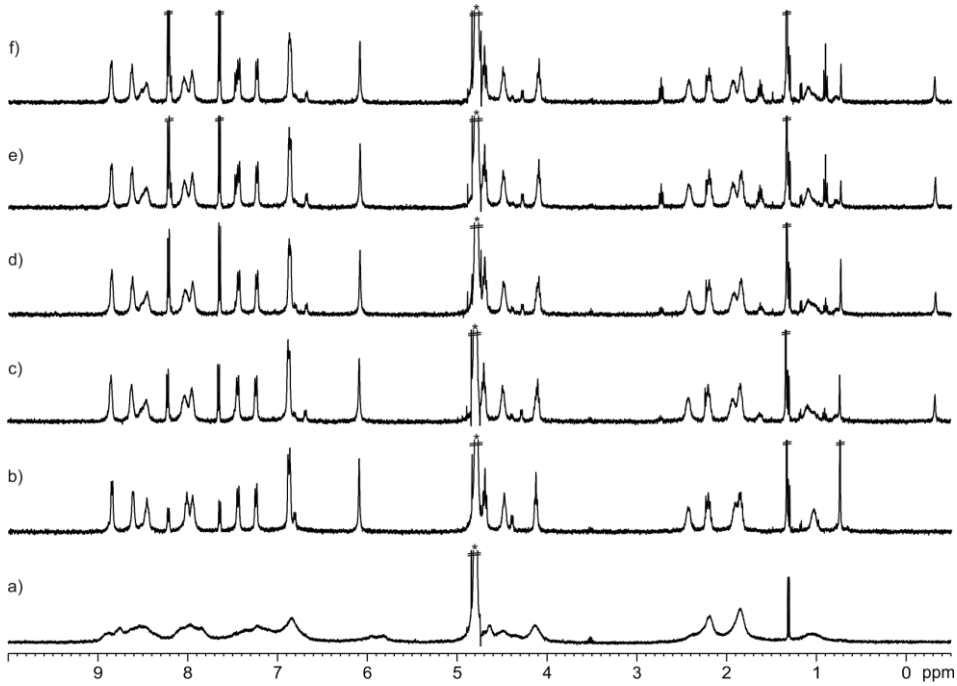

Figure 104. ^{1}H NMR (400 MHz, D_2O, 298 K) spectra of the pair-wise competitive experiment of **6**, **8b** and **8c**: a) **6**; b) **8c** + **6** (2.2:1 ratio); c) **8b** + **8c** + **6** (1:2.2:1 ratio); d) **8b** + **8c** + **6** (1:3.2:1 ratio); e) **8b** + **8c** + **6** (2:3.2:1 ratio) and f) **8b** + **8c** + **6** (2:5.6:1 ratio). *Residual solvent peak.

Integration of selected proton signals in the spectra of the pair-wise competitive experiments indicated that K_a (**8b**⊂**6**) = 10.0±0.5 x K_a (**8c**⊂**6**).

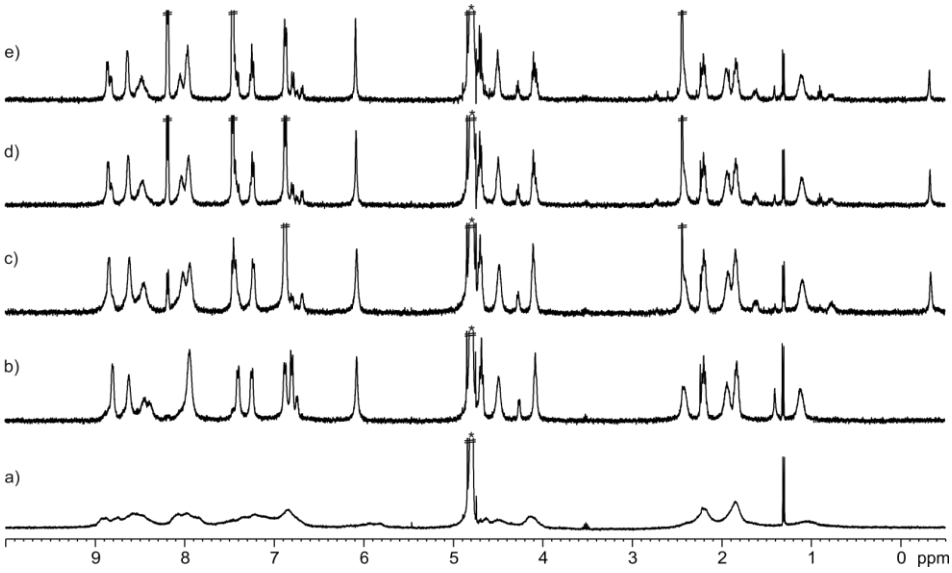

Figure 105. ^{1}H NMR (400 MHz, D_2O, 298 K) spectra of the pair-wise competitive experiment of **6**, **8b** and **8d**: a) **6**; b) **8d** + **6** (1.1:1 ratio); c) **8b** + **8d** + **6** (1:1.1:1 ratio); d) **8b** + **8d** + **6** (1:6:1 ratio) and e) **8b** + **8d** + **6** (1:12.7:1 ratio). *Residual solvent peak.

Integration of selected proton signals in the spectra of the pair-wise competitive experiments indicated that K_a (**8b**⊂**6**) = 60±10 x K_a (**8d**⊂**6**).

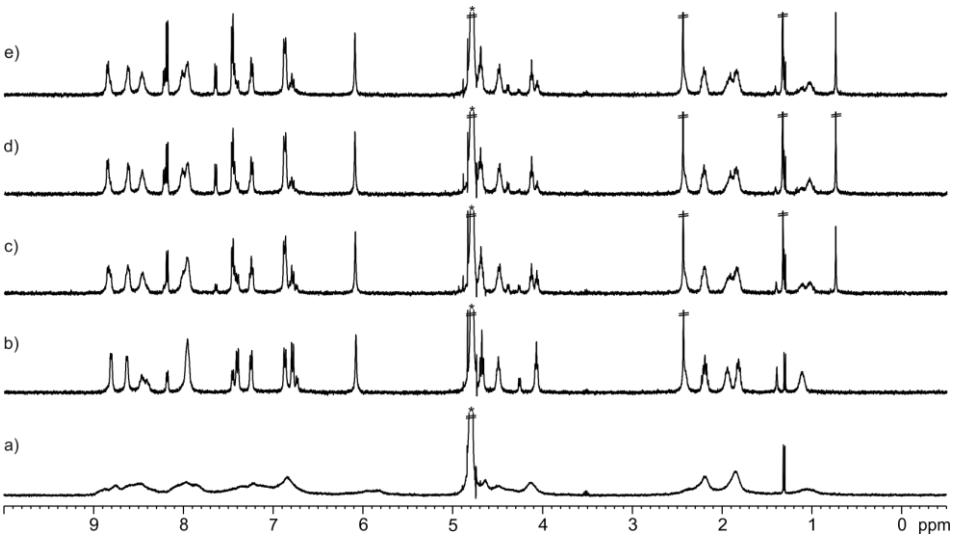

Figure 106. ^{1}H NMR (400 MHz, D_2O, 298 K) spectra of the pair-wise competitive experiment of **6**, **8c** and **8d**: a) **6**; b) **8d** + **6** (2.5:1 ratio); c) **8c** + **8d** + **6** (1.2:2.5:1 ratio); d) **8c** + **8d** + **6** (2.5:2.5:1 ratio) and e) **8c** + **8d** + **6** (2.5:3.9:1 ratio). *Residual solvent peak.

Integration of selected proton signals in the spectra of the pair-wise competitive experiments indicated that K_a (**8c**⊂**6**) = 4.5±0.4 x K_a (**8d**⊂**6**).

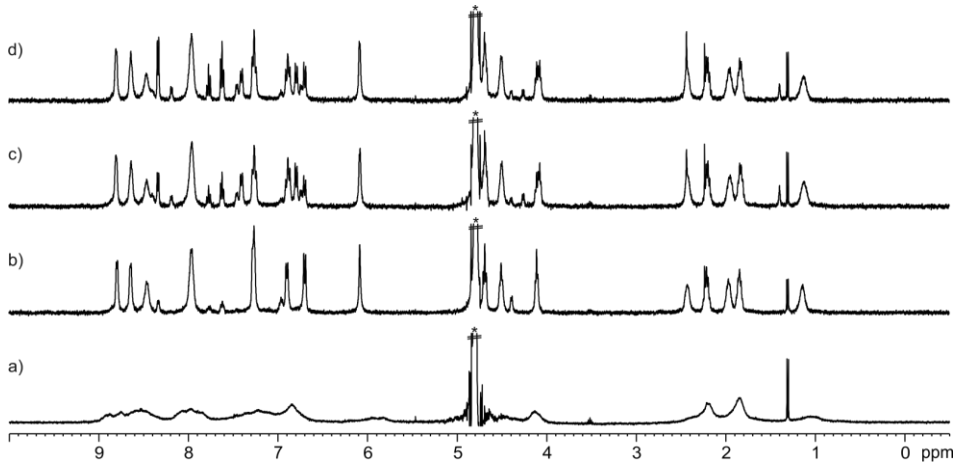

Figure 107. ^{1}H NMR (400 MHz, D_2O, 298 K) spectra of the pair-wise competitive experiment of **6**, **8d** and **8e**: a) **6**; b) **8e** + **6** (1.8:1 ratio); c) **8d** + **8e** + **6** (1.2:1.8:1 ratio) and d) **8d** + **8e** + **6** (1.2:3.2:1 ratio). *Residual solvent peak.

Integration of selected proton signals in the spectra of the pair-wise competitive experiments indicated that K_a (**8d**⊂**6**) = 3.7±0.2 x K_a (**8e**⊂**6**). This result is in line with that obtained from the ITC titration experiments.

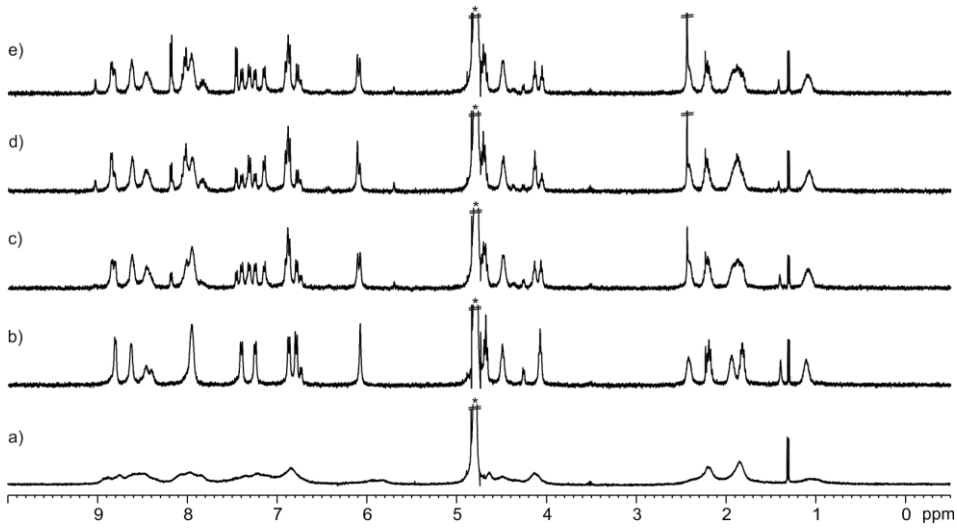

Figure 108. ^{1}H NMR (400 MHz, D_2O, 298 K) spectra of the pair-wise competitive experiment of **6**, **8d** and **8f**: a) **6**; b) **8d** + **6** (1:1 ratio); c) **8f** + **8d** + **6** (1:1:1 ratio); d) **8f** + **8d** + **6** (2:1:1 ratio) and e) **8f** + **8d** + **6** (2:2:1 ratio). *Residual solvent peak.

Chapter 3

Integration of selected proton signals in the spectra of the pair-wise competitive experiments indicated that K_a (**8f**⊂**6**) = 2.5±0.5 x K_a (**8d**⊂**6**). This result is in line with that obtained from the ITC titration experiments.

3.4.9 ITC titration experiments of octa-acid **5** with pyridyl *N*-oxides

ITC experiments were performed in a MicroCal VP-ITC MicroCalorimeter with the VP Viewer 2000 software. Titrations were carried out by adding small aliquots (8-10 µL) of a water solution of the guest into a solution of the host in the same solvent. The concentration of guest solutions was approximately seven to ten times more concentrated than receptor solutions ([H] = 0.05-0.10 mM). The association constants and the thermodynamic parameters were obtained from the fit of the titration data to the "one set of sites" binding model implemented in the Microcal ITC Data Analysis module.

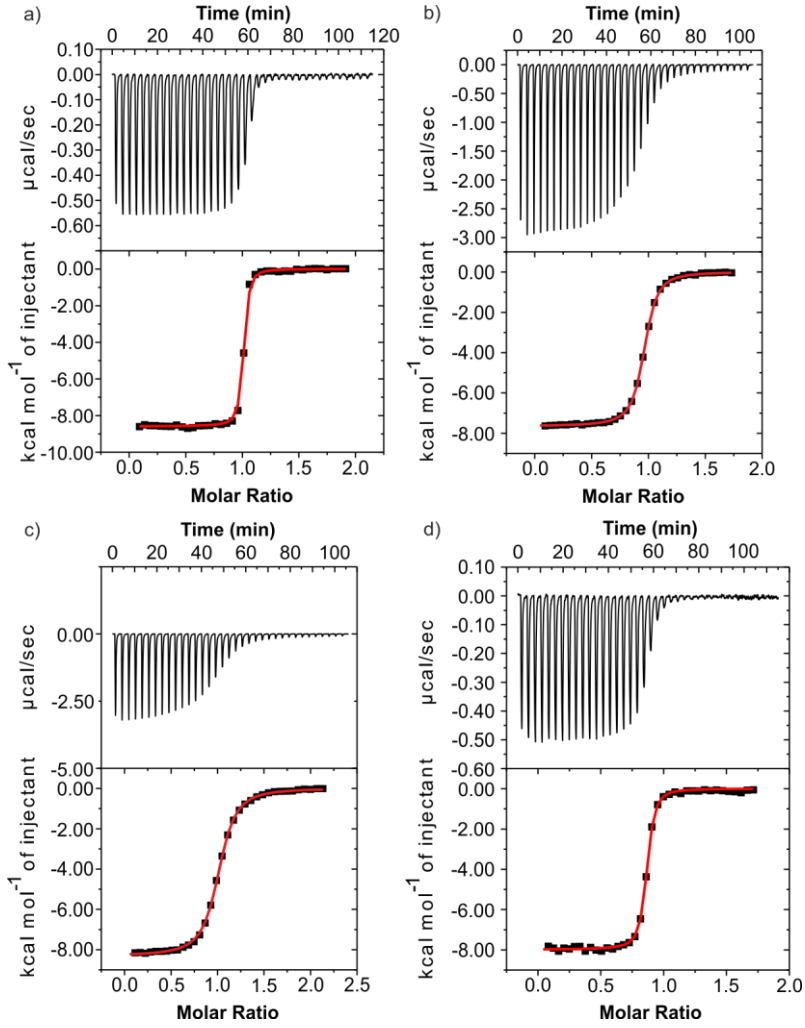

Figure 109. Top panels show raw data (heat *vs.* time) for the titration of guest into the host: a) **8b⊂5**; b) **8d⊂5**; c) **8e⊂5** and d) **8f⊂5** (H_2O at pH ~ 10). Titrations were performed at 298 K. Bottom panels represent integrated data fitted to the theoretical binding isotherm (red line) for a 1:1 binding model.

Table 15. Binding constants (K_a, M^{-1}) and thermodynamic parameters (ΔH, $T\Delta S$ and ΔG, kcal·mol^{-1}) determined from the combination of the ITC titration experiments and the pair-wise competitive experiments in water (pD or pH ~ 10) at 298 K. Errors in K_a and ΔG are reported as standard deviations.

Complex	K_a	ΔG	ΔH	$T\Delta S$
8a⊂5	>10^{7,a}		-12.5±0.1^{b}	
	1.2±0.5 x 10^{9,c}	-12.4±0.4^{c}		-0.1±0.4^{d}
8b⊂5	>10^{7,a}		-8.7±0.1^{b}	
	1.0±0.4 x 10^{8,c}	-10.9±0.2^{c}		2.2±0.2^{d}
8c⊂5	9.1±3.0 x 10^{6,c}	-9.5±0.2^{c}	n.d.	n.d.
8d⊂5	2.0±0.1 x 10^{6,b}	-8.6±0.1^{b}	-7.7±0.1^{b}	0.9±0.1^{b}
8e⊂5	8.6±0.5 x 10^{5,b}	-8.1±0.1^{b}	-8.4±0.1^{b}	-0.3±0.1^{b}
8f⊂5	2.2±0.2 x 10^{7,b}	-10.0±0.1^{b}	-7.8±0.2^{b}	2.2±0.2^{b}

[a] Estimated from ITC experiments; [b] determined by ITC experiments; [c] determined by pair-wise competitive experiments; [d] determined using the thermodynamic constants measured by ITC and pair-wise competitive experiments; n.d. = not determined.

3.4.10 ITC titration experiments of octa-pyridinium **6** with pyridyl *N*-oxides

ITC experiments were performed in a MicroCal VP-ITC MicroCalorimeter with the VP Viewer 2000 software. Titrations were carried out by adding small aliquots (8-10 μL) of a water solution of the guest into a solution of the host in the same solvent. The concentration of guest solutions was approximately seven to ten times more concentrated than receptor solutions ([H] = 0.05-0.10 mM). The association constants and the thermodynamic parameters were obtained from the fit of the titration data to the "one set of sites" binding model implemented in the Microcal ITC Data Analysis module.

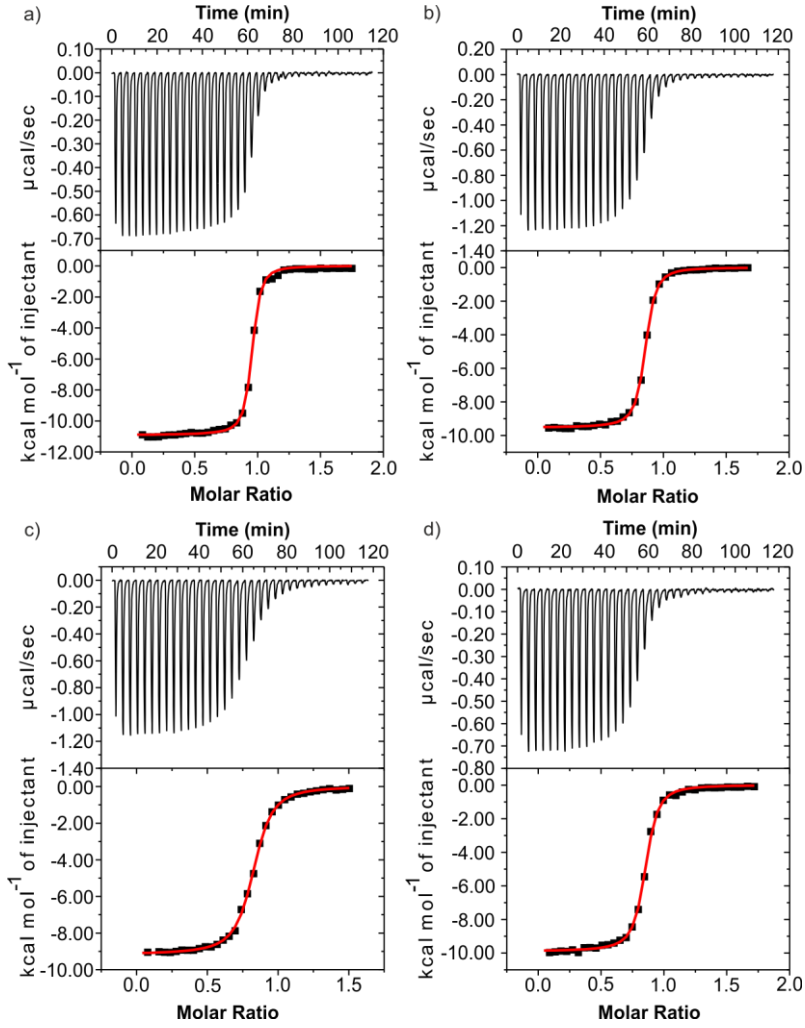

Figure 110. Top panels show raw data (heat *vs.* time) for the titration of guest into the host: a) **8b⊂6**; b) **8d⊂6**; c) **8e⊂6** and d) **8f⊂6** (H_2O). Titrations were performed at 298 K. Bottom panels represent integrated data fitted to the theoretical binding isotherm (red line) for a 1:1 binding model.

Table 16. Binding constants (K_a, M^{-1}) and thermodynamic parameters (ΔH, $T\Delta S$ and ΔG, kcal·mol^{-1}) determined from the combination of the ITC titration experiments and the pair-wise competitive experiments in water at 298 K. Errors in K_a and ΔG are reported as standard deviations.

Complex	K_a	ΔG	ΔH	$T\Delta S$
8a⊂6	>10^{7,a}		-15.1±0.1^{b}	
	2.6±0.6 x 10^{9,c}	-12.8±0.1^{c}		-2.3±0.1^{d}
8b⊂6	>10^{7,a}		-11.0±0.1^{b}	
	3.7±0.6 x 10^{8,c}	-11.7±0.1^{c}		0.7±0.1^{d}
8c⊂6	3.7±0.6 x 10^{7,c}	-10.3±0.1^{c}	n.d.	n.d.
8d⊂6	6.1±0.1 x 10^{6,b}	-9.2±0.1^{b}	-9.5±0.1^{b}	-0.3±0.1^{b}
8e⊂6	1.9±0.1 x 10^{6,b}	-8.6±0.1^{b}	-9.1±0.1^{b}	-0.5±0.1^{b}
8f⊂6	7.1±0.2 x 10^{6,b}	-9.3±0.1^{b}	-10.1±0.2^{b}	-0.8±0.2^{b}

[a] Estimated from ITC experiments; [b] determined by ITC experiments; [c] determined by pair-wise competitive experiments; [d] determined using the thermodynamic constants measured by ITC and pair-wise competitive experiments; n.d. = not determined.

3.4.11 VT ITC titration experiments of octa-pyridinium **6** with pyridyl *N*-oxide **8e**

ITC experiments were performed in a MicroCal VP-ITC MicroCalorimeter with the VP Viewer 2000 software. Titrations were carried out by adding small aliquots (8-10 μL) of a water solution of the guest into a solution of the host in the same solvent at different temperatures. The concentration of guest solutions was approximately seven to ten times more concentrated than receptor solutions ([H] = 0.05-0.10 mM). The association constants and the thermodynamic parameters were obtained from the fit of the titration data to the “one set of sites” binding model implemented in the Microcal ITC Data Analysis module.

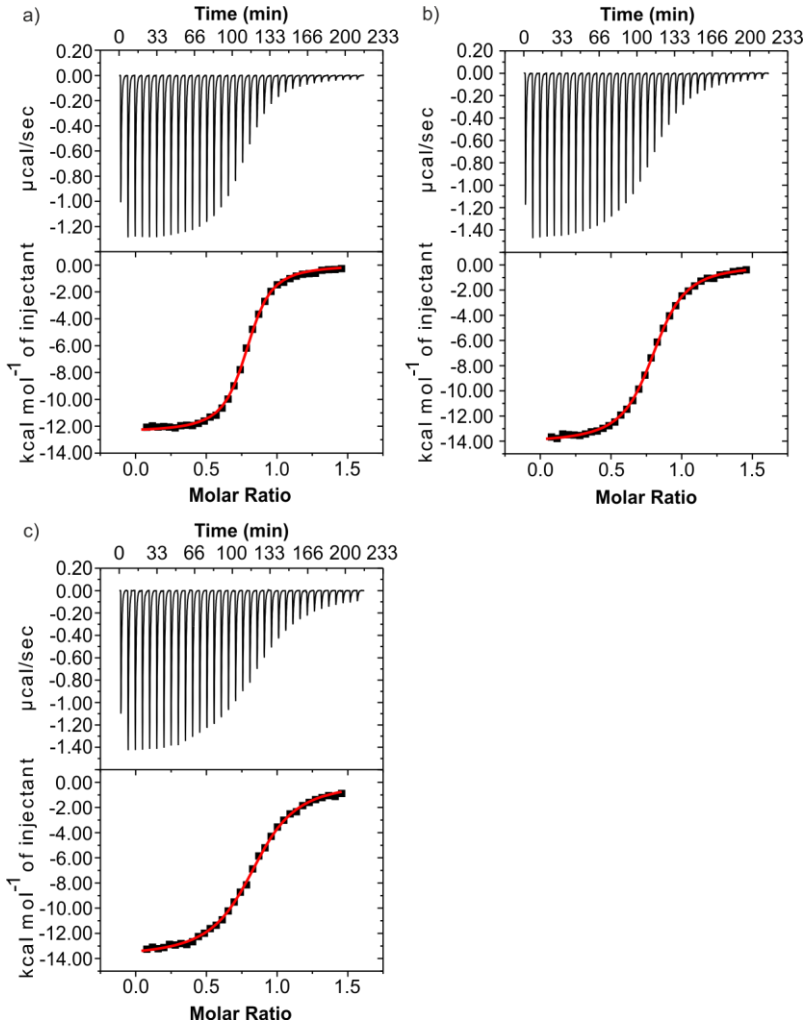

Figure 111. Top panels show raw data (heat *vs.* time) for the titration of guest into the host **8e⊂6**: a) 308; b) 318 and c) 328 K (H_2O). Bottom panels represent integrated data fitted to the theoretical binding isotherm (red line) for a 1:1 binding model.

Table 17. Binding constants (K_a, M^{-1}) and enthalpies (ΔH, kcal·mol^{-1}) determined from the VT ITC titration experiments (T, K) of pyridine *N*-oxide **8e** with octa-pyridinium **6** in neutral un-buffered water. Errors in K_a and ΔH are reported as standard deviations.

T	K_a	ΔH
298	1.9±0.1 x 10^6	-9.1±0.1
308	1.1±0.1 x 10^6	-12.3±0.3
318	6.4±0.2 x 10^5	-13.5±0.6
328	3.7±0.2 x 10^5	-14.3±0.4

3.4.12 Computational modelling

The energy-minimized structures shown in the chapter were obtained using Turbomole Version 7.0. The structures were optimized using DFT-Dispersion method (BP86-D3-def2-SVP DFT level of theory) and the water COSMO model.[45,46,47]

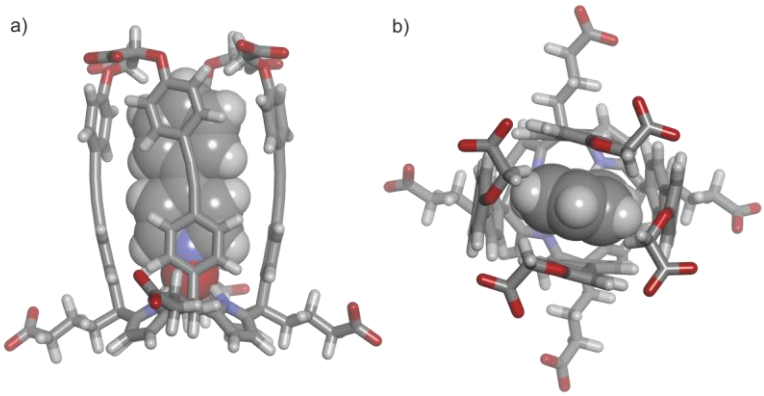

Figure 112. Energy minimized structure (BP86-D3-def2-SVP DFT level of theory, water COSMO model implemented in Turbomole Version 7.0) of the octa-anionic 1:1 inclusion complex **8a⊂5**: a) side and b) top views. The calix[4]pyrrole is depicted in stick representation and the *N*-oxide is shown as CPK model.

3.5 References and Notes

[1] K. N. Houk, A. G. Leach, S. P. Kim, X. Y. Zhang, *Angew. Chem., Int. Ed.* **2003**, *42*, 4872-4897.

[2] B. R. Stockwell, *Nature* **2004**, *432*, 846-854.

[3] S. L. Schreiber, *Nat. Chem. Biol.* **2005**, *1*, 64-66.

[4] D. Chandler, *Nature* **2002**, *417*, 491.

[5] D. Chandler, *Nature* **2005**, *437*, 640-647.

[6] G. V. Oshovsky, D. N. Reinhoudt, W. Verboom, *Angew. Chem., Int. Ed.* **2007**, *46*, 2366-2393.

[7] E. Persch, O. Dumele, F. Diederich, *Angew. Chem., Int. Ed.* **2015**, *54*, 3290-3327.

[8] W. Blokzijl, J. Engberts, *Angew. Chem., Int. Ed.* **1993**, *32*, 1545-1579.

[9] H. J. Bakker, *Nature* **2012**, *491*, 533-535.

[10] L. Yang, C. Adam, G. S. Nichol, S. L. Cockroft, *Nature Chem.* **2013**, *5*, 1006-1010.

[11] F. Biedermann, W. M. Nau, H. J. Schneider, *Angew. Chem., Int. Ed.* **2014**, *53*, 11158-11171.

[12] F. Biedermann, H.-J. Schneider, *Chem. Rev. (Washington, DC, U. S.)* **2016**, *116*, 5216-5300.

[13] D. Ben-Amotz, *Annu. Rev. Phys. Chem.* **2016**, *67*, 617-638.

[14] M. B. Hillyer, B. C. Gibb, *Annu. Rev. Phys. Chem.* **2016**, *67*, 307-329.

[15] C. Chothia, *Nature* **1974**, *248*, 338-339.

[16] C. Chothia, J. Janin, *Nature* **1975**, *256*, 705-708.

[17] A. E. Eriksson, W. A. Baase, X. J. Zhang, D. W. Heinz, M. Blaber, E. P. Baldwin, B. W. Matthews, *Science* **1992**, *255*, 178-183.

[18] C. N. Pace, *J. Mol. Biol.* **1992**, *226*, 29-35.

[19] S. M. Biros, J. Rebek, *Chem. Soc. Rev.* **2007**, *36*, 93-104.

[20] S. J. Barrow, S. Kasera, M. J. Rowland, J. del Barrio, O. A. Scherman, *Chem. Rev. (Washington, DC, U. S.)* **2015**, *115*, 12320-12406.

[21] J. Murray, K. Kim, T. Ogoshi, W. Yao, B. C. Gibb, *Chem. Soc. Rev.* **2017**, *46*, 2479-2496.

[22] E. A. Kataev, C. Muller, *Tetrahedron* **2014**, *70*, 137-167.

[23] P. S. Cremer, A. H. Flood, B. C. Gibb, D. L. Mobley, *Nature Chem.* **2017**, *10*, 8-16.

[24] C. F. Ke, H. Destecroix, M. P. Crump, A. P. Davis, *Nature Chem.* **2012**, *4*, 718-723.

[25] B. Sookcharoenpinyo, E. Klein, Y. Ferrand, D. B. Walker, P. R. Brotherhood, C. F. Ke, M. P. Crump, A. P. Davis, *Angew. Chem., Int. Ed.* **2012**, *51*, 4586-4590.

[26] T. J. Mooibroek, J. M. Casas-Solvas, R. L. Harniman, C. Renney, T. S. Carter, M. P. Crump, A. P. Davis, *Nature Chem.* **2016**, *8*, 69-74.

[27] R. A. Tromans, T. S. Carter, L. Chabanne, M. P. Crump, H. Li, J. V. Matlock, M. G. Orchard, A. P. Davis, *Nature Chem.* **2019**, *11*, 52-56.

[28] A. Lascaux, G. D. Leener, L. Fusaro, F. Topic, K. Rissanen, M. Luhmer, I. Jabin, *Org. Biomol. Chem.* **2016**, *14*, 738-746.

[29] G. B. Huang, S. H. Wang, H. Ke, L. P. Yang, W. Jiang, *J. Am. Chem. Soc.* **2016**, *138*, 14550-14553.

[30] L. L. Wang, Z. Chen, W. E. Liu, H. Ke, S. H. Wang, W. Jiang, *J. Am. Chem. Soc.* **2017**, *139*, 8436-8439.

[31] H. Yao, H. Ke, X. Zhang, S.-J. Pan, M.-S. Li, L.-P. Yang, G. Schreckenbach, W. Jiang, *J. Am. Chem. Soc.* **2018**, *140*, 13466-13477.

[32] S. Turega, W. Cullen, M. Whitehead, C. A. Hunter, M. D. Ward, *J. Am. Chem. Soc.* **2014**, *136*, 8475-8483.

[33] S. Mosca, Y. Yu, J. V. Gavette, K.-D. Zhang, J. Rebek, *J. Am. Chem. Soc.* **2015**, *137*, 14582-14585.

[34] A. J. Metherell, W. Cullen, N. H. Williams, M. D. Ward, *Chem.--Eur. J.* **2018**, *24*, 1554-1560.

[35] B. Verdejo, G. Gil-Ramirez, P. Ballester, *J. Am. Chem. Soc.* **2009**, *131*, 3178-3179.

[36] D. Hernandez-Alonso, S. Zankowski, L. Adriaenssens, P. Ballester, *Org. Biomol. Chem.* **2015**, *13*, 1022-1029.

[37] L. Escobar, A. Díaz-Moscoso, P. Ballester, *Chem. Sci.* **2018**, *9*, 7186-7192.

[38] G. Peñuelas-Haro, P. Ballester, *Chem. Sci.* **2019**, *10*, 2413-2423.

[39] L. Escobar, G. Aragay, P. Ballester, *Chem.--Eur. J.* **2016**, *22*, 13682-13689.

[40] A. Díaz-Moscoso, D. Hernández-Alonso, L. Escobar, F. A. Arroyave, P. Ballester, *Org. Lett.* **2017**, *19*, 226-229.

[41] A. Spurg, S. R. Waldvogel, *Eur. J. Org. Chem.* **2008**, 337-342.

[42] Y. He, S. Liu, A. Menon, S. Stanford, E. Oppong, A. M. Gunawan, L. Wu, D. J. Wu, A. M. Barrios, N. Bottini, A. C. B. Cato, Z.-Y. Zhang, *J. Med. Chem.* **2013**, *56*, 4990-5008.

[43] K.-D. Zhang, D. Ajami, J. Rebek, *J. Am. Chem. Soc.* **2013**, *135*, 18064-18066.

[44] M. B. Hillyer, C. L. D. Gibb, P. Sokkalingam, J. H. Jordan, S. E. Ioup, B. C. Gibb, *Org. Lett.* **2016**, *18*, 4048-4051.

[45] J. P. Perdew, *Phys. Rev. B* **1986**, *33*, 8822-8824.

[46] A. D. Becke, *Phys. Rev. A* **1988**, *38*, 3098-3100.

[47] R. Ahlrichs, M. Bar, M. Haser, H. Horn, C. Kolmel, *Chem. Phys. Lett.* **1989**, *162*, 165-169.

[48] E. A. Meyer, R. K. Castellano, F. Diederich, *Angew. Chem., Int. Ed.* **2003**, *42*, 1210-1250.

[49] L. M. Salonen, M. Ellermann, F. Diederich, *Angew. Chem., Int. Ed.* **2011**, *50*, 4808-4842.

[50] L. Escobar, D. Villarón, E. C. Escudero-Adán, P. Ballester, *Chem. Commun. (Cambridge, U. K.)* **2019**, *55*, 604-607.

[51] F. Diederich, K. Dick, *J. Am. Chem. Soc.* **1984**, *106*, 8024-8036.

[52] J. D. Dunitz, *Chem. Biol.* **1995**, *2*, 709-712.

[53] C. H. Haas, S. M. Biros, J. Rebek, *Chem. Commun. (Cambridge, U. K.)* **2005**, 6044-6045.

[54] M. Whitehead, S. Turega, A. Stephenson, C. A. Hunter, M. D. Ward, *Chem. Sci.* **2013**, *4*, 2744-2751.

[55] Y. Nozaki, C. Tanford, *J. Biol. Chem.* **1971**, *246*, 2211-2217.

[56] S. Damodaran, K. B. Song, *J. Biol. Chem.* **1986**, *261*, 7220-7222.

[57] S. K. Burley, G. A. Petsko, *Science* **1985**, *229*, 23-28.

[58] D. A. Stauffer, R. E. Barrans, D. A. Dougherty, *J. Org. Chem.* **1990**, *55*, 2762-2767.

[59] D. B. Smithrud, T. B. Wyman, F. Diederich, *J. Am. Chem. Soc.* **1991**, *113*, 5420-5426.

[60] T. Guinovart, D. Hernández-Alonso, L. Adriaenssens, P. Blondeau, M. Martínez-Belmonte, F. X. Rius, F. J. Andrade, P. Ballester, *Angew. Chem., Int. Ed.* **2016**, *55*, 2435-2440.

[61] J. S. Oakdale, L. Kwisnek, V. V. Fokin, *Macromolecules* **2016**, *49*, 4473-4479.

[62] T. Gibtner, F. Hampel, J.-P. Gisselbrecht, A. Hirsch, *Chem.--Eur. J.* **2002**, *8*, 408-432.

[63] G. R. Fulmer, A. J. M. Miller, N. H. Sherden, H. E. Gottlieb, A. Nudelman, B. M. Stoltz, J. E. Bercaw, K. I. Goldberg, *Organometallics* **2010**, *29*, 2176-2179.

[64] V. Fiandanese, G. Marchese, V. Martina, L. Ronzini, *Tetrahedron Lett.* **1984**, *25*, 4805-4808.

[65] B. Scheiper, M. Bonnekessel, H. Krause, A. Furstner, *J. Org. Chem.* **2004**, *69*, 3943-3949.

[66] D. A. Lightner, Nicolett.R, G. B. Quistad, E. Irwin, *Org. Mass Spectrom.* **1970**, *4*, 571-585.

[67] S. Duric, C. C. Tzschucke, *Org. Lett.* **2011**, *13*, 2310-2313.

UNIVERSITAT ROVIRA I VIRGILI
MOLECULAR CONTAINERS BASED ON ARYL-EXTENDED CALIX[4]PYRROLES
Luis Escobar González

Chapter 4

Self-Assembly of Mono-Metallic Pd(II)/Pt(II)-Cages Featuring Two Different Polar Binding Sites

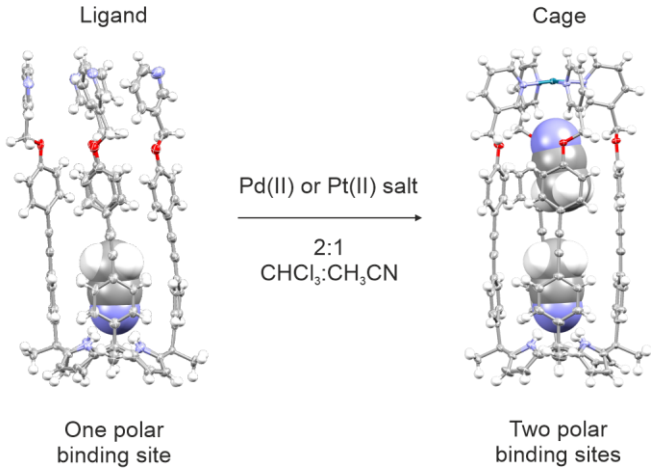

Part of this chapter has been published in:

L. Escobar, D. Villarón, E. C. Escudero-Adán, P. Ballester, *Chem. Commun.* **2019**, *55*, 604-607.

UNIVERSITAT ROVIRA I VIRGILI
MOLECULAR CONTAINERS BASED ON ARYL-EXTENDED CALIX[4]PYRROLES
Luis Escobar González

4.1 Introduction

Metal coordination is a methodology widely used for the self-assembly of molecular containers.[1,2,3,4] One of its aims is the design of molecular containers with tailored or external-stimuli controlled guest exchange dynamics. In this regard, understanding the exchange mechanisms that are operative in these assemblies allows their tuning to improve specific functions.[5,6,7,8,9,10,11,12,13,14,15,16] Among many applications,[17] metal-mediated assemblies are exploited for the stabilization of reactive species, the development of supramolecular catalysts and the controlled drug delivery of relevant substrates.[18,19,20,21,22]

In the construction of metal coordination assemblies, Pd(II) and Pt(II) are commonly used since they afford thermodynamically and kinetically stable metal junctions featuring square-planar geometry with pyridyl ligands.[23] The use of flat, multi-topic ligands yields Pd(II)/Pt(II)-coordination cages with large portals, allowing the reversible passage of guests.[2,24,25] On the other hand, concave and bowl-shaped multi-topic pyridyl ligands are more appropriate for the construction of metal-mediated molecular capsules, in which the in/out exchange of guests requires the dissociation of ligand-metal coordination bonds.[26] The pyridyl *N*-Pd(II) bond is labile, whereas the *N*-Pt(II) counterpart is more inert at ambient conditions.[24,27,28,29,30,31] For example, the energy barrier for the dissociation of pyridyl ligands is *ca.* 22 kcal·mol^{-1} in a banana-shaped $[L_4{\bullet}Pd_2]^{4+}$ cage.[32] In contrast, the octahedral $[L_4{\bullet}Pt_6]^{12+}$ cage (Figure 1a) does not show signs of dissociative processes at room temperature.[33,34,35]

Raymond and co-workers investigated the guest exchange mechanisms of a tetrahedral $[L_6{\bullet}Ga_4]^{12-}$ cage (Figure 1b). Small cationic guests (PEt_4^+, NEt_4^+ or $NMe_2Pr_2^+$) are bound reversibly to $[L_6{\bullet}Ga_4]^{12-}$ via a slippage mechanism (*i.e.* deformation of a cage's face) featuring exchange rate constants $k = 10^{-3}$ to 10 s^{-1} at room temperature. A sterically demanding guest, such as $[CoCp^*_2]^+$, which likely requires partial ligand-metal dissociation, has a dramatically decreased exchange rate, but the larger guest can still be displaced from the cage's cavity to the bulk solution.[5,36,37] Related exchange pathways were found by other groups using self-assembled capsules and cages.[11,38,39,40,41]

Atwood and Szumna devised mono-molecular capsules from resorcin[4]arene cavitands sealed by anion coordination (Figure 1c).[42] We thought that assembling mono-metallic Pd(II)/Pt(II)-mediated containers could be done similarly with upper rim, tetra-pyridyl substituted aryl-extended calix[4]pyrroles (C[4]Ps) as ligands. The cone conformation of tetra-*α* aryl-extended C[4]Ps has a deep aromatic cavity with a polar closed end.[43] The coordination of Pd(II) or Pt(II) at the upper rim of tetra-pyridyl derivatives could be used to close the open end and provide an additional polar binding site: a convergent array of four inwardly-directed *α*-CH pyridyl functions.[44,45,46,47]

Examples of metal coordination to calix[4]pyrrole scaffolds are known, but are scarce in the literature.[48,49,50,51,52] For example, Ji *et al.* reported the coordination of Pd(II) at the upper rim of a 2-

pyridyl substituted tetra-*α* aryl-extended C[4]P for the self-assembly of a bi-metallic cavitand.[48] An analogous C[4]P bearing 3-pyridyl substituents at the upper rim should assemble into a mono-metallic Pd(II)-cage suitable for the inclusion of sizeable polar guests.

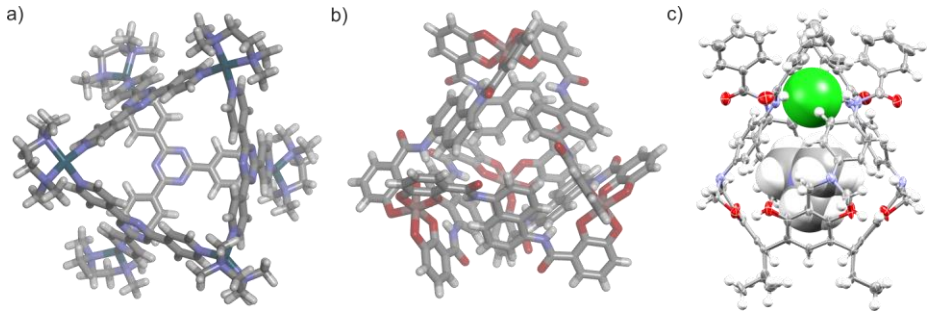

Figure 1. Energy minimized structures (MM3): a) Fujita's octahedral $[L_4{\bullet}Pt_6]^{12+}$ cage and b) Raymond's tetrahedral $[L_6{\bullet}Ga_4]^{12-}$ cage; c) X-ray crystal structure of the mono-molecular capsule sealed by anion coordination reported by Atwood and Szumna (chloride is bound to the amide NHs at the upper rim and tetra-methylammonium cation is encapsulated). The energy minimized structures are depicted in stick representation. The X-ray structure is shown in ORTEP view with thermal ellipsoids set at 50% probability and hydrogen atoms are shown as fixed-size spheres of 0.3 Å radius. Bound guests are shown as CPK models.

Here, we report the syntheses of the tetra-*α* isomers of aryl-extended and super aryl-extended calix[4]pyrroles bearing four 3-pyridyl substituents at their upper rims. We describe the results of coordination studies of the tetra-pyridyl calix[4]pyrroles with Pd(II) and Pt(II) salts. The super aryl-extended tetra-pyridyl C[4]P self-assembles into a mono-metallic Pd(II)/Pt(II)-cage, whereas the aryl-extended derivative produces ill-defined aggregates. We performed binding and kinetic ^{1}H NMR studies of a series of planar pyridyl *N*-oxides and quinuclidine *N*-oxide, a sterically more demanding guest, with the mono-metallic cages. Finally, we disclose the inclusion/exchange mechanisms involved in the reversible encapsulation of these neutral polar guests into the metallo-cages.

4.2 Results and Discussion

4.2.1 Synthesis

Tetra-pyridyl super aryl-extended calix[4]pyrrole (SAE-C[4]P) **1** was synthesized by quadruple Sonogashira coupling of pyridyl mono-acetylene derivative **2** with tetra-*α*-(4-iodophenyl) calix[4]pyrrole **3**[53] (Scheme 1a). In turn, **4** was prepared by reacting tetra-*α*-(4-hydroxyphenyl) calix[4]pyrrole **5**[51] with 3-(bromomethyl)pyridinium hydrobromide **6** (Scheme 1b). Tetra-pyridyl **1** and **4** were obtained in moderate yields (65 and 26%, respectively) and excellent purities. The compounds were fully characterized by a complete set of high-resolution spectra (NMR and HRMS).

Tetra-pyridyl SAE-C[4]P **1** was also characterized in the solid state by single crystal X-ray diffraction (Figure 2). **1** adopts a cone conformation with a bound acetonitrile molecule to the calix[4]pyrrole binding site. The pyrrole NHs of **1** establish four convergent hydrogen-bonding interactions with the nitrogen atom of the included CH_3CN, *d*(N···N) ~ 3.2 Å. The upper section of the aromatic cavity of **1** collapses owing to edge-to-face CH-π interactions.[54] Note that **1**, in a cone conformation, features a deep aromatic cavity with a single polar binding site.

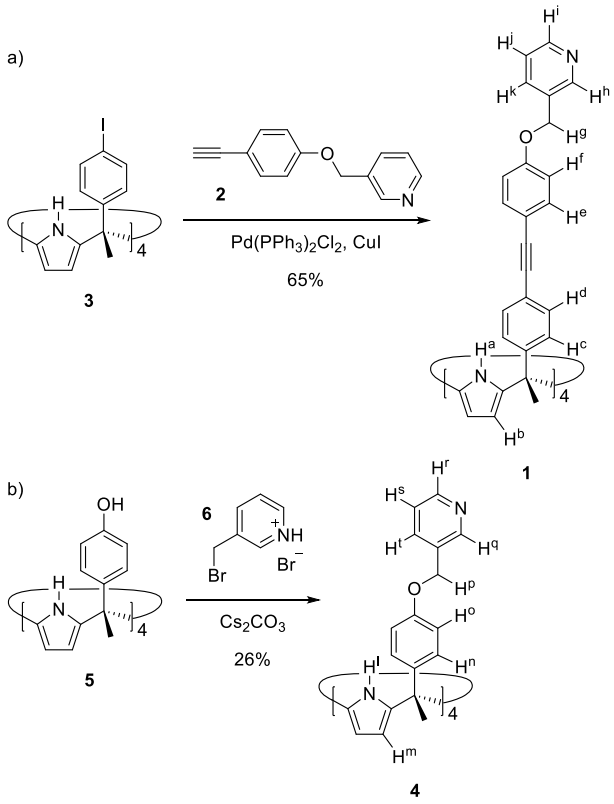

Scheme 1. Synthesis of a) tetra-pyridyl SAE-C[4]P **1** and b) tetra-pyridyl AE-C[4]P **4**.

4.2.2 Coordination studies

Tetra-pyridyl super aryl-extended calix[4]pyrrole **1**

We probed the coordination of Pd(II) with tetra-pyridyl SAE-C[4]P **1** in a 2:1 $CDCl_3$:CD_3CN solution mixture using ^{1}H NMR spectroscopy. We used this solvent mixture because **1** is not soluble in neat acetonitrile at typical NMR concentrations. The ^{1}H NMR spectrum of tetra-pyridyl **1** showed sharp and well-defined proton signals in agreement with a C_{4v} symmetry (Figure 3a). Based on previous findings[55] and its X-ray structure (Figure 2), **1** is expected to adopt the cone conformation by binding one CH_3CN molecule in its polar aromatic cavity. Not surprisingly, the ^{1}H NMR spectra of **1**

in pure $CDCl_3$ or in the solvent mixture above displayed different chemical shift values for the phenyl and pyridyl protons ($\Delta\delta$ ~ 0.25 ppm). The superposition of the aromatic signals of the two spectra revealed that the NH and *β*-pyrrole proton signals were sharper and experienced significant downfield shifts in the polar mixture (see Experimental Section). These observations indicate that in the solvent mixture, **1** is locked in a cone conformation by four hydrogen bonds between the pyrrole NHs and the nitrogen atom of the included CD_3CN molecule.

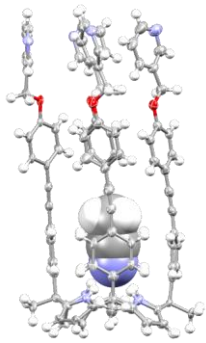

Figure 2. X-ray crystal structure of $CH_3CN\subset$**1**. The structure is shown in ORTEP view with thermal ellipsoids set at 50% probability. Hydrogen atoms are shown as fixed-size spheres of 0.3 Å radius. Bound CH_3CN is shown as CPK model. Solvent molecules and disordered atoms are omitted for clarity.

The addition of *ca.* 0.5 equiv. of $[Pd(CH_3CN)_4](BF_4)_2$ to a millimolar solution of **1** in the solvent mixture produced a set of new signals, which we assigned to the protons of bound **1**, together with another smaller set of signals. The thermal equilibration of the mixture for 24 h at 40°C led to the disappearance of the smaller signals, which we allocate to kinetically assembled aggregates of unknown structure. At this point, the intensities of the proton signals of free and bound receptor were almost identical (Figure 3b). The proton signals for bound **1** are also in agreement with a C_{4v} symmetry. Remarkably, the pyridyl proton signals of bound **1** displayed significant downfield shifts compared to those of the free counterpart. Specially, the *α*-pyridyl protons moved more than 0.7 ppm (Table 1). These chemical shift changes are consistent with pyridyl-Pd(II) coordination bonds as reported in the literature.[56] The addition of *ca.* 1 equiv. of Pd(II) and subsequent thermal equilibration induced the exclusive observation of the signals of bound **1** (Figure 3c). The addition of an excess of Pd(II) did not provoke further changes on the proton signals. Taken together, these results indicate that **1** forms a 1:1 complex with Pd(II). Most likely, the pyridyl substituents of **1** coordinate to Pd(II) producing a square-planar complex, $[\mathbf{1}\bullet Pd]^{2+}$. The equilibrium between free and bound **1** shows slow dynamics on the chemical shift timescale and the association constant of the complex can be estimated to be larger than 10^4 M^{-1}.

Based on the relative integral values of the protons in $[\mathbf{1}\bullet Pd]^{2+}$ and those of an internal standard (I.S.), we calculated that $[\mathbf{1}\bullet Pd]^{2+}$ was assembled to an extent larger than 70%. Large oligomeric metallo-aggregates are probably also present in equilibrium with $[\mathbf{1}\bullet Pd]^{2+}$.

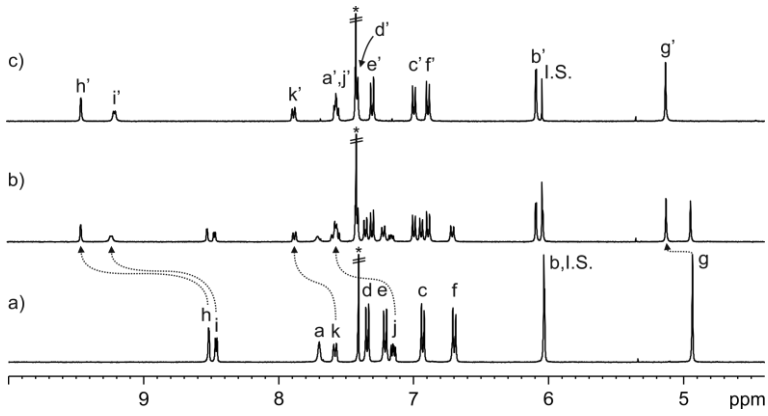

Figure 3. Selected region of the ^{1}H NMR (400 MHz, 2:1 $CDCl_3$:CD_3CN, 298 K) spectra: a) **1**; addition of Pd(II) to **1**: b) *ca.* 0.5 and c) *ca.* 1 equiv. after thermal equilibration (24 h at 40°C). Primed letters correspond to proton signals of [**1**•Pd]$^{2+}$. 1,3,5-Trimethoxybenzene (I.S.). See Scheme 1 for proton assignment. *Residual solvent peak.

Table 1. Chemical shifts (δ, ppm) and chemical shift changes ($\Delta\delta$, ppm) of the proton signals of the 3-pyridyl substituents of **1** upon metal coordination in 2:1 $CDCl_3$:CD_3CN. See Scheme 1 for proton assignment.

Signal	δ, **1**	δ, [**1**•Pd]$^{2+}$	$\Delta\delta$, [**1**•Pd]$^{2+}$	δ, [**1**•Pt]$^{2+}$	$\Delta\delta$, [**1**•Pt]$^{2+}$
h	8.51	9.45	+0.94	9.33	+0.82
i	8.46	9.16	+0.70	9.19	+0.73
j	7.15	7.56	+0.41	7.56	+0.41
k	7.58	7.87	+0.29	7.86	+0.28

In order to estimate the dimensions of [**1**•Pd]$^{2+}$, we undertook a series of ^{1}H DOSY NMR experiments[57] in 2:1 $CDCl_3$:CD_3CN solution. The calculated diffusion constant (-log *D*) for [**1**•Pd]$^{2+}$ was 9.28 (Figure 4a), whereas a value of 9.25 was calculated for the cone conformer of **1** (see Experimental Section), which features related dimensions. Similar diffusion constant values were obtained in $(CD_3)_2SO$ solutions for **1** and [**1**•Pd]$^{2+}$ (Figure 4b). However, the diffusion constant values determined in $(CD_3)_2SO$ and 2:1 $CDCl_3$:CD_3CN solutions are different. We attribute this finding to the different viscosity of the solvents.

The [**1**•Pd]$^{2+}$ cage is better represented by a cylindrical shaped object than a sphere. We determined the dimensions of the cylinder using Equations 1-3.[58,59,60] First, we estimated the length (a) and the radius (b) from the energy minimized structure (MM3) of $[(CH_3)_2SO]_2\subset$[**1**•Pd]$^{2+}$. These values were refined manually in order to minimize the difference between the calculated coefficient values and those measured experimentally ($D_{measured} - D_{calculated} < 10^{-12}$ $m^2 \cdot s^{-1}$). The cylindrical object corresponding to the optimized values was superimposed with the compound to

verify that the geometrical parameters have a physical significance. The experimentally measured diffusion constant is in agreement with one calculated for a cylindrical object with geometrical parameters coinciding with those determined from the energy minimized structure of [**1**•Pd]$^{2+}$ (5.1 Å radius and 21 Å height) (Figure 5a).

1) $R = [(3(a/2)b^2)/2]^{1/3}$; where a is the length and b is the radius.

2) $f = [(2/3)^{1/3}P^{2/3}]/[\ln(2P) - 0.3]$; $P = a/b$.

3) $D = (k_B T)/(6\pi\eta R f)$; k_B is the Boltzmann constant; T is the temperature and η is the viscosity of the solvent.

Note that these equations are valid to determine the dimensions of a cylinder from the diffusion constant when $2 < P < 20$.

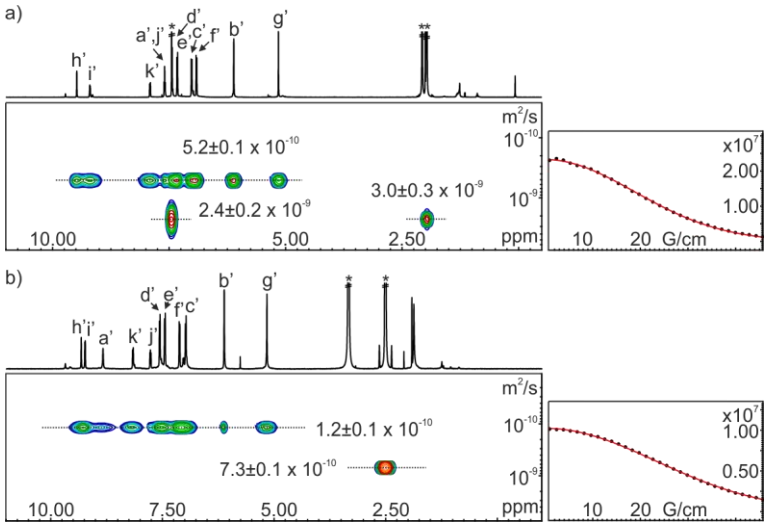

Figure 4. (left) ^{1}H pseudo 2D plot of DOSY (500 MHz with cryoprobe, 298 K): a) [**1**•Pd](BF$_4$)$_2$ in 2:1 $CDCl_3$:CD_3CN (D20 = 0.15 s; P30 = 0.80 ms) and b) [**1**•Pd](TFA)$_2$ in $(CD_3)_2SO$ (D20 = 0.15 s; P30 = 1.40 ms). (right) Fit of the decay of the signal b' to a mono-exponential function. Primed letters correspond to proton signals of [**1**•Pd]$^{2+}$. See Scheme 1 for proton assignment. Errors are indicated as standard deviations. *Residual solvent peaks.

The [**1**•Pd]$^{2+}$ complex was also characterized by ESI$^+$/TOF. The mass spectrum showed an intense ion peak at m/z = 803.2695, which coincides with the exact mass for the mono-isotopic peak of the doubly positive-charged cage. In addition, the isotopic distribution of the ion peak fully coincides with the theoretical one (see Experimental Section). These results support the formation of [**1**•Pd]$^{2+}$ in solution and its persistence in the gas phase.

We also obtained single crystals of [**1**•Pd](BF$_4$)$_2$ suitable for X-ray diffraction analysis. The data revealed the presence of the mono-Pd(II) cage (Figure 5b), and supports the structure determined in solution. In the solid state, the C[4]P core of [**1**•Pd](BF$_4$)$_2$ adopts the cone conformation with a

CH_3CN molecule bound to the four pyrrole NHs, *d*(N···N) ~ 3.3 Å. At the upper rim, the four pyridyl units are coordinated to Pd(II) with an average *d*(N···Pd) ~ 2.02 Å. We also observed a second CH_3CN molecule included in the cage's cavity. This molecule is bound to the four inwardly-directed *α*-pyridyl protons, *d*(N···C_α) ~ 3.5 Å, and oriented in opposite direction with respect to the other guest (Figure 5b). Additional electrostatic interactions (ion-dipole) between this CH_3CN molecule and the Pd(II) atom are also possible. The packing coefficient (*PC*) calculated for $[CH_3CN]_2\subset$[**1**•Pd]$(BF_4)_2$ is *ca.* 51%, consistent with the optimal 55% proposed for thermodynamically stable capsular complexes.[61] In short, SAE-C[4]P **1** tetra-chelates a Pd(II) ion at its upper rim, and defines a mono-metallic cage that features two different polar binding sites converging on the cavity. The cavity's space is adequate for the pair-wise encapsulation of CH_3CN guests.

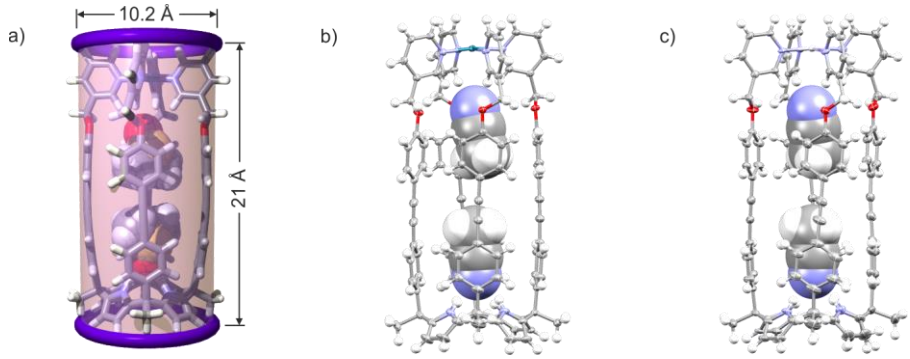

Figure 5. a) Energy minimized structure (MM3) of the putative $[(CH_3)_2SO]_2\subset$[**1**•Pd]$^{2+}$ cage complex and cylinder indicating its dimensions; X-ray crystal structures: b) $[CH_3CN]_2\subset$[**1**•Pd]$(BF_4)_2$ and c) $[CH_3CN]_2\subset$[**1**•Pt]$(BF_4)_2$. The energy minimized structure is depicted in stick representation. The X-ray structures are shown in ORTEP view with thermal ellipsoids set at 50% probability. Hydrogen atoms are shown as fixed-size spheres of 0.3 Å radius. Bound $(CH_3)_2SO$ and CH_3CN molecules are shown as CPK models. Anions, solvent molecules and disordered atoms are omitted for clarity.

Likewise, we also assembled the thermodynamically and kinetically more inert [**1**•Pt]$^{2+}$ cage by the addition of *ca.* 1 equiv. of $[Pt(CH_3CN)_4](BF_4)_2$ to a solution of **1** in 2:1 $CDCl_3$:CD_3CN and subsequent thermal equilibration, 50°C for 72 h or 80°C for 24 h. [**1**•Pt]$^{2+}$ was assembled in solution in an extent larger than 60% and fully characterized by a set of high-resolution spectra (NMR and HRMS). It is worth mentioning that the ^{1}H NMR spectrum of [**1**•Pt]$^{2+}$, even after thermal equilibration, showed small proton signals assigned to kinetically assembled aggregates of unknown structure.

The structure of [**1**•Pt]$^{2+}$ was also confirmed in the solid state by X-ray diffraction of a single crystal (Figure 5c). In the solid state, the four pyridyl substituents of ligand **1** are simultaneously coordinated to the Pt(II) metal center. Two opposite *N*-Pt(II) coordination bonds are shorter than the other two, d_1(N···Pt) ~ 1.97 Å and d_2(N···Pt) ~ 2.02 Å. In the case of [**1**•Pd]$^{2+}$, the four *N*-Pd(II)

bonds feature similar distances (see above). Two molecules of CH_3CN are included in the polar cavity of [**1**•Pt]$^{2+}$. One hydrogen bonds to the calix[4]pyrrole core and the other to the *α*-pyridyl protons. The X-ray structures of [**1**•Pt]$^{2+}$ and [**1**•Pd]$^{2+}$ are analogous.

Tetra-pyridyl aryl-extended calix[4]pyrrole **4**

We also investigated the coordination of Pd(II) to tetra-pyridyl AE-C[4]P **4** (Scheme 1b). In striking contrast to tetra-pyridyl SAE-C[4]P **1**, the incremental addition of Pd(II) to a solution of **2** in 2:1 $CDCl_3$:CD_3CN solvent mixture produced ^{1}H NMR spectra displaying broad signals (Figure 6). Thermal equilibration of the solutions at 40°C for 24 h did not produce changes on the ^{1}H NMR spectra. Changing the solvent to $(CD_3)_2SO$ produced similar results (see Experimental Section). These findings indicated that **4** and Pd(II) do not assemble into a mono-metallic cage to a significant extent but rather produce ill-defined aggregates.

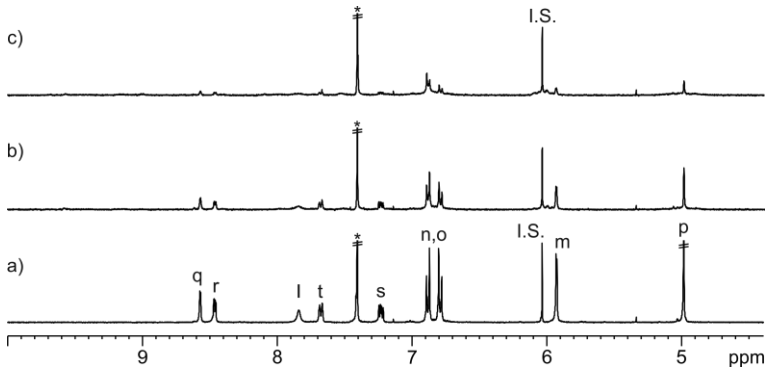

Figure 6. Selected region of the ^{1}H NMR (400 MHz, 2:1 $CDCl_3$:CD_3CN, 298 K) spectra: a) **4**; addition of Pd(II) to **4**: b) *ca.* 0.5 and c) *ca.* 1 equiv. 1,3,5-Trimethoxybenzene (I.S.). See Scheme 1 for proton assignment. *Residual solvent peak.

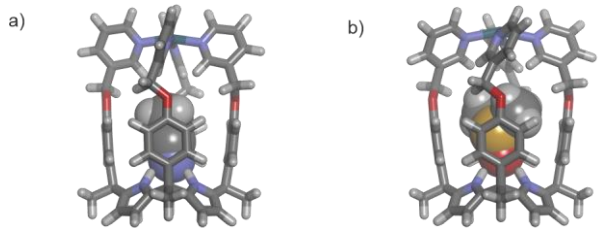

Figure 7. Energy minimized structures (MM3): a) $CH_3CN\subset$[**4**•Pd]$^{2+}$ and b) $(CH_3)_2SO\subset$[**4**•Pd]$^{2+}$. The cages are depicted in stick representation. Bound CH_3CN and $(CH_3)_2SO$ molecules are shown as CPK models.

Molecular modelling studies of the putative $CH_3CN\subset$[**4**•Pd]$^{2+}$ and $(CH_3)_2SO\subset$[**4**•Pd]$^{2+}$ cage complexes (Figure 7) showed a comfortable fit of the solvent molecules in the cavity (*PC* ~ 55%). The polar hetero-atoms of the bound solvent molecules, CH_3CN and $(CH_3)_2SO$, are hydrogen-

bonded to the pyrrole NHs of the calix[4]pyrrole unit. However, this arrangement does not satisfy the hydrogen-bonding characteristics of the inner *α*-pyridyl protons. We surmised that the assembly of C[4]P Pd(II)-cages requires the complementation of the hydrogen-bonding characteristics of both its opposed binding sites.

4.2.3 Formation of cage complexes

We examined the assembly of [**1**•Pd]$^{2+}$ using as precursor the 1:1 inclusion complexes of **1** with the pyridyl *N*-oxides **7**-**10** and quinuclidine *N*-oxide **11** (Figure 8). Previously, we showed that both aryl-extended and super aryl-extended calix[4]pyrroles form thermodynamically and kinetically stable 1:1 inclusion complexes with such *N*-oxides.[55]

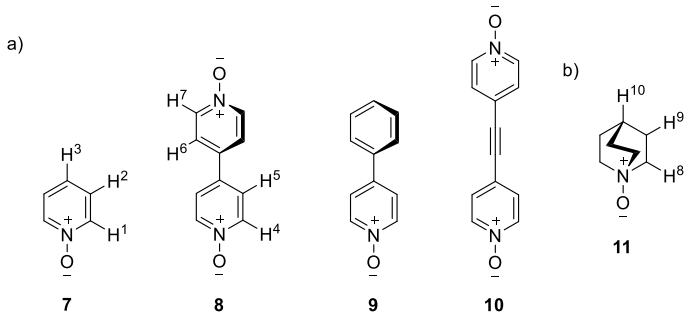

Figure 8. Line-drawing structures: a) pyridyl *N*-oxides **7**-**10** and b) quinuclidine *N*-oxide **11**.

Pyridyl *N*-oxides

The addition of 0.5 equiv. of pyridine *N*-oxide **7** to a solution of **1** in 2:1 $CDCl_3$:CD_3CN produced two set of proton signals of equal intensity corresponding to free **1** and the **7**⊂**1** inclusion complex. The pyrrole NHs of **7**⊂**1** experienced a large downfield shift due to the hydrogen bonds with the oxygen atom of **7**. At the same time, the proton signals of bound **7** appeared upfield shifted owing to the shielding effect exerted by the aromatic panels defining the cavity of **1**. The addition of 1 equiv. of **7** induced the quantitative formation of the **7**⊂**1** complex as expected. Addition of *ca.* 1 equiv. of Pd(II) to this solution gave, after thermal equilibration, the ^{1}H NMR spectrum showing a single set of signals for the protons of both **1** and **7**. Nevertheless, all proton signals experienced significant chemical shift changes with respect to those registered for the initial **7**⊂**1** complex (Figure 9). The pyridyl protons resonated at chemical shift values that were almost identical to those measured for [**1**•Pd]$^{2+}$. In addition, the chemical shifts of the protons of **7** were indicative of inclusion in the C[4]P's deep aromatic cavity. These observations support the quantitative assembly of the **7**⊂[**1**•Pd]$^{2+}$ cage complex.

The energy minimized structure of **7**⊂[**1**•Pd]$^{2+}$ begs for the co-inclusion of a CH_3CN molecule to satisfy the bonding requirements of the four inner *α*-pyridyl protons, and to provide a sensible *PC*

value (see Experimental Section). To find evidence for the co-inclusion of this CH_3CN molecule, we performed 1D GOESY NMR experiments using **7**⊂[**1**•Pd]$^{2+}$ in 2:1 $CDCl_3$:CH_3CN solution by selective excitation of the methyl group of CH_3CN. Unfortunately, the acquired GOESY spectra did not reveal the signal for the co-included CH_3CN molecule (see Experimental Section). Most likely, the chemical exchange between free and bound CH_3CN molecules is fast on the GOESY timescale. However, the X-ray structure of a single crystal that grew from the solution demonstrated the presence of the co-inclusion complex [**7**•CH_3CN]⊂[**1**•Pd]$(BF_4)_2$ (Figure 10).

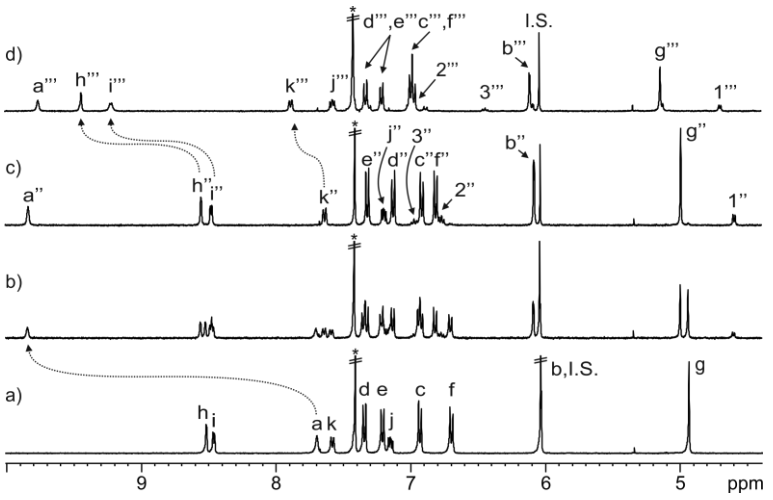

Figure 9. Selected region of the ^{1}H NMR (400 MHz, 2:1 $CDCl_3$:CD_3CN, 298 K) spectra: a) **1**; addition of **7** to **1**: b) 0.5 and c) 1 equiv.; addition of Pd(II) to **7**⊂**1**: d) *ca.* 1 equiv. after thermal equilibration. Doubly and triply primed letters and numbers correspond to proton signals of **7**⊂**1** and **7**⊂[**1**•Pd]$^{2+}$, respectively. 1,3,5-Trimethoxybenzene (I.S.). See Scheme 1 and Figure 8 for proton assignments. *Residual solvent peak.

Next, we studied the Pd(II)-cage assembly using as precursor the inclusion complex of **1** and 4,4'-bipyridine *N*,*N*'-dioxide **8** (Figure 8). Based on molecular modelling studies, **8** was a good fit for the cavity volume of [**1**•Pd]$^{2+}$ and could complement both the distal polar binding sites. Gratifyingly, the addition of *ca.* 1 equiv. of Pd(II) to a solution of **8**⊂**1** quantitatively produced the cage complex, **8**⊂[**1**•Pd]$^{2+}$. The signal of the NHs moved upfield in the cage complex compared to that on the **8**⊂**1** precursor (Figure 11), suggesting that **8** might be slightly too short to establish a perfect di-topic interaction with the two polar binding sites.

This hypothesis was confirmed by the observation of three structures for the **8**⊂[**1**•Pd]$(BF_4)_2$ complex in the solid state (Figure 12). In two of them, one oxygen atom of **8** is directly hydrogen-bonded to the four pyrrole NHs, d(O···$N_{pyrrole}$) ~ 3.0 Å. The other oxygen atom experiences electrostatic binding (ion-dipole) with the Pd(II) atom and is either weakly bound to only two *α*-pyridyl protons (Figure 12a), d(O···C_α) ~ 3.5 Å, or a co-included, hydrogen-bonded water molecules bridges that oxygen atom to the two remaining *α*-pyridyl hydrogens (Figure 12b). The

third structure of the **8**⊂[**1**•Pd]$(BF_4)_2$ cage complex displays one of the oxygen atoms of the *bis-N*-oxide **8** with an average distance to the four *α*-pyridyl protons that is significantly shorter to the one shown by the other oxygen to the pyrrole NHs (Figure 12c), *d*(O···C_α) ~ 3.1 Å and *d*(O···$N_{pyrrole}$) ~ 4.1 Å. The co-existence of these structures in solution would serve to explain the upfield shift of the NHs following the sealing of the cage with Pd(II). That is, the *bis-N*-oxide **8** is shuttling between the two distal binding sites of the cage complex, **8**⊂[**1**•Pd]$^{2+}$, while it is exclusively hydrogen-bonded to the pyrrole NHs in the **8**⊂**1** counterpart.

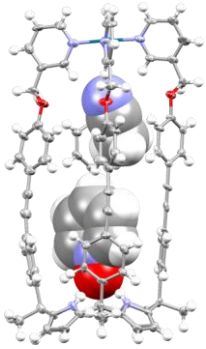

Figure 10. X-ray crystal structure of [**7**•CH_3CN]⊂[**1**•Pd]$(BF_4)_2$. The cage is shown in ORTEP view with thermal ellipsoids set at 50% probability. Hydrogen atoms are shown as fixed-size spheres of 0.3 Å radius. Bound molecules are shown as CPK models. Anions, solvent molecules and disordered atoms are omitted for clarity.

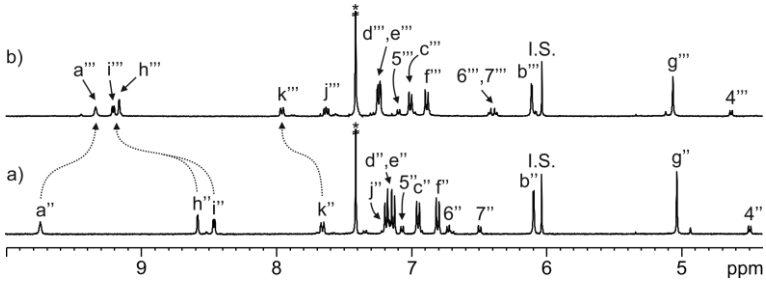

Figure 11. Selected region of the ^{1}H NMR (400 MHz, 2:1 $CDCl_3$:CD_3CN, 298 K) spectra: a) **8**⊂**1**; addition of Pd(II) to **8**⊂**1**: b) *ca.* 1 equiv. after thermal equilibration. Doubly and triply primed letters and numbers correspond to proton signals of **8**⊂**1** and **8**⊂[**1**•Pd]$^{2+}$, respectively. 1,3,5-Trimethoxybenzene (I.S.). See Scheme 1 and Figure 8 for proton assignments. *Residual solvent peak.

We also tested the use of 4-phenyl pyridine *N*-oxide **9** and *bis-N*-oxide **10** (Figure 8) to assemble the cage complexes. *N*-oxide **9** features a suitable volume to fill the cavity of [**1**•Pd]$^{2+}$ but it can only complement one polar binding site. In contrast, **10** is a di-topic guest but its length is larger than the distance between the two opposite polar binding sites of the [**1**•Pd]$^{2+}$ cage. The addition of *ca.* 1 equiv. of Pd(II) to separate solutions of **9**⊂**1** and **10**⊂**1** induced the almost complete disappearance of the proton signals and the emergence of a new set of signals of reduced

intensity (see Experimental Section). The diagnostic proton signals for [**1**•Pd]$^{2+}$, **9**⊂[**1**•Pd]$^{2+}$ or **10**⊂[**1**•Pd]$^{2+}$ were not present. Most likely, the addition of Pd(II) favored the formation of polymeric metallo-aggregates of the **9**⊂**1** and **10**⊂**1** inclusion complexes, respectively.

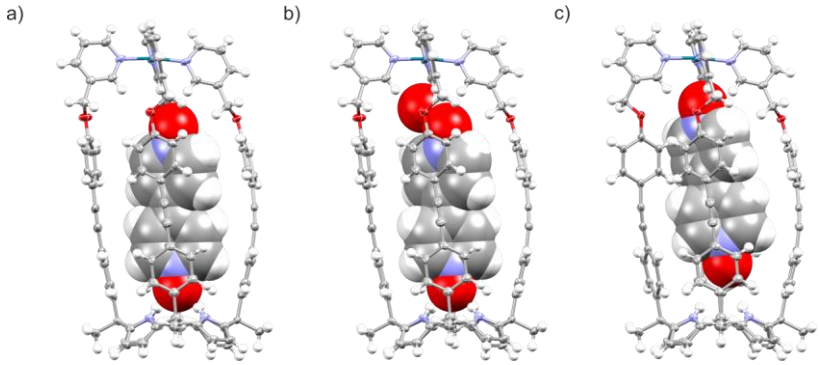

Figure 12. X-ray crystal structures: a) **8**⊂[**1**•Pd](BF$_4$)$_2$ (occupancy = 55%); b) [**8**•H$_2$O]⊂[**1**•Pd](BF$_4$)$_2$ (occupancy = 25%), there is a 12% occupancy of this structure lacking the water molecule and c) **8**⊂[**1**•Pd](BF$_4$)$_2$ (occupancy = 8%). The cages are shown in ORTEP view with thermal ellipsoids set at 50% probability. Hydrogen atoms are shown as fixed-size spheres of 0.3 Å radius. The H$_2$O molecule and the *bis*-*N*-oxide **8** are shown as CPK models. Anions, solvent molecules and disordered atoms are omitted for clarity.

Finally, the assignment of the proton signals to the cage complexes was unambiguously verified by assembling them through the addition of *ca.* 1 equiv. of *N*-oxides **7** or **8** to the pre-formed [**1**•Pd]$^{2+}$ cage. In both cases, the ^{1}H NMR spectroscopic analysis of the solutions evidenced the quantitative formation of the corresponding cage complexes (K_a > 10^4 M^{-1}). The analogous experiment performed with **9** produced the immediate appearance of a new set of sharp signals of reduced intensity, which we assigned to **9**⊂[**1**•Pd]$^{2+}$ (K_a ~ 5 x 10^2 M^{-1}). On the contrary, addition of *bis*-*N*-oxide **10** to [**1**•Pd]$^{2+}$ did not produce changes on the proton signals of [**1**•Pd]$^{2+}$, only the emergence of the signals corresponding to free **10**. This result confirmed that **10** is not complementary to the cavity dimensions of [**1**•Pd]$^{2+}$. Nevertheless, the time evolution of the mixtures, **9** or **10** with [**1**•Pd]$^{2+}$, produced the almost complete disappearance of all proton signals. As expected for these combinations, the thermodynamic equilibrium of the mixtures leads to the formation of large Pd(II)-mediated aggregates.

Likewise, addition of *N*-oxides **7** or **8** to the pre-assembled [**1**•Pt]$^{2+}$ cage in 2:1 $CDCl_3$:CD_3CN solvent mixture produced the quantitative formation of the corresponding Pt(II)-cage complexes **7**⊂[**1**•Pt]$^{2+}$ and **8**⊂[**1**•Pt]$^{2+}$, respectively (see Experimental Section).

Quinuclidine *N*-oxide

We assembled the **11**⊂[**1**•Pd]$^{2+}$ cage complex from the 1:1 inclusion complex of tetra-pyridyl **1** and quinuclidine *N*-oxide **11** (Figure 8b) in 2:1 $CDCl_3$:CD_3CN solution (Figure 13). The addition of 0.5

equiv. of **11** to a millimolar solution of tetra-pyridyl **1** produced a new set of separate proton signals for ligand **1**. The new set of signals corresponded to bound **1** in the **11⊂1** inclusion complex. The observation of two separate sets of signals for free and bound **1** indicates slow chemical exchange on the chemical shift timescale. The pyrrole NHs of bound **1** experienced a large downfield shift, $\Delta\delta$ = +2.75 ppm, supporting the formation of hydrogen bonds with the oxygen atom of bound **11**. On the other hand, all proton signals of **11** appeared highly upfield shifted compared to those of the free counterpart, with $\Delta\delta$ = -0.6 to -2.6 ppm. This observation supports the inclusion of **11** in the deep cavity of **1**. The protons of **11** experienced the shielding effect of the four aromatic walls of **1**. The addition of 1 equiv. of **11** induced the quantitative formation of **11⊂1** ($K_a > 10^4$ M^{-1}).

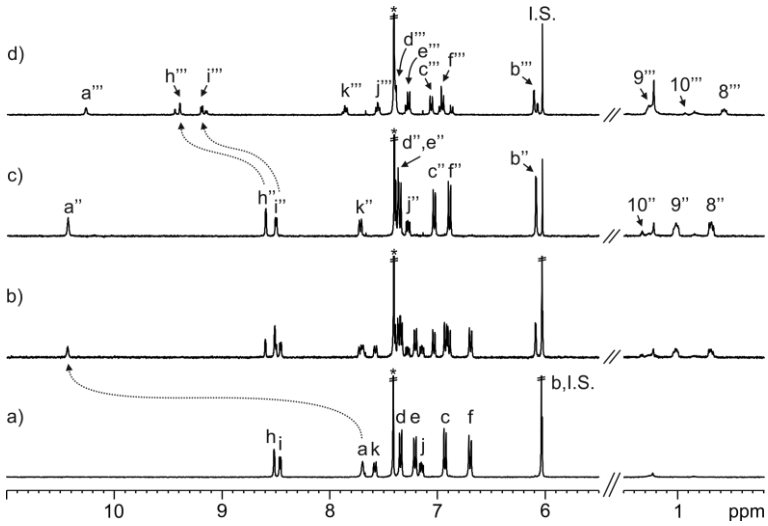

Figure 13. Selected regions of the ^{1}H NMR (400 MHz, 2:1 $CDCl_3$:CD_3CN, 298 K) spectra: a) **1**; addition of **11** to **1**: b) 0.5 and c) 1 equiv.; addition of Pd(II) to **11⊂1**: d) *ca.* 1 equiv. after thermal equilibration. Doubly and triply primed letters and numbers correspond to proton signals of **11⊂1** and **11⊂[1•**Pd**]**$^{2+}$, respectively. Small set of signals in d) corresponds to free [**1•**Pd**]**$^{2+}$. 1,3,5-Trimethoxybenzene (I.S.). See Scheme 1 and Figure 8 for proton assignments. *Residual solvent peak.

The subsequent addition of *ca*. 1 equiv. of $[Pd(CH_3CN)_4](BF_4)_2$ to the solution containing the **11⊂1** complex followed by thermal equilibration (24 h at 40°C), produced the disappearance of the original proton signals and the emergence of two new sets of signals for most of the protons of both binding partners. The two new sets of signals were of different intensity (Figure 13d). For example, the pyridyl protons *alpha* to the nitrogen atom, H^h and H^i, in the **11⊂1** complex split into two sets of downfield shifted signals with a *ca.* 70:30 ratio. We assigned the new sets of signals to the protons of the **11⊂[1•**Pd**]**$^{2+}$ cage complex and [**1•**Pd**]**$^{2+}$ cage, respectively. Based on this result, we estimated a stability constant of *ca.* 5 x 10^3 M^{-1} for the **11⊂[1•**Pd**]**$^{2+}$ cage complex.

Luckily, single crystals suitable for X-ray diffraction analysis grew from a 1,4-dichlorobenzene solution containing an equimolar mixture of **1**, **11** and the metal precursor $[Pd(CH_3CN)_4](BF_4)_2$ salt. The solution of the diffracted data revealed the presence of [**11**•BF_4]⊂[**1**•Pd](BF_4) cage complex in the crystal lattice (Figure 14). The structure featured the encapsulation of the quinuclidine *N*-oxide **11** in the polar cavity of the [**1**•Pd]$^{2+}$ cage that is defined by the calix[4]pyrrole unit. The oxygen atom of **11** is hydrogen-bonded to the four pyrrole NHs, $d(O\cdots N_{pyrrole})$ ~ 2.95 Å. In addition, the hydrogen atoms of **11** establish multiple CH-π interactions with the aromatic walls of [**1**•Pd]$^{2+}$.[54] Remarkably, a co-included tetrafluoroborate anion occupied the binding site defined by the inner *α*-CH pyridyl protons. The BF_4^- anion must be involved in Columbic and hydrogen-bonding interactions with the Pd(II) cationic center and the *α*-pyridyl hydrogens, respectively.[22] It is worth mentioning that ^{19}F NMR spectra indicated that tetrafluoroborate anions are free in the 2:1 $CDCl_3$:CD_3CN solutions of the [**1**•Pd]$^{2+}$ cage and its cage complexes (see Experimental Section).

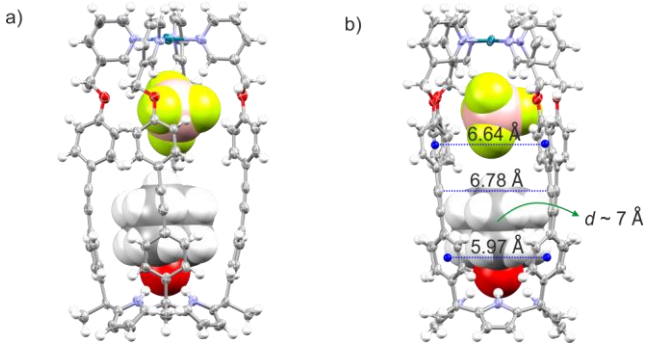

Figure 14. X-ray crystal structure of [**11**•BF_4]⊂[**1**•Pd](BF_4): a) side view and b) dimensions of **11** and the cage's portal. The cage is shown in ORTEP view with thermal ellipsoids set at 50% probability. Hydrogen atoms are shown as fixed-size spheres of 0.3 Å radius. Bound molecules and ions are shown as CPK models. Anions, solvent molecules and disordered atoms are omitted for clarity.

Likewise, the **11**⊂[**1**•Pt]$^{2+}$ cage complex was assembled from the **11**⊂**1** inclusion complex followed by the addition of the Pt(II) salt, $[Pt(CH_3CN)_4](BF_4)_2$. Thus, the equimolar mixture of Pt(II) salt and **11**⊂**1** afforded, after thermal equilibration (72 h at 50°C), a *ca.* 50:50 thermodynamic mixture of **11**⊂[**1**•Pt]$^{2+}$ and [**1**•Pt]$^{2+}$ (see Experimental Section). The binding constant of **11**⊂[**1**•Pt]$^{2+}$ is of the same order of magnitude than the analogous **11**⊂[**1**•Pd]$^{2+}$, which is in agreement with the experimentally measured distances for the cavity dimensions (see above).

4.2.4 Kinetic characterization of the cage complexes

<u>In/out exchange of pyridyl *N*-oxides</u>

We investigated the chemical exchange involved in **7**⊂**1** and **7**⊂[**1**•Pd]$^{2+}$ in 2:1 $CDCl_3$:CD_3CN by EXSY NMR spectroscopy. Chemical exchange cross-peaks between the NH protons of **1** and **7**⊂**1**

were present in the 2D EXSY NMR spectrum of an equimolar mixture (Figure 15a). In excess of **7**, the aromatic protons of the free *N*-oxide **7** and those in the **7⊂1** complex also showed chemical exchange (see Experimental Section). Based on the integral values of the diagonal and exchange cross-peaks, a rate constant $k_{exchange}$ = 1.4±0.1 s^{-1} ($\Delta G^{\ddagger}$ ~ 17.2 kcal·mol^{-1}) was determined for the magnetization exchange with the help of EXSYCalc software.[62]

Remarkably, the corresponding peaks were absent in analogous EXSY spectra of mixtures of the cage either with substoichiometric amount of **7**, [**1**•Pd]$^{2+}$ and **7⊂**[**1**•Pd]$^{2+}$, (Figure 15b) or an excess of **7**, **7** and **7⊂**[**1**•Pd]$^{2+}$, (see Experimental Section). The chemical exchange between free and bound pyridyl *N*-oxides in the cage complexes was slow on the EXSY timescale. Based on these results, we can estimate that the dissociation rate constant, k_{off}, must be smaller than 10^{-2} s^{-1} ($k_{exchange} = k' + k_{off} \sim 10^{-2}$ s^{-1}). This value assigns an energy barrier for the complex dissociation of *ca.* 20 kcal·mol^{-1} or more.[63] On the other hand, the formation of **7⊂**[**1**•Pd]$^{2+}$ was fast on the human timescale (< 30 s). This fact does not allow the accurate assessment of the corresponding second order rate constant, k_{on}, using kinetic ^{1}H NMR studies. Considering that a sensible estimate for the stability constant of the **7⊂**[**1**•Pd]$^{2+}$ cage complex is $K_a > 10^4$ M^{-1}, the k_{on} value can be deduced as $K_a \times k_{off} \sim 10^2$ $M^{-1}\cdot s^{-1}$. The estimated k_{on} indicates that the complex formation is not diffusion controlled and also serves to assign an energy barrier of $\Delta G^{\ddagger}$ ~ 15 kcal·mol^{-1} to the complex formation.

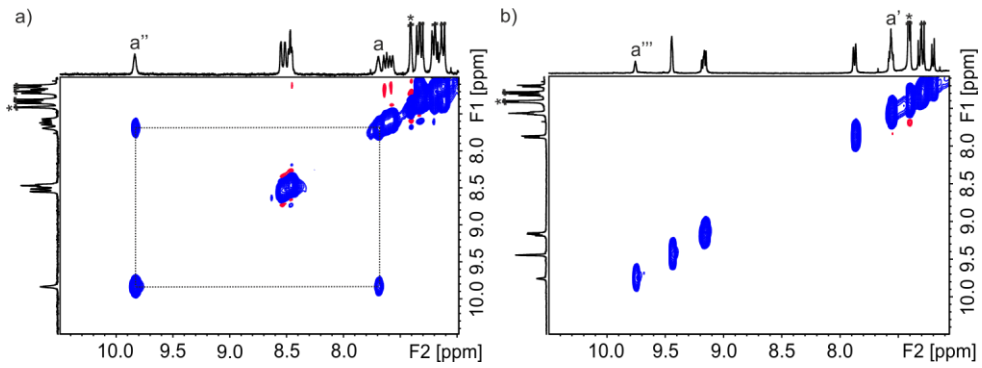

Figure 15. 2D ^{1}H-^{1}H EXSY NMR (300 MHz, 2:1 $CDCl_3$:CD_3CN, 298 K, t_{mix} = 0.3 s) spectra: a) **1** and **7⊂1** (1:1 ratio) and b) [**1**•Pd]$^{2+}$ and **7⊂**[**1**•Pd]$^{2+}$ (1:1 ratio). Primed letters correspond to proton signals of [**1**•Pd]$^{2+}$. Doubly and triply primed letters correspond to proton signals of **7⊂1** and **7⊂**[**1**•Pd]$^{2+}$, respectively. See Scheme 1 for proton assignment. *Residual solvent peak.

These results indicate an increase in the energy barrier of the magnetization exchange and thus, chemical exchange involving the cage, which is probably associated to a different exchange mechanism. In "four-wall" C[4]Ps, we proposed that the chemical exchange required the conformational change of the receptor (cone to alternate).[43] This pathway requires a higher activation energy for the Pd(II)-cage owing to the necessary dissociation of *N*-Pd(II) bonds.

Nevertheless, the formation of **7**⊂[**1**•Pd]$^{2+}$ or the analogous **7**⊂[**1**•Pt]$^{2+}$ is fast on the human timescale, indicating that ligand-metal dissociation involving the mono-metallic cage is not required for the in/out exchange of the planar pyridyl *N*-oxide. Taken together, we postulate that the inclusion/exchange of planar pyridyl *N*-oxides in the mono-metallic Pd(II)/Pt(II)-cages occurs through a "french doors" mechanism involving the rotation of the four *meso*-aromatic groups of the metallo-cage (see below).[64]

In/out exchange of quinuclidine *N*-oxide

Molecular modelling (MM3) of the X-ray structure of [**11**•BF_4]⊂[**1**•Pd](BF_4) suggested that the energy barrier for the in/out exchange process of the sterically demanding three-dimensional *N*-oxide **11** should be significantly larger than that of the planar *N*-oxide **7**, owing to the limited dimension of the cage's portal provided by the "french doors" mechanism (Figure 14).[65]

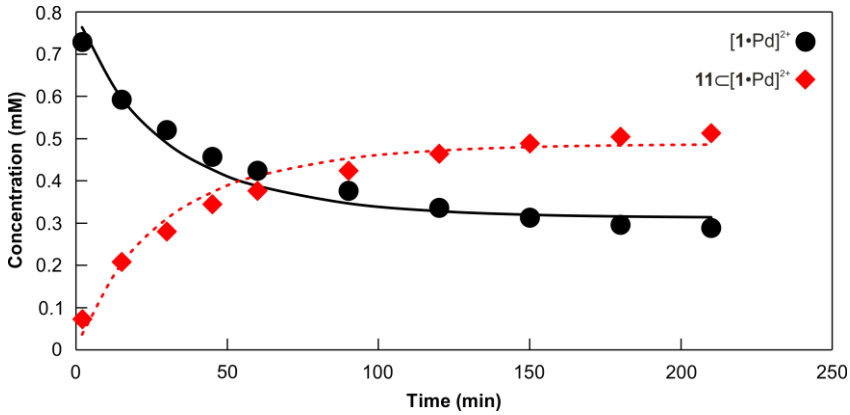

Figure 16. Concentration (mM) versus time (min) of free [**1**•Pd]$^{2+}$ (circles) and **11**⊂[**1**•Pd]$^{2+}$ cage complex (diamonds). Initial concentrations: [**1**•Pd]$^{2+}$ = 0.8 mM and [**11**] = 0.8 mM. The lines show the fit of the kinetic data.

In order to experimentally verify a putative change of mechanism for the encapsulation of **11** by [**1**•Pd]$^{2+}$, we assembled the **11**⊂[**1**•Pd]$^{2+}$ cage complex by adding *ca.* 1 equiv. of **11** to the pre-assembled [**1**•Pd]$^{2+}$ cage. The initial ^{1}H NMR spectrum (< 30 s) of the mixture revealed the exclusive presence of the proton signals of the two binding partners, **11** and [**1**•Pd]$^{2+}$, free in solution. Next, we monitored the kinetics of guest uptake by acquiring ^{1}H NMR spectra of the mixture at regular intervals.[9] The change in the concentration of [**1**•Pd]$^{2+}$ cage and the **11**⊂[**1**•Pd]$^{2+}$ cage complex was determined by integration of their corresponding proton signals (Figure 16). After *ca.* 4 h at r.t., the **11**⊂[**1**•Pd]$^{2+}$ was predominantly formed in solution (~ 70%) and its concentration did not change any further with time. We fit the kinetic data to a second order rate law considering the reversible formation of the cage complex ($v = k_{on}[H][G] - k_{off}[HG]$), for which we determined the thermodynamic stability constant above. It is worth mentioning here that kinetic ^{1}H NMR studies performed with different concentrations of **11** support the use of a second order

rate law in the range of investigated concentrations of **11** (see Experimental Section). The fit returned k_{on} = 0.5±0.1 $M^{-1}{\cdot}s^{-1}$ and k_{off} = 1.5±0.5 x 10^{-4} s^{-1}. These values are translated into energy barriers of *ca.* 18 and 23 kcal·mol^{-1}, respectively.

We also investigated the displacement of encapsulated **11** by the *bis*-*N*-oxide **8**. Starting from the thermodynamic mixture of **11**⊂[**1**•Pd]$^{2+}$ and [**1**•Pd]$^{2+}$ (70:30), the addition of 1 equiv. of **8** induced the instantaneous appearance of the cage complexes **11**⊂[**1**•Pd]$^{2+}$ and **8**⊂[**1**•Pd]$^{2+}$ in a *ca.* 70:30 ratio. This result indicated that the bound CH_3CN molecules in [**1**•Pd]$^{2+}$ were immediately replaced by **8**, however, all encapsulated **11** remained intact after the first 30 s. After 24 h, the analysis of the mixture showed the exclusive presence of **8**⊂[**1**•Pd]$^{2+}$ in solution (Figure 17).

Taken together, these results demonstrated that the uptake, release and exchange processes of the sterically demanding quinuclidine *N*-oxide **11** are energetically more costly than for the planar pyridyl *N*-oxide **7**.

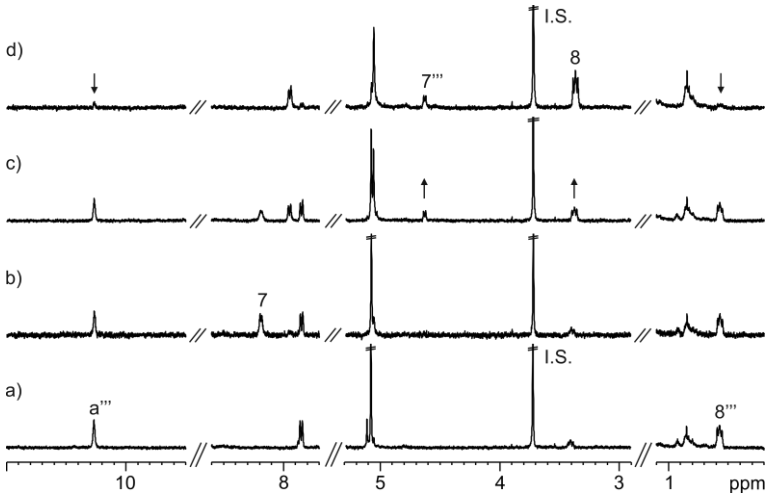

Figure 17. Selected regions of the ^{1}H NMR (400 MHz, 2:1 $CDCl_3$:CD_3CN, 298 K) spectra: a) **11**⊂[**1**•Pd]$^{2+}$ and [**1**•Pd]$^{2+}$ (*ca.* 7:3 ratio); addition of **8**: b) *ca.* 1 equiv.; after c) 5 and d) >24 h. Triply primed numbers correspond to proton signals of bound *N*-oxides in [**1**•Pd]$^{2+}$. Triply primed letter (a''') corresponds to the pyrrole NHs of **11**⊂[**1**•Pd]$^{2+}$. Arrows indicate increase and decrease in intensity of proton signals. 1,3,5-Trimethoxybenzene (I.S.). See Scheme 1 and Figure 8 for proton assignments.

Nevertheless, the measured modification of the kinetics for the in/out exchange processes of the quinuclidine *N*-oxide **11** is not enough to require a change of mechanism. A sterically demanding guest like **11** is expected to increase the energy barrier for the crossing of the passage provided by the rotated *meso*-phenyl groups. But the coincidence of energy between the formation of **11**⊂[**1**•Pd]$^{2+}$ and that described for the dissociation of pyridyl *N*-Pd(II) coordination bonds[32] hinted to the partial dissociation of the Pd(II)-cage for guest entrance.

In order to elucidate the change of mechanism for the uptake/release of **11**, we used the kinetically and thermodynamically more inert [**1**•Pt]$^{2+}$ cage. A "french doors" mechanism is viable in both cages, but a guest exchange mechanism involving the partial dissociation of the cage at r.t. can be ruled out for the [**1**•Pt]$^{2+}$ cage.[34] We attempted the assembly of **11**⊂[**1**•Pt]$^{2+}$ by adding 1 equiv. of **11** to the pre-assembled [**1**•Pt]$^{2+}$ cage. We used ^{1}H NMR spectroscopy to monitor the process. The equimolar solution of **11** and [**1**•Pt]$^{2+}$ did not produce the diagnostic proton signals expected for **11**⊂[**1**•Pt]$^{2+}$, even after standing for 5 days at r.t. (see Experimental Section). These results obtained with the [**1**•Pt]$^{2+}$ cage indicate that the "french doors" mechanism is associated with a very high energy barrier in the case of the in/out passage of **11**, which makes it inoperative, at least, at r.t. Consequently, an alternative, but energetically more costly mechanism, possibly involving the partial dissociation of the cage structure should be operative for the observed in/out processes of **11** with the [**1**•Pd]$^{2+}$ cage.

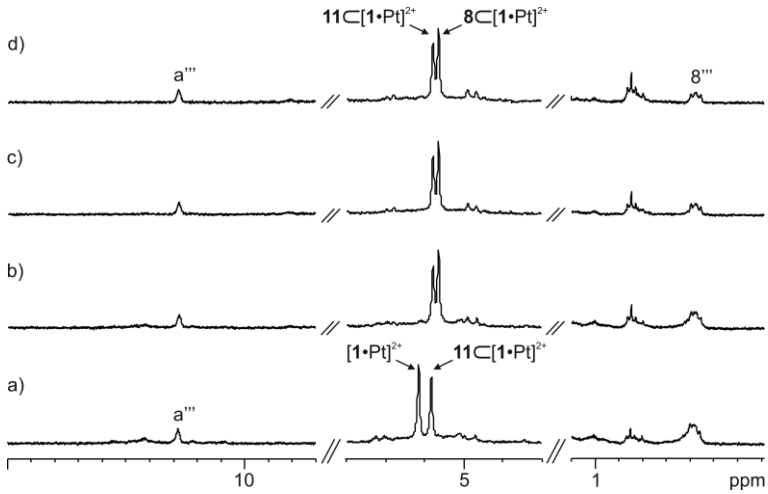

Figure 18. Selected regions of the ^{1}H NMR (400 MHz, 2:1 $CDCl_3$:CD_3CN, 298 K) spectra: a) **11**⊂[**1**•Pt]$^{2+}$ and [**1**•Pt]$^{2+}$ (*ca.* 1:1 ratio); addition of **8**: b) *ca.* 1 equiv.; after c) 5 and d) >24 h. Triply primed letter and number correspond to proton signals of **11**⊂[**1**•Pt]$^{2+}$. In the region between 4.9 and 5.2 ppm, the proton signals of the Pt(II)-cage and its cage complexes are labeled as [**1**•Pt]$^{2+}$, **8**⊂[**1**•Pt]$^{2+}$ and **11**⊂[**1**•Pt]$^{2+}$. See Scheme 1 and Figure 8 for proton assignments.

We also performed the displacement experiment of encapsulated **11** in **11**⊂[**1**•Pt]$^{2+}$ by *bis*-*N*-oxide **8**. The **11**⊂[**1**•Pt]$^{2+}$ cage complex was assembled from the **11**⊂**1** inclusion complex followed by the addition of the Pt(II) salt (see above). The addition of *ca.* 1 equiv. of the pyridyl *bis*-*N*-oxide **8** to the equimolar mixture of [**1**•Pt]$^{2+}$ carcerand and **11**⊂[**1**•Pt]$^{2+}$ carceplex induced the rapid formation of **8**⊂[**1**•Pt]$^{2+}$ that is present in solution as 50:50 mixture of **11**⊂[**1**•Pt]$^{2+}$, together with 0.5 equiv. of free **11**. In this case, the composition of the mixture did not change with time at ambient conditions (Figure 18) indicating that the *N*-Pt(II) bonds do not dissociate and, more interestingly, that the sterically demanding **11** is effectively imprisoned in the [**1**•Pt]$^{2+}$ cage.

4.2.5 Guest in/out exchange mechanisms of the mono-metallic Pd(II)/Pt(II)-cages

The chemical exchange of planar pyridyl *N*-oxides, **7** and **8**, in the mono-metallic Pd(II)/Pt(II)-cages is slow on both the chemical shift and EXSY timescales. Nevertheless, the entrance of the same guests into the parent metallo-cages is fast on the human timescale. In this regard, we postulate that a "french doors" mechanism, involving the rotation of the four *meso*-phenyl walls of the metallo-cages, allows the passage of the planar guests (Figure 19a).[40]

On the contrary, the encapsulation of quinuclidine *N*-oxide **11**, a more sterically demanding guest, is slower than pyridyl *N*-oxides in the Pd(II)-cage, and does not take place in the Pt(II)-counterpart. In this sense, we propose a modification of the inclusion/exchange mechanism of quinuclidine *N*-oxide **11**. This requires the partial dissociation of the Pd(II)-cage (Figure 19b).

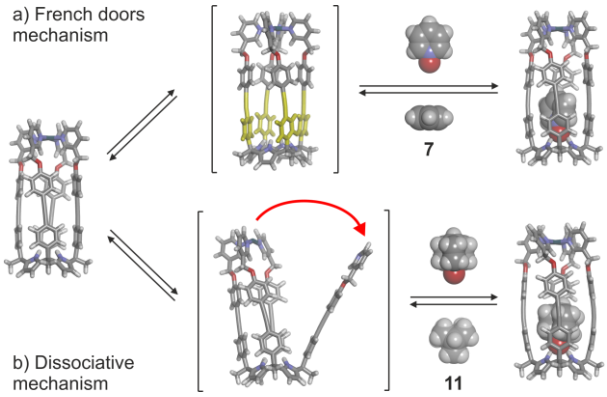

Figure 19. Proposed guest inclusion/exchange mechanisms for the [**1**•Pd]$^{2+}$ cage: a) "french doors" (highlighted in yellow) and b) dissociation of *N*-Pd(II) coordination bond. For the [**1**•Pt]$^{2+}$ cage, the dissociation mechanism becomes energetically unattainable at r.t. Encapsulated acetonitrile molecules are omitted for clarity. The models in brackets show the putative structures of the host in the transition state. The side and top view of the guests **7** and **11** as CPK models are shown above and below the equilibria arrows.

The different nature of the metal coordination bonds present in the two cages is responsible for their viable guest in/out mechanisms. Specifically, the high binding selectivity featured by [**1**•Pt]$^{2+}$ cage towards planar pyridyl *N*-oxides is related to the exclusive operation of the "french doors" mechanism for the in/out guest exchange processes.

4.2.6 Self-assembly of a water-soluble mono-metallic Pd(II)-cage

We aim at investigating the host-guest properties of analogous water-soluble mono-metallic cages. To this end, we designed a tetra-pyridyl SAE-C[4]P ligand **12** bearing four pyridinium cations at its lower rim (Scheme 2). We envisaged that the coordination of Pd(II) at the upper rim of **12** would produce the corresponding mono-metallic [**12**•Pd]$^{6+}$ cage. The four pyridinium cations at the lower rim and the Pd(II) ion, coordinated at the upper rim, should impart solubility in water to the

[**12**•Pd]$^{6+}$ cage. We synthesized the tetra-pyridyl ligand **12** starting from the tetra-*α*-(4-iodophenyl) tetra-(4-chlorobutyl) calix[4]pyrrole **13**.[66] The quadruple Sonogashira cross-coupling reaction between **13** and pyridyl mono-acetylene **2** gave tetra-pyridyl tetra-chloro **14** in 46% yield after column chromatography purification. Next, tetra-pyridinium tetra-pyridyl **12** was obtained in 85% yield by heating the parent tetra-chloro **14** in pyridine at 110°C for 24 h (Scheme 2). The tetra-pyridyl SAE-C[4]Ps **12** and **14** were characterized by a complete set of high-resolution spectra (NMR and HRMS).

The synthesized tetra-pyridinium tetra-pyridyl **12** showed low solubility in D_2O at millimolar concentrations. The ^{1}H NMR spectrum of a D_2O suspension of **12** displayed broad proton signals. Unfortunately, the addition of *ca.* 1 equiv. of $Pd(NO_3)_2$ to the later suspension of **12** induced the formation of an insoluble precipitate. Most likely, tetra-pyridyl **12** and Pd(II) formed insoluble metal-mediated aggregates in water (see Experimental Section).

Nevertheless, the addition of 1 equiv. of *bis*-*N*-oxide **8** to a millimolar D_2O suspension of **12** produced, after 2 h at 50°C, a solution containing, most likely, the putative **8⊂12** inclusion complex. Unfortunately, the ^{1}H NMR spectrum of the later D_2O solution displayed again broad proton signals. The addition of $(CD_3)_2SO$ (up to 5%) to the D_2O solution containing the equimolar mixture of **8** and **12** provoked the sharpening of two separate sets of signals that we assigned to the protons of free **8** and **8⊂12** (see Experimental Section). These results suggested that the **8⊂12** inclusion complex aggregates in water at millimolar concentrations.

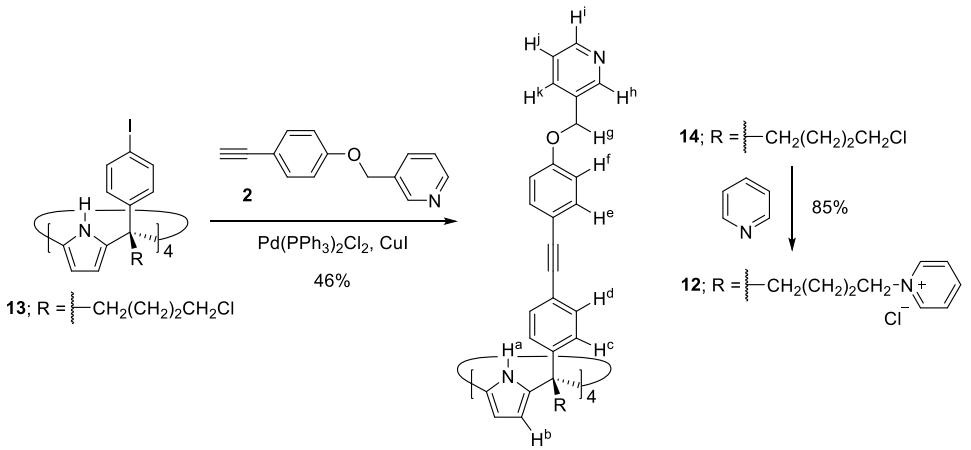

Scheme 2. Synthesis of tetra-pyridinium tetra-pyridyl super aryl-extended calix[4]pyrrole **12**.

Interestingly, the addition of *ca*. 1 equiv. of $Pd(NO_3)_2$ to the solution of **8⊂12** in pure D_2O produced changes in the ^{1}H NMR spectra. However, the proton signals were still broad for an unequivocal assignment (see Experimental Section). Note that, in this case, the equimolar mixture of **8**, **12** and Pd(II) in water did not induce the formation of a precipitate.

In order to investigate whether the **8**⊂[**12**•Pd]$^{6+}$ cage complex was assembled and its aggregation phenomena, we performed variable temperature (VT) ^{1}H NMR experiments on the above D_2O solution (Figure 20). The increase of the temperature produced ^{1}H NMR spectra displaying a set of sharp and well-defined proton signals in agreement with a C_{4v} symmetry. Specially, the signals of the *α*-pyridyl hydrogens, H^{h} and H^{i}, resonated at 9.08 and 9.04 ppm, respectively, suggesting the formation of pyridyl-Pd(II) coordination bonds. Additionally, the proton signals of **8** appeared upfield shifted, indicating the inclusion of the guest in the aromatic cavity of the SAE-C[4]P. The chemical shift values and signal pattern of the protons of *bis*-*N*-oxide **8** were similar to those observed in the ^{1}H NMR spectrum of **8**⊂[**1**•Pd]$^{2+}$ in 2:1 $CDCl_3$:CD_3CN solution.

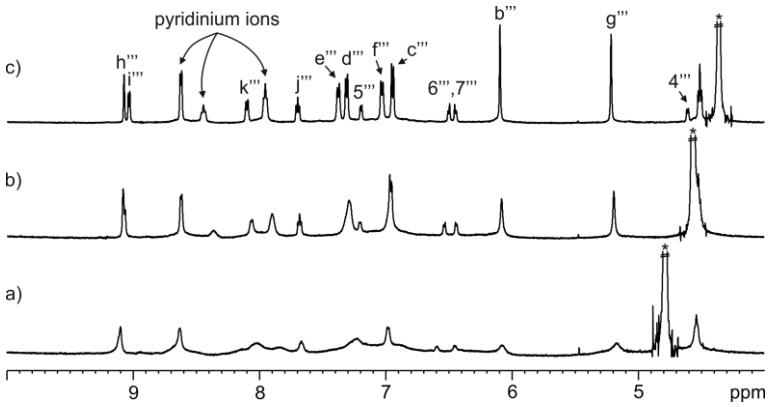

Figure 20. Selected region of the VT ^{1}H NMR (500 MHz, D_2O) spectra of **8**⊂[**12**•Pd]$^{6+}$: a) 298; b) 318 and c) 338 K. Triply primed letters and numbers correspond to proton signals of **8**⊂[**12**•Pd]$^{6+}$. See Scheme 2 and Figure 8 for proton assignments. *Residual solvent peak.

Taken together, these results suggested that the **8**⊂[**12**•Pd]$^{6+}$ cage complex was assembled in D_2O solution. In water, the mono-metallic [**12**•Pd]$^{6+}$ cage requires the use of a template for its assembly and experiences aggregation at millimolar concentrations at r.t.

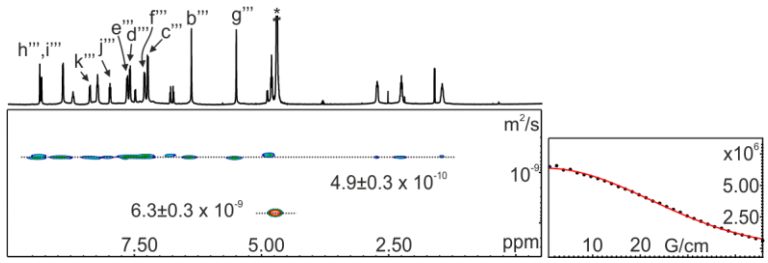

Figure 21. (left) ^{1}H pseudo 2D plot of DOSY (500 MHz with cryoprobe, D_2O, 333 K, D20 = 0.20 s; P30 = 0.60 ms) of **8**⊂[**12**•Pd]$^{6+}$. (right) Fit of the decay of the signal b''' to a mono-exponential function. Triply primed letters correspond to proton signals of **8**⊂[**12**•Pd]$^{6+}$. See Scheme 2 for proton assignment. Errors are indicated as standard deviations. *Residual solvent peak.

Finally, we analyzed the D_2O solution of **8**⊂[**12**•Pd]$^{6+}$ by 2D DOSY NMR spectroscopy at 60°C. The fit of the decay of the proton signals of the cage complex to a mono-exponential function returned a diffusion constant value D = 4.9±0.3 x 10^{-10} $m^2 \cdot s^{-1}$. This value is consistent with the one calculated for a discrete molecule of the cage complex in water solution.

The energy minimized structure (MM3) of the **8**⊂[**12**•Pd]$^{6+}$ cage complex shows the *bis*-*N*-oxide **8** included in the cavity of the metallo-cage. The *bis*-*N*-oxide **8** is involved in hydrogen-bonding interactions with both polar binding sites of the cage assembly. The metallo-cage features a large hydrophobic section provided by the *meso*-aromatic walls of the SAE-C[4]P ligand. The combination of four cationic groups at the lower rim and one Pd(II) ion at the upper rim does not warrant the solubility of **8**⊂[**12**•Pd]$^{6+}$ as discrete species in water at room temperature (Figure 22).

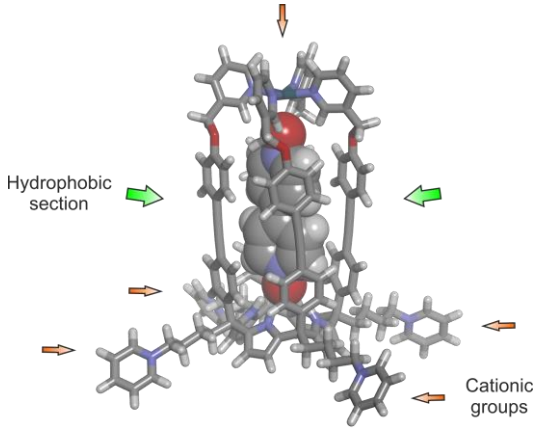

Figure 22. Energy minimized structure (MM3) of **8**⊂[**12**•Pd]$^{6+}$. The Pd(II)-cage is depicted in stick representation and the bound guest is shown as CPK model. Big (green) and small (orange) arrows indicate hydrophobic section and cationic groups of the cage complex, respectively.

4.3 Conclusions

In summary, we report the self-assembly of mono-metallic Pd(II)/Pt(II)-cages, [**1**•Pd]$^{2+}$ and [**1**•Pt]$^{2+}$. We demonstrate the reversible (co)inclusion of sizable polar guests in the cage's cavity. Replacing the super aryl-extended scaffold of **1** by the aryl-extended counterpart **4** prevents the cage assembly. The hydrogen-bonding needs of the two binding sites must be met for the efficient assembly and thermodynamic stability of the metallo-cages.

We demonstrate that the Pd(II)-cage features a switching from a "french doors" to a partial ligand-metal dissociation mechanism to accommodate the entrance/release of the sterically demanding quinuclidine *N*-oxide **11**. On the contrary, the isostructural Pt(II)-cage operates exclusively via a "french doors" mechanism avoiding the entrance and release of the bulky guest. The two mechanisms operating in [**1**•Pd]$^{2+}$ feature remarkably different kinetics, allowing the time-

dependent uptake/release processes for **11**. The obtained results highlight the importance of size-complementarity between guest dimensions and the metallo-cage portal. On the one hand, the reversible nature of the metal-ligand bonds present in the [**1**•Pd]$^{2+}$ cage enables two available mechanisms for guest entrance/release. These are reflected by the lack of selectivity in *N*-oxides binding. In contrast, the relative inertness of the metal-ligand interactions featured by the [**1**•Pt]$^{2+}$ cage provides high binding selectivity based on the premise of size-complementarity requested by the "french door" mechanism.

Finally, we show that a structurally related hexa-cationic Pd(II)-cage can be assembled in water solution using a suitable guest as template. The water-soluble cage complex aggregates owing to the large hydrophobic section provided by the SAE-C[4]P ligand. In order to reduce the aggregation, most likely, an increase in the number of charged groups at the periphery of the cage's structure is necessary.

4.4 Experimental Section

4.4.1 General information and instruments

Reagents were obtained from commercial suppliers and used without further purification unless otherwise stated. All solvents were commercially obtained and used without further purification except pyrrole which was distilled and freshly used. Dry solvents were taken from a solvent system MB SPS 800. THF, Et_3N, DIPEA and iPr$_2$NH were dried, distilled and degassed by three freeze-pump-thaw cycles before used in the cross-coupling reactions. CH_3CN and $CHCl_3$ were dried before used in the syntheses of the metallo-cages. Routine ^{1}H NMR and ^{13}C{^{1}H} NMR spectra were recorded on a Bruker Avance 300 (300 MHz for ^{1}H NMR and 75 MHz for ^{13}C NMR), Bruker Avance 400 (400 MHz for ^{1}H NMR and 100 MHz for ^{13}C NMR), Bruker Avance 500 (500 MHz for ^{1}H NMR and 125 MHz for ^{13}C NMR) or Bruker Avance 500 with cryoprobe (500 MHz for ^{1}H NMR and 125 MHz for ^{13}C NMR). Deuterated solvents used are indicated in the characterization and chemical shifts are given in ppm. Residual solvent peaks were used as reference.[67] All NMR *J* values are given in Hz. COSY, NOESY, ROESY, HMQC and HMBC experiments were recorded to help with the assignment of ^{1}H and ^{13}C signals. High-resolution mass spectra (HRMS) were obtained on a Bruker HPLC-TOF (MicroTOF Focus) and Bruker HPLC-QqTOF (MaXis Impact). Both using ESI as ionization mode. IR spectra were recorded on a Bruker Optics FTIR Alpha spectrometer equipped with a DTGS detector, KBr beamsplitter at 4 cm^{-1} resolution using a one bounce ATR accessory with diamond windows. Melting points were measured on a MP70 Melting Point System Mettler Toledo. Crystal structure determinations were carried out using a Rigaku MicroMax-007HF diffractometer equipped with a PILATUS 200K detector or a Bruker Apex II Duo equipped with an APEX II detector. Both using Mo*Kα* radiation. Crystal structure solution was achieved using VLD and Patterson methods as implemented in SIR2014 Version 14.10. Least-squares refinement on F2 using all measured intensities was carried out using the program

SHELX-2018/3. Column chromatography was performed with silica gel technical grade, pore size 60 Å, 230-400 mesh particle size, 40-63 μm particle size and Thin layer chromatography (TLC) analysis on silica gel 60 F254.

4.4.2 Determination of the rate constants from kinetic ^{1}H NMR studies

The uptake experiments of quinuclidine *N*-oxide **11** by the pre-assembled [**1**•Pd]$^{2+}$ cage were monitored by ^{1}H NMR spectroscopy. The concentration of the free and bound Pd(II)-cage throughout the kinetic experiment was determined by integration of their corresponding proton signals. 1,3,5-Trimethoxybenzene was used as internal standard in the kinetic ^{1}H NMR studies. The obtained data, concentration *vs.* time, were fit to a theoretical kinetic model using the Differential Kinetic Module of SPECFIT Software Version 3.0.40. This theoretical kinetic model considers the reversible formation of the bimolecular cage complex (Equations 4 and 5). The software requires the initial concentrations of the pre-assembled [**1**•Pd]$^{2+}$ cage and the quinuclidine *N*-oxide **11** used in the kinetic experiments.

4) [**1**•Pd]$^{2+}$ + **11** → **11**⊂[**1**•Pd]$^{2+}$; k_{on}

5) **11**⊂[**1**•Pd]$^{2+}$ → [**1**•Pd]$^{2+}$ + **11**; k_{off}

In this kinetic model, the ratio of the two rate constants, k_{on} and k_{off}, corresponds to the equilibrium constant $K_a = k_{on}/k_{off}$ for the formation of the cage complex **11**⊂[**1**•Pd]$^{2+}$. The calculated stability constant value K_a (**11**⊂[**1**•Pd]$^{2+}$), derived from the ratio of rate constants returned from the fit, is in perfect agreement with the one determined at the equilibrium for the formation of the cage complex.

4.4.3 Synthesis and characterization data

Tetra-pyridyl super aryl-extended calix[4]pyrrole 1: Tetra-*α* calix[4]pyrrole **3**[53] (55 mg, 0.05 mmol, 1 equiv.), $Pd(PPh_3)_2Cl_2$ (4.09 mg, 0.01 mmol, 0.03 equiv.), CuI (1.78 mg, 0.01 mmol, 0.05 equiv.) and 3-((4'-ethynylphenoxy)methyl)pyridine **2** (58.50 mg, 0.28 mmol, 1.5 equiv.) were kept under Argon atmosphere. Dry THF (5 mL) and dry diisopropylamine (5 mL) were added dropwise. The reaction was stirred at 45°C for 5 h. After that, the crude was concentrated, redissolved in CH_2Cl_2 (10 mL) and washed with brine (2x10 mL) and water (10 mL). The organic layer was dried (Na_2SO_4), filtered and concentrated. The crude was purified by column chromatography on silica gel (3 g, 9:1 CH_2Cl_2:isopropanol) and the product was further purified by recrystallization from 1:1 CH_2Cl_2:CH_3CN (4 mL) obtaining a white solid (47 mg, 0.03 mmol, 65% yield). Rf = 0.2 (95:5 CH_2Cl_2:isopropanol). ^{1}H NMR (500 MHz, $CDCl_3$, 298 K): *δ* (ppm): 8.66 (s, 4H); 8.58 (d, *J* = 5.0 Hz, 4H); 7.75 (d, *J* = 7.9 Hz, 4H); 7.68 (br s, 4H); 7.48-7.46 (m, 8H); 7.40-7.38 (m, 8H); 7.31 (dd, *J* = 7.9 Hz, *J* = 5.0 Hz, 4H); 7.11-7.09 (m, 8H); 6.93-6.91 (m, 8H); 5.77 (s, 8H); 5.08 (s, 8H); 1.98 (s, 12H). ^{13}C{^{1}H} NMR (125 MHz, $CDCl_3$, 298 K): *δ* (ppm): 158.5; 149.7; 149.1; 136.3; 135.4; 133.3;

132.3; 131.0; 127.6; 123.7; 121.8; 116.3; 115.0; 106.7; 89.2; 88.4; 67.7; 44.8; 28.1 (one carbon signal might be overlapped). HRMS (ESI-TOF) m/z: $[M+2H]^{2+}$ Calcd for $C_{104}H_{82}N_8O_4$ 753.3224; Found 753.3254. FTIR *v* (cm^{-1}): 1599; 1512; 1429; 1283; 1241; 1173; 1016; 827; 707. M.p. > 280°C (decompose).

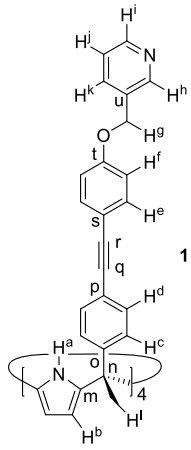

Figure 23. Line-drawing structure of tetra-pyridyl **1**.

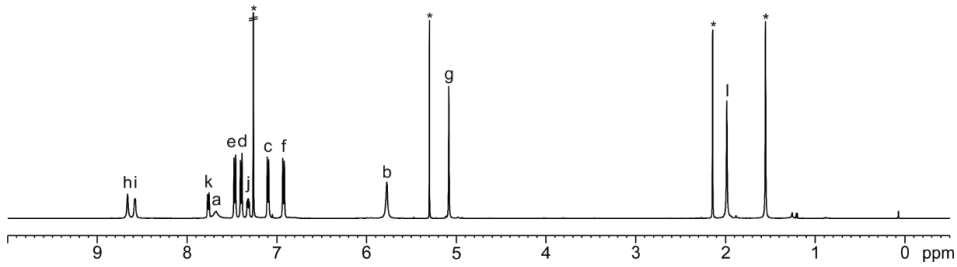

Figure 24. ^1H NMR (500 MHz, $CDCl_3$, 298 K) spectrum of **1**. See Figure 23 for proton assignment. *Residual solvent peaks.

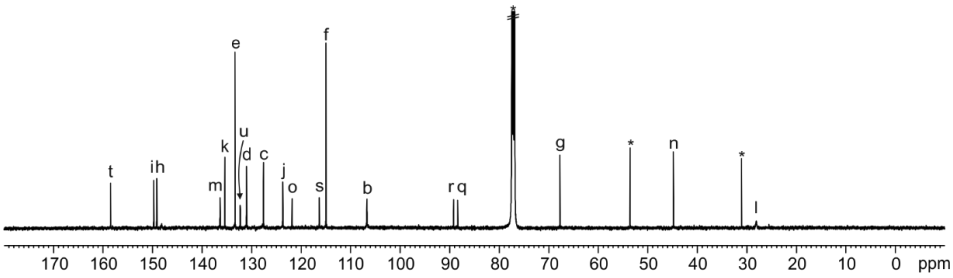

Figure 25. $^{13}C\{^{1}H\}$ NMR (500 MHz, $CDCl_3$, 298 K) spectrum of **1**. See Figure 23 for carbon assignment. *Residual solvent peaks.

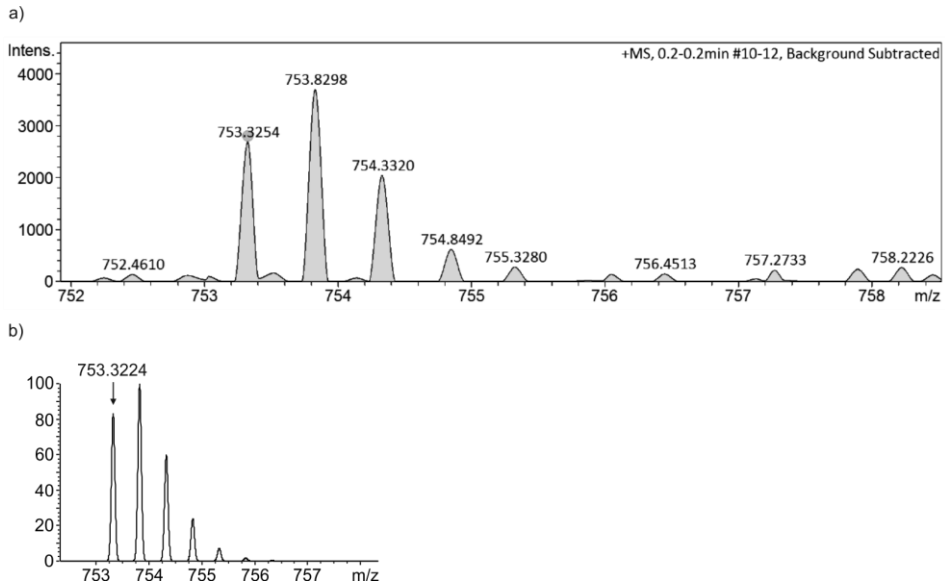

Figure 26. a) Experimental and b) theoretical isotopic distributions for $[M+2H]^{2+}$. The exact mass for the monoisotopic peak in a) and b) is indicated.

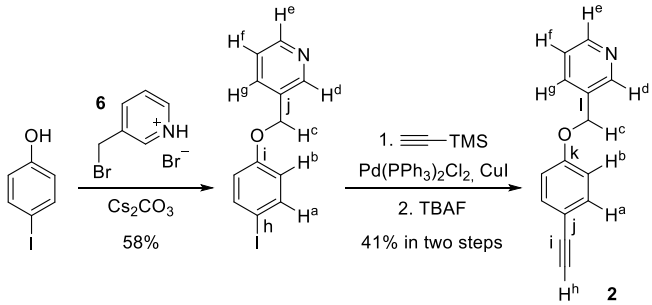

Scheme 3. Synthesis of mono-acetylene **2**.

3-((4'-Iodophenoxy)methyl)pyridine: 4-Iodophenol (400 mg, 1.82 mmol, 1 equiv.) and Cs_2CO_3 (889 mg, 2.73 mmol, 1.5 equiv.) were suspended in dry DMF (40 mL). The mixture was stirred under Argon atmosphere at 50°C for 30 min. 3-(Bromomethyl)pyridinium hydrobromide **6** (690 mg, 2.73 mmol, 1.5 equiv.) in DMF (20 mL) was added dropwise. The reaction was stirred at 60°C under Argon atmosphere for 5 h. The color changed from yellow to orange-brown. After that, the solvent was removed under vacuum and the solid was redissolved in CH_2Cl_2 (10 mL) and washed with brine (2x10 mL) and water (10 mL). The organic layer was dried (Na_2SO_4), filtered and concentrated. The crude was purified by column chromatography on silica gel (20 g, 9:1 CH_2Cl_2:EtOAc) affording the product as a white solid (326 mg, 1.58 mmol, 58% yield). Rf = 0.2 (9:1 CH_2Cl_2:EtOAc). ^{1}H NMR (300 MHz, $CDCl_3$, 298 K): *δ* (ppm): 8.67 (d, *J* = 1.9 Hz, 1H); 8.59 (dd, *J* = 4.8 Hz, *J* = 1.8 Hz, 1H); 7.76 (ddd, *J* = 7.8 Hz, *J* = 1.9 Hz, *J* = 1.9 Hz, 1H); 7.59-7.56 (m, 2H); 7.33 (dd, *J* = 7.8 Hz, *J* = 4.8 Hz, 1H); 6.77-6.74 (m, 2H); 5.05 (s, 2H). ^{13}C{^{1}H} NMR (100 MHz, $CDCl_3$, 298 K): *δ* (ppm): 158.4; 149.8; 149.1; 138.5; 135.3; 132.2; 123.7; 117.4; 83.7; 67.8. HRMS (ESI-TOF) m/z: $[M+H]^+$ Calcd for $C_{12}H_{11}INO$ 311.9880; Found 311.9872. FTIR *v* (cm^{-1}) = 1568; 1484; 1427; 1378; 1278; 1226; 1176; 1018; 793; 708. M.p. = 74-76°C.

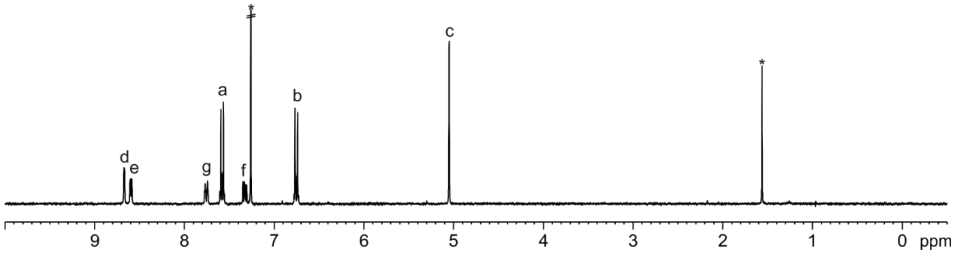

Figure 27. ^{1}H NMR (300 MHz, $CDCl_3$, 298 K) spectrum of 3-((4'-iodophenoxy)methyl)pyridine. See Scheme 3 for proton assignment. *Residual solvent peaks.

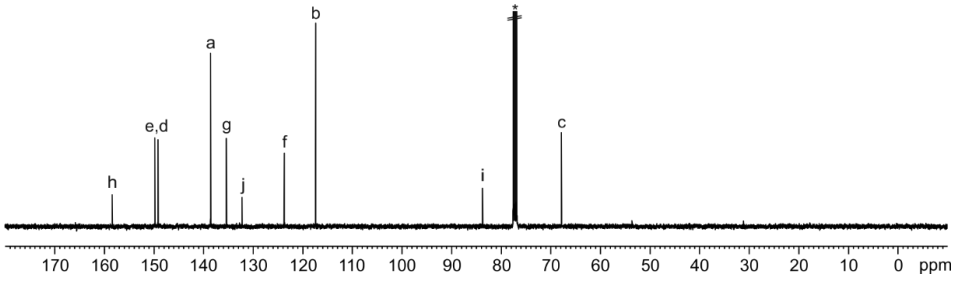

Figure 28. ^{13}C{^{1}H} NMR (100 MHz, $CDCl_3$, 298 K) spectrum of 3-((4'-iodophenoxy)methyl)pyridine. See Scheme 3 for carbon assignment. *Residual solvent peak.

3-((4'-Ethynylphenoxy)methyl)pyridine 2: Step 1. 3-((4'-Iodophenoxy)methyl)pyridine (300 mg, 0.96 mmol, 1 equiv.), $Pd(PPh_3)_2Cl_2$ (43.2 mg, 0.07 mmol, 0.07 equiv.) and CuI (49.6 mg, 0.26 mmol, 0.27 equiv.) were kept under Argon atmosphere for 5 min. Dry THF (7 mL) and dry DIPEA

(0.50 mL, 2.89 mmol, 3 equiv.) were added. Finally, ethynyltrimethylsilane (0.40 mL, 2.89 mmol, 3 equiv.) was added. The color of the mixture changed from orange to brown. The reaction was stirred at 45°C for 3 h. After that, the solvent was removed under vacuum and the crude was redissolved in CH_2Cl_2 (20 mL) and washed with brine (2x20 mL). The organic layer was dried (Na_2SO_4), filtered and concentrated. The crude was purified by column chromatography on silica gel (12 g, 85:15 CH_2Cl_2:EtOAc, product Rf = 0.4) affording the protected compound as brown oil (191 mg, 0.68 mmol, 70% yield). Step 2. The protected compound (119 mg, 0.42 mmol, 1 equiv.) was dissolved in dry THF (10 mL) and TBAF (0.47 mL from 1 M solution in THF, 0.47 mmol, 1.1 equiv.) was added dropwise. The reaction was stirred under Argon atmosphere. After 15 min, the reaction was quenched by adding aqueous saturated NH_4Cl (10 mL). The organic solvent was removed under vacuum and the crude was extracted with CH_2Cl_2 (2x10 mL). The organic layer was washed with brine (2x20 mL), dried (Na_2SO_4), filtered and concentrated. The crude was purified by column chromatography on silica gel (8 g, 8:2 CH_2Cl_2:EtOAc) affording the product as a yellow solid (50 mg, 0.24 mmol, 58% yield). Rf = 0.4 (8:2 CH_2Cl_2:EtOAc). ^{1}H NMR (400 MHz, $CDCl_3$, 298 K): δ (ppm): 8.69 (s, 1H); 8.61 (d, J = 4.8 Hz, 1H); 7.76 (d, J = 7.8 Hz, 1H); 7.45-7.43 (m, 2H); 7.33 (dd, J = 7.8 Hz, J = 4.8 Hz, 1H); 6.92-6.90 (m, 2H); 5.08 (s, 2H); 3.01 (s, 1H). ^{13}C{^{1}H} NMR (100 MHz, $CDCl_3$, 298 K): δ (ppm): 158.8; 149.8; 149.2; 135.4; 133.9; 132.2; 123.7; 115.1; 114.9; 83.5; 76.2; 67.7. HRMS (ESI-TOF) m/z: $[M+H]^+$ Calcd for $C_{14}H_{12}NO$ 210.0913; Found 210.0912. FTIR ν (cm^{-1}): 3173; 1605; 1577; 1505; 1429; 1379; 1286; 1243; 1170; 1048. M.p. = 76-78°C.

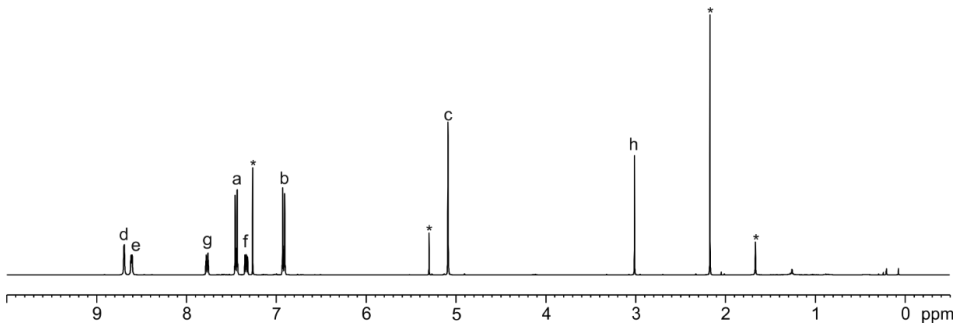

Figure 29. ^{1}H NMR (400 MHz, $CDCl_3$, 298 K) spectrum of **2**. See Scheme 3 for proton assignment. *Residual solvent peaks.

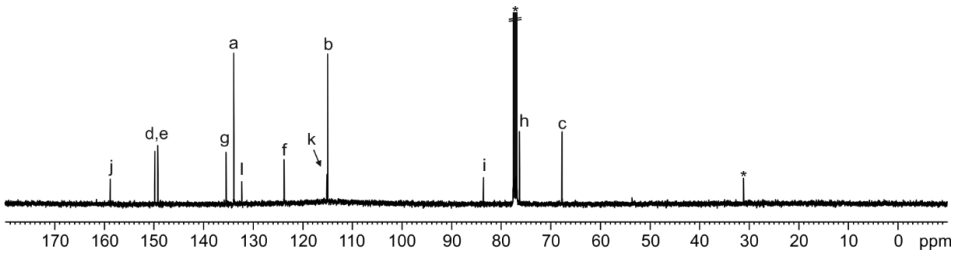

Figure 30. $^{13}C\{^{1}H\}$ NMR (100 MHz, $CDCl_3$, 298 K) spectrum of **2**. See Scheme 3 for carbon assignment. *Residual solvent peaks.

Tetra-pyridyl aryl-extended calix[4]pyrrole 4: Tetra-*α* tetra-(4-hydroxyphenyl) calix[4]pyrrole **5**[51,68] (100 mg, 0.14 mmol, 1 equiv.) and Cs_2CO_3 (1.32 g, 4.05 mmol, 7.5 equiv.) were suspended in dry DMF (2 mL) in a two-neck round-bottom flask. The mixture was stirred at 50°C under Argon atmosphere for 30 min. 3-(Bromomethyl)pyridinium hydrobromide **6** (273 mg, 1.08 mmol, 2 equiv.) in DMF (1 mL) was added dropwise and the reaction was stirred at 60°C under Argon atmosphere for 4 h. After that, the solvent was removed under vacuum and the crude was redissolved in CH_2Cl_2 (20 mL). The crude was washed with brine (2x20 mL) and water (20 mL). The organic layer was dried (Na_2SO_4), filtered and concentrated. The crude was purified by column chromatography on silica gel (4 g, 9:1 → 8:2 CH_2Cl_2:isopropanol) and the product was further purified by recrystallization from 1:1 CH_2Cl_2:CH_3CN affording a pale yellow solid (38 mg, 0.04 mmol, 26% yield). Rf = 0.2 (9:1 CH_2Cl_2:isopropanol). ^{1}H NMR (500 MHz, CD_2Cl_2, 298 K): *δ* (ppm): 8.64 (s, 4H); 8.53 (d, *J* = 4.7 Hz, 4H); 7.77 (d, *J* = 8.0 Hz, 4H); 7.71 (br s, 4H); 7.31 (dd, *J* = 8.0 Hz, *J* = 4.7 Hz, 4H); 7.06-7.04 (m, 8H); 6.86-6.84 (m, 8H); 5.74 (d, *J* = 2.7 Hz, 8H); 5.05 (s, 8H); 1.95 (s, 12H). $^{13}C\{^{1}H\}$ NMR (125 MHz, CD_2Cl_2, 298 K): *δ* (ppm): 157.5; 149.8; 149.4; 141.4; 137.1; 135.6; 133.1; 128.9; 123.8; 114.2; 106.6; 68.1; 44.5; 28.0. HRMS (ESI-TOF) m/z: $[M+H]^+$ Calcd for $C_{72}H_{65}N_8O_4$ 1105.5123; Found 1105.5129. FTIR *ν* (cm^{-1}): 2976; 1579; 1505; 1427; 1241; 1178; 1012; 832; 768; 708. M.p. > 138°C (decompose).

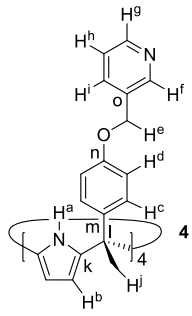

Figure 31. Line-drawing structure of tetra-pyridyl **4**.

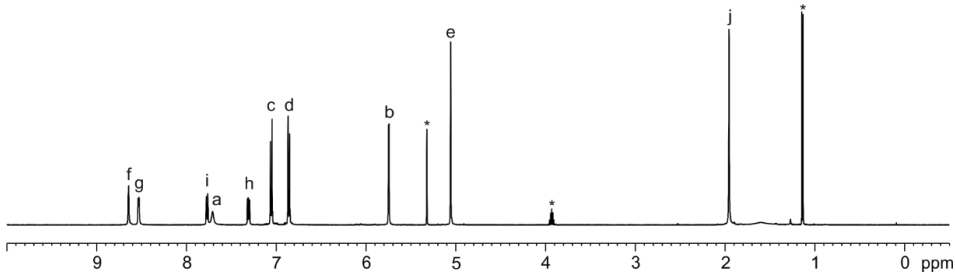

Figure 32. ^{1}H NMR (500 MHz, CD_2Cl_2, 298 K) spectrum of **4**. See Figure 31 for proton assignment. *Residual solvent peaks.

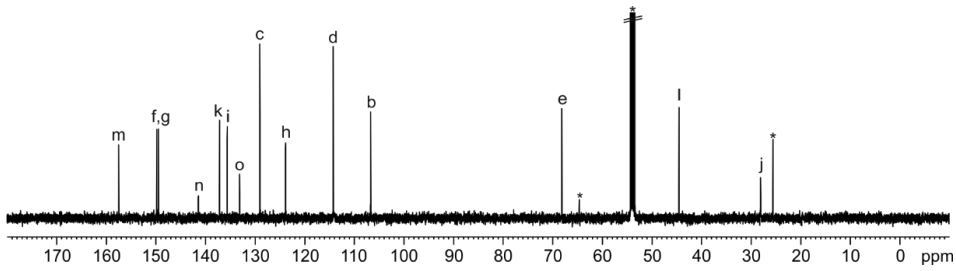

Figure 33. $^{13}C\{^{1}H\}$ NMR (125 MHz, CD_2Cl_2, 298 K) spectrum of **4**. See Figure 31 for carbon assignment. *Residual solvent peaks.

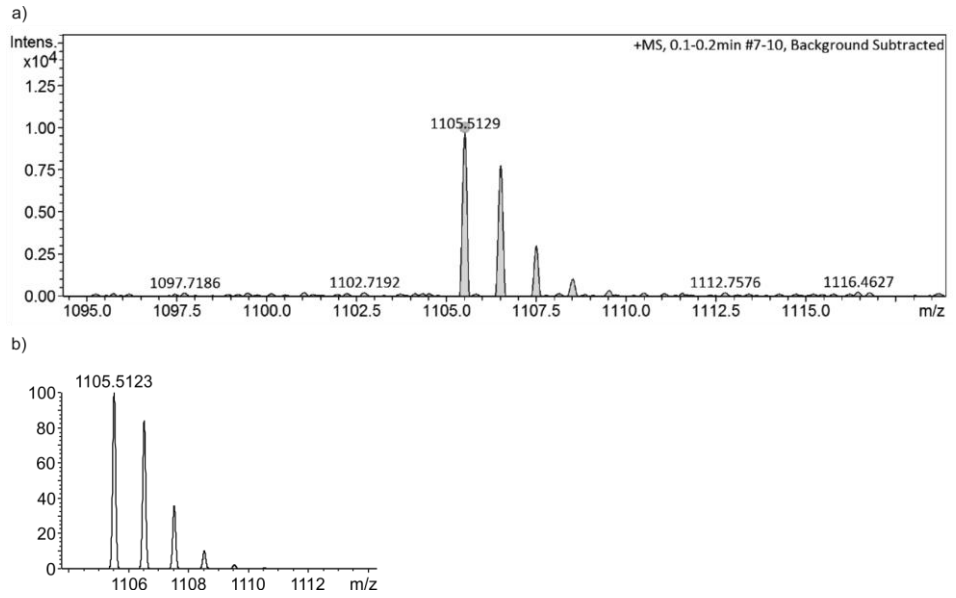

Figure 34. a) Experimental and b) theoretical isotopic distributions of $[M+H]^+$. The exact mass for the monoisotopic peak in a) and b) is indicated.

***Bis-N*-oxide 10:** The compound was synthesized following a described procedure in the literature.[69]

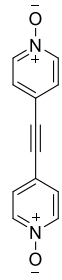

10

Figure 35. Line-drawing structure of *N*-oxide **10**.

Quinuclidine *N*-oxide 11: The experimental procedure for the synthesis of **11** is described in Chapter 2.

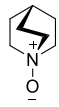

11

Figure 36. Line-drawing structure of *N*-oxide **11**.

Chapter 4

Tetra-pyridyl tetra-pyridinium super aryl-extended calix[4]pyrrole 12: Tetra-pyridyl tetra-chloro super aryl-extended calix[4]pyrrole **14** (20 mg, 0.011 mmol, 1 equiv.) was added to a dry-oven schlenk flask and kept under Argon atmosphere. Freshly distilled and dry pyridine (2.2 mL) was added and the reaction was stirred at 110°C overnight. After that, the reaction was stopped and allowed to reach r.t. The crude was concentrated and acetone (3 mL) was added and sonicated. The crude was filtered and washed with acetone (3 mL), CH_2Cl_2 (2x3 mL) and hexane (2x3 mL) affording the product as a pale brown solid (20 mg, 0.009 mmol, 85% yield). ^{1}H NMR (500 MHz with cryoprobe, CD_3OD, 298 K): δ (ppm) = 8.91 ppm (br s, 8H); 8.58-8.48 (m, 12H); 8.05 (br s, 8H); 7.89 (d, J = 7.6 Hz, 4H); 7.43-7.40 (m, 20H); 7.04-6.96 (m, 16H); 5.94 (s, 8H); 5.15 (s, 8H); 4.56 (t, J = 7.2 Hz, 8H); 2.50-2.47 (m, 8H); 2.00-1.96 (m, 8H); 1.26-1.22 (m, 8H). HRMS (ESI-TOF) m/z: $[M-4Cl]^{4+}$ Calcd for $C_{136}H_{120}N_{12}O_4$ 496.2383; Found 496.2398.

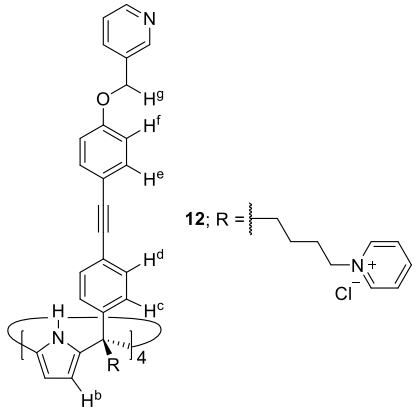

Figure 37. Line-drawing structure of tetra-pyridyl **12**.

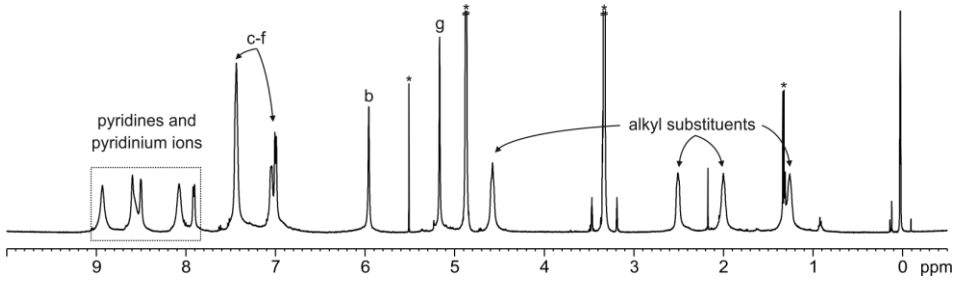

Figure 38. ^{1}H NMR (500 MHz with cryoprobe, CD_3OD, 298 K) spectrum of **12**. See Figure 37 for proton assignment. *Residual solvent peaks.

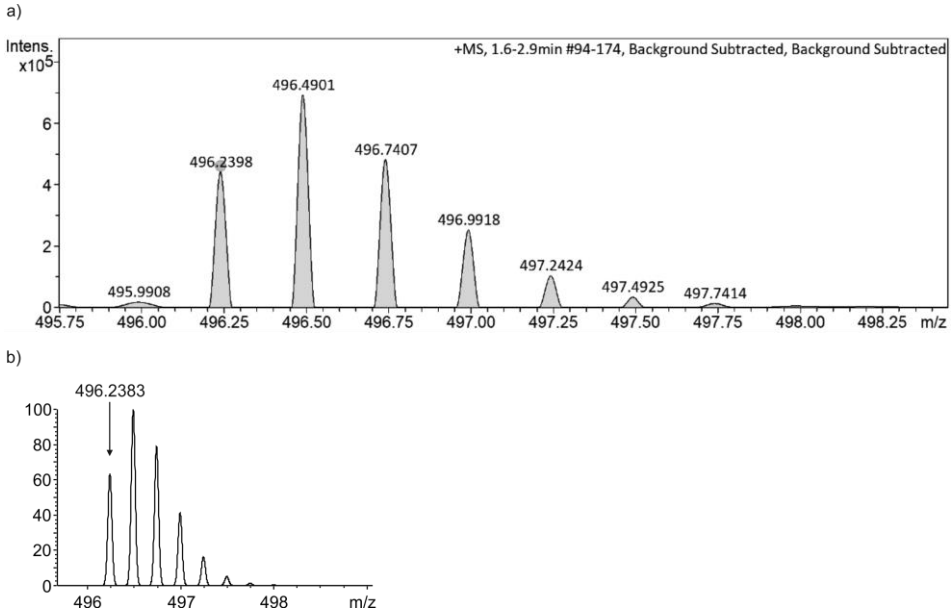

Figure 39. a) Experimental and b) theoretical isotopic distributions of $[M\text{-}4Cl]^{4+}$. The exact mass for the monoisotopic peak in a) and b) is indicated.

Tetra-pyridyl tetra-chloro super aryl-extended calix[4]pyrrole 14: Tetra-*α* tetra-(4-iodophenyl) tetra-(4-chlorobutyl) calix[4]pyrrole **13**[66] (50 mg, 0.03 mmol, 1 equiv.), $Pd(PPh_3)_2Cl_2$ (2.95 mg, 0.004 mmol, 0.03 equiv.), CuI (1.28 mg, 0.007 mmol, 0.05 equiv.) and 3-((4'-ethynylphenoxy)methyl)pyridine **2** (42.20 mg, 0.20 mmol, 1.5 equiv.) were kept under Argon atmosphere. Dry THF (3.6 mL) and dry diisopropylamine (3.6 mL) were added dropwise. The reaction was stirred at r.t. for 24 h. After that, the crude was concentrated, redissolved in CH_2Cl_2 (10 mL) and washed with brine (2x10 mL) and water (10 mL). The organic layer was dried (Na_2SO_4), filtered and concentrated. The crude was purified by column chromatography on silica gel (3 g, 90:10 → 85:15 CH_2Cl_2:isopropanol) to afford the product as a white solid (28 mg, 0.015 mmol, 46% yield). Rf = 0.4 (92:8 CH_2Cl_2:isopropanol). ^{1}H NMR (300 MHz, $CDCl_3$, 298 K): *δ* (ppm): 8.46 (br s, 8H); 7.74 (d, *J* = 7.8 Hz, 4H); 7.57 (br s, 4H); 7.37-7.29 (m, 20H); 7.05-7.02 (m, 8H); 6.89-6.86 (m, 8H); 5.92 (s, 8H); 5.04 (s, 8H); 3.49 (t, *J* = 6.5 Hz, 8H); 2.32-2.26 (m, 8H); 1.78-1.70 (m, 8H); 1.41-1.34 (m, 8H). ^{13}C{^{1}H} NMR (125 MHz with cryoprobe, $CDCl_3$, 298 K): *δ* (ppm): 158.5; 149.7; 149.0; 144.8; 135.5; 135.4; 133.4; 132.2; 130.9; 128.3; 123.7; 121.8; 116.2; 114.9; 106.7; 89.5; 88.2; 67.7; 48.9; 44.9; 39.8; 33.0; 22.7. MS (MALDI) m/z: $[M+H]^+$ Calcd for $C_{116}H_{101}N_8O_4Cl_4$ 1810.6; Found 1810.7. FTIR *ν* (cm^{-1}): 3430; 2950; 1602; 1513; 1428; 1281; 1247; 1018; 829; 771. M.p. > 220°C (decompose).

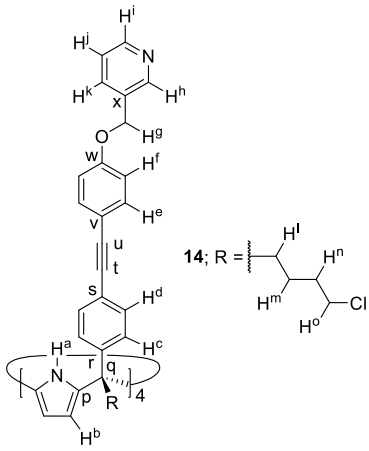

Figure 40. Line-drawing structure of tetra-pyridyl **14**.

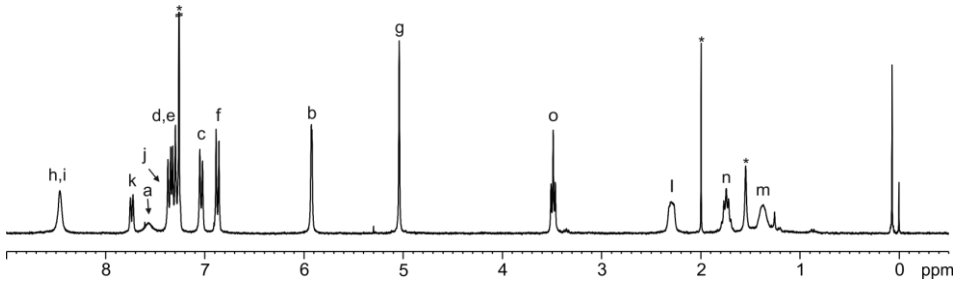

Figure 41. ^{1}H NMR (300 MHz, $CDCl_3$, 298 K) spectrum of **14**. See Figure 40 for proton assignment. *Residual solvent peaks.

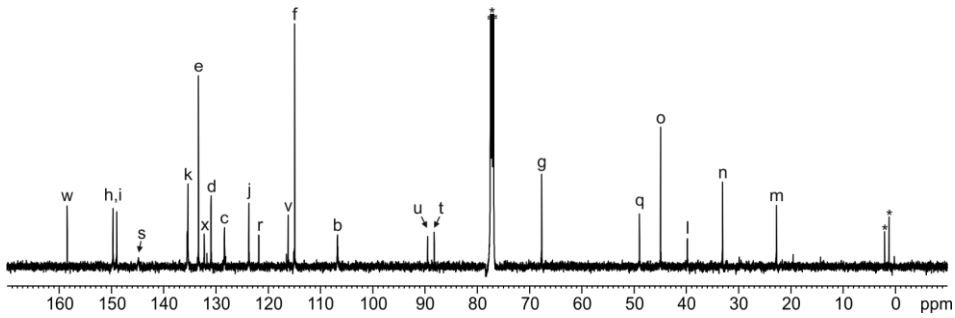

Figure 42. $^{13}C\{^{1}H\}$ NMR (125 MHz with cryoprobe, $CDCl_3$, 298 K) spectrum of **14**. See Figure 40 for carbon assignment. *Residual solvent peaks.

Cage [1•Pd](BF$_4$)$_2$: Procedure A. Tetra-pyridyl **1** (3 mg, 0.002 mmol, 1 equiv.) was dissolved in 2:1 $CDCl_3$:CD_3CN (1 mL) and added to a NMR tube (0.5 mL). $[Pd(CH_3CN)_4](BF_4)_2$ (0.21 mL from a 6 mM solution in 2:1 $CDCl_3$:CD_3CN, 0.0013 mmol, *ca.* 1 equiv.) was added to the calix[4]pyrrole's

solution. The NMR tube was hand-shaked for a few seconds and thermally equilibrated at 40°C for 24 h. A solution containing [**1**•Pd]$^{2+}$ was obtained (NMR yield > 70%). ^{1}H NMR (500 MHz with cryoprobe, 2:1 $CDCl_3$:CD_3CN, 298 K): *δ* (ppm): 9.45 (s, 4H); 9.16 (br d, 4H); 7.87 (d, *J* = 7.8 Hz, 4H); 7.56 (m, 8H); 7.41-7.39 (m, 8H); 7.30-7.28 (m, 8H); 6.99-6.97 (m, 8H); 6.88-6.86 (m, 8H); 6.08 (d, *J* = 2.4 Hz, 8H); 5.11 (s, 8H); 1.92 (s, 12H). ^{13}C{^{1}H} NMR (125 MHz with cryoprobe, 2:1 $CDCl_3$:CD_3CN, 298 K): *δ* (ppm): 158.3; 151.1; 150.1; 149.8; 139.3; 137.9; 137.2; 133.4; 130.8; 128.7; 127.5; 121.0; 116.5; 115.1; 105.3; 88.4; 88.0; 66.6; 44.8; 28.9. HRMS (ESI-TOF) m/z: [M-2(BF_4)]$^{2+}$ Calcd for $C_{104}H_{80}N_8O_4Pd$ 803.2674; Found 803.2695.

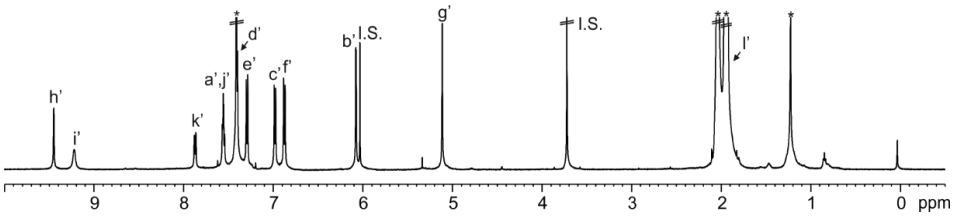

Figure 43. ^{1}H NMR (500 MHz with cryoprobe, 2:1 $CDCl_3$:CD_3CN, 298 K) spectrum of [**1**•Pd]$^{2+}$ from procedure A. Primed letters correspond to proton signals of [**1**•Pd]$^{2+}$. See Figure 23 for proton assignment. 1,3,5-Trimethoxybenzene (I.S.). *Residual solvent peaks.

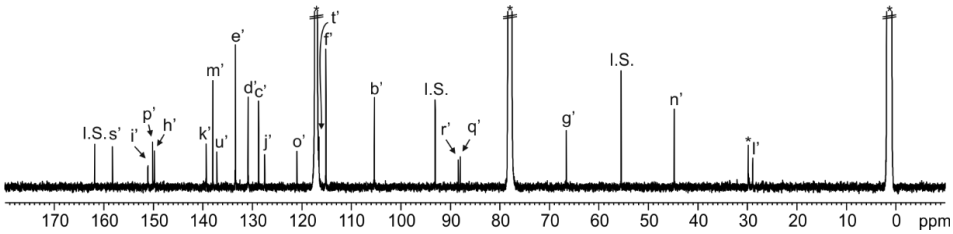

Figure 44. ^{13}C{^{1}H} NMR (500 MHz with cryoprobe, 2:1 $CDCl_3$:CD_3CN, 298 K) spectrum of [**1**•Pd]$^{2+}$ from procedure A. Primed letters correspond to proton signals of [**1**•Pd]$^{2+}$. See Figure 23 for carbon assignment. 1,3,5-Trimethoxybenzene (I.S.). *Residual solvent peaks.

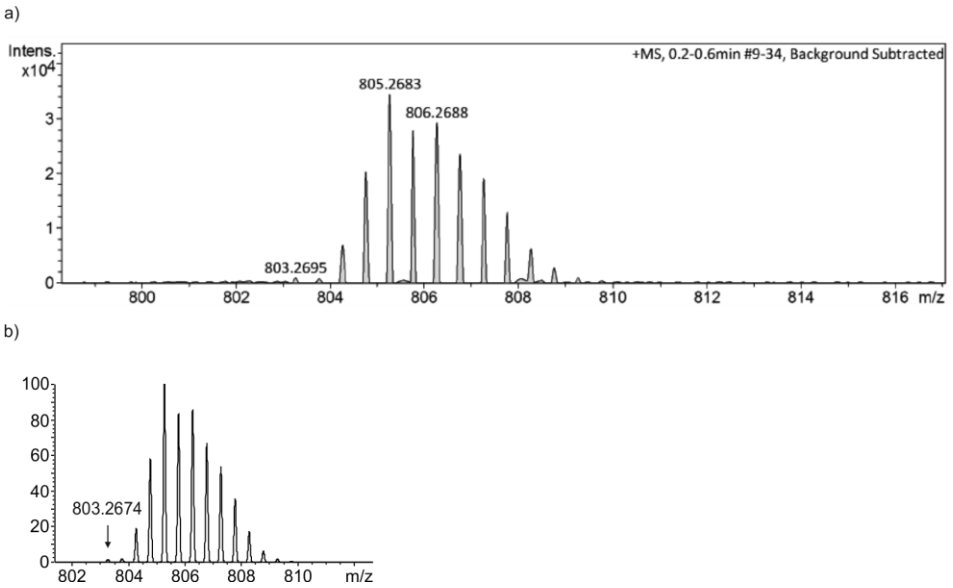

Figure 45. a) Experimental and b) theoretical isotopic distributions of $[M\text{-}2(BF_4)]^{2+}$. The exact mass for the monoisotopic peak in a) and b) is indicated.

Procedure B. Tetra-pyridyl **1** (20.66 mg, 0.014 mmol, 1 equiv.) was dissolved in dry 2:1 $CHCl_3$:CH_3CN (6.9 mL) in a Schlenk flask. $[Pd(CH_3CN)_4](BF_4)_2$ (4.2 mL from a 6 mM solution in 2:1 $CHCl_3$:CH_3CN, 0.025 mmol, *ca.* 1 equiv.) was added to the calix[4]pyrrole's solution. The reaction was stirred under Argon atmosphere at 40°C for 24 h. After that, the crude was filtered using extra 2:1 $CHCl_3$:CH_3CN (6 mL). The chloroform was removed under reduced pressure. Et_2O (6 mL) was added to the crude solution obtaining a white precipitate. The crude was filtered and the precipitate was washed with extra Et_2O (2 mL). The white solid was dried under high vacuum affording the [**1**•Pd]$^{2+}$ cage (15 mg, 0.0084 mmol, 60% yield). The ^1H and $^{13}C\{^1H\}$ NMR spectra in 2:1 $CDCl_3$:CD_3CN at 298 K of the isolated cage coincided with those obtained following the procedure A.

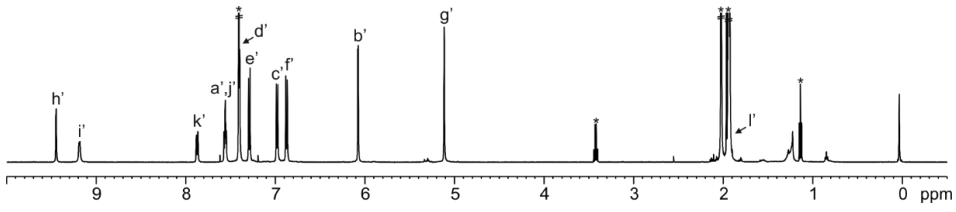

Figure 46. ^1H NMR (500 MHz with cryoprobe, 2:1 $CDCl_3$:CD_3CN, 298 K) spectrum of [**1**•Pd]$^{2+}$ from procedure B. Primed letters correspond to proton signals of [**1**•Pd]$^{2+}$. See Figure 23 for proton assignment. *Residual solvent peaks.

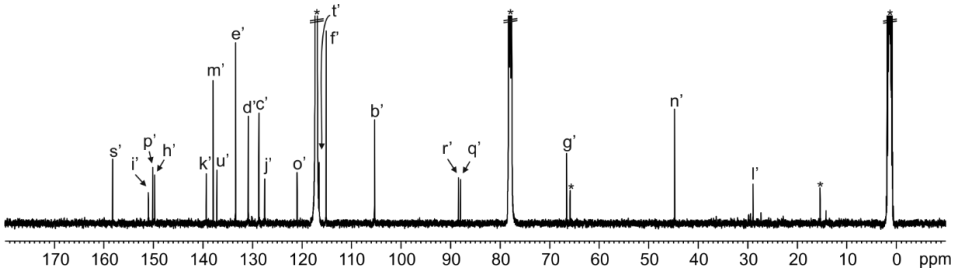

Figure 47. $^{13}C\{^{1}H\}$ NMR (500 MHz with cryoprobe, 2:1 $CDCl_3$:CD_3CN, 298 K) spectrum of [**1**•Pd]$^{2+}$ from procedure B. Primed letters correspond to proton signals of [**1**•Pd]$^{2+}$. See Figure 23 for carbon assignment. *Residual solvent peaks.

$$[Pt(CH_3CN)_2]Cl_2 + AgBF_4 \xrightarrow[71\%]{CH_3CN} [Pt(CH_3CN)_4](BF_4)_2$$

Scheme 4. Synthesis of $[Pt(CH_3CN)_4](BF_4)_2$.

Tetrakis(acetonitrile)platinum(II) tetrafluoroborate: A suspension of $AgBF_4$ (230 mg, 1.18 mmol, 2.06 equiv.) and $[Pt(CH_3CN)_2]Cl_2$ (200 mg, 0.56 mmol, 1 equiv.) in dry CH_3CN (40 mL) was refluxed overnight. After that, the reaction was allowed to reach r.t. and the crude was filtered through celite using additional CH_3CN (20 mL). The solution was concentrated under reduced pressure until 5 mL of volume. Et_2O (40 mL) was added obtaining a yellow precipitate. The precipitate was filtered, washed with Et_2O (20 mL) and the solid was dried under high vacuum affording the product as a pale orange solid (218 mg, 0.40 mmol, 71% yield). Analytical data are in agreement with those reported in the literature.[70,71]

Cage [1•Pt](BF$_4$)$_2$: Procedure A. Tetra-pyridyl **1** (3 mg, 0.002 mmol, 1 equiv.) was dissolved in 2:1 $CDCl_3$:CD_3CN (1 mL) and added to a NMR tube (0.5 mL). $[Pt(CH_3CN)_4](BF_4)_2$ (0.19 mL from a 6.8 mM solution in 2:1 $CDCl_3$:CD_3CN, 0.0013 mmol, *ca.* 1 equiv.) was added to the calix[4]pyrrole's solution. The NMR tube was hand-shaked for a few seconds and thermally equilibrated at 50°C for 72 h. A solution containing [**1**•Pt]$^{2+}$ was obtained (NMR yield > 60%). ^{1}H NMR (500 MHz with cryoprobe, 2:1 $CDCl_3$:CD_3CN, 298 K): δ (ppm): 9.33 (s, 4H); 9.19 (d, J = 5.7 Hz; 4H); 7.86 (d, J = 7.8 Hz, 4H); 7.57-7.54 (m, 8H); 7.41-7.39 (m, 8H); 7.28-7.26 (m, 8H); 6.99-6.97 (m, 8H); 6.88-6.86 (m, 8H); 6.08 (d, J = 2.6 Hz, 8H); 5.11 (s, 8H); 1.92 (s, 12H). $^{13}C\{^{1}H\}$ NMR (125 MHz with cryoprobe, 2:1 $CDCl_3$:CD_3CN, 298 K): δ (ppm): 158.2; 151.7; 150.7; 150.1; 139.4; 138.0; 137.5; 133.4; 130.9; 128.7; 127.8; 121.0; 116.5; 115.2; 105.4; 88.4; 88.0; 66.4; 44.7; 28.9. HRMS (ESI-TOF) m/z: $[M-2(BF_4)]^{2+}$ Calcd for $C_{104}H_{80}N_8O_4Pt$ 848.2951; Found 848.2986.

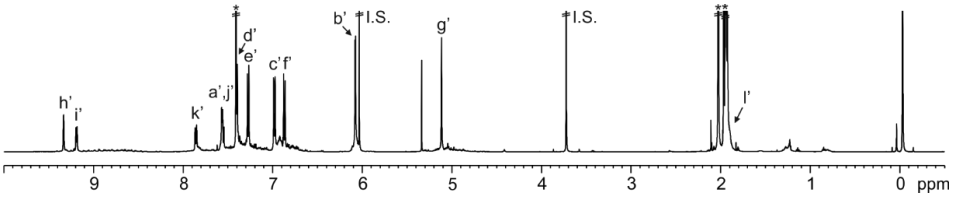

Figure 48. ^{1}H NMR (500 MHz with cryoprobe, 2:1 $CDCl_3$:CD_3CN, 298 K) spectrum of [**1**•Pt]$^{2+}$ from Procedure A. Primed letters correspond to proton signals of [**1**•Pt]$^{2+}$. See Figure 23 for proton assignment. 1,3,5-Trimethoxybenzene (I.S.). *Residual solvent peaks.

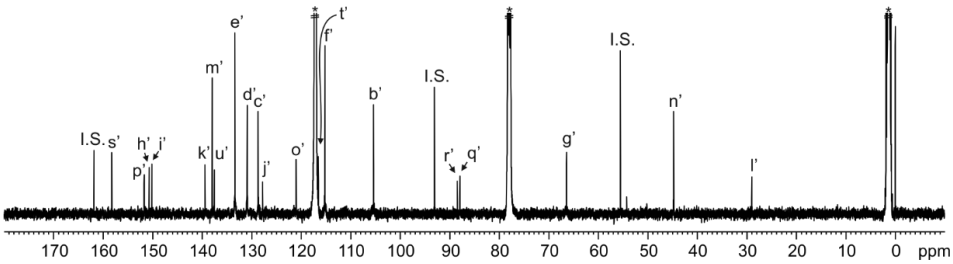

Figure 49. $^{13}C\{^{1}H\}$ NMR (125 MHz with cryoprobe, 2:1 $CDCl_3$:CD_3CN, 298 K) spectrum of [**1**•Pt]$^{2+}$ from Procedure A. Primed letters correspond to proton signals of [**1**•Pt]$^{2+}$. See Figure 23 for carbon assignment. 1,3,5-Trimethoxybenzene (I.S.). *Residual solvent peaks.

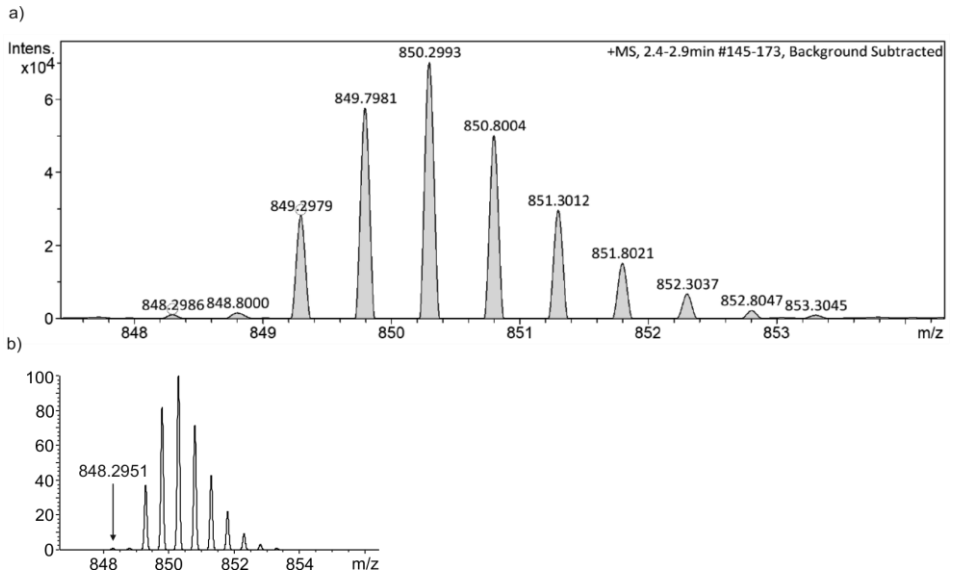

Figure 50. a) Experimental and b) theoretical isotopic distributions of [M-2(BF_4)]$^{2+}$. The exact mass for the monoisotopic peak in a) and b) is indicated.

Procedure B. Tetra-pyridyl **1** (20.21 mg, 0.013 mmol, 1 equiv.) was dissolved in dry 2:1 $CHCl_3$:CH_3CN (6.7 mL) in a Schlenk flask. $[Pt(CH_3CN)_4](BF_4)_2$ (2.9 mL from a 6 mM solution in 2:1 $CHCl_3$:CH_3CN, 0.017 mmol, *ca.* 1 equiv.) was added to the calix[4]pyrrole's solution. The reaction was stirred under Argon atmosphere at 50°C for 72 h. After that, the crude was filtered using extra 2:1 $CHCl_3$:CH_3CN (6 mL). Chloroform was removed under reduced pressure. Et_2O (6 mL) was added to the crude solution obtaining a white precipitate. The crude was filtered and the precipitate was washed with extra Et_2O (6 mL) and hexane (6 mL). The white solid was dried under high vacuum affording the [**1**•Pt]$^{2+}$ cage (15 mg, 0.0078 mmol, 60% yield). The ^{1}H NMR spectrum in 2:1 $CDCl_3$:CD_3CN at 298 K of the isolated cage coincided with that obtained following the procedure A.

4.4.4 NMR experiments of tetra-pyridyl **1**

Tetra-pyridyl **1** in $CDCl_3$ and 2:1 $CDCl_3$:CD_3CN

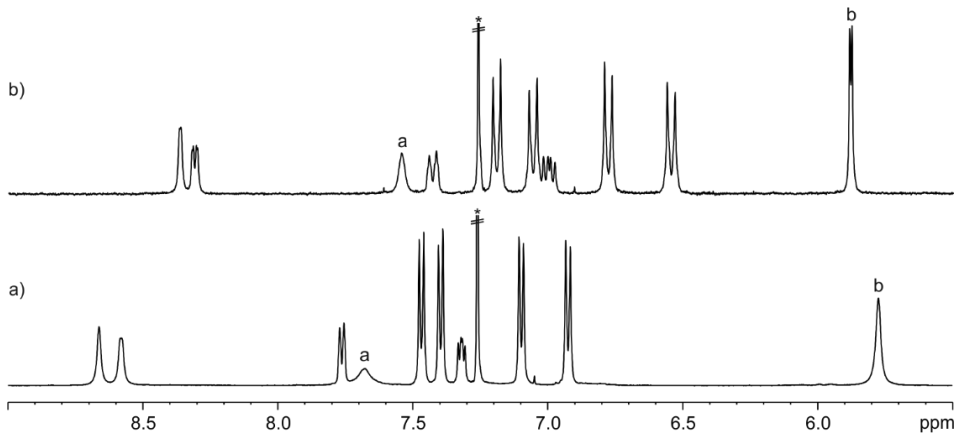

Figure 51. ^{1}H NMR (400 MHz, 298 K) spectra of tetra-pyridyl **1**: a) $CDCl_3$ and b) 2:1 $CDCl_3$:CD_3CN. See Figure 23 for proton assignment. *Residual solvent peak, δ ($CHCl_3$) = 7.26 ppm.

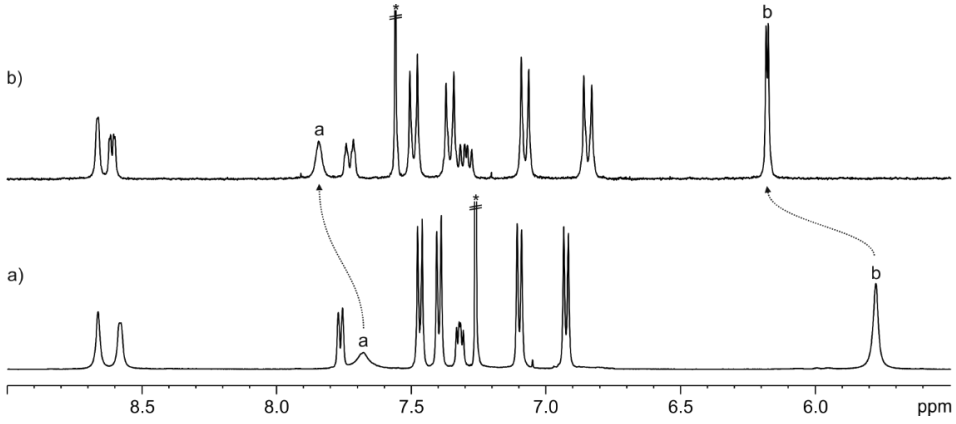

Figure 52. Superposition of the ^{1}H NMR (400 MHz, 298 K) spectra shown on Figure 51. The spectrum a) was referenced using the residual $CHCl_3$ signal at δ = 7.26 ppm. The spectrum b) was moved in the chemical shift scale. See Figure 23 for proton assignment. *Residual solvent peak.

Addition of Pd(II) to calix[4]pyrrole **1** in $(CD_3)_2SO$

A solution of the tetra-pyridyl **1** (1-2 mM) and 1,3,5-trimethoxybenzene (internal standard, 1-2 mM) was prepared in $(CD_3)_2SO$. Subsequently, 0.5 mL of the solution were transferred to a NMR tube. A solution of Pd(II) ($[Pd(CH_3CN)_4](BF_4)_2$, $Pd(TFA)_2$ or $Pd(NO_3)_2$) was prepared in $(CD_3)_2SO$ at 10-15 fold higher concentration (20-30 mM). Immediately, the 0.5 mL of the tetra-pyridyl's solution was titrated by manually injecting incremental amounts of the Pd(II) solution using a micro syringe. A ^{1}H NMR spectrum of the mixture was acquired after each injection and vigorous hand shaking of the NMR tube for few seconds.

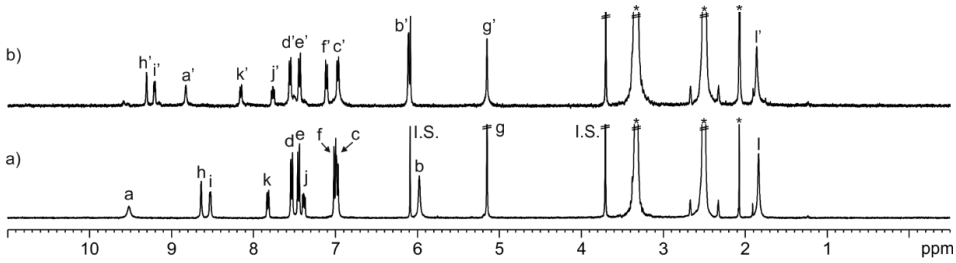

Figure 53. ^{1}H NMR (400 MHz, $(CD_3)_2SO$, 298 K) spectra: a) **1**; addition of $[Pd(CH_3CN)_4](BF_4)_2$ to **1**: b) *ca.* 1 equiv. Primed letters correspond to proton signals of $[\mathbf{1}\bullet Pd]^{2+}$. The $[\mathbf{1}\bullet Pd]^{2+}$ cage was formed in an extent larger than 70%. See Figure 23 for proton assignment. 1,3,5-Trimethoxybenzene (I.S.). *Residual solvent peaks.

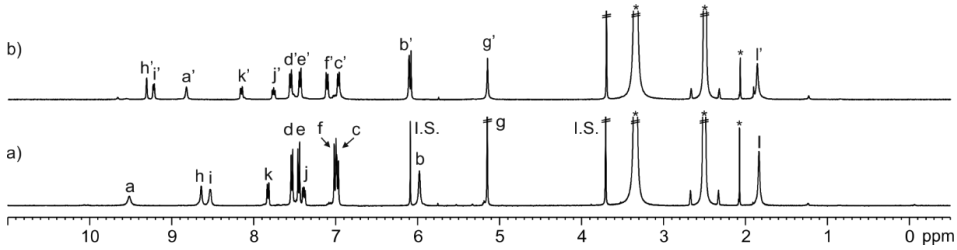

Figure 54. ^{1}H NMR (400 MHz, $(CD_3)_2SO$, 298 K) spectra: a) **1**; addition of $Pd(TFA)_2$ to **1**: b) *ca.* 1 equiv. Primed letters correspond to proton signals of $[\mathbf{1}\bullet Pd]^{2+}$. The $[\mathbf{1}\bullet Pd]^{2+}$ cage was formed in an extent larger than 70%. See Figure 23 for proton assignment. 1,3,5-Trimethoxybenzene (I.S.). *Residual solvent peaks.

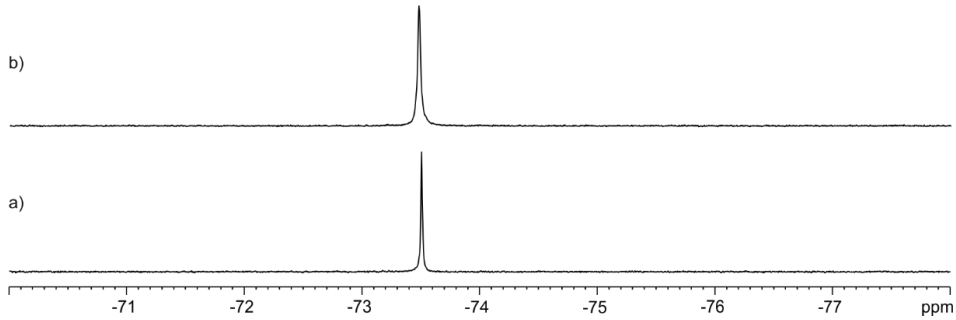

Figure 55. $^{19}F\{^{1}H\}$ NMR (376 MHz, $(CD_3)_2SO$, 298 K) spectra: a) $[\mathbf{1}\bullet Pd]^{2+}$ and b) $Pd(TFA)_2$.

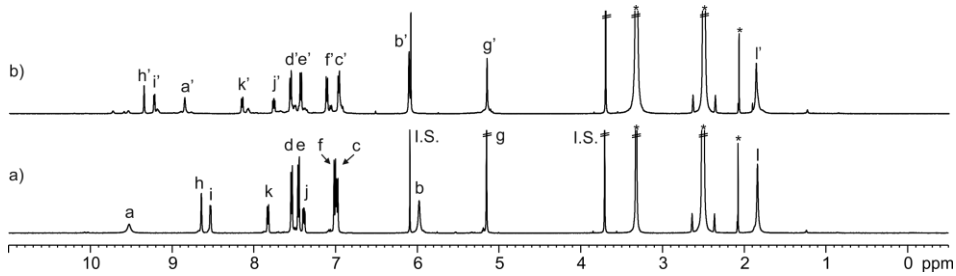

Figure 56. ^{1}H NMR (500 MHz, $(CD_3)_2SO$, 298 K) spectra: a) **1**; addition of $Pd(NO_3)_2$ to **1**: b) *ca.* 1 equiv. Primed letters correspond to proton signals of $[\mathbf{1}\bullet Pd]^{2+}$. The $[\mathbf{1}\bullet Pd]^{2+}$ cage was formed in an extent larger than 70%. See Figure 23 for proton assignment. 1,3,5-Trimethoxybenzene (I.S.). *Residual solvent peaks.

The ^{1}H NMR spectra of the tetra-pyridyl **1** with different Pd(II) salts in $(CD_3)_2SO$ were very similar and the number of proton signals was in agreement with a C_{4v} symmetry. Most likely, the tetra-pyridyl **1** and Pd(II) formed the $[\mathbf{1}\bullet Pd]^{2+}$ cage in $(CD_3)_2SO$, independently of the salt used, in an extent larger than 70%. The thermal equilibration at 40ºC of the $[\mathbf{1}\bullet Pd]^{2+}$ solutions in $(CD_3)_2SO$ did not produce further changes in the ^{1}H NMR spectra. The proton signals of low intensity were indicative of the formation of ill-defined aggregates that are in equilibrium with the cage assembly.

Table 2. Chemical shifts (δ, ppm) and chemical shift changes ($\Delta\delta$, ppm) of the proton signals of the 3-pyridyl substituents of **1** in $(CD_3)_2SO$. See Figure 23 for proton assignment.

Signal	δ, **1**	δ, [**1**•Pd]$^{2+}$	$\Delta\delta$, [**1**•Pd]$^{2+}$
h	8.64	9.32	+0.68
i	8.53	9.23	+0.70
j	7.39	7.77	+0.38
k	7.83	8.15	+0.32

Addition of Pd(II) to calix[4]pyrrole **1** in 2:1 $CDCl_3$:CD_3CN

A solution of the tetra-pyridyl **1** (1-2 mM) and 1,3,5-trimethoxybenzene (internal standard, 1-2 mM) was prepared in 2:1 $CDCl_3$:CD_3CN. Subsequently, 0.5 mL of the solution were transferred to a NMR tube. A solution of $[Pd(CH_3CN)_4](BF_4)_2$ was prepared in 2:1 $CDCl_3$:CD_3CN at higher concentration (5-7 mM). Immediately, the 0.5 mL of the tetra-pyridyl's solution was titrated by manually injecting incremental amounts of the Pd(II) solution using a micro syringe. A ^{1}H NMR spectrum of the mixture was acquired after each injection and vigorous hand shaking of the NMR tube for few seconds.

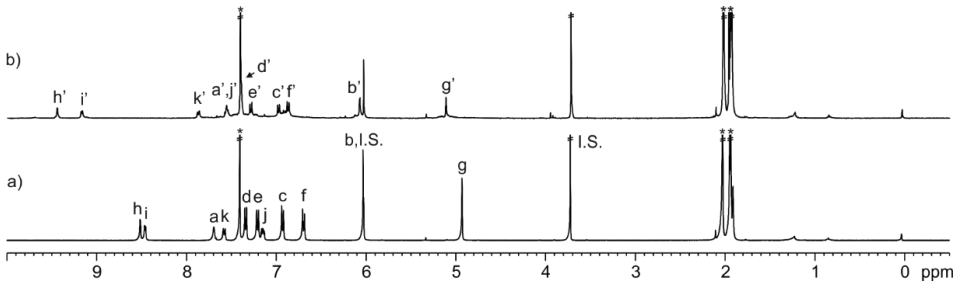

Figure 57. ^{1}H NMR (400 MHz, 2:1 $CDCl_3$:CD_3CN, 298 K) spectra: a) **1**; addition of $[Pd(CH_3CN)_4](BF_4)_2$ to **1**: b) *ca.* 1 equiv. Primed letters correspond to proton signals of [**1**•Pd]$^{2+}$. The [**1**•Pd]$^{2+}$ cage was formed in an extent larger than 60%. 1,3,5-Trimethoxybenzene (I.S.). See Figure 23 for proton assignment. *Residual solvent peaks.

Thermal equilibration experiment of the [**1**•Pd]$^{2+}$ cage

A solution of the tetra-pyridyl **1** (1-2 mM) and 1,3,5-trimethoxybenzene (internal standard, 1-2 mM) was prepared in 2:1 $CDCl_3$:CD_3CN. Subsequently, 0.5 mL of the solution were transferred to a NMR tube. A solution of $[Pd(CH_3CN)_4](BF_4)_2$ was prepared in 2:1 $CDCl_3$:CD_3CN at higher concentration (5-7 mM). Immediately, $[Pd(CH_3CN)_4](BF_4)_2$ (*ca.* 1 equiv.) was added to the calix[4]pyrrole's solution. A ^{1}H NMR spectrum of the mixture was acquired after the injection and

vigorous hand shaking of the NMR tube for few seconds. The mixture was thermally equilibrated at 40ºC in an oil bath for 24, 48 and 120 h and the ^{1}H NMR spectra were acquired.

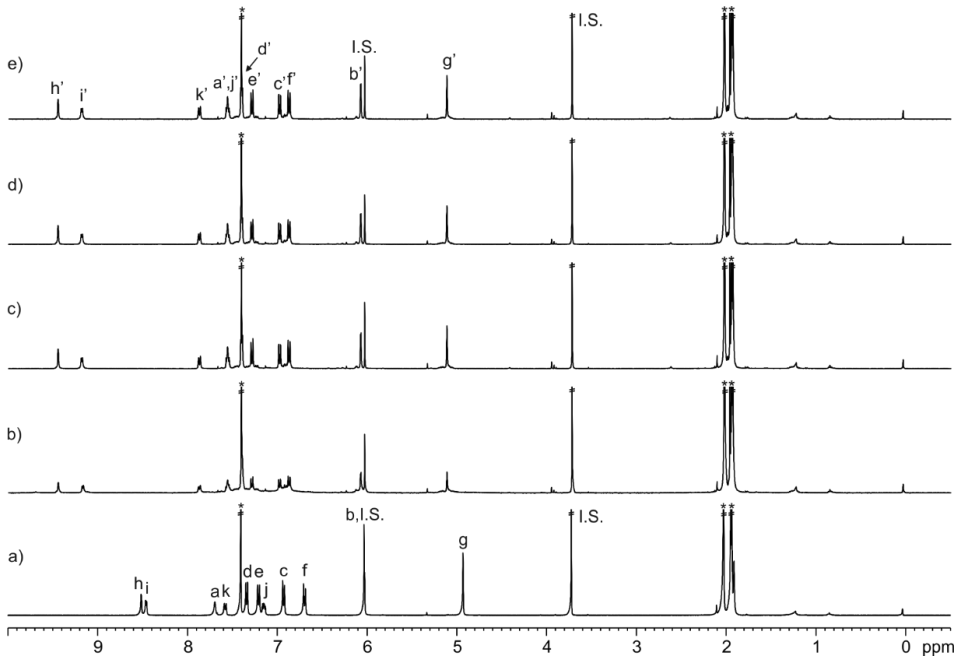

Figure 58. ^{1}H NMR (400 MHz, 2:1 $CDCl_3$:CD_3CN, 298 K) spectra: a) **1**; addition of $[Pd(CH_3CN)_4](BF_4)_2$ to **1**: b) *ca.* 1 equiv.; thermal equilibration of b) at 40ºC: c) 24; d) 48 and e) 120 h. Primed letters correspond to proton signals of [**1**•Pd]$^{2+}$. See Figure 23 for proton assignment. 1,3,5-Trimethoxybenzene (I.S.). *Residual solvent peaks.

The addition of $[Pd(CH_3CN)_4](BF_4)_2$ to a millimolar solution of tetra-pyridyl **1** produced the formation of the [**1**•Pd]$^{2+}$ cage (60%). The same solution was thermally equilibrated at 40ºC for 24 h. The ^{1}H NMR spectrum showed the formation of more than 70% of the [**1**•Pd]$^{2+}$ cage. The solution was thermally equilibrated at 40ºC for 48-120 h. However, the ^{1}H NMR spectra did not show further changes on the proton signals of the cage.

Chapter 4

^{1}H pseudo 2D DOSY NMR experiments of **1** and [**1**•Pd]$^{2+}$ cage

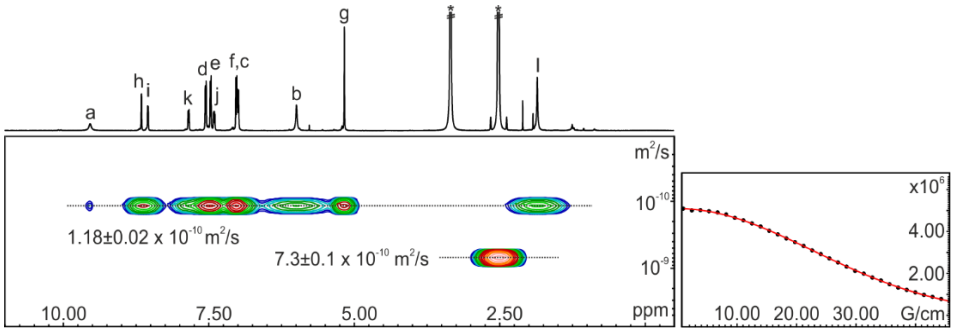

Figure 59. (left) ^{1}H pseudo 2D plot of DOSY (500 MHz with cryoprobe, $(CD_3)_2SO$, 298 K, D20 = 0.15 s; P30 = 1.40 ms) of tetra-pyridyl **1** (2 mM). (right) Fit of the decay of the signal b to a mono-exponential function. Errors are indicated as standard deviations. See Figure 23 for proton assignment. *Residual solvent peaks.

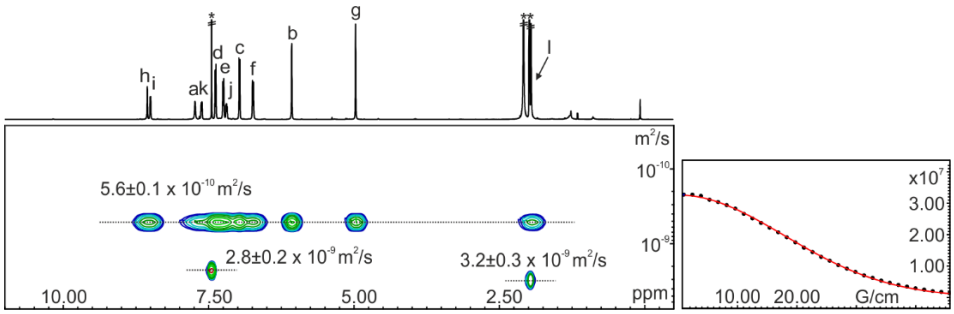

Figure 60. (left) ^{1}H pseudo 2D plot of DOSY (500 MHz with cryoprobe, 2:1 $CDCl_3$:CD_3CN, 298 K, D20 = 0.15 s; P30 = 0.80 ms) of tetra-pyridyl **1** (2 mM). (right) Fit of the decay of the signal b to a mono-exponential function. Errors are indicated as standard deviations. See Figure 23 for proton assignment. *Residual solvent peaks.

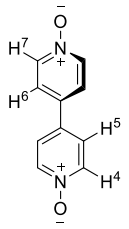

8

Figure 61. Line-drawing structure of *N*-oxide **8**.

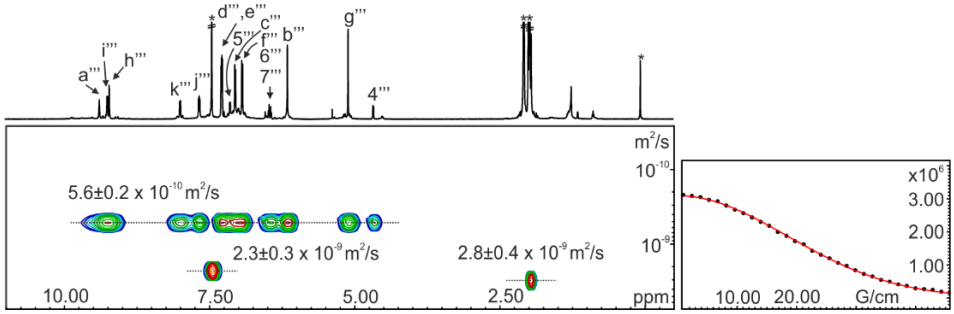

Figure 62. (left) ^{1}H pseudo 2D plot of DOSY (500 MHz with cryoprobe, 2:1 $CDCl_3$:CD_3CN, 298 K, D20 = 0.15 s; P30 = 0.80 ms) of **8**⊂[**1**•Pd]$^{2+}$ (2 mM). (right) Fit of the decay of the signal b''' to a mono-exponential function. Errors are indicated as standard deviations. Triply primed letters and numbers correspond to proton signals of **8**⊂[**1**•Pd]$^{2+}$. See Figure 23 and Figure 61 for proton assignments. *Residual solvent peaks.

The cylinders corresponding to the calculated diffusion coefficients in 2:1 $CDCl_3$:CD_3CN were not determined owing to the lack of an accurate value for the viscosity of this solvent mixture.

The diffusion coefficient values determined in $(CD_3)_2SO$ and 2:1 $CDCl_3$:CD_3CN solutions are different. We attribute this finding to the different viscosity of the solvents.

1D GOESY NMR experiments of the [**1**•Pd]$^{2+}$ cage

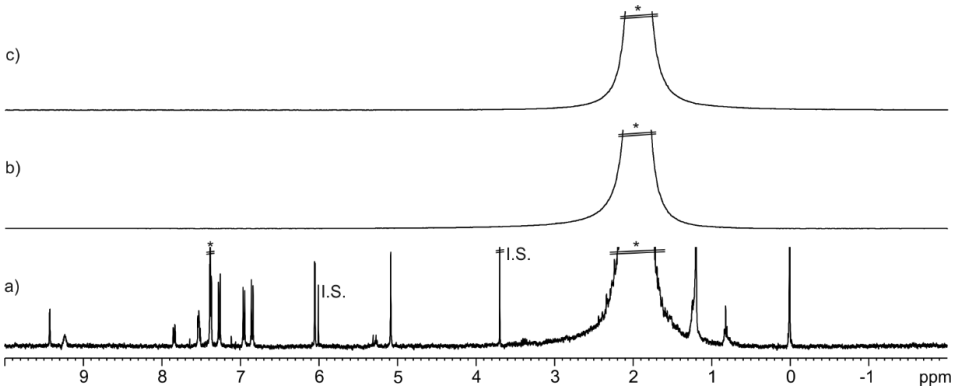

Figure 63. ^{1}H NMR (500 MHz, 2:1 $CDCl_3$:CH_3CN, 298 K) spectrum: a) [**1**•Pd]$^{2+}$; 1D GOESY NMR (500 MHz, 2:1 $CDCl_3$:CH_3CN, 298 K) spectra of [**1**•Pd]$^{2+}$: b) t_{mix} = 0.3 and c) t_{mix} = 0.6 s. 1,3,5-Trimethoxybenzene (I.S.). *Residual solvent peaks.

The 1D GOESY NMR spectra of [**1**•Pd]$^{2+}$ in 2:1 $CDCl_3$:CH_3CN at 298 K did not show the proton signals of included CH_3CN molecules in the cage. Most likely, the chemical exchange between free and bound CH_3CN molecules is fast on the GOESY timescale.

Chapter 4

Addition of Pt(II) to calix[4]pyrrole **1** in 2:1 $CDCl_3$:CD_3CN

A solution of tetra-pyridyl **1** (1-2 mM) and 1,3,5-trimethoxybenzene (internal standard, 1-2 mM) was prepared in 2:1 $CDCl_3$:CD_3CN. Subsequently, 0.5 mL of the solution were transferred to a NMR tube. A solution of $[Pt(CH_3CN)_4](BF_4)_2$ was prepared in 2:1 $CDCl_3$:CD_3CN at higher concentration (5-7 mM). Immediately, the 0.5 mL of the tetra-pyridyl's solution was titrated by manually injecting incremental amounts of the Pt(II) solution using a micro syringe. A ^{1}H NMR spectrum of the mixture was acquired after each injection and vigorous hand shaking of the NMR tube for few seconds. Finally, the mixture was thermally equilibrated for 72 h at 50°C and a ^{1}H NMR spectrum was acquired.

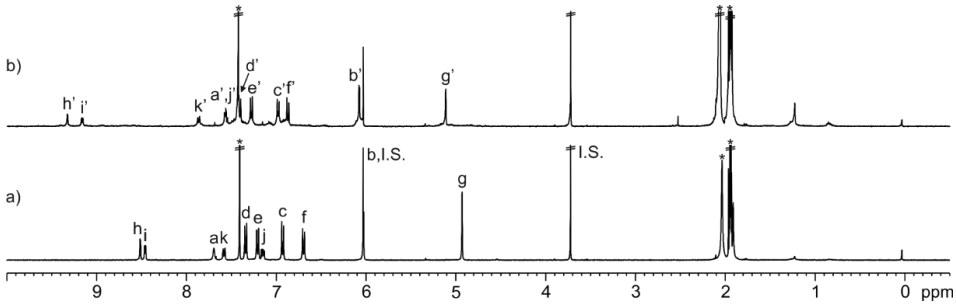

Figure 64. ^{1}H NMR (400 MHz, 2:1 $CDCl_3$:CD_3CN, 298 K) spectra: a) **1**; addition of $[Pt(CH_3CN)_4](BF_4)_2$ to **1**: b) *ca.* 1 equiv. after thermal equilibration (72 h at 50ºC). Primed letters correspond to proton signals of $[\mathbf{1}\bullet Pt]^{2+}$. The cage was formed in an extent larger than 60%. See Figure 23 for proton assignment. 1,3,5-Trimethoxybenzene (I.S.). *Residual solvent peaks.

Thermal equilibration experiment of the [**1**•Pt]$^{2+}$ cage

A solution of tetra-pyridyl **1** (1-2 mM) and 1,3,5-trimethoxybenzene (internal standard, 1-2 mM) was prepared in 2:1 $CDCl_3$:CD_3CN. Subsequently, 0.5 mL of the solution were transferred to a NMR tube. A solution of $[Pt(CH_3CN)_4](BF_4)_2$ was prepared in 2:1 $CDCl_3$:CD_3CN at higher concentration (5-7 mM). Immediately, $[Pt(CH_3CN)_4](BF_4)_2$ (*ca.* 1 equiv.) was added to the calix[4]pyrrole's solution. A ^{1}H NMR spectrum of the mixture was acquired after the injection and vigorous hand shaking of the NMR tube for few seconds. The mixture was thermally equilibrated at 80°C in an oil bath for 24, 48 and 72 h and the ^{1}H NMR spectra were acquired.

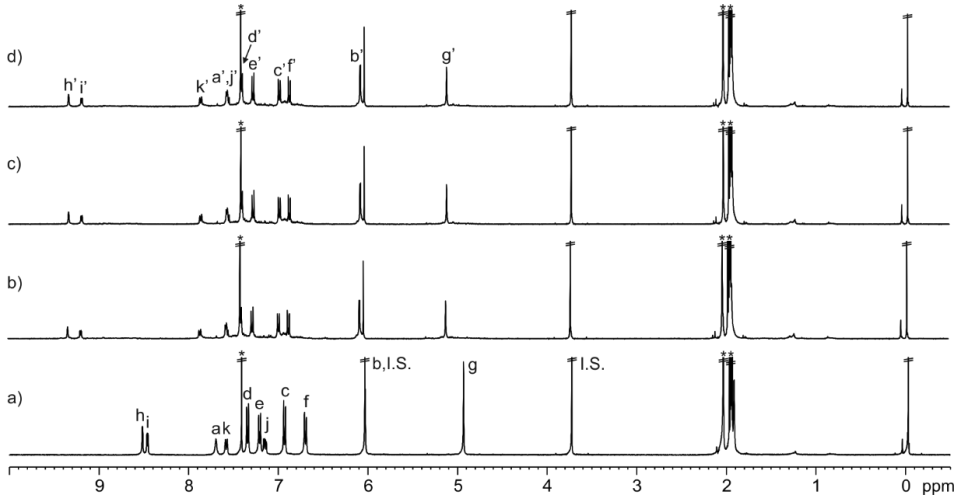

Figure 65. ^{1}H NMR (400 MHz, 2:1 $CDCl_3$:CD_3CN, 298 K) spectra: a) **1**; addition of $[Pt(CH_3CN)_4](BF_4)_2$ to **1**: *ca.* 1 equiv. after thermal equilibration of a) at 80°C: b) 24; c) 48 and d) 72 h. Primed letters correspond to proton signals of [**1**•Pt]$^{2+}$. The cage was formed in an extent larger than 60%. See Figure 23 for proton assignment. 1,3,5-Trimethoxybenzene (I.S.). *Residual solvent peaks.

4.4.5 NMR experiments of tetra-pyridyl **4**

Addition of Pd(II) to calix[4]pyrrole **4** in $(CD_3)_2SO$

A suspension of the tetra-pyridyl **4** (1-2 mM) and 1,3,5-trimethoxybenzene (internal standard, 1-2 mM) was prepared in $(CD_3)_2SO$. Subsequently, 0.5 mL of the suspension were transferred to a NMR tube. A solution of $[Pd(CH_3CN)_4](BF_4)_2$ was prepared in $(CD_3)_2SO$ at 10-15 fold higher concentration (20-30 mM). Immediately, the 0.5 mL of the tetra-pyridyl's suspension was titrated by manually injecting incremental amounts of the Pd(II) solution using a micro syringe. A ^1H NMR spectrum of the mixture was acquired after each injection and vigorous hand shaking of the NMR tube for few seconds.

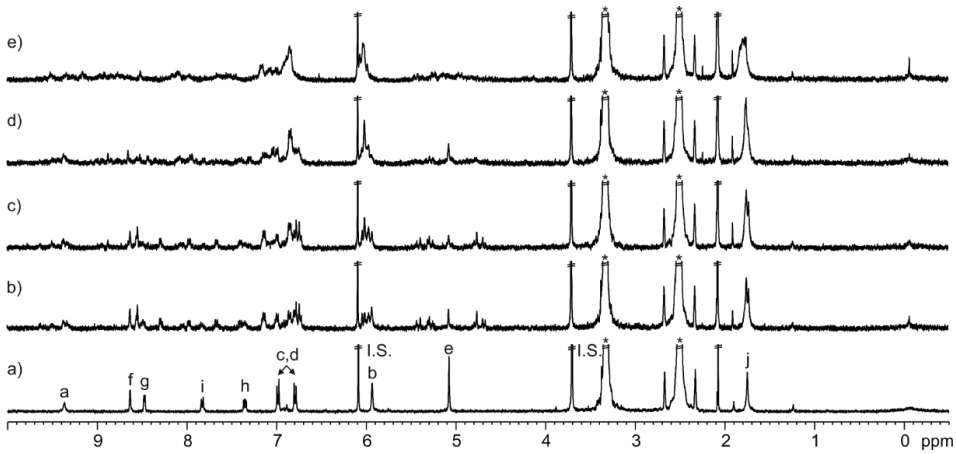

Figure 66. ^1H NMR (400 MHz, $(CD_3)_2SO$, 298 K) spectra: a) **4**; addition of $[Pd(CH_3CN)_4](BF_4)_2$ to **4**: b) 0.5; c) 1; d) 1.5 and e) 2 equiv. See Figure 31 for proton assignment. 1,3,5-Trimethoxybenzene (I.S.). *Residual solvent peaks.

The ^1H NMR spectrum of a millimolar suspension of tetra-pyridyl **4** in $(CD_3)_2SO$ showed sharp and well-defined proton signals, and its number was in agreement with a C_{4v} symmetry. The tetra-pyridyl **4** was not completely soluble in $(CD_3)_2SO$. The addition of incremental amounts of $[Pd(CH_3CN)_4](BF_4)_2$ to the suspension of **4** produced broad proton signals and the complete dissolution of the calix[4]pyrrole **4**. This result indicated that Pd(II) and **4** did not form the $[\mathbf{4}\bullet Pd]^{2+}$ cage. Probably, they formed ill-defined aggregates. The thermal equilibration of the mixture containing Pd(II) and **4** (2:1 ratio) at 40°C for 24 h did not produce changes in the ^1H NMR spectra.

4.4.6 NMR experiments of **1**, [**1**•Pd]$^{2+}$ and [**1**•Pt]$^{2+}$ with *N*-oxides in 2:1 $CDCl_3$:CD_3CN

Addition of *N*-oxides and Pd(II) or Pt(II) to calix[4]pyrrole **1**

A solution of the tetra-pyridyl **1** (1-2 mM) and 1,3,5-trimethoxybenzene (internal standard, 1-2 mM) was prepared in 2:1 $CDCl_3$:CD_3CN. Subsequently, 0.5 mL of the solution were transferred to a NMR tube. A solution of *N*-oxide **7**-**11** was prepared in 2:1 $CDCl_3$:CD_3CN using the tetra-pyridyl's solution at higher concentration ([G] = 10-30 mM and [**1**] = 1-2 mM). A solution of $[Pd(CH_3CN)_4](BF_4)_2$ or $[Pt(CH_3CN)_4](BF_4)_2$ was prepared in 2:1 $CDCl_3$:CD_3CN at higher concentration (5-7 mM). Immediately, the 0.5 mL of the tetra-pyridyl's solution was titrated by manually injecting incremental amounts of the *N*-oxide's solution using a micro syringe. A ^{1}H NMR spectrum of the mixture was acquired after each injection and vigorous hand shaking of the NMR tube for few seconds. After the formation of the corresponding 1:1 inclusion complex between the *N*-oxide and **1**, incremental amounts of Pd(II) or Pt(II) were added to the complex's solution using a micro syringe. A ^{1}H NMR spectrum of the mixture was acquired after each injection and vigorous hand shaking of the NMR tube for few seconds. Finally, the solution was thermally equilibrated at 40-50°C for 24-72 h and a ^{1}H NMR spectrum was acquired.

Pd(II)-cage

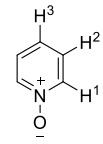

7

Figure 67. Line-drawing structure of *N*-oxide **7**.

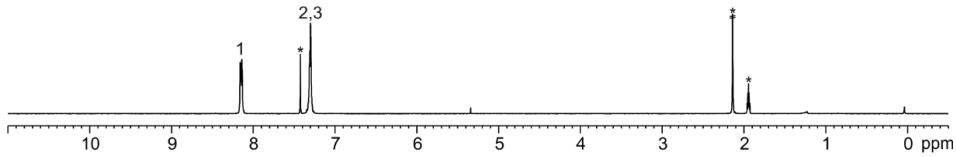

Figure 68. ^{1}H NMR (300 MHz, 2:1 $CDCl_3$:CD_3CN, 298 K) spectrum of **7**. See Figure 67 for proton assignment. *Residual solvent peaks.

Table 3. Chemical shifts (δ, ppm) of the protons of free and bound **7** (**7**⊂**1** and **7**⊂[**1**•Pd]$^{2+}$).

Signal	δ_{free}	δ, **7**⊂**1**	δ, **7**⊂[**1**•Pd]$^{2+}$
1	8.15	4.59	4.69
2	7.30	6.77	6.97
3	7.30	6.97	6.44

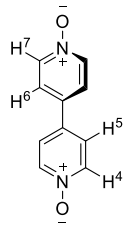

8

Figure 69. Line-drawing structure of *N*-oxide **8**.

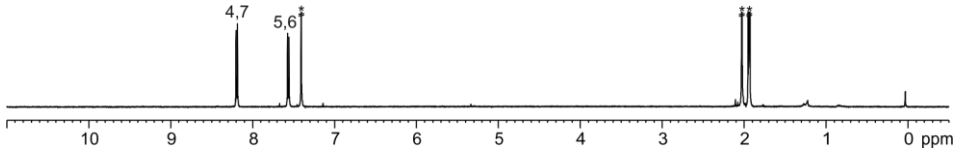

Figure 70. ^{1}H NMR (400 MHz, 2:1 $CDCl_3$:CD_3CN, 298 K) spectrum of **8**. See Figure 69 for proton assignment. *Residual solvent peaks.

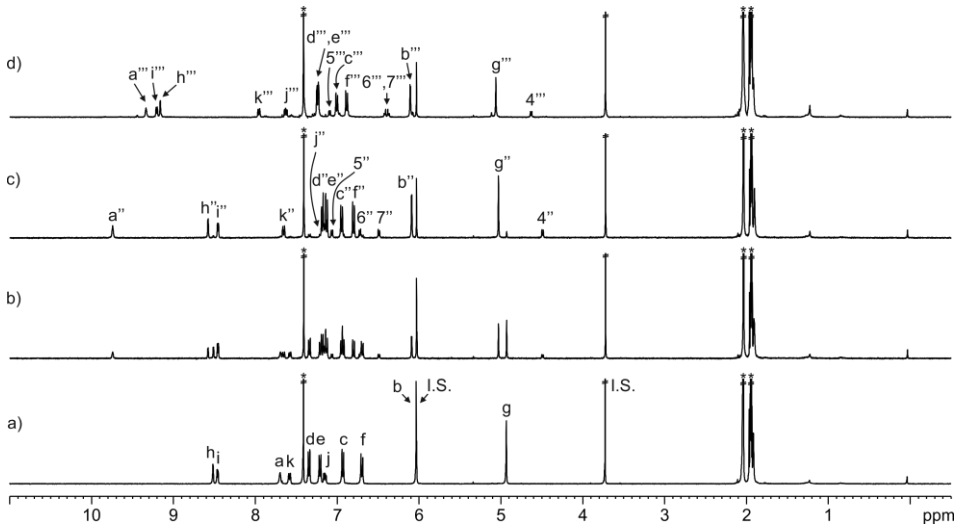

Figure 71. ^{1}H NMR (400 MHz, 2:1 $CDCl_3$:CD_3CN, 298 K) spectra: a) **1**; addition of **8** to **1**: b) 0.5 and c) 1 equiv.; addition of Pd(II) to **8⊂1**: d) *ca*. 1 equiv. after thermal equilibration (24 h at 40ºC). Doubly primed letters and numbers correspond to proton signals of **8⊂1**. Triply primed letters and numbers correspond to proton signals of **8⊂[1•**Pd**]**$^{2+}$. See Figure 23 and Figure 69 for proton assignments. 1,3,5-Trimethoxybenzene (I.S.). *Residual solvent peaks.

Table 4. Chemical shifts (δ, ppm) of the protons of free and bound **8** (**8⊂1** and **8⊂[1•**Pd**]**$^{2+}$).

Signal	δ_{free}	δ, **8⊂1**	δ, **8⊂[1•**Pd**]**$^{2+}$
4	8.19	4.49	4.63
5	7.57	7.06	7.10
6	7.57	6.72	6.40
7	8.19	6.49	6.40

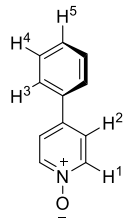

9

Figure 72. Line-drawing structure of *N*-oxide **9**.

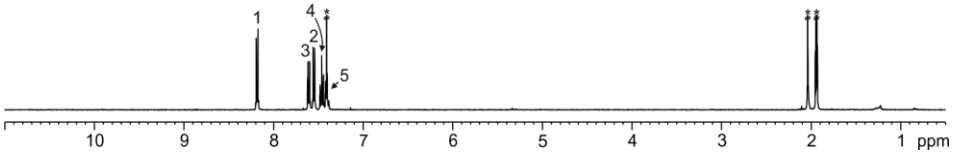

Figure 73. ^{1}H NMR (400 MHz, 2:1 $CDCl_3$:CD_3CN, 298 K) spectrum of **9**. See Figure 72 for proton assignment. *Residual solvent peaks.

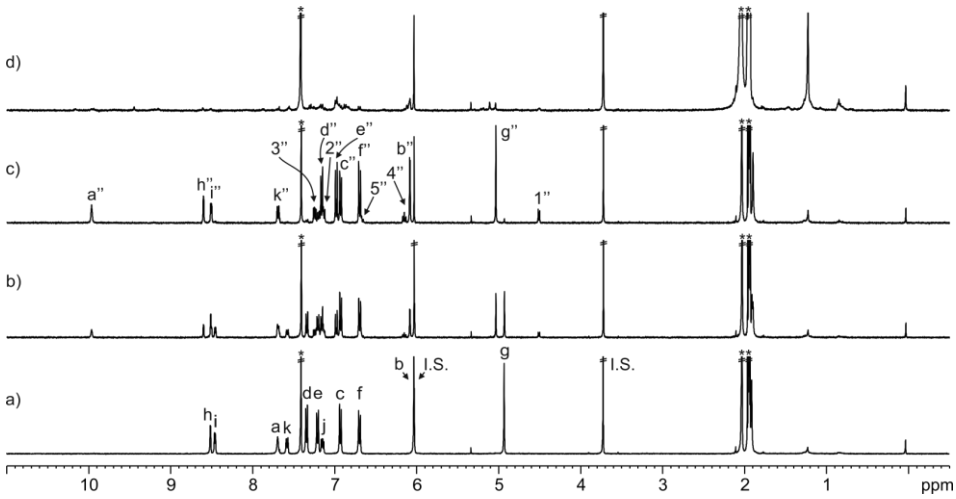

Figure 74. ^{1}H NMR (400 MHz, 2:1 $CDCl_3$:CD_3CN, 298 K) spectra: a) **1**; addition of **9** to **1**: b) 0.5 and c) 1 equiv.; addition of Pd(II) to **9⊂1**: d) *ca.* 1 equiv. after thermal equilibration (24 h at 40°C). Doubly primed letters and numbers correspond to proton signals of **9⊂1**. See Figure 23 and Figure 72 for proton assignments. 1,3,5-Trimethoxybenzene (I.S.). *Residual solvent peaks.

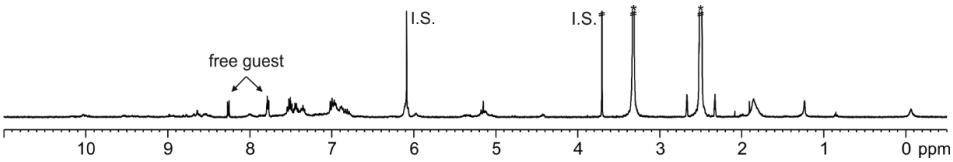

Figure 75. ^{1}H NMR (400 MHz, $(CD_3)_2SO$, 298 K) spectrum of the precipitate obtained after thermal equilibration (24 h at 40ºC) of a mixture containing *ca.* 1 equiv. of Pd(II), 1 equiv. of **9** and **1**. 1,3,5-Trimethoxybenzene (I.S.). *Residual solvent peaks.

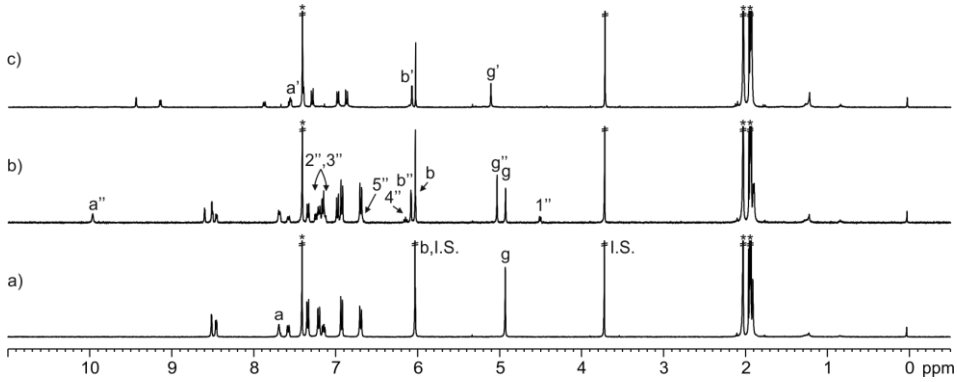

Figure 76. ^{1}H NMR (400 MHz, 2:1 $CDCl_3$:CD_3CN, 298 K) spectra: a) **1**; addition of **9** to **1**: b) 0.5 equiv.; addition of Pd(II) to b): c) *ca.* 1 equiv. after thermal equilibration (24 h at 40°C). Primed letters correspond to proton signals of [**1**•Pd]$^{2+}$. Doubly primed letters and numbers correspond to proton signals of **9⊂1**. See Figure 23 and Figure 72 for proton assignments. 1,3,5-Trimethoxybenzene. *Residual solvent peaks.

Table 5. Chemical shifts (δ, ppm) of the protons of free and bound **9** (**9⊂1**).

Signal	δ_{free}	δ, **9⊂1**
1	8.18	4.51
2	7.55	7.13
3	7.61	7.20
4	7.46	6.15
5	7.40	6.67

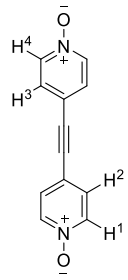

10

Figure 77. Line-drawing structure of *N*-oxide **10**.

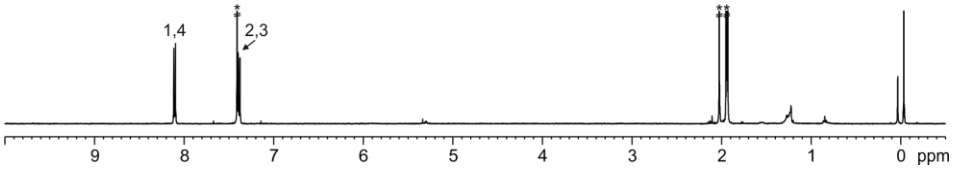

Figure 78. ^{1}H NMR (400 MHz, 2:1 $CDCl_3$:CD_3CN, 298 K) spectrum of **10**. See Figure 77 for proton assignment. *Residual solvent peaks.

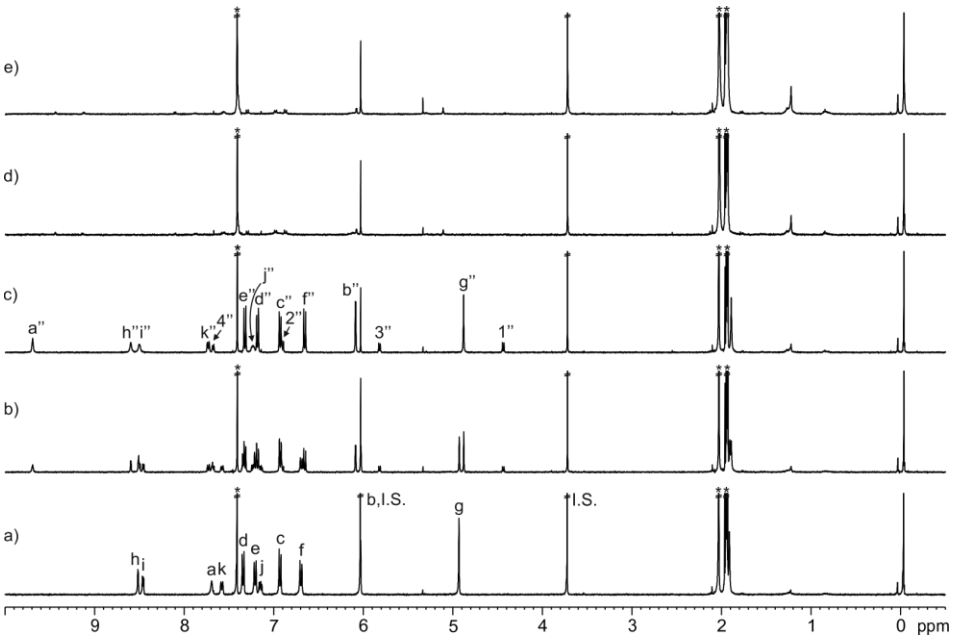

Figure 79. ^{1}H NMR (400 MHz, 2:1 $CDCl_3$:CD_3CN, 298 K) spectra: a) **1**; addition of **10** to **1**: b) 0.5 and c) 1 equiv.; addition of Pd(II) to **10⊂1**: d) *ca*. 1 equiv. and e) after thermal equilibration (24 h at 40°C). Doubly primed letters and numbers correspond to proton signals of **10⊂1**. See Figure 23 and Figure 77 for proton assignments. 1,3,5-Trimethoxybenzene (I.S.). *Residual solvent peaks.

Table 6. Chemical shifts (δ, ppm) of the protons of free and bound **10** (**10⊂1**).

Signal	δ_{free}	δ, **10⊂1**
1	8.11	4.45
2	7.39	6.90
3	7.39	5.82
4	8.11	7.68

Pt(II)-cage

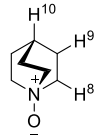

11

Figure 80. Line-drawing structure of *N*-oxide **11**.

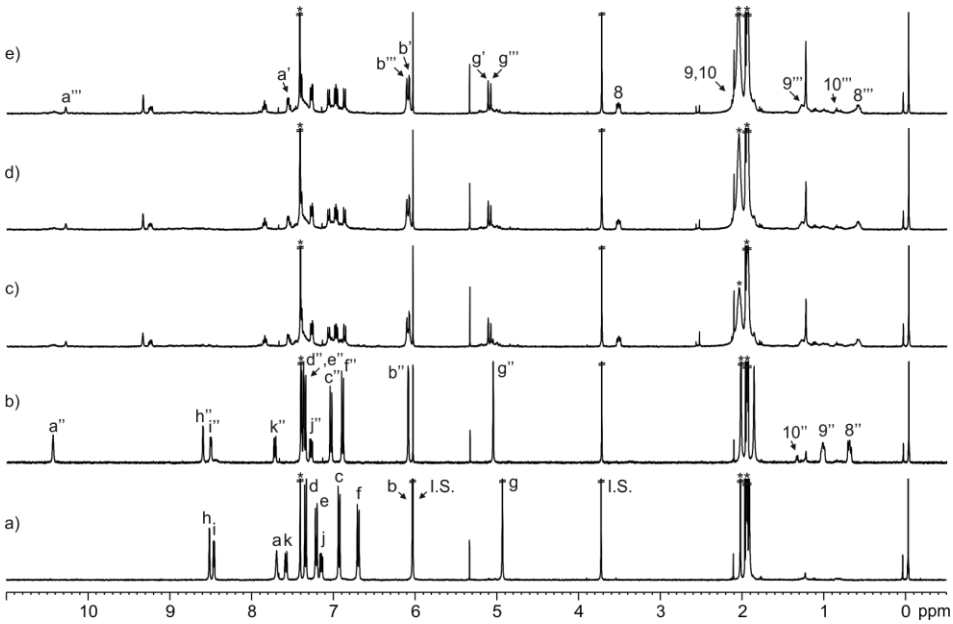

Figure 81. ^{1}H NMR (400 MHz, 2:1 $CDCl_3$:CD_3CN, 298 K) spectra: a) **1**; addition of **11** to **1**: b) 1 equiv.; addition of *ca.* 1 equiv. of Pt(II) to **11⊂1** after thermal equilibration at 50°C: c) 24; d) 48 and e) 72 h. Primed letters correspond to proton signals of [**1**•Pt]$^{2+}$. Doubly primed letters and numbers correspond to proton signals of **11⊂1**. Triply primed letters and numbers correspond to proton signals of **11⊂**[**1**•Pt]$^{2+}$. See Figure 23 and Figure 80 for proton assignments. 1,3,5-Trimethoxybenzene (I.S.). *Residual solvent peaks.

The addition of *ca.* 1 equiv. of $[Pt(CH_3CN)_4](BF_4)_2$ to a solution of **11⊂1** provoked chemical shift changes on the proton signals of the complex. The proton signals of **11** remained upfield shifted indicating that **11** was included in the aromatic cavity of the cage. The proton signals of the pyridyl substituents of **1** suffered the most noticeable chemical shift changes. This observation indicated that the pyridyl substituents were coordinated to a Pt(II) ion. The cage was formed in an extent larger than 60% (free and bound). The **11⊂**[**1**•Pt]$^{2+}$ cage complex was formed in *ca.* 50% extent (fraction of bound cage). We estimated a binding constant value K_a ~ 2 x 10^3 M^{-1} for the **11⊂**[**1**•Pt]$^{2+}$ cage complex.

Table 7. Chemical shifts (δ, ppm) of the protons of free and bound **11** (**11**⊂**1**, **11**⊂[**1**•Pd]$^{2+}$ and **11**⊂[**1**•Pt]$^{2+}$).

Signal	δ_{free}	δ, **11**⊂**1**	δ, **11**⊂[**1**•Pd]$^{2+}$	δ, **11**⊂[**1**•Pt]$^{2+}$
8	3.30	0.69	0.57	0.57
9	1.97	1.07	1.27	1.27
10	1.97	1.33	0.94	0.85

Addition of *N*-oxides to the [**1**•Pd]$^{2+}$ or [**1**•Pt]$^{2+}$ cage

A solution of the tetra-pyridyl **1** (1-2 mM) and 1,3,5-trimethoxybenzene (internal standard, 1-2 mM) was prepared in 2:1 $CDCl_3$:CD_3CN. Subsequently, 0.5 mL of the solution were transferred to a NMR tube. A solution of $[Pd(CH_3CN)_4](BF_4)_2$ or $[Pt(CH_3CN)_4](BF_4)_2$ was prepared in 2:1 $CDCl_3$:CD_3CN at higher concentration (5-7 mM). Immediately, the 0.5 mL of the tetra-pyridyl's solution was titrated by manually injecting incremental amounts of the Pd(II) or Pt(II) solution using a micro syringe. The solution of the [**1**•Pd]$^{2+}$ or [**1**•Pt]$^{2+}$ cage was thermally equilibrated at 40ºC for 24 h or 50ºC for 72 h, respectively. A solution of *N*-oxide **7**-**11** was prepared in 2:1 $CDCl_3$:CD_3CN at higher concentration (10-30 mM). The cage's solution was titrated by manually injecting incremental amounts of the *N*-oxide's solution using a micro syringe. A ^{1}H NMR spectrum of the mixture was acquired after each injection and vigorous hand shaking of the NMR tube for few seconds.

Pd(II)-cage

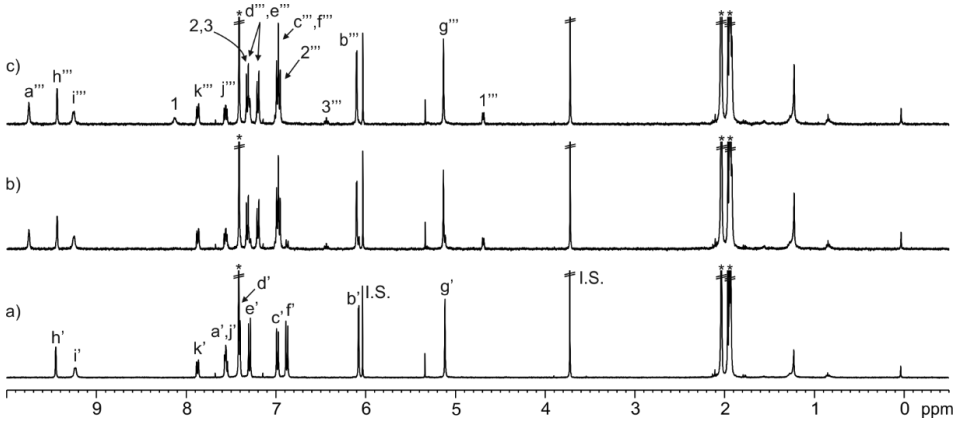

Figure 82. ^{1}H NMR (400 MHz, 2:1 $CDCl_3$:CD_3CN, 298 K) spectra: a) [**1**•Pd]$^{2+}$; addition of **7** to [**1**•Pd]$^{2+}$: b) 1 and c) 2 equiv. Primed letters correspond to proton signals of [**1**•Pd]$^{2+}$. Triply primed letters and numbers correspond to proton signals of **7**⊂[**1**•Pd]$^{2+}$. See Figure 23 and Figure 67 for proton assignments. 1,3,5-Trimethoxybenzene (I.S.). *Residual solvent peaks.

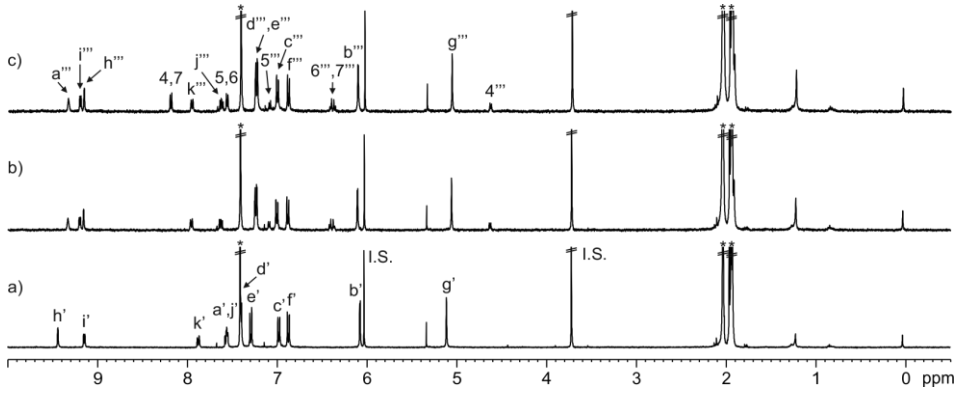

Figure 83. ^{1}H NMR (400 MHz, 2:1 $CDCl_3$:CD_3CN, 298 K) spectra: a) [**1**•Pd]$^{2+}$; addition of **8** to [**1**•Pd]$^{2+}$: b) 1 and c) 2 equiv. Primed letters correspond to proton signals of [**1**•Pd]$^{2+}$. Triply primed letters and numbers correspond to proton signals of **8**⊂[**1**•Pd]$^{2+}$. See Figure 23 and Figure 69 for proton assignments. 1,3,5-Trimethoxybenzene (I.S.). *Residual solvent peaks.

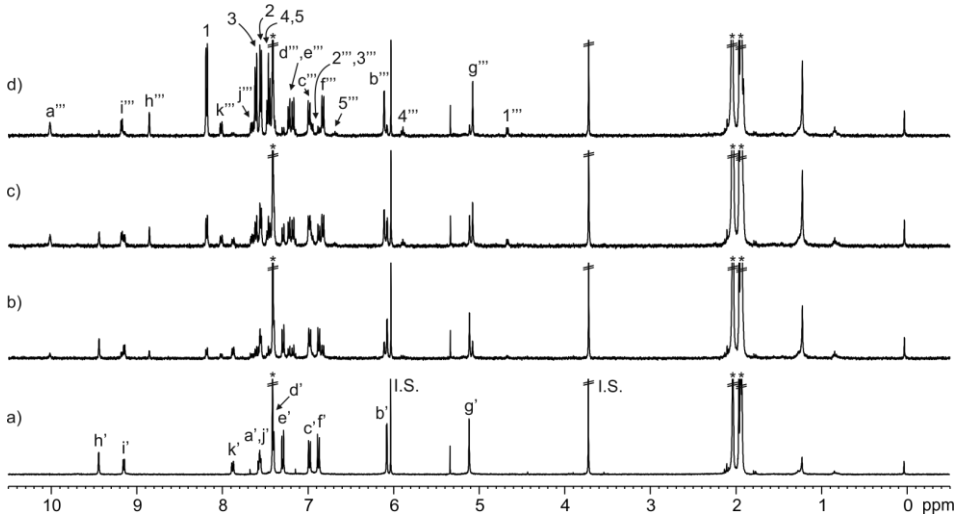

Figure 84. ^{1}H NMR (400 MHz, 2:1 $CDCl_3$:CD_3CN, 298 K) spectra: a) [**1**•Pd]$^{2+}$; addition of **9** to [**1**•Pd]$^{2+}$: b) 1; c) 2 and d) 5 equiv. Primed letters correspond to proton signals of [**1**•Pd]$^{2+}$. Triply primed letters and numbers correspond to proton signals of **9**⊂[**1**•Pd]$^{2+}$. See Figure 23 and Figure 72 for proton assignments. 1,3,5-Trimethoxybenzene (I.S.). *Residual solvent peaks.

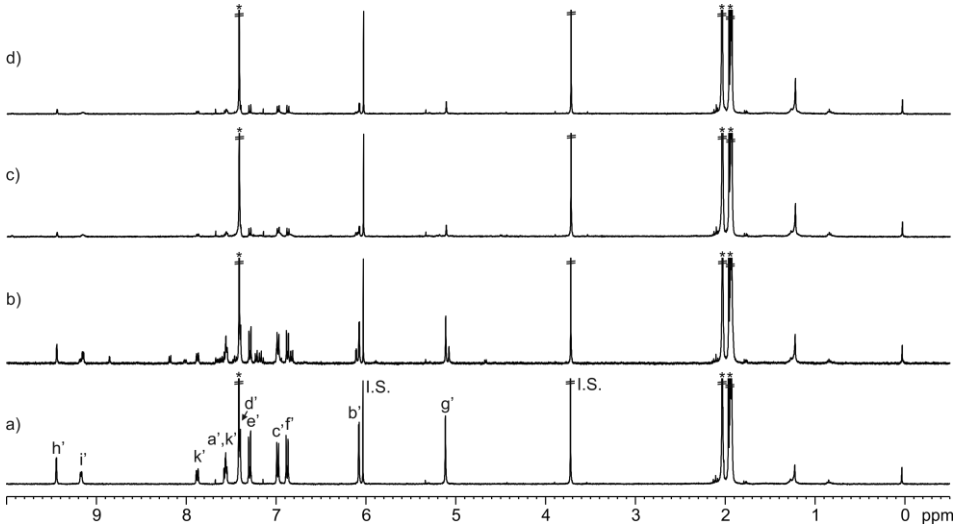

Figure 85. ^{1}H NMR (400 MHz, 2:1 $CDCl_3$:CD_3CN, 298 K) spectra: a) [**1**•Pd]$^{2+}$; addition of **9** to [**1**•Pd]$^{2+}$: b) 1 equiv. and after thermal equilibration at 40°C: c) 24 and d) 48 h. Primed letters correspond to proton signals of [**1**•Pd]$^{2+}$. See Figure 23 for proton assignment. 1,3,5-Trimethoxybenzene (I.S.). *Residual solvent peaks.

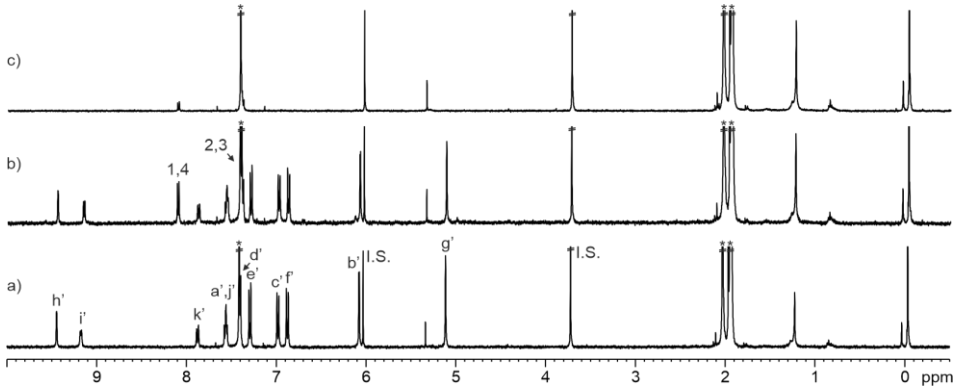

Figure 86. ^{1}H NMR (400 MHz, 2:1 $CDCl_3$:CD_3CN, 298 K) spectra: a) [**1**•Pd]$^{2+}$; addition of **10** to [**1**•Pd]$^{2+}$: b) 1 equiv. and c) after thermal equilibration (24 h at 40°C). Primed letters correspond to proton signals of [**1**•Pd]$^{2+}$. See Figure 23 and Figure 77 for proton assignments. 1,3,5-Trimethoxybenzene (I.S.). *Residual solvent peaks.

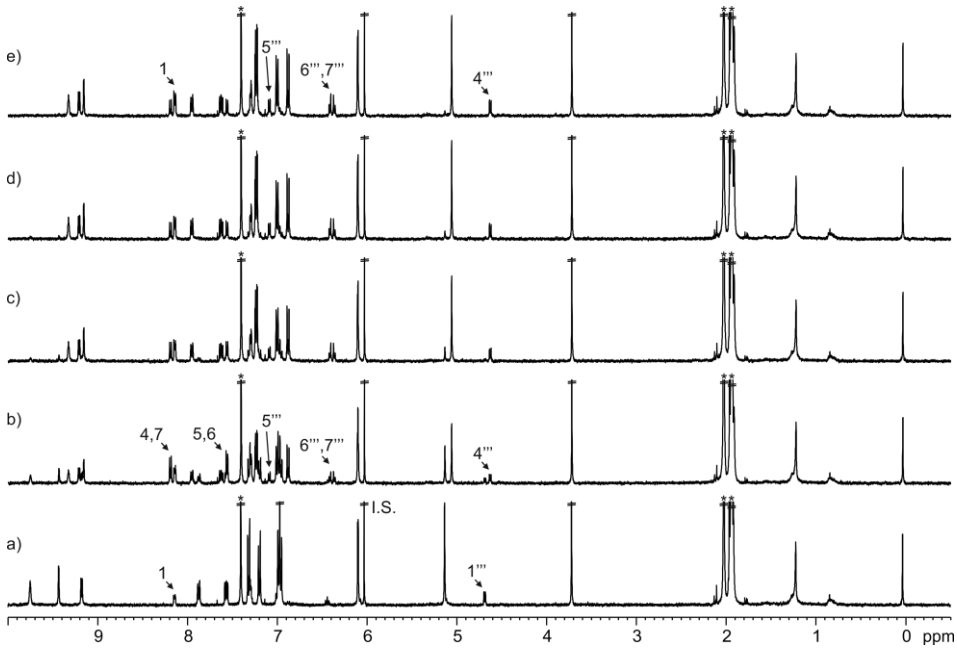

Figure 87. ^{1}H NMR (400 MHz, 2:1 $CDCl_3$:CD_3CN, 298 K) spectra: a) **7** and **7**⊂[**1**•Pd]$^{2+}$ (*ca*. 1.4:1 ratio); addition of **8** to a): b) *ca*. 1.2 equiv. and after: c) 10; d) 20 and e) 30 min. Triply primed numbers correspond to proton signals of bound *N*-oxides in [**1**•Pd]$^{2+}$. See Figure 67 and Figure 69 for proton assignments. 1,3,5-Trimethoxybenzene (I.S.). *Residual solvent peaks.

Addition of *bis*-*N*-oxide **8** to a solution of **7**⊂[**1**•Pd]$^{2+}$ produced the release of bound **7** to the bulk solution. Concomitantly, **8**⊂[**1**•Pd]$^{2+}$ was formed. More than 50% of bound **7** was released after the addition of **8**. The mixture evolved with time and, after 10 min, more than 80% of bound **7** was released.

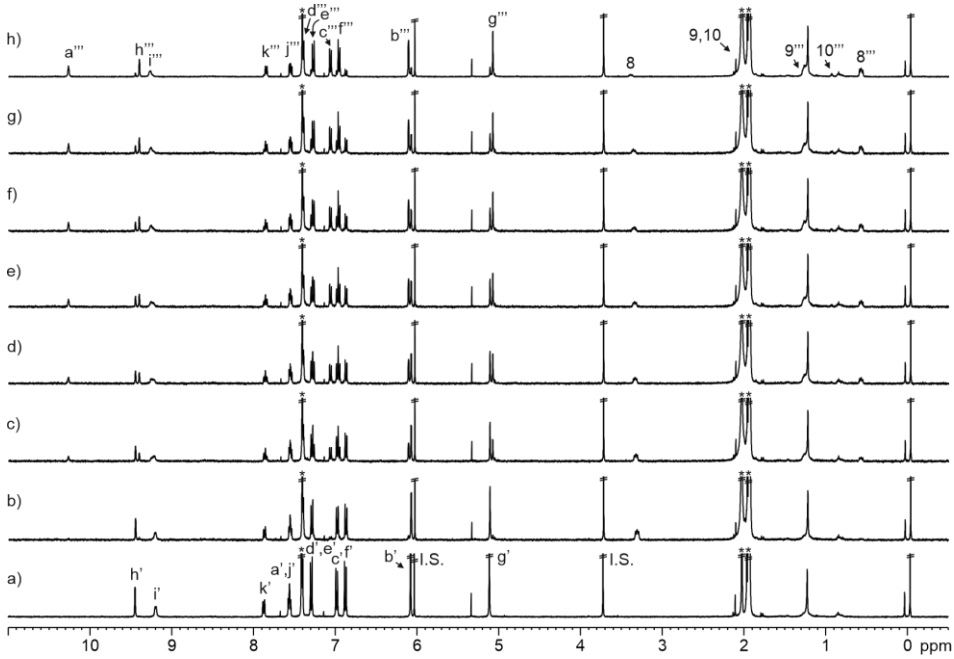

Figure 88. Selected ^{1}H NMR (400 MHz, 2:1 $CDCl_3$:CD_3CN, 298 K) spectra: a) [**1**•Pd]$^{2+}$ (0.8 mM); addition of **11** to [**1**•Pd]$^{2+}$: b) 1 equiv. and after: c) 30; d) 60; e) 90; f) 150; g) 210 min and h) 24 h. Primed letters correspond to proton signals of [**1**•Pd]$^{2+}$. Triply primed letters and numbers correspond to proton signals of **11**⊂[**1**•Pd]$^{2+}$. See Figure 23 and Figure 80 for proton assignments. 1,3,5-Trimethoxybenzene (I.S.). *Residual solvent peaks.

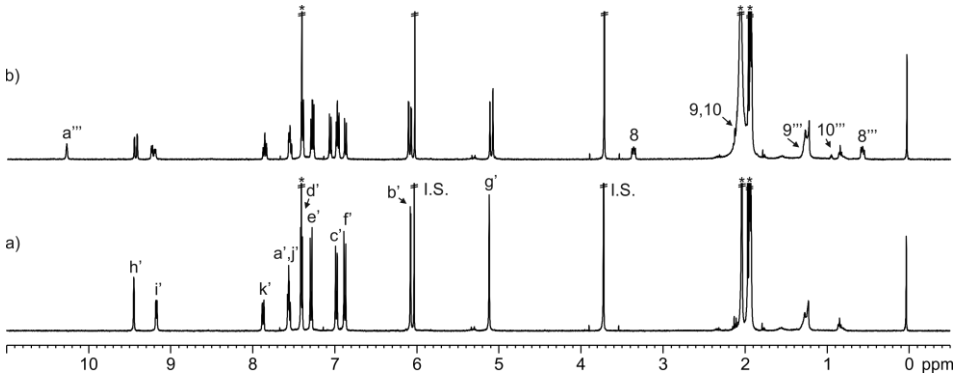

Figure 89. Selected ^{1}H NMR (400 MHz, 2:1 $CDCl_3$:CD_3CN, 298 K) spectra: a) [**1**•Pd]$^{2+}$ (1.4 mM); addition of 1.1 equiv. of **11** to [**1**•Pd]$^{2+}$ after b) 64 min. Primed letters correspond to proton signals of [**1**•Pd]$^{2+}$. Triply primed letters and numbers correspond to proton signals of **11**⊂[**1**•Pd]$^{2+}$. See Figure 23 and Figure 80 for proton assignments. 1,3,5-Trimethoxybenzene (I.S.). *Residual solvent peaks.

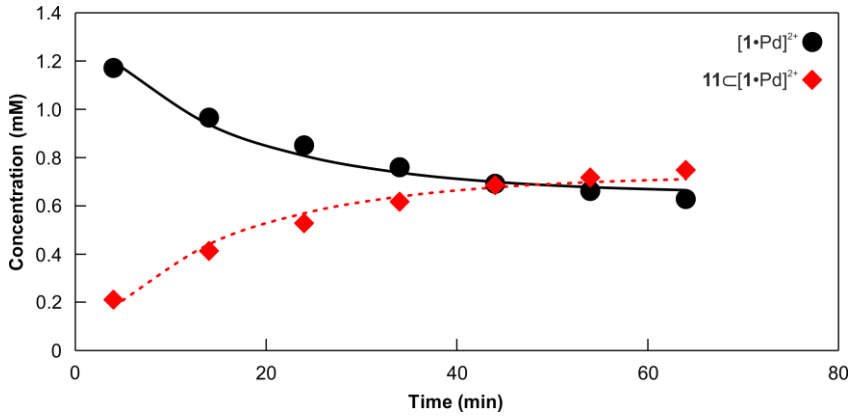

Figure 90. Concentration of free and bound [**1**•Pd]$^{2+}$ versus time (min) upon addition of quinuclidine *N*-oxide **11** ([H] = 1.4 mM and [G] = 1.4 mM). Lines represent fit of the kinetic data to a second order rate law considering the reversible formation of the cage complex.

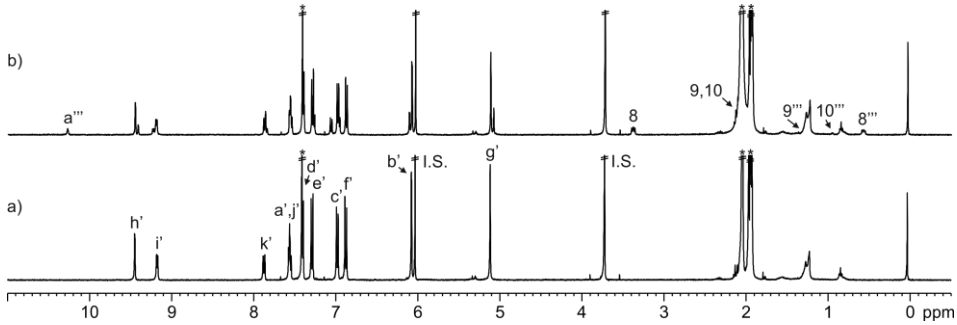

Figure 91. Selected ^{1}H NMR (400 MHz, 2:1 $CDCl_3$:CD_3CN, 298 K) spectra: a) [**1**•Pd]$^{2+}$ (1.4 mM); addition of 0.6 equiv. of **11** to [**1**•Pd]$^{2+}$ after b) 64 min. Primed letters correspond to proton signals of [**1**•Pd]$^{2+}$. Triply primed letters and numbers correspond to proton signals of **11**⊂[**1**•Pd]$^{2+}$. See Figure 23 and Figure 80 for proton assignments. 1,3,5-Trimethoxybenzene (I.S.). *Residual solvent peaks.

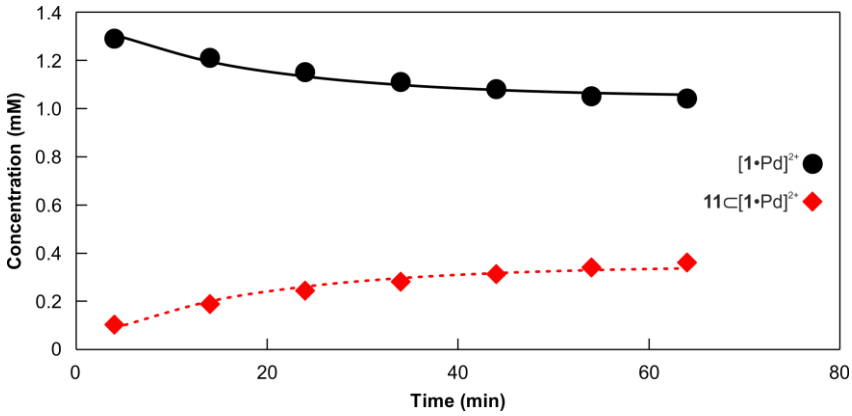

Figure 92. Concentration of free and bound [**1**•Pd]$^{2+}$ versus time (min) upon addition of quinuclidine *N*-oxide **11** ([H] = 1.4 mM and [G] = 0.8 mM). Lines represent fit of the kinetic data to a second order rate law considering the reversible formation of the cage complex.

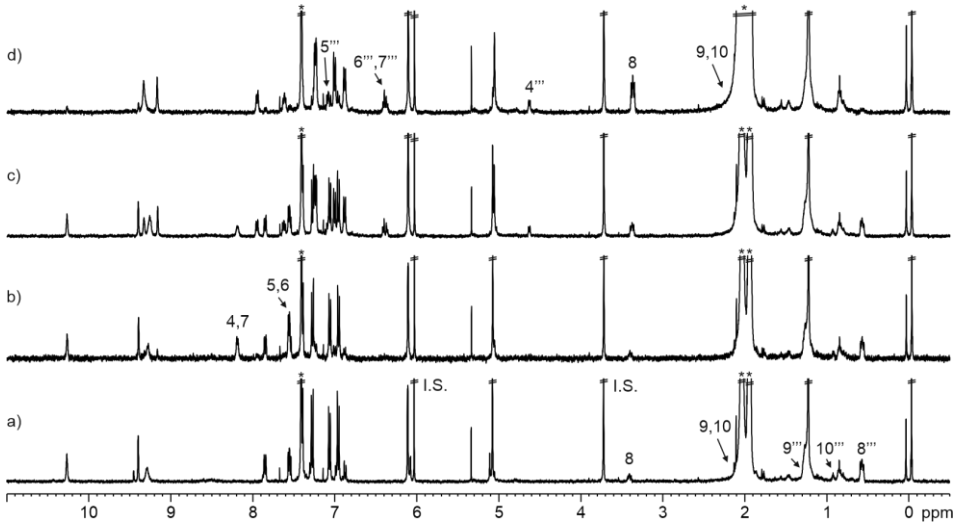

Figure 93. ^{1}H NMR (400 MHz, 2:1 $CDCl_3$:CD_3CN, 298 K) spectra: a) **11**⊂[**1**•Pd]$^{2+}$ and [**1**•Pd]$^{2+}$ (*ca.* 7:3 ratio); addition of **8** to a): b) 1 equiv. and after: c) 5 and d) >24 h. Triply primed numbers correspond to proton signals of bound *N*-oxides in [**1**•Pd]$^{2+}$. See Figure 69 and Figure 80 for proton assignments. 1,3,5-Trimethoxybenzene (I.S.). *Residual solvent peaks.

The addition of *bis*-*N*-oxide **8** to a millimolar solution containing **11**⊂[**1**•Pd]$^{2+}$ and [**1**•Pd]$^{2+}$ (*ca.* 7:3 ratio) produced the time-dependent release of **11** to the bulk solution and the formation of **8**⊂[**1**•Pd]$^{2+}$. After more than 24 h, the **8**⊂[**1**•Pd]$^{2+}$ cage complex was formed in an extent larger than 80%.

Pt(II)-cage

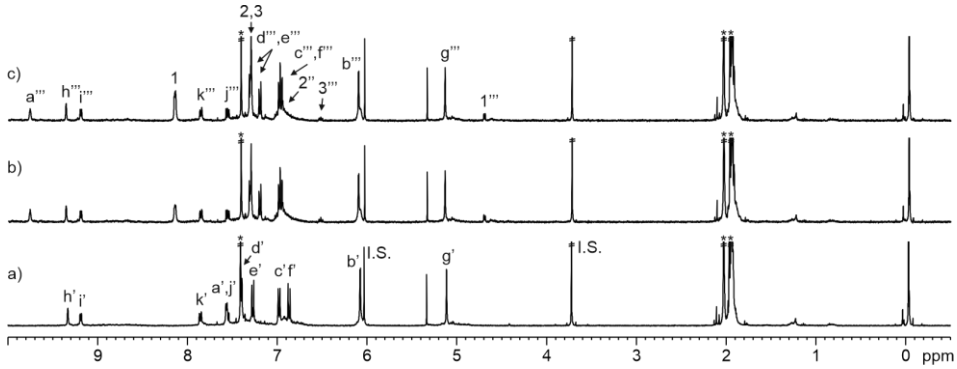

Figure 94. ^{1}H NMR (400 MHz, 2:1 $CDCl_3$:CD_3CN, 298 K) spectra: a) [**1**•Pt]$^{2+}$; addition of **7** to [**1**•Pt]$^{2+}$: b) 4 and c) 6 equiv. Primed letters correspond to proton signals of [**1**•Pt]$^{2+}$. Triply primed letters and numbers correspond to proton signals of **7**⊂[**1**•Pt]$^{2+}$. See Figure 23 and Figure 67 for proton assignments. 1,3,5-Trimethoxybenzene (I.S.). *Residual solvent peaks.

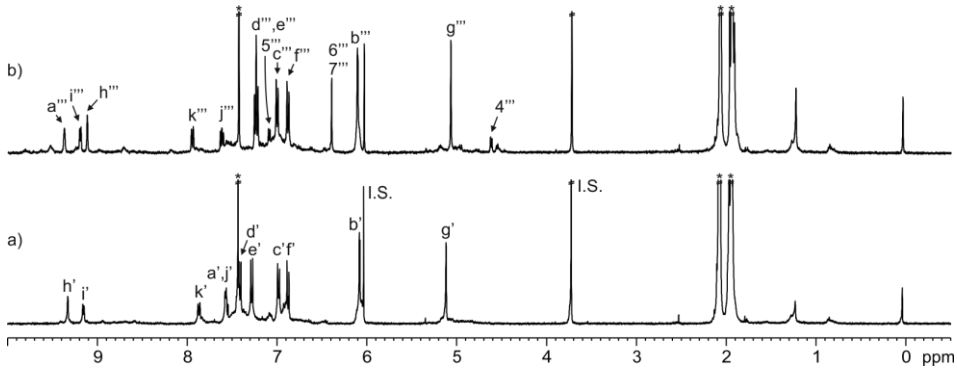

Figure 95. ^{1}H NMR (400 MHz, 2:1 $CDCl_3$:CD_3CN, 298 K) spectra: a) [**1**•Pt]$^{2+}$; addition of **8** to [**1**•Pt]$^{2+}$: b) 1 equiv. Primed letters correspond to proton signals of [**1**•Pt]$^{2+}$. Triply primed letters and numbers correspond to proton signals of **8**⊂[**1**•Pt]$^{2+}$. See Figure 23 and Figure 69 for proton assignments. 1,3,5-Trimethoxybenzene (I.S.). *Residual solvent peaks.

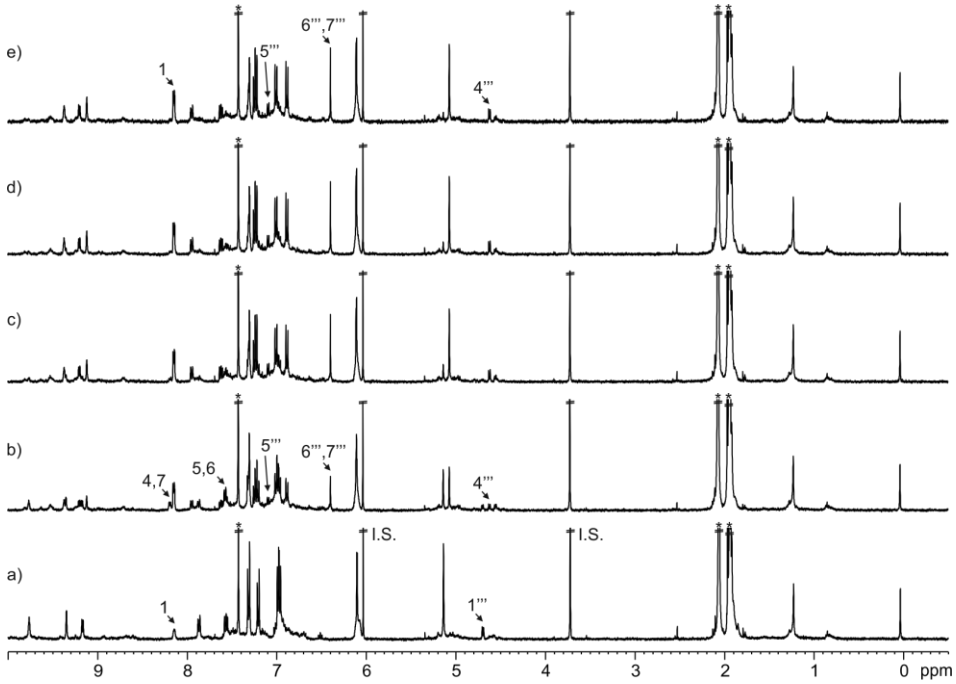

Figure 96. ^{1}H NMR (400 MHz, 2:1 $CDCl_3$:CD_3CN, 298 K) spectra: a) **7** and **7**⊂[**1**•Pt]$^{2+}$ (2:1 ratio); addition of **8** to a): b) *ca*. 1 equiv. and after: c) 10; d) 20 and e) 30 min. Triply primed numbers correspond to proton signals of bound *N*-oxides in [**1**•Pt]$^{2+}$. See Figure 67 and Figure 69 for proton assignments. 1,3,5-Trimethoxybenzene (I.S.). *Residual solvent peaks.

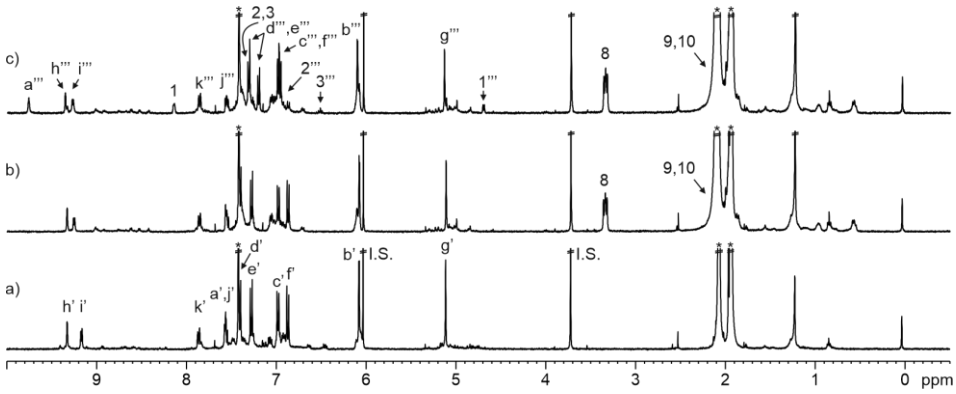

Figure 97. ^{1}H NMR (400 MHz, 2:1 $CDCl_3$:CD_3CN, 298 K) spectra: a) [**1**•Pt]$^{2+}$; addition of **11** to [**1**•Pt]$^{2+}$: b) *ca.* 2 equiv.; addition of **7** to b): c) *ca.* 2 equiv. Primed letters correspond to proton signals of [**1**•Pt]$^{2+}$. Triply primed letters and numbers correspond to proton signals of **7**⊂[**1**•Pt]$^{2+}$. See Figure 23, Figure 67 and Figure 80 for proton assignments. 1,3,5-Trimethoxybenzene (I.S.). *Residual solvent peaks.

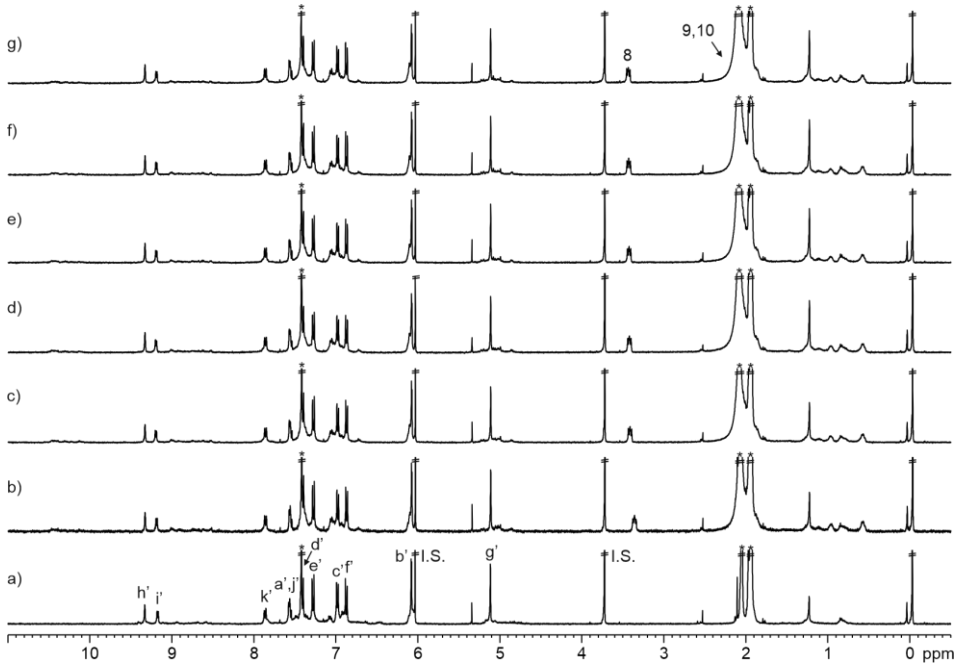

Figure 98. ^{1}H NMR (400 MHz, 2:1 $CDCl_3$:CD_3CN, 298 K) spectra: a) [**1**•Pt]$^{2+}$; addition of **11** to [**1**•Pt]$^{2+}$: b) 2 equiv. and after: c) 24; d) 48; e) 72; f) 96 and g) 120 h. Primed letters correspond to proton signals of [**1**•Pt]$^{2+}$. See Figure 23 and Figure 80 for proton assignments. 1,3,5-Trimethoxybenzene (I.S.). *Residual solvent peaks.

The addition of **11** to a millimolar solution of [**1**•Pt]$^{2+}$ did not produce changes on the proton signals of the [**1**•Pt]$^{2+}$ cage. The mixture did not evolve with time. Thus, **11** was not included in the [**1**•Pt]$^{2+}$ cage. Small signals in the initial solution of [**1**•Pt]$^{2+}$ correspond to protons of kinetically assembled aggregates that may feature an open cavity. A small fraction of **11** is bound in the cavity of these later species.

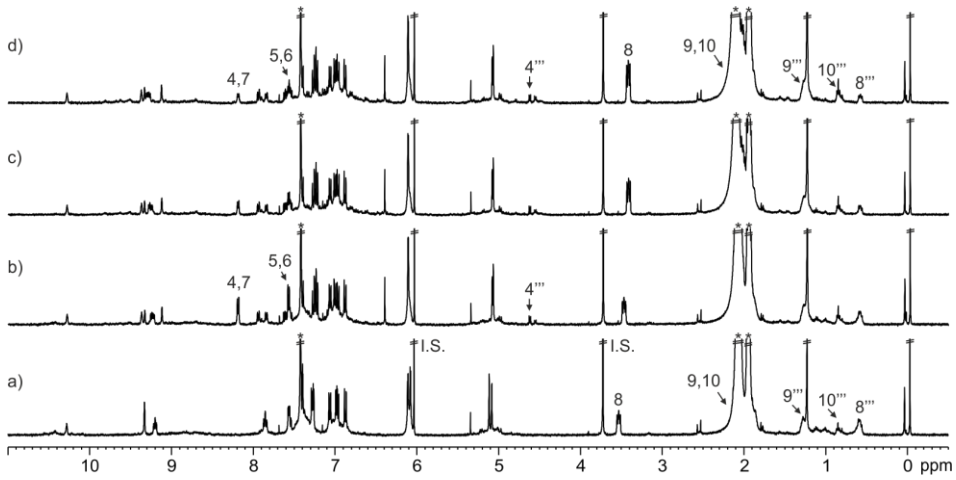

Figure 99. ^{1}H NMR (400 MHz, 2:1 $CDCl_3$:CD_3CN, 298 K) spectra: a) **11**⊂[**1**•Pt]$^{2+}$ and [**1**•Pt]$^{2+}$ (*ca.* 1:1 ratio); addition of **8** to a): b) 1 equiv. and after: c) 5 and d) >24 h. Triply primed numbers correspond to proton signals of bound *N*-oxides in [**1**•Pt]$^{2+}$. See Figure 69 and Figure 80 for proton assignments. 1,3,5-Trimethoxybenzene (I.S.). *Residual solvent peaks.

The addition of *bis*-*N*-oxide **8** to a millimolar solution containing **11**⊂[**1**•Pt]$^{2+}$ and [**1**•Pt]$^{2+}$ (*ca.* 1:1 ratio) produced a mixture of cage complexes **8**⊂[**1**•Pt]$^{2+}$ and **11**⊂[**1**•Pt]$^{2+}$ in *ca.* 1:1 ratio. Bound **11** in the [**1**•Pt]$^{2+}$ cage was not released to the bulk solution. Small proton signals corresponding to kinetically assembled aggregates evolved with time.

1D GOESY NMR experiments of [**1**•Pd]$^{2+}$ cage with pyridine *N*-oxide **7**

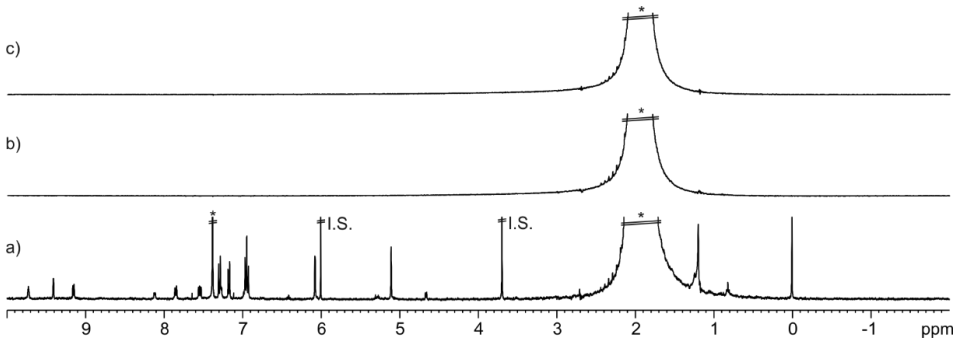

Figure 100. ^{1}H NMR (400 MHz, 2:1 $CDCl_3$:CH_3CN, 298 K) spectrum: a) **7**⊂[**1**•Pd]$^{2+}$; 1D GOESY NMR (400 MHz, 2:1 $CDCl_3$:CH_3CN, 298 K) spectra of a): b) t_{mix} = 0.3 and c) t_{mix} = 0.6 s. 1,3,5-Trimethoxybenzene (I.S.). *Residual solvent peaks.

VT ^{1}H NMR experiments of [**1**•Pd]$^{2+}$ and [**1**•Pt]$^{2+}$ with pyridine *N*-oxide **7**

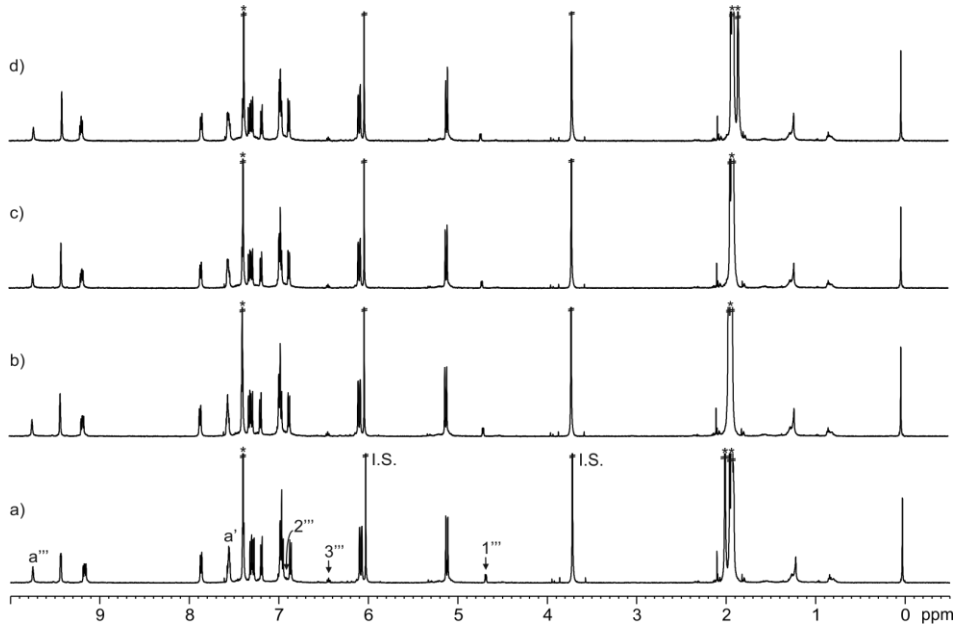

Figure 101. VT ^{1}H NMR (500 MHz, 2:1 $CDCl_3$:CD_3CN) spectra of **7**⊂[**1**•Pd]$^{2+}$ and [**1**•Pd]$^{2+}$ (1:1 ratio): a) 298; b) 308; c) 318 and d) 328 K. Primed letters correspond to proton signals [**1**•Pd]$^{2+}$. Triply primed letters and numbers correspond to proton signals of **7**⊂[**1**•Pd]$^{2+}$. See Figure 23 and Figure 67 for proton assignments. 1,3,5-Trimethoxybenzene (I.S.). *Residual solvent peaks.

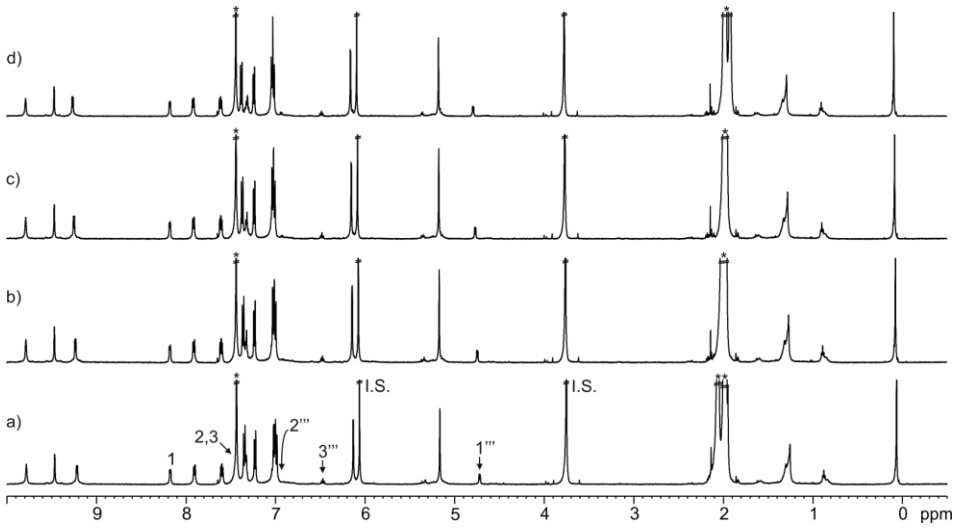

Figure 102. VT ^{1}H NMR (500 MHz, 2:1 $CDCl_3$:CD_3CN) spectra of **7** and **7**⊂[**1**•Pd]$^{2+}$ (1:1 ratio): a) 298; b) 308; c) 318 and d) 328 K. Triply primed numbers correspond to proton signals of **7**⊂[**1**•Pd]$^{2+}$. See Figure 67 for proton assignment. 1,3,5-Trimethoxybenzene (I.S.). *Residual solvent peaks.

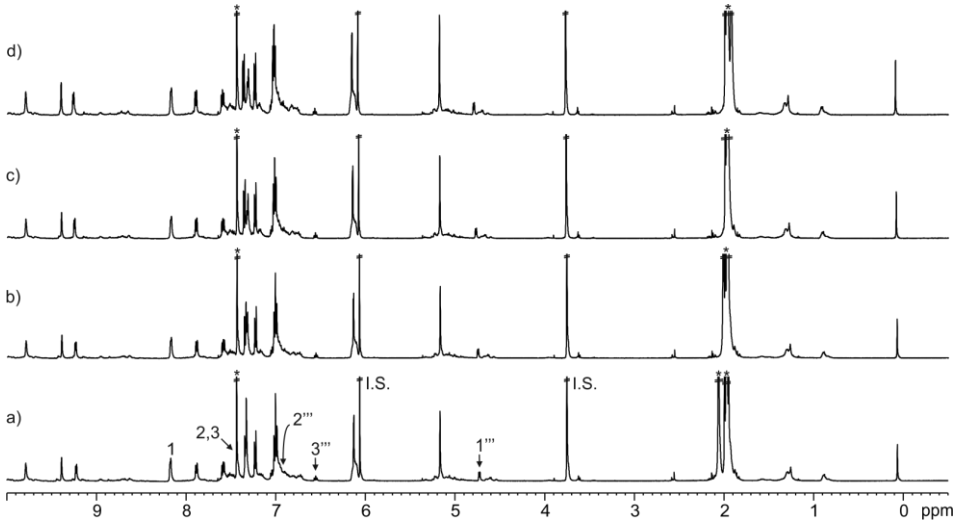

Figure 103. VT ^{1}H NMR (500 MHz, 2:1 $CDCl_3$:CD_3CN) spectra of **7** and **7**⊂[**1**•Pt]$^{2+}$ (1:1 ratio): a) 298; b) 308; c) 318 and d) 328 K. Triply primed numbers correspond to proton signals of **7**⊂[**1**•Pt]$^{2+}$. See Figure 67 for proton assignment. 1,3,5-Trimethoxybenzene (I.S.). *Residual solvent peaks.

No line-broadening effects were observed in the range of studied temperatures suggesting that the chemical exchange process between free and bound counterparts was very slow on the chemical shift timescale.

4.4.7 ^{19}F NMR experiments

^{19}F NMR spectra of $[Pd(CH_3CN)_4](BF_4)_2$ and cage complexes, **7**⊂[**1**•Pd]$^{2+}$, **8**⊂[**1**•Pd]$^{2+}$ and **11**⊂[**1**•Pd]$^{2+}$, were acquired in 2:1 $CDCl_3$:CD_3CN. Hexafluorobenzene was used as internal standard.

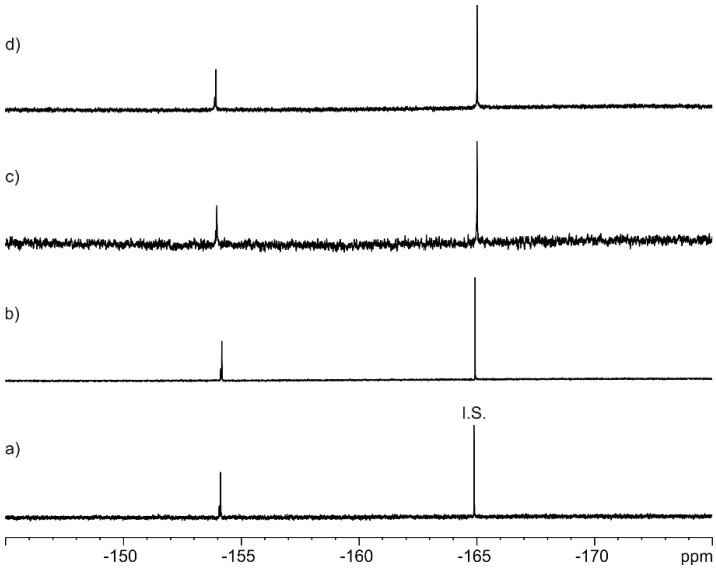

Figure 104. ^{19}F NMR (376 MHz, 2:1 $CDCl_3$:CD_3CN, 298 K) spectra: a) $[Pd(CH_3CN)_4](BF_4)_2$; b) **11**⊂[**1**•Pd]$^{2+}$ and [**1**•Pd]$^{2+}$ (*ca.* 7:3 ratio); c) **7**⊂[**1**•Pd]$^{2+}$ and d) **8**⊂[**1**•Pd]$^{2+}$. Hexafluorobenzene was used as internal standard (I.S.).

The ^{19}F signal corresponding to tetrafluoroborate anions did not experience appreciable chemical shift changes in the ^{19}F NMR spectra of the Pd(II)-cage complexes. These observations indicated that BF_4^- anions did not occupy the cavity of the Pd(II)-cage in 2:1 $CDCl_3$:CD_3CN solution.

4.4.8 Kinetic characterization of tetra-pyridyl **1**, [**1**•Pd]$^{2+}$ and [**1**•Pt]$^{2+}$ by EXSY NMR experiments

2D ^{1}H-^{1}H EXSY NMR experiment of the [**1**•Pd]$^{2+}$ cage

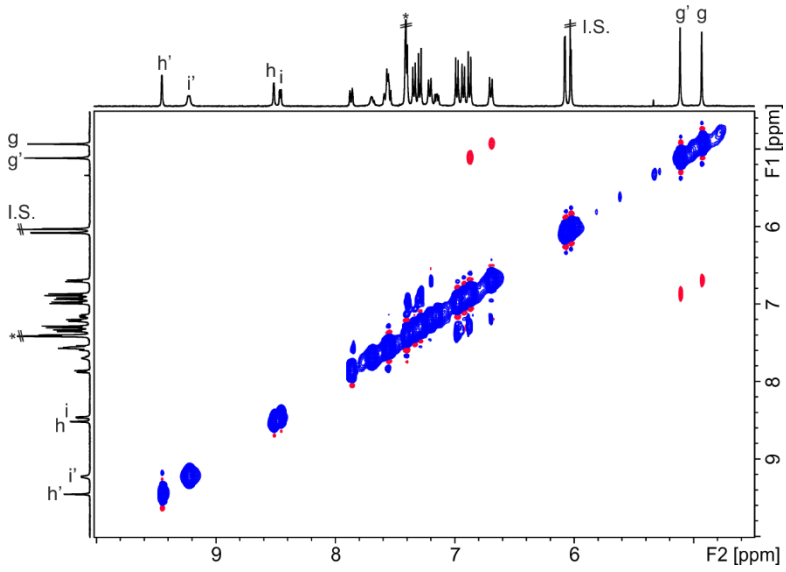

Figure 105. Selected region of the 2D ^{1}H-^{1}H EXSY NMR (400 MHz, 2:1 $CDCl_3$:CD_3CN, 298 K, t_{mix} = 0.3 s) spectrum of **1** and [**1**•Pd]$^{2+}$ (1:1 ratio). Primed letters correspond to proton signals of [**1**•Pd]$^{2+}$. See Figure 23 for proton assignment. 1,3,5-Trimethoxybenzene (I.S.). *Residual solvent peak.

The 2D ^{1}H-^{1}H EXSY NMR experiment did not show exchange cross-peaks between **1** and [**1**•Pd]$^{2+}$. This result indicated that the ligand exchange is slow on the EXSY timescale.

2D ^{1}H-^{1}H EXSY NMR experiments of **1**, [**1**•Pd]$^{2+}$ and [**1**•Pt]$^{2+}$ with pyridyl *N*-oxides

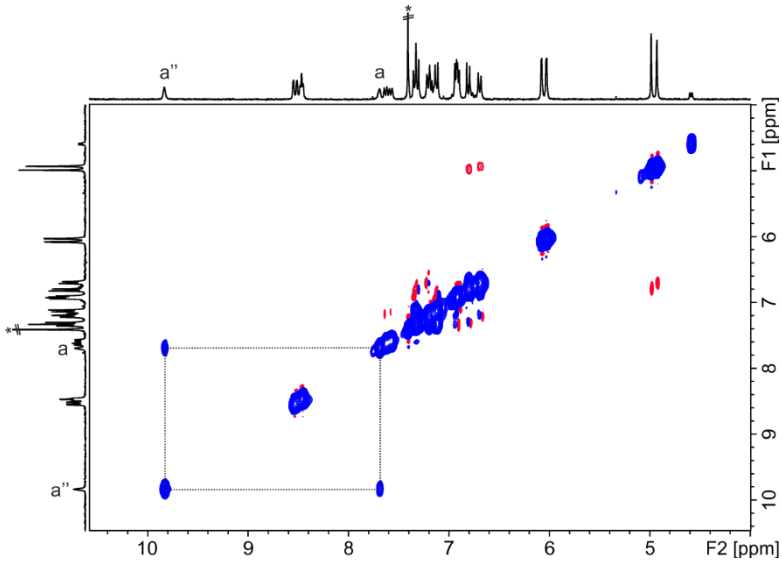

Figure 106. 2D ^{1}H-^{1}H EXSY NMR (300 MHz, 2:1 $CDCl_3$:CD_3CN, 298 K, t_{mix} = 0.3 s) spectrum of **7** and **1** (0.5:1 ratio). Doubly primed letters correspond to proton signals of **7**⊂**1**. See Figure 23 for proton assignment. *Residual solvent peak.

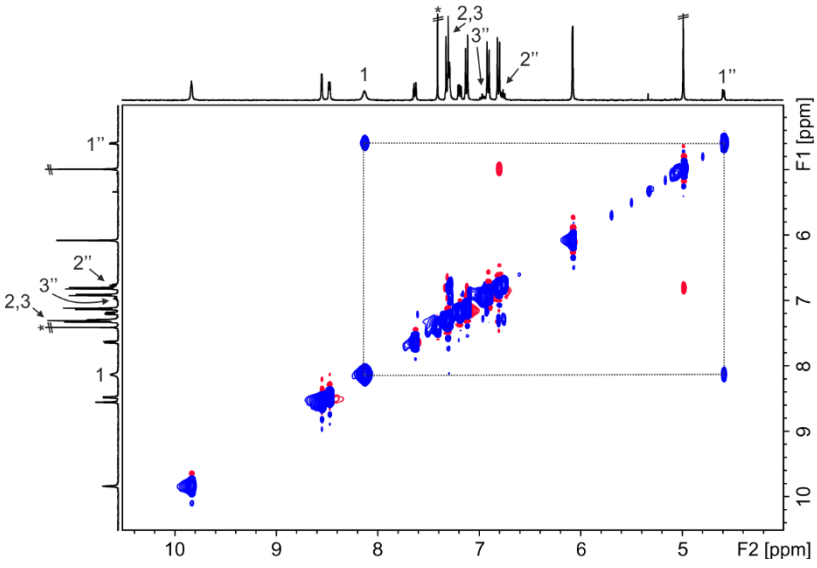

Figure 107. 2D ^{1}H-^{1}H EXSY NMR (400 MHz, 2:1 $CDCl_3$:CD_3CN, 298 K, t_{mix} = 0.3 s) spectrum of **7** and **1** (3:1 ratio). Doubly primed numbers correspond to proton signals of **7**⊂**1**. See Figure 67 for proton assignment. *Residual solvent peak.

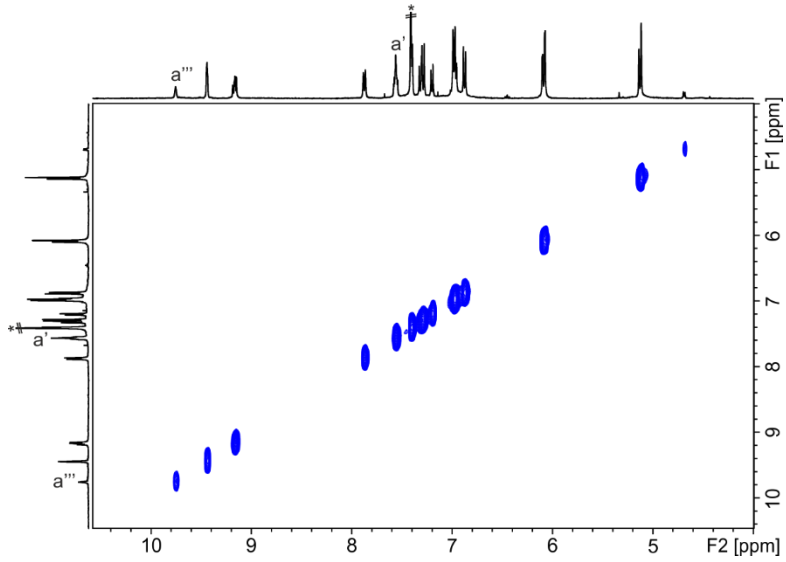

Figure 108. 2D ^{1}H-^{1}H EXSY NMR (300 MHz, 2:1 $CDCl_3$:CD_3CN, 298 K, t_{mix} = 0.3 s) spectrum of **7** and [**1**•Pd]$^{2+}$ (0.5:1 ratio). Primed letters correspond to proton signals of [**1**•Pd]$^{2+}$. Triply primed letters correspond to proton signals of **7**⊂[**1**•Pd]$^{2+}$. See Figure 23 for proton assignment. *Residual solvent peak.

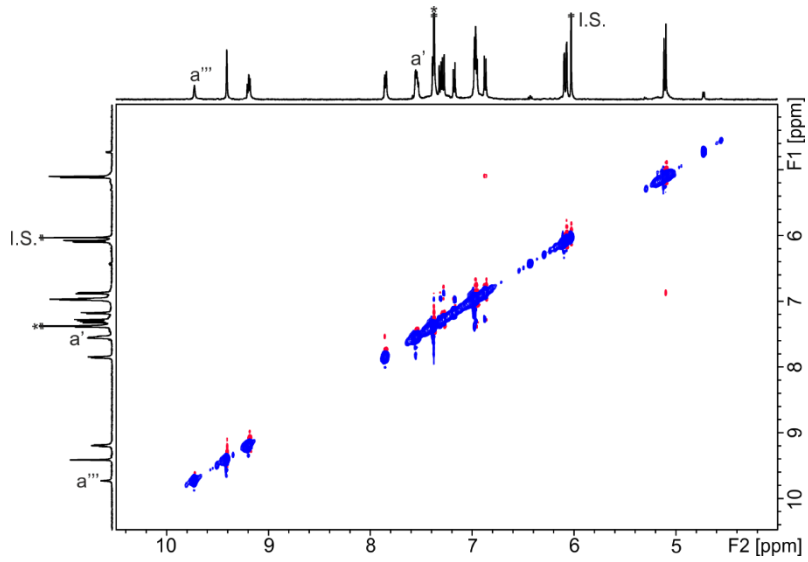

Figure 109. 2D ^{1}H-^{1}H EXSY NMR (300 MHz, 2:1 $CDCl_3$:CD_3CN, 328 K, t_{mix} = 0.3 s) spectrum of **7** and [**1**•Pd]$^{2+}$ (0.5:1 ratio). Primed letters correspond to proton signals of [**1**•Pd]$^{2+}$. Triply primed letters correspond to proton signals of **7**⊂[**1**•Pd]$^{2+}$. See Figure 23 for proton assignment. 1,3,5-Trimethoxybenzene (I.S.). *Residual solvent peak.

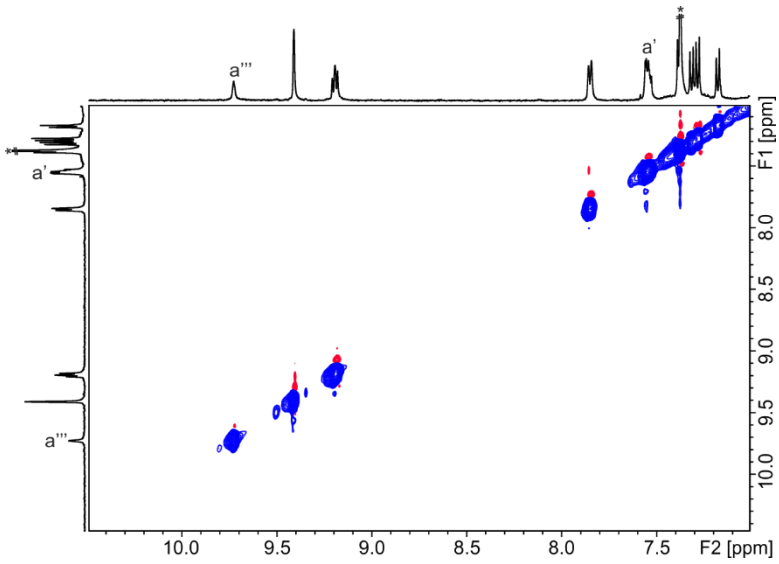

Figure 110. Selected region of the 2D ^{1}H-^{1}H EXSY NMR (500 MHz, 2:1 $CDCl_3$:CD_3CN, 328 K, t_{mix} = 0.3 s) spectrum of **7** and [**1**•Pd]$^{2+}$ (0.5:1 ratio). Primed letters correspond to proton signals of [**1**•Pd]$^{2+}$. Triply primed letters correspond to proton signals of **7**⊂[**1**•Pd]$^{2+}$. See Figure 23 for proton assignment. *Residual solvent peak.

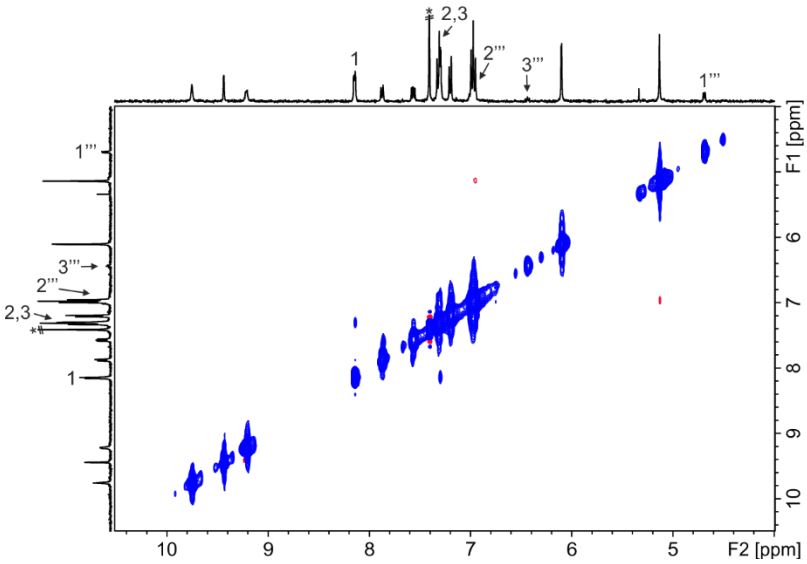

Figure 111. 2D ^{1}H-^{1}H EXSY NMR (400 MHz, 2:1 $CDCl_3$:CD_3CN, 298 K, t_{mix} = 0.3 s) spectrum of **7** and [**1**•Pd]$^{2+}$ (4:1 ratio). Triply primed numbers correspond to proton signals of **7**⊂[**1**•Pd]$^{2+}$. See Figure 67 for proton assignment. *Residual solvent peak.

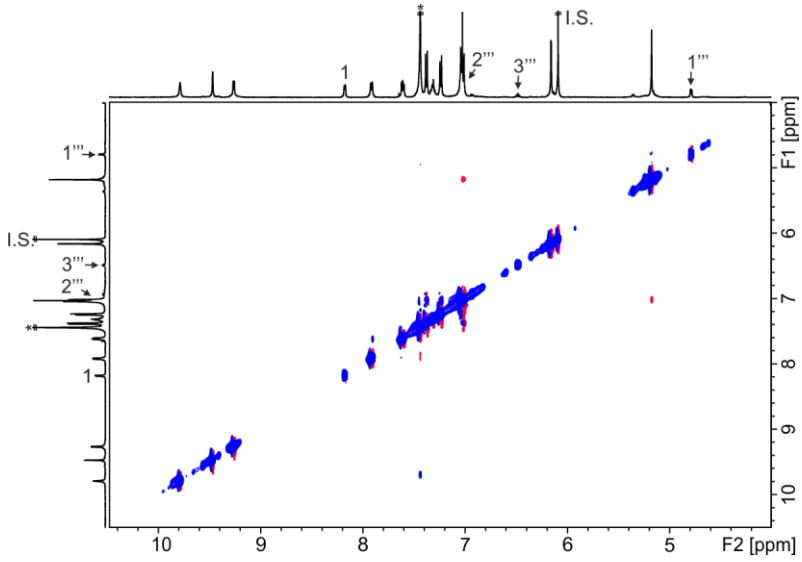

Figure 112. 2D ^{1}H-^{1}H EXSY NMR (500 MHz, 2:1 $CDCl_3$:CD_3CN, 328 K, t_{mix} = 0.3 s) spectrum of **7** and [**1**•Pd]$^{2+}$ (2:1 ratio). Triply primed numbers correspond to proton signals of **7**⊂[**1**•Pd]$^{2+}$. See Figure 67 for proton assignment. 1,3,5-Trimethoxybenzene (I.S.). *Residual solvent peak.

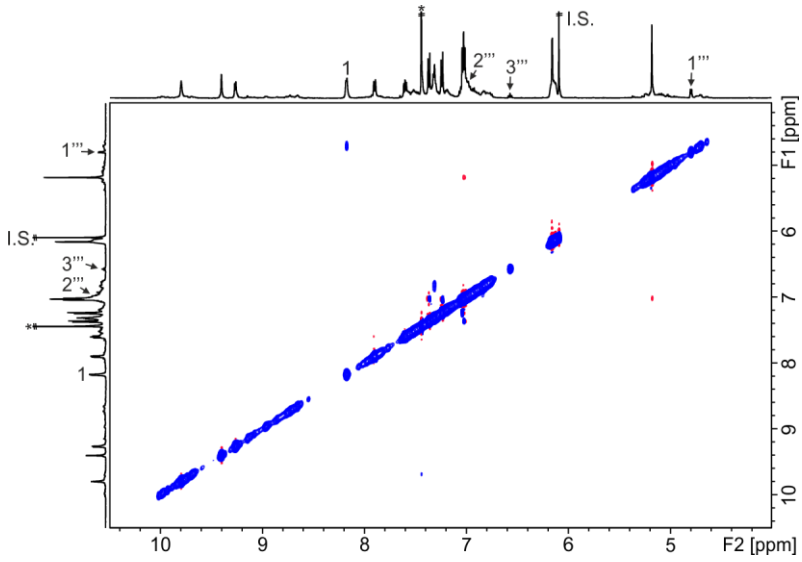

Figure 113. 2D ^{1}H-^{1}H EXSY NMR (500 MHz, 2:1 $CDCl_3$:CD_3CN, 328 K, t_{mix} = 0.3 s) spectrum of **7** and [**1**•Pt]$^{2+}$ (2:1 ratio). Triply primed numbers correspond to proton signals of **7**⊂[**1**•Pt]$^{2+}$. See Figure 67 for proton assignment. 1,3,5-Trimethoxybenzene (I.S.). *Residual solvent peak.

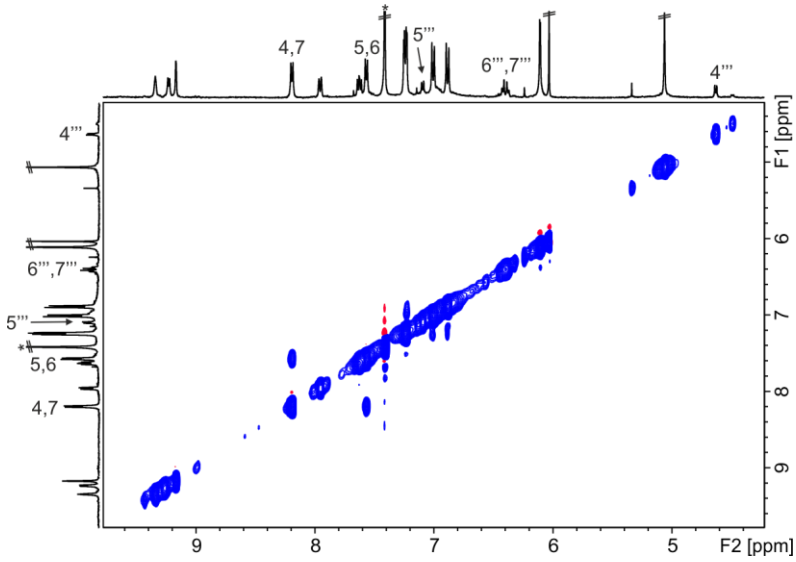

Figure 114. 2D ^{1}H-^{1}H EXSY NMR (400 MHz, 2:1 $CDCl_3$:CD_3CN, 298 K, t_{mix} = 0.3 s) spectrum of **8** and [**1**•Pd]$^{2+}$ (2:1 ratio). Triply primed numbers correspond to proton signals of **8**⊂[**1**•Pd]$^{2+}$. See Figure 69 for proton assignment *Residual solvent peak.

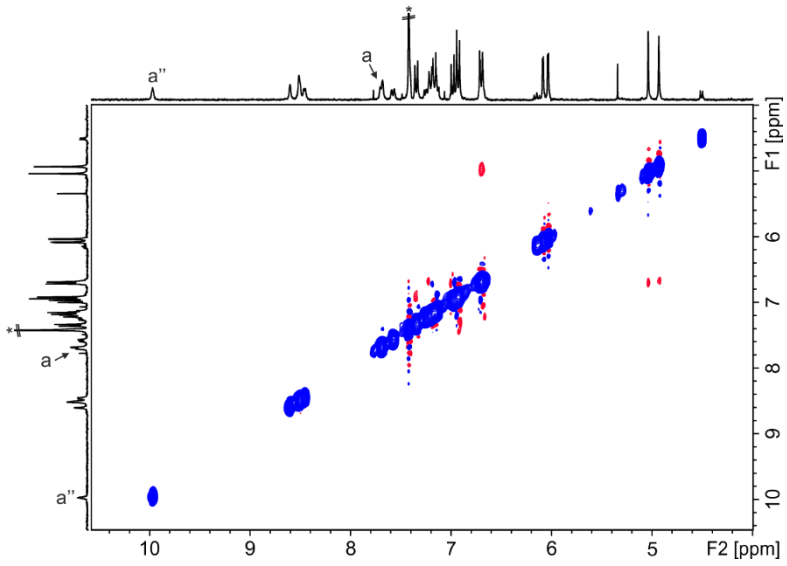

Figure 115. 2D ^{1}H-^{1}H EXSY NMR (300 MHz, 2:1 $CDCl_3$:CD_3CN, 298 K, t_{mix} = 0.3 s) spectrum of **9** and **1** (0.5:1 ratio). Doubly primed letters correspond to proton signals of **9**⊂**1**. See Figure 23 for proton assignment. *Residual solvent peak.

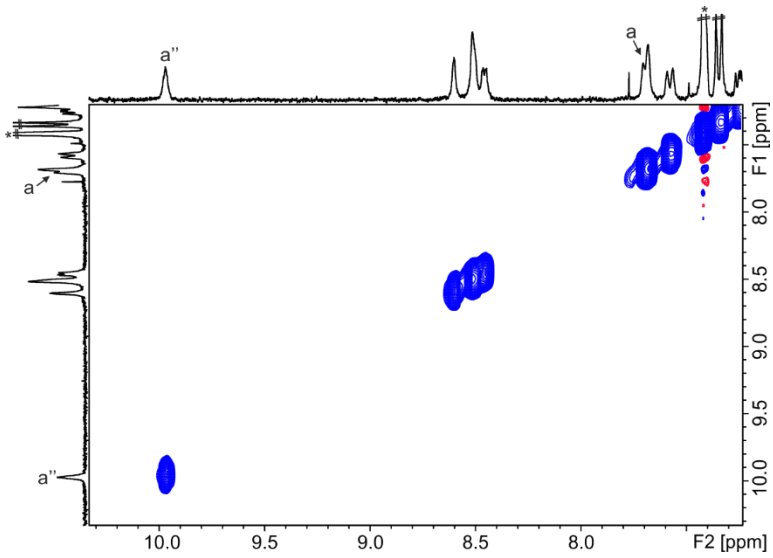

Figure 116. Selected region of the 2D ^{1}H-^{1}H EXSY NMR (300 MHz, 2:1 $CDCl_3$:CD_3CN, 298 K, t_{mix} = 0.3 s) spectrum of **9** and **1** (0.5:1 ratio). Doubly primed letters correspond to proton signals of **9⊂1**. See Figure 23 for proton assignment. *Residual solvent peak.

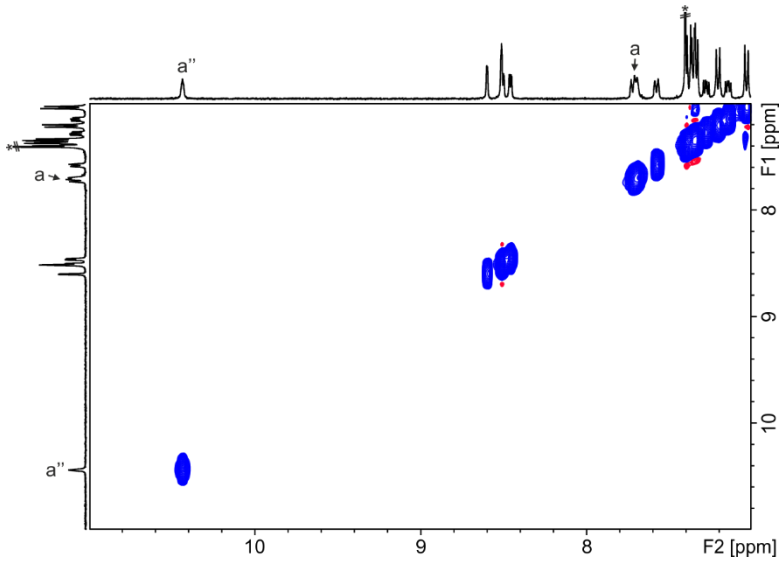

Figure 117. Selected region of the 2D ^{1}H-^{1}H EXSY NMR (400 MHz, 2:1 $CDCl_3$:CD_3CN, 298 K, t_{mix} = 0.3 s) spectrum of **11** and **1** (0.5:1 ratio). Doubly primed letters correspond to proton signals of **11⊂1**. See Figure 23 for proton assignment. *Residual solvent peak.

We did not observe cross-peaks due to chemical exchange in the range of studied temperatures suggesting that the chemical exchange process between free and bound components of the cage complexes was also slow on the EXSY timescale.

4.4.9 Energy minimized structures and packing coefficients of cage complexes

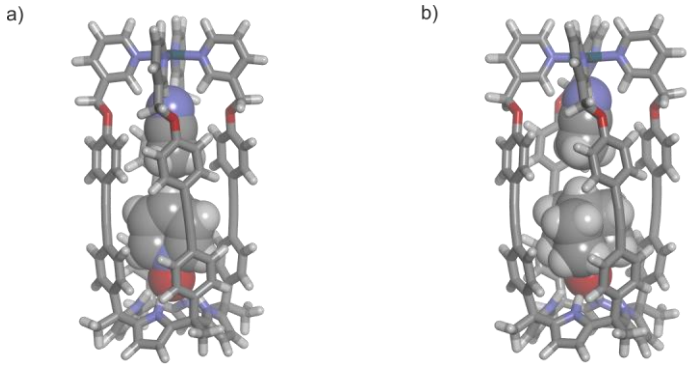

Figure 118. Energy minimized structures (MM3): a) [**7**•CH_3CN]⊂[**1**•Pd]$^{2+}$ and b) [**11**•CH_3CN]⊂[**1**•Pd]$^{2+}$. The cages are depicted in stick representation. Bound molecules are shown as CPK models.

Table 8. Packing coefficients (*PC* = ($V_{guest/s}$/V_{host}) x 100) of the [**1**•Pd]$^{2+}$ cage complexes obtained from their energy minimized structures (MM3). The volumes of the host and the guest/s were determined using SwissPDB Version 4.10.

Cage complex	V_{host} (Å^3)[a]	$V_{guest/s}$ (Å^3)	*PC* (%)
[$(CH_3)_2SO]_2$⊂[**1**•Pd]$^{2+}$	292	153	52
[$CH_3CN]_2$⊂[**1**•Pd]$^{2+}$	172	93	54
[**7**•CH_3CN]⊂[**1**•Pd]$^{2+}$	205	134	65
8⊂[**1**•Pd]$^{2+}$	252	161	64
9⊂[**1**•Pd]$^{2+}$	251	158	63
[**11**•CH_3CN]⊂[**1**•Pd]$^{2+}$	296	181	61

[a] The volume of the cage complexes was determined by replacing the *ortho*-protons of adjacent *meso*-aromatic walls by methyl groups.

4.4.10 X-ray structures

CCDC 1876531 (CH_3CN⊂**1**); 1876530 ([$CH_3CN]_2$⊂[**1**•Pd]$(BF_4)_2$); 1943204 ([$CH_3CN]_2$⊂[**1**•Pt]$(BF_4)_2$); 1876528 ([**7**•CH_3CN]⊂[**1**•Pd]$(BF_4)_2$); 1876529 (**8**⊂[**1**•Pd]$(BF_4)_2$) and 1943205 ([**11**•BF_4]⊂[**1**•Pd](BF_4)) contain the supplementary crystallographic data for this chapter. These data can be obtained free of charge from The Cambridge Crystallographic Data Centre.

4.4.11 NMR experiments of tetra-pyridyl **12** and [**12**•Pd]$^{6+}$

A suspension of the tetra-pyridinium tetra-pyridyl **12** was prepared in D_2O (1 mM). The suspension of **12** was stirred at 50°C for 24 h. After that, the mixture was filtered and the ^{1}H NMR spectrum was acquired.

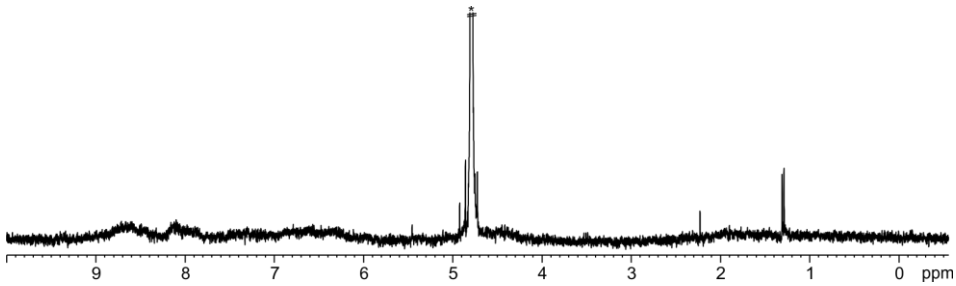

Figure 119. ^{1}H NMR (400 MHz, D_2O, 298 K) spectrum of **12**. *Residual solvent peak.

Tetra-pyridinium tetra-pyridyl **12** (1 mM) and 1 equiv. of *bis*-*N*-oxide **8** were suspended in D_2O. The suspension was stirred at 50°C for 2 h leading to a solution of the putative **8**⊂**12** inclusion complex. After that, a ^{1}H NMR spectrum of the solution was acquired. A solution of $Pd(NO_3)_2$ was prepared in D_2O at 20-30 fold higher concentration (20-30 mM). Pd(II) (*ca.* 1 equiv.) was added to the previous solution and a ^{1}H NMR spectrum of the mixture was acquired after the injection and vigorous hand shaking of the NMR tube for few seconds.

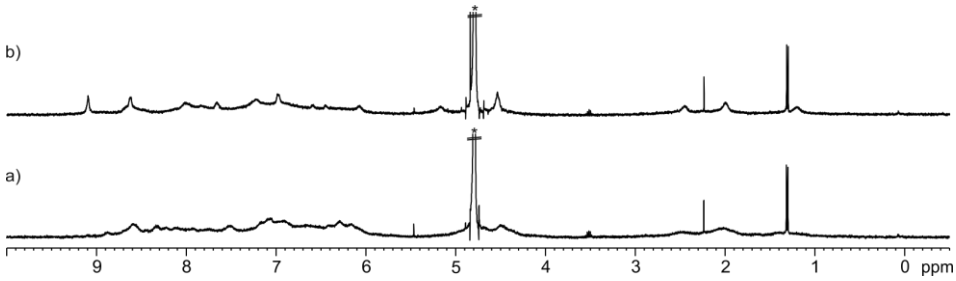

Figure 120. ^{1}H NMR (400 MHz, D_2O, 298 K) spectra: a) **8** and **12** (1:1 ratio); addition of Pd(II) to a): *ca.* 1 equiv. *Residual solvent peak.

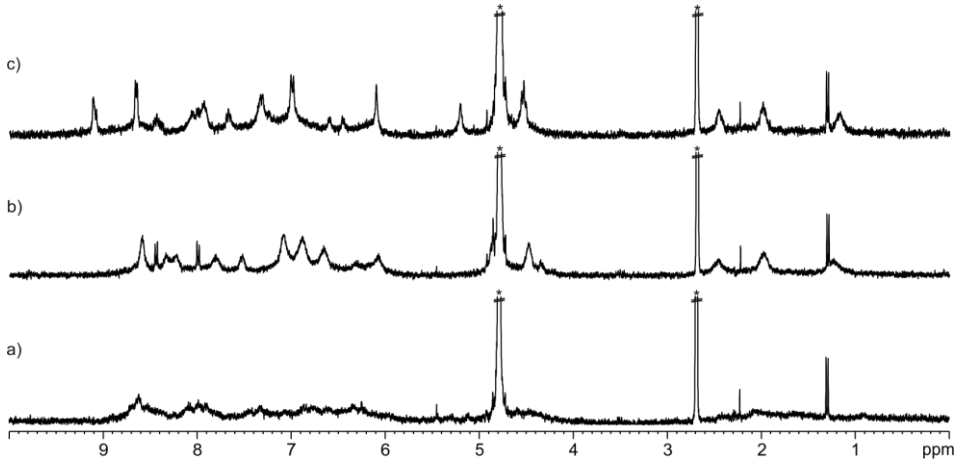

Figure 121. ^{1}H NMR (400 MHz, 95:5 D_2O:$(CD_3)_2SO$, 298 K) spectra: a) **12**; addition of **8** to **12**: b) 1 equiv.; addition of Pd(II) to b): c) *ca*. 1 equiv. *Residual solvent peaks.

4.5 References and Notes

[1] J. M. Lehn, *Chem. Soc. Rev.* **2007**, *36*, 151-160.

[2] M. Han, D. M. Engelhard, G. H. Clever, *Chem. Soc. Rev.* **2014**, *43*, 1848-1860.

[3] T. R. Cook, P. J. Stang, *Chem. Rev. (Washington, DC, U. S.)* **2015**, *115*, 7001-7045.

[4] L. L. K. Taylor, I. A. Riddell, M. M. J. Smulders, *Angew. Chem., Int. Ed.* **2019**, *58*, 1280-1307.

[5] A. V. Davis, K. N. Raymond, *J. Am. Chem. Soc.* **2005**, *127*, 7912-7919.

[6] S. Zarra, M. M. J. Smulders, Q. Lefebvre, J. K. Clegg, J. R. Nitschke, *Angew. Chem., Int. Ed.* **2012**, *51*, 6882-6885.

[7] J. K. Clegg, J. Cremers, A. J. Hogben, B. Breiner, M. M. J. Smulders, J. D. Thoburn, J. R. Nitschke, *Chem. Sci.* **2013**, *4*, 68-76.

[8] M. X. Han, R. Michel, B. He, Y. S. Chen, D. Stalke, M. John, G. H. Clever, *Angew. Chem., Int. Ed.* **2013**, *52*, 1319-1323.

[9] S. Loffler, J. Lubben, L. Krause, D. Stalke, B. Dittrich, G. H. Clever, *J. Am. Chem. Soc.* **2015**, *137*, 1060-1063.

[10] V. Croue, S. Goeb, G. Szaloki, M. Allain, M. Salle, *Angew. Chem., Int. Ed.* **2016**, *55*, 1746-1750.

[11] A. M. Castilla, T. K. Ronson, J. R. Nitschke, *J. Am. Chem. Soc.* **2016**, *138*, 2342-2351.

[12] S. Akine, M. Miyashita, T. Nabeshima, *J. Am. Chem. Soc.* **2017**, *139*, 4631-4634.

[13] L. K. S. von Krbek, D. A. Roberts, B. S. Pilgrim, C. A. Schalley, J. R. Nitschke, *Angew. Chem., Int. Ed.* **2018**, *57*, 14121-14124.

[14] R. J. Li, J. J. Holstein, W. G. Hiller, J. Andreasson, G. H. Clever, *J. Am. Chem. Soc.* **2019**, *141*, 2097-2103.

[15] G. Moncelsi, P. Ballester, *ChemPhotoChem* **2019**, *3*, 304-317.

[16] R. Djemili, L. Kocher, S. Durot, A. Peuronen, K. Rissanen, V. Heitz, *Chem.--Eur. J.* **2019**, *25*, 1481-1487.

[17] J. E. Beves, B. A. Blight, C. J. Campbell, D. A. Leigh, R. T. McBurney, *Angew. Chem., Int. Ed.* **2011**, *50*, 9260-9327.

[18] C. J. Brown, F. D. Toste, R. G. Bergman, K. N. Raymond, *Chem. Rev. (Washington, DC, U. S.)* **2015**, *115*, 3012-3035.

[19] A. J. McConnell, C. S. Wood, P. P. Neelakandan, J. R. Nitschke, *Chem. Rev. (Washington, DC, U. S.)* **2015**, *115*, 7729-7793.

[20] A. Galan, P. Ballester, *Chem. Soc. Rev.* **2016**, *45*, 1720-1737.

[21] C. M. Hong, R. G. Bergman, K. N. Raymond, F. D. Toste, *Acc. Chem. Res.* **2018**, *51*, 2447-2455.

[22] F. J. Rizzuto, L. K. S. von Krbek, J. R. Nitschke, *Nat. Rev. Chem.* **2019**, *3*, 204-222.

[23] N. B. Debata, D. Tripathy, D. K. Chand, *Coord. Chem. Rev.* **2012**, *256*, 1831-1945.

[24] M. Fujita, M. Tominaga, A. Hori, B. Therrien, *Acc. Chem. Res.* **2005**, *38*, 369-378.

[25] P. D. Frischmann, M. J. MacLachlan, *Chem. Soc. Rev.* **2013**, *42*, 871-890.

[26] K. Kobayashi, M. Yamanaka, *Chem. Soc. Rev.* **2015**, *44*, 449-466.

[27] M. Fujita, *Chem. Soc. Rev.* **1998**, *27*, 417-425.

[28] M. Chas, D. Abella, V. Blanco, E. Pia, G. Blanco, A. Fernandez, C. Platas-Iglesias, C. Peinador, J. M. Quintela, *Chem.--Eur. J.* **2007**, *13*, 8572-8582.

[29] T. Weilandt, N. L. Löw, G. Schnakenburg, J. Daniels, M. Nieger, C. A. Schalley, A. Lützen, *Chem.--Eur. J.* **2012**, *18*, 16665-16676.

[30] A. Baba, T. Kojima, S. Hiraoka, *J. Am. Chem. Soc.* **2015**, *137*, 7664-7667.

[31] J. Mendez-Arroyo, A. I. d'Aquino, A. B. Chinen, Y. D. Manraj, C. A. Mirkin, *J. Am. Chem. Soc.* **2017**, *139*, 1368-1371.

[32] S. Kai, V. Marti-Centelles, Y. Sakuma, T. Mashiko, T. Kojima, U. Nagashima, M. Tachikawa, P. J. Lusby, S. Hiraoka, *Chem.--Eur. J.* **2018**, *24*, 663-671.

[33] M. Fujita, J. Yazaki, K. Ogura, *Chem. Lett.* **1991**, 1031-1032.

[34] M. Fujita, F. Ibukuro, K. Yamaguchi, K. Ogura, *J. Am. Chem. Soc.* **1995**, *117*, 4175-4176.

[35] F. Ibukuro, T. Kusukawa, M. Fujita, *J. Am. Chem. Soc.* **1998**, *120*, 8561-8562.

[36] A. V. Davis, R. M. Yeh, K. N. Raymond, *Proc. Natl. Acad. Sci. U. S. A.* **2002**, *99*, 4793-4796.

[37] A. V. Davis, D. Fiedler, G. Seeber, A. Zahl, R. van Eldik, K. N. Raymond, *J. Am. Chem. Soc.* **2006**, *128*, 1324-1333.

[38] S. L. Craig, S. Lin, J. Chen, J. Rebek, *J. Am. Chem. Soc.* **2002**, *124*, 8780-8781.

[39] M. D. Pluth, K. N. Raymond, *Chem. Soc. Rev.* **2007**, *36*, 161-171.

[40] S. Rieth, K. Hermann, B.-Y. Wang, J. D. Badjic, *Chem. Soc. Rev.* **2011**, *40*, 1609-1622.

[41] M. M. J. Smulders, S. Zarra, J. R. Nitschke, *J. Am. Chem. Soc.* **2013**, *135*, 7039-7046.

[42] J. L. Atwood, A. Szumna, *Chem. Commun. (Cambridge, U. K.)* **2003**, 940-941.

[43] D. S. Kim, J. L. Sessler, *Chem. Soc. Rev.* **2015**, *44*, 532-546.

[44] J. E. M. Lewis, E. L. Gavey, S. A. Cameron, J. D. Crowley, *Chem. Sci.* **2012**, *3*, 778-784.

[45] D. P. August, G. S. Nichol, P. J. Lusby, *Angew. Chem., Int. Ed.* **2016**, *55*, 15022-15026.

[46] Y.-H. Li, Y. Zhang, Y.-M. Legrand, A. van der Lee, J.-J. Jiang, C.-X. Chen, C.-Y. Su, M. Barboiu, *Dalton Trans.* **2017**, *46*, 15204-15207.

[47] S. Kusaba, M. Yamashina, M. Akita, T. Kikuchi, M. Yoshizawa, *Angew. Chem., Int. Ed.* **2018**, *57*, 3706-3710.

[48] X. K. Ji, D. S. Black, S. B. Colbran, G. D. Willett, P. Turner, *Inorg. Chem. Commun.* **2006**, *9*, 469-472.

[49] N. Kiriyama, M. Ebihara, T. Udagawa, H. Miyaji, *RSC Adv.* **2016**, *6*, 19794-19796.

[50] J. Lee, N. W. Waggoner, L. Polanco, G. R. You, V. M. Lynch, S. K. Kim, S. M. Humphrey, J. L. Sessler, *Chem. Commun. (Cambridge, U. K.)* **2016**, *52*, 8514-8517.

[51] J. Aguilera-Sigalat, C. Saenz de Pipon, D. Hernandez-Alonso, E. C. Escudero-Adan, J. Ramon Galan-Mascaros, P. Ballester, *Cryst. Growth Des.* **2017**, *17*, 1328-1338.

[52] T. Hirao, D. S. Kim, X. D. Chi, V. M. Lynch, K. Ohara, J. S. Park, K. Yamaguchi, J. L. Sessler, *Nat. Commun.* **2018**, *9*, 823.

[53] A. Galan, G. Aragay, P. Ballester, *Chem. Sci.* **2016**, *7*, 5976-5982.

[54] L. M. Salonen, M. Ellermann, F. Diederich, *Angew. Chem., Int. Ed.* **2011**, *50*, 4808-4842.

[55] L. Escobar, G. Aragay, P. Ballester, *Chem.--Eur. J.* **2016**, *22*, 13682-13689.

[56] P. Liao, B. W. Langloss, A. M. Johnson, E. R. Knudsen, F. S. Tham, R. R. Julian, R. J. Hooley, *Chem. Commun. (Cambridge, U. K.)* **2010**, *46*, 4932-4934.

[57] L. Avram, Y. Cohen, *Chem. Soc. Rev.* **2015**, *44*, 586-602.

[58] M. M. Tirado, J. García de la Torre, *J. Chem. Phys.* **1979**, *71*, 2581-2587.

[59] M. M. Tirado, C. L. Martinez, J. García de la Torre, *J. Chem. Phys.* **1984**, *81*, 2047-2052.

[60] S. Hansen, *J. Chem. Phys.* **2004**, *121*, 9111-9115.

[61] M. Sandro, J. J. Rebek, *Chem.--Eur. J.* **1998**, *4*, 1016-1022.

[62] J. C. Cobas, M. Martín-Pastor, EXSYCalc Version 1.0.

[63] A. Pastor, E. Martinez-Viviente, *Coord. Chem. Rev.* **2008**, *252*, 2314-2345.

[64] K. N. Houk, K. Nakamura, C. Sheu, A. E. Keating, *Science* **1996**, *273*, 627-629.

[65] D. J. Cram, M. E. Tanner, C. B. Knobler, *J. Am. Chem. Soc.* **1991**, *113*, 7717-7727.

[66] L. Escobar, P. Ballester, *Org. Chem. Front.* **2019**, *6*, 1738-1748.

[67] G. R. Fulmer, A. J. M. Miller, N. H. Sherden, H. E. Gottlieb, A. Nudelman, B. M. Stoltz, J. E. Bercaw, K. I. Goldberg, *Organometallics* **2010**, *29*, 2176-2179.

[68] L. Bonomo, E. Solari, G. Toraman, R. Scopelliti, M. Latronico, C. Floriani, *Chem. Commun. (Cambridge, U. K.)* **1999**, 2413-2414.

[69] A. Galan, E. C. Escudero-Adan, P. Ballester, *Chem. Sci.* **2017**, *8*, 7746-7750.

[70] A. Derenzi, A. Panunzi, A. Vitagliano, G. Paiaro, *J. Chem. Soc., Chem. Commun.* **1976**, 47-47.

[71] T. E. Muller, J. C. Green, D. M. P. Mingos, C. M. McPartlin, C. Whittingham, D. J. Williams, T. M. Woodroffe, *J. Organomet. Chem.* **1998**, *551*, 313-330.

UNIVERSITAT ROVIRA I VIRGILI
MOLECULAR CONTAINERS BASED ON ARYL-EXTENDED CALIX[4]PYRROLES
Luis Escobar González

Chapter 5

Conformational Selectivity and High-Affinity Binding in the Complexation of *N*-Phenyl Amides in Water by a Phenyl Extended Calix[4]pyrrole

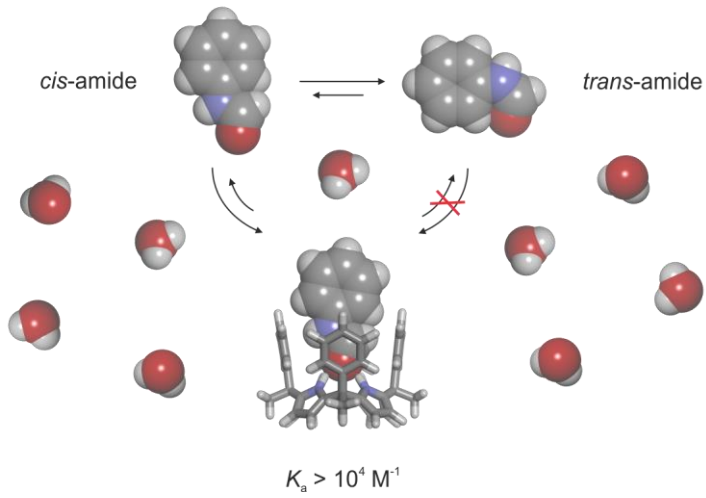

Part of this chapter has been published in:

L. Escobar, A. Díaz-Moscoso, P. Ballester, *Chem. Sci.* **2018**, *9*, 7186-7192.

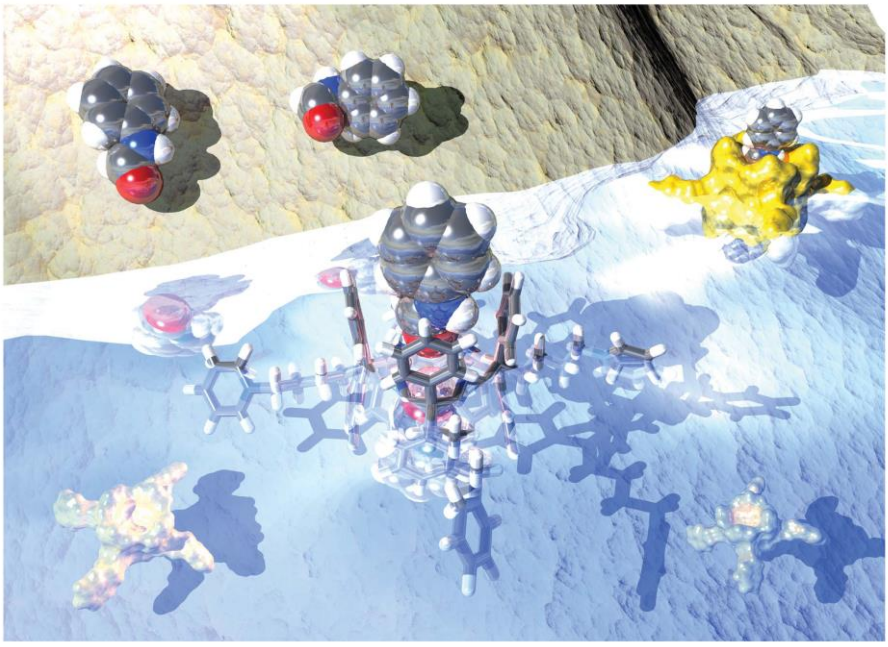

Showcasing research from Professor Ballester's laboratory, Institute of Chemical Research of Catalonia (ICIQ), Tarragona, Spain.

Conformational selectivity and high-affinity binding in the complexation of *N*-phenyl amides in water by a phenyl extended calix[4]pyrrole

We report the synthesis of a tetrapyridinium phenyl extended calix[4]pyrrole showing high selectivity and binding affinity for the *cis*-conformers of *N*-phenyl-amides in water. The conformational selectivity is remarkable owing to the energetic preference of the amides to adopt the *trans*-conformation. In turn, the high binding affinities derived from the combination of hydrogen bonding interactions and the hydrophobic effect. We used two binding models for the mathematical analyses of the titration data and rationalized the different magnitudes calculated for the corresponding binding constants (apparent and intrinsic).

As featured in:

See P. Ballester *et al.*, *Chem. Sci.*, 2018, **9**, 7186.

ROYAL SOCIETY OF CHEMISTRY

rsc.li/chemical-science

Registered charity number: 207890

5.1 Introduction

Carboxamides (*a.k.a* organic amides) are important functional groups in both natural (*e.g.* peptides) and synthetic (*e.g.* nylon) polymers. The existence of many methods for their synthesis, together with their high thermodynamic stability in a wide range of chemical conditions render amides very useful covalent linkers in many chemical constructs. The pseudo-double-bond character of the carbon(C=O)-nitrogen σ-bond restricts its rotation and, therefore, secondary and tertiary amides exist as two isomeric *cis-trans* rotamers (Scheme 1a). In solution, secondary amides show marked preference for the *trans*-rotamer (*Z*-isomer).[1,2] On the one hand, the energetic difference between the two rotamers lies in the range of 0.5 to 2.5 kcal·mol^{-1} for the secondary and tertiary amides.[3] On the other hand, because the free energy barrier for the *cis-trans* interconversion is moderate ($\Delta G^{\ddagger}$ = 16-22 kcal·mol^{-1}) the process is typically slow on the NMR chemical shift timescale but fast on the human timescale.[3] Steric contributions on either side of the amide group seem to be the most significant factors for easing the barrier crossing, as well as controlling the relative population of *cis-trans* isomers.

The *cis-trans* isomerization of the amide bond plays an important role in determining folding,[4] function[5] and ligand interactions in proteins and peptides.[6,7,8,9,10] Likewise, the photo-physical behavior of simple phenanthrene carboxamides was shown to be dependent on the amide conformation.[11] The equilibrium between secondary amide rotamers is known to be solvent dependent.[12] In addition, *cis*-amide rotamers have been stabilized by intramolecular CH-π interactions,[13] lone pair-π interactions[14,15] and the hydrophobic effect.[16]

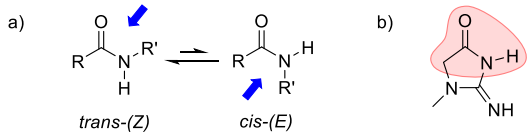

Scheme 1. a) Equilibrium between *trans*-(*Z*) and *cis*-(*E*) conformers of a secondary amide. Arrows (blue) indicate areas of steric clashes. b) Structural analogy of the *cis*-(*E*) isomer with the lactam tautomeric form of creatinine is highlighted (red).

In organic solvents, the formation of host-guest hydrogen-bonded complexes has also been studied to stabilize *cis*-amides.[14,17,18,19,20] In water, the combination of hydrogen-bonding interactions and the hydrophobic effect has provided thermodynamically stable complexes of synthetic receptors with small linear and cyclic peptides (Figure 1a).[21,22] However, to the best of our knowledge, synthetic receptors displaying selective binding of *cis*-rotamers of mono-amides in water and producing thermodynamically highly stable complexes are not known.

Sessler *et al.* described the binding of small tertiary amides (*i.e.* di-methyl formamide and di-methyl acetamide) using octa-methyl calix[4]pyrrole in benzene solution. The resulting complexes displayed binding affinities in the order of 10 M^{-1} and were mainly stabilized by the establishment

of hydrogen-bonding interactions between the pyrrole NHs and the oxygen atom of the amide's carbonyl group.[23] More recently, we reported the use of phosphonate calix[4]pyrrole cavitands, featuring a polar aromatic cavity, for the efficient binding of creatinine in organic solvents (Figure 1b).[24] In solution and in the solid state, the inclusion of creatinine in the cavity of the receptor was mainly driven by the establishment of multiple hydrogen bonds. Nevertheless, the additional intermolecular CH-π interactions were also present in the above creatinine complex. To us, the lactam tautomer of bound creatinine resembled a *cis*-rotamer of a secondary amide and suggested the potential use of aryl-extended calix[4]pyrroles for its selective binding in water solution (Scheme 1b).

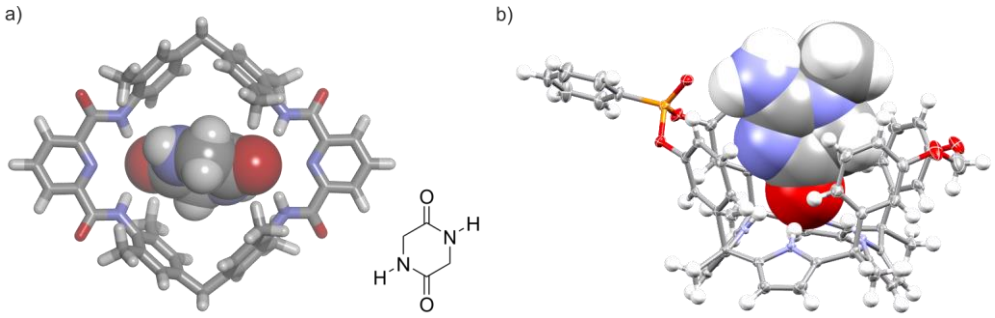

Figure 1. a) Energy minimized structure of the Hunter's cyclophane bound to a cyclic di-amide. The receptor is depicted in stick representation. Water-solubilizing groups are omitted for clarity. b) X-ray crystal structure of the complex between creatinine and phosphonate calix[4]pyrrole cavitand. The cavitand is shown in ORTEP view with thermal ellipsoids set at 50% probability. Hydrogen atoms are shown as fixed-size spheres of 0.3 Å radius. Bound guests are shown as CPK models.

Herein, we report the synthesis of a water-soluble tetra-cationic pyridinium aryl-extended calix[4]pyrrole receptor. We also describe the results of the binding studies of the tetra-pyridinium calix[4]pyrrole with a series of acyclic mono-amides in water. The conformational selectivity displayed by the aryl-extended calix[4]pyrrole in the exclusive binding of the *cis*-rotamers of *N*-phenyl amides with affinity constants larger than 10^3 M^{-1} is highlighted. Finally, we investigate the binding of a long-chain di-formamide to a water-soluble super aryl-extended calix[4]pyrrole receptor in water.

5.2 Results and Discussion

5.2.1 Synthesis of tetra-pyridinium calix[4]pyrrole **1**

Water-soluble aryl-extended calix[4]pyrroles bearing ionizable carboxylic acid functions have been previously described in literature.[25,26,27] These receptors required basic media for their water solubilization. In order to avoid these conditions, not compatible with biological standards, we designed the tetra-*α* tetra-phenyl calix[4]pyrrole **1** featuring four *meso*-(3-pyridiniumpropyl)

substituents at its lower rim (Scheme 2). The water solubilization of calix[4]pyrrole **1** was inspired by previous works on water-soluble deep cavitands bearing benzimidazolones at their upper rims.[28] In these examples, the deep cavitands were rendered water soluble by converting the lower rim tetra-chloride derivatives into quaternary ammonium salts by treatment with excess of pyridine. Receptor **1** was synthesized in two steps from commercially available starting materials (Scheme 2).

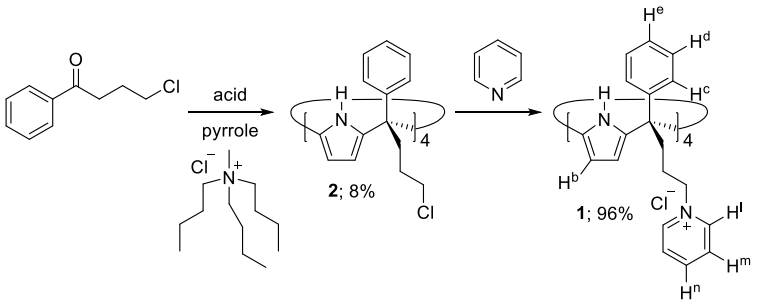

Scheme 2. Synthesis of tetra-phenyl tetra-pyridinium calix[4]pyrrole **1**.

To start, the tetra-*α* tetra-chloro calix[4]pyrrole **2** was prepared using a synthetic methodology recently developed by us that involves the use of methyltributylammonium chloride as template in the cyclocondensation step.[29] Treatment of the tetra-chloro **2** at 110°C in excess of pyridine provided the tetra-pyridinium calix[4]pyrrole salt **1** as yellow precipitate in excellent yield and purity. Calix[4]pyrrole **1** was soluble in water at concentrations up to 15 mM. However, some foam appeared in the solution after vigorous shaking at high concentrations indicating the amphiphilic nature of the tetra-pyridinium calix[4]pyrrole **1**. In order to avoid misleading results, we performed our experiments at concentration below 5 mM. A dilution experiment (1 mM to 0.4 mM) showed negligible changes in the proton signals of the acquired ^{1}H NMR spectra (see Experimental Section). At diluted concentrations, the proton signals of **1** are sharp and well-defined and their number is in agreement with C_{4v} symmetry. Most likely, both alternate and cone conformation of **1** are present in solution. The two conformers are in equilibrium and display a fast chemical exchange on the chemical shift timescale.[30,31]

5.2.2 Binding studies of tetra-pyridinium tetra-phenyl **1** with formamides in water

Molecular modelling studies

Earlier studies with aryl-extended calix[4]pyrroles related to **1** and their cavitand derivatives demonstrated that, in the solid state and organic media, *N*,*N*-di-methyl formamide[32] and creatinine[24] were suitable guests for inclusion in their polar aromatic cavities defined by the four *meso*-phenyl substituents. Based on these precedents, we envisaged that tetra-*α* aryl-extended

calix[4]pyrrole **1** might show conformational selectivity in the recognition of size and shape complementary secondary and tertiary small amides in water (Figure 2).

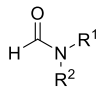

3; R^1 = H; R^2 = Ph
4; R^1 = Ph; R^2 = Ph
5; R^1 = CH_3; R^2 = Ph
6; R^1 = H; R^2 = CH_3
7; R^1 = CH_3; R^2 = CH_3

Figure 2. Line-drawing structures of formamides **3**-**7**. When applicable only the *cis*-rotamer is depicted. See Scheme 1 for the *cis*/*trans* equilibrium.

Simple molecular modelling studies revealed that the inclusion of *N*-phenyl formamide **3** in the aromatic cavity of the cone conformation of **1** was energetically more favorable for the *cis*-rotamer, ΔE = 7.3 kcal·mol^{-1} (Figure 3a). The *cis*-**3**⊂**1** complex is stabilized by four hydrogen-bonding interactions established between the amide carbonyl oxygen atom and the NHs of the four pyrrole units. Additional CH-π and NH-π interactions[18,33,34] are also established between the included *cis*-**3** amide and the *meso*-phenyl walls of **1**.[35] On the other hand, the inclusion of *trans*-**3** in the cone conformation of **1**, *trans*-**3**⊂**1** complex, evidenced steric clashes between the *N*-phenyl substituent and two of the four *meso*-phenyl groups of the receptor (Figure 3b).

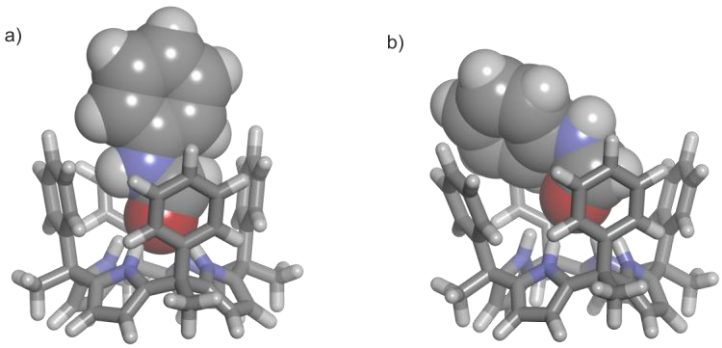

Figure 3. Energy minimized structures (PM3, water COSMO model as implement in SCIGRESS Version FJ 2.6) of the inclusion complexes: a) *cis*-**3**⊂**1** and b) *trans*-**3**⊂**1**. Calix[4]pyrrole **1** is shown in stick representation and amides (*cis*-**3** and *trans*-**3**) as CPK models. Water-solubilizing groups were pruned to methyl groups to ease the calculations.

<u>^{1}H NMR spectroscopy titrations</u>

We decided to experimentally probe the interaction of **1** with *N*-phenyl formamide **3** in water using ^{1}H NMR titration experiments. We mentioned above that the steric factors are usually the most important contributors to the relative population of the *cis*/*trans* rotamers in small secondary and tertiary amides, and that the isomer ratio is also affected by the solvent.[36] In this respect, the ^{1}H NMR spectrum of a 10 mM solution of *N*-phenyl formamide **3** in water showed a 32:68 *cis*/*trans* ratio, based on the integral values of the two singlets resonating at δ = 8.65 and 8.28 ppm,

respectively, which are assigned to the hydrogen atoms of the formyl group in each rotamer (Figure 4).

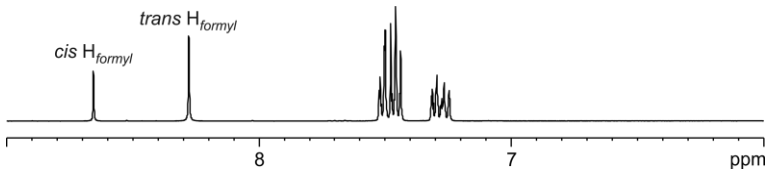

Figure 4. Selected region of the ^{1}H NMR (400 MHz, D_2O, 298 K) spectrum of **3**. The proton signals of the formyl protons of the *cis*- and *trans*-rotamer are indicated.

The incremental addition of formamide **3** to a 1 mM water solution of tetra-pyridinium receptor **1** induced significant chemical shift changes to several proton signals of the receptor. In particular, the triplet of the *para*-aromatic proton (H^e) of the *meso*-phenyl groups of **1** moved upfield ($\Delta\delta_{max}$ = -0.21 ppm). In contrast, the *β*-pyrrole protons (H^b) moved downfield ($\Delta\delta_{max}$ = +0.09 ppm). The pyridinium proton signals also displayed chemical shift changes upon addition of incremental amounts of the guest. These observations indicated the existence of a fast chemical exchange on the ^{1}H NMR timescale between free and bound receptor **1**. Remarkably, after the addition of 0.6 equiv. of **3** only the sharp singlet corresponding to the hydrogen atom of the formyl group for the free *trans*-isomer became visible. At this point, we also observed a complex signal of aromatic protons resonating at δ = 7.5 ppm that was assigned to the phenyl group of the formamide. The signals assigned to *trans*-**3** grew in intensity as the concentration of **3** was increased (Figure 5). In contrast, the signal of the formyl proton in the free *cis*-rotamer was not observed even when 2 equiv. of **3** were added.

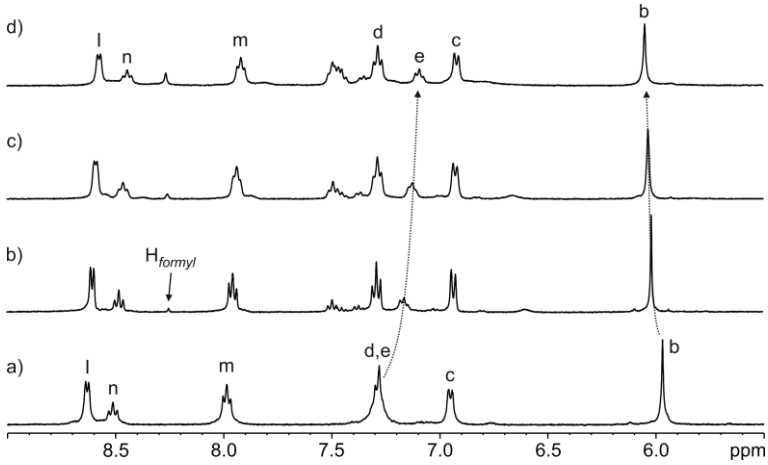

Figure 5. Selected region of the ^{1}H NMR (400 MHz, D_2O, 298 K) spectra of the titration of **1** with **3**: a) 0; b) 0.6; c) 1.0 and d) 2.0 equiv. The H_{formyl} signal corresponds to the hydrogen atom of the formyl group for *trans*-**3**. See Scheme 2 and Figure 2 for proton assignments.

The titration data were mathematically analyzed using HypNMR 2008 software Version 4.0.66.[37] The fit of the chemical shift changes experienced by selected proton signals of the receptor **1** (H^b, H^c, H^d and H^e) to a binding isotherm of a theoretical 1:1 binding model was good (Figure 6). We estimated an apparent binding constant value $K_a > 10^4$ M^{-1} for the formed complex and determined the chemical shift values of the protons of the receptor in the complex (see Experimental Section). These later values allowed the calculation of the corresponding complexation induced shifts (CIS).

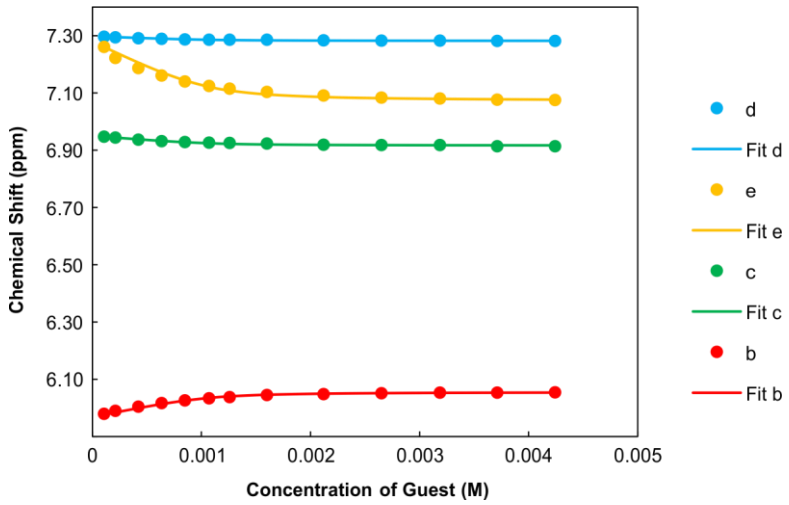

Figure 6. Chemical shifts of the proton signals of **1** upon incremental amounts of **3** (circles) and fit of the titration data to a theoretical 1:1 binding model (lines).

At first sight, the determined magnitude of the apparent binding constant might be considered as the weighted-average of two putative 1:1 inclusion complexes: *cis*-**3**⊂**1** and *trans*-**3**⊂**1**. In order to assess the conformational selectivity exhibited by receptor **1** in the binding of **3**, we decided to titrate it against the tertiary *N*,*N*-di-phenyl formamide **4** (Figure 2). The hydrogen-bonding inclusion of formamide **4** in the cavity of **1** should produce the **4**⊂**1** complex exhibiting a binding geometry closely resembling that of the *trans*-**3**⊂**1** complex (Figure 3b). Our idea was to use the binding constant value of **4**⊂**1** as reference for the *trans*-**3**⊂**1** counterpart.

The extensive sonication of a suspension of *N*,*N*-di-phenyl formamide **4** with a 1.7 mM solution of **1** led to the dissolution of *ca*. 2 equiv. of **4** but did not induce appreciable changes in the chemical shift values of the receptor's protons. Thus, we estimated a binding constant value K_a (**4**⊂**1**) < 10 M^{-1}. On the one hand, this result strongly supports a conformational selectivity towards the *cis*-rotamer in the binding of the *N*-phenyl formamide **3** with receptor **1**. On the other hand, it also requested a change in the mathematical analysis of the titration data in order to assess a more accurate value of the binding constant for the *cis*-**3**⊂**1** complex.

Therefore, we reanalyzed the titration data of **1** with **3** using a theoretical binding model that considers the existence of the equilibrium between the two rotamers of **3** and the exclusive formation of a 1:1 complex with the *cis*-rotamer and receptor **1**.

In doing so a theoretical binding isotherm was calculated from the simulated speciation profile produced with the SPECFIT software Version 3.0.40 (see Section 5.2.5). We considered the equilibrium constant between the two rotamers of **3** and the determined chemical shift values for the protons in the free and bound receptor **1** as fixed values. The value of *K* (*cis*-**3**/*trans*-**3**) = 32/68 = 0.47 was determined from the ^{1}H NMR spectrum of **3** (Figure 4). The complexation induced shifts (CIS) for the protons of **1** were those calculated from the previous fit (see Experimental Section). The fit of the experimental titration data to the more elaborated theoretical binding model only served to estimate that the binding constant value K_a (*cis*-**3**⊂**1**) was larger than 10^4 M^{-1} (Figure 7). The magnitude of this estimate represents a remarkable binding affinity for the complexation of a small polar molecule in water using a synthetic receptor.[38,39]

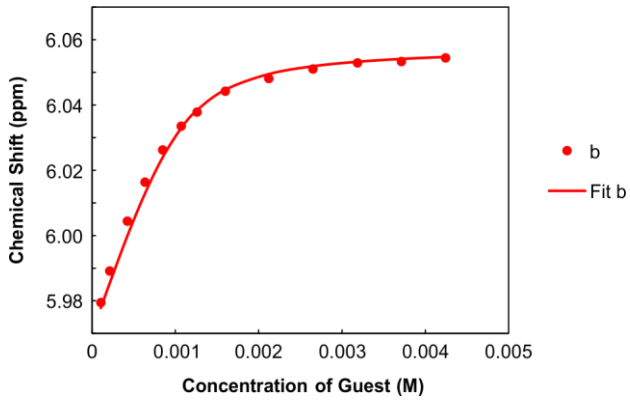

Figure 7. Chemical shift of the proton signal b of **1** upon incremental amounts of **3** (circles) and fit of the titration data to a theoretical binding model considering the *cis*/*trans* equilibrium and the exclusive formation of the *cis*-rotamer⊂**1** complex (line).

The fact that the *cis*-rotamer is present in solution to a significant extent (32%) is the main reason for the observed coincidence between the binding constant values estimated using the two binding models, that is K_a (*cis*-**3**⊂**1**) ~ K_{app}. We will show below that when the *cis*-rotamer is present in solution at low levels, the mathematical analyses of the titration data using the two binding models will produce very different values for K_a (*cis*-rotamer⊂**1**) and K_{app}.

Next, we performed a reverse titration of *N*-phenyl formamide **3** with receptor **1** (Figure 8). The ^{1}H NMR spectrum of a 1.2 mM solution of **3** containing just 0.05 equiv. of **1** (Figure 8b) showed the formyl proton of the *trans*-**3** rotamer as a sharp singlet resonating at the same chemical shift as in the absence of **1**. On the contrary, the formyl singlet assigned to the *cis*-**3** rotamer was not detectable at this stage of the titration. This observation indicated that while the equilibrium

involving the two free rotamers of **3** displayed slow chemical exchange on the chemical shift timescale, the *cis*-**3** rotamer was also involved in a binding equilibrium, probably with bound *cis*-**3**, featuring intermediate chemical exchange on the chemical shift timescale. The intermediate kinetics of the latter chemical exchange process produced broadening beyond detection for the formyl proton in the *cis*-**3** rotamer. This result also provides irrefutable support to the selective binding of the *cis*-**3** rotamer by receptor **1**.

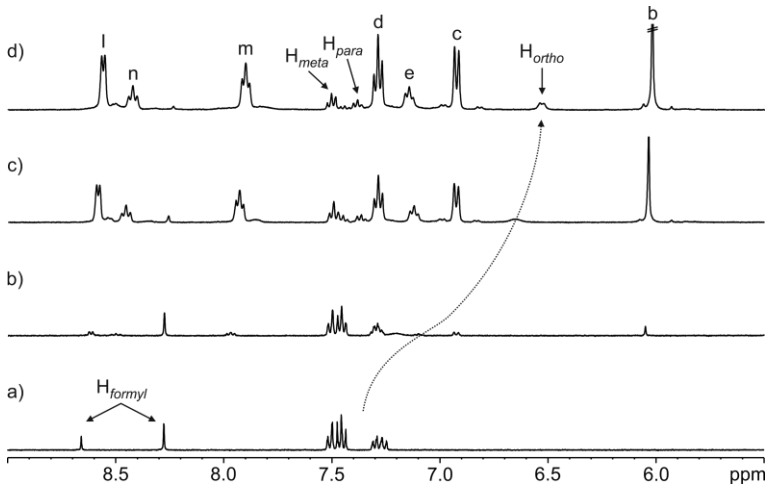

Figure 8. Selected region of the ^{1}H NMR (400 MHz, D_2O, 298 K) spectra of the titration of **3** with **1**: a) 0; b) 0.05; c) 1.0 and d) 2.0 equiv. In a) the H_{formyl} signals correspond to *cis*-**3** (left) and *trans*-**3** (right) providing a 32:68 ratio. In d) the *ortho*-, *meta*-, and *para*-phenyl protons of bound **3** are also indicated. See Scheme 2 and Figure 2 for proton assignments.

In complete agreement with the previous statement, an increase in the concentration of **1** did not affect the appearance and chemical shift value of the formyl proton signal for the *trans*-**3** rotamer, however, its intensity decreased. We also observed an increase in intensity of three aromatic signals, two triplets moving downfield and one doublet that shifted upfield. We assigned these signals to the protons of the *N*-phenyl group of the *cis*-**3** rotamer, which are involved in a fast chemical exchange on the chemical shift timescale between its free and bound states. The different kinetics of the chemical exchanges experienced by the protons of the *cis*-**3** rotamer, that is, the formyl proton is involved in an intermediate exchange and the aromatic protons are involved in a fast exchange, result from notable different CISs. The formyl proton of bound *cis*-**3** is included in the aromatic cavity of **1** experiencing a strong magnetic shielding exerted by the *meso*-phenyl substituents. We assigned a broad signal resonating at δ = 5.32 ppm to the formyl proton of bound *cis*-**3**. The computationally determined chemical shift value (DFT level of theory) of this proton in the inclusion complex *cis*-**3**⊂**1** is in complete agreement with the assignment.

On the other hand, the *N*-phenyl unit of bound *cis*-**3** resides almost completely outside of the aromatic cavity of **1**, with its *ortho*-protons being the only ones affected by the shielding effect (Figure 8d).

In order to evaluate the scope of the conformational selectivity featured by tetra-phenyl calix[4]pyrrole receptor **1** in the binding of other formamides, we investigated the complexation of **1** with *N*-methyl-*N*-phenyl formamide **5**. Based on the integral values of the two separate formyl protons, formamide **5** is present in water as an 82:18 *cis*/*trans* mixture of rotamers (*K* (*cis*-**5**/*trans*-**5**) = 4.56).

The direct ^{1}H NMR titration of **1** with incremental amounts of **5** showed an analogous behaviour with respect to the chemical shift changes of the proton signals of receptor **1** to the one previously described for **3**. The mathematical analysis of the titration data using the binding model that considers the equilibrium between the rotamers and the exclusive observation of a 1:1 complex with the *cis*-**5** isomer allowed us to estimate that the affinity constant value K_a (*cis*-**5**⊂**1**) must be larger than 10^4 M^{-1}. We also performed an ITC titration experiment for formamide **5** and calix[4]pyrrole **1** (Figure 9). The calculated apparent binding constant was 8.6±0.1 x 10^3 M^{-1}, a value that is in line with the estimated one from the ^{1}H NMR titration analysis. The ITC results showed that the binding process was enthalpically driven (ΔH = -7.11±0.04 kcal·mol^{-1}) and entropically opposed ($-T\Delta S$ = 1.75±0.04 kcal·mol^{-1}). Clearly, this thermodynamic signature is not the expected one for purely hydrophobic binding.[40]

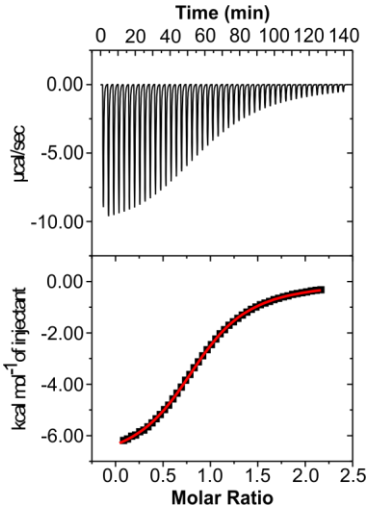

Figure 9. Top panels show raw data (heat *vs.* time) for the titration of guest into the host: **5**⊂**1** (H_2O). Titration was performed at 298 K. Bottom panels represent integrated data fitted to the theoretical binding isotherm (red line) for a 1:1 binding model.

We also performed a reverse titration by adding increasing amounts of **1** to a 2.9 mM water solution of **5**. The proton signals assigned to the *trans*-**5** rotamer did not experience noticeable chemical shift changes. In contrast, those of the *cis*-**5** counterpart, specially the formyl proton and the methyl protons, moved significantly upfield. From these titration data, we could estimate the CISs experienced by these protons because, although their signals broadened beyond detection in the initial and middle phases of the titration, they became observable again in the presence of 2 equiv. of **1**. In the *cis*-**5**⊂**1** complex, the formyl group resonates at δ = 5.01 ppm ($\Delta\delta$ = -3.39 ppm) and the methyl resonates at δ = 1.25 ppm ($\Delta\delta$ = -2.07 ppm). The large calculated CISs confirm the deep inclusion of *cis*-**5** in the aromatic cavity of **1**.

A 2D NOESY experiment showed intermolecular cross-peaks between the singlet of the methyl protons of bound *cis*-**5** and the aromatic protons (H^c and H^d) of the *meso*-phenyl substituents of the calix[4]pyrrole **1** (Figure 10). The computed chemical shift values of the protons of bound *cis*-**5** in the *cis*-**5**⊂**1** complex are in agreement with the experimental ones.

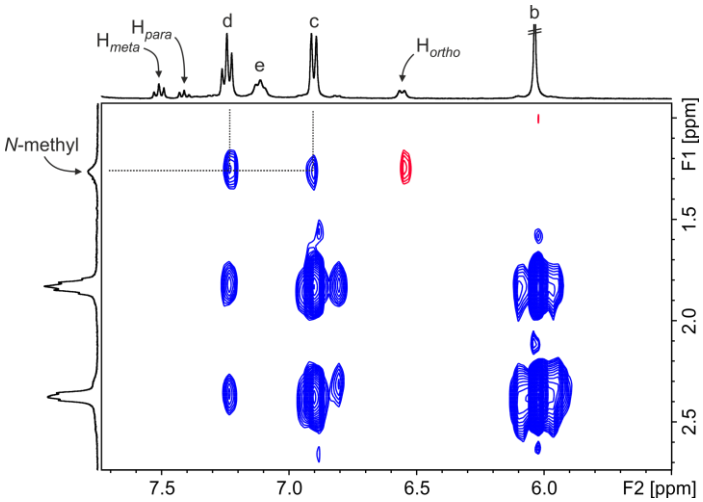

Figure 10. Selected region of the 2D ^{1}H-^{1}H NOESY NMR (400 MHz, D_2O, 298 K, t_{mix} = 0.4 s) spectrum of *N*-methyl-*N*-phenyl formamide **5** and calix[4]pyrrole **1** (2:1 ratio).

We also assessed the affinity constant of calix[4]pyrrole **1** for *N*-methyl formamide **6**. Formamide **6** is present in water as an 8:92 mixture of *cis*/*trans* rotamers. Nevertheless, molecular modelling studies (Figure 11) and the previous results obtained in the binding of the secondary and tertiary formamides **3** and **5**, respectively, strongly supported the inclusion of both isomers of **6** in receptor **1**. The energy minimized 1:1 inclusion complexes, *cis*-**6**⊂**1** and *trans*-**6**⊂**1**, featured close to isoenergetic values (*ca.* 146 kcal·mol^{-1}).

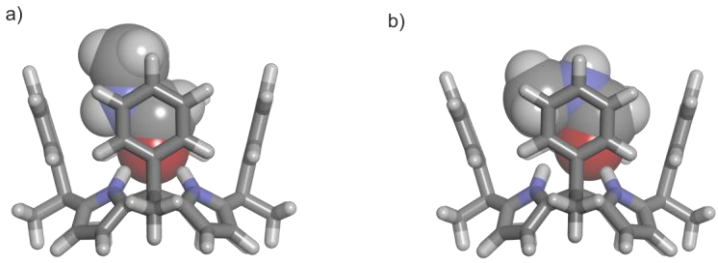

Figure 11. Energy minimized structures (PM3, water COSMO model as implement in SCIGRESS Version FJ 2.6) of the inclusion complexes: a) *cis*-**6**⊂**1** and b) *trans*-**6**⊂**1**. Calix[4]pyrrole **1** is shown in stick representation and amides (*cis*-**6** and *trans*-**6**) as CPK models. Water-solubilizing groups were pruned to methyl groups to ease the calculations.

Therefore, the ^{1}H NMR titration data for the interaction of **1** with **6** were analyzed using a simple 1:1 binding model obtaining a good fit and returning an affinity constant value of K_{app} (**6**⊂**1**) = 4.4 x 10^3 M^{-1}. The removal of the phenyl group in **6** compared to **5** slightly diminished the binding affinity for receptor **1**. Probably, this difference is caused by a combination of reduction in hydrophobicity and the hydrogen-bonding accepting character of the oxygen atom in formamide **6** (secondary *vs*. tertiary).

In agreement with this hypothesis, the addition of an extra methyl group in *N*,*N*-di-methyl formamide **7** increased its binding affinity for **1**, compared to **6**, placing it at the same level observed for the analogous but more lipophilic *N*-phenyl derivatives **3** and **5**.

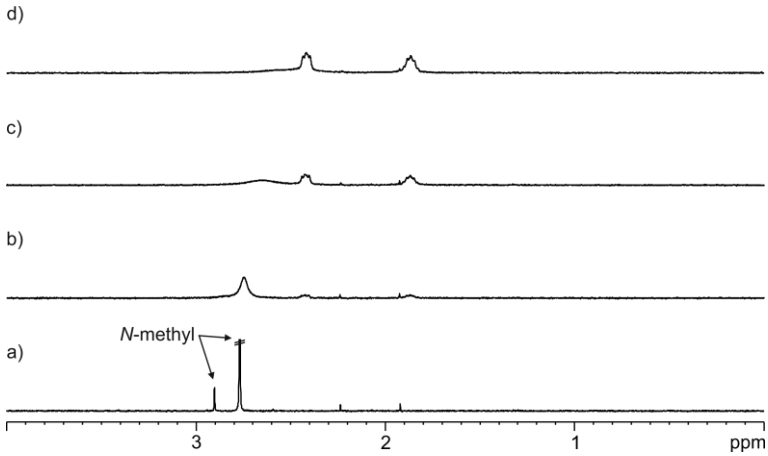

Figure 12. Selected region of the ^{1}H NMR (400 MHz, D_2O, 298 K) spectra of the titration of **6** with **1**: a) 0; b) 0.05; c) 0.2 and d) 0.4 equiv. In a) the *N*-methyl signals correspond to *cis*-**6** (left) and *trans*-**6** (right) providing 8:92 ratio.

It is worth noting that in the reverse ^{1}H NMR titration of *N*-methyl formamide **6** with receptor **1**, after the first addition of the receptor, the separate methyl proton signals of the two rotamers of **6** coalesce into a broad singlet that shifted upfield upon increasing the concentration of **1** (Figure

12). This result clearly supports the binding of two rotamers of **6**, which are involved in a chemical exchange equilibrium with the free counterparts featuring fast/intermediate dynamics on the chemical shift timescale.

Also note that, in the examples of *N*-phenyl formamides **3** and **5**, only the proton signals assigned to the *cis*-rotamer experienced broadening and chemical shift changes. We used this observation as evidence of the conformational selectivity in the binding process. The results described above indicate that receptor **1** might be considered as a minimal synthetic chaperone selecting the *cis*-conformation of the bound *N*-phenyl formamides and increasing their relative concentration in solution in the bound form.

Table 1. *Cis*/*trans* rotamer ratio in water at 298 K for the formamides used as guests in this study and binding constant values (M^{-1}) of the 1:1 inclusion complexes with receptor **1**. See Figure 2 for the line-drawing of the molecular structures of the amides.

Formamides	R^1	R^2	*cis*/*trans* ratio	K_a (*cis*⊂**1**)[a]	K_{app}[b]	$K_{a(1:1)}$[b]
3	H	Ph	32:68	> 10^4	> 10^4	
4	Ph	Ph	n.a.			< 10
5	Me	Ph	82:18	> 10^4	> 10^4	
6	H	Me	8:92		4.4 x 10^{3}[c]	
7	Me	Me	n.a.			> 10^4

[a] Theoretical binding model considering the *cis*/*trans* equilibrium between amide rotamers and the exclusive formation of the *cis*⊂**1** complex was used; [b] using a 1:1 theoretical binding model and [c] weighted-average of K_a (*cis*⊂**1**) and K_a (*trans*⊂**1**). Errors (standard deviations) are estimated to be lower than 20%. n.a. = not applicable.

5.2.3 Binding studies of tetra-pyridinium tetra-phenyl **1** with acetamides in water

Molecular modelling studies

Molecular modelling studies suggested that acetamide **8** and the *cis*-rotamer of *N*-methyl acetamide **9**, as well as those of other secondary *N*-aryl amide derivatives like **10**-**13** (Figure 13), were suitable candidates for the inclusion in the aromatic cavity of **1** (Figure 14a). The modelled acetamides closely resembled the *cis*-rotamer of *N*-methyl formamides in terms of size complementarity with the dimensions of the aromatic cavity of **1** in the cone conformation.

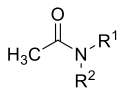

8; R^1 = H; R^2 = H
9; R^1 = H; R^2 = CH_3
10; R^1 = H; R^2 = Ph
11; R^1 = H; R^2 = 2'-CH_3Ph
12; R^1 = H; R^2 = 2',4'-di-CH_3Ph
13; R^1 = H; R^2 = 2',6'-di-CH_3Ph
14; R^1 = CH_3; R^2 = CH_3

Figure 13. Line-drawing structures of acetamides **8**-**14**. When applicable only the *cis*-rotamer is depicted. See Scheme 1 for the *cis*/*trans* equilibrium.

In contrast, tertiary *N*,*N*-di-methyl acetamide **14** presents an additional methyl group to be included in the cavity of **1**. The energy minimized structure of the **14⊂1** complex displayed a severe distortion of the cone conformation of the receptor owing to steric clashes between the *meso*-phenyl substituents and the two included methyl groups of the amide (Figure 14b).

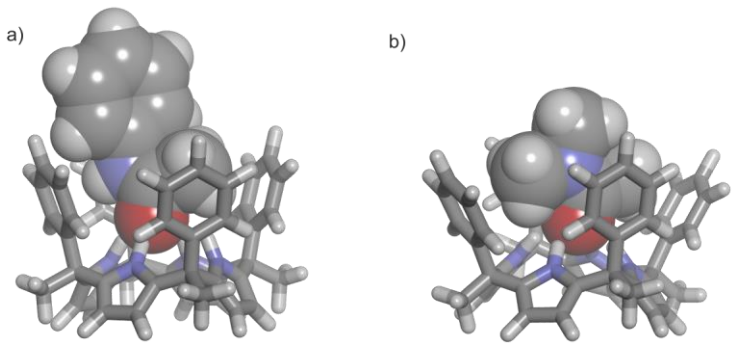

Figure 14. Energy minimized structures (PM3, water COSMO model as implement in SCIGRESS Version FJ 2.6) of the inclusion complexes: a) *cis*-**10⊂1** and b) **14⊂1**. Calix[4]pyrrole **1** is shown in stick representation and amides (*cis*-**10** and **14**) as CPK models. Water-solubilizing groups were pruned to methyl groups to ease the calculations.

^{1}H NMR spectroscopy titrations

The titration of receptor **1** with increasing amounts of acetamide **8** afforded exclusively the **8⊂1** complex and, accordingly, it was analyzed using a simple 1:1 binding model returning K_a = 6.8 x 10^3 M^{-1}. The magnitude of the binding constant is in agreement with the value determined for the isosteric *N*-methyl formamide K_a (**6⊂1**) = 4.4 x 10^3 M^{-1}.

In water, *N*-methyl acetamide **9** and *N*-phenyl acetamide **10** displayed *cis*/*trans* isomeric ratios of 2:98 and 1:99, respectively, based on the integral values of their methyl acetamide proton signals. In particular, the assignment of the methyl proton signal for the *cis*-**10** rotamer to a small singlet resonating at δ = 1.90 ppm was confirmed by magnetization transfer experiments (see Experimental Section). The titration data of **1** with both acetamides, **9** and **10**, were analyzed in an analogous manner. For the sake of brevity, we will only describe in detail the titration experiments performed with **10** and the corresponding data analyses.

The incremental addition of **10** (up to 15 equiv.) to a 1.2 mM solution of **1** in water produced very small changes in the chemical shift values of the diagnostic proton signals of the receptor (H^b, H^c, H^d and H^e) used for signalling of complex formation in the formamide series (see Experimental Section).

We also performed a reverse ^{1}H NMR titration experiment adding incremental amounts of calix[4]pyrrole **1** to a 1.5 mM solution of **10** (see Experimental Section). As expected, the proton signals of *trans*-**10** did not experience chemical shift changes and only a small reduction of their intensities was observed. Unfortunately, it was not possible to accurately quantify the amount of *trans*-**10** rotamer that has been isomerized into the *cis*-**10** counterpart using the integral values of selected signals in the acquired ^{1}H NMR spectra due to its selective complexation.

We rationalize these results assuming that, as expected, receptor **1** does not bind the *trans*-**10** rotamer and that, owing to the low concentration of the *cis*-**10** rotamer in solution, the formation of the *cis*-**10**⊂**1** complex (in the direct and reverse titrations) takes place to a reduced extent. To verify our hypothesis, we simulated the speciation profile of a direct titration considering *K* (*cis*-**10**/*trans*-**10**) = 0.01 and K_a (*cis*-**10**⊂**1**) = 1.0 x 10^4 M^{-1}. Surprisingly to us, the simulated profile indicated a significant formation of the *cis*-**10**⊂**1** complex in the concentration range used for the experimental titration (see Experimental Section).

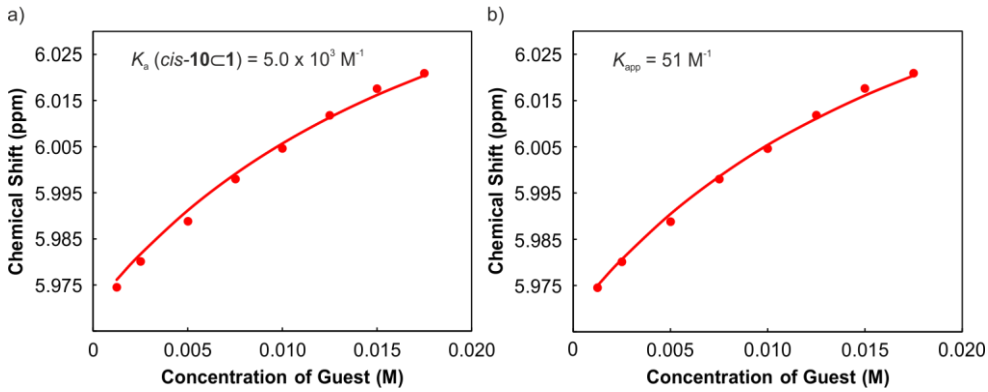

Figure 15. Chemical shift of the proton signal b of **1** upon incremental amounts of **10** (circles) and fit of the titration data (lines): a) theoretical binding model considering the *cis*/*trans* equilibrium and the exclusive formation of *cis*-rotamer⊂**1** and b) simple 1:1 binding model.

Owing to the low saturation levels of complex formation attained during the direct and reverse titration of **1** with **10**, we could not determine an accurate binding constant value for the *cis*-**10**⊂**1** complex. Nevertheless, we obtained a reasonable fit of the experimental data using the theoretical binding model that considers the equilibrium between rotamers and the exclusive formation of a 1:1 complex with the *cis*-isomer. The fit was performed by fixing the values of *K* (*cis*-**10**/*trans*-**10**), δ_{free} and δ_{bound} (0.01; 5.97 ppm and 6.08 ppm). We considered that the chemical shift value of the

β-pyrrole protons in the *cis*-**5**⊂**1** complex was a good estimate for the δ_{bound} value in *cis*-**10**⊂**1**. The only variable to refine was K_a (*cis*-**10**⊂**1**). The best fit was obtained assuming K_a (*cis*-**10**⊂**1**) = 5.0 x 10^3 M^{-1} (Figure 15a). This result suggest a reduction in the binding constant of the inclusion of the *cis*-rotamer of acetamide **10** compared to the isosteric *N*-methyl-*N*-phenyl formamide **5**. Remarkably, the mathematical analysis of the same titration data using the simple 1:1 binding model provided an apparent binding constant of 51 M^{-1} (Figure 15b).

This example showcases the significant difference in the calculated values of K_a (*cis*-**10**⊂**1**) and K_{app} when the *cis*-rotamer is present in solution at very low concentration. It also serves to justify the use of the elaborated binding model in the estimation or accurate determination of K_a (*cis*-rotamer⊂**1**) values.

Table 2. *Cis*/*trans* rotamer ratio in water at 298 K for the acetamides used as guests in this study and binding constant values (M^{-1}) of the 1:1 inclusion complexes with receptor **1**. See Figure 2 for the line-drawing of the molecular structures of the amides.

Acetamides	R^1	R^2	*cis*/*trans* ratio	K_a (*cis*⊂**1**)[a]	K_{app}[b]	$K_{a(1:1)}$[b]
8	H	H	n.a.			6.8×10^3
9	H	Me	2:98	1.2×10^4	2.1×10^2	
10	H	Ph	1:99	5.0×10^3	51	
14	Me	Me	n.a.			27

[a] Theoretical binding model considering the *cis*/*trans* equilibrium between amide rotamers and the exclusive formation of the *cis*⊂**1** complex was used and [b] using a 1:1 theoretical binding model. Errors (standard deviations) are estimated to be lower than 20%. n.a. = not applicable.

We also determined the *cis*/*trans* ratios of the *N*-aryl acetamide derivatives **11**-**13** in water (Figure 13). We expected to observe an increase in the amount of the *cis*-rotamer compared to **10** as was previous described in organic solvents.[20] Unfortunately, in water, the percentage of the *cis*-isomers for the series of acetamides **11**-**13** did not increase over 3% (see Experimental Section). This limitation precluded the undertaking of the experimental quantification of the corresponding K_a (*cis*-rotamer⊂**1**) values for these *N*-aryl acetamides.

Finally, the affinity constant value of receptor **1** for *N*,*N*-di-methyl acetamide **14** was determined to be K_a (**14**⊂**1**) = 27 M^{-1} using a simple 1:1 binding model. This value supports the conformational selectivity of the receptor in the binding of *cis*-**9**. It also serves to quantify in three orders of magnitude the selectivity expressed by receptor **1** in the binding of *N*,*N*-di-methyl formamide **7** compared to the homologated and more hydrophobic *N*,*N*-di-methyl acetamide **14**.

5.2.4 Binding of a long-chain di-formamide to a water-soluble super aryl-extended calix[4]pyrrole

We envisaged that the thermodynamic and kinetic stability of formamide⊂calix[4]pyrrole complexes could be enhanced using a water-soluble super aryl-extended calix[4]pyrrole receptor and a long-chain formamide. Octa-pyridinium super aryl-extended calix[4]pyrrole **15** features a deeper aromatic cavity than the aryl-extended counterpart **1**, enhancing the hydrophobic effect (Figure 16a).[41] In the same vein, a long *N*-alkyl substituent in the formamide guest increases its hydrophobicity and leads to an increase in the number of attractive interactions established in the host-guest complex.

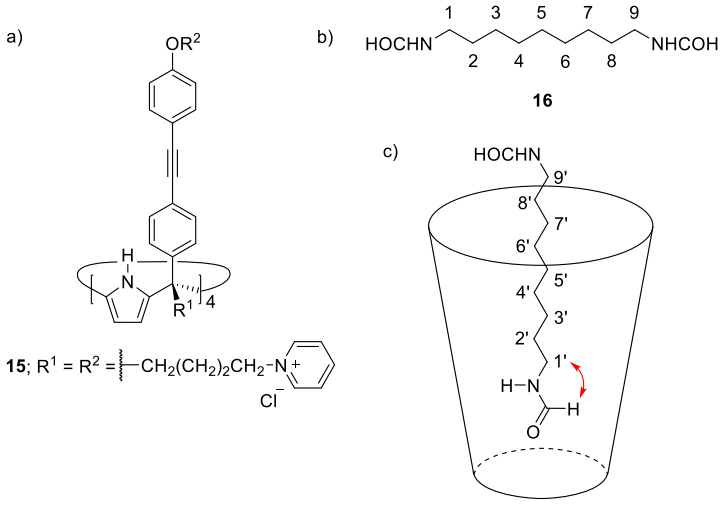

Figure 16. Line drawing structures: a) octa-pyridinium **15** and b) di-formamide **16**. c) Cartoon representation of the 1:1 inclusion complex, **16⊂15**. Bound formamide group of **16** to the calix[4]pyrrole core is the *cis*-rotamer. The proximity between the buried formyl hydrogen and the *α*-methylene protons is highlighted (double red arrow).

We selected di-formamide **16** having a linear *N*,*N*'-nonyl group for this study (Figure 16b). Di-formamide **16** is present in water as a mixture of three isomers: *trans*,*trans*, *trans*,*cis* and *cis*,*cis*. The ^{1}H NMR spectrum of **16** in D_2O shows a 20:80 *cis*/*trans* ratio, *K* (*cis*/*trans*) = 0.25, based on the integral values of the formyl proton signals. From this ratio, we calculated the isomerization constants of di-formamide **16**: *K* (*cis*,*trans*-**16**/*trans*,*trans*-**16**) = 0.5 and *K* (*cis*,*cis*-**16**/*cis*,*trans*-**16**) = 0.125. These constant values translate into the following statistical distribution of isomers: 64% *trans*,*trans*; 32% *trans*,*cis* and 4% *cis*,*cis*. The latter is rarely observed directly due to overlapped signals and its low intensity.

We probed the complexation of the octa-pyridinium **15** and the di-formamide **16** (Figure 16) using ^{1}H NMR spectroscopy. Owing to the limited solubility of **16** in D_2O, a solution of **16** was prepared in $(CD_3)_2SO$ and used for the titration experiment. The addition of 1 equiv. of di-formamide **16** to a millimolar solution of octa-pyridinium **15** in D_2O produced the sharpening of the proton signals of

the receptor. This observation suggests the lock of the receptor in the cone conformation. The proton signals of **16** appeared upfield shifted with respect to those for free **16** in solution. The signal pattern for the protons of bound **16** was not symmetric owing to the different magnetic environments experienced along the super aryl-extended cavity. The addition of 2 equiv. of **16** did not produce further changes in the signals of the bound components, but produced a new set of proton signals corresponding to the protons of free di-formamide (Figure 17). The observation of separate sets of signals for the protons of free and bound di-formamide **16** was indicative of slow chemical exchange on the ^{1}H NMR chemical shift timescale. Taken together, these observations indicated that **15** and **16** form a thermodynamically and kinetically stable 1:1 inclusion complex for which we estimated a binding constant value larger than 10^4 M^{-1}.

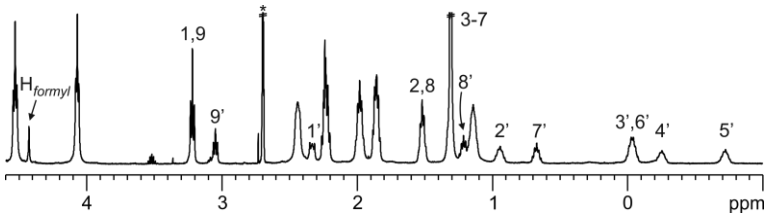

Figure 17. Selected region of the ^{1}H NMR (500 MHz with cryoprobe, D_2O, 298 K) spectrum of di-formamide **16** and octa-pyridinium **15** (2:1 ratio). Primed letters correspond to proton signals of bound *trans*,*cis*-**16**. *Residual solvent peak.

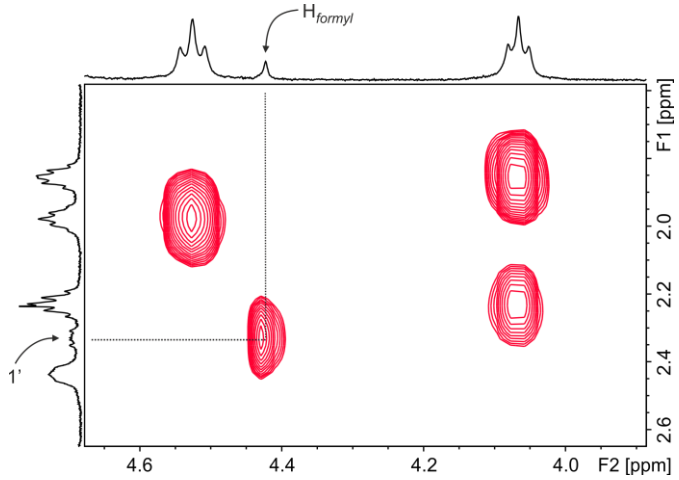

Figure 18. Selected region of the 2D ^{1}H-^{1}H ROESY NMR (400 MHz, D_2O, 298 K, spin-lock = 0.4 s) spectrum of calix[4]pyrrole **15** and di-formamide **16** (2:1 ratio).

Analysis of the ^{1}H NMR titration spectra revealed the binding geometry of the **16⊂15** complex. The *α*-methylene protons ($H^{1'}$) with respect to one formamide group appeared at δ = 2.33 ppm ($\Delta\delta$ = -0.89 ppm). On the other hand, the *α*-methylene protons ($H^{9'}$) with respect to the other formamide showed a reduced upfield shift, $\Delta\delta$ = -0.17 ppm. These observations indicated that one end of the

di-formamide **16** is deeply included in the aromatic cavity of **15**, whereas the other end is near the top of the receptor's cavity.

2D NOESY and ROESY experiments were consistent with an extended conformation of the bound di-formamide **16** (see Experimental Section). The signal of the buried formyl proton (H_{formyl}) appeared at δ = 4.43 ppm ($\Delta\delta$ = -3.54 ppm) and showed a selected cross-peak with the α-methylene protons ($H^{1'}$) in the 2D ROESY spectrum (Figure 18). This observation confirmed that the formamide group of **16** bound to the calix[4]pyrrole core of **15** adopts the *cis*-conformation. This finding also supports the selective binding of the *cis*-rotamer of the formamides by aryl-extended and super aryl-extended calix[4]pyrrole receptors. The proton signal of the formamide group of **16** at the top of the receptor's cavity did not display noticeable chemical shift changes. The binding geometry of the bound formamide is depicted in Figure 16c.

The selective conformational binding of the *cis*-rotamer for one of the formamide groups of **16** produces two possible complexes: *trans*,*cis*-**16⊂15** and *cis*,*cis*-**16⊂15** in a statistical 80:20 ratio, respectively. The more intense proton signals correspond to the *trans*,*cis*-**16⊂15** complex. The proton signals of *cis*,*cis*-**16⊂15** are expected to display low intensity and possibly overlap with those of the *trans*,*cis*-counterpart.

5.2.5 Assessment of the binding constants from the ^{1}H NMR titration data of the water-soluble tetra-phenyl calix[4]pyrrole **1** using a complete binding model

The ^{1}H NMR titration data obtained from the addition of incremental amounts of the guest to a solution of the host was fit to a theoretical 1:1 binding model using HypNMR 2008 software Version 4.0.66. The chemical shifts for the proton signals of the free receptor (δ_{free}) were fixed. The binding constant (K_a) and the chemical shifts for the proton signals of the bound host (δ_{bound}) were refined as variables. The HypNMR software returned the values for the variable parameters (K_a and δ_{bound}).

For non-symmetrical amide derivatives, the binding constants returned from the fit using HypNMR software to a 1:1 binding model are apparent values (K_{app}). The equilibrium between rotamers and the exclusive binding of the *cis*-rotamer cannot be implemented in the binding model of the software.

In order to simulate speciation profiles of titrations taking into account the equilibrium between the two non-symmetrical amide rotamers and the exclusive binding of the *cis*-rotamer by the receptor, we used the SPECFIT software Version 3.0.40, in particular the differential kinetics module. We introduce the theoretical kinetic model shown below that takes in consideration the existence of four rate constants that are pairwise related by two reversible equilibrium constants:

1) *trans* $\rightarrow$ *cis*; k_1

2) *cis* $\rightarrow$ *trans*; k_2

3) *cis* + **1** $\rightarrow$ *cis*⊂**1**; k_3

4) *cis*⊂**1** $\rightarrow$ *cis* + **1**; k_4

K (*trans*/*cis*) = k_1/k_2 and K_a (*cis*⊂**1**) = k_3/k_4

k_1 and k_2 are the rate constant values for the isomerization process between the *trans* and *cis* non-symmetrical amides. Assuming a typical energy barrier of 20 kcal·mol^{-1} for the *trans* to *cis* interconversion this translates into a k_1 = 1.3 x 10^{-2} s^{-1}. The value of k_2 is calculated based on the known relationship of rate constants and equilibrium constant, K (*trans*/*cis*) = k_1/k_2. For example, if K (*trans*/*cis*) determined experimentally is 99, then k_2 = 1.3 x 10^{-2} s^{-1}/99 = 1.3 x 10^{-4} s^{-1}. With respect to the kinetics of the binding process, we assume a dissociation rate k_4 in the order of 3 s^{-1}. For a K_a (*cis*⊂**1**) = 10^4 M^{-1} it will translate into k_3 = 10^4 M^{-1} x 3 s^{-1} = 3 x 10^4 M^{-1}·s^{-1}. We also need to provide the software with initial concentrations of the amide and the receptor. We used an equilibration time of 10 s for the kinetic system to reach the equilibrium and return the concentration of all the species at equilibrium. We calculated the theoretical speciation at each point of the experimental titration assuming different values of K_a (*cis*⊂**1**) (concentration of **1** is constant for all simulated speciation but the amide concentration increases in the case of a direct titration).

The concentrations of the free (H_{free}) and the bound host (H_{bound}) determined from the theoretical speciation at each point of the titration were used to calculate the theoretical chemical shift values (δ_{calc}) by means of the following equation:

5) δ_{calc} (ppm) = [x(H_{free}) x δ_{free}] + [x(H_{bound}) x δ_{bound}]; x(H_{free}) = [H_{free}]/[H] and x(H_{bound}) = [H_{bound}]/[H]

x(H_{free}) and x(H_{bound}) are the molar fractions of free host (H_{free}) and the complex (H_{bound}), respectively. The value of δ_{free} was obtained from the ^{1}H NMR spectra of the free host. The value of δ_{bound} is the chemical shift of the fully bound host determined from the fit to a simple 1:1 model.

The series of calculated chemical shifts (δ_{calc}) produced different theoretical binding isotherms as a function of the K_a (*cis*⊂**1**) value considered in the simulation. The theoretically predicted isotherms were compared to the experimentally measured one, which is defined by the observed chemical shift values (δ_{obs}) experienced by selected proton signals during the titrations.

We performed multiple isotherm simulations for each one of the experimental titrations to be analyzed. We simply varied the value of K_a (*cis*⊂**1**) until obtaining a good fit between the theoretically and experimentally determined binding isotherms. The goodness of each fit was evaluated from the sum of the residual values and its simple visual inspection.

5.3 Conclusions

In summary, we report the synthesis of a tetra-*α* aryl-extended calix[4]pyrrole **1** bearing four *meso*-(3-pyridiniumpropyl) groups providing water solubility. We studied the binding of a series of primary, secondary and tertiary formamides and acetamides with receptor **1** in water. The mathematical analyses of the ^{1}H NMR titrations of *N*-phenyl formamides **3** and **5** using a simple 1:1 binding model, K_{app}, or a more elaborated theoretical model including the *cis*/*trans* isomerization and the exclusive formation of the *cis*-rotamer⊂**1** complex, K_a (*cis*⊂**1**), returned similar values, which were typically larger than 10^3 M^{-1}. We demonstrated that calix[4]pyrrole **1** selectively binds the *cis*-rotamers of these two formamides. In contrast, both rotamers of formamides **6** and **7**, the *N*-methyl analogues of **3** and **5**, are bound by receptor **1** without substantial changes in affinity values. Remarkably, primary (**8**) and secondary (**9** and **10**) acetamides are also bound in water by receptor **1** with high affinities. For the secondary acetamides, **9** and **10**, receptor **1** also features conformational selectivity for their *cis*-rotamers. In these examples, the mathematical analyses of the ^{1}H NMR titration data for the secondary acetamides provided very different binding constant values depending on the binding model used. We showed that this result is a direct consequence of the low level of *cis*-rotamer present in solution. *N*,*N*-Di-phenyl formamide **4** and *N*,*N*-di-methyl acetamide **14** show a reduced affinity for **1** owing to size complementary issues with the receptor's polar cavity. Taken together, the reported findings demonstrate that calix[4]pyrrole **1** functions as a minimal chaperone analogue increasing the amount of amide *cis*-rotamers in solution through selective binding. The reported association constant values for most of the amide⊂**1** complexes are among the highest reported to date for the binding of small polar molecules[38] and even small peptides[42,43,44,45,46,47] in water using synthetic receptors. The amides are bound in the functionalized aromatic cavity of calix[4]pyrrole **1** by a combination of hydrogen-bonding, NH-π and CH-π interactions and the hydrophobic effect.

Finally, we hypothesized that the elaboration of the aromatic cavity of water-soluble aryl-extended calix[4]pyrroles would have an impact on improving their recognition properties, affinity and selectivity, in the binding of the *cis*-rotamer of amides in water. In this regard, we showed that the octa-pyridinium super aryl-extended calix[4]pyrrole **15** efficiently binds the long-chain di-formamide **16** forming a thermodynamically and kinetically highly stable 1:1 inclusion complex in water.

5.4 Experimental Section

5.4.1 General information and instruments

Reagents and solvents were purchased from commercial sources and used without further purification unless otherwise stated. When required, dried and deoxygenated solvents supplied by a Solvent Purification System (SPS) were employed. Pyrrole was freshly distilled under vacuum prior to use. Methyltributylammonium chloride was purchased as aqueous solution, dried under vacuum and employed as a solid. Thin layer chromatography (TLC) was performed on silica gel 60 F254. Silica gel 60 Å for chromatography was employed in flash column chromatography. ^{1}H, $^{13}C\{^{1}H\}$, COSY, NOESY, HSQC and HMBC NMR spectra were recorded using a Bruker 400 UltrashieldTM (400 MHz for ^{1}H and 100 MHz for ^{13}C), Bruker Avance 500 UltrashieldTM (500 MHz for ^{1}H and 125 MHz for ^{13}C) or Bruker Avance 500 with cryoprobe (500 MHz for ^{1}H and 125 MHz for ^{13}C) spectrometers. Residual solvent peaks were employed for calibration of NMR spectra.[48] Mass spectrometry experiments were performed on a LCT Premier, Waters-Micromass ESI. FTIR measurements were carried out on a Bruker Optics ATR FTIR Alpha-p spectrometer equipped with a DTGS detector, KBr beam splitter at 4 cm^{-1} resolution.

5.4.2 Synthesis and characterization data

Tetra-phenyl tetra-(3-pyridiniumpropyl) calix[4]pyrrole 1: Tetra-chloro calix[4]pyrrole **2** (80 mg, 0.086 mmol, 1 equiv.) was dissolved in pyridine (20 mL) and protected from the light by covering the flask with foil. The mixture was stirred at 110°C under Argon atmosphere for 24 h. After that, the crude was concentrated and the solid was washed with acetone (2x5 mL), CH_2Cl_2 (2x5 mL) and hexane (2x5 mL). The solid was dried under high vacuum affording **1** as yellow solid (103 mg, 0.083 mmol, 96% yield). ^{1}H NMR (500 MHz, $(CD_3)_2SO$, 298 K): δ (ppm) = 9.08 (br s, 4H); 9.06 (dd, *J* = 6.7 Hz, *J* = 1.2 Hz, 8H); 8.60 (tt, *J* = 7.8 Hz, *J* = 1.2 Hz, 4H); 8.15 (dd, *J* = 7.8 Hz, *J* = 6.7 Hz, 8H); 7.25 (dd, *J* = 8.3 Hz, *J* = 7.3 Hz, 8H); 7.11 (tt, *J* = 7.3 Hz, *J* = 1.4 Hz, 4H); 6.80 (dd, *J* = 8.3 Hz, *J* = 1.4 Hz, 8H); 5.96 (d, *J* = 2.6 Hz, 8H); 4.53 (t, *J* = 7.1 Hz, 8H); 2.28-2.23 (m, 8H); 1.55-1.50 (m, 8H). $^{13}C\{^{1}H\}$ NMR (125 MHz, $(CD_3)_2SO$, 298 K): δ (ppm) = 145.6; 145.2; 144.6; 136.3; 128.2 (three signals); 127.0; 104.8; 60.5; 47.3; 36.6; 27.2. HRMS (ESI-TOF) m/z: $[M\text{-}2Cl]^{2+}$ Calcd for $C_{76}H_{76}Cl_2N_8$ 585.2780; Found 585.2801. FTIR *v* (cm^{-1}) = 3386; 3210; 3130; 3055; 2974; 2930; 2868; 1631; 1578; 1485; 1447; 1159; 767; 706; 684. M.p > 210°C (decompose).

Chapter 5

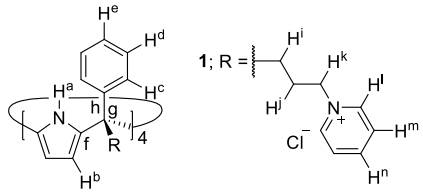

Figure 19. Line-drawing structure of tetra-*α* **1**.

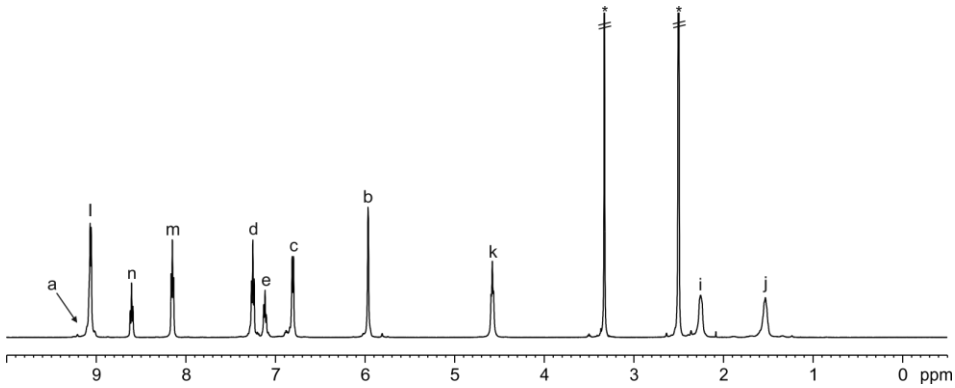

Figure 20. ^{1}H NMR (500 MHz, $(CD_3)_2SO$, 298 K) spectrum of tetra-*α* **1**. See Figure 19 for proton assignment. *Residual solvent peaks.

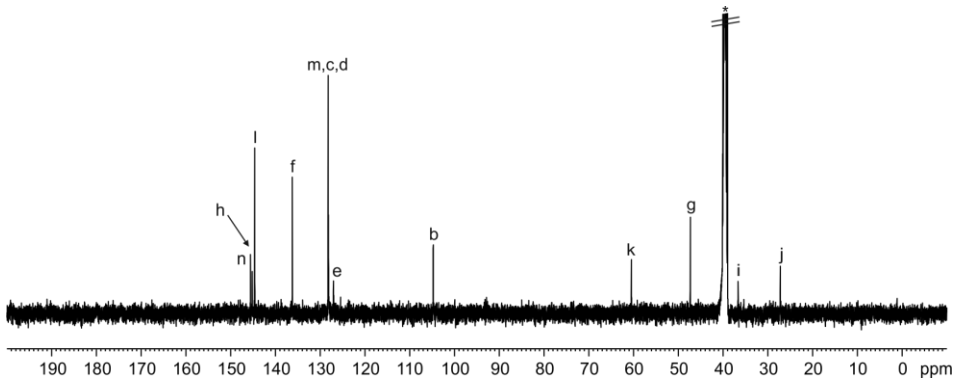

Figure 21. $^{13}C\{^{1}H\}$ NMR (125 MHz, $(CD_3)_2SO$, 298 K) spectrum of tetra-*α* **1**. See Figure 19 for carbon assignment. *Residual solvent peak.

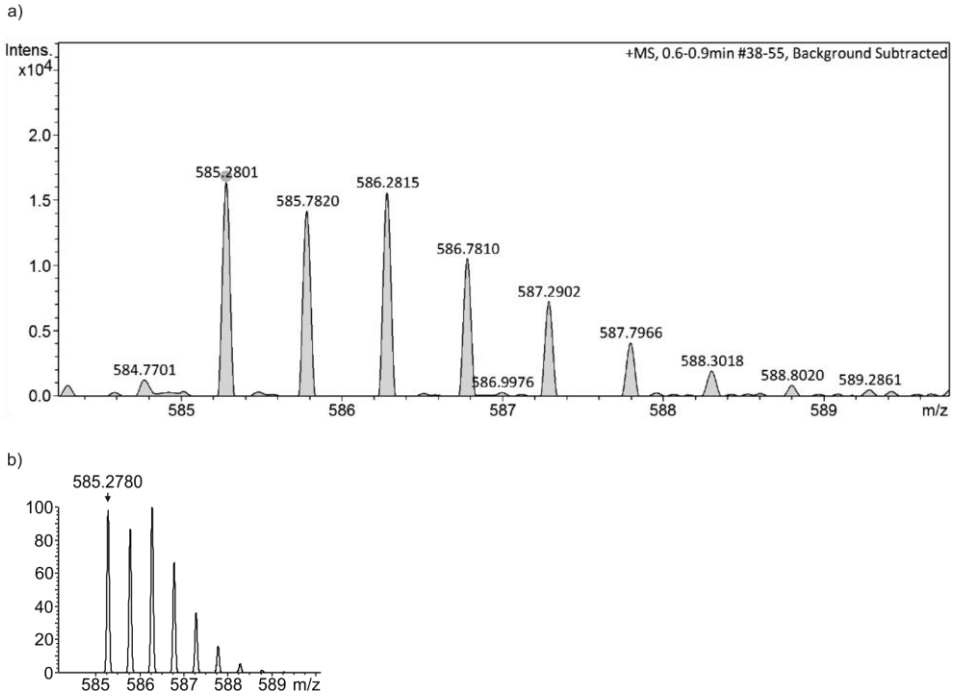

Figure 22. a) Experimental and b) theoretical isotopic distributions of $[M\text{-}2Cl]^{2+}$. The exact mass for the monoisotopic peak in a) and b) is indicated.

Tetra-phenyl tetra-(3-chloropropyl) calix[4]pyrrole 2: The compound was prepared following a procedure previously reported in the literature.[29]

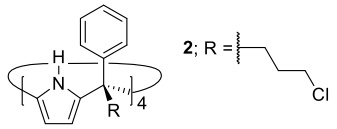

Figure 23. Line-drawing structure of tetra-*α* **2**.

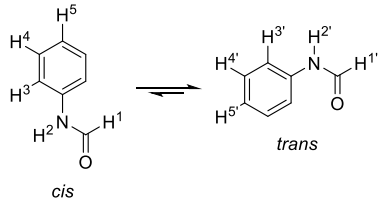

Figure 24. Conformational isomers of *N*-phenyl formamide **3**.

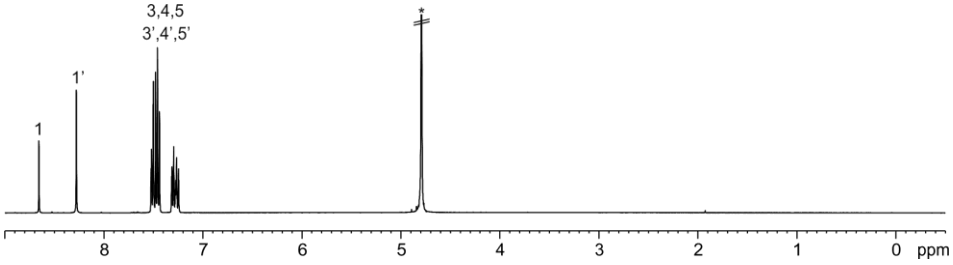

Figure 25. ^{1}H NMR (400 MHz, D_2O, 298 K) spectrum of **3**. See Figure 24 for proton assignment. *Residual solvent peak.

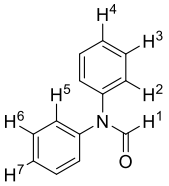

Figure 26. Line-drawing structure of *N*,*N*-di-phenyl formamide **4**.

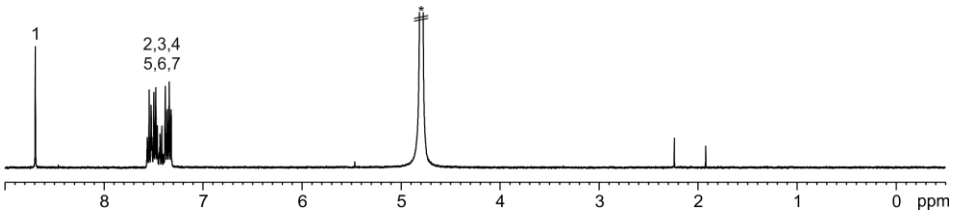

Figure 27. ^{1}H NMR (400 MHz, D_2O, 298 K) spectrum of **4**. See Figure 26 for proton assignment. *Residual solvent peak.

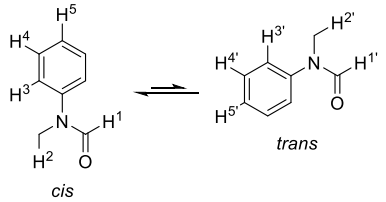

Figure 28. Conformational isomers of *N*-methyl-*N*-phenyl formamide **5**.

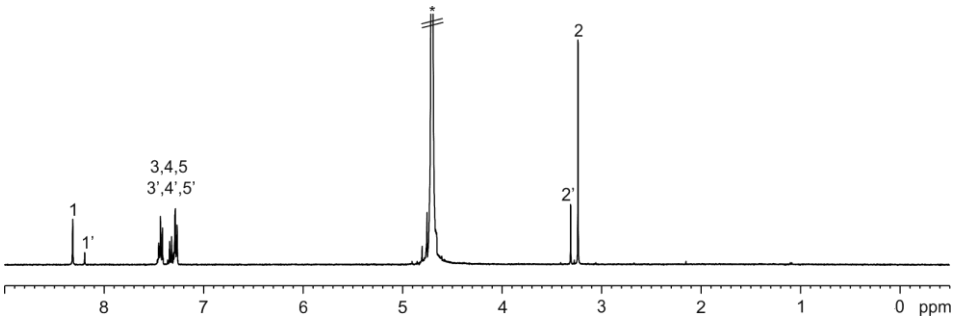

Figure 29. ^{1}H NMR (400 MHz, D_2O, 298 K) spectrum of **5**. See Figure 28 for proton assignment. *Residual solvent peak.

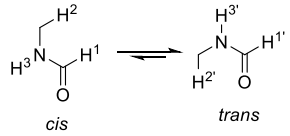

Figure 30. Conformational isomers of *N*-methyl formamide **6**.

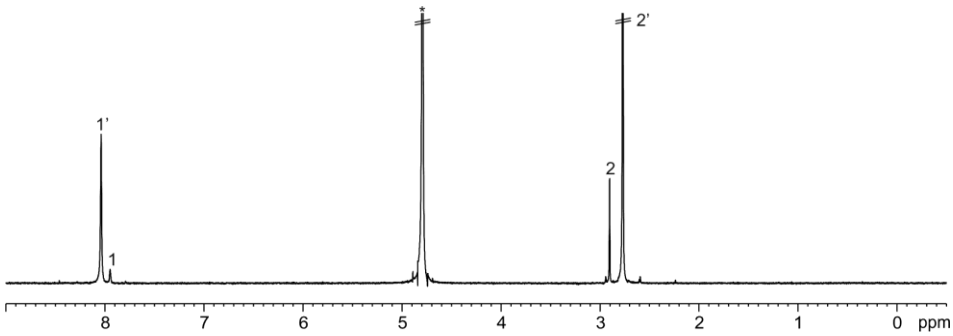

Figure 31. ^{1}H NMR (400 MHz, D_2O, 298 K) spectrum of **6**. See Figure 30 for proton assignment. *Residual solvent peak.

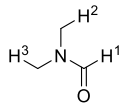

Figure 32. Line-drawing structure of *N*,*N*-di-methyl formamide **7**.

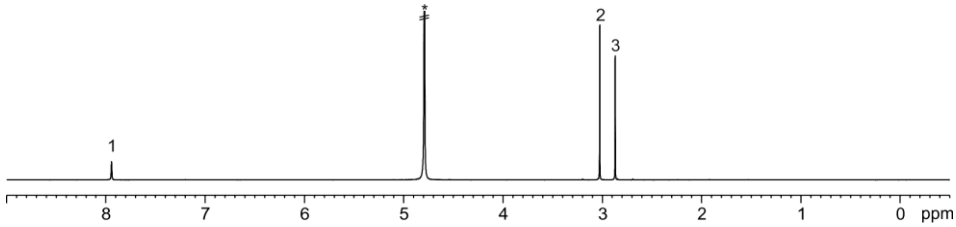

Figure 33. ^{1}H NMR (400 MHz, D_2O, 298 K) spectrum of **7**. See Figure 32 for proton assignment. *Residual solvent peak.

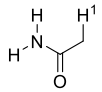

Figure 34. Line-drawing structure of acetamide **8**.

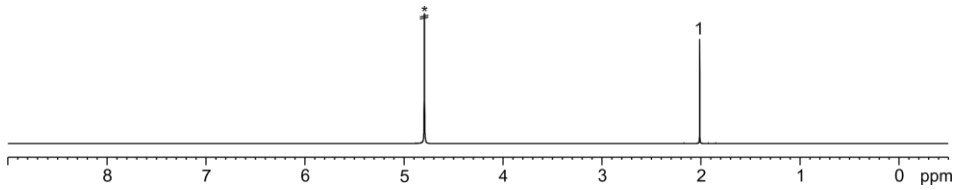

Figure 35. ^{1}H NMR (400 MHz, D_2O, 298 K) spectrum of **8**. See Figure 34 for proton assignment. *Residual solvent peak.

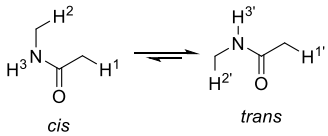

Figure 36. Conformational isomers of *N*-methyl acetamide **9**.

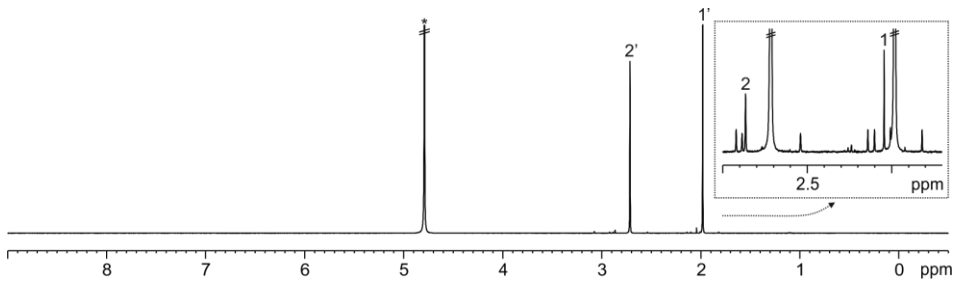

Figure 37. ^{1}H NMR (400 MHz, D_2O, 298 K) spectrum of **9**. See Figure 36 for proton assignment. *Residual solvent peak.

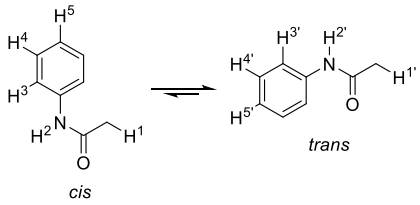

Figure 38. Conformational isomers of *N*-phenyl acetamide **10**.

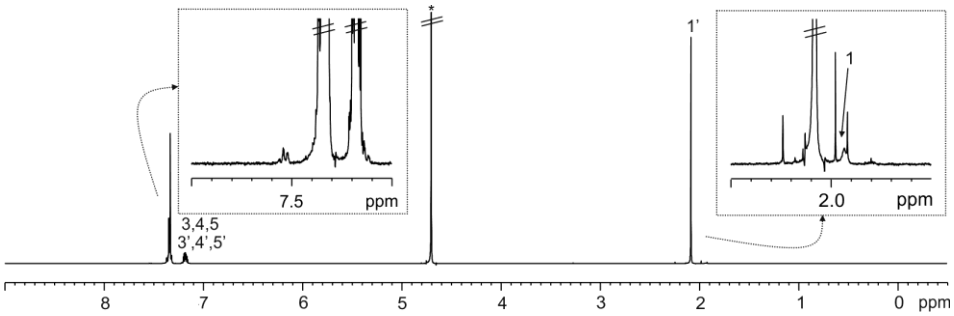

Figure 39. ^{1}H NMR (400 MHz, D_2O, 298 K) spectrum of **10**. See Figure 38 for proton assignment. The calculated chemical shift for the CH_3 protons (H^1) of *cis*-**10** is 1.77 ppm, which is in agreement with the assignment of the proton signals in the spectrum. *Residual solvent peak.

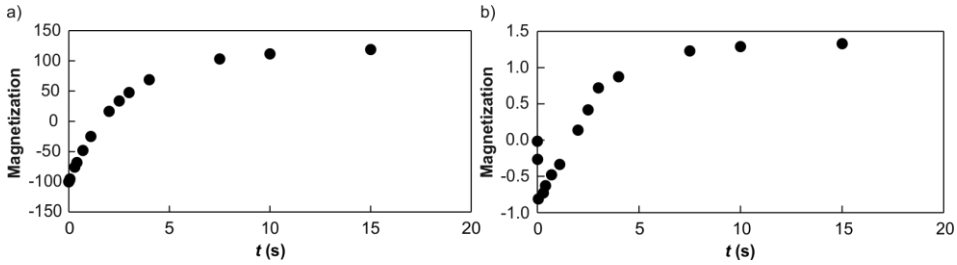

Figure 40. Magnetization *vs.* time (s) for the selective inversion recovery (SIR) NMR experiment of **10**: a) *trans*-rotamer and b) *cis*-rotamer. The signal at 2.10 ppm ($H^{1'}$) corresponding to *trans*-**10** was selectively pulsed (a). The signal at 1.90 ppm suffered a magnetization transfer due to chemical exchange (b) indicating that this proton signal (H^1) corresponded to *cis*-**10**.

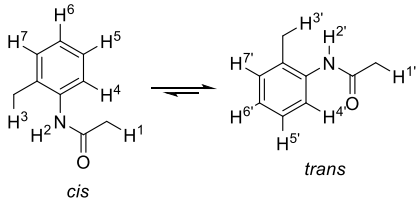

Figure 41. Conformational isomers of *O*-acetotoluidide **11**.

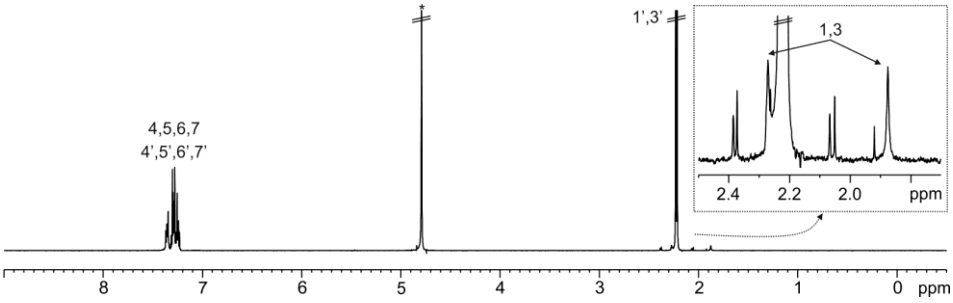

Figure 42. ^{1}H NMR (400 MHz, D_2O, 298 K) spectrum of **11**. See Figure 41 for proton assignment. *Residual solvent peak.

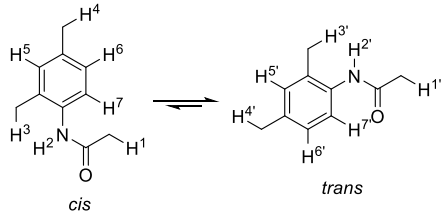

Figure 43. Conformational isomers of *N*-(2',4'-di-methylphenyl) acetamide **12**.

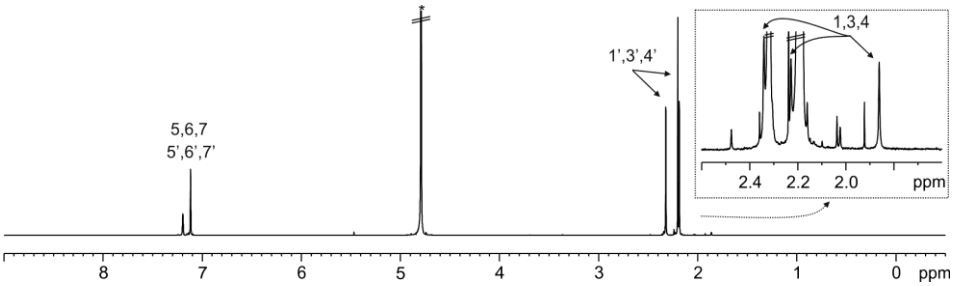

Figure 44. ^{1}H NMR (400 MHz, D_2O, 298 K) spectrum of **12**. See Figure 43 for proton assignment. *Residual solvent peak.

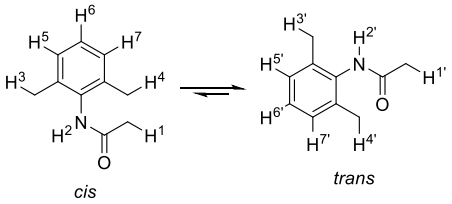

Figure 45. Conformational isomers of *N*-(2',6'-di-methylphenyl) acetamide **13**.

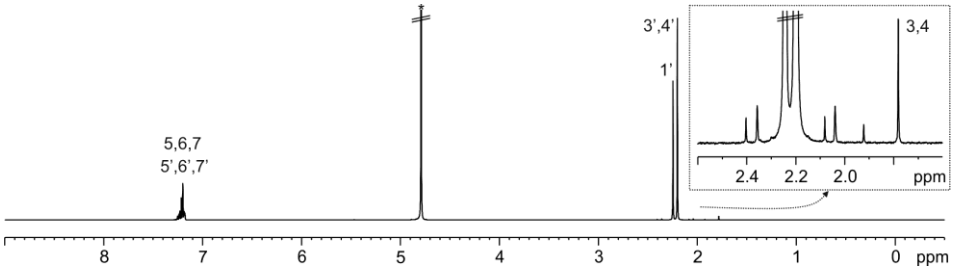

Figure 46. ^{1}H NMR (400 MHz, D_2O, 298 K) spectrum of **13**. See Figure 45 for proton assignment. *Residual solvent peak.

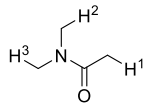

Figure 47. Line-drawing structure of *N*,*N*-di-methyl acetamide **14**.

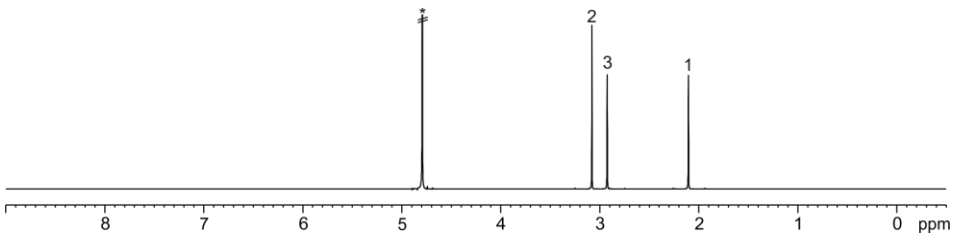

Figure 48. ^{1}H NMR (400 MHz, D_2O, 298 K) spectrum of **14**. See Figure 47 for proton assignment. *Residual solvent peak.

Table 3. Molar ratio of the conformational isomers (*cis*/*trans*) of the amides in D_2O determined by integration of the ^{1}H NMR spectra and isomerization constant values (K_{iso} = [*cis*-amide]/[*trans*-amide]). The amides **4**, **7**, **8** and **14** bear identical *N*-substituents.

Amide	**3**	**4**	**5**	**6**	**7**	**8**	**9**	**10**	**11**	**12**	**13**	**14**
Molar ratio	32/68	-	82/18	8/92	-	-	1.6/98.4	1/99	2.3/97.7	2.7/97.3	2.2/97.8	-
K_{iso}	0.47	-	4.56	0.09	-	-	0.02	0.01	0.02	0.03	0.02	-

Chapter 5

Octa-pyridinium super aryl-extended calix[4]pyrrole 15: The compound was prepared following a procedure previously reported in the literature.[41]

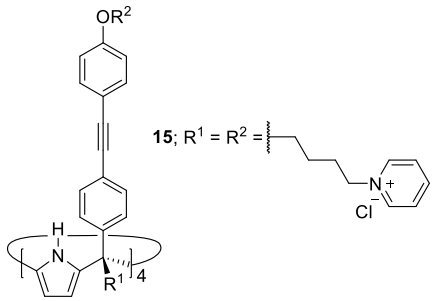

Figure 49. Line-drawing structure of tetra-*α* **15**.

Di-formamide 16: The compound was provided by the group of Prof. Rebek.

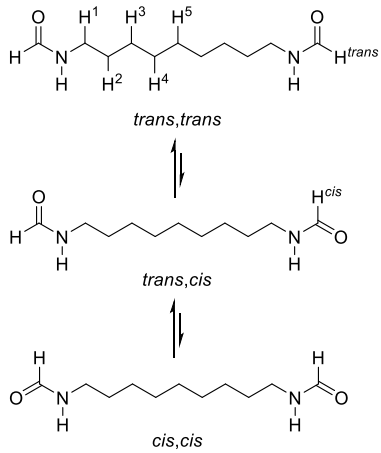

Figure 50. Conformational isomers of di-formamide **16**.

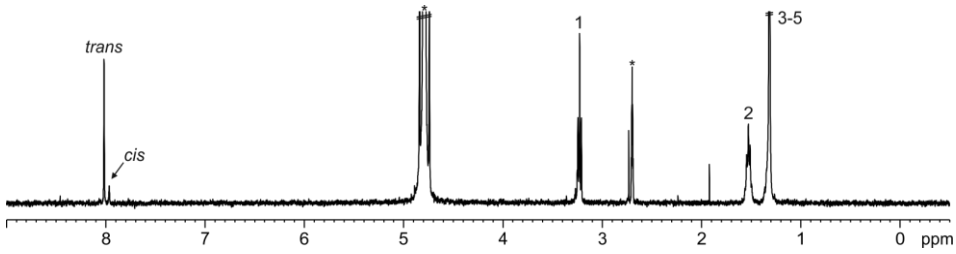

Figure 51. ^{1}H NMR (400 MHz, D_2O, 298 K) spectrum of **16** (added from a $(CD_3)_2SO$ solution). See Figure 50 for proton assignment. *Residual solvent peaks.

5.4.3 NMR experiments of tetra-pyridinium calix[4]pyrrole **1** in D_2O

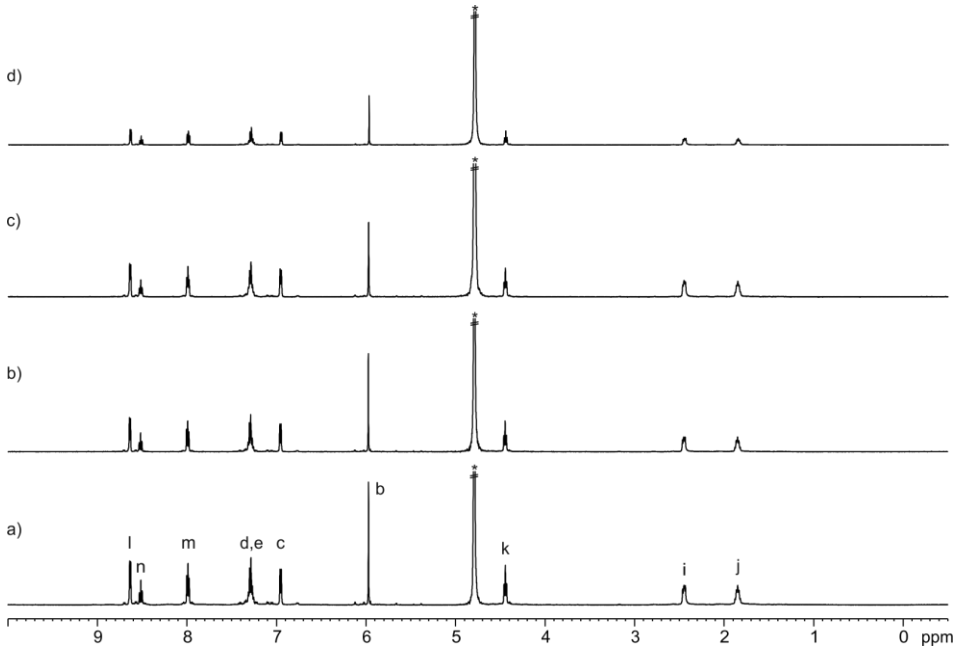

Figure 52. ^{1}H NMR (500 MHz with cryoprobe, D_2O, 298 K) spectra of the dilution experiment of **1**: a) 1; b) 0.8; c) 0.6 and d) 0.4 mM. See Figure 19 for proton assignment. *Residual solvent peak.

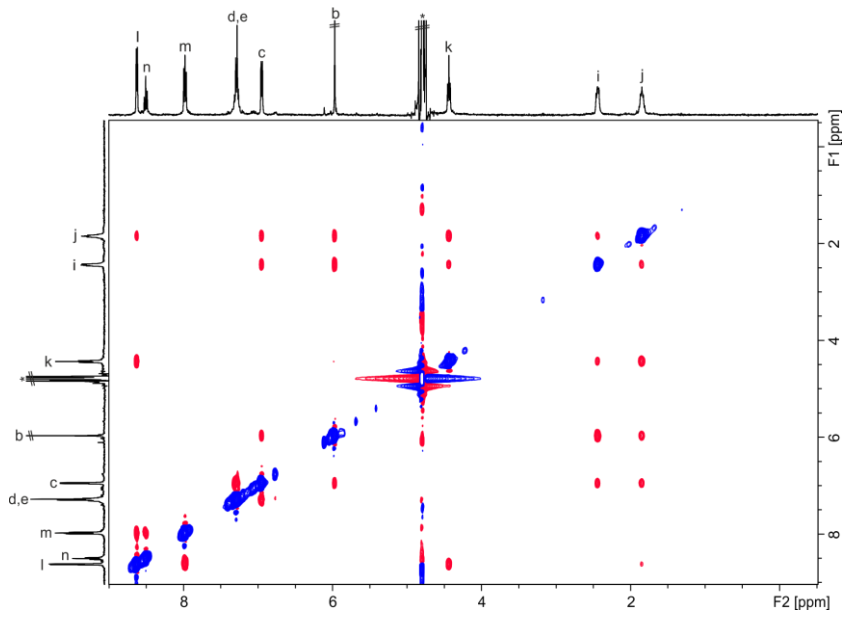

Figure 53. 2D ^{1}H-^{1}H ROESY (400 MHz, D_2O, 298 K, spin lock = 0.4 s) spectrum of **1**. See Figure 19 for proton assignment. *Residual solvent peak.

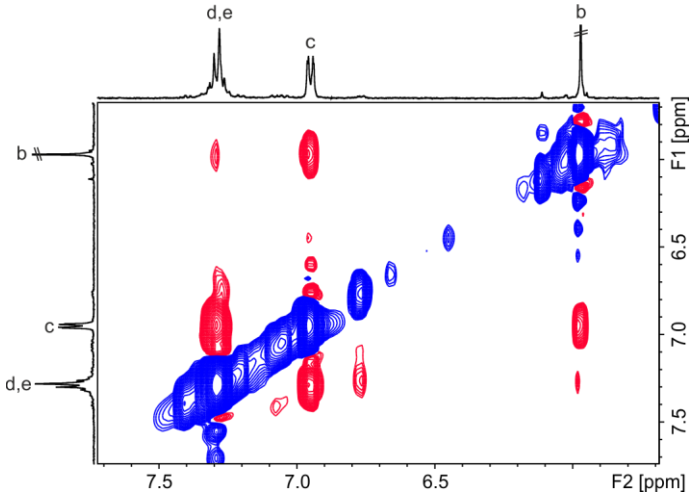

Figure 54. Selected region of the 2D ^{1}H-^{1}H ROESY (400 MHz, D_2O, 298 K, spin lock = 0.4 s) spectrum of **1**. See Figure 19 for proton assignment.

The 2D ^{1}H-^{1}H ROESY NMR spectrum of **1** showed cross-peaks between the H^b and H^c protons indicating proximity. Also, cross-peaks between H^b and H^d protons of **1** were observed.

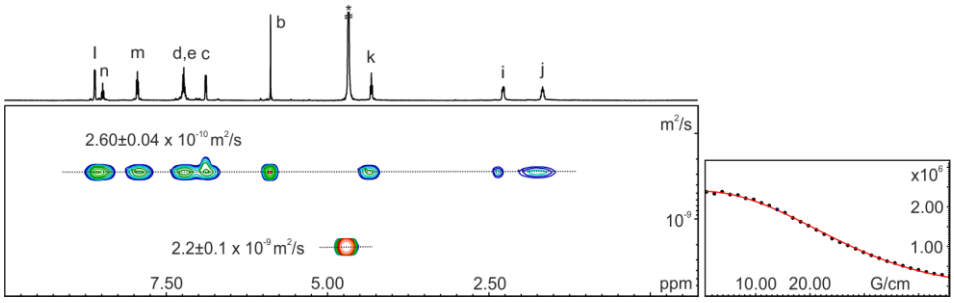

Figure 55. (left) ^{1}H pseudo 2D plot of DOSY (500 MHz with cryoprobe, D_2O, 298 K, D20 = 0.15 s, P30 = 1 ms) of **1** (1 mM); (right) fit of the decay of the signal of proton b to a mono-exponential function. Errors are indicated as standard deviations. See Figure 19 for proton assignment. *Residual solvent peak.

The dilution and DOSY NMR experiments of **1** at millimolar concentrations indicated that the calix[4]pyrrole was soluble in water as discrete species.

5.4.4 ^{1}H NMR titration experiments with formamides

^{1}H NMR titrations were carried out by adding aliquots of a D_2O solution of the guest into a solution of the host in the same solvent or viceversa (see the corresponding figures for details). The aliquots were added to the NMR tube (initial volume = 0.5 mL) with a glass micro syringe and NMR spectra were directly recorded after the additions. The concentration of the host or the guest (depending on the experiment) was maintained constant throughout the titration.

^{1}H NMR titration of calix[4]pyrrole **1** with *N*-phenyl formamide **3**

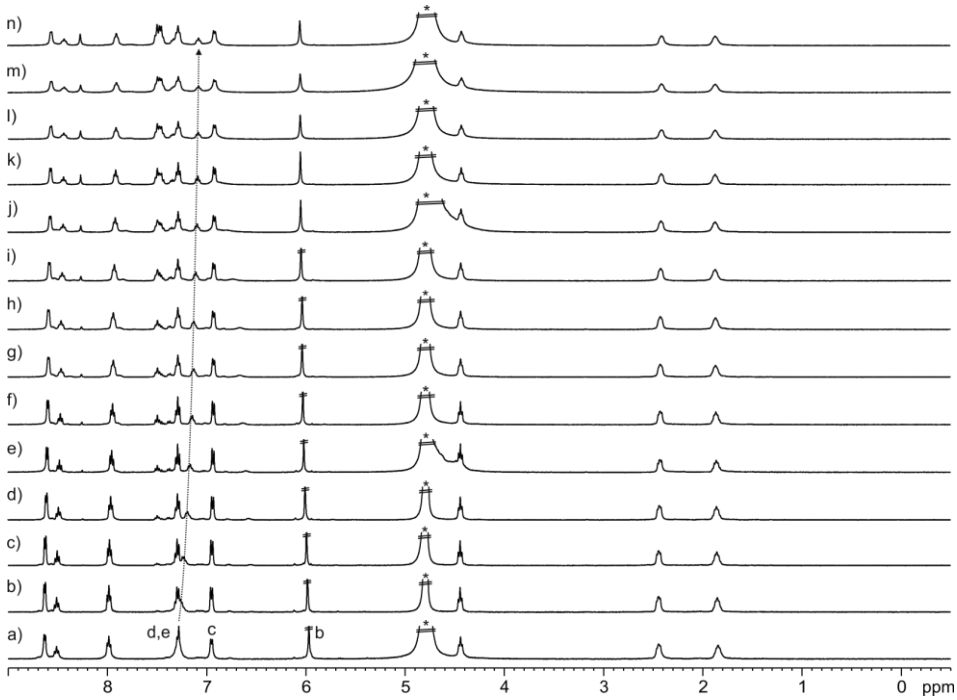

Figure 56. ^{1}H NMR (400 MHz, D_2O, 298 K) spectra of the titration of **1** with **3**: a) 0; b) 0.1; c) 0.2; d) 0.4; e) 0.6; f) 0.8; g) 1.0; h) 1.2; i) 1.5; j) 2.0; k) 2.5; l) 3.0; m) 3.5 and n) 4.0 equiv. See Figure 19 for proton assignment. *Residual solvent peak.

Table 4. Chemical shifts for the proton signals of bound host **1** (δ_{bound}, ppm) obtained from the fit of the ^{1}H NMR titration data (calix[4]pyrrole **1** with **3**) to a theoretical 1:1 binding model and induced chemical shifts ($\Delta\delta = \delta_{bound} - \delta_{free}$, ppm).

Signal	δ_{free}	δ_{bound}	$\Delta\delta$
b	5.97	6.06	+0.09
c	6.95	6.92	-0.03
d	7.30	7.28	-0.02
e	7.28	7.07	-0.21

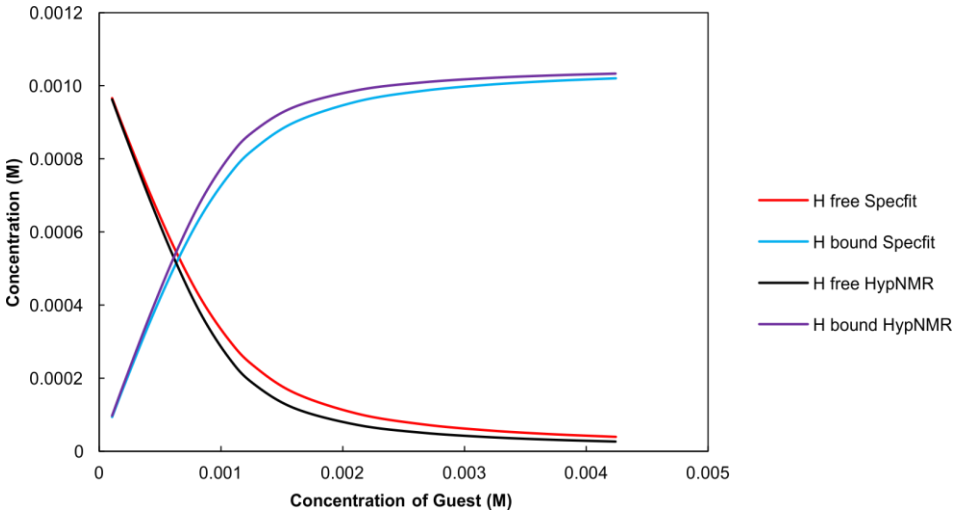

Figure 57. Calculated host (H) speciation profiles using the simple 1:1 binding model (HypNMR) and the theoretical binding model considering the *cis*/*trans* equilibrium and the exclusive formation of the *cis*-**3**⊂**1** complex (Specfit).

The speciation profiles obtained using the simple 1:1 binding model and the theoretical binding model considering the *cis*/*trans* equilibrium and the exclusive formation of the *cis*⊂**1** complex were similar. Accordingly, the two binding models returned similar estimates for the binding constant values.

^{1}H NMR titration of *N*-phenyl formamide **3** with calix[4]pyrrole **1**

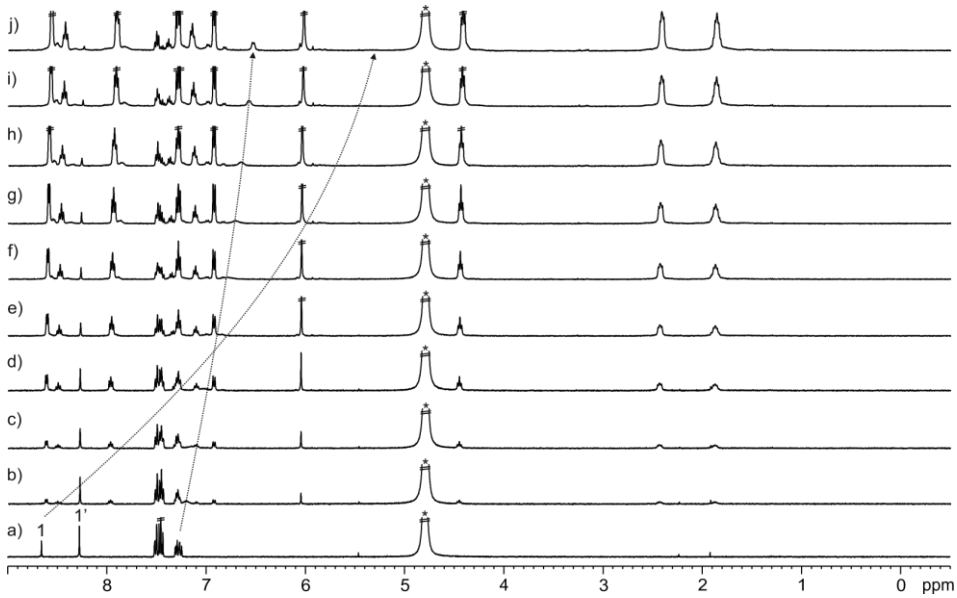

Figure 58. ^{1}H NMR (400 MHz, D_2O, 298 K) spectra of the titration of **3** with **1**: a) 0; b) 0.05; c) 0.1; d) 0.2; e) 0.4; f) 0.6; g) 0.8; h) 1.0; i) 1.5 and j) 2.0 equiv. See Figure 24 for proton assignment. *Residual solvent peak.

Table 5. Experimental (δ_{obs}, ppm), theoretical (δ_{calc}, ppm) and complexation induced chemical shifts ($\Delta\delta$, ppm) for the proton signals of bound *cis*-**3** to **1**. Experimental values were obtained from a mixture of **1** and **3** in a 2:1 ratio.

Signal	δ_{free}	δ_{obs}	$\Delta\delta$	δ_{calc}
1	8.65	5.32[a]	-3.33	4.56
2	-	-	-	3.88
3	7.28	6.53	-0.75	6.10
4	-	7.50	-	6.82
5	-	7.38	-	6.64

[a] The experimental chemical shift of H^1 in the 2:1 mixture of **1** and **3** was assigned to a broad signal at 5.32 ppm with the help of chemical shift calculations of the *cis*-**3**⊂**1** complex.

Chapter 5

^{1}H NMR titration of calix[4]pyrrole **1** with *N*,*N*-di-phenyl formamide **4**

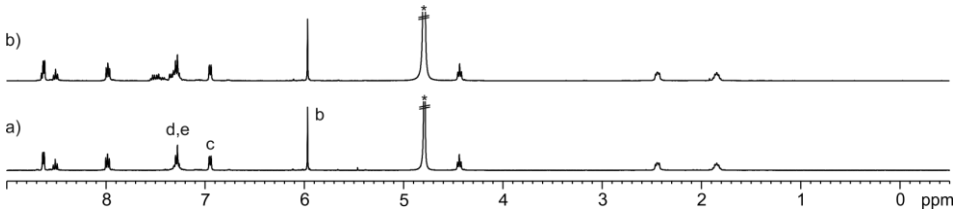

Figure 59. ^{1}H NMR (400 MHz, D_2O, 298 K) spectra of the titration of **1** with **4**: a) 0 and b) excess. The NMR tube was sonicated for 15 min before acquisition of spectrum b). See Figure 19 for proton assignment. *Residual solvent peak.

The *N*,*N*-di-phenyl formamide **4** was added as a solid to a millimolar solution of **1** due to its limited solubility in water (< 5 mM).

^{1}H NMR titration of calix[4]pyrrole **1** with *N*-methyl-*N*-phenyl formamide **5**

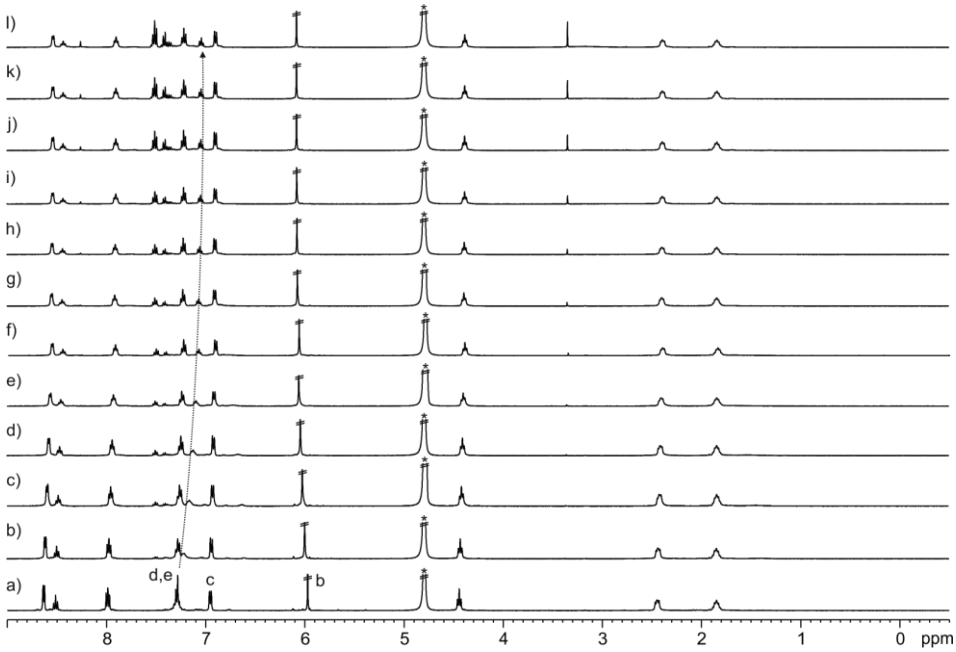

Figure 60. ^{1}H NMR (400 MHz, D_2O, 298 K) spectra of the titration of **1** with **5**: a) 0; b) 0.2; c) 0.4; d) 0.6; e) 0.8; f) 1.0; g) 1.2; h) 1.5; i) 2.0; j) 2.5; k) 3.0 and l) 4.0 equiv. See Figure 19 for proton assignment. *Residual solvent peak.

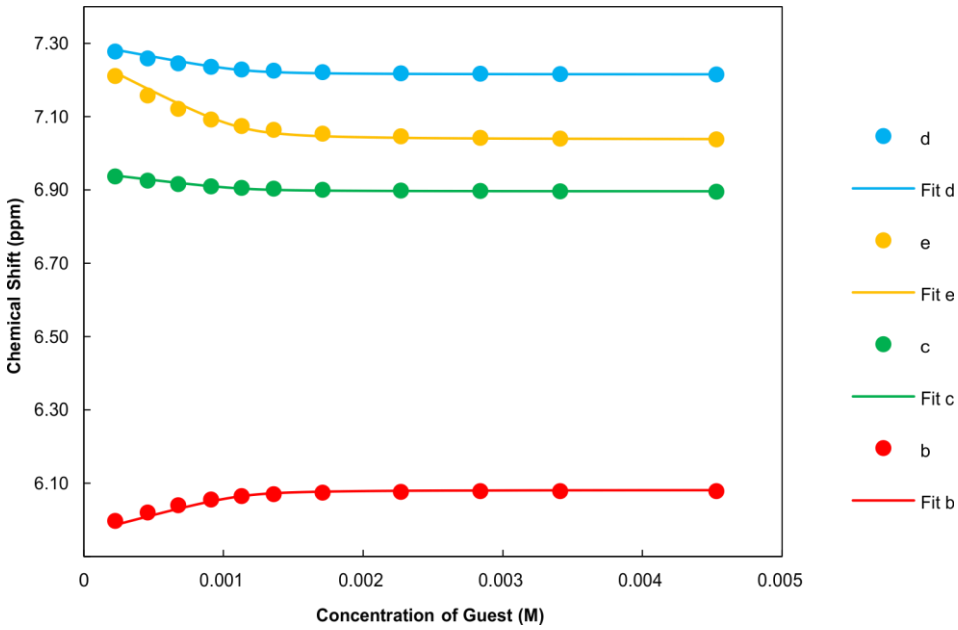

Figure 61. Chemical shifts of the proton signals of **1** upon incremental amounts of **5** (circles) and fit of the titration data to a theoretical 1:1 binding model (lines).

Table 6. Chemical shifts for the proton signals of bound host **1** (δ_{bound}, ppm) obtained from the fit of the ^{1}H NMR titration data (calix[4]pyrrole **1** with **5**) to a theoretical 1:1 binding model and induced chemical shifts ($\Delta\delta = \delta_{bound} - \delta_{free}$, ppm).

Signal	δ_{free}	δ_{bound}	$\Delta\delta$
b	5.97	6.08	+0.11
c	6.95	6.90	-0.05
d	7.30	7.21	-0.09
e	7.28	7.04	-0.24

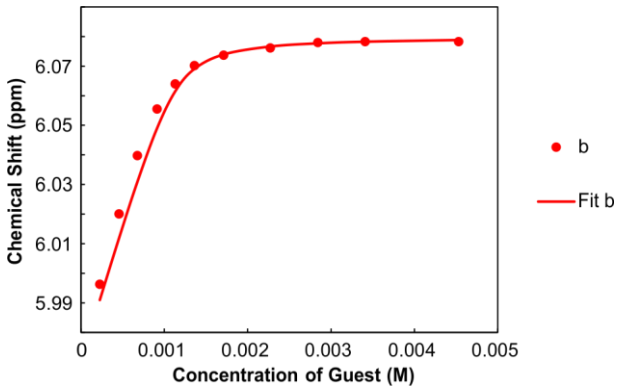

Figure 62. Chemical shift of the proton signal b of **1** upon incremental amounts of **5** (circles) and fit of the titration data to a theoretical binding model considering the *cis*/*trans* equilibrium and the exclusive formation of the *cis*-rotamer⊂**1** (line).

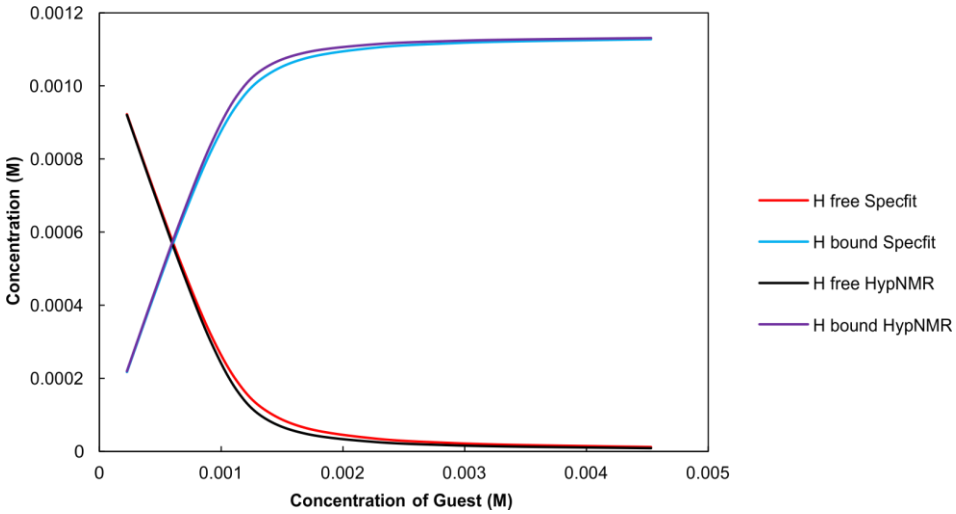

Figure 63. Calculated host (H) speciation profiles using the simple 1:1 binding model (HypNMR) and the theoretical binding model considering the *cis*/*trans* equilibrium and the exclusive formation of the *cis*-**5**⊂**1** complex (Specfit).

The speciation profiles obtained using the simple 1:1 binding model and the theoretical binding model considering the *cis*/*trans* equilibrium and the exclusive formation of the *cis*⊂**1** complex were similar. Accordingly, the two binding models returned similar estimates for the binding constant values.

^{1}H NMR titration of *N*-methyl-*N*-phenyl formamide **5** with calix[4]pyrrole **1**

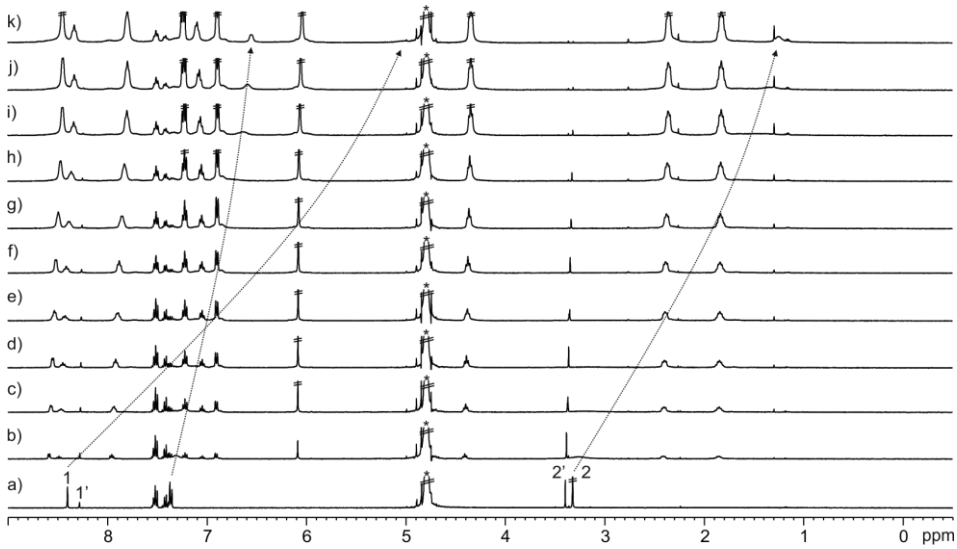

Figure 64. ^{1}H NMR (400 MHz, D_2O, 298 K) spectra of the titration of **5** with **1**: a) 0; b) 0.07; c) 0.13; d) 0.2; e) 0.26; f) 0.33; g) 0.5; h) 0.66; i) 1.0; j) 1.32 and k) 2.0 equiv. See Figure 28 for proton assignment. *Residual solvent peak.

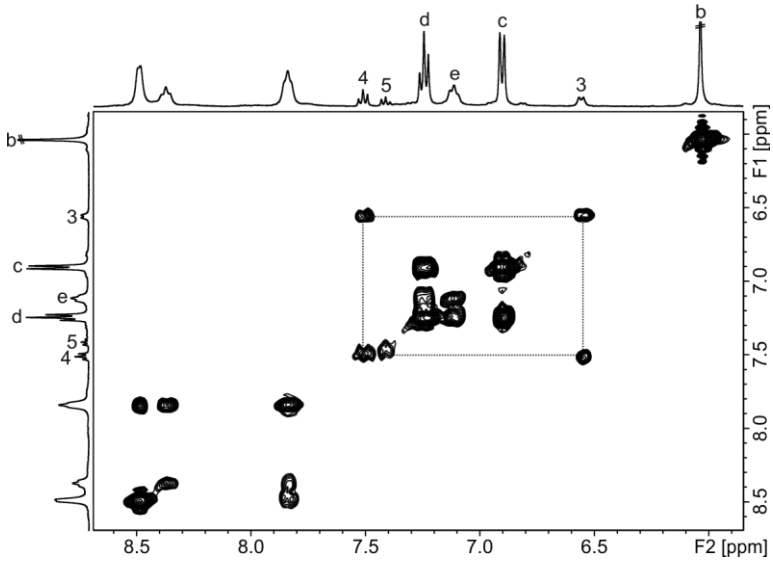

Figure 65. Selected region of the 2D ^{1}H-^{1}H COSY NMR (400 MHz, D_2O, 298 K) spectrum of **1** and **5** (2:1 ratio). COSY cross-peaks between H^3 and H^4 of bound **5** are observed. See Figure 19 and Figure 28 for proton assignments.

Table 7. Experimental (δ_{obs}, ppm), theoretical (δ_{calc}, ppm) and complexation induced chemical shifts ($\Delta\delta$, ppm) for the proton signals of bound *cis*-**5** to **1**. Experimental values were obtained from a mixture of **1** and **5** in a 2:1 ratio.

Signal	δ_{free}	δ_{obs}	$\Delta\delta$	δ_{calc}
1	8.40	5.01[a]	-3.39	4.70
2	3.32	1.25	-2.07	1.06
3	7.36	6.55	-0.81	5.85
4	-	7.43	-	6.80
5	-	7.33	-	6.69

[a] The experimental chemical shift of H^1 in the 2:1 mixture of **1** and **5** was assigned to a broad signal at 5.01 ppm with the help of chemical shift calculations of the *cis*-**5**⊂**1** complex.

^{1}H NMR titration of calix[4]pyrrole **1** with *N*-methyl formamide **6**

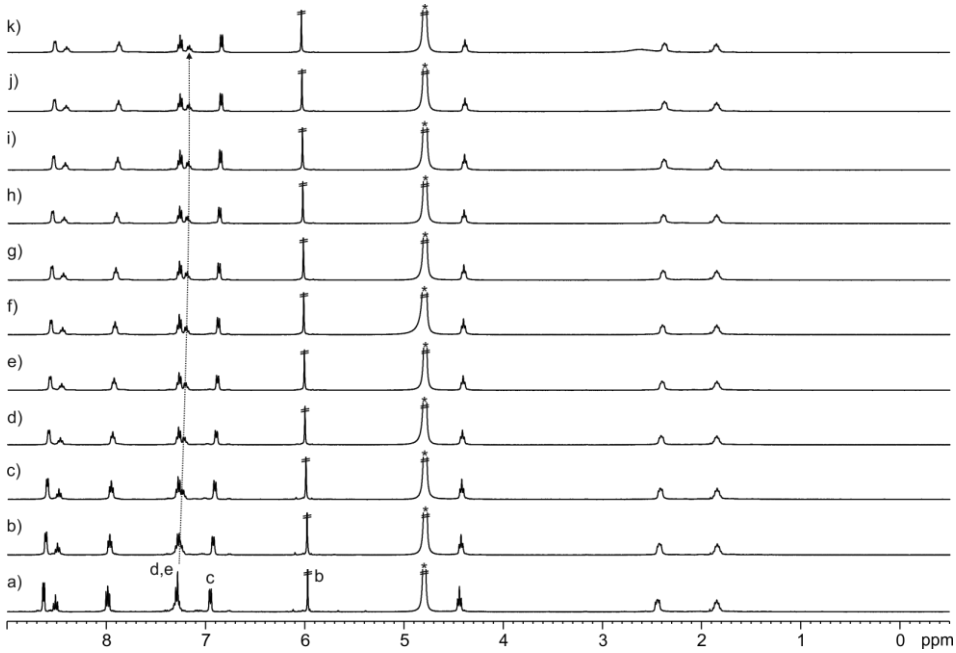

Figure 66. ^{1}H NMR (400 MHz, D_2O, 298 K) spectra of the titration of **1** with **6**: a) 0; b) 0.2; c) 0.4; d) 0.6; e) 0.8; f) 1.0; g) 1.2; h) 1.5; i) 2.0; j) 3.0 and k) 5.0 equiv. See Figure 19 for proton assignment. *Residual solvent peak.

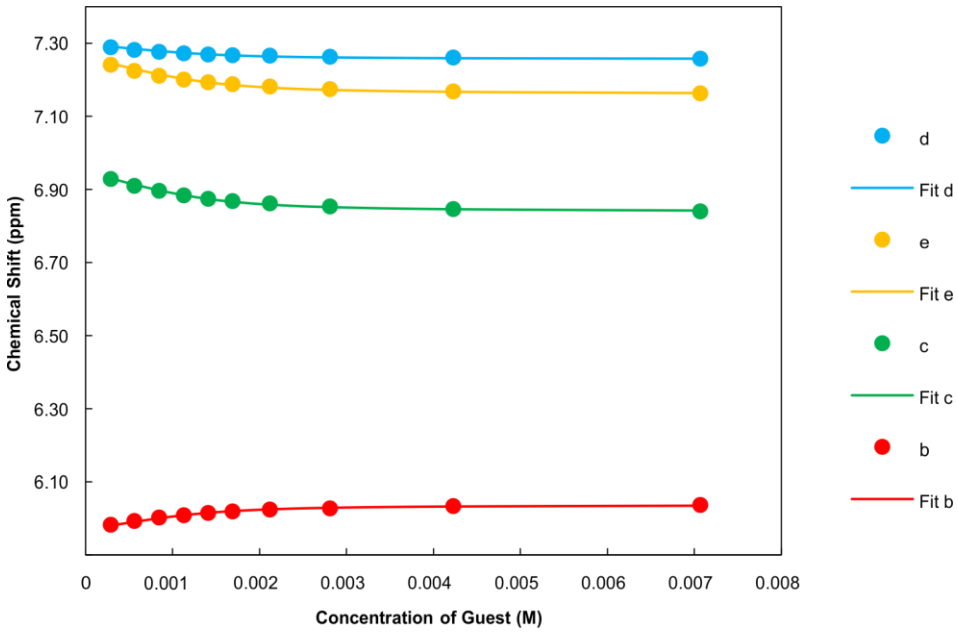

Figure 67. Chemical shifts of the proton signals of **1** upon incremental amounts of **6** (circles) and fit of the titration data to a theoretical 1:1 binding model (lines).

Table 8. Chemical shifts for the proton signals of bound host **1** (δ_{bound}, ppm) obtained from the fit of the ^{1}H NMR titration data (calix[4]pyrrole **1** with **6**) to a theoretical 1:1 binding model and induced chemical shifts ($\Delta\delta = \delta_{bound} - \delta_{free}$, ppm).

Signal	δ_{free}	δ_{bound}	$\Delta\delta$
b	5.97	6.04	+0.07
c	6.95	6.84	-0.11
d	7.30	7.26	-0.04
e	7.28	7.16	-0.12

Chapter 5

^{1}H NMR titration of *N*-methyl formamide **6** with calix[4]pyrrole **1**

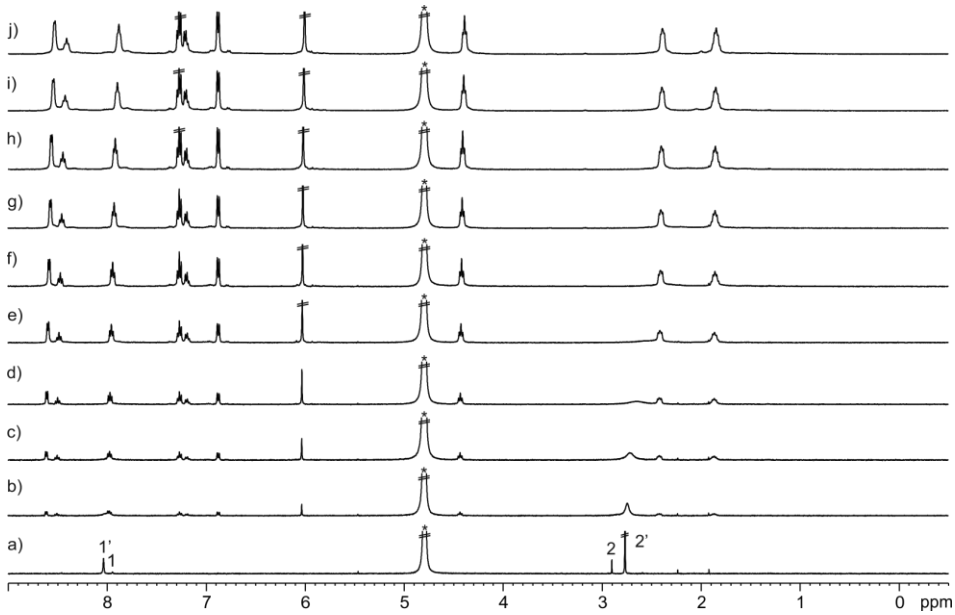

Figure 68. ^{1}H NMR (400 MHz, D_2O, 298 K) spectra of the titration of **6** with **1**: a) 0; b) 0.05; c) 0.1; d) 0.2; e) 0.4; f) 0.6; g) 0.8; h) 1.0; i) 1.5 and j) 2.0 equiv. See Figure 30 for proton assignment. *Residual solvent peak.

^{1}H NMR titration of calix[4]pyrrole **1** with *N*,*N*-di-methyl formamide **7**

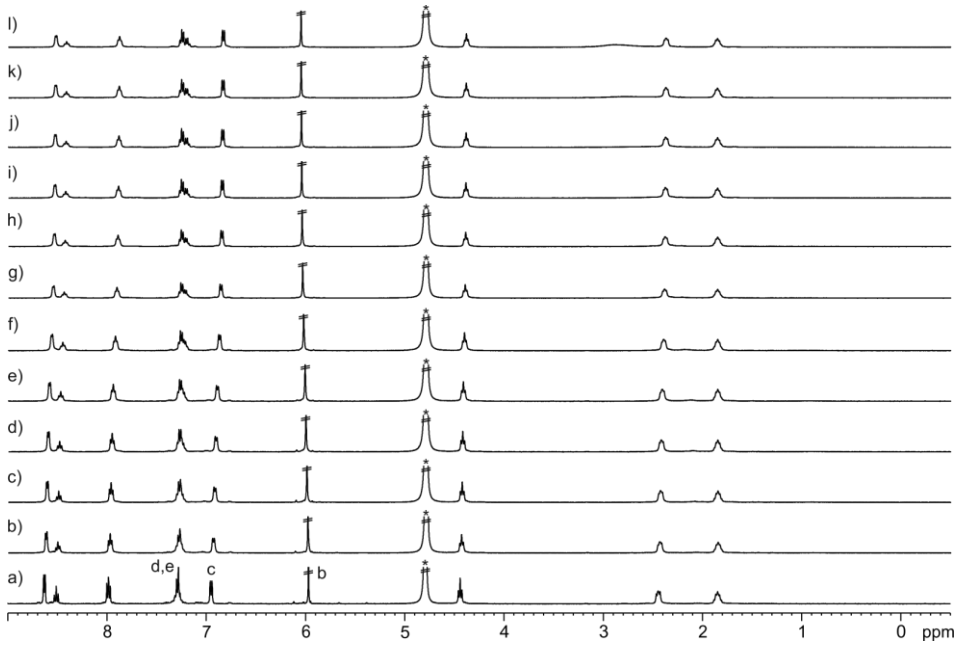

Figure 69. ^{1}H NMR (400 MHz, D_2O, 298 K) spectra of the titration of **1** with **7**: a) 0; b) 0.1; c) 0.2; d) 0.3; e) 0.4; f) 0.6; g) 0.8; h) 1.0; i) 1.2; j) 1.5; k) 2.0 and l) 3.0 equiv. See Figure 19 for proton assignment. *Residual solvent peak.

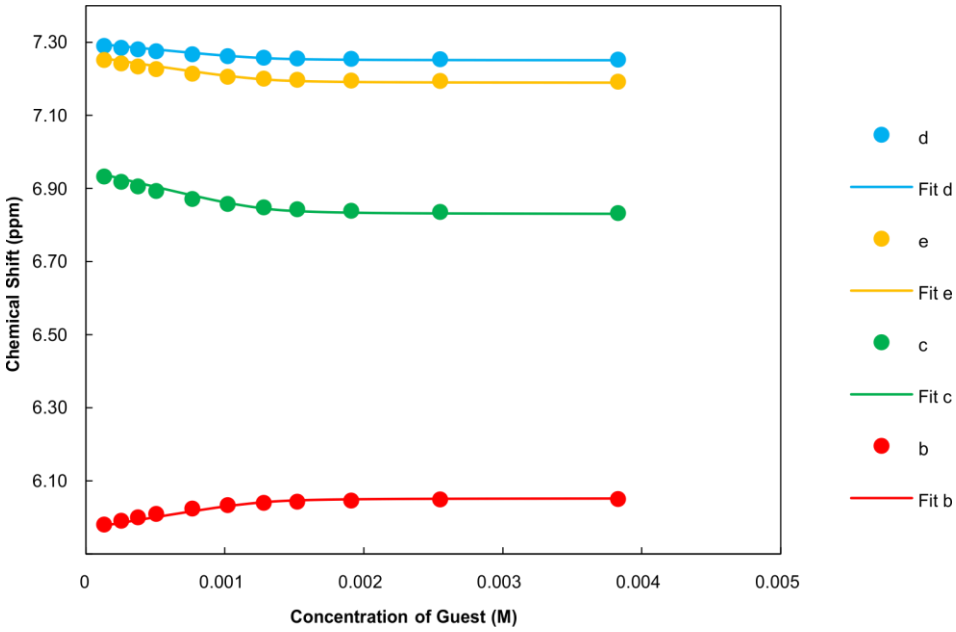

Figure 70. Chemical shifts of the proton signals of **1** upon incremental amounts of **7** (circles) and fit of the titration data to a theoretical 1:1 binding model (lines).

Table 9. Chemical shifts for the proton signals of bound host **1** (δ_{bound}, ppm) obtained from the fit of the ^{1}H NMR titration data (calix[4]pyrrole **1** with **7**) to a theoretical 1:1 binding model and induced chemical shifts ($\Delta\delta = \delta_{bound} - \delta_{free}$, ppm).

Signal	δ_{free}	δ_{bound}	$\Delta\delta$
b	5.97	6.05	+0.08
c	6.95	6.83	-0.18
d	7.30	7.25	-0.05
e	7.28	7.19	-0.11

5.4.5 ^{1}H NMR titration experiments with acetamides

^{1}H NMR titrations were carried out by adding aliquots of a D_2O solution of the guest into a solution of the host in the same solvent or viceversa (see the corresponding figures for details). The aliquots were added to the NMR tube (initial volume = 0.5 mL) with a glass micro syringe and NMR spectra were directly recorded after the additions. The concentration of the host or the guest (depending on the experiment) was maintained constant throughout the titration.

^{1}H NMR titration of calix[4]pyrrole **1** with acetamide **8**

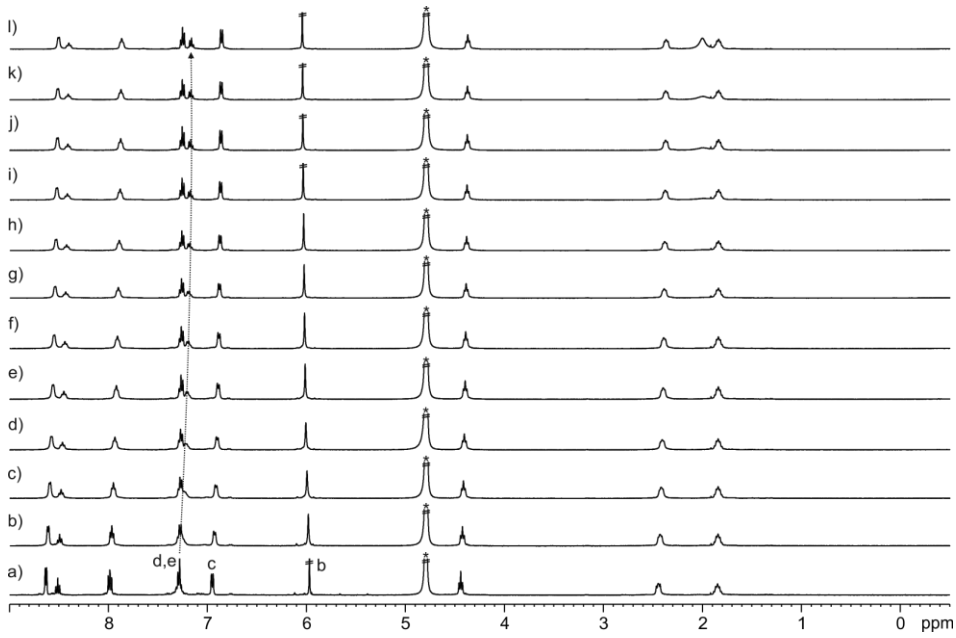

Figure 71. ^{1}H NMR (400 MHz, D_2O, 298 K) spectra of the titration of **1** with **8**: a) 0; b) 0.2; c) 0.4; d) 0.6; e) 0.8; f) 1.0; g) 1.2; h) 1.5; i) 2.0; j) 2.5; k) 3.0 and l) 5.0 equiv. See Figure 19 for proton assignment. *Residual solvent peak.

The protons (H^1) of the bound acetamide **8** appeared as a broad signal at *ca.* -0.5 ppm.

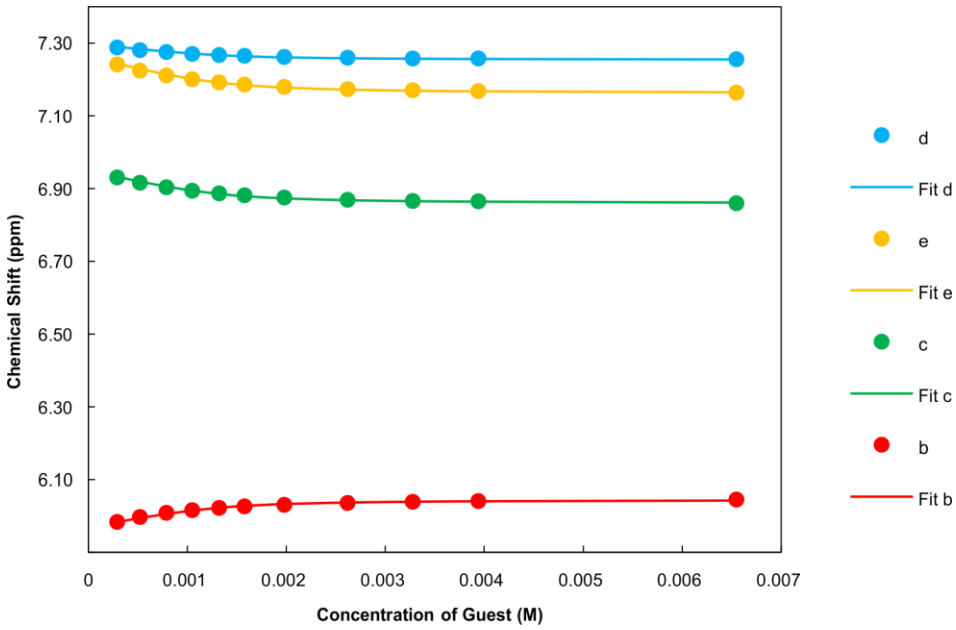

Figure 72. Chemical shifts of the proton signals of **1** upon incremental amounts of **8** (circles) and fit of the titration data to a theoretical 1:1 binding model (lines).

Table 10. Chemical shifts for the proton signals of bound host **1** (δ_{bound}, ppm) obtained from the fit of the ^{1}H NMR titration data (calix[4]pyrrole **1** with **8**) to a theoretical 1:1 binding model and induced chemical shifts ($\Delta\delta = \delta_{bound} - \delta_{free}$, ppm).

Signal	δ_{free}	δ_{bound}	$\Delta\delta$
b	5.97	6.04	+0.07
c	6.95	6.86	-0.09
d	7.30	7.25	-0.05
e	7.28	7.16	-0.12

^{1}H NMR titration of calix[4]pyrrole **1** with *N*-methyl acetamide **9**

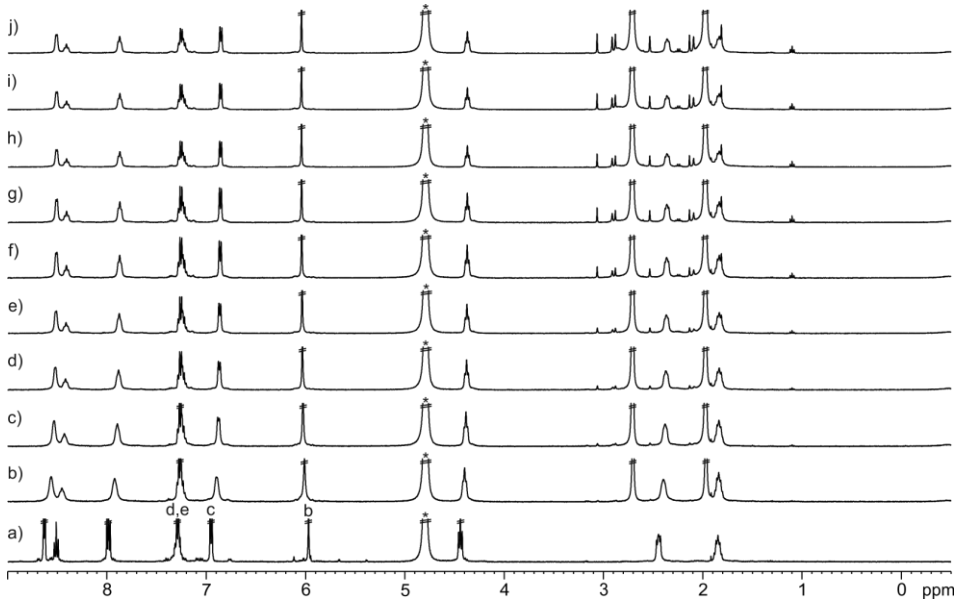

Figure 73. ^{1}H NMR (400 MHz, D_2O, 298 K) spectra of the titration of **1** with **9**: a) 0; b) 5; c) 10; d) 15; e) 20; f) 30; g) 40; h) 50; i) 60 and j) 80 equiv. See Figure 19 for proton assignment. *Residual solvent peak.

The protons (H^1) of the bound *cis*-acetamide **9** appeared as a broad signal at *ca.* -0.5 ppm.

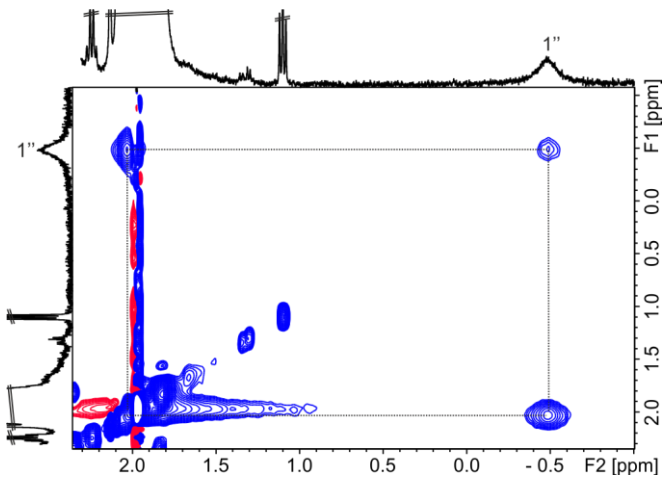

Figure 74. Selected region of the 2D ^{1}H-^{1}H EXSY NMR (400 MHz, D_2O, 298 K, t_{mix} = 0.4 s) spectrum of **1** and **9** (80:1 ratio). Doubly primed number correspond to proton signal of bound *cis*-**9**. See Figure 36 for proton assignment.

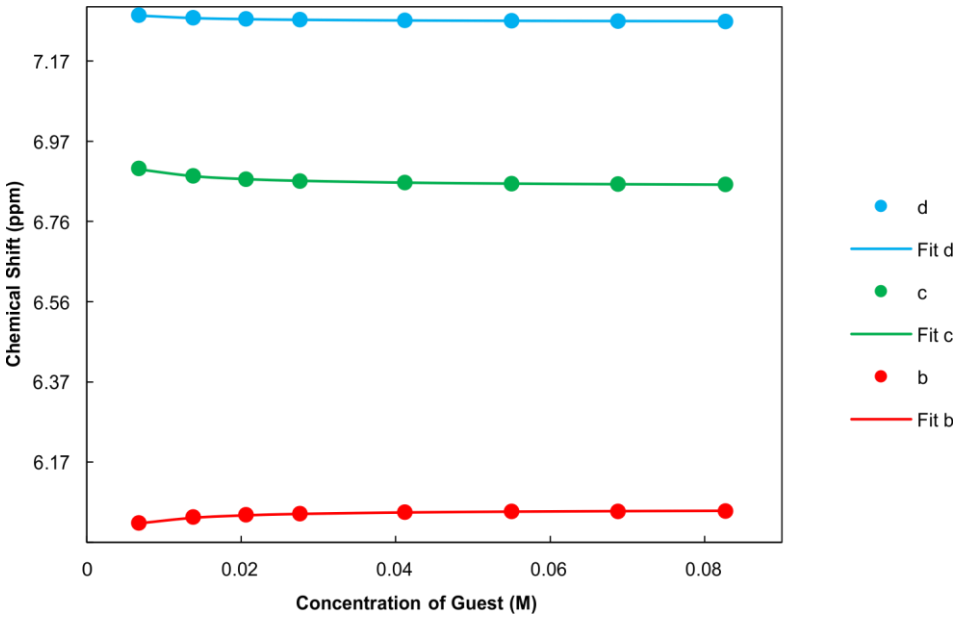

Figure 75. Chemical shifts of the proton signals of **1** upon incremental amounts of **9** (circles) and fit of the titration data to a theoretical 1:1 binding model (lines).

Table 11. Chemical shifts for the proton signals of bound host **1** (δ_{bound}, ppm) obtained from the fit of the ^{1}H NMR titration data (calix[4]pyrrole **1** with **9**) to a theoretical 1:1 binding model and induced chemical shifts ($\Delta\delta = \delta_{bound} - \delta_{free}$, ppm).

Signal	δ_{free}	δ_{bound}	$\Delta\delta$
b	5.97	6.05	+0.08
c	6.95	6.85	-0.10
d	7.30	7.26	-0.04

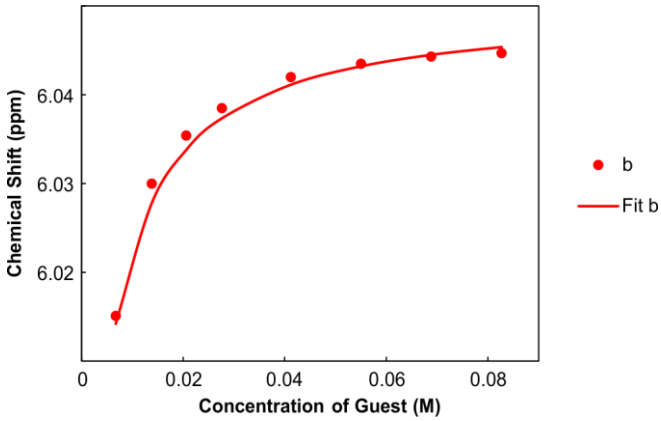

Figure 76. Chemical shift of the proton signal b of **1** upon incremental amounts of **9** (circles) and fit of the titration data to a theoretical binding model considering the *cis*/*trans* equilibrium and the exclusive formation of the *cis*-rotamer⊂**1** (line). We considered that the chemical shift value of the *β*-pyrrole protons in the *cis*-**9**⊂**1** complex is similar to the δ_{bound} value determined from the fit of the titration data to the simple 1:1 binding model.

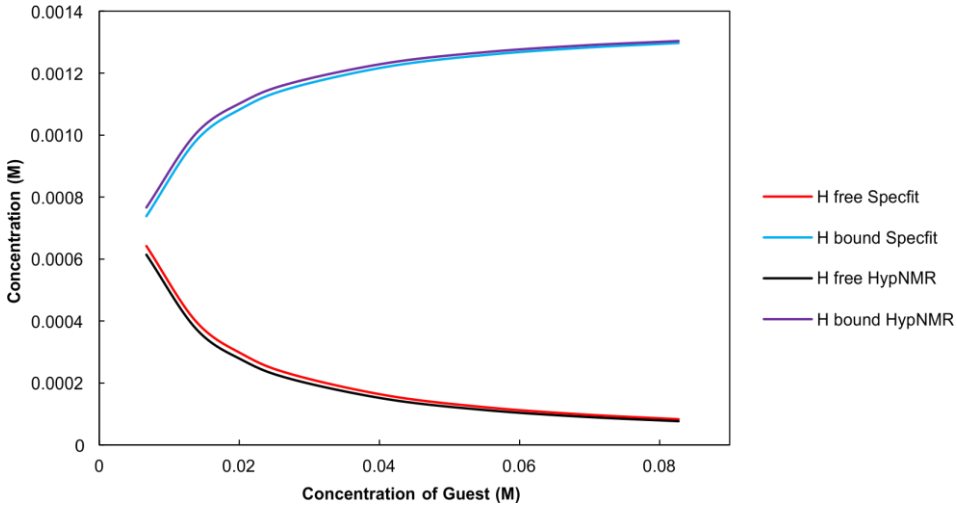

Figure 77. Calculated host (H) speciation profiles using the simple 1:1 binding model (HypNMR) and the theoretical binding model considering the *cis*/*trans* equilibrium and the exclusive formation of the *cis*-**9**⊂**1** complex (Specfit).

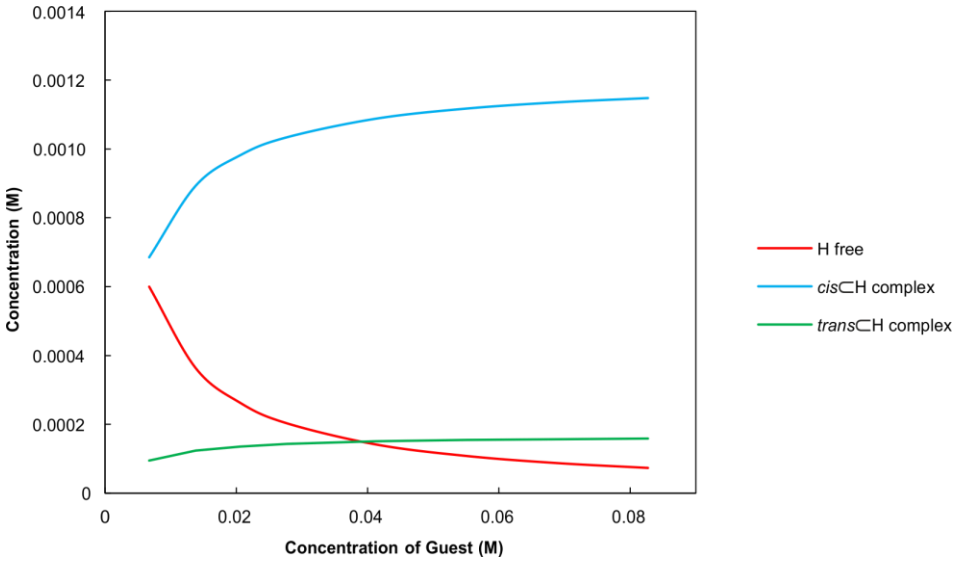

Figure 78. Calculated host (H) speciation profile using the theoretical binding model considering the *cis*/*trans* equilibrium and the formation of the *cis*-**9⊂1** and *trans*-**9⊂1** complexes (Specfit): K_a (*cis*⊂**1**) > 10^4 M^{-1}; K_a (*trans*⊂**1**) = 27 M^{-1}; *cis*/*trans* ratio = 1.6/98.4; [H] = 1.38 x 10^{-3} M.

The value of K_a (*trans*-**9⊂1**) was considered similar to the binding constant for the **14⊂1** complex. The speciation profile showed that the *trans*-**9⊂1** complex was formed in a reduced extent. For this reason, the *trans*-**9⊂1** complex was not included in the fit of the ^{1}H NMR titration data to the theoretical binding model, considering only the *cis*/*trans* equilibrium and the formation of the *cis*-**9⊂1** complex.

^{1}H NMR titration of calix[4]pyrrole **1** with *N*-phenyl acetamide **10**

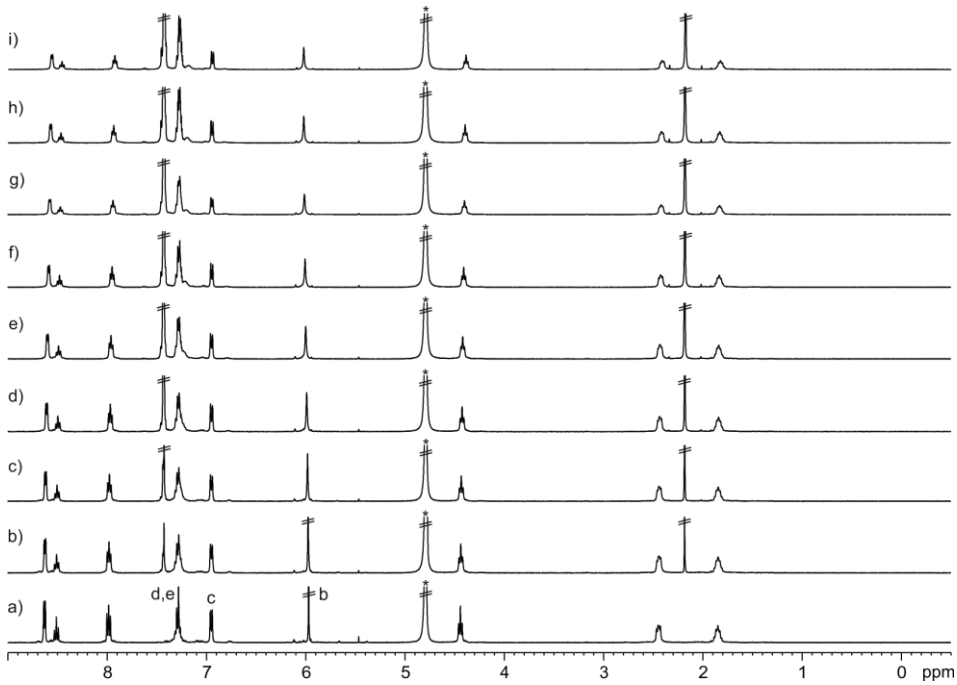

Figure 79. ^{1}H NMR (400 MHz, D_2O, 298 K) spectra of the titration of **1** with **10**: a) 0; b) 1; c) 2; d) 4; e) 6; f) 8; g) 10; h) 12 and i) 14 equiv. See Figure 19 for proton assignment. *Residual solvent peak.

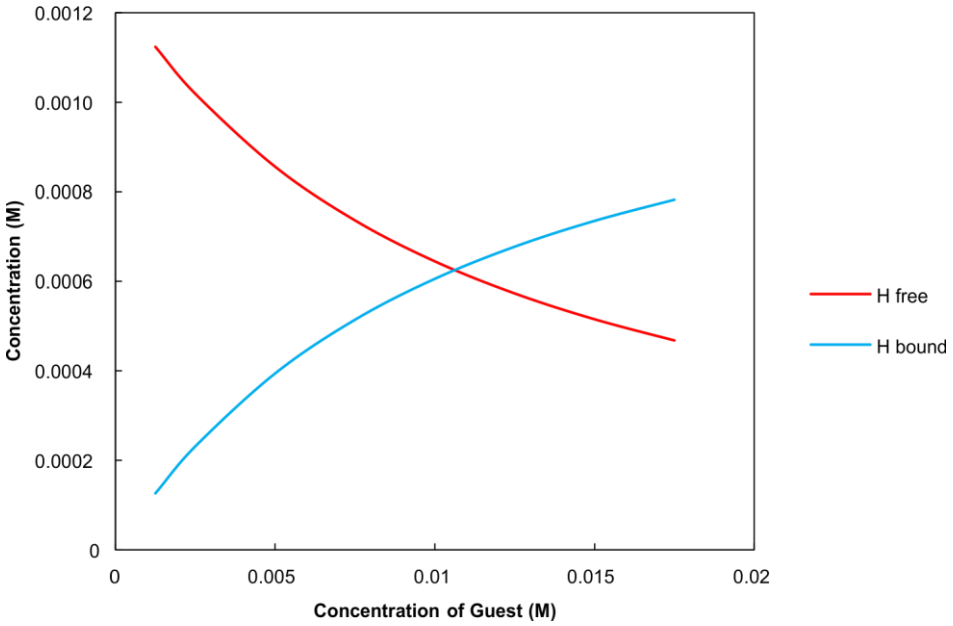

Figure 80. Calculated host (H) speciation profile using the theoretical binding model considering the *cis*/*trans* equilibrium and the exclusive formation of the *cis*-**10**⊂**1** complex (Specfit): K_a (*cis*⊂**1**) = 10^4 M^{-1}; *cis*/*trans* ratio = 1/99; [H] = 1.20 x 10^{-3} M. The simulated speciation profile indicates the formation of the *cis*-**10**⊂**1** complex in a considerable extent.

Table 12. Chemical shift for the proton signal of bound host **1** (δ_{bound}, ppm) obtained from the fit of the ^{1}H NMR titration data (calix[4]pyrrole **1** with **10**) to a theoretical 1:1 binding model and induced chemical shifts ($\Delta\delta = \delta_{bound} - \delta_{free}$, ppm).

Signal	δ_{free}	δ_{bound}	$\Delta\delta$
b	5.97	6.08[a]	+0.11

[a] We considered that the chemical shift value of the *β*-pyrrole protons in the *cis*-**5**⊂**1** complex is a good estimate for δ_{bound} in the *cis*-**10**⊂**1** complex.

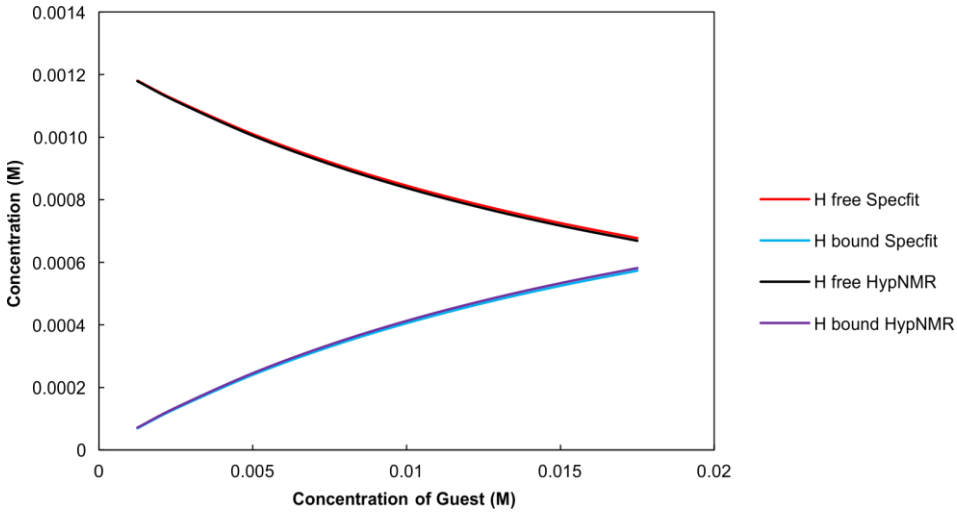

Figure 81. Calculated host (H) speciation profiles using the simple 1:1 binding model (HypNMR) and the theoretical binding model considering the *cis*/*trans* equilibrium and the exclusive formation of the *cis*-**10**⊂**1** complex (Specfit).

^{1}H NMR titration of *N*-phenyl acetamide **10** with calix[4]pyrrole **1**

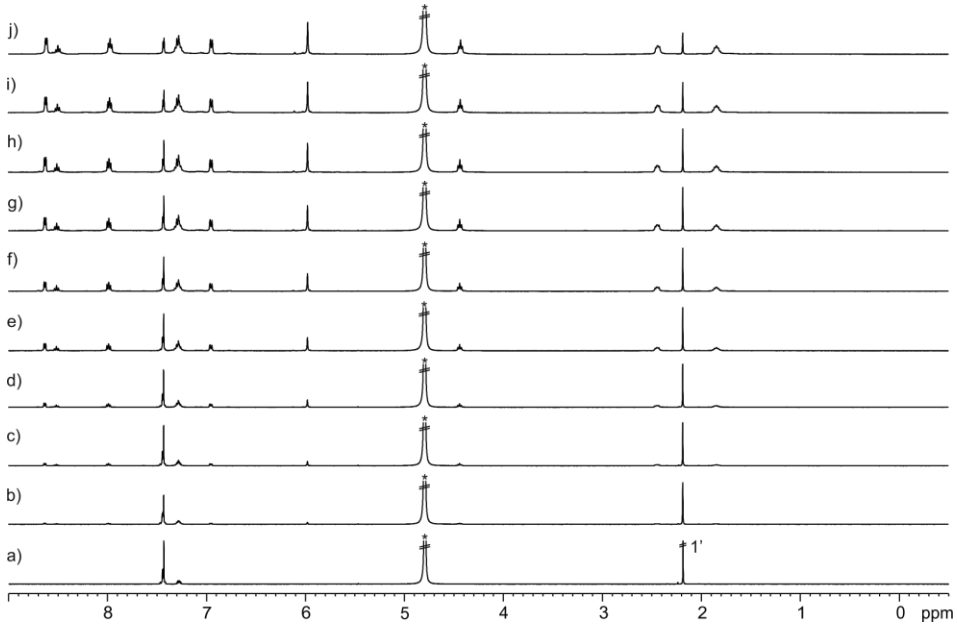

Figure 82. ^{1}H NMR (400 MHz, D_2O, 298 K) spectra of the titration of **10** with **1**: a) 0; b) 0.05; c) 0.1; d) 0.2; e) 0.4; f) 0.6; g) 0.8; h) 1.0; i) 1.5 and j) 2.0 equiv. See Figure 38 for proton assignment. *Residual solvent peak.

Chapter 5

^{1}H NMR titration of calix[4]pyrrole **1** with *O*-acetotoluidide **11**

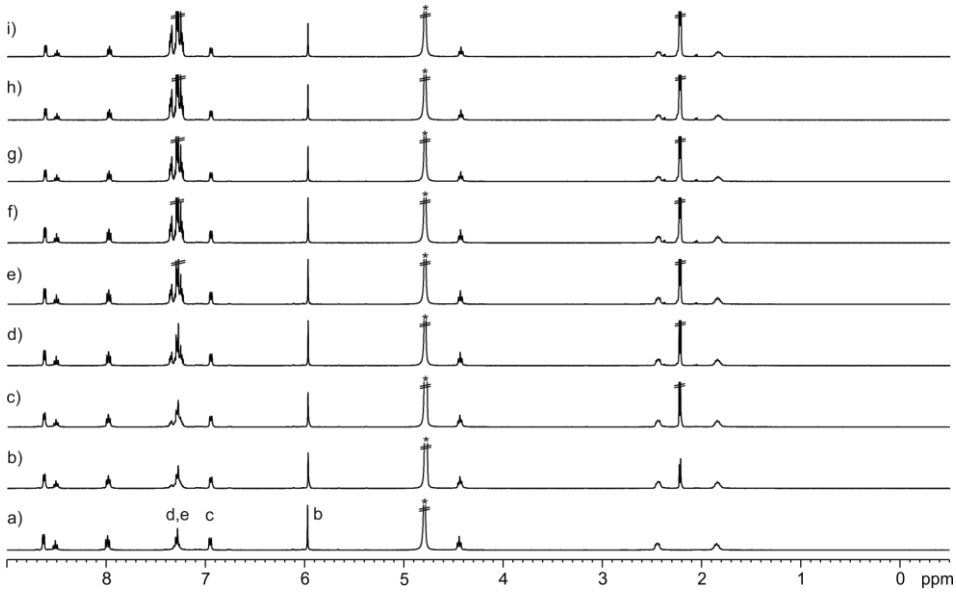

Figure 83. ^{1}H NMR (400 MHz, D_2O, 298 K) spectra of the titration of **1** with **11**: a) 0; b) 1; c) 2; d) 4; e) 6; f) 8; g) 10; h) 12 and i) 12.7 equiv. See Figure 19 for proton assignment. *Residual solvent peak.

^{1}H NMR titration of *O*-acetotoluidide **11** with calix[4]pyrrole **1**

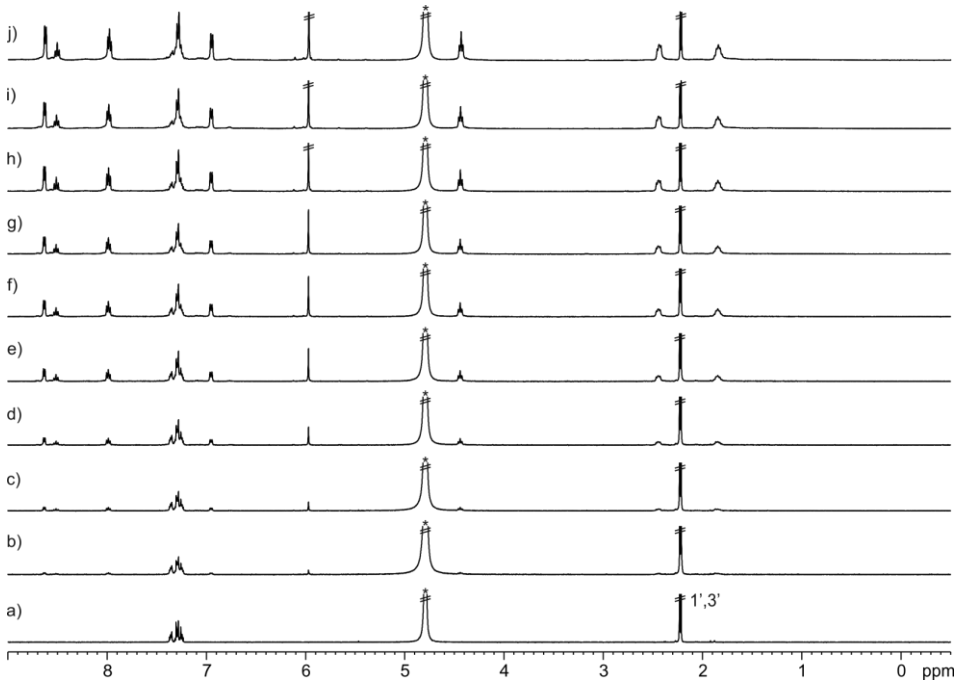

Figure 84. ^{1}H NMR (400 MHz, D_2O, 298 K) spectra of the titration of **11** with **1**: a) 0; b) 0.05; c) 0.1; d) 0.2; e) 0.4; f) 0.6; g) 0.8; h) 1.0; i) 1.5 and j) 2.0 equiv. See Figure 41 for proton assignment. *Residual solvent peak.

Chapter 5

^{1}H NMR titration of calix[4]pyrrole **1** with *N*,*N*-di-methyl acetamide **14**

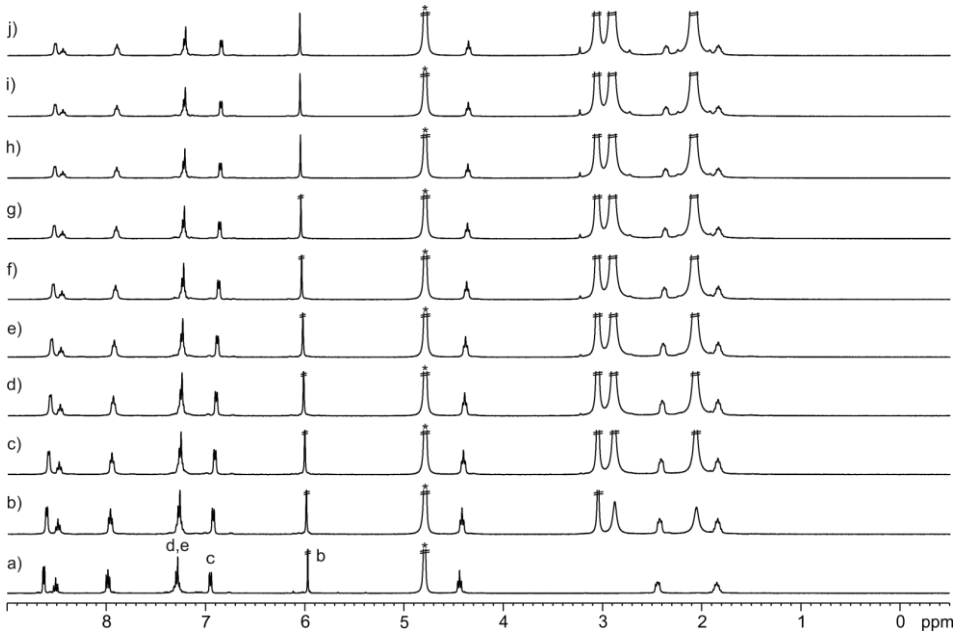

Figure 85. ^{1}H NMR (400 MHz, D_2O, 298 K) spectra of the titration of **1** with **14**: a) 0; b) 5; c) 10; d) 15; e) 20; f) 30; g) 40; h) 50; i) 60 and j) 70 equiv. See Figure 19 for proton assignment. *Residual solvent peak.

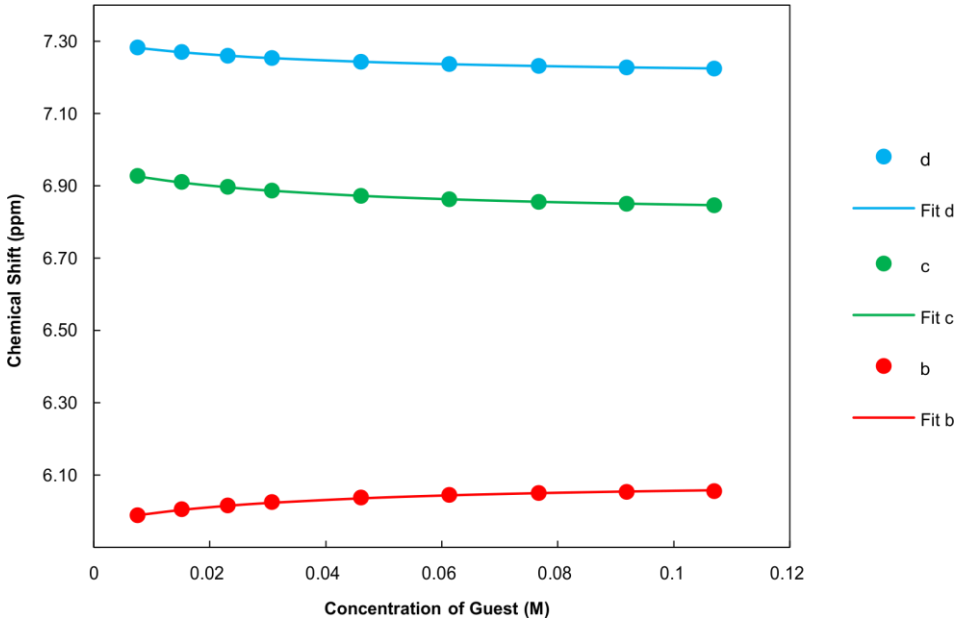

Figure 86. Chemical shifts of the proton signals of **1** upon incremental amounts of **14** (circles) and fit of the titration data to a theoretical 1:1 binding model (lines).

Table 13. Chemical shifts for the proton signals of bound host **1** (δ_{bound}, ppm) obtained from the fit of the ^{1}H NMR titration data (calix[4]pyrrole **1** with **14**) to a theoretical 1:1 binding model and induced chemical shifts ($\Delta\delta = \delta_{bound} - \delta_{free}$, ppm).

Signal	δ_{free}	δ_{bound}	$\Delta\delta$
b	5.97	6.09	+0.12
c	6.95	6.81	-0.14
d	7.30	7.20	-0.10

5.4.6 NMR spectra with di-formamide

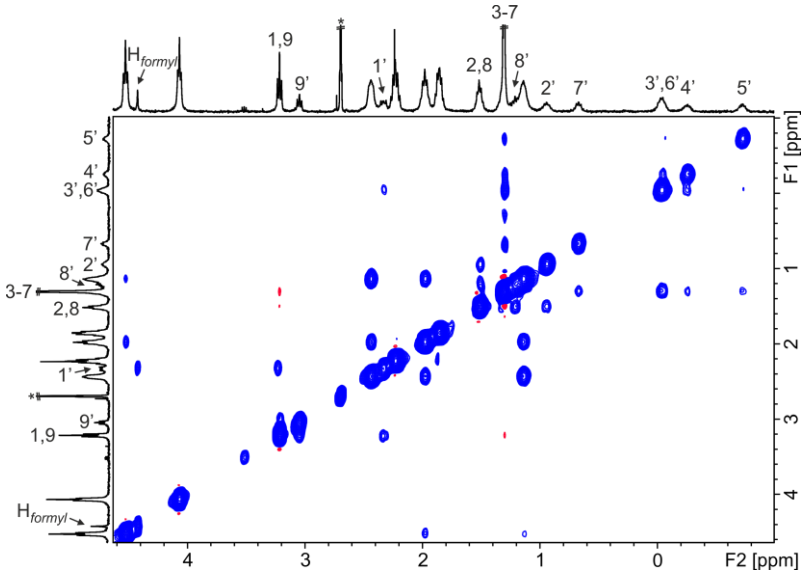

Figure 87. Selected region of the 2D ^{1}H-^{1}H NOESY NMR (400 MHz, D_2O, 298 K, t_{mix} = 0.6 s) spectrum of calix[4]pyrrole **15** and di-formamide **16** (2:1 ratio). Primed letters correspond to proton signals of bound *trans*,*cis*-**16**. See Figure 50 for proton assignment. *Residual solvent peak.

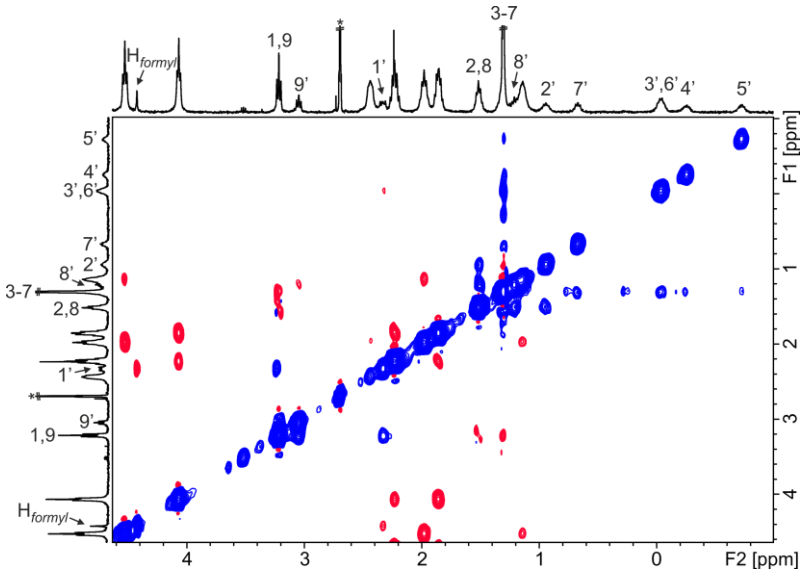

Figure 88. Selected region of the 2D ^{1}H-^{1}H ROESY NMR (400 MHz, D_2O, 298 K, spin-lock = 0.4 s) spectrum of calix[4]pyrrole **15** and di-formamide **16** (2:1 ratio). Primed letters correspond to proton signals of bound *trans*,*cis*-**16**. See Figure 50 for proton assignment. *Residual solvent peak.

Table 14. Chemical shifts (δ, ppm) of the protons of free and bound *trans,cis*-**16** (*trans,cis*-**16**⊂**15**) and complexation induced shifts ($\Delta\delta$, ppm).

Signal	δ_{free}	δ_{bound}	$\Delta\delta$
cis	7.97	4.43	-3.54
1	3.23	2.33	-0.90
2	1.53	0.94	-0.59
3	1.31	-0.03	-1.34
4	1.31	-0.26	-1.57
5	1.31	-0.72	-2.03
6	1.31	-0.03	-1.34
7	1.31	0.67	-1.98
8	1.53	1.21	-0.32
9	3.23	3.05	-0.18

5.4.7 ITC titration experiments

ITC experiments were performed in a MicroCal VP-ITC MicroCalorimeter with the VP Viewer 2000 software. Titrations were carried out by adding small aliquots (6-16 μL) of a water solution of the guest into a solution of the host in the same solvent. The concentration of guest solutions was approximately seven to ten times more concentrated than receptor solutions ([H] = 1 mM). The association constants and the thermodynamic parameters were obtained from the fit of the titration data to the "one set of sites" binding model implemented in the Microcal ITC Data Analysis module.

5.4.8 Molecular modelling structures

The energy minimized structures (PM3, water COSMO model) of the inclusion complexes were obtained using SCIGRESS Version FJ 2.6. The theoretical chemicals shifts for the proton signals of free and bound amides were computed from the energy minimized structures at the DFT level of theory (BP86-D3-def2-SVP) using Turbomole Version 7.0.[49,50] Tetramethylsilane (TMS) has been calculated with the same conditions and employed as reference. Alkyl chains and pyridinium groups were pruned to methyl groups to ease the calculations.

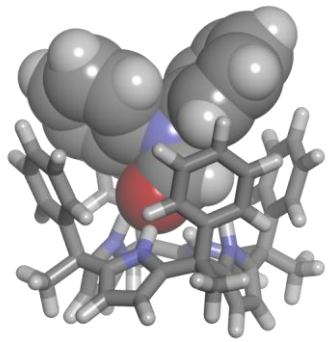

Figure 89. Energy minimized structure (PM3, water COSMO model) of the inclusion complex **4⊂1**. The calix[4]pyrrole is depicted in stick representation and bound amide is shown as CPK model.

Table 15. Energy of the **4⊂1** complex (PM3, water COSMO model)**.**

Complex	*E* (kcal·mol^{-1})
4⊂1	213.6

5.5 References and Notes

[1] G. Fischer, *Chem. Soc. Rev.* **2000**, *29*, 119-127.

[2] C. Dugave, L. Demange, *Chem. Rev. (Washington, DC, U. S.)* **2003**, *103*, 2475-2532.

[3] W. E. Stewart, T. H. Siddall, *Chem. Rev. (Washington, DC, U. S.)* **1970**, *70*, 517-551.

[4] G. E. S. Schulz, R. H., *Principles of Protein Structure*, Springer-Verlag, New York, **1979**.

[5] O. Tchaicheeyan, *FASEB J.* **2004**, *18*, 783-789.

[6] H. Kagechika, T. Himi, E. Kawachi, K. Shudo, *J. Med. Chem.* **1989**, *32*, 2292-2296.

[7] W. L. Cody, J. X. He, M. D. Reily, S. J. Haleen, D. M. Walker, E. L. Reyner, B. H. Stewart, A. M. Doherty, *J. Med. Chem.* **1997**, *40*, 2228-2240.

[8] M. Keller, C. Boissard, L. Patiny, N. N. Chung, C. Lemieux, M. Mutter, P. W. Schiller, *J. Med. Chem.* **2001**, *44*, 3896-3903.

[9] J. Chatterjee, D. Mierke, H. Kessler, *J. Am. Chem. Soc.* **2006**, *128*, 15164-15172.

[10] E. Biron, J. Chatterjee, O. Ovadia, D. Langenegger, J. Brueggen, D. Hoyer, H. A. Schmid, R. Jelinek, C. Gilon, A. Hoffman, H. Kessler, *Angew. Chem., Int. Ed.* **2008**, *47*, 2595-2599.

[11] F. D. Lewis, E. L. Burch, *J. Am. Chem. Soc.* **1994**, *116*, 1159-1160.

[12] E. Bairaktari, D. F. Mierke, S. Mammi, E. Peggion, *J. Am. Chem. Soc.* **1990**, *112*, 5383-5383.

[13] A. Jabs, M. S. Weiss, R. Hilgenfeld, *J. Mol. Biol.* **1999**, *286*, 291-304.

[14] C. C. Forbes, A. M. Beatty, B. D. Smith, *Org. Lett.* **2001**, *3*, 3595-3598.

[15] B. C. Gorske, J. R. Stringer, B. L. Bastian, S. A. Fowler, H. E. Blackwell, *J. Am. Chem. Soc.* **2009**, *131*, 16555-16567.

[16] R. R. Gardner, S. L. McKay, S. H. Gellman, *Org. Lett.* **2000**, *2*, 2335-2338.

[17] C. Vicent, S. C. Hirst, F. Garciatellado, A. D. Hamilton, *J. Am. Chem. Soc.* **1991**, *113*, 5466-5467.

[18] F. H. Beijer, R. P. Sijbesma, J. A. J. M. Vekemans, E. W. Meijer, H. Kooijman, A. L. Spek, *J. Org. Chem.* **1996**, *61*, 6371-6380.

[19] G. J. Pernía, J. D. Kilburn, J. W. Essex, R. J. Mortishire-Smith, M. Rowley, *J. Am. Chem. Soc.* **1996**, *118*, 10220-10227.

[20] M. J. Deetz, J. E. Fahey, B. D. Smith, *J. Phys. Org. Chem.* **2001**, *14*, 463-467.

[21] W. C. Still, *Acc. Chem. Res.* **1996**, *29*, 155-163.

[22] C. Allott, H. Adams, C. A. Hunter, J. A. Thomas, P. L. Bernad Jr, C. Rotger, *Chem. Commun. (Cambridge, U. K.)* **1998**, 2449-2450.

[23] W. E. Allen, P. A. Gale, C. T. Brown, V. M. Lynch, J. L. Sessler, *J. Am. Chem. Soc.* **1996**, *118*, 12471-12472.

[24] T. Guinovart, D. Hernández-Alonso, L. Adriaenssens, P. Blondeau, M. Martínez-Belmonte, F. X. Rius, F. J. Andrade, P. Ballester, *Angew. Chem., Int. Ed.* **2016**, *55*, 2435-2440.

[25] B. Verdejo, G. Gil-Ramírez, P. Ballester, *J. Am. Chem. Soc.* **2009**, *131*, 3178-3179.

[26] K. D. Bhatt, D. J. Vyas, B. A. Makwana, S. M. Darjee, V. K. Jain, *Spectrochim. Acta, Part A* **2014**, *121*, 94-100.

[27] D. Hernandez-Alonso, S. Zankowski, L. Adriaenssens, P. Ballester, *Org. Biomol. Chem.* **2015**, *13*, 1022-1029.

[28] K.-D. Zhang, D. Ajami, J. Rebek, *J. Am. Chem. Soc.* **2013**, *135*, 18064-18066.

[29] A. Díaz-Moscoso, D. Hernández-Alonso, L. Escobar, F. A. Arroyave, P. Ballester, *Org. Lett.* **2017**, *19*, 226-229.

[30] J. R. Blas, M. Márquez, J. L. Sessler, F. J. Luque, M. Orozco, *J. Am. Chem. Soc.* **2002**, *124*, 12796-12805.

[31] J. R. Blas, J. M. López-Bes, M. Márquez, J. L. Sessler, F. J. Luque, M. Orozco, *Chem.--Eur. J.* **2007**, *13*, 1108-1116.

[32] G. Gil-Ramirez, E. C. Escudero-Adan, J. Benet-Buchholz, P. Ballester, *Angew. Chem., Int. Ed.* **2008**, *47*, 4114-4118.

[33] H. Adams, F. J. Carver, C. A. Hunter, N. J. Osborne, *Chem. Commun. (Cambridge, U. K.)* **1996**, 2529-2530.

[34] I. Alfonso, M. I. Burguete, F. Galindo, S. V. Luis, L. Vigara, *J. Org. Chem.* **2007**, *72*, 7947-7956.

[35] L. M. Salonen, M. Ellermann, F. Diederich, *Angew. Chem., Int. Ed.* **2011**, *50*, 4808-4842.

[36] V. P. Manea, K. J. Wilson, J. R. Cable, *J. Am. Chem. Soc.* **1997**, *119*, 2033-2039.

[37] C. Frassineti, S. Ghelli, P. Gans, A. Sabatini, M. S. Moruzzi, A. Vacca, *Anal. Biochem.* **1995**, *231*, 374-382.

[38] G.-B. Huang, S.-H. Wang, H. Ke, L.-P. Yang, W. Jiang, *J. Am. Chem. Soc.* **2016**, *138*, 14550-14553.

[39] L.-L. Wang, Z. Chen, W.-E. Liu, H. Ke, S.-H. Wang, W. Jiang, *J. Am. Chem. Soc.* **2017**, *139*, 8436-8439.

[40] P. S. Cremer, A. H. Flood, B. C. Gibb, D. L. Mobley, *Nature Chem.* **2017**, *10*, 8.

[41] L. Escobar, P. Ballester, *Org. Chem. Front.* **2019**, *6*, 1738-1748.

[42] X. Cha, K. Ariga, T. Kunitake, *J. Am. Chem. Soc.* **1996**, *118*, 9545-9551.

[43] A. T. Wright, E. V. Anslyn, *Org. Lett.* **2004**, *6*, 1341-1344.

[44] H. Imai, H. Munakata, Y. Uemori, N. Sakura, *Inorg. Chem.* **2004**, *43*, 1211-1213.

[45] C. P. Mandl, B. König, *J. Org. Chem.* **2005**, *70*, 670-674.

[46] C. Schmuck, U. Machon, *Chem.--Eur. J.* **2005**, *11*, 1109-1118.

[47] M. E. Bush, N. D. Bouley, A. R. Urbach, *J. Am. Chem. Soc.* **2005**, *127*, 14511-14517.

[48] G. R. Fulmer, A. J. M. Miller, N. H. Sherden, H. E. Gottlieb, A. Nudelman, B. M. Stoltz, J. E. Bercaw, K. I. Goldberg, *Organometallics* **2010**, *29*, 2176-2179.

[49] A. D. Becke, *Phys. Rev. A* **1988**, *38*, 3098-3100.

[50] R. Ahlrichs, M. Bar, M. Haser, H. Horn, C. Kolmel, *Chem. Phys. Lett.* **1989**, *162*, 165-169.

UNIVERSITAT ROVIRA I VIRGILI
MOLECULAR CONTAINERS BASED ON ARYL-EXTENDED CALIX[4]PYRROLES
Luis Escobar González

Chapter 6

Synthesis and Binding Studies of a Tetra-*α* Aryl-Extended Photoresponsive Calix[4]pyrrole Receptor Bearing *meso*-Alkyl Substituents

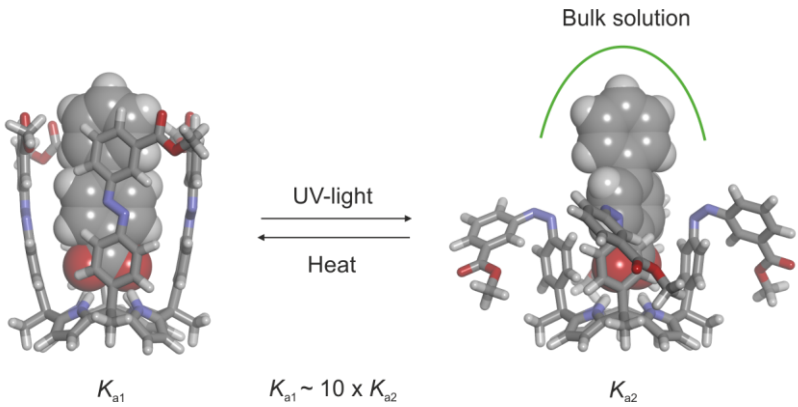

Part of this chapter has been published in:

L. Escobar, F. A. Arroyave, P. Ballester, *Eur. J. Org. Chem.* **2018**, 1097-1106.

EurJOC
European Journal of Organic Chemistry

A Journal of
ChemPubSoc Europe

9/2018
www.eurjoc.org

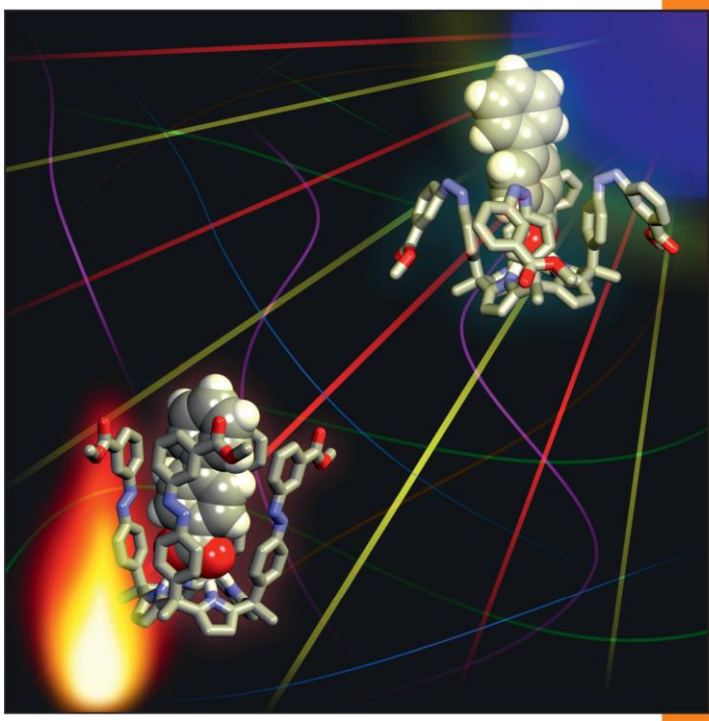

Front Cover

Pablo Ballester et al.
Synthesis and Binding Studies of a Tetra-α Aryl-Extended Photoresponsive Calix[4]pyrrole Receptor Bearing *meso*-Alkyl Substituents

Supported by
ACES Asian Chemical Editorial Society

WILEY-VCH

6.1 Introduction

Photoresponsive functional molecular systems couple external light stimuli with the modification of their molecular and supramolecular properties.[1] The coupling requires the intermediacy of photochromic units, also known as molecular switches, experiencing a significant change in shape and spectroscopic properties upon light-irradiation.[2] The study of photoswitchable molecular catalyst,[3,4] as well as light-modulated host-guest systems is of current interest.[5,6] This later function enabled the realization of light-induced molecular motions in mechanically interlocked molecules and the light-controlled delivery/uptake of molecular cargo in supramolecular encapsulation complexes.[7,8] Different photoresponsive groups (*e.g.* azobenzenes, dithienylethenes and anthracenes) were incorporated in the scaffolds of supramolecular and unimolecular receptors.[1,2] The photo-isomerization process of the properly positioned photoswitches served to control the hosts' binding affinities by changing their geometries and/or inner space properties.[9,10] Alternatively, the light-controlled modulation of the binding properties of host-guest systems might involve the use of photoswitchable guests.[11] However, this later approach results in the release of structurally modified cargo (guest).

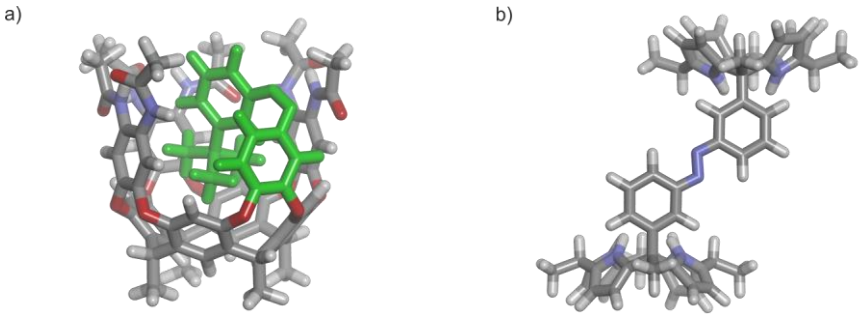

Figure 1. Energy minimized structures (MM3): a) Rebek's resorcin[4]arene cavitand bearing an azobenzene unit (introverted *cis*-azobenzene is highlighted) and b) Kohnke's dimeric calix[4]pyrrole receptor (*trans*-azobenzene). The receptors are depicted in stick representation.

Main azobenzenes are stable photochromic units that have been employed extensively as photoswitches in the development of host-guest systems.[12,13,14,15,16] Examples of their incorporation in calix[4]arene,[17,18,19] and resorcin[4]arene derivatives are abundant.[11,20] For example, we described the attachment of four terminal azobenzene groups to tetra-urea calix[4]arenes. These photoswitchable molecules self-assembled into dimeric capsules and showed that their *trans*-to-*cis* photoisomerization induced the release of the encapsulated organic cation (*e.g.* tetra-methylphosphonium) to the bulk solution.[21] Rebek and co-workers attached one azobenzene group to a deep cavitand derived from a resorcin[4]arene scaffold (Figure 1a).[22,23] They showed that the *trans*/*cis* photo-isomerization regulated the binding of adamantane derivatives. Resorcin[4]arenes bearing four azobenzene substituents have been also synthesized and studied the light-induced isomerization of the self-assembled hexameric capsules.[24] Recently,

a resorcin[4]arene carcerand having four azobenzene groups in its walls was described.[25] In this case, the photo-isomerization process provoked the distortion of the carcerand's structural geometry.

Azobenzene groups have also been appended to calix[4]pyrrole units but to a lesser extent. In this vein, Kohnke and co-workers synthesized a calix[4]pyrrole dimeric receptor bearing an azobenzene group as spacer (Figure 1b).[26] The *trans*-isomer complexed aliphatic *bis*-carboxylates (*e.g*. adipate, succinate and glutarate) forming 1:1 complexes with association constant values in the range of 10^3-10^4 M^{-1} in $(CH_3)_2SO$ solution. The *cis*-counterpart showed noticeable improvements in its binding affinities for the shorter di-topic guests. The reported affinity values indicated a three-fold increase in the case of glutarate and a gain of almost two orders of magnitude for the succinate. Lately, our research group produced tetra-urea aryl-extended calix[4]pyrroles with terminal azobenzene groups demonstrating their capacity to self-assemble into photoresponsive homo- and hetero-dimeric capsules.[27,28]

Tetra-azobenzene extended calix[4]pyrroles bearing *meso*-methyl substituents were previously reported in literature, however, their molecular recognition and photo-isomerization properties were not explored.[29,30] Herein, we describe an alternative synthetic route for the preparation of a tetra-azobenzene extended calix[4]pyrrole. The prepared receptor was isolated as pure tetra-*α* configurational isomer bearing *meso*-alkyl substituents functionalized with terminal ethyl ester groups. We also report the results of light-induced isomerization studies of the all-*trans* receptor that were monitored using ^{1}H NMR and UV/Vis spectroscopies. We selected 4-phenyl pyridine *N*-oxide and tetra-methylammonium 1,1'-bi-phenyl 4-carboxylate as guests. We describe the binding properties of the all-*trans* isomer, as well as of the *cis*-enriched isomeric mixture produced by light-irradiation at 365 nm, in which the all-*cis* isomer is present to an extent larger than 80%. The binding studies were performed in both dichloromethane and acetonitrile solutions by means of ^{1}H NMR spectroscopy titrations and isothermal titration calorimetry (ITC) experiments.

6.2 Results and Discussion

6.2.1 Synthesis

Tetra-*α* 4-nitrophenyl calix[4]pyrrole **1a** was prepared by acid-catalyzed (4 M HCl in dioxane) cyclocondensation of pyrrole and ethyl 5-(4'-nitrophenyl)-5-oxopentanoate **2**[31] (Scheme 1). The cyclocondensation reaction was carried out in two consecutive steps in order to improve the yield of the tetra-*α* isomer. First, both reactants were stirred for 24 h in dry ethanol and HCl yielding a complex mixture of aryl-extended calix[4]pyrrole stereoisomers and open oligomers. Next, the isolated crude reaction mixture was redissolved in dry CH_2Cl_2 and stirred for an additional 48 h at room temperature in the presence of HCl. After work-up, the crude reaction mixture was purified by column chromatography. Further purification by crystallization provided calix[4]pyrrole **1a** in 11%

yield. The catalytic hydrogenation of the tetra-nitro compound **1a** using 10% Pd/C afforded tetra-aniline calix[4]pyrrole **1b** in high yield (Scheme 1).

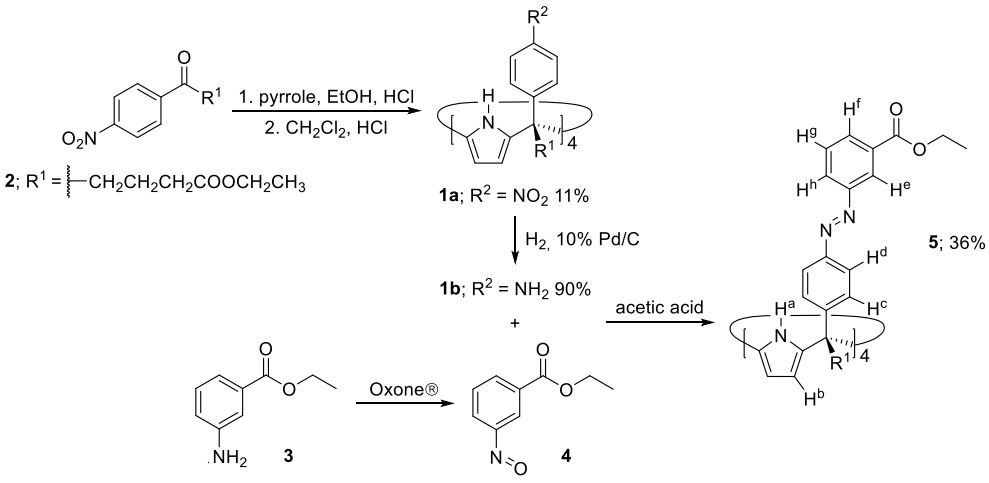

Scheme 1. Synthesis of the aryl-extended calix[4]pyrroles **1a** and **1b**, and the tetra-azobenzene extended calix[4]pyrrole **5**.

The Oxone® mediated oxidation of aniline **3** provided the labile nitroso-arene derivative **4**, which was treated without further purification with tetra-aniline calix[4]pyrrole **1b**, under Mills reaction conditions. Tetra-azobenzene extended calix[4]pyrrole **5** was obtained as a mixture of *cis-trans* stereoisomers in 36% yield after column chromatography purification of the crude reaction mixture (Scheme 1). All compounds, except nitroso-arene **4**, were fully characterized by a set of high-resolution spectra (NMR and HRMS).

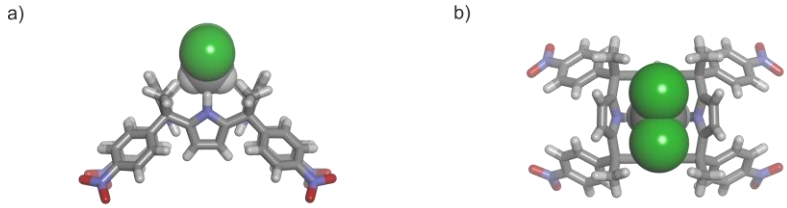

Figure 2. Preliminary solution of the X-ray crystal structure of $CH_2Cl_2 \subset$ **1a**: a) side and b) top views. The calix[4]pyrrole is depicted in stick representation and the CH_2Cl_2 molecule is shown as CPK model. Alkyl substituents are pruned to methyl groups for clarity.

In the case of tetra-nitro calix[4]pyrrole **1a**, single crystals suitable for X-ray diffraction analysis were obtained by slow evaporation of dichloromethane from a solution of **1a**. The preliminary solution of the diffracted data confirmed that the isolated tetra-nitro calix[4]pyrrole **1a** was the tetra-*α* isomer. **1a** adopts a 1,3-alternate conformation in the crystal packing with a bound CH_2Cl_2

molecule (Figure 2). Most likely, the hydrogen atoms of the solvent molecule are involved in CH-π interactions with two opposite pyrrole units of the calix[4]pyrrole core.

6.2.2 Photo-isomerization studies of tetra-azobenzene calix[4]pyrrole **5**

We investigated the photo-isomerization process of tetra-azobenzene calix[4]pyrrole **5** by means of ^{1}H NMR and UV/Vis spectroscopies. The ^{1}H NMR spectrum of the isolated mixture of *cis*-*trans* stereoisomers of **5** in CD_2Cl_2 solution showed, after thermal equilibration at 60°C in the dark for 24 h, a single set of sharp and well-resolved proton signals in agreement with a C_{4v} symmetry. The observed set of proton signals was assigned to the exclusive presence of all-*trans*-**5** isomer (*tttt*-**5**) (Figure 3a). Next, the CD_2Cl_2 solution of *tttt*-**5** was photo-irradiated with UV light (365 nm) for 30 min (Figure 3b,c). We acquired a ^{1}H NMR spectrum of the light-irradiated solution every 5 min. During the irradiation experiment, we observed the gradual disappearance of the proton signals assigned to *tttt*-**5** and the emergence of several sets of new proton signals, which in turn evolved with time. We assigned these new sets of signals to the formation of five possible *cis*-enriched isomers of **5** (*i.e. tttc*-, *ttcc*-, *tctc*-, *tccc*- and *cccc*-isomers of **5**). The photostationary state (*PSS*) was reached within 15-20 min, as evidenced by the fact that the ^{1}H NMR spectra of the mixture remained unchanged after this period of time (Figure 3c). We attributed the most intense set of proton signals, which are in agreement with a C_{4v} symmetry, to the *cccc*-**5** isomer. The signals of the two protons *ortho* to the azo groups in the terminal phenyl substituent of the azobenzene unit (H^e and H^h) in *cccc*-**5** experienced an upfield shift of *ca*. 1.0 ppm with respect to those in the *tttt*-**5** counterpart. The aromatic protons of the *meso*-phenyl substituents, H^c and H^d, also moved upfield. These observations are in agreement with the *trans*-to-*cis* isomerization of the azo groups in *tttt*-**5**. The *cis*-azo isomer adopted a tilted U-shaped conformation directing the protons *ortho* to the azo group in one of its phenyl substituent towards the shielding cone of the other. Most likely, the deshielding of H^c in *cccc*-**5** is due to the close proximity in space of the *cis*-isomerized azobenzene units. The integral value of the proton signals remaining for *trans*-azo groups at the *PSS* with respect to those of the *β*-pyrrole protons in all isomers enabled us to estimate that the *cis*-isomerization of the azo groups occurred to an extent close to 85%. This result suggested that in *tttt*-**5** each azo group experiences an independent *cis*-isomerization process.

The *cis*-enriched mixture of **5** was thermally equilibrated in the dark and analyzed by ^{1}H NMR spectroscopy. We observed a single set of proton signals diagnostic of the exclusive presence of the *tttt*-**5** isomer in solution (Figure 3d). This result demonstrated the reversibility of the photo-isomerization process and the photostability of tetra-azobenzene **5** under these light-irradiation conditions. The photo-isomerization and thermal equilibration was repeated several times without **5** showing signs of degradation. It is worth mentioning here that typically, aryl-extended calix[4]pyrroles readily decompose under UV light. In complete agreement with our previous findings in the case of tetra-urea calix[4]pyrroles equipped with azobenzene units,[28] the incorporation of the photoswitch seemed to endow photostability to the calix[4]pyrrole **5**. We

suggest that the azobenzene units might act as inner filters absorbing the high-energy photons produced by the light source.

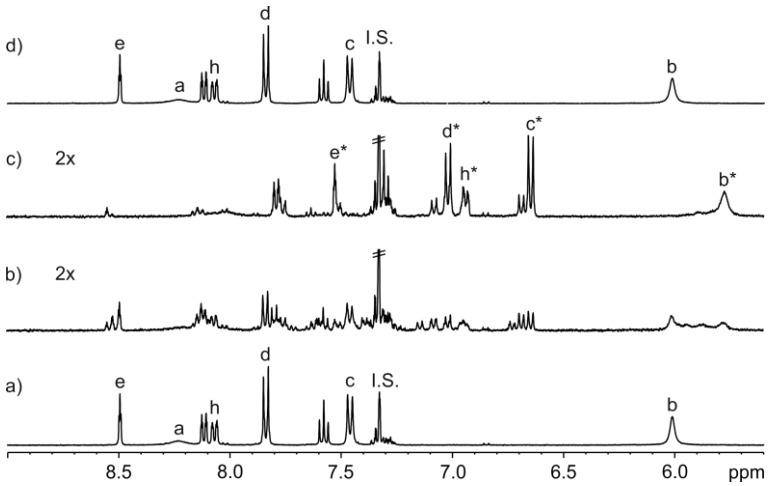

Figure 3. Selected region of the ^{1}H NMR (400 MHz, CD_2Cl_2, 298 K) spectra of **5**: a) after thermal equilibration; after photo-irradiation (365 nm): b) 5 and c) 20 min; d) after thermal re-equilibration. Letters with an asterisk correspond to protons of *cccc*-**5**. Benzyl methyl ether (I.S.). See Scheme 1 for proton assignment.

We also performed the switching between the different states of **5** (*tttt*-**5** and mixture of *cis*-enriched isomers at the *PSS*) using CD_3CN solutions and obtaining quite similar results (see Experimental Section).

Additionally, the photo-isomerization of tetra-azobenzene extended calix[4]pyrrole **5** in dichloromethane solution was studied using UV/Vis spectroscopy. The UV/Vis absorption spectrum of *tttt*-**5** obtained after thermal equilibration of the solution (Figure 4a) showed a strong band centered at 326 nm commonly attributed to the allowed π-π* transition of *trans*-azobenzenes.[13] Photo-irradiation of the sample at 365 nm for 3 min (Figure 4c) provoked a decrease in the intensity of the band and a concomitant hypsochromic shift ($\Delta\lambda$ = -24 nm) of its maximum. Simultaneously, a new band centered at 436 nm grew in intensity. This emerging band was attributed to the allowed n-π* transition of *cis*-azobenzenes.[13] Prolonged photo-irradiation times did not produce further changes in the UV/Vis spectrum. We concluded that the *PSS* was reached after three minutes of UV irradiation owing to the diluted conditions used in the experiment. In contrast, NMR spectroscopic experiments required 15-20 min of photo-irradiation to achieve the *PSS* (see above).

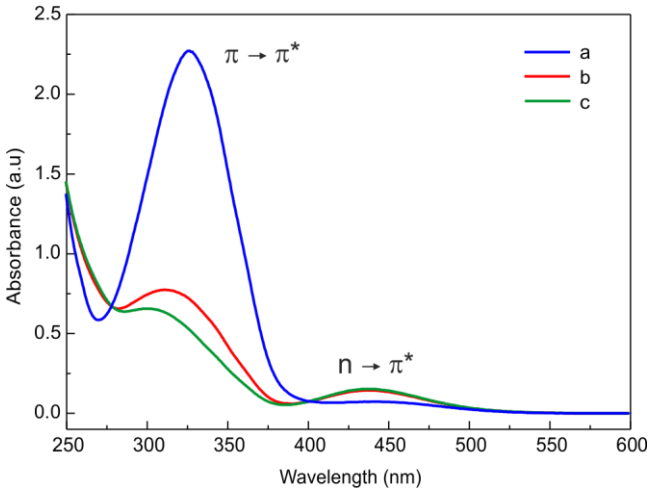

Figure 4. UV/Vis spectra of a dichloromethane solution of **5** (25 μM): a) after thermal equilibration; photo-irradiation (365 nm): b) 1 and c) 3 min.

6.2.3 Binding studies of tetra-azobenzene extended calix[4]pyrrole **5** by ^{1}H NMR spectroscopy

We probed the interaction of *tttt*-**5** with 4-phenyl pyridine *N*-oxide **6** and tetra-methylammonium 1,1'-bi-phenyl 4-carboxylate **7**•NMe_4 (Figure 5) in both CD_2Cl_2 and CD_3CN solutions by ^{1}H NMR spectroscopy titrations.

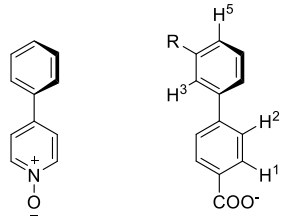

6

7•NMe_4; R = H^4
8•NMe_4; R = F

Figure 5. Line-drawing structures of 4-phenyl pyridine *N*-oxide **6** and tetra-methylammonium carboxylates **7**•NMe_4 and **8**•NMe_4.

The ^{1}H NMR spectrum of a 1 mM solution of **5** in CD_3CN after thermal equilibration showed the diagnostic signals for the *tttt*-**5** isomer (Figure 6a). Typically, in polar solvents (*e.g.* acetone and acetonitrile), aryl-extended calix[4]pyrroles adopt the cone conformation[31,32,33,34] being pre-organized for the inclusion of suitable electron-rich neutral and anionic guests. The addition of 0.4 equiv. of carboxylate salt **7**•NMe_4 to the above CD_3CN solution (Figure 6b) produced the appearance of a new set of signals that were assigned to the protons of the bound host. The

observation of separate proton signals for the free and bound receptor was indicative of a binding equilibrium featuring slow chemical exchange dynamics on the NMR chemical shift timescale. Significantly, the pyrrole NHs (H^a) in the bound host appeared downfield shifted ($\Delta\delta$ = +4.2 ppm) suggesting their involvement in hydrogen-bonding interactions with the carboxylate group of **7**.

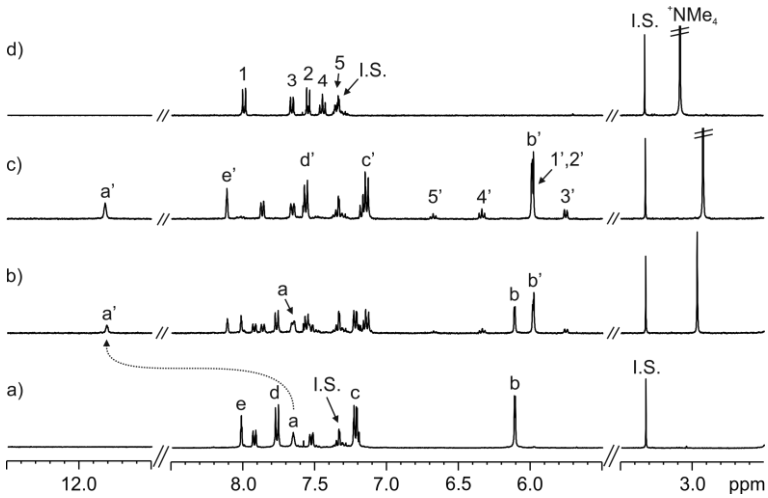

Figure 6. Selected regions of the ^{1}H NMR (400 MHz, CD_3CN, 298 K) spectra of the titration of *tttt*-**5** with **7**•NMe_4: a) 0; b) 0.4 and c) 1 equiv.; d) **7**•NMe_4. Primed letters and numbers correspond to proton signals of bound components. See Scheme 1 and Figure 5 for proton assignments. Benzyl methyl ether (I.S.).

We also observed that the aromatic protons of the added carboxylate **7** resonated as a single set of upfield shifted signals with respect to those of **7**•NMe_4 free in solution. The protons H^1, *alpha* to the carboxylate, moved to δ = 5.98 ppm experiencing the largest upfield shift ($\Delta\delta$ = -2.02 ppm). Protons H^2, H^3 and H^4 also shifted more than 1 ppm upfield. In contrast, the resonance of H^5 suffered a more reduced upfield shift of *ca.* 0.7 ppm. These observations indicated that carboxylate **7** was deeply included in the aromatic cavity of *tttt*-**5**. The aromatic protons H^1-H^4 were maximally exposed to the π-systems of the aromatic rings and the azo bond, while H^5 is located near the upper rim of the cavity and pointed away from it. At this point, the protons of the tetra-methylammonium cation, $^+NMe_4$, resonated as a sharp singlet at δ = 2.92 ppm. Their reduced upfield chemical shift change ($\Delta\delta$ = -0.16 ppm) suggested that the cation was not bound to a significant extent in the shallow and electron-rich aromatic cavity defined by the pyrrole rings in cone conformation that is opposite to the included carboxylate. In short, the inclusion complex formed by **7**•NMe_4 and *tttt*-**5** in acetonitrile solution was not extensively ion-paired mainly having an anionic character.

The intensity of the proton signals of bound *tttt*-**5** grew at the expenses of the original ones as the salt concentration was increased. Thus, when 1 equiv. of carboxylate salt **7**•NMe_4 (Figure 6c) was added, only the proton signals for bound *tttt*-**5** were observed. This result indicated that the anionic

inclusion complex had a 1:1 stoichiometry, **7**⊂*tttt*-**5**, and its binding constant could be estimated as larger than 10^4 M^{-1}.

The addition of an excess of **7**•NMe_4 did not produce further changes in the proton signals of the bound partners, *tttt*-**5** and **7**, but provoked a reduced downfield chemical shift change in the singlet corresponding to the methyl groups of the $^+NMe_4$ cation. The organic cation was involved in a fast chemical exchange between the free and minimally bound counterpart. In contrast but in agreement with the slow dynamics featured by the binding process producing the **7**⊂*tttt*-**5** anionic complex, the emergence of the proton signals corresponding to free carboxylate **7** was readily observed in the ^{1}H NMR spectrum of the mixture in the presence of an excess of the salt. We obtained a similar behaviour (dynamics and chemical shift changes) in the titration of *tttt*-**5** with the neutral *N*-oxide **6** performed in CD_3CN solution (see Experimental Section).

We also studied the binding of *tttt*-**5** with both guests, **6** and **7**•NMe_4, in CD_2Cl_2 solutions. In non-polar solvents, such as dichloromethane or chloroform, calix[4]pyrrole *tttt*-**5** is expected to adopt an alternate conformation[34,35] and the binding of a polar guest, *i.e. N*-oxide **6** or carboxylate **7**, induces the receptor to adopt the cone conformation. The results of the ^{1}H NMR titrations revealed that both guests also formed thermodynamically and kinetically highly stable 1:1 complexes with *tttt*-**5** in CD_2Cl_2 solution for which we estimated K_a values larger than 10^4 M^{-1} (see Experimental Section). The most noticeable difference for the titration of *tttt*-**5** with **7**•NMe_4 in acetonitrile and dichloromethane solutions, was the observation of a sharp singlet appearing at δ = 1.81 ppm in the later case. This signal corresponded to the protons of the bound tetra-methylammonium cation when sub-stoichiometric amounts of **7**•NMe_4 were added. The large upfield chemical shift ($\Delta\delta$ = -1.64 ppm) experienced by the methyl groups of $^+NMe_4$ in CD_2Cl_2 solution located the cation in the shallow aromatic cavity surrounded by the pyrrole rings and opposite to the bound carboxylate **7**. This observation is also indicative that in CD_2Cl_2 solution the formed complex features a receptor separated ion-paired geometry **7**⊂*tttt*-**5**•NMe_4.[36] The incremental addition of more than 1 equiv. of **7**•NMe_4 produced a gradual downfield chemical shift and broadening of the singlet. This is due to the chemical exchange process between free and bound tetra-methylammonium cations featuring intermediate dynamics on the NMR timescale owing to the shallow inclusion of the bound counterpart.

Simple molecular modelling studies (MM3) showed that **6** and **7** are perfectly shape, size and function complementary to the aromatic polar cavity of *tttt*-**5**. The two energy minimized inclusion complexes, **6**⊂*tttt*-**5** and **7**⊂*tttt*-**5**•NMe_4, displayed the bi-phenyl scaffolds of the guests fully included in the deep and polar three-dimensional aromatic cavity featured by *tttt*-**5** in cone conformation (Figure 7). The included guests experience multiple CH-π and π-π interactions with the aromatic walls of the container. The pyrrole NHs are involved in hydrogen-bonding interactions with the oxygen atoms of the polar groups of the included guests (carboxylate and *N*-oxide). Additionally, the structure of the **7**⊂*tttt*-**5**•NMe_4 complex exposed the excellent fit of one of the

methyl groups of the tetra-methylammonium cation in the shallow aromatic cavity opposed to the bound carboxylate.

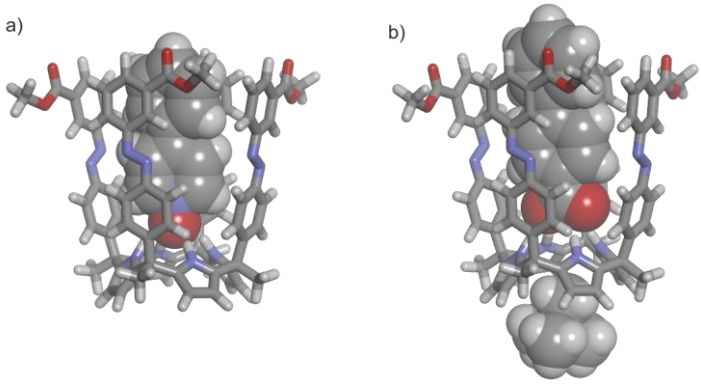

Figure 7. Energy minimized structures (MM3) of the inclusion complexes: a) **6**⊂*tttt*-**5** and b) **7**⊂*tttt*-**5**•NMe_4. Included guest molecules (**6** and **7**•NMe_4) are shown as CPK models and **5** is depicted in stick representation. For clarity, *meso*-alkyl substituents are pruned to methyl groups.

6.2.4 Light-irradiation experiments of the inclusion complexes of *tttt*-**5**

The ^{1}H NMR analysis of an equimolar mixture of the thermally stabilized *tttt*-**5** and **7**•NMe_4 in CD_3CN solution showed the quantitative formation of the anionic complex **7**⊂*tttt*-**5**. The solution was light-irradiated at 365 nm with the acquisition of a ^{1}H NMR spectrum of the mixture every 5 min (Figure 8a,b). The *PSS* was reached within 20 min. The light-irradiation produced the appearance of multiple sets of proton signals in the aromatic region of the ^{1}H NMR spectra for the bound host. The sharp singlet corresponding to the NH protons of bound *tttt*-**5** converted into a complex multiplet. The protons of the bound carboxylate also split into several sets of signals, none of them coinciding with free **7** in CD_3CN solution. All together, these observations suggested that light-irradiation of **7**⊂*tttt*-**5** induced the appearance of *cis*-enriched isomeric complexes (*tttc*-, *ttcc*-, *tctc*-, *tccc*- and *cccc*-isomers) without promoting the release of free **7** to the bulk solution. Thus, the *trans*-to-*cis* isomerization of the azo groups in **7**⊂*tttt*-**5** did not provoke a reduction in thermodynamic stability of the corresponding *cis*-enriched inclusion complexes leading to a significant guest release at millimolar concentration.

Following the photo-irradiation experiment, the sample was thermally equilibrated in the dark for 24 h at 60°C and the final solution re-analyzed by ^{1}H NMR spectroscopy (Figure 8c). The exclusive observation of the proton signals corresponding to the 1:1 complex of **7**⊂*tttt*-**5** with identical intensity to those of the original complex proved the photostability of both binding partners and the reversibility of the photo-isomerization process. Analogous results were observed in the case of the photo-irradiation and thermal equilibration of the inclusion complex of the 4-phenyl pyridine *N*-oxide, **6**⊂*tttt*-**5**, also in CD_3CN solution. We repeated the photo-isomerization

experiments of the inclusion complexes **6**⊂*tttt*-**5** and **7**⊂*tttt*-**5**•NMe_4 using CD_2Cl_2 as solvent (see Experimental Section). Both inclusion complexes showed analogous behaviors to the CD_3CN solutions. However, the thermal equilibration of the photo-irradiated solution of the *cis*-enriched isomers of **7**⊂*tttt*-**5**•NMe_4 did not exclusively produce the starting complex, but a mixture of the **7**⊂*tttt*-**5**•NMe_4 and Cl⊂*tttt*-**5**•NMe_4 complexes in a 75:25 ratio was observed. The presence of the Cl⊂*tttt*-**5**•NMe_4 complex was attributed to a secondary reaction of the carboxylate **7** with the CD_2Cl_2 solvent during the thermal equilibration process. This reaction produces the chloromethyl ester of the carboxylate and the tetra-methylammonium chloride complex, Cl⊂*tttt*-**5**•NMe_4 (see Experimental Section).

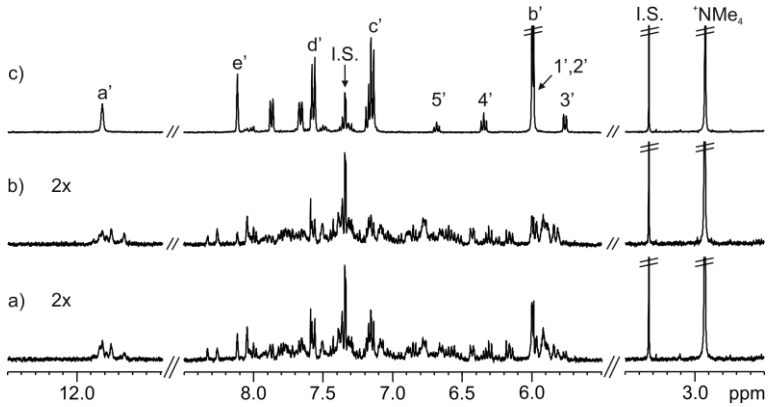

Figure 8. Selected regions of the ^{1}H NMR (400 MHz, CD_3CN, 298 K) spectra of **7**⊂*tttt*-**5** after photo-irradiation (365 nm): a) 10 and b) 20 min; c) after thermal equilibration. Primed letters and numbers correspond to proton signals of bound components. See Scheme 1 and Figure 5 for proton assignments. Benzyl methyl ether (I.S.).

It is worth mentioning that photo-irradiation of 4-phenyl pyridine *N*-oxide **6** in dichloromethane or acetonitrile produced its decomposition. However, decomposition did not happen when **6** was bound to **5** because the azobenzene groups of the receptor absorbed the high-energy photons emitted by the light source.

We also investigated the kinetics of the thermal equilibration processes for the mixture of *cis*-enriched **6**⊂**5** complexes and the free receptor **5** in CD_2Cl_2 solution at 40°C using ^{1}H NMR spectroscopy. The concentration changes of the *cis*- and *trans*-azo units at different time intervals were determined by integration. The fit of the concentration changes obeyed a first-order rate law and enabled the calculation of similar rate constant values for both processes, $k \sim 2 \times 10^{-2}$ h^{-1} (Figure 9). Thus, we calculated an energy barrier for the *cis*-to-*trans* thermal isomerization processes of the order of *ca.* 26 kcal·mol^{-1} (see Experimental Section). We mentioned above that the free receptor *tttt*-**5** and its inclusion complex, **6**⊂*tttt*-**5**, reached the *PSS* within 15-20 min at 1 mM concentrations. All together, these results indicate that the inclusion of the guest does not

have a significant effect on the kinetics of photo-isomerization and thermal equilibration of the bound receptor.

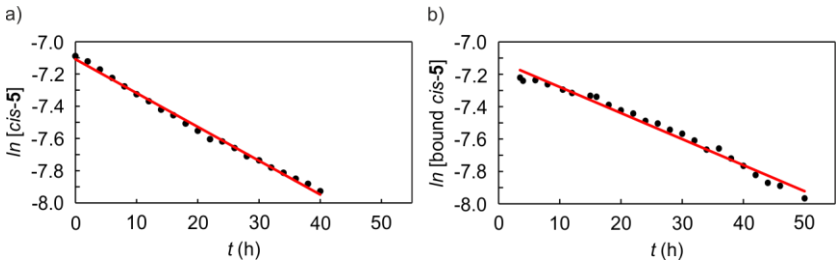

Figure 9. Thermal equilibration processes: a) *ln* [*cis*-**5**] and b) *ln* [bound *cis*-**5**] *vs.* time (h) (circles). The data were fitted to a first-order kinetic equation (red line). The *cis*-**5** and bound *cis*-**5** species correspond to the *cis*-enriched isomeric mixtures.

The inclusion complex of the fluoro carboxylate derivative, **8**⊂*tttt*-**5**, in CD_3CN solution was used to investigate the effect of the included guest in the composition of the mixture of *cis*-enriched isomers obtained at the *PSS* in comparison to the one produced using the free receptor *tttt*-**5**. The photo-isomerized solution of **8**⊂*tttt*-**5** was analyzed using $^{19}F\{^1H\}$ NMR spectroscopy. Unexpectedly, the $^{19}F\{^1H\}$ NMR spectrum of the *cis*-enriched mixture of inclusion complexes at the *PSS* showed the presence of five singlets. One of them corresponded to the original **8**⊂*tttt*-**5** complex (Figure 10a,b).

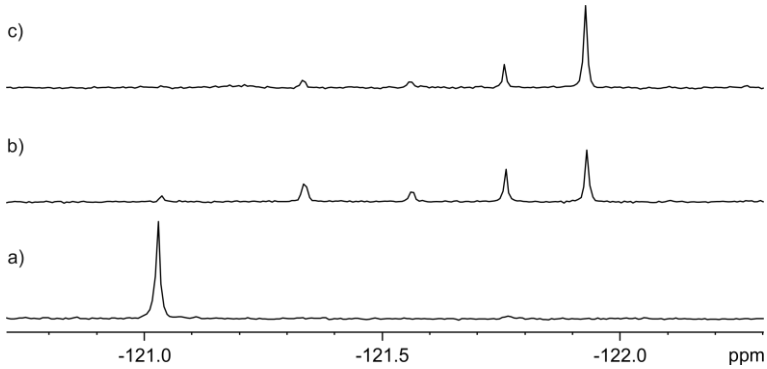

Figure 10. $^{19}F\{^1H\}$ NMR (471 MHz with cryoprobe, CD_3CN, 298 K) spectra: a) **8**⊂*tttt*-**5**; b) photo-irradiation (365 nm) of **8**⊂*tttt*-**5** for 20 min and c) photo-irradiation of *tttt*-**5** for 20 min followed by the addition of 1 equiv. of **8**•NMe_4.

Based on the integral values of the five singlets and the number of *cis*-azo groups present in each isomeric complex, we calculated that the light-irradiation produced the *trans*-to-*cis* isomerization of 65% of the azo groups. In turn, the mixture of inclusion complexes produced by the addition of 1 equiv. of the fluoro derivative salt **8**•NMe_4 to a photo-irradiated CD_3CN solution of the free receptor **5** at the *PSS* was also analyzed using NMR spectroscopy (Figure 10c). The $^{19}F\{^1H\}$ NMR

spectrum displayed only four fluorine signals. The singlet corresponding to **8**⊂*tttt*-**5** complex was not detected and the one assigned to the **8**⊂*cccc*-**5** complex was by far the more intense. We calculated that the *trans*-to-*cis* isomerization of the azo groups in free *tttt*-**5** progressed in more than 80%. In short, the inclusion of the guest in the cavity of *tttt*-**5** plays a significant role in the composition of the mixture of *cis*-enriched isomers produced at the *PSS*.

Molecular modelling studies (MM3) of the conformations of the complexes **6**⊂*cccc*-**5** and **7**⊂*cccc*-**5**•NMe_4 (Figure 11) showed that the 4-phenyl substituents of the included guests were totally exposed to the solvent. This result supported the downfield chemical shift changes observed for their aromatic protons and the lack of π-π and CH-π interactions with the terminal phenyl group of the *cis*-azobenzene units. In the inclusion complexes of the *tttt*-**5** isomer, the terminal phenyl groups of the *trans*-azo units enlarge its aromatic cavity by defining an upper section that engages in π-π and CH-π interactions with the 4-phenyl substituent of the included guests. The reduction of intermolecular interactions in the inclusion complexes of *cis*-enriched **5** is expected to translate in a diminution of their binding affinities with respect to the *tttt*-**5** isomer.

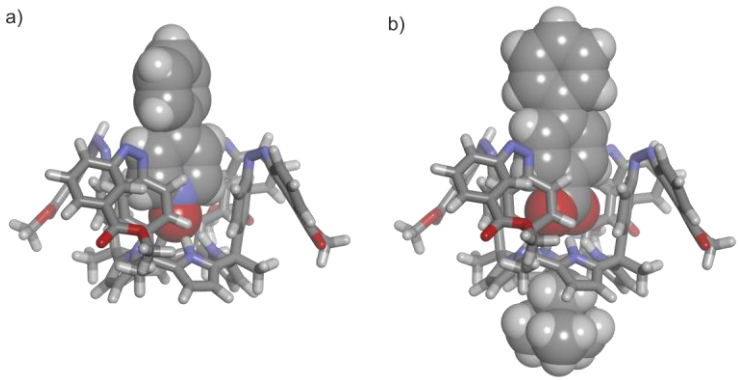

Figure 11. Energy minimized structures (MM3) of the inclusion complexes: a) **6**⊂*cccc*-**5** and b) **7**⊂*cccc*-**5**•NMe_4. Included guest molecules (**6** and **7**•NMe_4) are shown as CPK models and **5** is depicted in stick representation. For clarity, *meso*-alkyl substituents are pruned to methyl groups.

6.2.5 ITC binding studies

In order to assess the diminution in binding affinity induced by the *trans*-to-*cis* isomerization of the azobenzene groups in the inclusion complexes of *tttt*-**5**, we performed a series of isothermal titration calorimetry (ITC) experiments. ITC is a suitable technique for the accurate determination of binding constants of 1:1 complexes with values larger than 10^4 M^{-1}. We had estimated above that the binding constants for the inclusion complexes of two studied guests, **6** and **7**•NMe_4, with the all-*trans* and the *cis*-enriched isomers of **5** were indeed larger than 10^4 M^{-1}. In previous investigations, we determined that “four-wall” aryl-extended calix[4]pyrroles bind pyridine *N*-oxide derivatives with association constant values larger than 10^4 M^{-1} in both organic solvent and

water.[35,37] However, to the best of our knowledge, the binding affinities of aromatic carboxylates for "four-wall" aryl-extended calix[4]pyrrles have not been reported. In this vein, we are aware of several binding studies that address the complexation of carboxylates with *bis*-calix[4]pyrrole dimers,[26,38,39,40] a chiral strapped calix[4]pyrrole[41] and a self-assembled metallo-cage by dimerization of a "two-wall" di-pyridyl calix[4]pyrrole.[42]

Using ITC experiments, we first determined the thermodynamic parameters of the complexations of the *tttt*-**5** isomer with *N*-oxide **6** and tetra-methylammonium carboxylate **7**•NMe_4 (Figure 12) both in dichloromethane and acetonitrile solutions.

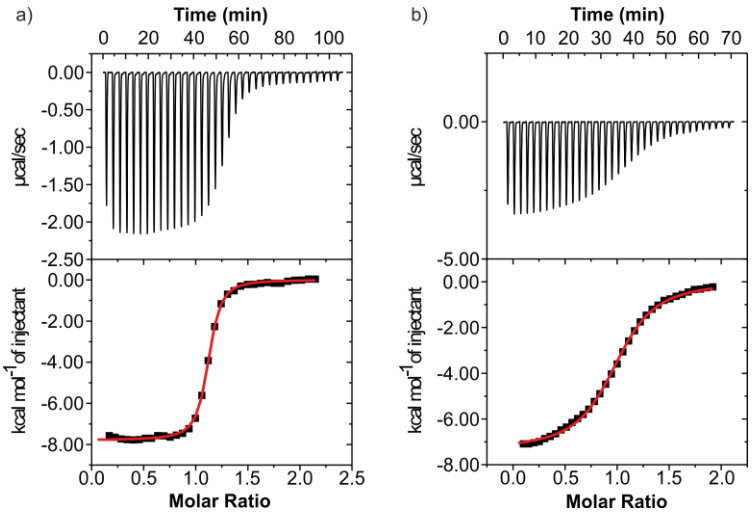

Figure 12. Top panels show raw data (heat *vs.* time) for the titration of guest into the host (CH_3CN): a) **7**⊂*tttt*-**5** and b) **7**⊂*cccc*-**5** (*cis*-enriched mixture of **5**). Titrations were performed at 298 K. Bottom panels represent integrated data fitted to the theoretical binding isotherm (red line) for a 1:1 binding model.

We repeated the ITC experiments by placing in the cell of the calorimeter a light-irradiated (365 nm) solution of the *tttt*-**5** isomer that reached the *PSS*. As described above, at the *PSS* this solution contains a mixture of *cis*-enriched isomers of **5**, in which the *cccc*-**5** isomer accounts for more than 80% and the *tttt*-**5** isomer is negligible. Thus, the determined affinity constant value using the mixture of *cis*-enriched isomers of **5** is considered to be a weighted-average of constant values for the *cis*-isomers. Because we expect a drop in the affinity constant as a function of the number of *cis*-azo groups present in receptor **5**, the determined constant value is a maximum estimate for the *cccc*-**5** isomer. Table 1 summarizes all the thermodynamic parameters determined from the ITC experiments.

From the analysis of the tabulated data several general conclusions can be drawn. All binding processes involving *tttt*-**5** were enthalpically driven. Entropy opposed binding in the case of the *N*-oxide **6** in both solvents. On the other hand, entropy favored binding of the carboxylate salt,

7•NMe_4, in dichloromethane solution and had a negligible effect in acetonitrile. We attributed the entropy changes to important solvation effects in the case of the salt, as well as to the deep inclusion nature of the final complex. In general, enthalpy-entropy compensation effects[43] were also present in the studied binding processes of *tttt*-**5**.

Table 1. Binding constants (K_a, M^{-1}) and thermodynamic parameters (ΔH, $T\Delta S$ and ΔG, kcal·mol^{-1}) determined from the ITC experiments performed in dichloromethane (T = 288 K) and acetonitrile (T = 298 K) solutions. Error values are reported as standard deviations.

Solvent	Complex	K_a	ΔH	$T\Delta S$	ΔG
CH_2Cl_2	**6**⊂*tttt*-**5**	7.0±2.0 x 10^6	-12.6±0.3	-3.6±0.4	-9.0±0.2
	6⊂*cccc*-**5**	5.0±0.5 x 10^5	-11.0±1.0	-3.5±1.0	-7.5±0.1
	7⊂*tttt*-**5**•NMe_4	5.1±0.6 x 10^6	-6.0±0.7	2.8±0.7	-8.8±0.1
	7⊂*cccc*-**5**•NMe_4	3.3±0.1 x 10^5	-4.4±0.2	2.9±0.2	-7.3±0.1
CH_3CN	**6**⊂*tttt*-**5**	>10^7	-12.4±0.3		
	6⊂*cccc*-**5**	2.9±0.1 x 10^6	-13.1±0.1	-4.3±0.1	-8.8±0.1
	7⊂*tttt*-**5**	3.9±0.7 x 10^6	-7.6±0.2	1.4±0.2	-9.0±0.1
	7⊂*cccc*-**5**	1.8±0.1 x 10^5	-7.3±0.1	-0.1±0.1	-7.2±0.1

The affinity constant values for the *cccc*-**5** isomer (*cis*-enriched mixture of isomers) with both guests and in the two solvents show a drop of one order of magnitude compared to *tttt*-**5**. For example, in dichloromethane solution the stability constant value for **6**⊂*tttt*-**5** complex was determined to be 7.0 x 10^6 M^{-1}. A maximum estimate for the magnitude of the stability constant of the **6**⊂*cccc*-**5** complex is of the order of 5.0 x 10^5 M^{-1}. Previously, we determined a binding constant value as large as 10^7 M^{-1} for the complexation of pyridyl *N*-oxide derivatives with a super aryl-extended calix[4]pyrrole receptor in chloroform solution. The ratio of the binding constant values for the complexes of 4-methyl pyridine *N*-oxide and 4-phenyl pyridine *N*-oxide with the super aryl-extended receptor was *ca.* 4.[35] This corresponds to an energy difference of *ca.* 1 kcal·mol^{-1} which was attributed to the lack of CH-π and π-π interactions in the case of the methyl substituted *N*-oxide. In the present study, the *trans*-to-*cis* isomerization of the azobenzene units in *tttt*-**5** produced a related loss of CH-π and π-π interactions for the complexes of the *cccc*-**5** isomer, which are in average ten-fold thermodynamically less stable. This drop in thermodynamic stability can be quantified as 1.3 kcal·mol^{-1}, a value in close agreement with our previous estimate. The energy difference of the two estimates (0.3 kcal·mol^{-1}) could be related to the entropic penalty

associated with the reduction of the free rotation of the four single bonds N_{azo}-$C_{para\text{-}meso\text{-}phenyl}$ in the case of the inclusion complexes with *cccc*-**5** isomer.

For a given receptor, *tttt*-**5** or *cccc*-**5**, the binding constant values for its pair of complexes with any of the two guests, **6** or **7**•NMe_4, are different by one order of magnitude in acetonitrile solution. In contrast, the same pair of complexes has almost identical binding constant values in dichloromethane solution. For example, in acetonitrile solution, the association constant value of the **6**⊂*tttt*-**5** complex is estimated to be larger 10^7 M^{-1} while the carboxylate salt **7**•NMe_4 is bound by the same receptor with an affinity constant of just 3.9 x 10^6 M^{-1}. On the other hand, the same pair of complexes **6**⊂*tttt*-**5** and **7**⊂*tttt*-**5**•NMe_4 in dichloromethane solution have similar affinity constant values, 7.0 x 10^6 and 5.1 x 10^6 M^{-1}, respectively. The coincidence of binding constant values determined in dichloromethane but not in acetonitrile solution must be related to the solvent separated ion-paired binding mode featured by the carboxylate complex in the less polar solvent.[36] In dichloromethane solution, *tttt*-**5** and *cccc*-**5** acted as hetero-ditopic receptors for the salt **7**•NMe_4, while in acetonitrile they mainly formed anionic inclusion complexes **7**⊂**5**.

Finally, the fact that the *N*-oxide **6** is strongly bound by *tttt*-**5** or *cccc*-**5** in a polar solvent such as acetonitrile than in the non-polar dichloromethane counterpart is assigned to the pre-organized cone conformation adopted by the free receptor in the polar solvent.

6.3 Conclusions

We described the synthesis and characterization of the tetra-azobenzene extended calix[4]pyrrole *tttt*-**5**. Photo-isomerization studies revealed that at 1 mM concentration calix[4]pyrrole *tttt*-**5** reached the *PSS* within 15-20 min of photo-irradiation at 365 nm. We determined that *ca.* 85% of azobenzene groups adopted the *cis*-configuration in the *PSS* and that the switching process was fully reversible by thermal equilibration of the mixture in the dark.

The results of ^{1}H NMR titrations of *tttt*-**5** and *cccc*-**5** (mixture of *cis*-enriched isomers) with *N*-oxide **6** and carboxylate salt **7**•NMe_4 in CD_2Cl_2 and CD_3CN solutions, revealed the formation of thermodynamically and kinetically highly stable 1:1 complexes. ITC experiments enabled the accurate determination of binding constants for all inclusion complexes. The affinity constant values for the complexes of *tttt*-**5**, with any of the two guests, are one order of magnitude larger than the corresponding ones with the *cccc*-**5** isomer.

On the other hand, the two pair of inclusion complexes involving one receptor isomer, *tttt*-**5** or *cccc*-**5**, and the two guests show identical binding constant values in dichloromethane solution but show an order of magnitude difference in acetonitrile favoring *N*-oxide binding. Finally, the binding constants determined for the inclusion complexes of the *N*-oxide are one order of magnitude larger in acetonitrile than in dichloromethane solution.

The *para*-phenyl substituents of bound **6** and **7**•NMe_4 are shielded from the bulk solvent by being included in the upper aromatic cavity of *tttt*-**5**. The photo-isomerization process of the azo groups in the *cis*-enriched complexes produces the partial/total exposure of the phenyl substituents to the bulk solution.

We envisage that the switching of the contact surface between the guest and the receptor's isomer could have potential applications, such as, control of the reactivity of functional groups located in the terminal phenyl substituent of the guest depending on the *trans*-to-*cis* geometry of the receptor.

6.4 Experimental Section

6.4.1 General information and instruments

Reagents were obtained from commercial suppliers and used without further purification unless otherwise stated. All solvents were commercially obtained and used without further purification except pyrrole that was distilled and freshly used. Dry solvents were taken from a solvent system MB SPS 800. Routine ^{1}H NMR, $^{19}F\{^{1}H\}$ NMR and $^{13}C\{^{1}H\}$ NMR spectra were recorded on a Bruker Avance 300 (300 MHz for ^{1}H NMR and 75 MHz for ^{13}C NMR), Bruker Avance 400 (400 MHz for ^{1}H NMR, 376 MHz for ^{19}F and 100 MHz for ^{13}C NMR), Bruker Avance 500 (500 MHz for ^{1}H NMR, 471 MHz for ^{19}F and 125 MHz for ^{13}C NMR) or Bruker Avance 500 with cryoprobe (500 MHz for ^{1}H NMR, 471 MHz for ^{19}F and 125 MHz for ^{13}C NMR). Deuterated solvents used are indicated in the characterization and chemical shifts are given in ppm. Residual solvent peaks were used as reference.[44] All NMR *J* values are given in Hz. COSY, NOESY, HMQC and HMBC experiments were recorded to help in the assignment of ^{1}H and ^{13}C signals. High-resolution mass spectra (HRMS) were obtained on a Bruker HPLC-TOF (MicroTOF Focus) and Bruker HPLC-QqTOF (MaXis Impact). Both using ESI as ionization mode. IR spectra were recorded on a Bruker Optics FTIR Alpha spectrometer equipped with a DTGS detector, KBr beam splitter at 4 cm^{-1} resolution using a one bounce ATR accessory with diamond windows. Melting points were measured on a MP70 Melting Point System Mettler Toledo. Photo-irradiation of the solutions was carried out using a 4 W UV lamp having a light intensity of 6.9 mW at 365 nm. ITC titrations were carried out on a Microcal VP-ITC MicroCalorimeter. Column chromatography purifications were performed using silica gel technical grade, pore size 60 Å, 230-400 mesh particle size, 40-63 μm particle size and Thin layer chromatography (TLC) analyses on silica gel 60 F254.

6.4.2 Synthesis and characterization data

Tetra-(4-nitrophenyl) calix[4]pyrrole 1a: A solution of ethyl 5-(4'-nitrophenyl)-5-oxopentanoate **2** (500 mg, 1.89 mmol, 1 equiv.) in EtOH (5 mL) was stirred under Argon atmosphere and protected from light. Then, 4 M HCl in dioxane (0.94 mL, 3.77 mmol, 2 equiv.) was added dropwise over 5 min. Finally, distilled pyrrole (0.13 mL, 1.89 mmol, 1 equiv.) was added dropwise over 5 min. The mixture was stirred at r.t. under Argon atmosphere for 24 h. The crude was concentrated at r.t. and the resulting solid was washed with CH_3OH. The solid was dissolved in CH_2Cl_2 (5 mL) and stirred under Argon atmosphere and protected from the light. 4 M HCl in dioxane (0.94 mL, 3.77 mmol, 2 equiv.) was added dropwise over 5 min. After 48 h, the reaction was stopped and the reaction crude was concentrated. The crude was redissolved in CH_2Cl_2 (10 mL) and washed with saturated $NaHCO_3$ (2x10 mL) and water (10 mL). The organic layer was dried (Na_2SO_4), filtered and concentrated to dryness. The crude was purified by column chromatography on silica gel (20 g, $CH_2Cl_2 \rightarrow$ 99:1 CH_2Cl_2:Et_2O) to afford the product as a pale yellow solid, that was further purified by crystallization in 3:1 CH_3OH:Et_2O (65.40 mg, 0.05 mmol, 11% yield). Rf = 0.4 (99:1 CH_2Cl_2:Et_2O). ^{1}H NMR (400 MHz, $CDCl_3$, 298 K): δ (ppm) = 8.27 (br s, 4H); 8.08-8.06 (m, 8H); 7.43-7.41 (m, 8H); 5.90 (s, 8H); 4.10 (c, J = 7.1 Hz, 8H); 2.38 (m, 8H); 2.31 (tt, J = 6.7 Hz; J = 6.7 Hz, 8H); 1.56 (m, 8H); 1.23 (t, J = 7.1 Hz, 12H). ^{13}C{^{1}H} NMR (100 MHz, $CDCl_3$, 298 K): δ (ppm) = 173.9; 153.0; 146.9; 134.8; 129.5; 122.8; 107.3; 60.7; 49.7; 38.1; 33.3; 20.1; 14.4. HRMS (ESI-TOF) m/z: $[M-H]^-$ Calcd for $C_{68}H_{71}N_8O_{16}$ 1255.4994; Found 1255.4994. FTIR ν (cm^{-1}) = 3390; 2943; 1730; 1518; 1349; 1206; 1177; 1148; 1114; 857; 842; 770. M.p > 140ºC (decompose).

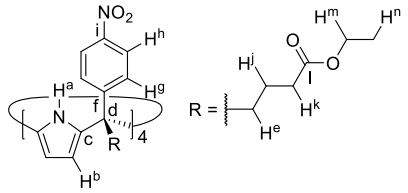

1a

Figure 13. Line-drawing structure of tetra-*α* **1a**.

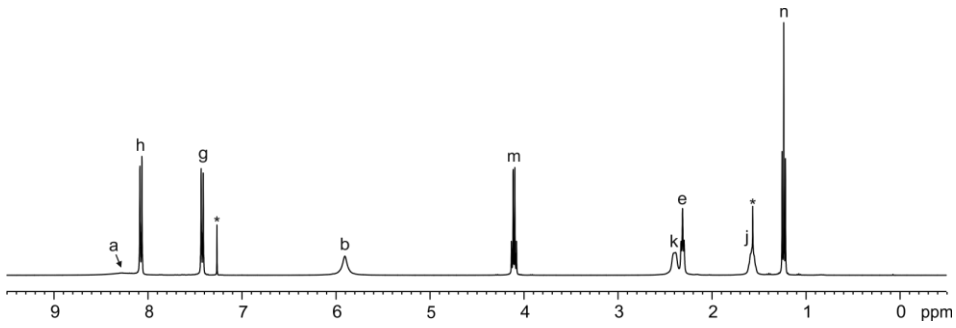

Figure 14. ^{1}H NMR (400 MHz, $CDCl_3$, 298 K) spectrum of tetra-*α* **1a**. See Figure 13 for proton assignment. *Residual solvent peaks.

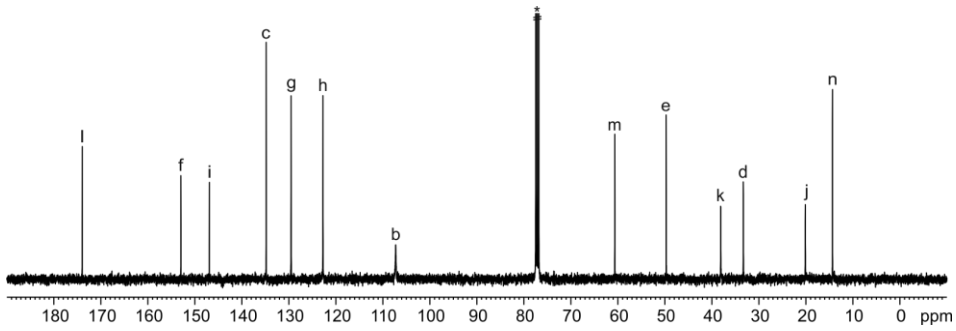

Figure 15. $^{13}C\{^{1}H\}$ NMR (100 MHz, $CDCl_3$, 298 K) spectrum of tetra-*α* **1a**. See Figure 13 for carbon assignment. *Residual solvent peak.

Tetra-(4-aminophenyl) calix[4]pyrrole 1b: Tetra-nitro calix[4]pyrrole **1a** (130 mg, 0.10 mmol, 1 equiv.) was added to a high-pressure glass reactor and dissolved in EtOAc (60 mL). 10% Palladium on carbon (110 mg, 0.10 mmol, 1 equiv.) was added. The reaction was carried out in a low pressure PARR hydrogenator at 4 bar for 24 h. After that, the reaction was stopped and filtered through celite under nitrogen atmosphere. The celite was flushed with EtOAc until no more product came out (seen by TLC). The product was concentrated and kept in a vial under Argon atmosphere (103 mg, 0.09 mmol, 90% yield). ^{1}H NMR (400 MHz, $CDCl_3$, 298 K): δ (ppm) = 7.77 (br s, 4H); 6.96-6.94 (m, 8H); 6.52-6.50 (m, 8H); 5.81 (d, J = 2.5 Hz, 8H); 4.08 (c, J = 7.2 Hz, 8H); 3.55 (s, 8H); 2.25 (m, 8H); 2.25 (m, 8H); 1.60 (m, 8H); 1.22 (t, J = 7.2 Hz, 12H). $^{13}C\{^{1}H\}$ NMR (100 MHz, $CDCl_3$, 298 K): δ (ppm) = 173.9; 144.7; 135.9; 135.6; 129.7; 114.3; 106.1; 60.3; 48.4; 39.2; 34.1; 20.6; 14.4. HRMS (ESI-TOF) m/z: $[M+H+Na]^{2+}$ Calcd for $C_{68}H_{81}N_8NaO_8$ 580.3032; Found 580.3018. FTIR v (cm^{-1}) = 3369; 2974; 1719; 1620; 1511; 1255; 1182; 1147; 1031; 813; 768; 523. M.p > 130ºC (decompose).

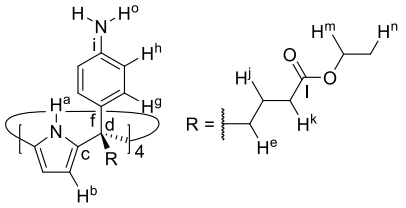

1b

Figure 16. Line-drawing structure of tetra-*α* **1b**.

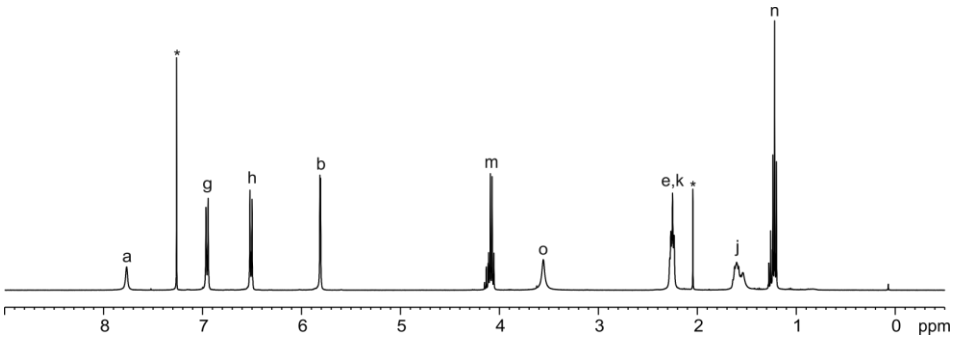

Figure 17. ^{1}H NMR (400 MHz, $CDCl_3$, 298 K) spectrum of tetra-*α* **1b**. See Figure 16 for proton assignment. *Residual solvent peaks.

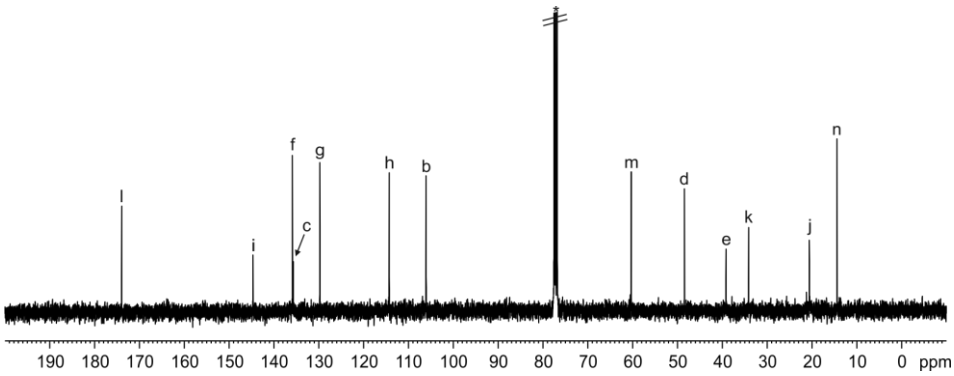

Figure 18. $^{13}C\{^{1}H\}$ NMR (100 MHz, $CDCl_3$, 298 K) spectrum of tetra-*α* **1b**. See Figure 16 for carbon assignment. *Residual solvent peak.

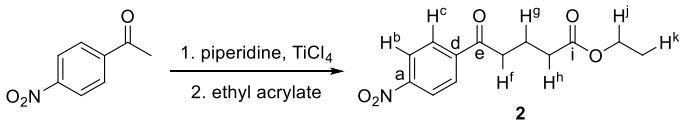

Scheme 2. Synthesis of compound **2**.

Ethyl 5-(4'-Nitrophenyl)-5-oxopentanoate 2: Step 1. 4-Nitroacetophenone (20 g, 121 mmol, 1 equiv.) was dissolved in piperidine (60 mL, 606 mmol, 5 equiv.) and hexane (500 mL) was added. The mixture was stirred at 0ºC for 10 min. Then, $TiCl_4$ (8 mL, 72.7 mmol, 0.6 equiv.) was added slowly during 5 min. The reaction was stirred for 30 min at 0ºC and 24 h at r.t. Then, the solids were filtered off and washed with hexane (200 mL). The combined organic phases were concentrated under vacuum. The resulting enamine was obtained as brown oil (24.3 g, 105 mmol, 87% yield). Step 2. The enamine (20 g, 86 mmol, 1 equiv.) was dissolved in dry EtOH (40 mL). The solution was stirred under Argon atmosphere at r.t. and ethyl acrylate (11.3 mL, 103 mmol, 1.2 equiv.) was added. Then, the reaction was stirred at r.t. for 7 days. After that, water (100 mL), acetic acid (27 mL) and EtOAc (40 mL) were added and the reaction was heated at 45ºC for 1 h. Additional EtOAc (60 mL) was added and the phases were separated. The organic phase was washed with 1 N HCl (2x100 mL) and water (100 mL). The organic layer was dried (Na_2SO_4), filtered and concentrated. The product was purified by column chromatography on silica gel (CH_2Cl_2 → 99:1 CH_2Cl_2:TBME) affording the product as a brown solid (5.58 g, 18.36 mmol, 21% yield). Rf = 0.5 (99:1 CH_2Cl_2:TBME). ^{1}H NMR (400 MHz, $CDCl_3$, 298 K): δ (ppm) = 8.31 (m, 2H); 8.12 (m, 2H); 4.14 (c, J = 7.2 Hz, 2H); 3.11 (t, J = 7.1 Hz, 2H); 2.45 (t, J = 7.1 Hz, 2H); 2.09 (tt, J = 7.1 Hz, J = 7.1 Hz, 2H); 1.26 (t, J = 7.2 Hz, 3H). ^{13}C{^{1}H} NMR (100 MHz, $CDCl_3$, 298 K): δ (ppm) = 198.0; 173.2; 150.5; 141.3; 129.2; 124.0; 60.6; 38.2; 33.2; 19.2; 14.4. HRMS (ESI-TOF) m/z: $[M+Na]^+$ Calcd for $C_{13}H_{15}NNaO_5$ 288.0851; Found 288.0851. FTIR v (cm^{-1}) = 3101; 3071; 3049; 2950; 1727; 1682; 1602; 1521; 1345; 1318; 1202; 1184; 1154; 871; 854; 744. M.p. = 46-47ºC.

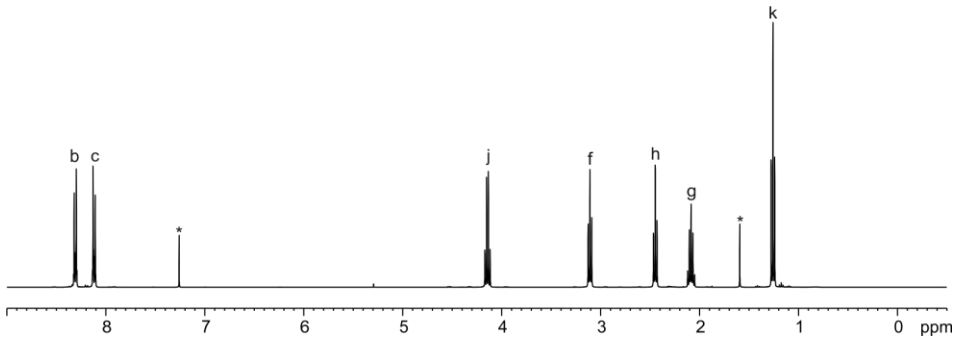

Figure 19. ^{1}H NMR (400 MHz, $CDCl_3$, 298 K) spectrum of **2**. See Scheme 2 for proton assignment. *Residual solvent peaks.

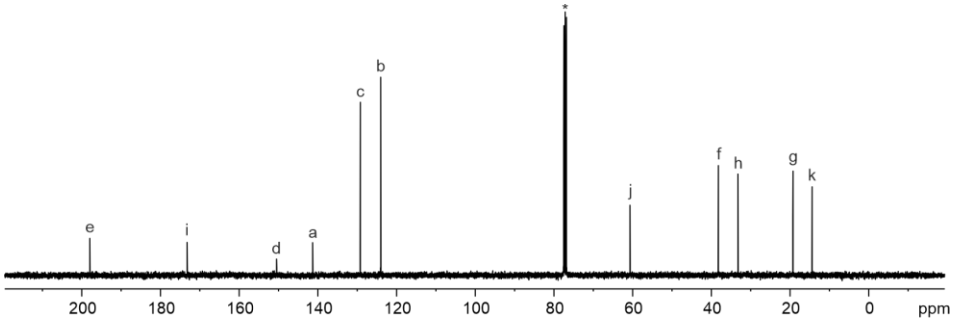

Figure 20. $^{13}C\{^{1}H\}$ NMR (100 MHz, $CDCl_3$, 298 K) spectrum of **2**. See Scheme 2 for carbon assignment. *Residual solvent peak.

Ethyl 3-nitrosobenzoate 4: Oxone® (3.72 g, 12.11 mmol, 2 equiv.) was dissolved in water (80 mL) and ethyl 3-aminobenzoate (1 g, 6.05 mmol, 1 equiv.) was dissolved in CH_2Cl_2 (20 mL). The oxone solution was added to the dichloromethane solution and the mixture was stirred vigorously at r.t. for 24 h. After that, the organic layer was washed with water (3x20 mL), 1 N HCl (20 mL) and brine (20 mL). The organic layer was dried (Na_2SO_4), filtered and concentrated to dryness, affording the product as a brown solid (0.77 g, 4.30 mmol, 71% yield). The compound was used in the synthesis of **5** without further purification due to the reduced stability of nitroso compounds.

Tetra-azobenzene extended calix[4]pyrrole 5: Tetra-amine calix[4]pyrrole **1b** (40 mg, 0.04 mmol, 1 equiv.) and ethyl 3-nitrosobenzoate **4** (37.80 mg, 0.21 mmol, 1.5 equiv.) were dissolved in acetic acid (5 mL). The reaction was stirred at r.t. under Argon atmosphere for 24 h. After that, the reaction was stopped and water (5 mL) was added. $NaHCO_3$ (10 mL) was added and the product was extracted with EtOAc (2x10 mL). The organic layer was washed with $NaHCO_3$ (10 mL) and water (10 mL), dried (Na_2SO_4), filtered and concentrated. The crude was purified by column chromatography on silica gel (6 g, 98:2 CH_2Cl_2:TBME → 95:5 CH_2Cl_2:TBME) and size exclusion column chromatography (Bio-beads SX-3, THF) to afford the product as an orange solid that was washed with CH_3OH and hexane (22.56 mg, 0.01 mmol, 36% yield). Rf = 0.4–0.1 (98:2 CH_2Cl_2:TBME). Characterization of *tttt*-**5**: ^{1}H NMR (500 MHz with cryoprobe, CD_2Cl_2, 298 K): δ (ppm) = 8.49 (dd, J = 1.7, J = 1.7 Hz, 4H); 8.22 (br s, 4H); 8.12 (ddd, J = 7.7 Hz, J = 1.7 Hz; J = 1.7 Hz, 4H); 8.07 (ddd, J = 7.7, J = 1.7, J = 1.7 Hz, 4H); 7.84-7.82 (m, 8H); 7.58 (dd, J = 7.7, J = 7.7 Hz, 4H); 7.47-7.45 (m, 8H); 6.00 (s, 8H); 4.38 (c, J = 7.1 Hz, 8H); 4.09 (c, J = 7.1 Hz, 8H); 2.49 (m, 8H); 2.34 (tt, J = 6.7 Hz; J = 6.7 Hz, 8H); 1.65 (m, 8H); 1.39 (t, J = 7.1 Hz, 12H); 1.22 (t, J = 7.1 Hz, 12H). $^{13}C\{^{1}H\}$ NMR (125 MHz with cryoprobe, CD_2Cl_2, 298 K): δ (ppm) = 174.0; 166.3; 153.1; 151.6; 149.7; 136.1; 132.2; 131.8; 130.0; 129.6; 127.1; 124.1; 122.3; 107.2; 61.7; 60.7; 49.9; 38.4; 33.9; 20.7; 14.5; 14.5. HRMS (ESI-TOF) m/z: $[M]^{-+}$ Calcd for $C_{104}H_{108}N_{12}O_{16}$ 1780.8006; Found 1780.8003. FTIR ν (cm^{-1}) = 3392; 2977; 1717; 1599; 1418; 1368; 1293; 1268; 1179; 1148; 1013; 757. M.p > 130°C (decompose).

Chapter 6

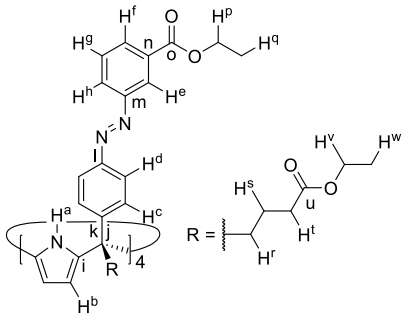

5

Figure 21. Line-drawing structure of *tttt*-**5**.

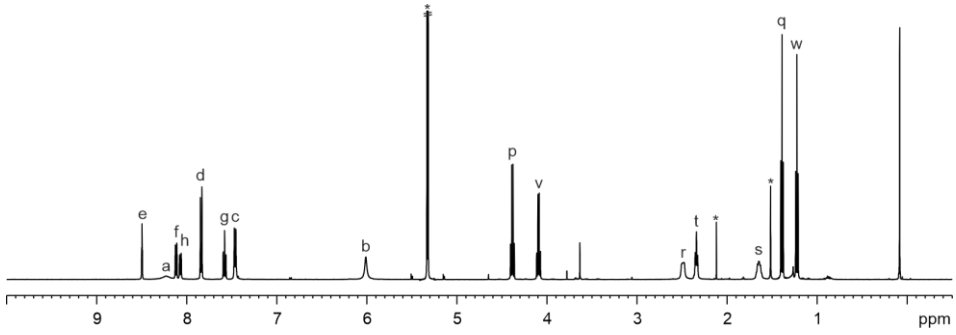

Figure 22. ^{1}H NMR (500 MHz with cryoprobe, CD_2Cl_2, 298 K) spectrum of *tttt*-**5**. See Figure 21 for proton assignment. *Residual solvent peaks.

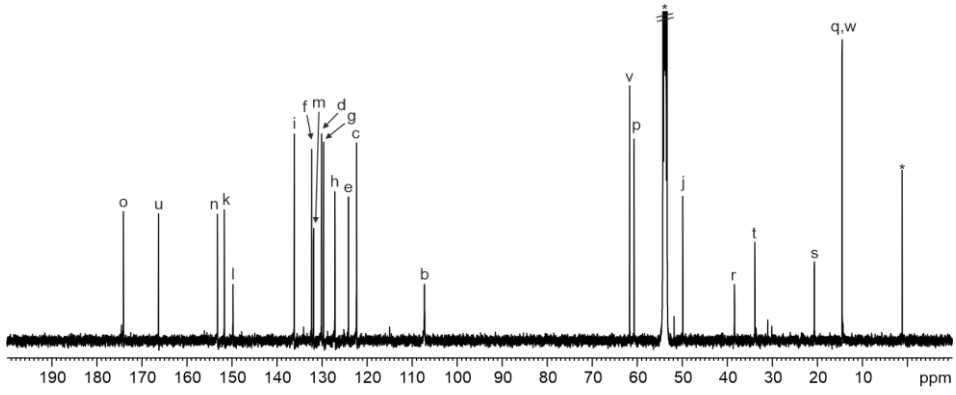

Figure 23. $^{13}C\{^{1}H\}$ NMR (125 MHz with cryoprobe, CD_2Cl_2, 298 K) spectrum of *tttt*-**5**. See Figure 21 for carbon assignment. *Residual solvent peaks.

Tetra-methylammonium 1,1'-bi-phenyl 4-carboxylate 7•NMe$_4$: Bi-phenyl carboxylic acid (100 mg, 0.50 mmol, 1 equiv.) and tetra-methylammonium hydroxide (91 mg, 0.50 mmol, 1 equiv.) were added to a round-bottom flask. CH_3OH (10 mL) was added and the reaction was stirred at r.t. for 2 h. After that, the solvent was removed and the solid was washed with hexane (5 mL), affording the product as a white solid that was dried (P_2O_5) and kept under Argon atmosphere (117 mg, 0.43 mmol, 85% yield). ^{1}H NMR (500 MHz with cryoprobe, CD_3CN, 298 K): δ (ppm) = 8.00-7.98 (m, 2H); 7.65 (d, J = 7.2 Hz, 2H); 7.56-7.53 (m, 2H); 7.45 (t, J = 7.2 Hz, 2H); 7.35 (t, J = 7.2 Hz, 1H); 3.12 (s, 12H). ^{13}C{^{1}H} NMR (125 MHz with cryoprobe, CD_3CN, 298 K): δ (ppm) = 170.2; 142.2; 142.0; 141.5; 130.7; 129.8; 128.2; 127.9; 126.7; 56.1. FTIR v (cm^{-1}) = 3324; 3027; 1591; 1575; 1543; 1493; 1365; 952; 834; 746; 697; 601.

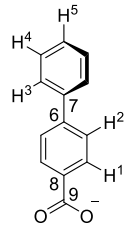

7•NMe$_4$

Figure 24. Line-drawing structure of **7**•NMe$_4$.

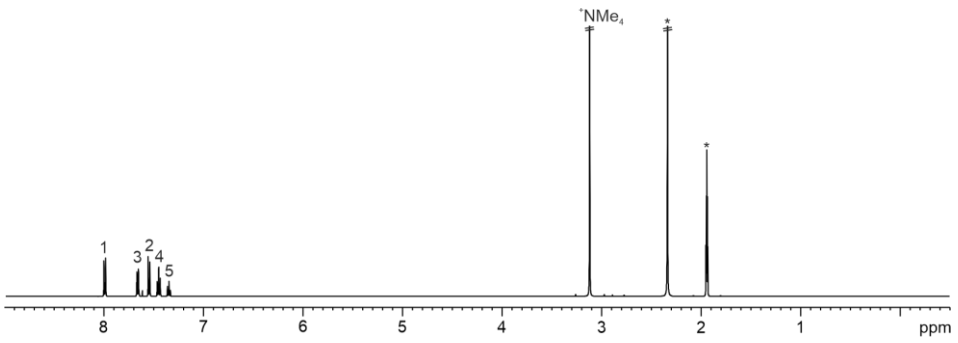

Figure 25. ^{1}H NMR (500 MHz with cryoprobe, CD_3CN, 298 K) spectrum of **7**•NMe$_4$. See Figure 24 for proton assignment. *Residual solvent peaks.

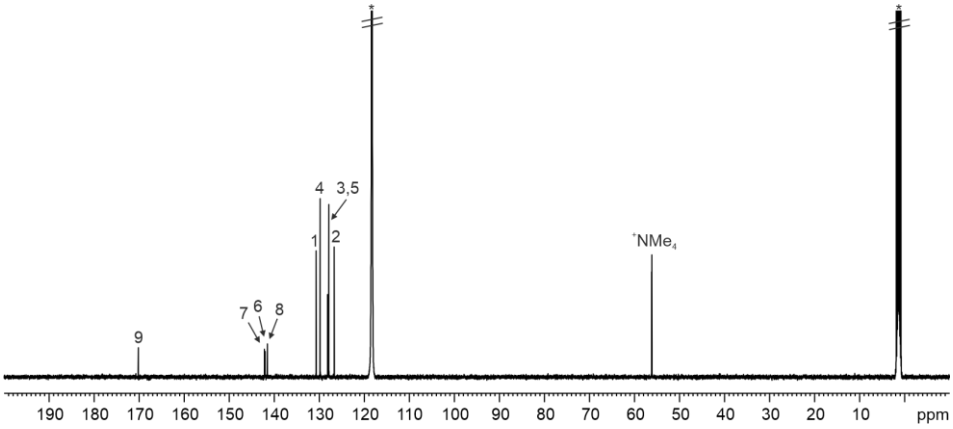

Figure 26. $^{13}C\{^{1}H\}$ NMR (125 MHz with cryoprobe, CD_3CN, 298 K) spectrum of **7**•NMe_4. See Figure 24 for carbon assignment. *Residual solvent peaks.

Tetra-methylammonium 3'-fluoro-(1,1'-bi-phenyl) 4-carboxylate 8•NMe$_4$: 3'-Fluoro-(1,1'-bi-phenyl) 4-carboxylic acid (183 mg, 0.85 mmol, 1 equiv.) and tetra-methylammonium hydroxide (153 mg, 0.85 mmol, 1 equiv.) were added to a round-bottom flask. CH_3OH (20 mL) was added and the reaction was stirred at r.t. for 2 h. After that, the solvent was removed and the solid was washed with hexane (5 mL), affording the product as a white solid that was dried (P_2O_5) and kept under Argon atmosphere (200 mg, 0.70 mmol, 82% yield). ^{1}H NMR (400 MHz, CD_3CN, 298 K): δ (ppm) = 7.80-7.78 (m, 1H); 7.71-6.68 (m, 1H); 7.59-7.56 (m, 2H); 7.48-7.44 (m, 2H); 7.40-7.36 (m, 2H); 3.09 (s, 12H). $^{13}C\{^{1}H\}$ NMR (125 MHz with cryoprobe, CD_3CN, 298 K): δ (ppm) = 168.9 (d, J = 6.5 Hz); 161.2; 159.2; 144.9 (d, J = 23 Hz), 137.1; 130.4 (d, J = 13 Hz); 129.9 (d, J = 11 Hz); 129.4; 129.3; 128.9; 128.6; 126.2 (d, J = 12 Hz); 117.1 (d, J = 87 Hz); 56.1 (m). $^{19}F\{^{1}H\}$ NMR (376 MHz, CD_3CN, 298 K): δ (ppm) = -121.85 (s, 1F). FTIR ν (cm^{-1}) = 3405; 3016; 2953; 1598; 1578; 1543; 1492; 1347; 1206; 949; 780; 764.

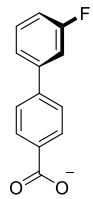

8•NMe_4

Figure 27. Line-drawing structure of **8**•NMe_4.

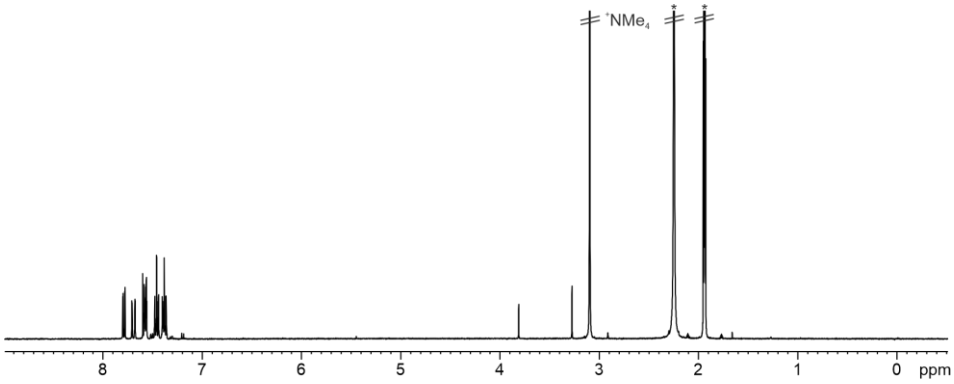

Figure 28. ^{1}H NMR (400 MHz, CD_3CN, 298 K) spectrum of **8**•NMe_4. *Residual solvent peaks.

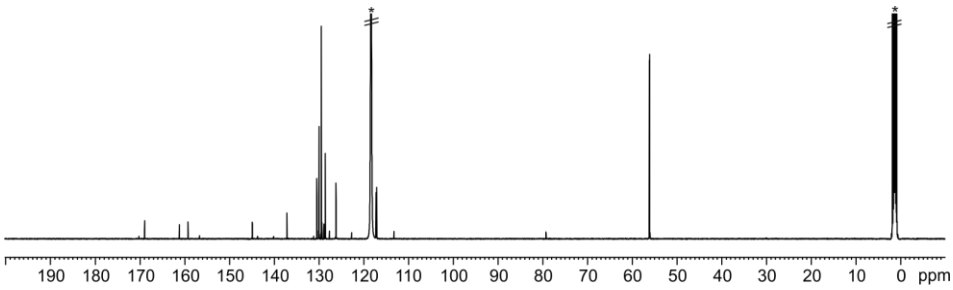

Figure 29. $^{13}C\{^{1}H\}$ NMR (125 MHz with cryoprobe, CD_3CN, 298 K) spectrum of **8**•NMe_4. *Residual solvent peaks.

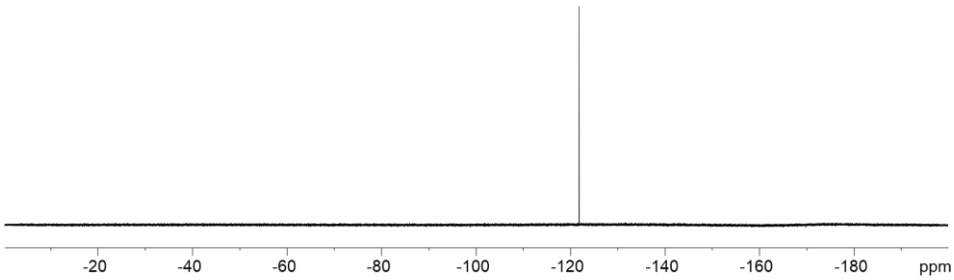

Figure 30. $^{19}F\{^{1}H\}$ NMR (376 MHz, CD_3CN, 298 K) spectrum of **8**•NMe_4.

6.4.3 Photo-isomerization studies by ^{1}H NMR spectroscopy

The isolated calix[4]pyrrole **5** was dissolved in CD_2Cl_2 or CD_3CN. The resulting solutions (1-2 mM) were placed in *J* Young NMR tubes and benzyl methyl ether was added as internal standard (1-2 mM). The solutions were heated at 60°C for 24 h. At the end of the thermal equilibration process, the exclusive presence of the *tttt*-**5** isomer was verified by acquiring a ^{1}H NMR spectrum. Next, the NMR tubes were light-irradiated at 365 nm for 30 min using a hand-held UV lamp. The irradiated solutions were monitored using ^{1}H NMR spectroscopy by acquiring the corresponding spectra every 5 min. The photostability of the guests was also investigated by performing identical light-irradiation experiments excluding the initial thermal equilibration process.

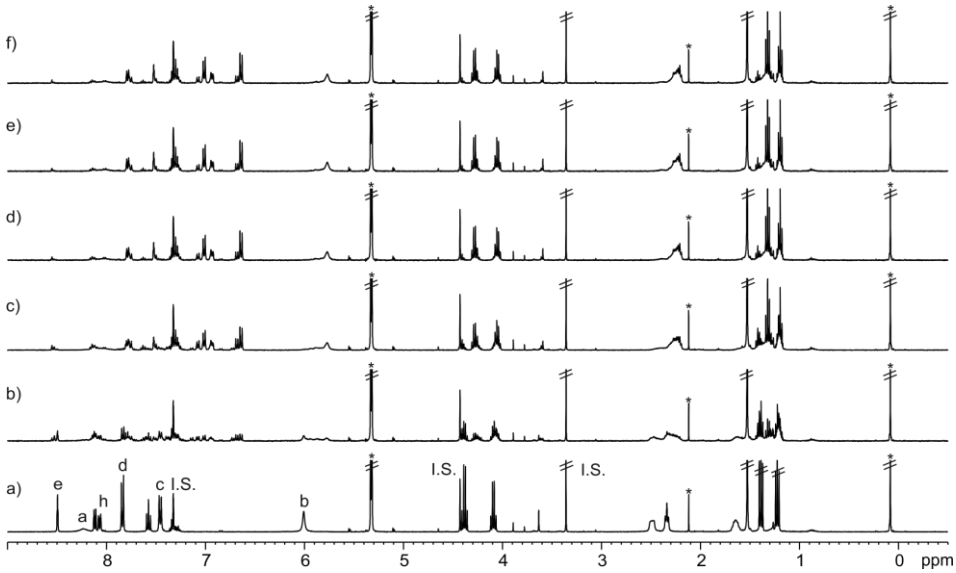

Figure 31. ^{1}H NMR (400 MHz, CD_2Cl_2, 298 K) spectra of **5**: a) thermal equilibration; photo-irradiation (365 nm): b) 5; c) 10; d) 15; e) 20 and f) 30 min. *PSS* was reached within 15-20 min of photo-irradiation. See Figure 21 for proton assignment. Benzyl methyl ether (I.S.). *Residual solvent peaks.

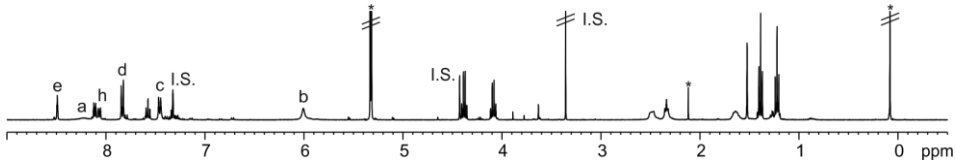

Figure 32. ^{1}H NMR (400 MHz, CD_2Cl_2, 298 K) spectra of **5** after thermal re-equilibration. See Figure 21 for proton assignment. Benzyl methyl ether (I.S.). *Residual solvent peaks.

Composition of the *cis*-enriched mixture of **5** in the *PSS* (CD_2Cl_2):

Figure 31e shows the proton signals of the *cis*-enriched mixture of **5** after 20 min of photo-irradiation (365 nm). The integral value of the proton signals remaining for the *trans*-azo groups at the *PSS* (I_{trans} = 0.6, δ = 8.25-8.15 ppm corresponding to the proton signals H^e of **5**) with respect to those of the β-pyrrole protons ($I_{\beta\text{-pyrrole}}$ = 8, δ = 6.05-5.75 ppm) in all isomers allowed us to estimate that the *cis*-isomerization of the azo-groups occurred to an extent close to 85%.

trans-azo groups = (I_{trans}/4) x 100 = 15%

cis-azo groups = 100% - 15% = 85%

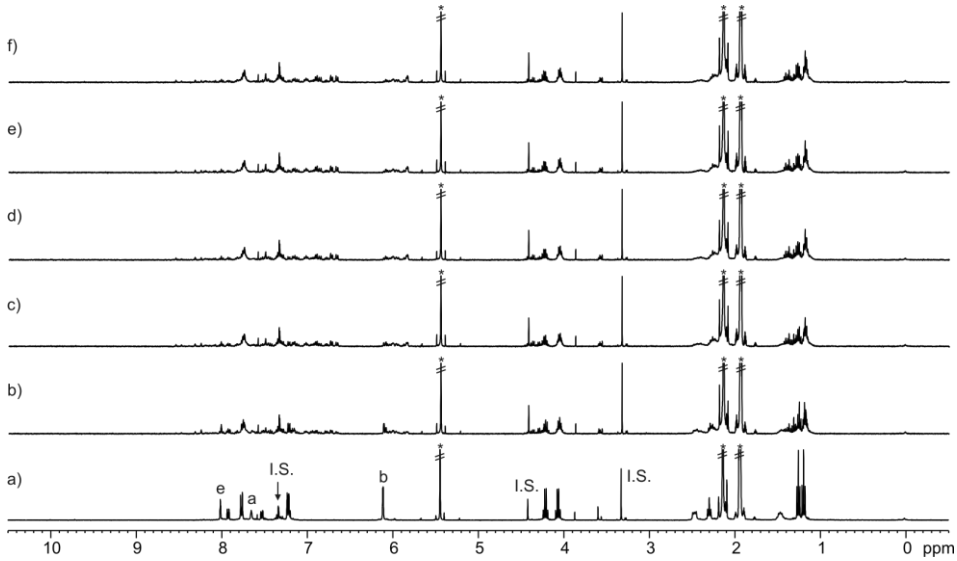

Figure 33. ^{1}H NMR (400 MHz, CD_3CN, 298 K) spectra of **5**: a) thermal equilibration; photo-irradiation (365 nm): b) 5; c) 10; d) 15; e) 20 and f) 30 min. *PSS* was reached within 15-20 min of irradiation. See Figure 21 for proton assignment. Benzyl methyl ether (I.S.). *Residual solvent peaks.

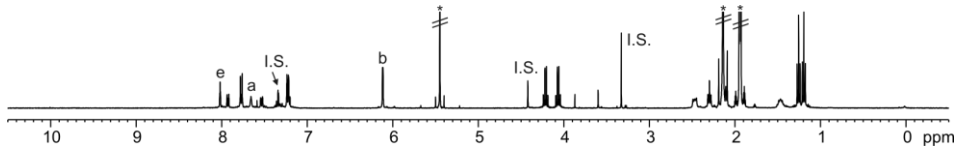

Figure 34. ^{1}H NMR (400 MHz, CD_3CN, 298 K) spectra of **5** after thermal re-equilibration. See Figure 21 for proton assignment. Benzyl methyl ether (I.S.). *Residual solvent peaks.

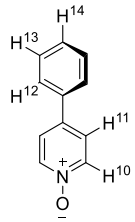

6

Figure 35. Line-drawing structure of **6**.

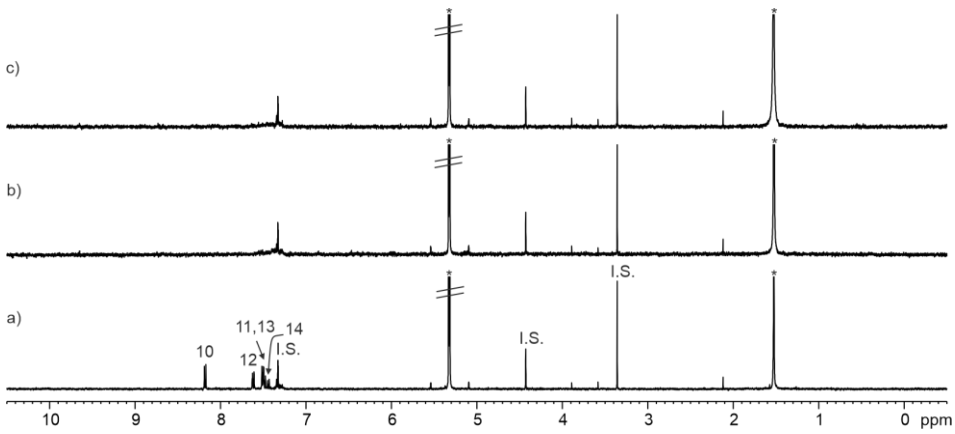

Figure 36. ^{1}H NMR spectra (400 MHz, CD_2Cl_2, 298 K) acquired during the photo-irradiation (365 nm) of **6**: a) 0; b) 10 and c) 20 min. See Figure 35 for proton assignment. Benzyl methyl ether (I.S.). *Residual solvent peaks.

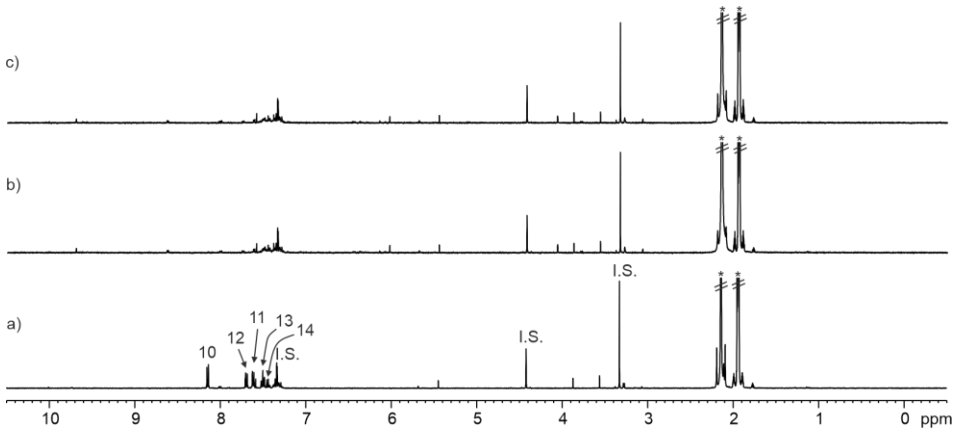

Figure 37. ^{1}H NMR spectra (400 MHz, CD_3CN, 298 K) acquired during the photo-irradiation (365 nm) of **6**: a) 0; b) 10 and c) 20 min. See Figure 35 for proton assignment. Benzyl methyl ether (I.S.). *Residual solvent peaks.

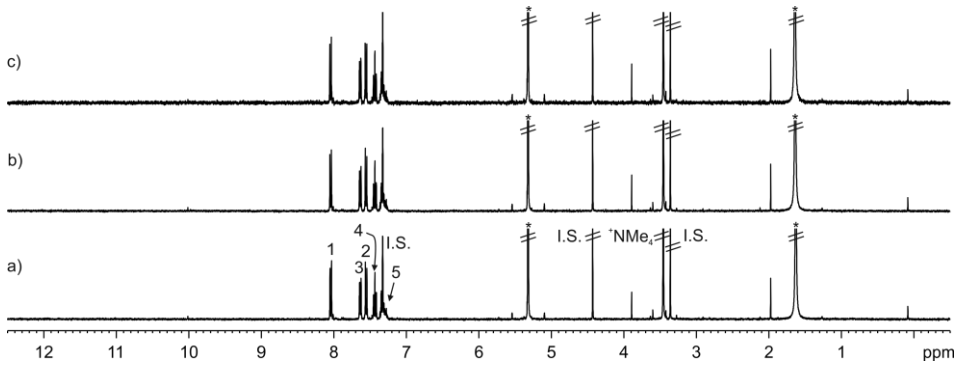

Figure 38. ^{1}H NMR spectra (400 MHz, CD_2Cl_2, 298 K) acquired during the photo-irradiation (365 nm) of **7**•NMe_4: a) 0; b) 10 and c) 20 min. See Figure 24 for proton assignment. Benzyl methyl ether (I.S.). *Residual solvent peaks.

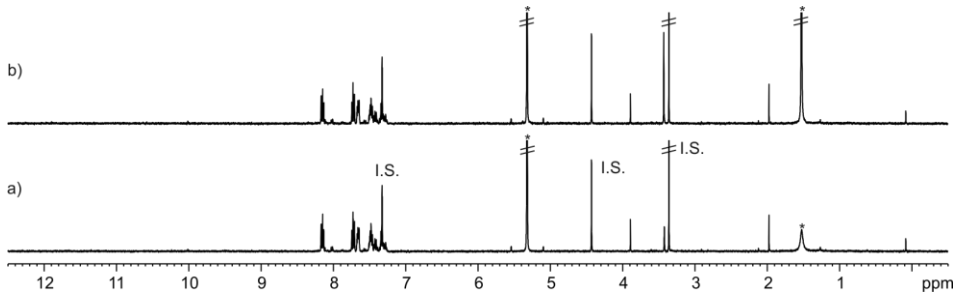

Figure 39. ^{1}H NMR (400 MHz, CD_2Cl_2, 298 K) spectra of **7**•NMe_4 after heating at 60ºC: a) 24 and b) 48 h. Benzyl methyl ether (I.S.). *Residual solvent peaks.

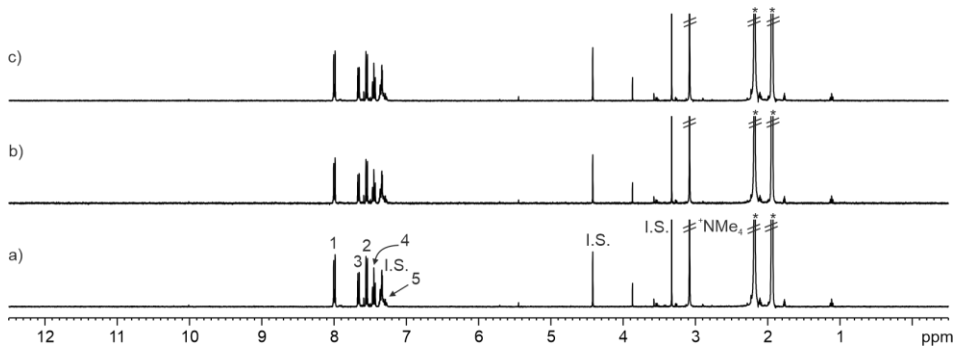

Figure 40. ^{1}H NMR (400 MHz, CD_3CN, 298 K) spectra acquired during the photo-irradiation (365 nm) of **7**•NMe_4: a) 0; b) 10 and c) 20 min. See Figure 24 for proton assignment. Benzyl methyl ether (I.S.). *Residual solvent peaks.

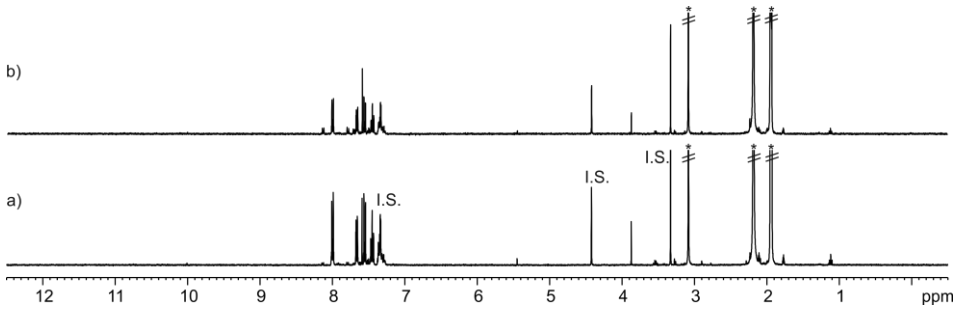

Figure 41. ^{1}H NMR (400 MHz, CD_3CN, 298 K) spectra of **7**•NMe_4 after heating at 60ºC: a) 24 and b) 48 h. Benzyl methyl ether (I.S.). *Residual solvent peaks.

6.4.4 Photo-isomerization studies by UV/VIS spectroscopy

A solution of the synthesized calix[4]pyrrole **5** in CH_2Cl_2 (0.01-0.03 mM) was heated at 60ºC for 24 h in a sealed flask. After cooling at r.t. the solution was transferred to a standard UV/Vis cuvette and its UV/Vis spectrum recorded. The solution was light-irradiated in the cuvette at 365 nm using a hand-held UV lamp. UV/Vis spectra of the solution was acquired after 1 and 3 min of irradiation.

6.4.5 ^{1}H NMR binding studies and light-irradiation experiments

A solution of the host **5** (1-2 mM) in CD_2Cl_2 or CD_3CN was thermally equilibrated at 60ºC for 24 h. Subsequently, 0.5 mL of the solution were transferred to a *J* Young NMR tube to which benzyl methyl ether was added as internal standard (1-2 mM). The remaining CD_2Cl_2 or CD_3CN solutions of the thermally equilibrated host were used to prepare the titrants' solution, which contained the *N*-oxide **6**, carboxylates **7**•NMe_4 or **8**•NMe_4 at 10-15 fold higher concentration ([G] = 20-30 mM and [*tttt*-**5**] = 1-2 mM). In this manner the concentration of the host was maintained constant throughout the titration. Immediately, the 0.5 mL of the host solution was titrated by manually injecting incremental amounts of the titrants' solutions using a micro syringe. A ^{1}H NMR spectrum of the mixture was acquired after each injection and vigorous hand shaking of the NMR tube for few seconds.

Equimolar mixtures of the guests and the *tttt*-**5** isomer (1-2 mM), which led to the quantitative formation of the corresponding 1:1 complexes, were also light-irradiated and analyzed using ^{1}H NMR spectroscopy as described above for the separate binding partners. The reversibility of the photo-isomerization processes and the photostability of the binding partners was evaluated by submitting the light-irradiated solutions of the complexes to the same thermal equilibration conditions applied to the free receptor and subsequent analysis of the solutions using ^{1}H NMR spectroscopy.

4-Phenyl pyridine *N*-oxide **6**

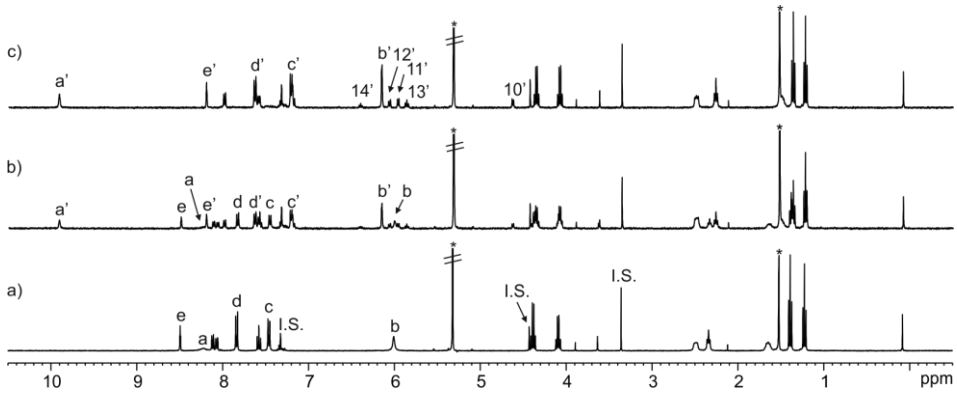

Figure 42. ^{1}H NMR (400 MHz, CD_2Cl_2, 298 K) spectra of the titration of *tttt*-**5** with **6**: a) 0; b) 0.5 and c) 1 equiv. Primed letters and numbers correspond to proton signals of bound components. See Figure 21 and Figure 35 for proton assignments. Benzyl methyl ether (I.S.). *Residual solvent peaks.

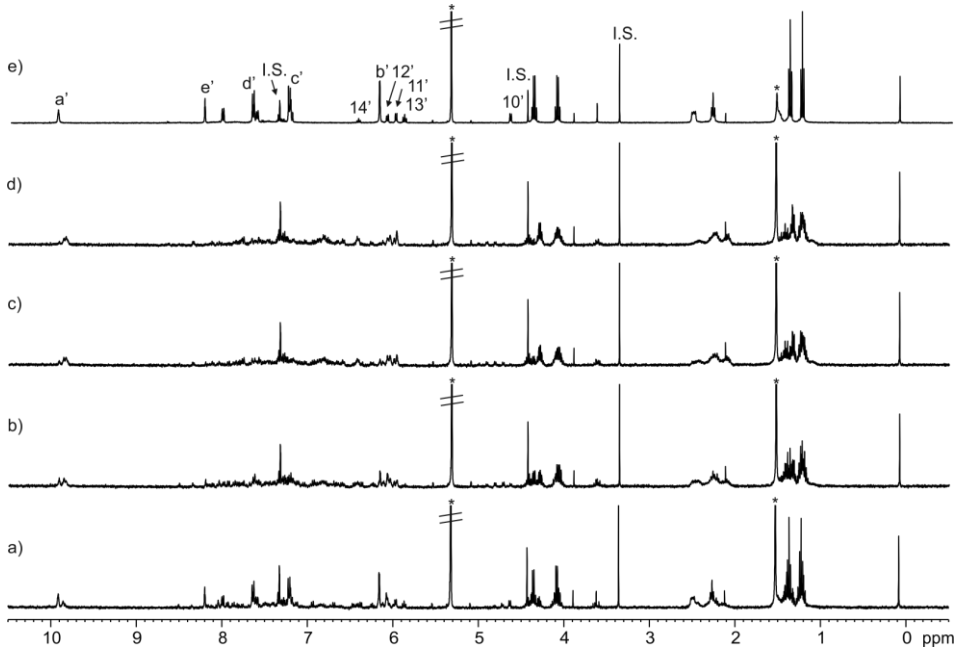

Figure 43. ^{1}H NMR (400 MHz, CD_2Cl_2, 298 K) spectra of the photo-irradiation (365 nm) of **6**⊂*tttt*-**5**: a) 5; b) 10; c) 15 and d) 20 min; e) thermal re-equilibration. Primed letters and numbers correspond to proton signals of bound components. See Figure 21 and Figure 35 for proton assignments. Benzyl methyl ether (I.S.). *Residual solvent peaks.

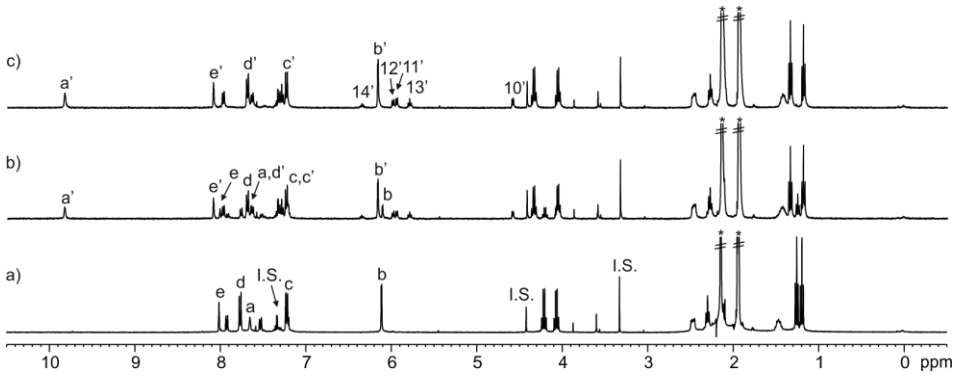

Figure 44. ^{1}H NMR (400 MHz, CD_3CN, 298 K) spectra of the titration of *tttt*-**5** with **6**: a) 0; b) 0.7 and c) 1 equiv. Primed letters and numbers correspond to proton signals of bound components. See Figure 21 and Figure 35 for proton assignments. Benzyl methyl ether (I.S.). *Residual solvent peaks.

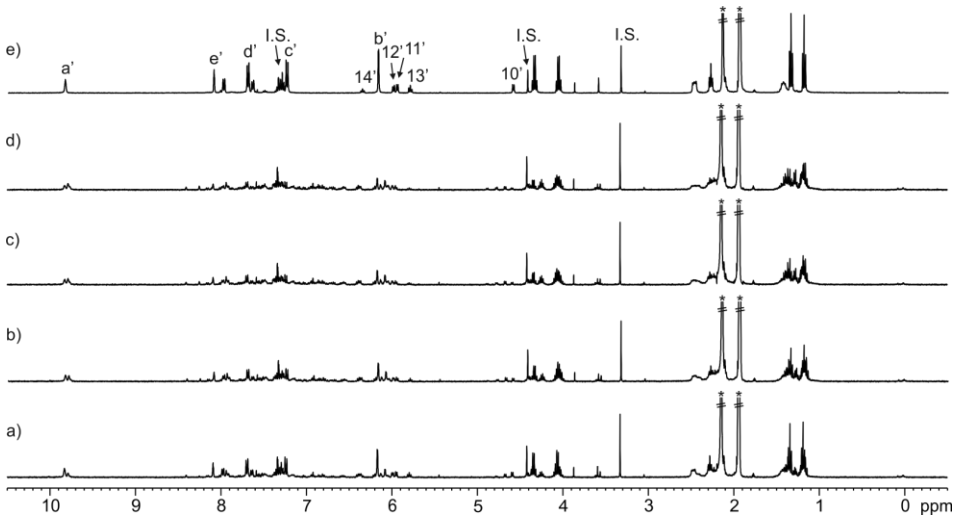

Figure 45. ^{1}H NMR (400 MHz, CD_3CN, 298 K) spectra of the photo-irradiation (365 nm) of **6**⊂*tttt*-**5**: a) 5; b) 10; c) 15 and d) 20 min; e) thermal re-equilibration. Primed letters and numbers correspond to proton signals of bound components. See Figure 21 and Figure 35 for proton assignments. Benzyl methyl ether (I.S.). *Residual solvent peaks.

Table 2. Chemical shifts (δ, ppm) of the protons of free and bound **6** (**6**⊂*tttt*-**5**) and complexation induced shifts ($\Delta\delta$, ppm).

Signal	Solvent	δ_{free}	δ_{bound}	$\Delta\delta$	Solvent	δ_{free}	δ_{bound}	$\Delta\delta$
10		8.17	4.63	-3.54		8.15	4.58	-3.57
11		7.49	5.97	-1.52		7.62	5.94	-1.68
12	CD_2Cl_2	7.61	6.07	-1.54	CD_3CN	7.70	5.99	-1.71
13		7.47	5.87	-1.60		7.50	5.79	-1.71
14		7.42	6.40	-1.00		7.44	6.35	-1.10

Tetra-methylammonium 1,1'-bi-phenyl 4-carboxylate **7**•NMe_4

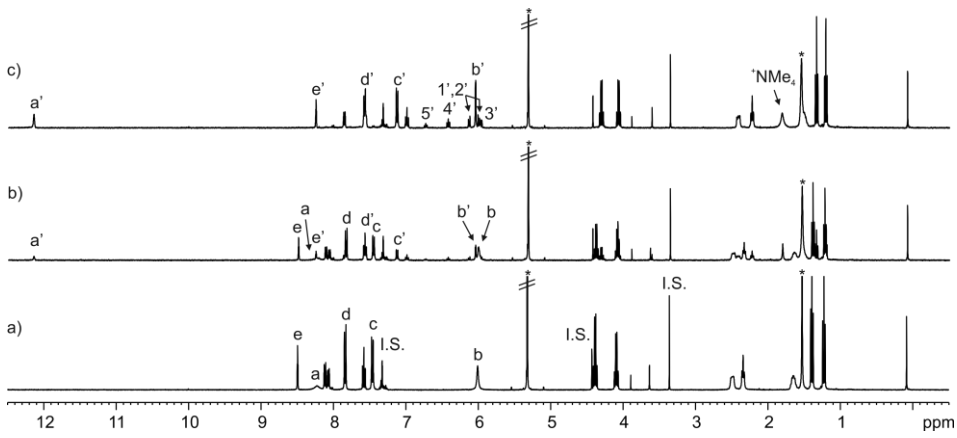

Figure 46. ^{1}H NMR (400 MHz, CD_2Cl_2, 298 K) spectra of the titration of *tttt*-**5** with **7**•NMe_4: a) 0; b) 0.5 and c) 1 equiv. Primed letters and numbers correspond to proton signals of bound components. See Figure 21 and Figure 24 for proton assignments. Benzyl methyl ether (I.S.). *Residual solvent peaks.

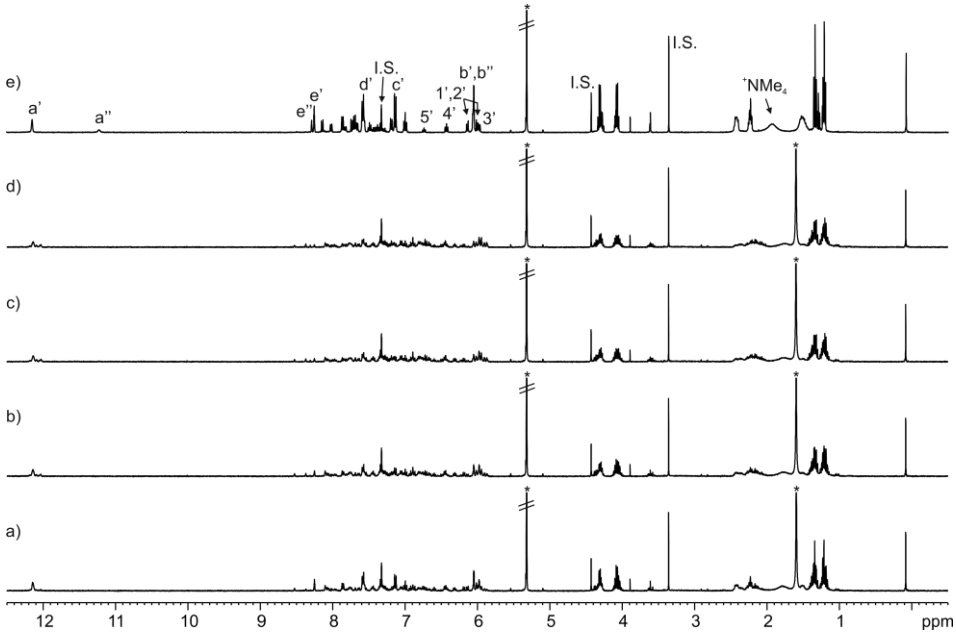

Figure 47. ^{1}H NMR (400 MHz, CD_2Cl_2, 298 K) spectra of the photo-irradiation (365 nm) of **7**⊂*tttt*-**5**•NMe_4: a) 5; b) 10; c) 15 and d) 20 min; e) thermal re-equilibration. Thermal re-equilibration produced a mixture of two complexes: **7**⊂*tttt*-**5**•NMe_4 and Cl⊂*tttt*-**5**•NMe_4 (75:25 ratio). Primed letters and numbers correspond to proton signals of **7**⊂*tttt*-**5**•NMe_4. Doubly primed letters correspond to proton signals of Cl⊂*tttt*-**5**•NMe_4. See Figure 21 and Figure 24 for proton assignments. Benzyl methyl ether (I.S.). *Residual solvent peaks.

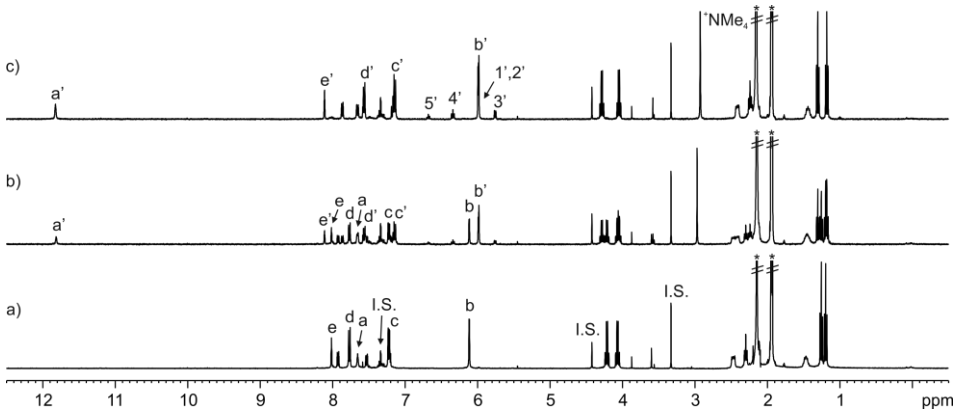

Figure 48. ^{1}H NMR (400 MHz, CD_3CN, 298 K) spectra of the titration of *tttt*-**5** with **7**•NMe_4: a) 0; b) 0.4 and c) 1 equiv. Primed letters and numbers correspond to proton signals of bound components. See Figure 21 and Figure 24 for proton assignments. Benzyl methyl ether (I.S.). *Residual solvent peaks.

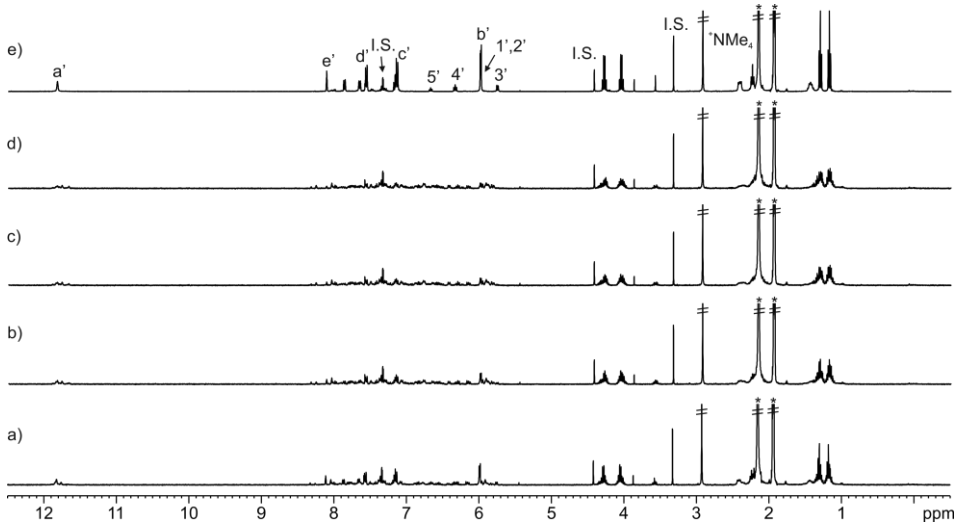

Figure 49. ^{1}H NMR (400 MHz, CD_3CN, 298 K) spectra of the photo-irradiation (365 nm) of **7**⊂*tttt*-**5**•NMe_4: a) 5; b) 10; c) 15 and d) 20 min; e) thermal re-equilibration. Primed letters and numbers correspond to proton signals of bound components. See Figure 21 and Figure 24 for proton assignments. Benzyl methyl ether (I.S.). *Residual solvent peaks.

Table 3. Chemical shifts (δ, ppm) of the protons of free and bound **7**•NMe_4 (**7**⊂*tttt*-**5**•NMe_4) and complexation induced shifts ($\Delta\delta$, ppm).

Signal	Solvent	δ_{free}	δ_{bound}	$\Delta\delta$	Solvent	δ_{free}	δ_{bound}	$\Delta\delta$
1		8.04	6.14-6.00	-1.97 (approx.)		8.00	5.98	-2.02
2		7.55	6.14-6.00	-1.48 (approx.)		7.55	5.98	-1.57
3		7.63	5.97	-1.66		7.66	5.76	-1.90
	CD_2Cl_2				CD_3CN			
4		7.43	6.43	-1.00		7.45	6.34	-1.11
5		7.33	6.74	-0.59		7.34	6.68	-0.66
$^{+}NMe_4$		3.45	1.81	-1.64		3.08	2.92	-0.16

Chapter 6

Tetra-methylammonium 3'-fluoro-(1,1'-bi-phenyl) 4-carboxylate **8**•NMe_4

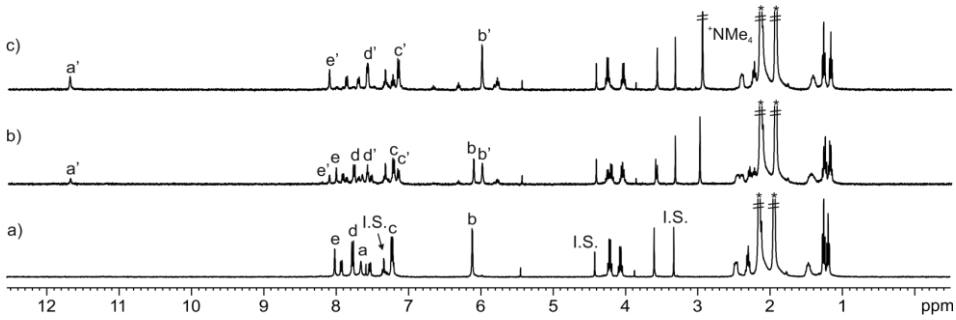

Figure 50. ^{1}H NMR (400 MHz, CD_3CN, 298 K) spectra of the titration of *tttt*-**5** with **8**•NMe_4: a) 0; b) 0.5 and c) 1 equiv. Primed letters correspond to proton signals of bound components. See Figure 21 for proton assignment. Benzyl methyl ether (I.S.). *Residual solvent peaks.

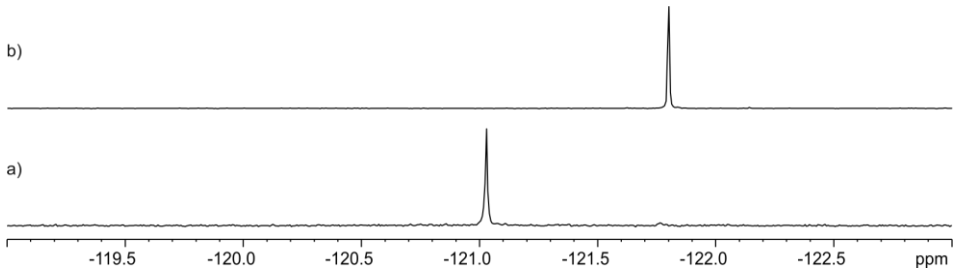

Figure 51. $^{19}F\{^1H\}$ NMR (471 MHz with cryoprobe, CD_3CN, 298 K) spectra of the titration of *tttt*-**5** with **8**•NMe_4: a) 1 equiv. and b) **8**•NMe_4.

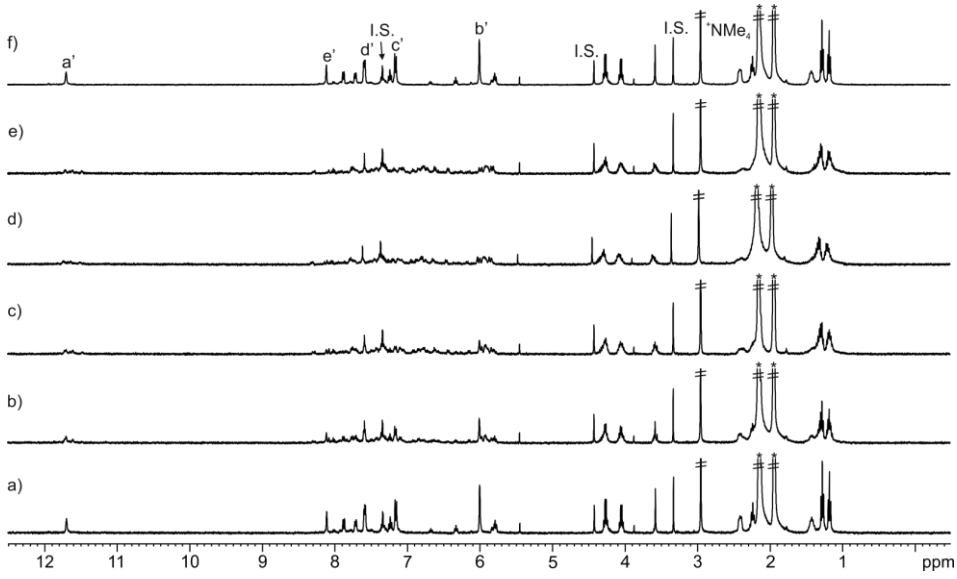

Figure 52. ^{1}H NMR (400 MHz, CD_3CN, 298 K) spectra of the photo-irradiation (365 nm) of **8**⊂*tttt*-**5**: a) 5; b) 10; c) 15 and d) 20 min; e) thermal re-equilibration. Primed letters correspond to proton signals of bound components. See Figure 21 for proton assignment. Benzyl methyl ether (I.S.). *Residual solvent peaks.

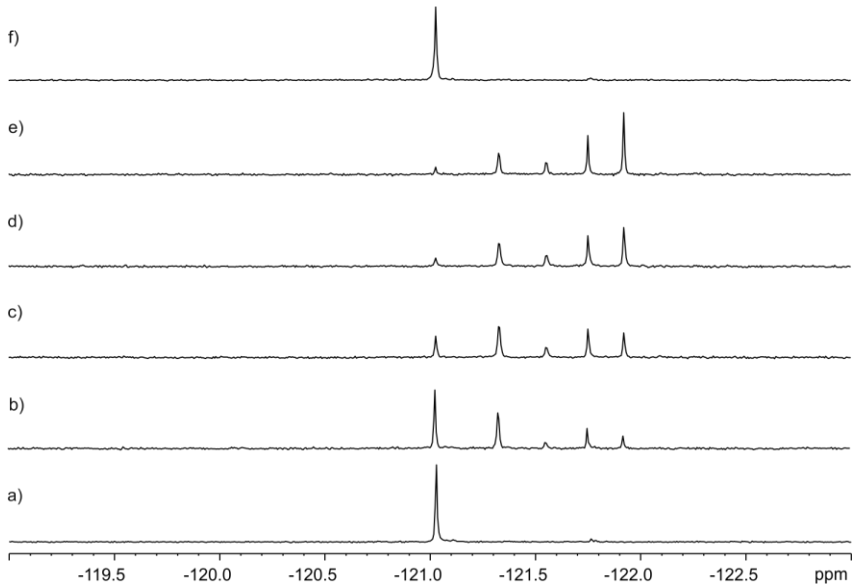

Figure 53. $^{19}F\{^{1}H\}$ NMR (471 MHz with cryoprobe, CD_3CN, 298 K) spectra of the photo-irradiation (365 nm) of **8**⊂*tttt*-**5**: a) 5; b) 10; c) 15 and d) 20 min; e) thermal re-equilibration.

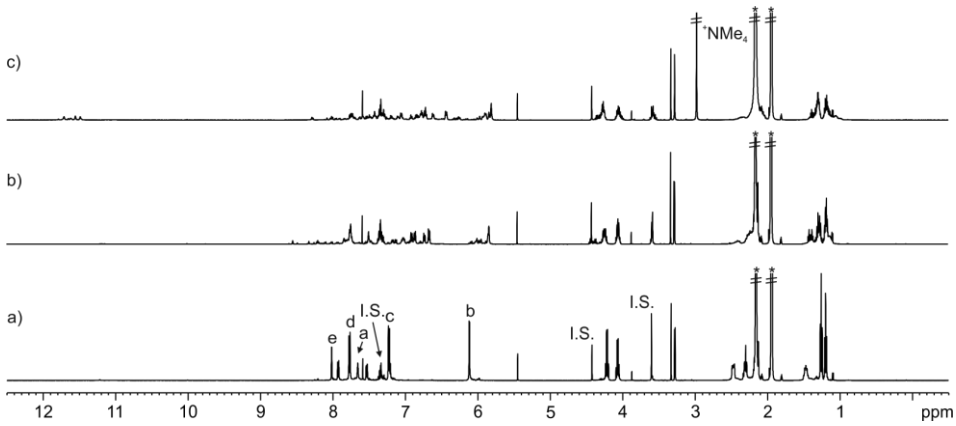

Figure 54. ^{1}H NMR (400 MHz, CD_3CN, 298 K) spectra of the titration of *tttt*-**5** with **8**•NMe_4: a) *tttt*-**5**; photo-irradiation (365 nm): b) 20 min and c) addition of 1 equiv. of **8**•NMe_4. See Figure 21 for proton assignment. Benzyl methyl ether (I.S.). *Residual solvent peaks.

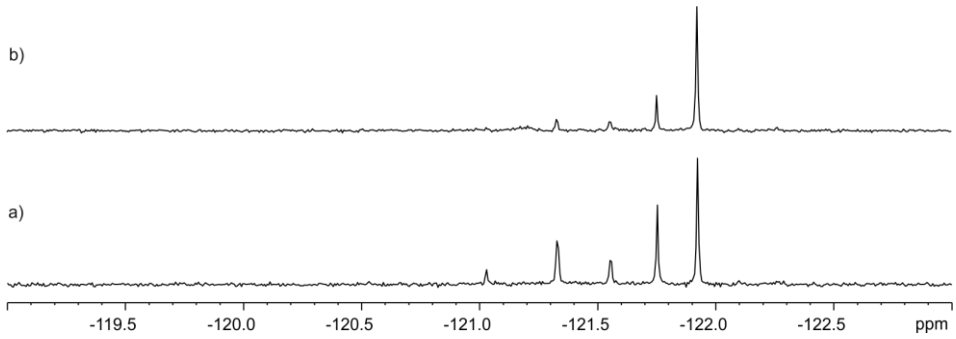

Figure 55. $^{19}F\{^{1}H\}$ NMR (471 MHz with cryoprobe, CD_3CN, 298 K) spectra of **8**⊂**5**: a) photo-irradiation of **8**⊂*tttt*-**5** for 20 min and b) photo-irradiation of *tttt*-**5** for 20 min followed by the addition of 1 equiv. of **8**•NMe_4.

Composition of the *cis*-enriched mixture of **5** in the *PSS* (CD_3CN):

Figure 55 shows the $^{19}F\{^{1}H\}$ signals of the *cis*-enriched mixture of **8**⊂**5** produced by: a) photo-irradiation of **8**⊂*tttt*-**5** for 20 min and b) photo-irradiation of *tttt*-**5** for 20 min followed by the addition of 1 equiv. of **8**•NMe_4. The signals were assigned to different isomeric complexes of **5** and **8** (*tttt*-, *tttc*-, *ttcc*- and *tctc*-, *tccc*- and *cccc*-isomers ordered from higher to lower chemical shifts). Based on the integral values of the signals and the number of *cis*-azo groups present in each isomeric complex, we calculated that the light-irradiation in a) produced the *trans*-to-*cis* isomerization of 65% of the azo groups of **5**. However, the light-irradiation in b) produced an 85% of the azo groups of **5** in the *cis*-configuration.

If the sum of integrals is 1:

cis-azo groups = [I_{cccc} + (3/4) x I_{tccc} + (2/4) x $I_{ttcc,tctc}$ + (1/4) x I_{tttc} + (0/4) x I_{tttt}] x 100

trans-azo groups = 100 - % *cis*-azo groups

6.4.6 Kinetic experiments of *cis*-to-*trans* isomerizations

A solution of **5** or **6**⊂**5** (1-2 mM) in CD_2Cl_2 was thermally equilibrated at 60ºC for 24 h. Benzyl methyl ether (1-2 mM) was used as internal standard. The sample was photo-irradiated with UV light (365 nm) for 20 min at r.t. and a ^{1}H NMR spectrum of the solution was acquired. Next, the NMR tube was heated at 40ºC in the spectrometer probe and a ^{1}H NMR spectrum was acquired every hour for 40-50 h. The concentration of *cis*-azo groups was determined from the signals assigned to the *trans*-azo counterparts and applying the mass balance [**5**] = [*trans*-**5**] + [*cis*-**5**] or [**5**] = [bound *trans*-**5**] + [bound *cis*-**5**]. The concentration changes of the *cis*-azo groups were fit to a first-order kinetic equation and the rate constant (k) (Equation 3), half-live ($t_{1/2}$) (Equation 4) and energy barrier ($\Delta G^{\ddagger}$) (Equation 5) values were determined.

1) *cis*-**5** → *trans*-**5** or bound *cis*-**5** → bound *trans*-**5**

2) d[*trans*-**5**]/dt = -d[*cis*-**5**]/dt = k_1 x [*cis*-**5**] or d[bound *trans*-**5**]/dt = -d[bound *cis*-**5**]/dt = k_2 x [bound *cis*-**5**]

3) ln [*cis*-**5**] = ln [*cis*-**5**]$_0$ - k_1 x t or ln [bound *cis*-**5**] = ln [bound *cis*-**5**]$_0$ - k_2 x t; k = rate constant

4) $t_{1/2}$ = ln 2/k; $t_{1/2}$ = half-live

5) k = ($k_B T$/h) x e^[-$\Delta G^{\ddagger}$/(RT)]; k_B = Boltzmann's constant; h = Planck's constant; R = Gas constant; T = Temperature and $\Delta G^{\ddagger}$ = Energy barrier.

Table 4. Rate constant (k, h^{-1}), half-live ($t_{1/2}$, h) and energy barrier ($\Delta G^{\ddagger}$, kcal·mol^{-1}) of the *cis*-to-*trans* isomerizations of **5** and **6**⊂**5** obtained from the fit of the data to a first-order kinetic equation.

Compound	k	$t_{1/2}$	$\Delta G^{\ddagger}$
5	2.1 x 10^{-2}	33	25.9
6⊂**5**	1.6 x 10^{-2}	43	26.0

6.4.7 ITC titration experiments

All titrations were performed by injecting small aliquots (8 µL) of dichloromethane or acetonitrile solutions of the guests from a computer controlled micro syringe into the solution of the host in the same solvent placed in the cell. The solution of the host was previously thermally equilibrated (*tttt*-**5**) or photo-irradiated (*cis*-enriched mixture of **5**) at 365 nm. The concentrations of the guest solutions were approximately seven to ten times more concentrated than the receptor ones ([H] = 0.05-0.50 mM). The association constants and enthalpy values were derived from the fit of the titration data to a 1:1 binding model using the Microcal ITC Data Analysis module.

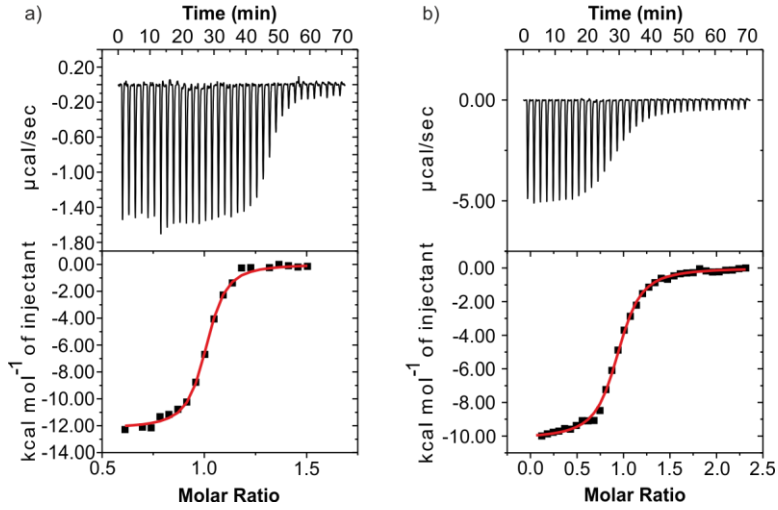

Figure 56. Top panels show raw data (heat *vs.* time) for the titration of guest into the host: a) **6**⊂*tttt*-**5** and b) **6**⊂*cccc*-**5** (*cis*-enriched mixture of **5**) (CH_2Cl_2). Titrations were performed at 288 K. Bottom panels represent integrated data fitted to the theoretical binding isotherm (red line) for a 1:1 binding model.

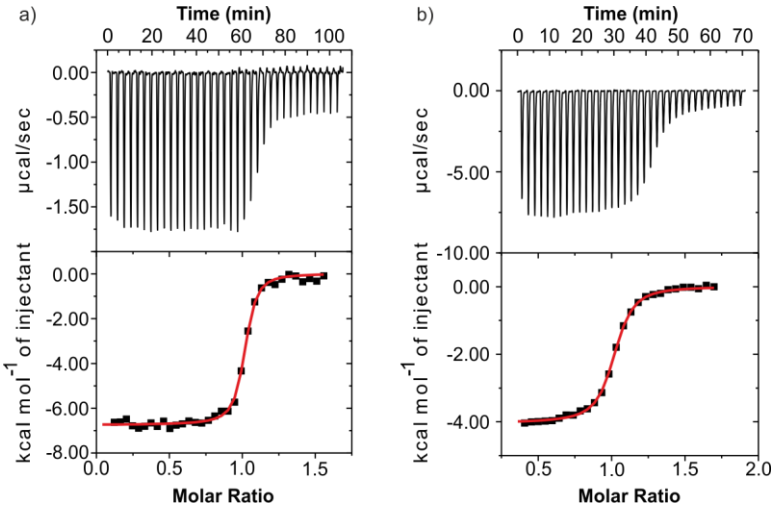

Figure 57. Top panels show raw data (heat *vs.* time) for the titration of guest into the host: a) **7**⊂*tttt*-**5**•NMe_4 and b) **7**⊂*cccc*-**5**•NMe_4 (*cis*-enriched mixture of **5**) (CH_2Cl_2). Titrations were performed at 288 K. Bottom panels represent integrated data fitted to the theoretical binding isotherm (red line) for a 1:1 binding model.

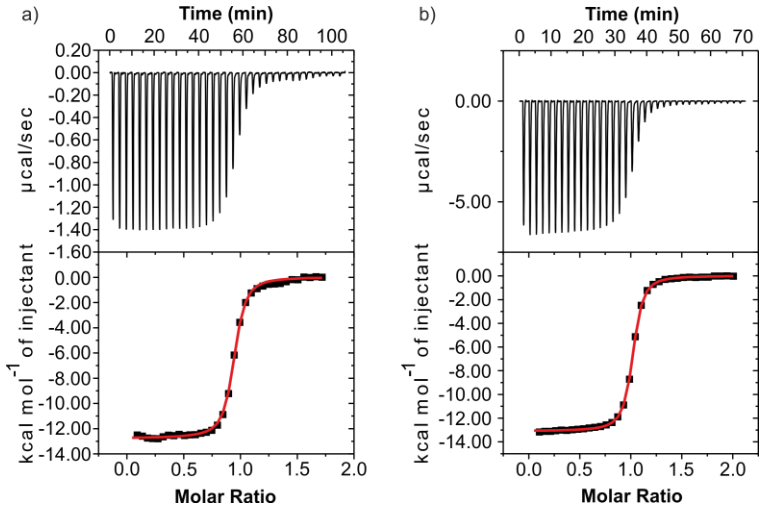

Figure 58. Top panels show raw data (heat *vs.* time) for the titration of guest into the host: a) **6**⊂*tttt*-**5** and b) **6**⊂*cccc*-**5** (*cis*-enriched mixture of **5**) (CH_3CN). Titrations were performed at 298 K. Bottom panels represent integrated data fitted to the theoretical binding isotherm (red line) for a 1:1 binding model.

6.4.8 Stability of **7**•NMe_4 in CD_2Cl_2 and CD_3CN solutions

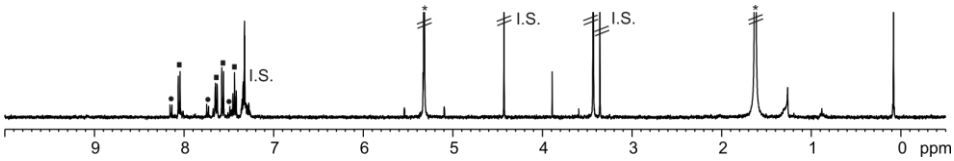

Figure 59. ^{1}H NMR (400 MHz, CD_2Cl_2, 298 K) spectrum of **7**•NMe_4 after 24 h at r.t. The mixture contained **7**•NMe_4 (squares) and chloromethyl 1,1'-bi-phenyl 4-carboxylate **9** (circles) in a 83:17 ratio. Benzyl methyl ether (I.S.). *Residual solvent peaks.

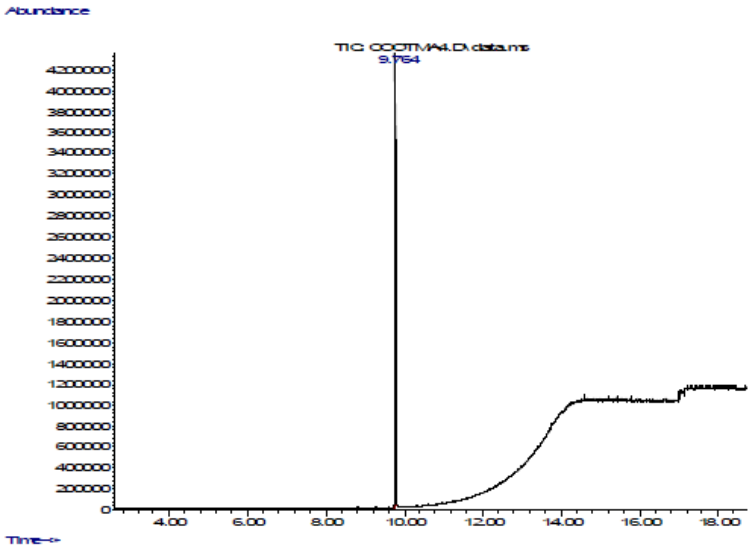

Figure 60. GC (column: HP5 30 m x 0.25 mm, 0.25 μm; flux = 1.5 mL·min^{-1}; temperature gradient: 20°C·min^{-1} from 50°C to 325°C) chromatogram of **7**•NMe_4 after 24 h at r.t. in CH_2Cl_2. Retention time of **9** = 9.76 min.

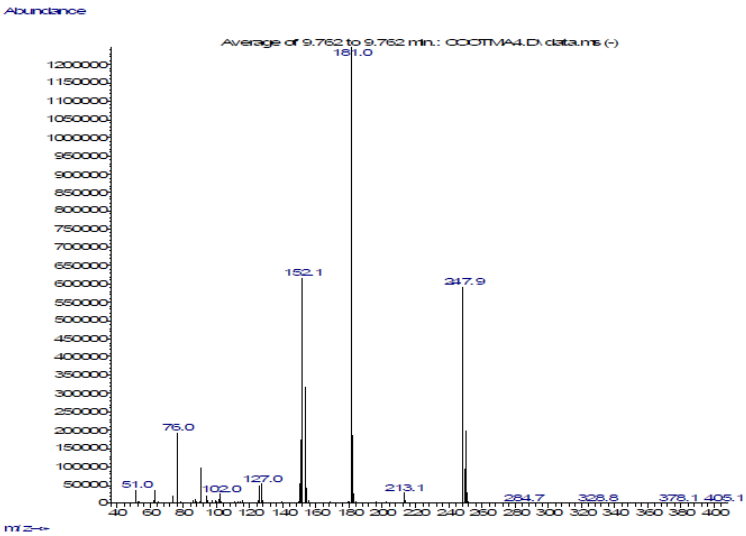

Figure 61. MS (electron impact; negative mode) analysis after GC of **7**•NMe_4 after 24 h at r.t. in CH_2Cl_2. The mass of the ions corresponded to the fragmentation of **9**. The peaks at m/z = 247.9 and 249.9 corresponded to the molecular ion of **9**, $[M]^{\cdot-}$ and $[M+2]^{\cdot-}$.

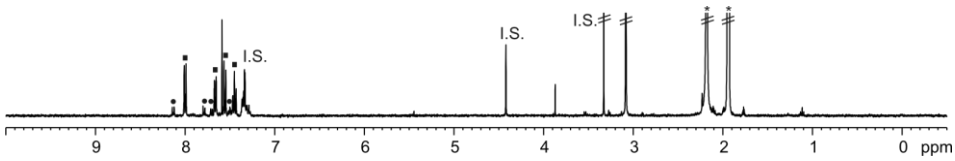

Figure 62. ^1H NMR (400 MHz, CD_3CN, 298 K) spectrum of **7**•NMe_4 after heating at 60ºC for 24 h. The mixture contained **7**•NMe_4 (squares) and methyl 1,1'-bi-phenyl 4-carboxylate **10** (circles) in a 87:12 ratio. Benzyl methyl ether (I.S.). *Residual solvent peaks.

Chapter 6

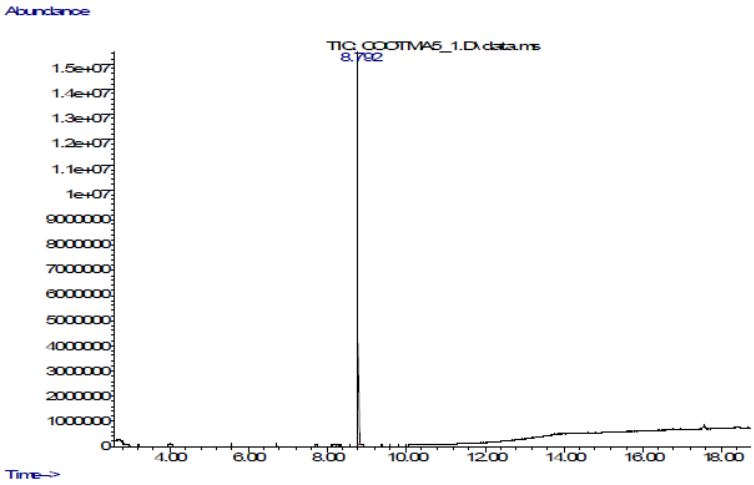

Figure 63. GC (column: HP5 30 m x 0.25 mm, 0.25 μm; flux = 1.5 mL·min^{-1}; temperature gradient: 20°C·min^{-1} from 50°C to 325°C) chromatogram of **7**•NMe_4 after heating at 60°C for 24 h. Retention time of **10** = 8.79 min.

Figure 64. MS (electron impact; negative mode) analysis after GC of **7**•NMe_4 after heating at 60°C for 24 h in CH_3CN. The mass of the ions corresponded to the fragmentation of **10**. The peaks at m/z = 212.1 corresponded to the molecular ion of **10**, $[M]^{\cdot-}$.

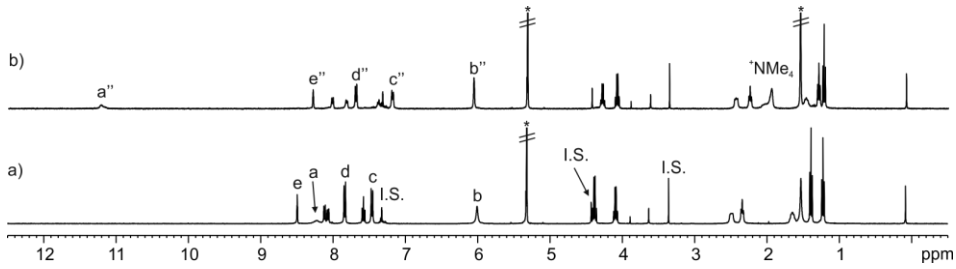

Figure 65. ^{1}H NMR (400 MHz, CD_2Cl_2, 298 K) spectra of the titration of *tttt*-**5** and tetra-methylammonium chloride (NMe_4Cl): a) 0; b) excess of NMe_4Cl. Proton signals of Cl⊂*tttt*-**5**•NMe_4 (doubly primed letters) are in agreement with the new set of signals observed after thermal re-equilibration of the **7**⊂**5**•NMe_4 complex in CD_2Cl_2. See Figure 21 for proton assignments. Benzyl methyl ether (I.S.). *Residual solvent peaks.

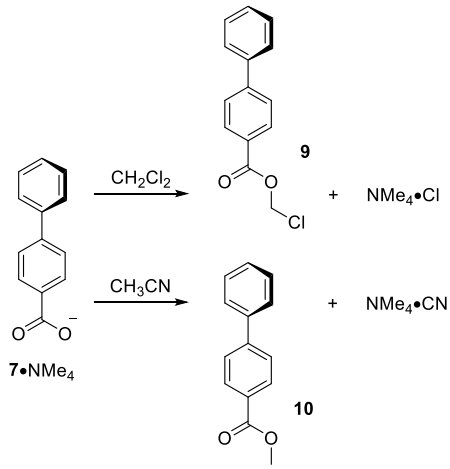

Scheme 3. Proposed products derived from **7**•NMe_4 in CH_2Cl_2 and CH_3CN. Chloromethyl 1,1'-bi-phenyl 4-carboxylate **9** and methyl 1,1'-bi-phenyl 4-carboxylate **10** were detected by GC/MS.

6.5 References and Notes

[1] D. H. Qu, Q. C. Wang, Q. W. Zhang, X. Ma, H. Tian, *Chem. Rev. (Washington, DC, U. S.)* **2015**, *115*, 7543-7588.

[2] M. Kathan, S. Hecht, *Chem. Soc. Rev.* **2017**, *46*, 5536-5550.

[3] R. S. Stoll, S. Hecht, *Angew. Chem., Int. Ed.* **2010**, *49*, 5054-5075.

[4] S. F. Pizzolato, B. S. L. Collins, T. van Leeuwen, B. L. Feringa, *Chem.--Eur. J.* **2017**, *23*, 6174-6184.

[5] M. Natali, S. Giordani, *Chem. Soc. Rev.* **2012**, *41*, 4010-4029.

[6] S. J. Wezenberg, B. L. Feringa, *Org. Lett.* **2017**, *19*, 324-327.

[7] V. Balzani, A. Credi, M. Venturi, *Chem. Soc. Rev.* **2009**, *38*, 1542-1550.

[8] A. Diaz-Moscoso, P. Ballester, *Chem. Commun. (Cambridge, U. K.)* **2017**, *53*, 4635-4652.

[9] T. Murase, S. Sato, M. Fujita, *Angew. Chem., Int. Ed.* **2007**, *46*, 5133-5136.

[10] M. Han, R. Michel, B. He, Y.-S. Chen, D. Stalke, M. John, G. H. Clever, *Angew. Chem., Int. Ed.* **2013**, *52*, 1319-1323.

[11] O. B. Berryman, H. Dube, J. Rebek Jr., *Isr. J. Chem.* **2011**, *51*, 700-709.

[12] A. A. Beharry, G. A. Woolley, *Chem. Soc. Rev.* **2011**, *40*, 4422-4437.

[13] E. Merino, M. Ribagorda, *Beilstein J. Org. Chem.* **2012**, *8*, 1071-1090.

[14] H. M. D. Bandara, S. C. Burdette, *Chem. Soc. Rev.* **2012**, *41*, 1809-1825.

[15] J. García-Amorós, D. Velasco, *Beilstein J. Org. Chem.* **2012**, *8*, 1003-1017.

[16] M. X. Dong, A. Babalhavaeji, S. Samanta, A. A. Beharry, G. A. Woolley, *Acc. Chem. Res.* **2015**, *48*, 2662-2670.

[17] T. Jin, *Mater. Lett.* **2007**, *61*, 805-808.

[18] H. Galán, G. Hennrich, J. de Mendoza, P. Prados, *Eur. J. Org. Chem.* **2010**, *2010*, 1249-1257.

[19] K.-i. Yuyama, L. Marcelis, P.-M. Su, W.-S. Chung, H. Masuhara, *Langmuir* **2017**, *33*, 755-763.

[20] O. B. Berryman, A. C. Sather, A. Lledo, J. Rebek, *Angew. Chem., Int. Ed.* **2011**, *50*, 9400-9403.

[21] F. A. Arroyave, P. Ballester, *J. Org. Chem.* **2015**, *80*, 10866-10873.

[22] O. B. Berryman, A. C. Sather, J. Rebek, *Chem. Commun. (Cambridge, U. K.)* **2011**, *47*, 656-658.

[23] E. Busseron, J. Lux, M. Degardin, J. Rebek, *Chem. Commun. (Cambridge, U. K.)* **2013**, *49*, 4842-4844.

[24] T. Sakano, T. Ohashi, M. Yamanaka, K. Kobayashi, *Org. Biomol. Chem.* **2015**, *13*, 8359-8364.

[25] S. N. Sahu, A. B. Rozhenko, J. Eberhard, J. Mattay, *J. Photochem. Photobiol., A* **2016**, *331*, 165-174.

[26] G. Cafeo, F. H. Kohnke, G. Mezzatesta, A. Profumo, C. Rosano, A. Villari, A. J. P. White, *Chem.--Eur. J.* **2015**, *21*, 5323-5327.

[27] L. Osorio-Planes, M. Espelt, M. A. Pericas, P. Ballester, *Chem. Sci.* **2014**, *5*, 4260-4264.

[28] A. Diaz-Moscoso, F. A. Arroyave, P. Ballester, *Chem. Commun. (Cambridge, U. K.)* **2016**, *52*, 3046-3049.

[29] V. Jain, H. Mandalia, *J. Inclusion Phenom. Macrocyclic Chem.* **2009**, *63*, 27-35.

[30] V. Jain, H. Mandalia, N. Bhojak, *Fibers Polym.* **2010**, *11*, 363-371.

[31] A. Díaz-Moscoso, D. Hernández-Alonso, L. Escobar, F. A. Arroyave, P. Ballester, *Org. Lett.* **2017**, *19*, 226-229.

[32] P. Anzenbacher, K. Jursikova, V. M. Lynch, P. A. Gale, J. L. Sessler, *J. Am. Chem. Soc.* **1999**, *121*, 11020-11021.

[33] L. Bonomo, E. Solari, G. Toraman, R. Scopelliti, M. Latronico, C. Floriani, *Chem. Commun. (Cambridge, U. K.)* **1999**, 2413-2414.

[34] G. Gil-Ramirez, E. C. Escudero-Adan, J. Benet-Buchholz, P. Ballester, *Angew. Chem., Int. Ed.* **2008**, *47*, 4114-4118.

[35] L. Escobar, G. Aragay, P. Ballester, *Chem.--Eur. J.* **2016**, *22*, 13682-13689.

[36] D. S. Kim, J. L. Sessler, *Chem. Soc. Rev.* **2015**, *44*, 532-546.

[37] D. Hernandez-Alonso, S. Zankowski, L. Adriaenssens, P. Ballester, *Org. Biomol. Chem.* **2015**, *13*, 1022-1029.

[38] W. Sato, H. Miyaji, J. L. Sessler, *Tetrahedron Lett.* **2000**, *41*, 6731-6736.

[39] R. Gotor, A. M. Costero, P. Gavina, S. Gil, M. Parra, *Eur. J. Org. Chem.* **2013**, 1515-1520.

[40] G. Cafeo, G. Gattuso, F. H. Kohnke, G. Papanikolaou, A. Profumo, C. Rosano, *Chem.--Eur. J.* **2014**, *20*, 1658-1668.

[41] H. Miyaji, S. J. Hong, S. D. Jeong, D. W. Yoon, H. K. Na, J. Hong, S. Ham, J. L. Sessler, C. H. Lee, *Angew. Chem., Int. Ed.* **2007**, *46*, 2508-2511.

[42] N. Kiriyama, M. Ebihara, T. Udagawa, H. Miyaji, *RSC Adv.* **2016**, *6*, 19794-19796.

[43] J. D. Dunitz, *Chem. Biol.* **1995**, *2*, 709-712.

[44] G. R. Fulmer, A. J. M. Miller, N. H. Sherden, H. E. Gottlieb, A. Nudelman, B. M. Stoltz, J. E. Bercaw, K. I. Goldberg, *Organometallics* **2010**, *29*, 2176-2179.

Chapter 7

Self-Assembly of Hydrogen-Bonded Dimeric Capsules Derived From a Tetra-Urea Super Aryl-Extended Calix[4]pyrrole

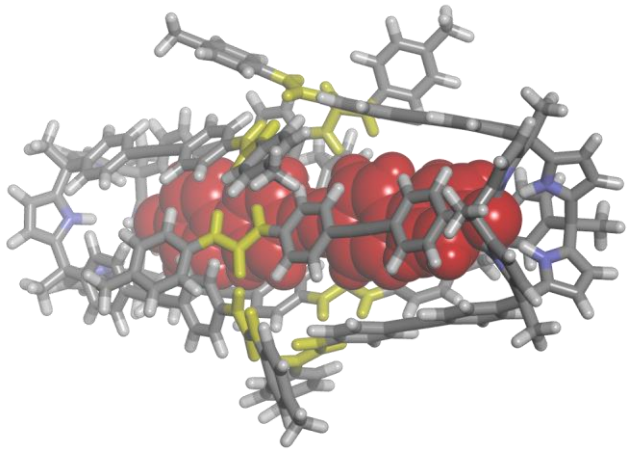

Unpublished results

UNIVERSITAT ROVIRA I VIRGILI
MOLECULAR CONTAINERS BASED ON ARYL-EXTENDED CALIX[4]PYRROLES
Luis Escobar González

7.1 Introduction

Self-assembly is a supramolecular strategy for the construction of large molecular architectures from smaller, individual components under thermodynamic control. The information for the assembly is encoded in the binding motifs of the sub-units, whose reversible interaction leads to the self-assembled architecture. The hydrophobic effect, ion-pairing, metal-ligand or hydrogen-bonding interactions are involved in the assembly process.[1,2]

Non-covalent, self-assembled capsules feature enclosed cavities. Their inner volumes are suitable for size, shape and function complementary guests, which are isolated from the bulk solution upon encapsulation. In the liquid state, thermodynamically stable encapsulation complexes obey the 55% packing coefficient rule. Additionally, encapsulation complexes are generally kinetically stable because guest exchange requires partial/total dissociation of the capsular assembly, *i.e.* breaking of multiple non-covalent interactions.[1,2,3,4]

Dimeric capsules have been designed using concave molecular scaffolds and self-complementary hydrogen-bonding functions, such as urea groups. The urea group features two NH hydrogen bond donors and one hydrogen bond acceptor in the oxygen atom of the C=O group (Figure 1a). The interaction between urea groups features a head-to-tail binding geometry (Figure 1b). Thus, concave molecular scaffolds decorated with urea groups have encoded information for their assembly into capsules.[5]

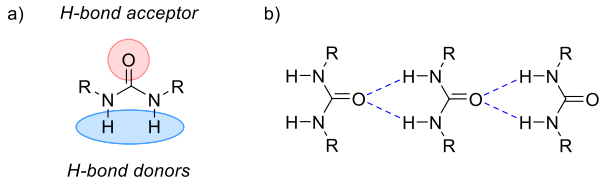

Figure 1. a) Structure of a urea group highlighting the donor and acceptor hydrogen-bonding atoms; b) head-to-tail hydrogen-bonding pattern of urea groups.

In this regard, Rebek and Böhmer reported independently the self-assembly of a calix[4]arene decorated with four urea groups at its upper rim into dimeric capsules (Figure 2a). The tetra-urea calix[4]arene hemispheres are held together by a unidirectional belt of sixteen hydrogen bonds. The calix[4]arene capsule features a spherical volume of *ca.* 200 Å^3 suitable for the encapsulation of small molecules (*e.g.* $CHCl_3$ and benzene).[6,7,8,9,10] The group of Rebek also designed a cylindrical dimeric capsule from resorcin[4]arene cavitands bearing upper rim urea (or imide) groups. In this case, the capsule is stabilized by a seam of bifurcated hydrogen-bonding interactions. The cylindrical capsule offers an inner space of *ca.* 415 Å^3 suitable for the encapsulation of a large guest or the co-inclusion of two guests.[2,11,12,13] Both calix[4]arene and

resorcin[4]arene dimeric capsules display non-polar inner environments and their binding selectivity obeys mainly the size and shape complementarity principles.

The control of the location and the orientation of encapsulated guests requires the functionalization of the capsule's cavity with endohedral polar groups. In this sense, dimeric capsules with polar interiors follow the size and shape principles, but also obey the complementarity of polar functional groups.[10] Our group reported dimeric capsules assembled from tetra-urea aryl-extended calix[4]pyrroles (Figure 2b). In the cone conformation, the calix[4]pyrrole cores at the poles of the dimer offer polar functions defined by the inwardly-oriented pyrrole NHs. Thus, a molecule of a di-topic guest (*e.g.* 4,4'-bipyridyl *bis*-*N*-oxide) or two molecules of a mono-topic guest (*e.g.* tri-methylamine *N*-oxide) template the formation of the dimeric capsule. The halves of the dimer form a seam of hydrogen bonds similar to that discussed above for the tetra-urea calix[4]arene capsule. The calix[4]pyrrole capsule provides a polar cavity with an inner volume of *ca.* 340 Å^3.[14] Owing to the analogy in the self-assembly mode of tetra-urea calix[4]arene and tetra-urea calix[4]pyrrole capsules, our group also showed that an equimolar solution containing the two different tetra-ureas and suitable templating guests leads to the exclusive formation of a hetero-dimeric calix[4]arene-calix[4]pyrrole capsule. In this case, the hybrid capsular assembly features only one polar hemisphere and its volume is *ca.* 280 Å^3.[10,15]

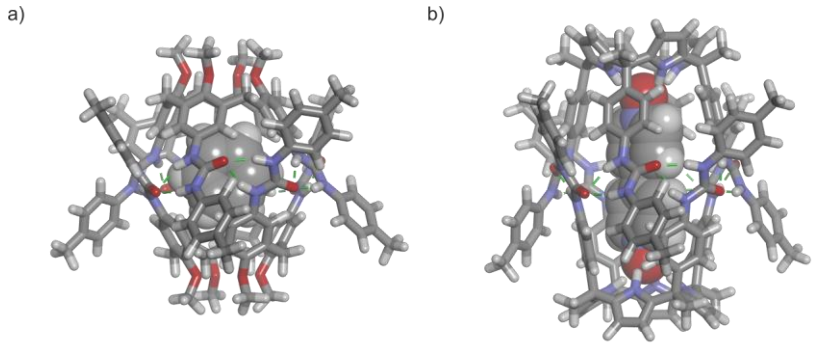

Figure 2. Energy minimized structures (MM3): a) Dimeric capsule of tetra-urea calix[4]arene (benzene is encapsulated) and b) dimeric capsule of tetra-urea calix[4]pyrrole (4,4'-bipyridine *bis*-*N*-oxide is encapsulated). The structures of the calix[4]arene and calix[4]pyrrole are depicted in stick representation. Bound guests are shown as CPK models.

Interestingly, larger hydrogen-bonded molecular capsules have been reported in literature.[10,16,17] For example, Atwood and co-workers showed that a simple resorcin[4]arene forms an hexameric self-assembled capsule with eight water molecules. Remarkably, a total of sixty hydrogen bonds held together the hexamer in which the water molecules participate. The volume of the cavity of the hexameric capsule is *ca*. 1375 Å^3.[16,18,19,20]

Self-assembled capsules have been applied in selective binding, control of guest uptake/release, stabilization of reactive species and as molecular reactors, among others. Applications in catalysis

have been reported but this field remains challenging owing to the issue of product inhibition.[21,22,23,24,25]

Herein, we report the synthesis of a tetra-urea super aryl-extended calix[4]pyrrole (SAE-C[4]P) bearing *meso*-alkyl substituents. We describe solution studies of the tetra-urea SAE-C[4]P with mono- and di-topic pyridyl *N*-oxides as templating guests for its self-assembly into homo-dimeric capsules of *ca.* 640 Å^3 volume. We also show that the tetra-urea SAE-C[4]P and a tetra-urea calix[4]arene self-assemble into a hetero-dimeric capsule having a volume of *ca.* 470 Å^3. The inner volumes of either the homo- or hetero-dimeric SAE-C[4]P capsules are significantly larger than those reported for calix[4]arene or calix[4]pyrrole derivatives.

7.2 Results and Discussion

7.2.1 Synthesis

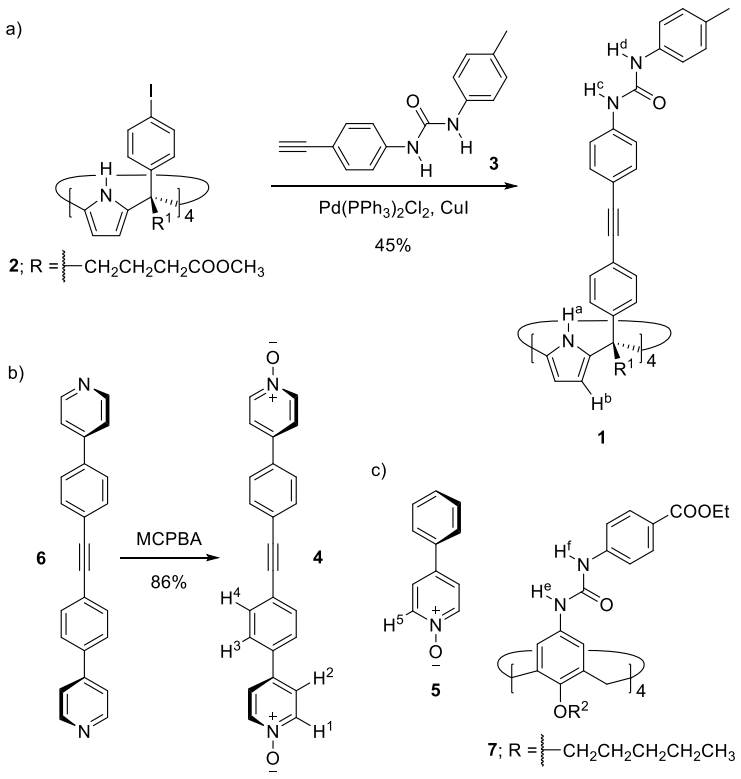

Scheme 1. Synthesis of a) tetra-urea SAE-C[4]P **1** and b) *bis*-*N*-oxide **4**; c) line-drawing structures of 4-phenyl pyridine *N*-oxide **5** and tetra-urea calix[4]arene **7**.

We envisaged that dimeric capsules with polar interiors and inner volumes larger than *ca.* 340 Å^3 (tetra-urea calix[4]pyrrole capsule) could be assembled from tetra-urea derivatives of super aryl-

extended calix[4]pyrroles.[26] The urea groups could be installed at the upper rim of the SAE-C[4]P scaffolds. In the presence of a suitable templating guest, two tetra-urea SAE-C[4]Ps should assemble into dimeric capsules by the establishment of a cyclic seam of sixteen intermolecular hydrogen bonds between their urea groups.

Tetra-urea super aryl-extended calix[4]pyrrole **1** was synthesized by the quadruple Sonogashira cross-coupling reaction between tetra-*α*-(4-iodophenyl) tetra-ester calix[4]pyrrole **2**[27] and 1-(4-ethynylphenyl)-3-(*para*-tolyl)urea **3**. Tetra-urea **1** was isolated in 45% yield after column chromatography purification (Scheme 1a). It is worth mentioning that the purification of tetra-urea SAE-C[4]P **1** resulted problematic owing to its high polarity.

The tetra-urea SAE-C[4]P **1** was characterized by NMR spectroscopy and HRMS. The ^{1}H NMR spectrum of **1** in $(CD_3)_2CO$ solution showed a set of sharp and well-defined proton signals, whose number is in agreement with C_{4v} symmetry (Figure 3). The pyrrole NHs (H^a) appeared as a sharp singlet at δ = 8.24 ppm, suggesting their involvement in hydrogen-bonding interactions. Most likely, SAE-C[4]P **1** adopts the cone conformation by binding one acetone molecule in its polar aromatic cavity.[23,28] The *β*-pyrrole protons (H^b) resonated at δ = 6.11 ppm as a sharp signal. On the other hand, the urea NHs ($H^{c,d}$) appeared at δ = 9.00 and δ = 8.67 ppm. The downfield chemical shift of the urea NH protons suggest that they are also involved in hydrogen-bonding interactions with solvent molecules. Taken together, these observations suggest that tetra-urea **1** exists mainly as a monomer in acetone solution.

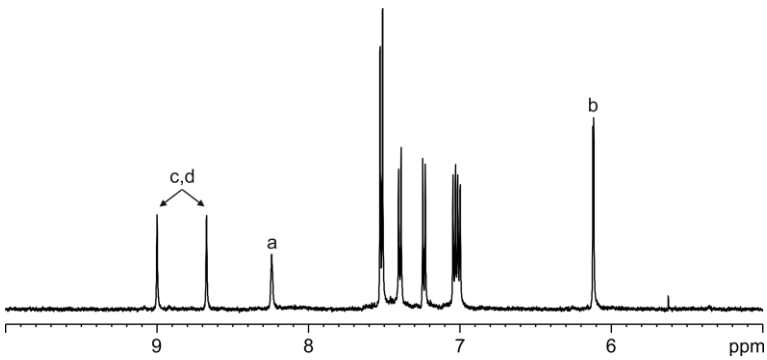

Figure 3. Selected region of the ^{1}H NMR (400 MHz, $(CD_3)_2CO$, 298 K) spectrum of tetra-urea **1**. See Scheme 1 for proton assignment.

The energy minimized structure (MM3) of the putative $(CH_3)_2CO\subset$**1** complex shows the receptor in the cone conformation. The pyrrole NHs of SAE-C[4]P **1** stablish four convergent hydrogen bonds with the oxygen atom of the bound $(CH_3)_2CO$ molecule. The *meso*-aromatic walls of **1** are engaged in CH-π interactions with the methyl groups of bound $(CH_3)_2CO$ (Figure 4).

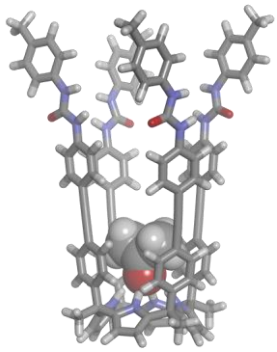

Figure 4. Energy minimized structure (MM3) of the putative $(CH_3)_2CO\subset$**1** complex. Tetra-urea SAE-C[4]P **1** is depicted in stick representation and bound acetone is shown as CPK model. Alkyl substituents are pruned to methyl groups to ease the calculation.

7.2.2 Self-assembly of tetra-urea SAE-C[4]P **1** into homo-dimeric capsules

Tetra-urea aryl-extended calix[4]pyrroles form dimers in the presence of suitable guests in non-polar solvents, such as methylene chloride or chloroform.[6,14] We thought that tetra-urea SAE-C[4]P **1** should assemble into dimeric capsules when using appropriate templating guests. Based on simple molecular modelling studies (MM3), we selected a long *bis*-pyridyl *bis*-*N*-oxide **4** and 4-phenyl pyridine *N*-oxide **5** as possible templating guests (Scheme 1b,c). The *bis*-*N*-oxide **4** is a di-topic guest that complements the two distal polar binding sites of the dimeric capsule formed by two units of **1**. On the contrary, **5** is a mono-topic guest that complements only one polar binding site of the dimeric capsule and thus, two guest molecules are necessary for its assembly.

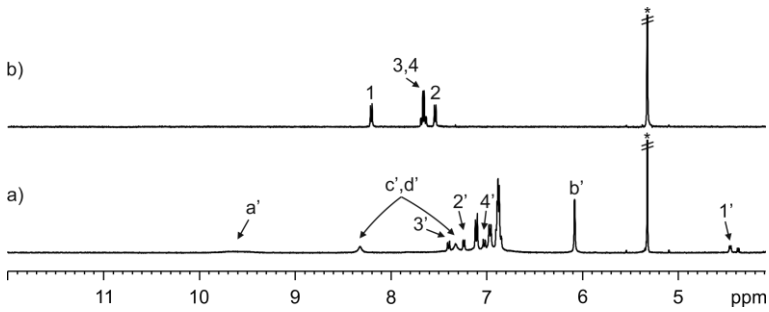

Figure 5. Selected region of the ^{1}H NMR (400 MHz, CD_2Cl_2, 298 K) spectra: a) tetra-urea **1** and *bis*-*N*-oxide **4** (2:1 ratio) and b) *bis*-*N*-oxide **4**. Primed letters and numbers correspond to proton signals of **4**$\subset$**1**$_2$. See Scheme 1 for proton assignments. *Residual solvent peak.

Briefly, *bis*-*N*-oxide **4** was synthesized by oxidation of *bis*-pyridyl **6**[29,30] with MCPBA (Scheme 1b). **4** was isolated by alumina column chromatography in good yield and excellent purity. 4-Phenyl pyridine *N*-oxide **5** is commercially available.

First, we probed the interaction between tetra-urea **1** and *bis*-*N*-oxide **4** in CD_2Cl_2 solution. Tetra-urea **1** was not totally soluble in CD_2Cl_2 at millimolar concentration. This observation indicates that **1** forms insoluble high-order aggregates owing to the hydrogen-bonding interactions between the upper rim urea groups. Nevertheless, the addition of 0.5 equiv. of *bis*-*N*-oxide **4** to a suspension of tetra-urea **1** in CD_2Cl_2 produced, after sonication for 10 min, a solution that was analyzed by ^{1}H NMR spectroscopy (Figure 5a). The ^{1}H NMR spectrum of the 2:1 mixture of tetra-urea **1** and *bis*-*N*-oxide **4** showed a set of well-resolved proton signals. The *β*-pyrrole protons (H^b) resonated as a sharp signal at δ = 6.08 ppm, whereas the pyrrole NHs (H^a) appeared as a broad signal centered at δ = 9.60 ppm. Two singlets appearing at δ = 8.32 and δ = 7.32 ppm corresponded to the urea NHs (H^c and H^d) of **1**. The proton signals of tetra-urea **1** do not provide evidence for the formation of a simple 1:1 inclusion complex or a homo-dimeric encapsulation complex. In this regard, we analyzed the chemical shifts and signal pattern for the protons of *bis*-*N*-oxide **4**. The proton signals of **4** appeared upfield shifted with respect to those of the free guest in CD_2Cl_2 solution (Figure 5b). In particular, the *α*-protons (H^1) respect to the *N*-oxide ends of **4** resonated at δ = 4.45 ppm. These protons experienced the largest complexation induced shift, $\Delta\delta$ = -3.75 ppm, indicating the deep inclusion of **4** in the aromatic cavity of SAE-C[*4*]P **1** in the cone conformation. The other aromatic proton signals of **4** (H^2-H^4) appeared between 7.5 and 7.0 ppm.

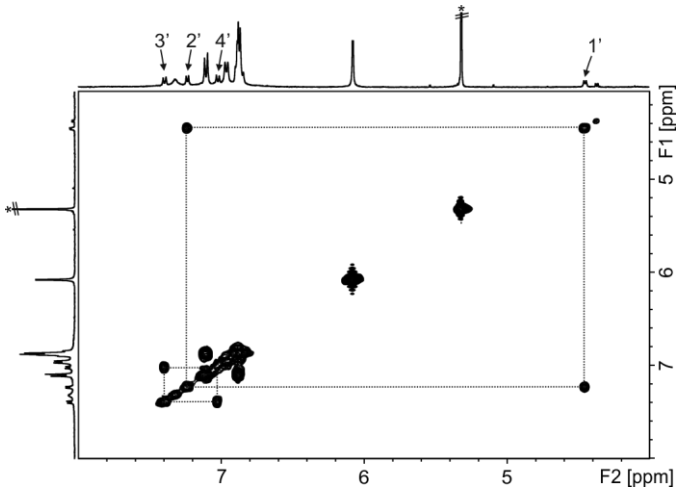

Figure 6. Selected region of 2D ^{1}H-^{1}H COSY (400 MHz, CD_2Cl_2, 298 K) spectrum of **4⊂1**$_2$. Primed numbers correspond to proton signals of **4⊂1**$_2$. See Scheme 1 for proton assignments. *Residual solvent peak.

The signal pattern for the protons of bound **4** indicates that the two ends of the bound *bis*-*N*-oxide are equivalent and, in other words, they enjoy identical magnetic environments, which is supported by a 2D COSY NMR spectrum of the later solution (Figure 6). This result points out that two tetra-urea SAE-C[4]Ps assemble into a homo-dimeric encapsulation complex, **4⊂1**$_2$, and rules out the assignment of the proton signals to a simple 1:1 inclusion complex, **4⊂1**. Note that in the 1:1

inclusion complex, the proton signals of the two ends of bound *bis*-*N*-oxide **4** should not be equivalent owing to the different magnetic environments along the aromatic cavity of **1**.

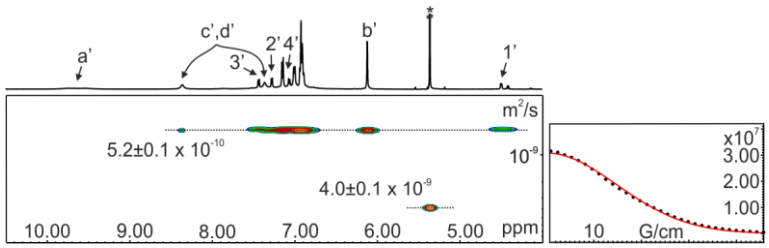

Figure 7. (left) ^{1}H pseudo 2D plot of DOSY (500 MHz with cryoprobe, CD_2Cl_2, 298 K, D20 = 0.15 s; P30 = 1 ms) of **4⊂1**$_2$. (right) Fit of the decay of the signal b' to a mono-exponential function. Primed letters and numbers correspond to proton signals of **4⊂1**$_2$. See Scheme 1 for proton assignments. Errors are indicated as standard deviations. *Residual solvent peak.

The CD_2Cl_2 solution containing tetra-urea **1** and *bis*-*N*-oxide **4** (2:1 ratio) was analyzed by DOSY NMR technique.[31] The decay of the proton signals was well-fitted to a mono-exponential function. The fit returned a diffusion constant value D = 5.2±0.1 x 10^{-10} $m^2 \cdot s^{-1}$ (Figure 7). This value is lower than that reported for homo-dimeric capsules of tetra-urea aryl-extended calix[4]pyrroles[32] and supports the formation of the **4⊂1**$_2$ encapsulation complex.

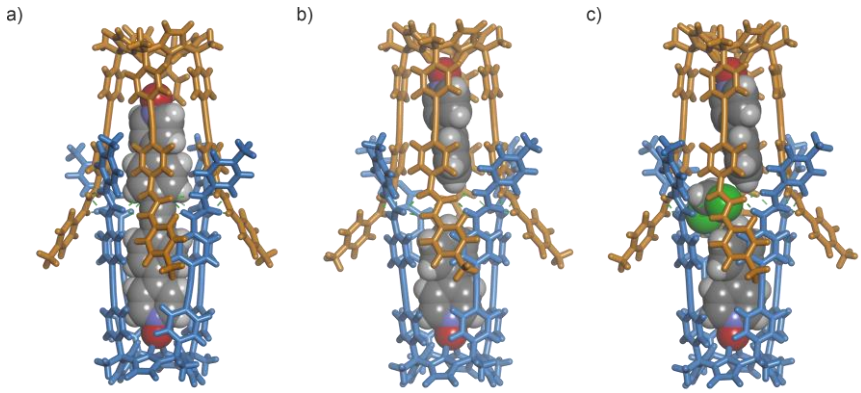

Figure 8. Energy minimized structures (MM3): a) **4⊂1**$_2$; b) **5**$_2$**⊂1**$_2$ and c) [**5**$_2$•CH_2Cl_2]**⊂1**$_2$ The tetra-urea SAE-C[4]Ps are depicted in stick representation. Bound molecules are shown as CPK models. Hydrogen bonds between the urea groups are highlighted (green lines). Alkyl substituents were pruned to methyl groups to ease the calculations.

The energy minimized structure (MM3) of **4⊂1**$_2$ shows the two tetra-urea SAE-C[4]Ps in the cone conformation (Figure 8a). The upper rim urea groups of **1** are involved in intermolecular hydrogen-bonding interactions in the equator of the dimeric assembly. The *bis*-*N*-oxide **4** seems to be slightly too short to stablish a perfect di-topic interaction with the two opposite calix[4]pyrrole cores of the capsular assembly. Thus, **4** may be shuttling between the two distal polar binding sites. This

observation may explain the broadening of the pyrrole NHs observed in the ^{1}H NMR spectrum of **4⊂1**$_2$. A packing coefficient of *ca.* 52% was calculated for the homo-dimeric encapsulation complex, **4⊂1**$_2$, which is in close agreement with the value reported for thermodynamically stable capsular complexes in the liquid state.[4] The volume of the cavity provided by **1**$_2$ is *ca.* 640 Å^3.

Next, we investigated the dimerization of tetra-urea SAE-C[4]P **1** using a mono-topic templating guest, 4-phenyl pyridine *N*-oxide **5**. Brief sonication of equimolar amounts of tetra-urea **1** and *N*-oxide **5** in CD_2Cl_2 produced a solution that was analyzed by ^{1}H NMR spectroscopy. The ^{1}H NMR spectrum of the CD_2Cl_2 solution showed well-resolved proton signals (Figure 9). The *β*-pyrrole protons (H^b) appeared as a sharp signal at *δ* = 6.10 ppm. Contrary to the result obtained for **4⊂1**$_2$, the pyrrole NHs resonated as a sharp singlet at *δ* = 9.92 ppm. The downfield chemical shift of the pyrrole NHs of **1** suggests that they are involved in hydrogen-bonding interactions, probably with the oxygen atom of the pyridyl *N*-oxide guest. The proton signals of the pyridyl *N*-oxide **5** appeared upfield shifted owing its deep inclusion in the polar aromatic cavity of **1** in the cone conformation. For example, the *α*-protons respect to the *N*-oxide appeared at *δ* = 4.61 ppm (Δ*δ* = -3.5 ppm).

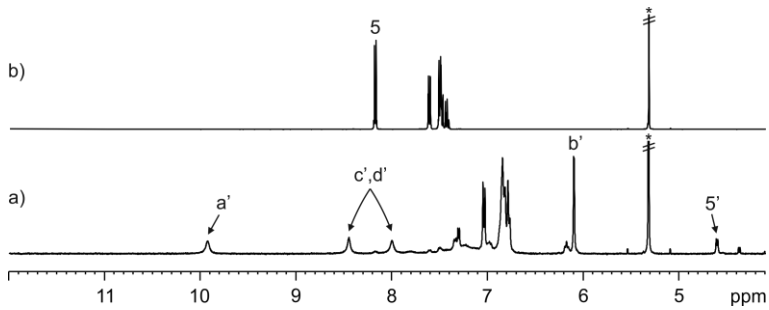

Figure 9. Selected region of the ^{1}H NMR (400 MHz, CD_2Cl_2, 298 K) spectra: a) tetra-urea **1** and *N*-oxide **5** (*ca.* 1:1 ratio) and b) *N*-oxide **5**. Primed letters and number correspond to proton signals of **5**$_2$⊂**1**$_2$. See Scheme 1 for proton assignments. *Residual solvent peak.

Integration of the proton signals of the two binding partners indicated that the complex had a 1:1 stoichiometry. In this case, the integral values does not provide evidence for the assignment of the observed signals in the ^{1}H NMR spectrum to a simple 1:1 inclusion complex or a 2:2 homo-dimeric encapsulation complex.

Nevertheless, the DOSY NMR experiment of the equimolar solution of tetra-urea **1** and *N*-oxide **5** in CD_2Cl_2 assigned a diffusion constant value $D = 4.9\pm0.3 \times 10^{-10}$ m^2·s^{-1} for the complex (Figure 10). This constant value is in line with that determined for **4⊂1**$_2$ and supports the formation of a 2:2 encapsulation complex, **5**$_2$⊂**1**$_2$.

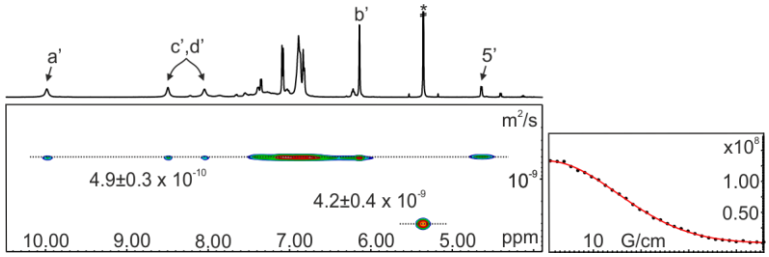

Figure 10. (left) ^{1}H pseudo 2D plot of DOSY (500 MHz with cryoprobe, CD_2Cl_2, 298 K, D20 = 0.15 s; P30 = 1 ms) of $\mathbf{5}_2\subset\mathbf{1}_2$. (right) Fit of the decay of the signal b' to a mono-exponential function. Primed letters and number correspond to proton signals of $\mathbf{5}_2\subset\mathbf{1}_2$. See Scheme 1 for proton assignments. Errors are indicated as standard deviations. *Residual solvent peak.

The energy minimized structure (MM3) of $\mathbf{5}_2\subset\mathbf{1}_2$ shows the two pyridyl *N*-oxides bound to the opposite calix[4]pyrrole cores of the dimeric capsule (Figure 8b). The oxygen atoms of the *N*-oxides stablish hydrogen-bonding interactions with the pyrrole NHs of the distal calix[4]pyrrole binding sites. In this case, the two polar guests satisfy the hydrogen-bonding characteristics of the capsular assembly, which may explain the sharpening of the signal corresponding to the bound pyrrole NHs in the ^{1}H NMR spectrum of $\mathbf{5}_2\subset\mathbf{1}_2$.

The calculated packing coefficient of $\mathbf{5}_2\subset\mathbf{1}_2$ is relatively low, *ca.* 40%. This result suggest that the cavity of the homo-dimeric encapsulation complex must be occupied by a solvent molecule to satisfy the 55% packing coefficient rule.[4] Most likely, a dichloromethane molecule is encapsulated in the equator of the homo-dimeric capsule (Figure 8c). The *PC* value of the $[\mathbf{5}_2\bullet CH_2Cl_2]\subset\mathbf{1}_2$ capsule is *ca.* 54%.

Table 1. Packing coefficient values (*PC*, %) determined from the energy minimized structures (MM3) of the encapsulation complexes (SwissPDB Version 4.10).

Complex	*PC*
$\mathbf{4}\subset\mathbf{1}_2$	52
$\mathbf{5}_2\subset\mathbf{1}_2$	40
$[\mathbf{5}_2\bullet CH_2Cl_2]\subset\mathbf{1}_2$	54

7.2.3 Self-assembly of tetra-urea SAE-C[4]P **1** and tetra-urea C[4]A **7** into a hetero-dimeric capsule

Our group showed that a tetra-urea aryl-extended calix[4]pyrrole and a tetra-urea calix[4]arene exclusively self-assemble into a hetero-dimeric capsule in dichloromethane solution.[15] We thought that tetra-urea SAE-C[4]P **1** should assemble into a hetero-dimeric capsule using tetra-urea calix[4]arene **7** and 4-phenyl pyridine *N*-oxide **5** (Scheme 1c). The *N*-oxide **5** should bind to the calix[4]pyrrole hemisphere and, most probably, a dichloromethane molecule should be included in the calix[4]arene hemisphere to satisfy the packing coefficient rule.

The ^{1}H NMR spectrum of a millimolar solution of tetra-urea calix[4]arene **7** in CD_2Cl_2 solution showed broad proton signals assigned to ill-defined aggregates (Figure 11a). Previously, we and others reported that the homo-dimeric capsule of similar tetra-urea calix[4]arenes is disrupted in dichloromethane solution.[15,33] Nevertheless, an equimolar CD_2Cl_2 solution of tetra-urea **1**, tetra-urea **7** and *N*-oxide **5**, produced after sonication for 10 min, gave a set of well-resolved signals in the ^{1}H NMR spectrum. Interestingly, the set of signals does not coincide with that of the homo-dimeric $\mathbf{5}_2\subset\mathbf{1}_2$ encapsulation complex and hints to the formation of a new, well-defined complex. The pyrrole NHs (H^a) of **1** appeared downfield shifted, δ = 9.95 ppm. The four signals corresponding to the urea NH protons of both **1** and **7** resonated at 8.23, 7.82 (x2) and 7.39 ppm. The chemical shifts of the urea protons of **1** and **7** indicated their involvement in hydrogen-bonding interactions. On the other hand, the proton signals of the pyridyl *N*-oxide **5** moved upfield. The upfield shift of the *α*-pyridyl protons (H^5), $\Delta\delta$ = -3.5 ppm, indicated the deep inclusion of **5** in the aromatic cavity of the cone conformer of **1**. Taken together, these observations suggest the formation of the hetero-dimeric encapsulation complex **5**⊂[**1**•**7**].

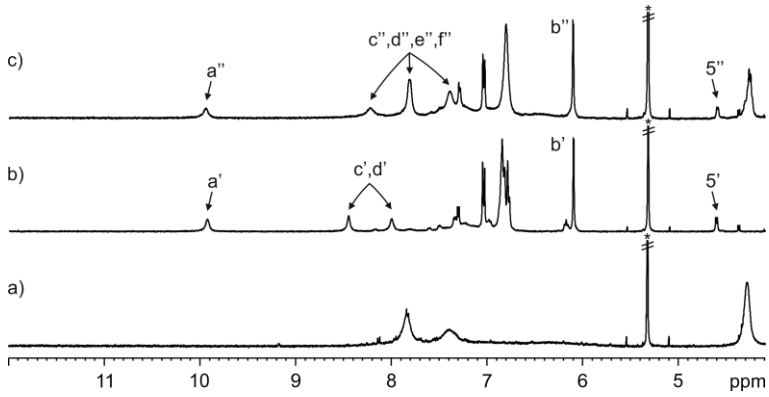

Figure 11. Selected region of the ^{1}H NMR (400 MHz, CD_2Cl_2, 298 K) spectra: a) **7**; b) $\mathbf{5}_2\subset\mathbf{1}_2$ and c) **5**⊂[**1**•**7**]. Primed letters and number correspond to proton signals of $\mathbf{5}_2\subset\mathbf{1}_2$. Doubly primed letters and number correspond to proton signals of **5**⊂[**1**•**7**]. See Scheme 1 for proton assignments. *Residual solvent peak.

The replacement of one half of the homo-capsule $\mathbf{1}_2$ by the tetra-urea calix[4]arene **7** to produce the hetero-capsule [**1•7**] should induce a significant change in the diffusion constant value. Thus, we analyzed the later equimolar solution of **1**, **5** and **7** by DOSY NMR spectroscopy. The returned diffusion constant value was 5.9±0.1 x 10^{-10} $m^2 \cdot s^{-1}$ (Figure 12). This value is larger than those determined for the homo-capsules **4**⊂$\mathbf{1}_2$ and $\mathbf{5}_2$⊂$\mathbf{1}_2$, and supports the assembly of the hetero-capsule **5**⊂[**1•7**].

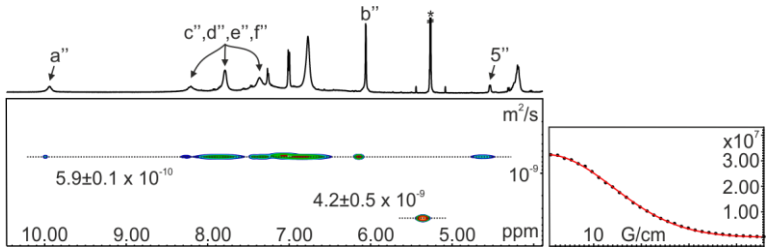

Figure 12. (left) ^{1}H pseudo 2D plot of DOSY (500 MHz with cryoprobe, CD_2Cl_2, 298 K, D20 = 0.15 s; P30 = 1 ms) of **5**⊂[**1•7**]. (right) Fit of the decay of the signal b'' to a mono-exponential function. Doubly primed letters and number correspond to proton signals of **5**⊂[**1•7**]. See Scheme 1 for proton assignments. Errors are indicated as standard deviations. *Residual solvent peak.

The energy minimized structure (MM3) of the hetero-dimeric capsule suggests that a CH_2Cl_2 molecule must be co-included in its cavity (Figure 13). The packing coefficient of [**5**•CH_2Cl_2]⊂[**1•7**] is *ca*. 47% and the hetero-capsule [**1•7**] features a cavity volume of *ca.* 470 Å^3. This volume is reduced more than 160 Å^3 when one half of the homo-capsule $\mathbf{1}_2$ is replaced by tetra-urea calix[4]arene **7** in the hetero-capsule [**1•7**].

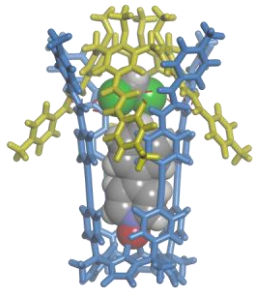

Figure 13. Energy minimized structure (MM3) of [**5**•CH_2Cl_2]⊂[**1•7**]. The tetra-ureas **1** and **7** are depicted in stick representation. Bound molecules are shown as CPK models. Hydrogen bonds between the urea groups are highlighted (red lines). Alkyl substituents were pruned to methyl groups to ease the calculation.

7.2.4 Synthesis of lipophilic calix[4]pyrrole scaffolds for the preparation of tetra-urea SAE-C[4]Ps

One of the main issues of tetra-urea SAE-C[4]P **1** is its low solubility in non-polar solvents, complicating the purification by standard techniques, such as chromatography, and the investigation of self-assembly processes by ^{1}H NMR spectroscopy. In this regard, we propose the use of a more lipophilic aryl-extended calix[4]pyrrole scaffold in the construction of tetra-urea SAE-C[4]Ps. Replacing the *meso*-alkyl ester groups at the lower rim of tetra-*α* 4-iodophenyl calix[4]pyrrole **2** by *meso*-dodecyl chains should improve the solubility of the tetra-urea derivative in non-polar solvents.

In this sense, we describe the synthesis of tetra-*α* tetra-(4-iodophenyl) tetra-dodecyl calix[4]pyrrole **8** (Scheme 2). 4-Iodophenyl dodecyl ketone **9** was prepared in two synthetic steps starting from 4-iodobenzaldehyde. 4-Iodobenzaldehyde was reacted with dodecyl magnesium bromide, prepared in situ, to give the corresponding alcohol **10** in 51% yield. Next, **10** was oxidized with pyridinium chlorochromate (PCC) to produce the desired 4-iodophenyl dodecyl ketone **9**. Compound **9** was isolated in 90% yield after filtration through Fluorosil®. Finally, tetra-(4-iodophenyl) calix[4]pyrrole **8** was synthesized from ketone **9** and pyrrole using a methodology recently described by our research group that involves the use of 4 M HCl (in dioxane solution) and methyltributylammonium chloride salt in the cyclocondensation step.[34] The tetra-*α* isomer of **8** was isolated in 19% yield by silica gel column chromatography. All the synthesized compounds were characterized by a complete set of high-resolution spectra (NMR and HRMS).

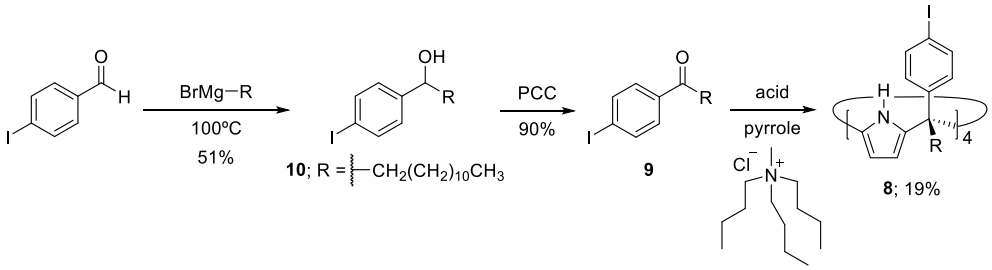

Scheme 2. Synthesis of tetra-(4-iodophenyl) tetra-dodecyl calix[4]pyrrole **8**.

7.3 Conclusions

In summary, we described the self-assembly of a super aryl-extended calix[4]pyrrole **1** decorated with urea groups at its upper rim into dimeric capsules in CD_2Cl_2 solution. Either a molecule of di-topic *bis*-*N*-oxide **4** or two molecules of mono-topic pyridyl *N*-oxide **5** served as templating guests for the efficient assembly of the homo-dimeric capsule. We also showed the self-assembly of tetra-urea SAE-C[4]P **1** and tetra-urea C[4]A **7** into a hetero-dimeric capsule. The hetero-capsule is templated by one molecule of *N*-oxide **5** and, most likely, by a co-encapsulated solvent molecule.

The two homo- and hetero-dimeric capsules feature polar interiors with cavity volumes larger than 450 Å^3. These properties suggest the application of self-assembled capsules derived from tetra-urea SAE-C[4]P **1** as nano-reactors to mediate chemical transformations, such as the alkyne-azide cycloaddition reaction.

7.4 Experimental Section

7.4.1 General information and instruments

All reagents were obtained from commercial suppliers and used without further purification unless otherwise stated. All solvents were commercially obtained and used without further purification excess pyrrole that was distilled and freshly used. Dry solvents were taken from a solvent system MB SPS 800 or obtained after drying with appropriate desiccants. Routine ^{1}H NMR and ^{13}C{^{1}H} NMR spectra were recorded on a Bruker Avance 300 (300 MHz for ^{1}H NMR and 75 MHz for ^{13}C NMR), Bruker Avance 400 (400 MHz for ^{1}H NMR and 100 MHz for ^{13}C NMR), Bruker Avance 500 (500 MHz for ^{1}H NMR and 125 MHz for ^{13}C NMR) or Bruker Avance 500 with cryoprobe (500 MHz for ^{1}H NMR and 125 MHz for ^{13}C NMR). Deuterated solvents used are indicated in the characterization and chemical shifts are given in ppm. Residual solvent peaks were used as reference.[35] All NMR *J* values are given in Hz. COSY, NOESY, ROESY, HMQC and HMBC were recorded to help with the assignment of ^{1}H and ^{13}C signals. High-resolution mass spectra (HRMS) were obtained on a Bruker HPLC-TOF (MicroTOF Focus) and Bruker HPLC-QqTOF (MaXis Impact). Both with ESI as ionization mode. IR spectra were recorded on a Bruker Optics FTIR Alpha spectrometer equipped with a DTGS detector, KBr beam splitter at 4 cm^{-1} resolution using a one bounce ATR accessory with diamond windows. Melting points were measured on a MP70 Melting Point System Mettler Toledo instrument. Column chromatography purifications were performed with silica gel technical grade, pore size 60 Å, 230-400 mesh particle size, 40-63 μm particle size and Thin layer chromatography (TLC) analyses on silica gel 60 F254.

7.4.2 Synthesis and characterization data

Tetra-urea super aryl-extended calix[4]pyrrole 1: Tetra-iodo **2** (50 mg, 0.03 mmol, 1 equiv.), 1-(4-ethynylphenyl)-3-(*para*-tolyl)urea **3** (49 mg, 0.20 mmol, 1.5 equiv.), $Pd(PPh_3)_2Cl_2$ (2.88 mg, 0.004 mmol, 0.03 equiv.) and CuI (1.25 mg, 0.007 mmol, 0.05 equiv.) were kept under Argon atmosphere. Dry and degassed THF (5 mL) and *i*Pr_2NH (5 mL) were added. The reaction was stirred at 45ºC under Argon atmosphere. After 20 h, the crude was concentrated and redissolved in CH_2Cl_2 (30 mL). The organic layer was washed with 0.5 N HCl (20 mL), brine (20 mL) and water (20 mL). The organic layer was dried (Na_2SO_4), filtered and concentrated. The crude was purified by silica gel column chromatography (6 g, 98:2 → 96:4 CH_2Cl_2:THF) affording the product as a white solid (30 mg, 0.015 mmol, 45% yield). ^{1}H NMR (500 MHz, $(CD_3)_2CO$, 298 K): δ (ppm) = 9.00 (s, 4H); 8.67 (s, 4H); 8.24 (br s, 4H); 7.52-7.50 (m, 16H); 7.40-7.38 (m, 8H); 7.24-7.23 (m, 8H); 7.04-7.00 (m, 16H); 6.11 (d, *J* = 2.5 Hz, 8H); 3.60 (s, 12H); 2.44 (m, 8H); 2.31 (m, 8H); 2.23 (s,

12H); 1.48 (m, 8H). HRMS (ESI-TOF) m/z: $[M+2Na]^{2+}$ Calcd for $C_{128}H_{116}N_{12}O_{12}Na_2$ 1029.4310; Found 1029.4334.

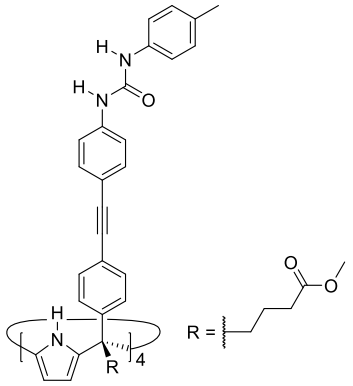

1

Figure 14. Line-drawing structure of tetra-urea SAE-C[4]P **1**.

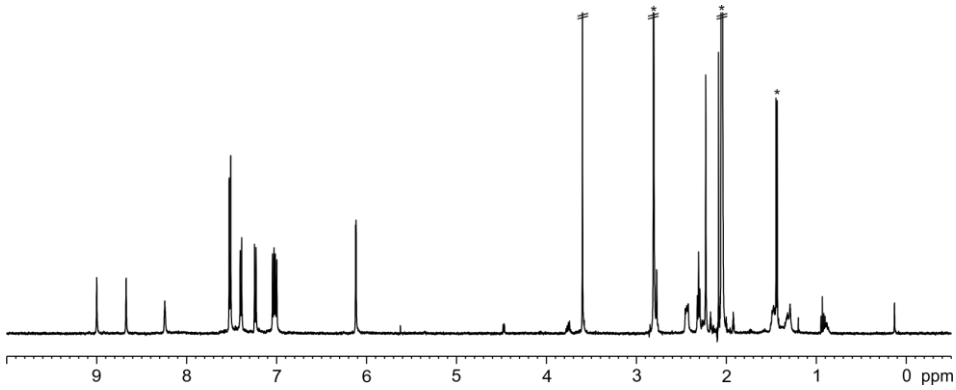

Figure 15. ^{1}H NMR (500 MHz, $(CD_3)_2CO$, 298 K) spectrum of **1**. *Residual solvent peaks.

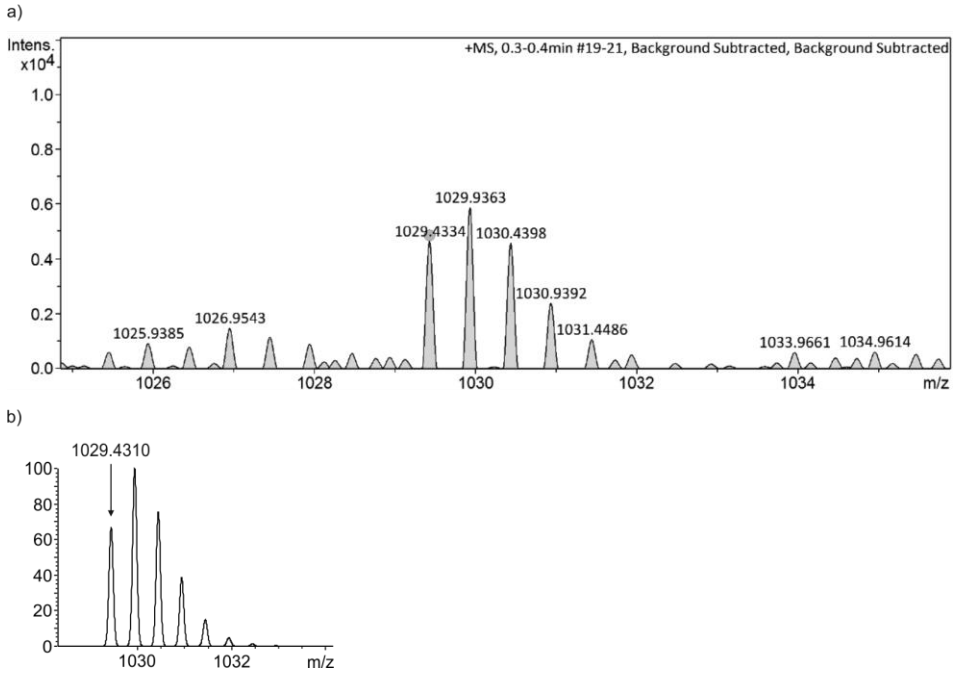

Figure 16. a) Experimental and b) theoretical isotopic distributions of $[M+2Na]^{2+}$. The exact mass for the monoisotopic peak in a) and b) is indicated.

Tetra(4-iodophenyl) calix[4]pyrrole 2: The experimental procedure for the synthesis of **2** is described in Chapter 3.

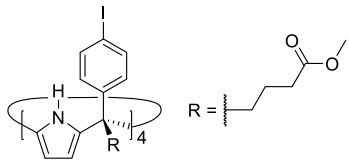

2

Figure 17. Line-drawing structure of tetra-*α* **2**.

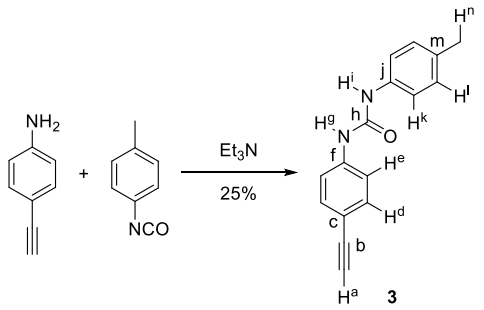

Scheme 3. Synthesis of 1-(4-ethynylphenyl)-3-(*para*-tolyl)urea **3**.

1-(4-Ethynylphenyl)-3-(*para*-tolyl)urea 3: 4-Ethynyl aniline (220 mg, 1.88 mmol, 1 equiv.) was dissolved in dry CH_2Cl_2 (25 mL). Et_3N (0.1 mL, 0.75 mmol, 0.4 equiv.) was added to the previous solution. Finally, 1-isocyanato-4-methyl-benzene (250 mg, 1.88 mmol, 1 equiv.) was dissolved in dry CH_2Cl_2 (25 mL) and added dropwise to the previous mixture. The reaction was stirred under Argon atmosphere and heated under reflux conditions for 24 h. After that, the reaction was stopped and the crude was neutralized using 1 N HCl. The crude was concentrated, triturated with hexane (20 mL) and filtered to afford the product as a white solid (112 mg, 0.45 mmol, 25% yield). ^{1}H NMR (400 MHz, $(CD_3)_2CO$, 298 K): δ (ppm) = 8.25 (br s, 1H); 8.06 (br s, 1H); 7.56-7.54 (m, 2H); 7.41-7.38 (m, 4H); 7.10-7.08 (m, 2H); 3.51 (s, 1H); 2.26 (s, 3H). ^{13}C{^{1}H} NMR (100 MHz, $(CD_3)_2CO$, 298 K): δ (ppm) = 153.2; 141.7; 138.0; 133.4; 132.4; 130.0; 119.7; 119.0; 116.3; 84.4; 77.8; 20.7. HRMS (ESI-TOF) m/z: $[M-H]^-$ Calcd for $C_{16}H_{13}N_2O$ 249.1033; Found 249.1030. FTIR ν (cm^{-1}) = 3281; 1637; 1581; 1551; 1508; 1403; 1306; 1288; 1233; 820; 640; 503.

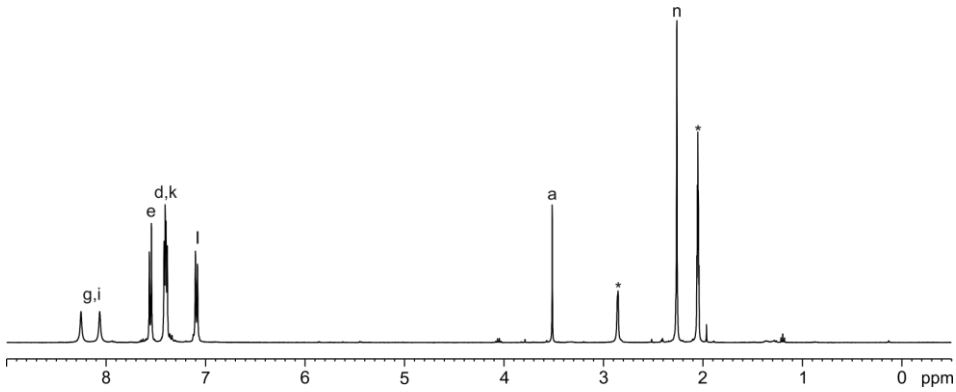

Figure 18. ^{1}H NMR (400 MHz, $(CD_3)_2CO$, 298 K) spectrum of **3**. See Scheme 3 for proton assignment. *Residual solvent peaks.

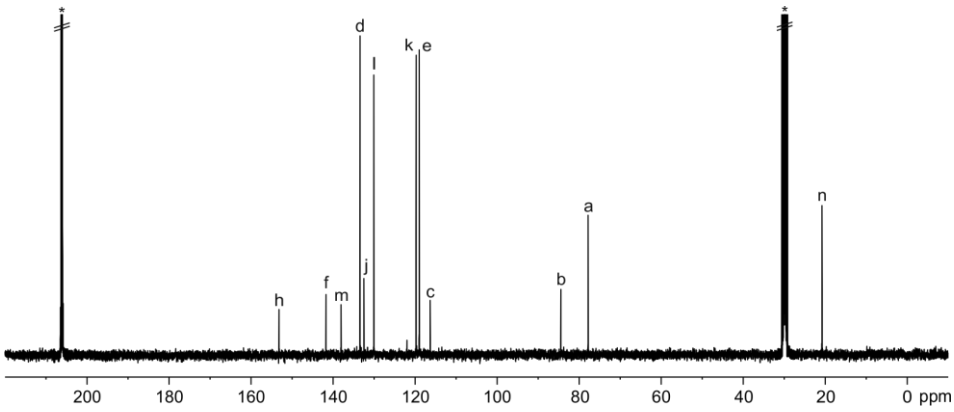

Figure 19. $^{13}C\{^{1}H\}$ NMR (100 MHz, $(CD_3)_2CO$, 298 K) spectrum of **3**. See Scheme 3 for carbon assignment. *Residual solvent peaks.

***Bis-N*-oxide 4:** *Bis*-pyridine **6** (40 mg, 0.12 mmol, 1 equiv.) was dissolved in distilled $CHCl_3$ (3 mL). The solution was cooled at 0ºC and *meta*-chloroperbenzoic acid (MCPBA) (81 mg, 0.36 mmol, 1.5 equiv.) was added portionwise. The reaction was stirred at 0ºC for 2.5 h. After that, the reaction was stopped and diluted with $CHCl_3$ (2.5 mL). The crude was purified by neutral alumina column chromatography (6 g; 9:1 $CHCl_3$:isopropanol) affording the product as a pale yellow solid (37.8 mg, 0.10 mmol, 86% yield). ^{1}H NMR (400 MHz, $CDCl_3$, 298 K): δ (ppm) = 8.28-8.26 (m, 4H); 7.67-7.65 (m, 4H); 7.61-7.59 (m, 4H); 7.54-7.52 (m, 4H). $^{13}C\{^{1}H\}$ NMR (125 MHz with cryoprobe, $CDCl_3$, 298 K): δ (ppm) = 139.6; 137.7; 136.1; 132.7; 126.5; 124.0; 123.7; 90.8. HRMS (ESI-TOF) m/z: $[M+Na]^+$ Calcd for $C_{24}H_{16}N_2O_2Na$ 387.1104; Found 387.1112.

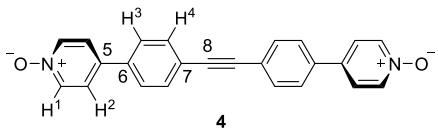

4

Figure 20. Line-drawing structure of *bis-N*-oxide **4**.

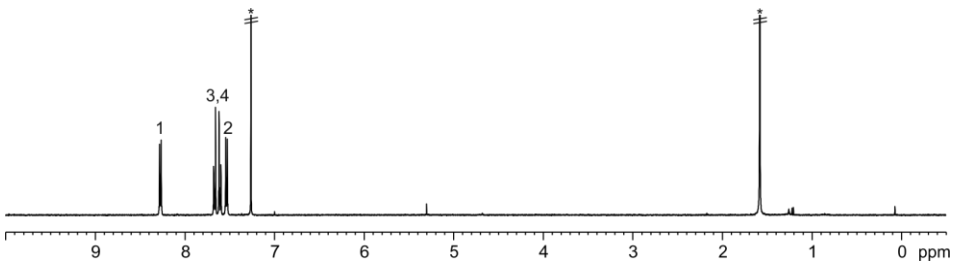

Figure 21. ^{1}H NMR (400 MHz, $CDCl_3$, 298 K) spectrum of **4**. See Figure 20 for proton assignment. *Residual solvent peaks.

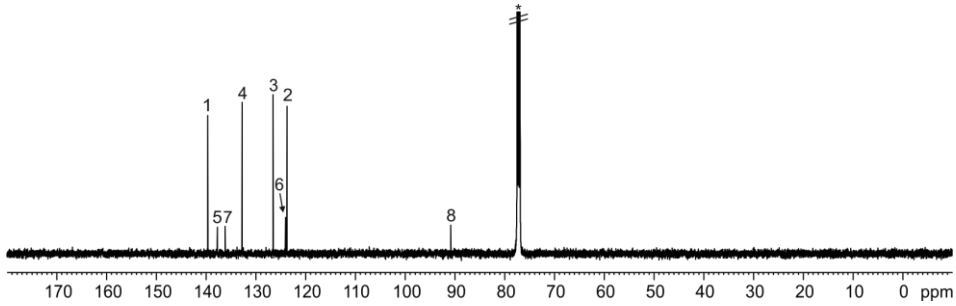

Figure 22. $^{13}C\{^1H\}$ NMR (125 MHz with cryoprobe, $CDCl_3$, 298 K) spectrum of **4**. See Figure 20 for carbon assignment. *Residual solvent peak.

Tetra-urea calix[4]arene 7: The compound was provided by the group of Prof. Ballester.

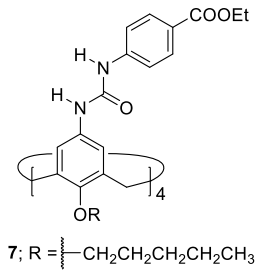

Figure 23. Line-drawing structure of tetra-urea **7**.

Tetra(4-iodophenyl) calix[4]pyrrole 8: Compound *αααα*-**8** was synthesized following a methodology previously described by our research group.[32] 4-Iodophenyl dodecyl ketone **9** (1 g, 2.50 mmol, 1 equiv.) and methyltributylammonium chloride (1.77 g, 7.50 mmol, 3 equiv.) were dissolved in dry CH_2Cl_2 (10 mL). The mixture was stirred at r.t. under Argon atmosphere and pyrrole (0.17 mL, 2.50 mmol, 1 equiv.) was added dropwise. HCl (1.87 mL from a 4 M solution in dioxane, 7.50 mmol, 3 equiv.) was added dropwise. The flask was covered with foil and stirred for 72 h. After that, the crude was diluted with CH_2Cl_2 (20 mL) and washed with aqueous saturated $NaHCO_3$ (2x20 mL) and water (20 mL). The organic layer was dried (Na_2SO_4), filtered and concentrated. The crude was purified by column chromatography on silica gel (80 g, 96:4 → 95:5 Hexane:CH_2Cl_2). The product was further purified by recrystallization from 2:3 CH_2Cl_2:CH_3CN affording *αααα*-**8** as a white solid (213 mg, 0.12 mmol, 19% yield). Rf = 0.2 (95:5 Hexane:CH_2Cl_2). ^1H NMR (500 MHz, $CDCl_3$, 298 K): δ (ppm) = 7.52-7.50 (m, 8H); 7.24 (br s, 4H); 6.87-6.85 (m, 8H); 5.80 (d, J = 2.5 Hz, 8H); 2.19-2.17 (m, 8H); 1.29-1.20 (m, 80H); 0.88 (t, J = 7.1 Hz, 12H). $^{13}C\{^1H\}$ NMR (125 MHz, $CDCl_3$, 298 K): δ (ppm) = 144.8; 136.7; 135.3; 130.6; 106.6; 92.4; 48.9; 40.5; 32.1; 30.6; 29.9-29.8 (several signals); 29.5; 25.5; 22.8; 14.3. HRMS (ESI-TOF) m/z: $[M-H]^-$ Calcd for $C_{92}H_{127}I_4N_4$ 1795.6245; Found 1795.6237. FTIR ν (cm^{-1}) = 3408; 2920; 2850; 1569; 1483; 1465; 1390; 1004; 766; 720; 509. M.p. = 98-100ºC.

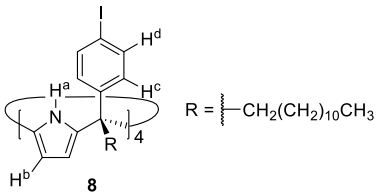

8

Figure 24. Line-drawing structure of tetra-*α* **8**.

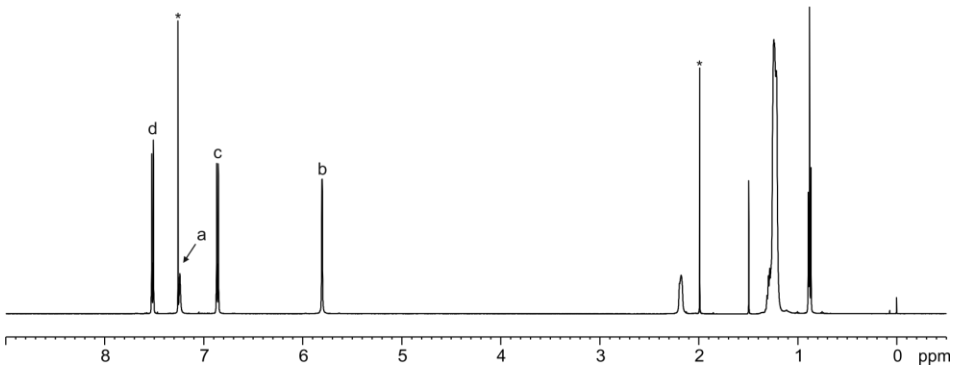

Figure 25. ^{1}H NMR (500 MHz, $CDCl_3$, 298 K) spectrum of tetra-*α* **8**. See Figure 24 for proton assignment. *Residual solvent peaks.

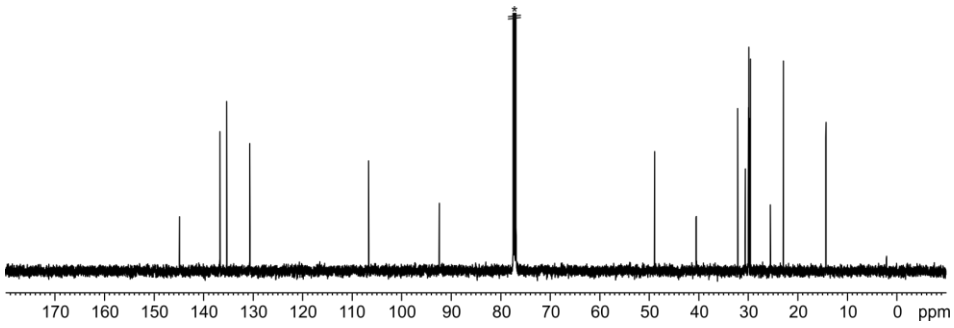

Figure 26. $^{13}C\{^{1}H\}$ NMR (125 MHz, $CDCl_3$, 298 K) spectrum of tetra-*α* **8**. *Residual solvent peak.

1-(4-Iodophenyl)tridecanone 9: 4-Iodophenyl alcohol **10** (1.80 g, 4.47 mmol, 1 equiv.) was added to a dry-oven round-bottom flask and purged with Argon. Dry CH_2Cl_2 (30 mL) was added and the solution was stirred at r.t. PCC (1.93 g, 8.95 mmol, 2 equiv.) was added in one portion to the solution of the alcohol. After the addition of PCC, the color changed to orange. After 1 h, Et_2O (30 mL) was added and the mixture was stirred for an additional 1 h. The crude was filtered through Fluorosil® (20 g, CH_2Cl_2). The product was obtained as a white solid (1.61 g, 4.02 mmol, 90% yield). ^{1}H NMR (300 MHz, $CDCl_3$, 298 K): δ (ppm) = 7.83-7.81 (m, 2H); 7.67-7.65 (m, 2H); 2.91 (t, J = 7.4 Hz, 2H); 1.73-1.69 (m, 2H); 1.32-1.26 (m, 18H); 0.88 (t, J = 6.7 Hz, 3H). $^{13}C\{^{1}H\}$ NMR (75

MHz, $CDCl_3$, 298 K): δ (ppm) = 200.0; 138.0; 136.5; 129.6; 100.9; 38.7; 32.1; 29.8-29.4 (several signals); 24.4; 22.8; 14.3. HRMS (ESI-TOF) m/z: $[M+Na]^+$ Calcd for $C_{19}H_{29}IONa$ 423.1155; Found 423.1163. FTIR ν (cm^{-1}) = 2915; 2848; 1679; 1579; 1560; 1462; 1392; 1259; 1185; 820; 790. M.p. = 82-84ºC.

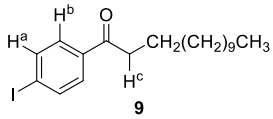

9

Figure 27. Line-drawing structure of ketone **9**.

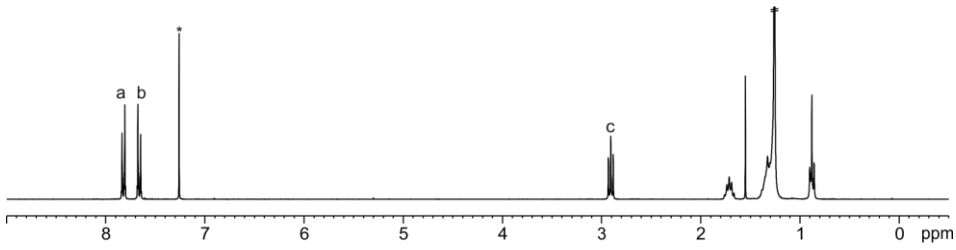

Figure 28. ^1H NMR (300 MHz, $CDCl_3$, 298 K) spectrum of **9**. See Figure 27 for proton assignment. *Residual solvent peak.

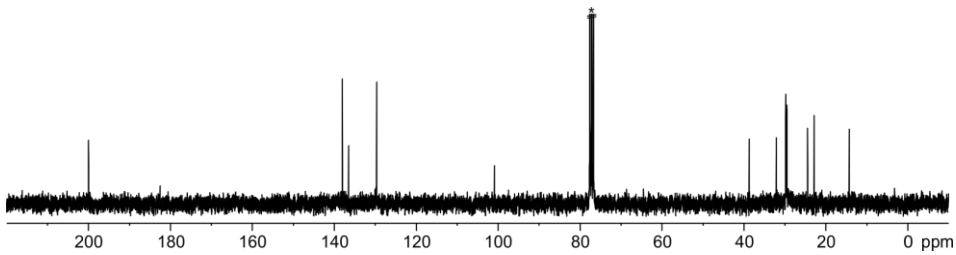

Figure 29. $^{13}C\{^1H\}$ NMR (75 MHz, $CDCl_3$, 298 K) spectrum of **9**. *Residual solvent peak.

1-(4-Iodophenyl)tridecanol 10: Part 1. Magnesium turnings (0.21 g, 8.62 mmol, 1 equiv.) were added to an dry-oven round-bottom flask and purged with Argon. Dry THF (2 mL) was added and the mixture was sonicated for 10 min. Then, the flask was connected to an addition funnel and the mixture was stirred at 100ºC under Argon atmosphere. 1-Bromododecane (2.07 mL, 8.62 mmol, 1 equiv.) was added to the addition funnel and diluted with dry THF (5 mL). The 1-bromododecane solution was added dropwise to the magnesium for 30 min. After the addition, dry THF (1.6 mL) was added to the addition funnel and added dropwise to the reaction. The reaction was stirred at r.t. for 1 h and the magnesium was totally consumed. Part 2. 4-Iodobenzaldehyde (2 g, 8.62 mmol, 1 equiv.) was added to a dry-oven flask and THF (6 mL) was added. The solution was added to an addition funnel connected to the flask of the prepared Grignard reagent. The reaction was heated

at 100ºC and the aldehyde was added dropwise. Extra THF (2.6 mL) was added to the addition funnel and, subsequently, added to the reaction mixture. After 2 h, the reaction was stopped and allowed to reach r.t. The reaction was quenched with aqueous saturated NH_4Cl (40 mL) and the organic layer was removed under vacuum. The crude was extracted with EtOAc (3x40 mL) and the organic layer was washed with water (40 mL). The organic layer was dried (Na_2SO_4), filtered and concentrated. The crude was purified by silica gel column chromatography (140 g, 4:6 CH_2Cl_2:Hexane) affording the product as a transparent oil (1.80 g, 4.40 mmol, 51% yield). Rf = 0.3 (4:6 CH_2Cl_2:Hexane). ^{1}H NMR (300 MHz, $CDCl_3$, 298 K): δ (ppm) = 7.67-7.64 (m, 2H); 7.08-7.06 (m, 2H); 4.62-4.57 (m, 1H); 1.98 (d, J = 3.4 Hz, 1H); 1.74-1.64 (m, 2H); 1.37-1.24 (m, 20 H); 0.88 (t, J = 6.9 Hz, 3H). ^{13}C{^{1}H} NMR (75 MHz, $CDCl_3$, 298 K): δ (ppm) = 144.7; 137.6; 128.0; 92.8; 74.2; 39.2; 32.0; 29.7-29.5 (several signals); 25.8; 22.8; 14.3. HRMS (ESI-TOF) m/z: $[M-H]^+$ Calcd for $C_{19}H_{30}IO$ 401.1336; Found 401.1333. FTIR ν (cm^{-1}) = 3345; 2915; 2849; 1469; 1401; 1059; 1004; 959; 820; 716; 550. M.p. = 55-57ºC.

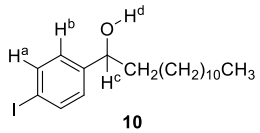

10

Figure 30. Line-drawing structure of alcohol **10**.

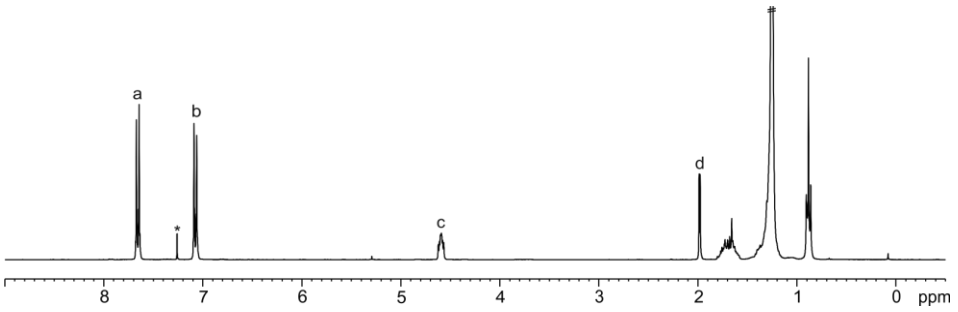

Figure 31. ^{1}H NMR (300 MHz, $CDCl_3$, 298 K) spectrum of **10**. See Figure 30 for proton assignment. *Residual solvent peak.

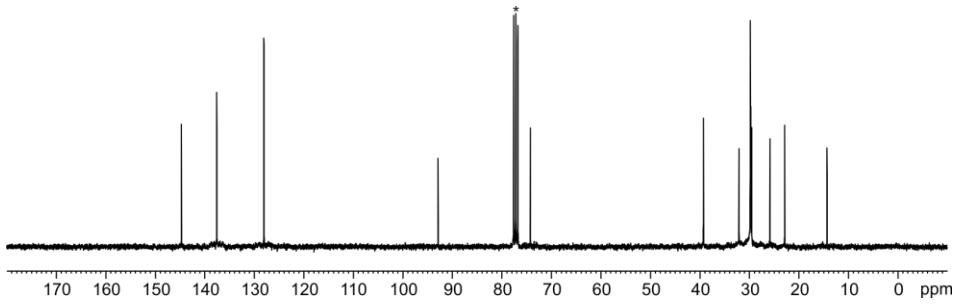

Figure 32. $^{13}C\{^{1}H\}$ NMR (75 MHz, $CDCl_3$, 298 K) spectrum of **10**. *Residual solvent peak.

7.4.3 ^{1}H NMR studies of self-assembled dimeric capsules

Homo-dimeric capsules: Tetra-urea **1** was suspended in CD_2Cl_2 (theoretical [H] = 1-2 mM). Solutions of *bis*-*N*-oxide **4** or pyridyl *N*-oxide **5** were prepared in CD_2Cl_2 at higher concentration ([G] = 10-30 mM). Guest **4** (0.5 equiv.) or **5** (1 equiv.) were added to the suspension of **1**. The mixture was sonicated for 10 min and filtered. A ^{1}H NMR spectrum of the solution was acquired.

Hetero-dimeric capsule: Tetra-urea **1** and tetra-urea **7** were suspended in CD_2Cl_2 (theoretical concentration of each compound = 1-2 mM). A solution of pyridyl *N*-oxide **5** was prepared in CD_2Cl_2 at higher concentration ([G] = 10-30 mM). Guest **5** (1 equiv.) was added to the equimolar suspension of **1** and **7**. The mixture was sonicated for 10 min and filtered. A ^{1}H NMR spectrum of the solution was acquired.

Table 2. Chemical shifts (δ, ppm) of the protons of free and bound **4** (**4**⊂**1**$_2$) and complexation induced shifts ($\Delta\delta$, ppm).

Signal	δ_{free}	δ_{bound}	$\Delta\delta$
1	8.20	4.45	-3.75
2	7.53	7.23	-0.30
3	7.65	7.39	-0.26
4	7.65	7.02	-0.63

7.4.4 Energy minimized structures and calculation of cavity volumes

The energy minimized structures (MM3) shown in this chapter were obtained using SCIGRESS Version FJ 2.6.

The cavity volumes of the homo-dimeric and hetero-dimeric self-assembled capsules were calculated with the help of SwissPDB Version 4.10.

7.5 References and Notes

[1] F. Hof, S. L. Craig, C. Nuckolls, J. Rebek, *Angew. Chem., Int. Ed.* **2002**, *41*, 1488-1508.

[2] J. Rebek, *Acc. Chem. Res.* **2009**, *42*, 1660-1668.

[3] M. M. Conn, J. Rebek, *Chem. Rev. (Washington, DC, U. S.)* **1997**, *97*, 1647-1668.

[4] M. Sandro, J. J. Rebek, *Chem.--Eur. J.* **1998**, *4*, 1016-1022.

[5] J. Rebek, *Chem. Commun. (Cambridge, U. K.)* **2000**, 637-643.

[6] K. D. Shimizu, J. Rebek, *Proc. Natl. Acad. Sci. U. S. A.* **1995**, *92*, 12403-12407.

[7] O. Mogck, V. Böhmer, W. Vogt, *Tetrahedron* **1996**, *52*, 8489-8496.

[8] B. C. Hamann, K. D. Shimizu, J. Rebek Jr., *Angew. Chem., Int. Ed.* **1996**, *35*, 1326-1329.

[9] O. Mogck, E. F. Paulus, V. Bohmer, I. Thondorf, W. Vogt, *Chem. Commun. (Cambridge, U. K.)* **1996**, 2533-2534.

[10] L. Adriaenssens, P. Ballester, *Chem. Soc. Rev.* **2013**, *42*, 3261-3277.

[11] T. Heinz, D. M. Rudkevich, J. Rebek, *Nature* **1998**, *394*, 764-766.

[12] W. Jiang, K. Tiefenbacher, D. Ajami, J. Rebek, *Chem. Sci.* **2012**, *3*, 3022-3025.

[13] K.-D. Zhang, D. Ajami, J. Rebek, *J. Am. Chem. Soc.* **2013**, *135*, 18064-18066.

[14] P. Ballester, G. Gil-Ramírez, *Proc. Natl. Acad. Sci. U. S. A.* **2009**, *106*, 10455-10459.

[15] M. Chas, G. Gil-Ramírez, P. Ballester, *Org. Lett.* **2011**, *13*, 3402-3405.

[16] L. R. MacGillivray, J. L. Atwood, *Nature* **1997**, *389*, 469-472.

[17] G. Gil-Ramírez, J. Benet-Buchholz, E. C. Escudero-Adán, P. Ballester, *J. Am. Chem. Soc.* **2007**, *129*, 3820-3821.

[18] J. L. Atwood, L. J. Barbour, A. Jerga, *Proc. Natl. Acad. Sci. U. S. A.* **2002**, *99*, 4837-4841.

[19] A. Shivanyuk, J. Rebek, *J. Am. Chem. Soc.* **2003**, *125*, 3432-3433.

[20] T. Evan-Salem, I. Baruch, L. Avram, Y. Cohen, L. C. Palmer, J. Rebek, *Proc. Natl. Acad. Sci. U. S. A.* **2006**, *103*, 12296-12300.

[21] J. Kang, J. Rebek, *Nature* **1997**, *385*, 50-52.

[22] Q. Zhang, K. Tiefenbacher, *J. Am. Chem. Soc.* **2013**, *135*, 16213-16219.

[23] D. S. Kim, J. L. Sessler, *Chem. Soc. Rev.* **2015**, *44*, 532-546.

[24] Q. Zhang, K. Tiefenbacher, *Nature Chem.* **2015**, *7*, 197-202.

[25] A. Galan, P. Ballester, *Chem. Soc. Rev.* **2016**, *45*, 1720-1737.

[26] L. Escobar, G. Aragay, P. Ballester, *Chem.--Eur. J.* **2016**, *22*, 13682-13689.

[27] L. Escobar, P. Ballester, *Org. Chem. Front.* **2019**, *6*, 1738-1748.

[28] G. Gil-Ramirez, E. C. Escudero-Adan, J. Benet-Buchholz, P. Ballester, *Angew. Chem., Int. Ed.* **2008**, *47*, 4114-4118.

[29] J. E. Lovett, M. Hoffmann, A. Cnossen, A. T. J. Shutter, H. J. Hogben, J. E. Warren, S. I. Pascu, C. W. M. Kay, C. R. Timmel, H. L. Anderson, *J. Am. Chem. Soc.* **2009**, *131*, 13852-13859.

[30] H. L. Ozores, M. Amorín, J. R. Granja, *J. Am. Chem. Soc.* **2017**, *139*, 776-784.

[31] L. Avram, Y. Cohen, *Chem. Soc. Rev.* **2015**, *44*, 586-602.

[32] A. Díaz-Moscoso, F. A. Arroyave, P. Ballester, *Chem. Commun. (Cambridge, U. K.)* **2016**, *52*, 3046-3049.

[33] Y. Rudzevich, M. O. Vysotsky, V. Böhmer, M. S. Brody, J. J. Rebek, F. Broda, I. Thondorf, *Org. Biomol. Chem.* **2004**, *2*, 3080-3084.

[34] A. Díaz-Moscoso, D. Hernández-Alonso, L. Escobar, F. A. Arroyave, P. Ballester, *Org. Lett.* **2017**, *19*, 226-229.

[35] G. R. Fulmer, A. J. M. Miller, N. H. Sherden, H. E. Gottlieb, A. Nudelman, B. M. Stoltz, J. E. Bercaw, K. I. Goldberg, *Organometallics* **2010**, *29*, 2176-2179.

General Conclusions

In summary, we report the syntheses of aryl-extended (AE) and super aryl-extended (SAE) calix[4]pyrroles (C[4]Ps) bearing ionizable or charged groups at either the lower or upper rim, or both. We investigated the molecular recognition properties of the synthesized AE-C[4]P and SAE-C[4]P receptors with polar molecules in organic solvents and water. We assessed the binding constant values, K_a, and the thermodynamic parameters, ΔH, $T\Delta S$ and ΔG, which govern the equilibria of the investigated host-guest complexes. We also determined the rate constants for the formation, k_{on}, and dissociation, k_{off}, of the complexes derived from SAE-C[4]P receptors. Based on these results, we proposed viable inclusion/exchange mechanisms that allow the reversible passage of guests in the SAE-C[4]P complexes.

In particular, we found in **Chapter 2** that SAE-C[4]P receptors form thermodynamically and kinetically highly stable inclusion complexes with pyridyl *N*-oxides in chloroform solution, featuring binding constant values $K_a > 10^6$ M^{-1}. The results of the binding experiments indicated that the CH-π and π-π interactions established between the four terminal phenyl substituents that defined the upper section of the cavity of the SAE-C[4]P receptors and the *para*-phenyl residue of a pyridyl *N*-oxide guest can be estimated to be in the order of 1 kcal·mol^{-1}. Thus, the extension of the aromatic cavity in the SAE-C[4]Ps endowed these receptors with superior binding properties towards *N*-oxides versus the parent AE-C[4]Ps. We also determined the kinetic stability of the inclusion complexes of SAE-C[4]Ps with pyridyl *N*-oxides. The formation of these inclusion complexes was close to diffusion control, suggesting that super aryl-extended calix[4]pyrroles adopt a 1,3-alternate conformation in chloroform solution. We proposed that the TS structure for the dissociation of the complexes involves the SAE-C[4]P in a 1,3-alternate conformation with the polar guest interacting with the receptor just by establishing two hydrogen bonds. We also learnt that the incorporation of four ionizable or charged residues at the upper rim of the super aryl-extended calix[4]pyrroles is not enough for their water solubilization at concentrations required for NMR characterization.

We report in **Chapter 3** the synthesis of SAE-C[4]Ps bearing eight ionizable or charged groups at the periphery of their scaffolds. These SAE-C[4]P derivatives are soluble in neutral or basic water solution at millimolar concentrations. We showed that the free SAE-C[4]P receptors display different rates in their conformational equilibria owing to the different nature of the installed water-solubilizing groups. We investigated the binding properties of the water-soluble SAE-C[4]Ps with a series of pyridyl *N*-oxides having different non-polar residues at their *para*-position. The binding constant values of these complexes were larger than 10^5 M^{-1}. We analyzed the relationship between the free energies of binding and the surface area of the non-polar *para*-substituents of the guests. This relationship allowed the quantification of the hydrophobic effect operating in these SAE-C[4]P complexes. Remarkably, the SAE-C[4]P receptors displayed nanomolar affinities for the complexation of 4-phenyl pyridine *N*-oxide. The later complexes are stabilized by additional 2

kcal·mol^{-1} with respect to our estimate based on the reduction of solvent surface accessibility of the phenyl group.

We applied a water-soluble AE-C[4]P receptor for the selective recognition of the *cis*-rotamer of *N*-phenyl amides in **Chapter 5**. We studied the binding of a series of primary, secondary and tertiary formamides and acetamides with the AE-C[4]P receptor in water. We analyzed the ^{1}H NMR titrations using a simple 1:1 binding model, K_{app}, and a complete theoretical model including the *cis*/*trans* isomerization and the exclusive formation of the 1:1 complex of the *cis*-rotamer, K_a. The determined binding constant values K_a for the formation of the *cis*-isomer⊂AE-C[4]P complexes were larger than 10^3 M^{-1}. We showed that a simple AE-C[4]P binds selectively the *cis*-rotamers of formamides and acetamides in water solution with high-binding affinity. These findings demonstrated that the AE-C[4]P receptor functions as a minimal chaperone analogue increasing the concentration of amide *cis*-rotamers in solution through selective binding.

We sealed the cavity of the super aryl-extended calix[4]pyrrole receptors by metal coordination in **Chapter 4**. We described the coordination studies of Pd(II)/Pt(II) salts with a SAE-C[4]P ligand bearing four pyridyl substituents at the upper rim. The tetra-pyridyl SAE-C[4]P ligand self-assembles into a mono-metallic Pd(II)/Pt(II)-cage featuring two inner binding sites of different polarity. We studied the (co)inclusion of sizable polar guests in the cage's cavity. The kinetic characterization of the cage complexes allowed the determination of their formation and dissociation rate constants, k_{on} and k_{off}. Based on these results, we proposed that the Pd(II)-cage features two guest inclusion/exchange mechanisms: 1) a "french doors" involving the rotation of the *meso*-phenyl substituents of the cage and 2) a partial ligand-metal dissociation. On the contrary, the isostructural Pt(II)-cage operates exclusively via a "french doors" mechanism. These results highlight the importance of size-complementarity between guest dimensions and the metallo-cage portal. On the one hand, the reversible nature of the metal-ligand bonds present in the Pd(II)-cage enables two available mechanisms for guest entrance/release. These are reflected by the lack of selectivity in *N*-oxides binding. In contrast, the relative inertness of the metal-ligand interactions featured by the Pt(II)-cage provides high-binding selectivity based on the premise of size-complementarity requested by the "french doors" mechanism.

Following the idea of designing molecular containers with enclosed cavities, we report initial studies on the self-assembly of a tetra-urea super aryl-extended calix[4]pyrrole into homo- and hetero-dimeric capsules in **Chapter 7**. We found that two molecules of a mono-topic guest (4-phenyl pyridine *N*-oxide) or one molecule of a di-topic guest (*bis*-*N*-oxide) template the formation of the homo-dimeric capsular assembly in dichloromethane solution. Interestingly, the combination of a tetra-urea calix[4]arene with the tetra-urea SAE-C[4]P and the mono-topic guest produced the exclusive formation of the corresponding hetero-dimeric encapsulation complex.

We also coupled the switching process of photo-responsive units to the binding performance of deep-cavity calix[4]pyrroles in **Chapter 6**. We described the synthesis and characterization of a tetra-azobenzene calix[4]pyrrole. From the photo-isomerization studies, we observed that the *tttt*-calix[4]pyrrole reached the *PSS* within 15-20 min of photo-irradiation at 365 nm and we determined that, in the *PSS*, *ca.* 85% of the azobenzene groups adopted the *cis*-configuration. The switching process was fully reversible by thermal equilibration of the mixture in the dark. We performed ^{1}H NMR and ITC titration experiments with the *tttt*- and *cccc*-receptor (mixture of *cis*-enriched isomers) and two polar guests, 4-phenyl pyridine *N*-oxide and bi-phenyl carboxylate, in dichloromethane and acetonitrile solutions. The affinity constant values for the complexes of the all-*trans*-receptor, with any of the two guests, were one order of magnitude larger than those of the corresponding ones with the *cccc*-counterpart.

In this Thesis, we have demonstrated the synthetic accessibility in the functionalization of aryl-extended and super aryl-extended calix[4]pyrroles at either the upper or lower rim, or both. The incorporation of appropriate groups in the calix[4]pyrrole scaffolds improved their solubility in common organic solvents or imparted solubility in water. In addition, the functionalization of super aryl-extended calix[4]pyrroles with specific binding motifs afforded self-assembled metallo-cages and non-covalent capsules. We augur that the properties of the enclosed cavities of the later assemblies, *i.e.* volume and polarity, will have potential applications in the stabilization of reactive species and the development of molecular reaction vessels.

UNIVERSITAT ROVIRA I VIRGILI
MOLECULAR CONTAINERS BASED ON ARYL-EXTENDED CALIX[4]PYRROLES
Luis Escobar González

List of Abbreviations

AE	–	Aryl-Extended
ATR	–	Attenuated Total Reflectance
B3LYP	–	Beckee, 3-parameter, Lee-Yang-Parr
°C	–	Celsius
C[4]P	–	Calix[4]pyrrole
CIS	–	Complexation Induced Shift
COSMO	–	COnductor-like Screening MOdel
COSY	–	COrrelated SpectroscopY
CPK	–	Corey-Pauling-Koltun model
DFT	–	Density Functional Theory
DMF	–	Di-Methyl Formamide
DMSO	–	Di-Methyl Sulfoxide
DOSY	–	Diffusion Ordered SpectroscopY
Equiv.	–	Equivalent
ESI	–	ElectroSpray Ionization
EXSY	–	EXchange SpectroscopY
FTIR	–	Fourier-Transform InfraRed spectroscopy
GOESY	–	Gradient-enhanced nuclear Overhauser Effect SpectroscopY
HMBC	–	Heteronuclear Multiple Bond Correlation
HMQC	–	Heteronuclear Multiple-Quantum Correlation
HPLC	–	High-Performance Liquid Chromatography
HSQC	–	Heteronuclear Single-Quantum Correlation

HRMS	–	High-Resolution Mass Spectrometry
IR	–	InfraRed
ITC	–	Isothermal Titration Calorimetry
K	–	Kelvin
kcal	–	Kilocalorie
MALDI	–	Matrix-Assisted Laser Desorption Ionization
MHz	–	MegaHertz
MM	–	Molecular Mechanics force field
MS	–	Mass Spectrometry
NMe_4	–	Tetramethylammonium
NMR	–	Nuclear Magnetic Resonance
NOE	–	Nuclear Overhauser Effect
NOESY	–	Nuclear Overhauser Enhancement SpectroscopY
NSIR	–	Non-Selective Inversion Recovery
ORTEP	–	Oak Ridge Thermal Ellipsoid Plot
PC	–	Packing Coefficient
PM	–	Parameterized Model
PSS	–	PhotoStationary State
ROE	–	Rotating-frame Overhauser Effect
ROESY	–	Rotating-frame Overhauser Enhancement SpectroscopY
r.t.	–	Room Temperature
SAE	–	Super Aryl-Extended
SIR	–	Selective Inversion Recovery

SPS	–	Solvent Purification System
TFA	–	Trifluoroacetate
THF	–	TetraHydroFuran
TLC	–	Thin Layer Chromatography
TMS	–	TetraMethylSilane
TS	–	Transition State
UV	–	UltraViolet
Vis	–	Visible

UNIVERSITAT ROVIRA I VIRGILI
MOLECULAR CONTAINERS BASED ON ARYL-EXTENDED CALIX[4]PYRROLES
Luis Escobar González

UNIVERSITAT ROVIRA I VIRGILI
MOLECULAR CONTAINERS BASED ON ARYL-EXTENDED CALIX[4]PYRROLES
Luis Escobar González

UNIVERSITAT ROVIRA I VIRGILI
MOLECULAR CONTAINERS BASED ON ARYL-EXTENDED CALIX[4]PYRROLES
Luis Escobar González